

ACS SYMPOSIUM SERIES 452

Fluid Catalytic Cracking II

Concepts in Catalyst Design

Mario L. Ocelli, *EDITOR*
Unocal Corporation

Developed from a symposium sponsored
by the Division of Petroleum Chemistry, Inc.
at the 200th National Meeting
of the American Chemical Society,
Washington, DC, August 26–31, 1990



American Chemical Society, Washington, DC 1991



Library of Congress Cataloging-in-Publication Data

Fluid catalytic cracking II: concepts in catalyst design
Mario L. Occelli, editor.

p. cm.—(ACS symposium series, ISSN 0097-6156; 452).

Developed from a symposium sponsored by the Division of Petroleum Chemistry, Inc. at the 200th National Meeting of the American Chemical Society, Washington, D.C., August 26-31, 1990."

Includes bibliographical references and index.


ISBN 0-8412-1908-7

1. Catalytic cracking—Congresses.

I. Occelli, Mario L., 1942- .II. American Chemical Society.
Division of Petroleum Chemistry.III. Series.

TP690.4.F56 1991
665.5'33—dc20

90-23463
CIP

The paper used in this publication meets the minimum requirements of American National Standard for Information Sciences—Permanence of Paper for Printed Library Materials, ANSI Z39.48-1984. 

Copyright © 1991

American Chemical Society

All Rights Reserved. The appearance of the code at the bottom of the first page of each chapter in this volume indicates the copyright owner's consent that reprographic copies of the chapter may be made for personal or internal use or for the personal or internal use of specific clients. This consent is given on the condition, however, that the copier pay the stated per-copy fee through the Copyright Clearance Center, Inc., 27 Congress Street, Salem, MA 01970, for copying beyond that permitted by Sections 107 or 108 of the U.S. Copyright Law. This consent does not extend to copying or transmission by any means—graphic or electronic—for any other purpose, such as for general distribution, for advertising or promotional purposes, for creating a new collective work, for resale, or for information storage and retrieval systems. The copying fee for each chapter is indicated in the code at the bottom of the first page of the chapter.

The citation of trade names and/or names of manufacturers in this publication is not to be construed as an endorsement or as approval by ACS of the commercial products or services referenced herein; nor should the mere reference herein to any drawing, specification, chemical process, or other data be regarded as a license or as a conveyance of any right or permission to the holder, reader, or any other person or corporation, to manufacture, reproduce, use, or sell any patented invention or copyrighted work that may in any way be related thereto. Registered names, trademarks, etc., used in this publication, even without specific indication thereof, are not to be considered unprotected by law.

PRINTED IN THE UNITED STATES OF AMERICA

American Chemical Society
Library
1155 16th St., N.W.
Washington, D.C. 20036

ACS Symposium Series

M. Joan Comstock, *Series Editor*

1991 ACS Books Advisory Board

V. Dean Adams
Tennessee Technological
University

Paul S. Anderson
Merck Sharp & Dohme
Research Laboratories

Alexis T. Bell
University of California—Berkeley

Malcolm H. Chisholm
Indiana University

Natalie Foster
Lehigh University

Dennis W. Hess
University of California—Berkeley

Mary A. Kaiser
E. I. du Pont de Nemours and
Company

Gretchen S. Kohl
Dow-Corning Corporation

Michael R. Ladisch
Purdue University

Bonnie Lawlor
Institute for Scientific Information

John L. Massingill
Dow Chemical Company

Robert McGorin
Kraft General Foods

Julius J. Menn
Plant Sciences Institute,
U.S. Department of Agriculture

Marshall Phillips
Office of Agricultural Biotechnology,
U.S. Department of Agriculture

Daniel M. Quinn
University of Iowa

A. Truman Schwartz
Macalaster College

Stephen A. Szabo
Conoco Inc.

Robert A. Weiss
University of Connecticut

Foreword

The ACS SYMPOSIUM SERIES was founded in 1974 to provide a medium for publishing symposia quickly in book form. The format of the Series parallels that of the continuing ADVANCES IN CHEMISTRY SERIES except that, in order to save time, the papers are not typeset but are reproduced as they are submitted by the authors in camera-ready form. Papers are reviewed under the supervision of the Editors with the assistance of the Series Advisory Board and are selected to maintain the integrity of the symposia; however, verbatim reproductions of previously published papers are not accepted. Both reviews and reports of research are acceptable, because symposia may embrace both types of presentation.

Preface

IN A PARENT VOLUME TO THIS ONE (ACS Symposium Series, Vol. No. 375), it was reported that refiners worldwide are meeting crude oil quality problems as well as environmental issues and regulations by developing, in cooperation with catalyst manufacturers, new fluid catalytic cracking (FCC) formulations that will help improve air and water quality. The focus of this volume has not changed. In fact, the reauthorization of the U.S. Clean Air Act of 1970 will likely mandate the reformulation of gasoline and the implementation of even stricter sulfur emission tolerance levels in the 1990s. Furthermore, the ever increasing dependence of western nations on Middle Eastern crudes, together with recent developments in Kuwait, have once more reaffirmed the need to process residual oil and, most importantly, readily available but metal-contaminated crudes from Central and South America. Thus, the demand for new, custom-designed FCC will probably continue to increase in the years to come.

In this volume, theoretical as well as applied aspects of cracking have been discussed in chapters dealing with the origin and effects of strong acidity, modeling, catalyst testing, residue processing and additive usage for gasoline octane enhancement. Novel concepts and catalyst design, together with modern characterization techniques such as laser Raman spectroscopy, solid-state NMR (MASNMR), X-ray photoelectron spectroscopy (XPS) and secondary ion mass spectrometry (SIMS), have been used to provide guidance in the difficult problem of cracking metal-contaminated feedstocks.

I would like to thank Professor S. L. Suib, Dr. A. Corma and Dr. A. Peters for helping to chair the symposium from which this volume was developed. The views and conclusions expressed in this book are those of the authors and I thank them, too, for the effort they have made, both in presenting their work at the symposium and in preparing the camera-ready manuscripts used in this volume. I would like to express my gratitude to G. Smith for her inestimable secretarial help and to my colleagues at Unocal and elsewhere for acting as technical referees.

MARIO L. OCCELLI
Unocal Science & Technology Division
P.O. Box 76
Brea, CA 92621

October 9, 1990

Chapter 1

Origin of Strong Acidity in Dealuminated Zeolite-Y

Jack H. Lunsford

Department of Chemistry, Texas A&M University,
College Station, TX 77843

Dealumination processes which leave residual extraframework aluminum in a Y-type zeolite result in a decrease in the overall number of Brønsted acid sites but an increase in the strength of the remaining acid sites. The net effect is an increase in activity for acid-catalyzed reactions up to a maximum at ca. 32 framework Al atoms per unit cell. A model for strong Brønsted acidity is proposed which includes (i) the presence of framework Al atoms that have no other Al atoms in a 4-membered ring and (ii) complex Al cations in the β cages. The essential role of extraframework aluminum is evident from recent studies in which framework Al has been completely removed from zeolite-Y and by experiments on the related ZSM-20 zeolite.

The commercial utilization of dealuminated Y-type zeolites has generated renewed interest in the origin of strong acidity in these materials. It is now evident that a carefully prepared H-Y zeolite, with its full complement of protons but with no extraframework Al, exhibits very little activity for acid-catalyzed reactions such as the dealkylation of cumene or the cracking of hexane (1,2). If these zeolites are dealuminated to ca. 32 framework aluminum atoms per unit cell ($Al_f/u.c.$), either by steaming or by treatment with silicon tetrachloride, their activities for these reactions increase remarkably. This framework Al concentration corresponds to a Si/Al ratio of 5.0 or a unit cell dimension, a_0 , of 24.54 Å. Even if zeolites are not purposely dealuminated at the outset, they become dealuminated to an equilibrium level during their regeneration in a catalytic cracking unit (3).

Early theoretical arguments of Dempsey (4) and also of Mikovsky and Marshall (5) suggested that the acid strength was related to the Al distribution in the framework and that only Al_f atoms with no second-neighbor Al_f atoms in the 4-rings are responsible for strong Brønsted acidity. The number of aluminum atoms with 0, 1, 2 and 3 aluminum second neighbors in the 4-rings has been calculated by Beagley *et al.* (6), and the results are shown in Figure 1. The disordered unit cell, referred to in the figure caption, indicates that a random distribution of Si and Al atoms was assumed, with the only constraint being that an Al-O-Al linkage did not exist (Loewenstein's Rule). In the unique structures model it was assumed

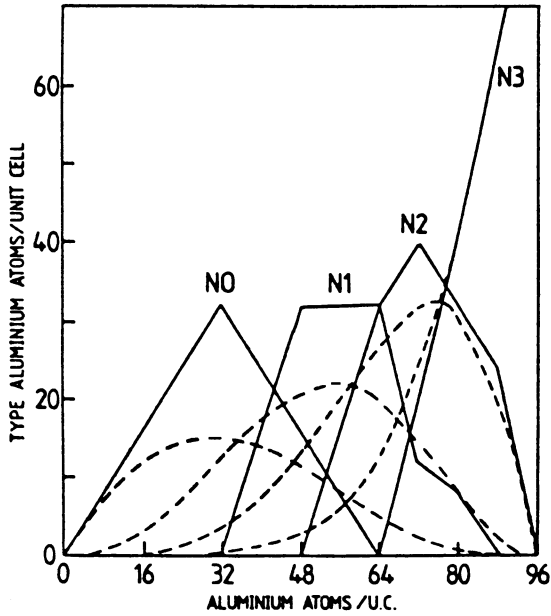
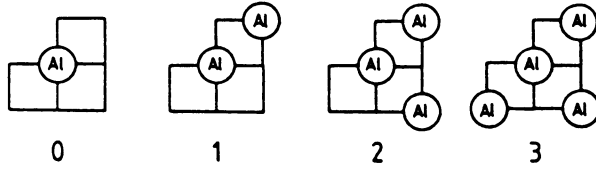


Figure 1. Distribution of types of Al atoms in faujasites: (-), unique structures of Cambridge group; (---), disordered unit cell.

that Al-Al repulsion across 4-rings or 6-rings resulted in energetically preferred structures. Thus, if the hypothesis of Dempsey and of Mikovsky and Marshall (herein referred to as the DMM model) is correct and if one assumes the distribution indicated by the unique structures model, one would expect that the number of strongly acidic protons would increase to a maximum level at 32 Al_f/u.c. and would decrease to zero at 64 Al_f/u.c.

The dealumination process, whether by steaming or by treatment with SiCl₄, not only changes the Al_f distribution but also introduces extraframework Al into the zeolite cavities. This extraframework Al, which may be present in several forms, also has the potential for increasing or decreasing both the number and acid strength of the protons. The problem of separating the effects of the Al_f and the various forms of extraframework Al has been formidable; however, considerable progress has been made in several laboratories. It is the purpose of this review to summarize these results and to suggest a model of strong acidity that appears to fit much of the available data. The data include catalytic results on faujasite-type zeolites prepared by several methods, poisoning studies, and infrared studies of hydroxyl groups.

Effect of Framework Aluminum Concentration

Early studies in our laboratory (1,2) focused on the effect of dealumination, effected either by steaming or by treatment with SiCl₄, on the activity of the zeolite for three test reactions: methanol dehydration, cumene dealkylation and hexane cracking. These reactions were chosen because they require increasing acid strength, with hexane cracking being the most demanding. Unfortunately, it is not possible (at least in our hands) to prepare from a normal zeolite-Y crystalline materials having Al_f values over the entire range between 0 and 54 Al_f/u.c. In particular, the zeolites in the range from about 32 to 52 Al_f/u.c. are inaccessible. Nevertheless, as shown by the data in Figure 2 on cumene dealkylation, the activity increased in an almost linear manner with respect to the framework Al concentration up to 32 Al_f/u.c. The DY550 series and the DY-(Si/Al) series were prepared by dealumination of a NH₄Na-Y Zeolite with SiCl₄ under different conditions, followed by ion exchange with NH₄⁺ to a residual Na⁺ ion content <0.05 wt.%. The SDY zeolite was prepared by steaming the zeolite at 600°C, followed by NH₄⁺ ion exchange. All of these dealuminated zeolites retained a high degree of crystallinity. The normal H-Y zeolite exhibited an activity that was only 6% of the SDY zeolite and comparable to that of a DY zeolite containing ca. 2 Al_f/u.c., which confirms that the acid strength of the protons in normal H-Y zeolite is not adequate for promoting the rapid dealkylation of cumene. Qualitatively similar results were obtained during the cracking of hexane, although higher temperatures were required to obtain comparable reaction rates. In the methanol dehydration reaction, the conversion over the H-Y zeolite was about 60% of that obtained over the SDY zeolite, which demonstrates that differences in acid strength are important even for less demanding reactions.

A linear relationship between the carbonium ion rate in isobutane conversion and the framework Al concentration up to 32 Al_f/u.c. has been more recently reported by Beyerlein *et al.* (7). This type of linear relationship, which is analogous to that observed during hexane cracking over H-ZSM-5 zeolites (8), led us to suggest that in the dealuminated Y-type zeolites each Al_f gave rise to an equivalent Brønsted acid site having a constant turnover frequency (1,2). These results also seem to support the DMM model. The solid line in Figure 2, which is the N(0) distribution from Figure 1, fits the data reasonably well. Other results, however, indicate that the situation is more complex and that only a fraction of the Al_f atoms are involved in creating active centers. The analogy between these dealuminated zeolite-Y samples and normal H-ZSM-5 is, in fact, not

correct because the former catalyst has extraframework aluminum, whereas the latter does not.

Poisoning Studies

Poisoning studies carried out by several groups have shown that the equivalents of poison needed to quench the catalytic activity of the dealuminated Y-type zeolites are much less than the number of Al_f atoms. Beyerlein *et al.* (9) reported that residual sodium cations extensively decreased the isobutane cracking activity of steam-dealuminated Y-type zeolites. From their results it was concluded that only one-third of the Al_f atoms were associated with strong acidity throughout the $Si/Al \geq 5$ composition domain.

More recently, Fritz and Lunsford (10) studied the effect that sodium poisoning had on hexane cracking over a series of Y-type zeolites that had been modified by dealumination with $SiCl_4$ or by steaming. The results, depicted in Figure 3, indicate that each sodium ion added back to the zeolite effectively neutralizes the catalytic activity previously thought to be due to five Brønsted acid sites. The abscissa in Figure 1 represents the number of framework Al atoms which remains unpoisoned after the addition of sodium. For example, if each Al_f atom had a strongly acidic proton associated with it, the A-series sample, which in the pure form had 15 $Al_f/u.c.$, would have required that same number Na^+ ions to neutralize the acidity. In fact, only about 3 Na^+ ions/u.c. ($Al_f - Na = 12$) destroyed the activity. Based on NH_4^+ poisoning experiments, Lombardo *et al.* (11) concluded that approximately 10% of the potential Brønsted sites, counted as Al_f ions, were involved in the catalytic decomposition of neopentane.

The effect of steaming and of extensive poisoning by alkali metal ions is not limited to Y-type zeolites, as Lago *et al.* (12) have observed similar phenomena with mildly steamed H-ZSM-5. The activity for hexane cracking increased by about a factor of four upon mild steaming of the catalyst. Selective Cs poisoning indicated that the concentration of a more active site in the steamed sample was only about 6% of the tetrahedral framework aluminum. These sites exhibited a specific activity 45-75 times greater than that of a normal site in H-ZSM-5.

Two possible mechanisms for the effectiveness of the poisons have been postulated. First, the poison may be effective through a long range interaction. Evidence for this hypothesis is given by Dyer and Singh (13), who found that K^+ ions had a much greater effect on activity than Na^+ ions. This was attributed to differences in cationic radii and electronegativities. A second possibility is that even in zeolites having isolated Al_f atoms, only a fraction of the Brønsted sites are associated with strong acidity. Strong evidence favoring the second possibility is found in the infrared studies to be discussed in the next section.

Hydroxyl Infrared Bands

Infrared bands of dealuminated zeolites in the O-H stretching region have been extensively studied (14-17); however, emphasis will be placed on the study by Fritz and Lunsford (10), which describes the effect of Na^+ on these infrared bands. Perhaps the most informative example is the $SiCl_4$ -treated zeolite (series A of Figure 3). The $SiCl_4$ -treated zeolites have less extraframework aluminum than do the steamed samples; therefore, the infrared spectra in the O-H stretching region are less complicated.

The effect of added Na^+ on the infrared spectra of the $SiCl_4$ -treated zeolite is shown in Figure 4. At least five major hydroxyl bands are apparent in the spectra. There are two silanol bands: one at 3745 cm^{-1} , which results from terminal hydroxyl groups in the lattice (18), and one at 3739 cm^{-1} , which is possibly due to hydroxyl nests. The two bands at 3635 and 3560 cm^{-1} are associated with the

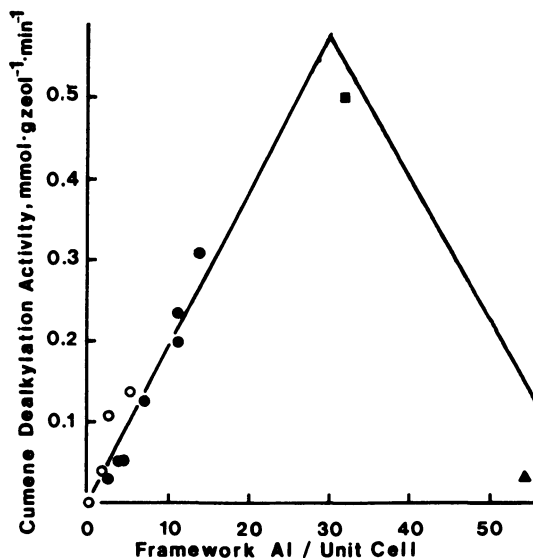


Figure 2. Dependence of catalytic activity for cumene conversion at 290°C on framework aluminum content: (○) DY550 series, (●) DY-(Si/Al) series, (■) SDY, (▲) HY.

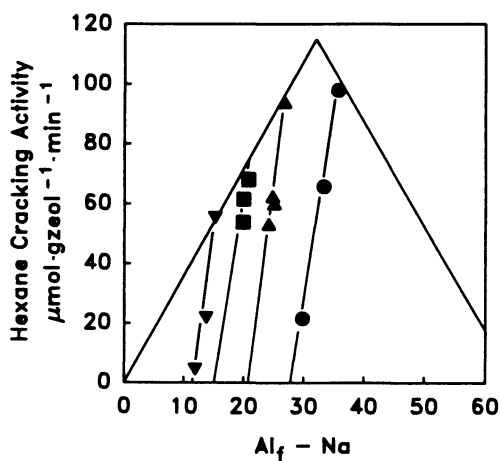


Figure 3. The dependence of hexane cracking activity on the framework Al content for four series of Na⁺-poisoned catalysts. Each Na⁺ is assumed to poison one framework Al atom. (▼) A series, (■) B series, (▲) C series, (●) D series. The solid line represents the theoretical activity based on isolated Al atoms (6). Reproduced with permission from Ref. 10.

Copyright 1989 Academic Press.

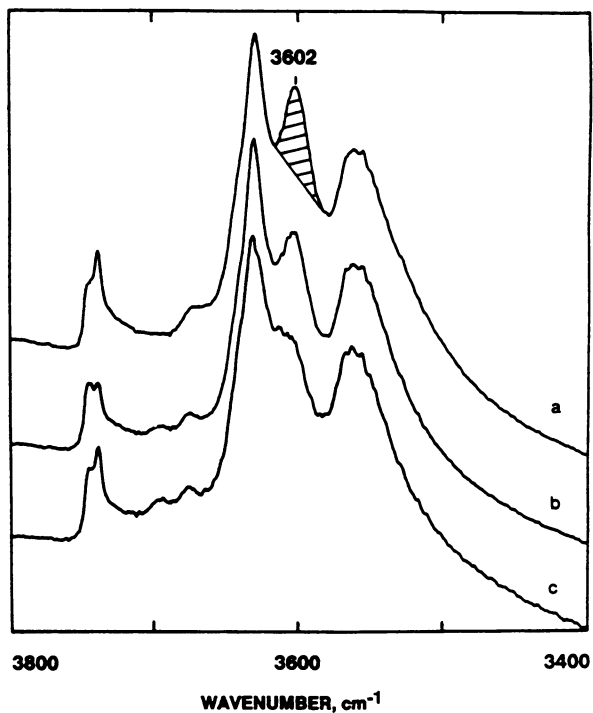


Figure 4. Infrared spectra of the hydroxyl region for a SiCl_4 -treated zeolite (series A, with $\text{Al}_T = 15.3$) with various amounts of Na^+ added as a poison: (a) 0.02 wt% Na^+ , (b) 0.23 wt% Na^+ , (c) 0.49 wt% Na^+ . The ordinate is absorbance in arbitrary units. Reproduced with permission from Ref. 10. Copyright 1989 Academic Press.

traditional Brønsted sites found in a normal H-Y zeolite. The fifth band, which is the most sensitive to Na^+ addition, is found at 3602 cm^{-1} . This band decreased upon addition of small amounts of Na^+ in a manner that paralleled the decrease in catalytic activity (Figure 3), whereas the bands at 3635 and 3560 cm^{-1} were not significantly affected by the introduction of small amounts of Na^+ . More complete ion exchange with Na^+ would have resulted in a decreased amplitude of the 3635 and 3560 cm^{-1} bands.

With respect to the mechanism by which sodium poisons the acidic zeolite, it is important to note that at least three different types of acidic protons are present, and that one form is affected much more by sodium poisoning than are the other two. Thus, only a fraction of the Brønsted sites is strongly acidic, even in zeolites having only the N(O) configuration in the 4-rings (Figure 1). The question arises as to what, in addition to the Al_f distribution, is essential for a strongly acidic site. Since dealumination by steaming or by treatment with SiCl_4 generates extraframework aluminum in various forms, it is reasonable to suspect that one of these types of extraframework aluminum may be involved in the development of strong acidity.

Evidence for the Role of Extraframework Aluminum

Evidence that something more than a proper Al_f distribution is needed to create strong acidity first came from the experiments of Beyerlein *et al.* (7). Using the acid-catalyzed conversion of isobutane as a measure of strong acidity, they found that a dealuminated zeolite prepared by treatment with ammonium hexafluorosilicate (AHF) exhibited much less carbonium ion activity than might be expected, based on the number of Al_f atoms. This treatment leaves very little extraframework Al in the zeolite. When the sample was mildly steamed, the activity became considerably greater. The authors concluded that the enhanced acidity was a result of a synergism between the framework Brønsted sites and the Lewis sites associated with extraframework aluminum.

Experiments to further demonstrate the critical role of extraframework Al, or another polyvalent cation, have recently been carried out in our laboratory (19,20). A series of faujasite-type zeolites was prepared that had Al_f concentrations between 21 and 54 per u.c. At the low end of the range, AHF was used to remove the framework Al, and an H-ZSM-20 zeolite with 42 $\text{Al}_f/\text{u.c.}$ was synthesized. ZSM-20 is an intergrowth of the cubic faujasite structure and the hexagonal variant known as Breck's structure six (BSS) (21). Thus, it is a faujasite-like material. The catalytic activities of these zeolites for hexane cracking are compared in Figure 5 (lower data set) with the activities of zeolites prepared by steaming or by treatment with SiCl_4 (upper data set). The solid lines represent N(O) distributions. The samples without extraframework Al exhibited very modest activity, even though some of them had a favorable N(O) concentration.

The amount of extraframework Al that is needed to develop a strongly acidic H-ZSM-20 zeolite is actually quite small, as indicated by the results of Figure 6. Dealumination of an H-ZSM-20 zeolite from an original concentration of 41 $\text{Al}_f/\text{u.c.}$ to 31 $\text{Al}_f/\text{u.c.}$ resulted in the maximum increase in activity for hexane cracking. This increase is almost the mirror image of the decreases that were noted previously for Na^+ poisoning. The 10 Al atoms that have been removed from the framework correspond to about 1.3 Al per small cavity. As more Al_f atoms are removed, the activity decreased in a manner consistent with the N(O) distribution that is indicated by the solid line in Figure 6.

Fritz and Lunsford (10), as well as Lombardo *et al.* (11), have suggested that the effective extraframework Al is present in the β cages as cations that are bridge-bonded through oxygen atoms. In order to test this hypothesis, one would like to ion-exchange Al^{3+}

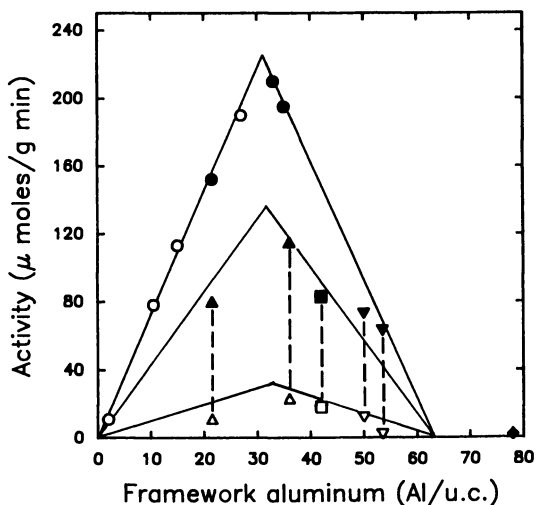


Figure 5. Hexane cracking activity as a function of framework aluminum content: O, Y-type zeolite dealuminated with SiCl_4 ; ●, Y-type zeolite prepared by steaming; Δ, Y-type zeolite dealuminated with ammonium hexafluorosilicate; ▲, after La^{3+} exchange to level of maximum activity; □, ZSM-20; ■, after La^{3+} exchange to level of maximum activity; ▽, as synthesized zeolite Y; ▼, after exchange to level of maximum activity; ◆, HLa-X. Reproduced with permission from Ref. 20.

Copyright 1990 Academic Press.

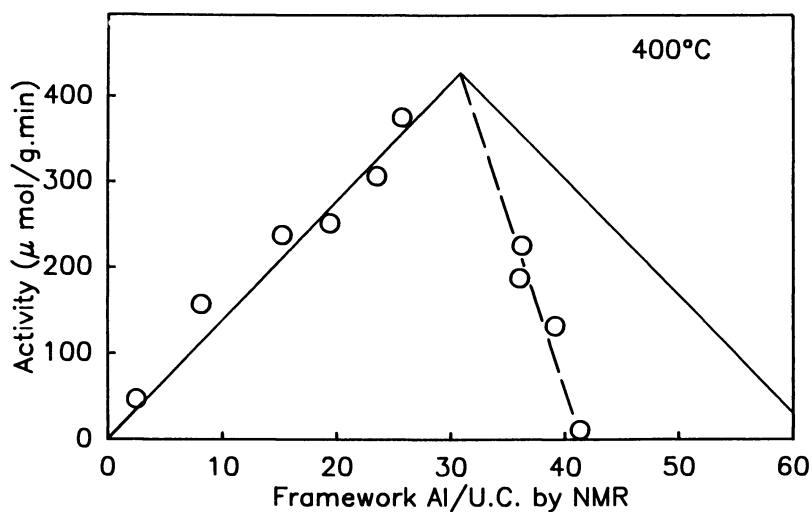


Figure 6. Dependence of hexane cracking activity on framework aluminum content for steam-dealuminated H-ZSM-20.

into a series of faujasite-type zeolites having a range of Al_f values, but this is probably not possible because Al^{3+} hydrolyzes extensively. As an alternative, we have ion exchanged La^{3+} ions into the series of zeolites described previously for the data of Figure 5. Lanthanum-exchanged zeolites are particularly attractive because of the structural information that is available on the location of the cations. When La-Y zeolites are heated to approximately $300^\circ C$, the hydration sphere is lost, and the lanthanum ions migrate into the β cages where they are preferentially attached to sites I' and take on an effective charge of +2.5 (22). Species such as $[La \leftarrow \underset{O}{\overset{O}{\text{O}}}\text{La}]^{2+}$, $[La \leftarrow \underset{OH}{\overset{OH}{\text{O}}}\text{La}]^{4+}$, and $La(OH)^{2+}$ have been proposed. There is neutron diffraction evidence to support both the location of the La ion and the presence of extraframework oxygen and hydrogen in the β cages (23).

When the series of NH_4 -Y or NH_4 -ZSM-20 zeolites having 21 to 54 Al_f atoms per u.c., and almost no extraframework Al, was exchanged with La^{3+} ions to various extents, the activity for hexane cracking first increased and then decreased with the extent of ion exchange. The maxima in activity for each zeolite are plotted as the middle set of data in Figure 5. Again, the results are reasonably well approximated by the N(O) distribution, with data now being available for the range of 35 to 54 Al_f /u.c. The HLa-X samples were almost completely inactive, which is consistent with the results expected from the N(O) distribution. The samples containing La^{3+} were less active than the samples dealuminated with $SiCl_4$ or by steaming, but this is expected because the polarizing or inductive effect of the smaller Al^{3+} ion is much greater than that of the La^{3+} ion. These results support a model of strong acidity that involves the withdrawal of electrons from structural O-H bonds by polyvalent cations that are present in the β cages.

Model for Strong Acidity

The evidence to date suggests that the development of strong Brønsted acidity in Y-type zeolites requires both isolated Al_f atoms and the presence of extraframework aluminum. Extraframework aluminum may, of course, exist in several forms, including a boehmite-like material (24) and several ionic species, such as those described previously. It seems unlikely that pseudo-boehmite or even alumina in the large cavities would be capable of generating strongly acidic sites in the zeolite framework, whereas through inductive effects the ionic forms of Al in the β cages should have a profound effect on the electron distribution in the framework. The extent of these interactions could profitably be explored by theoretical calculations. While the cationic forms of Al may promote the acid strength, they simultaneously decrease the number of protons needed to maintain charge neutrality.

As a numerical example, consider a partially dealuminated H-Y zeolite that contains 32 Al_f /u.c., all of which are isolated, and 8 extraframework Al cations/u.c. This example is similar to the case of the partially dealuminated H-ZSM-20 zeolite in Figure 6 if one assumes that most of the extraframework Al is present in the cationic form. If the extraframework Al is complexed such that each Al has an equivalent charge of +2, 16 protons would be required to balance the framework charge. Here it is assumed that the cationic extraframework Al is present as $[Al \leftarrow \underset{OH}{\overset{OH}{\text{O}}}\text{Al}]^{4+}$. An examination of two representative β -cages in this zeolite reveals that one cage contains the $[Al \leftarrow \underset{OH}{\overset{OH}{\text{O}}}\text{Al}]^{4+}$ complex cation, whereas the other is empty. If the Al_f atoms are distributed such that the β -cage with the complex cation has 6 Al_f atoms and the other β -cage has 2, the cage with the complex cation would have 2 highly acidic protons, and the remaining cage would have 2 weakly acidic protons. Thus, for the 8 Al_f atoms there would be only 2 highly acidic protons, which is consistent with the

Na⁺-poisoning experiments. The presence of a larger number of weakly acidic protons is also consistent with the infrared results.

As the number of Al_f/u.c. is increased, the probability of having isolated Al_f atoms decreases; thus, the activity would decrease. It is at the lower Al_f concentrations, however, that a simple statistical treatment fails to predict the observed linear relationship between catalytic activity and Al_f concentration. For example, at 8 Al_f/u.c. it is difficult to imagine how there would be a significant concentration of strongly acidic centers. There must be β-cages that contain at least 3 Al_f atoms and one Al(OH)²⁺ cation in order for there to be a strongly acidic proton. But this proton may be even more acidic than in the case described previously. Even within the more acidic materials, there may be subsets of strongly acidic sites. The net effect may be the observed linear relationship between catalytic activity and Al_f content. Clearly, more theoretical and experimental work is needed to test the validity of these models.

Acknowledgments

The author is indebted to several associates who carried out many of the experiments described here and who were involved in the development of the concepts. These include Steven DeCanio, Paul Fritz, S. J. Sohn, and Sun Yao. The research in our laboratory was supported in part by the U. S. Army Research Office and by the Regents of Texas A&M University through the AUF-sponsored Materials Science and Engineering Program.

Literature Cited

1. DeCanio, S. J.; Sohn, J. R.; Fritz, P. O.; Lunsford, J. H. J. Catal. 1986, **101**, 132.
2. Sohn, J. R.; DeCanio, S. J.; Fritz, P. O.; Lunsford; J. H. J. Phys. Chem. 1986, **90**, 4847.
3. Pine, L. A.; Maher, P. J.; Wachter, W. A. J. Catal. 1984, **85**, 466.
4. Dempsey, E. J. Catal. 1974, **33**, 497; 1975, **39**, 155.
5. Mikovsky, R. J.; Marshall, J. F. J. Catal. 1976, **44**, 170.
6. Beagley, B.; Dwyer, J.; Fitch, F. R.; Mann, R.; Walters, J. J. Phys. Chem. 1984, **88**, 1744.
7. Beyerlein, R. A.; McVicker, G. B.; Yacullo, L. N.; Ziemiak, J. J. Phys. Chem. 1988, **92**, 1967.
8. Haag, W. O.; Lago, R. M.; Weisz, P. B. Nature (London) 1984, **309**, 589.
9. Beyerlein, R. A.; McVicker, G. B.; Yacullo, L. N.; Ziemiak, J. J. ACS Meeting, Div. Petrol. Chem., New York, 1986; Vol. 31, p. 190.
10. Fritz, P. O.; Lunsford, J. H. J. Catal. 1989, **118**, 85.
11. Lombardo, E. A.; Sill, G. A.; Hall, W. K. J. Catal. 1989, **119**, 426.
12. Lago, R. M.; Haag, W. O.; Mikovsky, R. J.; Olson, D. H.; Helling, S. D.; Schmitt, K. D.; Kerr, G. T. In Proceedings 7th Intl. Zeo. Conf.; Murakami, Y.; Iijima, A.; Ward, J. W., Ed.; Kodansha Ltd.: Tokyo, 1986; p. 677.
13. Dyer, A.; Singh, A. P. Zeolites 1988, **8**, 242.
14. Jacobs, P. A.; Uytterhoeven, J. B. J. Chem. Soc. Faraday Trans. 1 1973, **2**, 373.
15. Anderson, M. A.; Klinowski, J. Zeolites 1986, **6**, 455.
16. Lohse, U.; Löffler, E.; Hunger, M.; Stöchner, J.; Patzelová, V. Zeolites 1987, **7**, 11.
17. Corma, A.; Fornés, V.; Perez-Pariente, J.; Sastre, E.; Martens, J. A.; Jacobs, P. A. ACS Symp. Ser. 1988, **368**, 555.
18. Jacobs, P. A. Carboniogenic Activity of Zeolites; Elsevier: Amsterdam, 1977.
19. Sun, Y.; Lunsford, J. H. unpublished results.
20. Carvajal, R.; Chu, P.-J.; Lunsford, J. H. J. Catal., in press.

21. Newsam, J. M.; Treacy, M. M. J.; Vaughan, D. E. W.; Strohmaier, K. G.; Mortier, W. J. J. Chem. Soc., Chem. Commun. 1989, 493.
22. Marynen, P.; Maes, A.; Cremers, A. Zeolites 1984, 4, 287.
23. Cheetham, A. K.; Eddy, M. M.; Thomas, J. M. J. Chem. Soc., Chem. Commun. 1984, 1337.
24. Shannon, R. D.; Gardner, K. H.; Staley, R. H.; Bergeret, G.; Gallezot, P.; Auroux, A. J. Phys. Chem. 1985, 89, 4778.

RECEIVED September 17, 1990

Chapter 2

Influence of Superacid Sites in Ultrastable Y Zeolites on Gas Oil Cracking

A. Corma, V. Fornés, F. A. Mocholí, J. B. Montón, and F. Rey

Instituto de Tecnología Química, UPV-CSIC, Universidad Politécnica de Valencia, Camino Vera S/N, 46071 Valencia, Spain

Gasoil Cracking has been carried out on two USY samples with unit cell sizes of 24.47 and 24.31 Å, which were steamed at 650° and 650° plus 725°C, respectively. The results were compared with those obtained with the same series of samples after removing most of the extraframework aluminum (EFAL) by $(\text{NH}_4)_2\text{SiF}_6$ treatment. In the zeolite steamed at lower temperature, the chemical treatment produces a strong decrease on the cracking activity. This decrease is not due to surface framework dealumination, as shown by XPS analysis and n-heptane cracking, but to the absence of EFAL. The removal of EFAL also produces an increase in gas and coke formation. Much less marked effects are observed on the high temperature steamed zeolites after being chemically treated. Gasoil cracking, activity and selectivity of the 24.47 Å USY sample after removing EFAL and being subject to an ulterior high temperature steaming gives slightly less gases and coke and more gasoline than a USY sample with the same unit cell size but containing all the EFAL.

Most of the actual refineries are using high octane catalysts based on ultrastable Y zeolite (USY). Ultrastabilization is achieved by increasing the framework Si/Al ratio of the zeolite by either steam (1,2), chemical treatments (3-5) or a combination of both (6). If a partial dealumination of the Y zeolite is carried out during the manufacturing of the catalyst, the ulterior dealumination in the FCC unit becomes slower, and more crystallinity is retained. If partially NH_4^+ exchanged NH_4NaY zeolite is steam calcined, a slow

framework dealumination occurs while silicon migration to stabilize the defects sites takes place (1). Following this procedure, the extraframework aluminum (EFAL) remains in the zeolite and its exact nature and therefore its catalytic role depends on the method and conditions used for its formation (7,8). The catalytic role of EFAL during gasoil cracking is a matter of discussion. There are studies which claim a negative role for the EFAL component (9) as responsible for a non selective cracking. Others (8,10) claim that some EFAL plays a positive role by enhancing the Brönsted acidity of the HF and LF hydroxyl groups. This role is specially effective in samples steamed at moderated temperatures (11). The EFAL present in an equilibrium catalyst is in the form of condensed types of alumina, and it is believed (11) that it is active for bottoms conversion and Light Cycle Oil (LCO) production, but on the other hand gives coke and dry gas. In order to eliminate the negative effects, a procedure based on an $(\text{NH}_4)_2\text{SiF}_6$ treatment (4) has been commercially developed which is able to extract aluminum while replacing by silicon and removing the EFAL from the zeolite. However, and by following this treatment, no more than 40% of the Al contained in a Y zeolite can be removed under economically competing procedures (12). Nevertheless, when the predealumination is carried out by this procedure, the equilibrium catalyst has still EFAL present when the zeolite becomes further dealuminated in the unit. It is possible to eliminate the EFAL formed during the ultrastabilization by steam treatment, by acid leaching (6,13). However, the procedure will also remove Al from the framework, and probably will generate a framework Si/Al gradient along the crystal.

In a previous paper (14) we have shown that by an adequate treatment of steam dealuminated Y zeolites with $(\text{NH}_4)_2\text{SiF}_6$ it is possible to remove selectively the EFAL. The physicochemical characterization of these samples shows that the presence of EFAL is the responsible for the formation of superacid sites, as well as for the neutralization of a part of framework hydroxyls.

In this work we have studied the effect of the elimination of the EFAL on the gasoil cracking behaviour of the zeolites.

Experimental

Samples USY-1, USY-2 and U1F-25, U2F-15, U2F-35 were obtained following the procedure described in the previous paper (14). Moreover, a new USY sample (U1F-25S) was obtained by steaming sample U1F-25 at 750°C and 100% steam during 5 hours. Acidity measurements were carried out on wafers of 10 mg.cm⁻² previously degassed in a I.R. cell at 400°C and 10⁻³ Pa, overnight. 6.66.10² Pa of pyridine were introduced into the cell at room temperature. After equilibrium, the samples were

outgassed at temperatures of 250, 350 and 400°C under vacuum, and the spectra in the 1800-1300 cm^{-1} region recorded at room temperature. Intensities of the bands at 1540 cm^{-1} (Brönsted sites) and 1450 cm^{-1} (Lewis sites) and apparent extinction coefficients reported by Hughes and White (15) were used to determine the amount of acid centers.

XPS measurements were performed following the experimental conditions previously published (16).

Cracking catalysts were prepared by diluting the zeolites in a high surface silica matrix. A vacuum gasoil was cracked at 482°C in a tubular fixed bed reactor. The catalyst to oil ratio (g.zeolite/g.gasoil) was varied between 0.1 and 1.1 g.g^{-1} , in order to obtain different levels of conversion, the time on stream was always kept at 60 seconds. In this way it is possible to obtain the yields of gasoline, diesel, gases and coke, at different levels of conversion, and therefore to compare the selectivities of the different catalysts at the same level of conversion. The catalysts were regenerated "in situ" after each experiment by passing 6 ml.h^{-1} flow of air at 530°C for 5 hours. Gases were analyzed by GC and separated with a Poropak-Q plus silica column. Liquids were analyzed by Simulated Distillation.

Cracking of n-heptane was carried out on catalysts USY-1 and U1F-25 in a continuous flow, fixed bed reactor (15), at 450°C and atmospheric pressure. In all experiments, 0.223 g of zeolite catalyst, and 8.625 g of n-heptane were used. With each catalyst the reaction was performed at 75, 150 and 375 seconds of time on stream. The catalyst was regenerated "in situ" after each experiment by passing flow of air at 520°C during 4 hours, and liquids were analyzed by GC by means of a Porapak-Q silica and a S-30 columns respectively.

Results and Discussion

The characteristics of all samples are given in Table 1, while acidity measurements at different degassing temperatures are summarized in Table 2.

Cracking activity

Figure 1a shows the activity of samples USY-1 and UF1-25 for gasoil cracking. It becomes apparent that the extraction of EFAL by the $(\text{NH}_4)_2\text{SiF}_6$ treatment has decreased the activity of the zeolite catalyst, eventhough the bulk framework Si/Al ratio has remained practically unchanged after the chemical treatment (Table 1). If one tries to explain this behaviour only on the bases of the framework Al, and since the gasoil cracking takes place mainly at the external surface of the zeolite crystallites, one could think that eventhough the bulk framework Si/Al has not been changed by the chemical

Table 1. Physicochemical characteristics of the samples

Sample	Crist. %	a_0 nm	FAL/u.c. ¹	Si-O	FAL/u.c. ²	Framework Si/Al	EFAL ³	XPS Surface Si/Al
USY-1	80	2.447	27	1053	26	6	18	0.72
U1F-25	85	2.445	24	1055	24	7	2	4.8
U1F-25S	80	2.428	5	1078	6	35	21	-
USY-2	85	2.431	9	1074	10	21	25	1.3
U2F-15	65	2.431	9	1073	10	21	14	5.0
U2F-35	65	2.431	9	1074	10	21	4	13.9
USY-3	65	2.430	8	1076	8	23	41	-

¹ From unit cell parameter and Fichtner-Smittler equation (20).

² From Si-O asymmetric stretching frequency and Sohn et al. equation (21).

³ Calculated from FAL (1) and total aluminum by chemical analysis.

treatment, the $(\text{NH}_4)_2\text{SiF}_6$, besides removing the EFAL has dealuminated preferentially the framework of the surface of the crystallites. In order to check that possibility the surface Si/Al ratio of samples USY-1 and U1F-25 have been measured by XPS and the results are given in Table 1. They show that, as has been previously presented (17,18), in the case of steam dealuminated samples, a sensible amount of EFAL migrates to the surface of crystallites decreasing the surface Si/Al ratio with respect to that of the bulk. The XPS analysis of the

Table 2. Brönsted and Lewis acidity, measured as mmols of pyridine adsorbed at different temperatures

SAMPLE	Brönsted			Lewis		
	250°C	350°C	400°C	250°C	350°C	400°C
USY-1	167	109	60	52	40	35
U1F-25	302	169	101	23	19	19
U1F-25S	10	5	4	4	2	2
USY-2	26	16	8	23	15	9
U2F-15	134	80	30	83	75	68
U2F-35	145	74	23	27	25	25
USY-3	14	7	4	15	6	4

zeolite after the $(\text{NH}_4)_2\text{SiF}_6$ treatment of the steamed sample, does not indicate unequivocally a preferential dealumination of the framework at the surface. In fact, the surface Si/Al ratio is close, but slightly lower, than that of the bulk, something which can be explained by the remaining 2 EFAL per unit cell which have not been extracted. The XPS results are in favor of the hypothesis that the $(\text{NH}_4)_2\text{SiF}_6$ has been used to extract EFAL and very little, if any, in extracting framework Al from the crystallites surface. However, on the bases of the XPS results we can not completely ruled out the possibility of a framework dealumination at the surface and therefore to reject completely the hypothesis made above. What becomes clear, however is that, even if a certain depletion of the FAL has occurred at the surface of the crystallites, most of the bulk framework Si/Al ratio has remained practically unchanged. Then, if we perform a cracking reaction with a reactant, n-heptane, which can easily penetrate inside of the zeolite, if the sites associated to framework Al are the only responsible for the cracking we should not expect differences in activity between samples USY-1 and U1F-25. In any case, it is clear that in this case the surface effect claimed for the gasoil would be negligible.

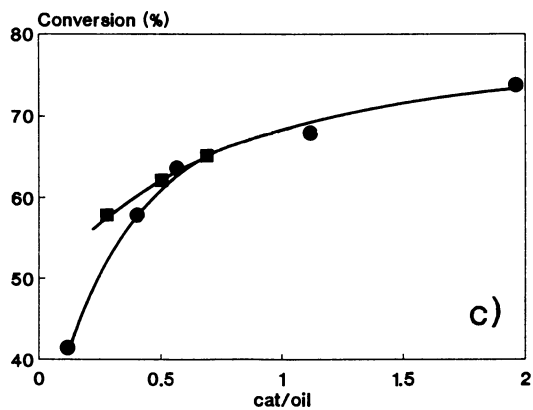
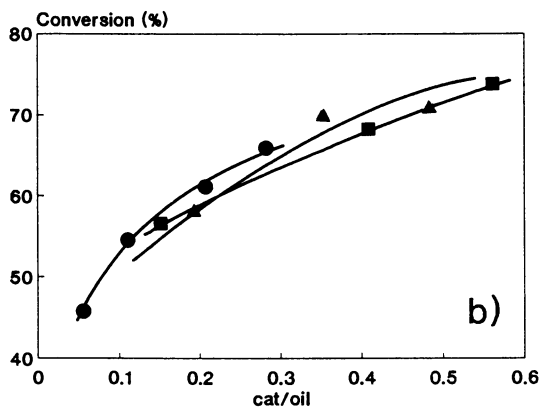
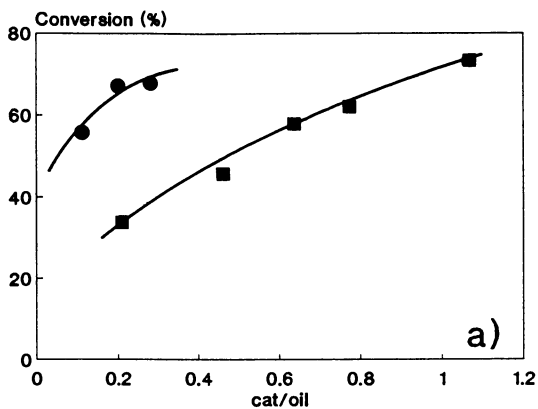


Figure 1. Gas-oil cracking activity of samples : a) USY-1 (●) and U1F-25 (■); b) USY-2 (●), U2F-15 (■) and U2F-35 (▲); c) USY-3 (●) and U1F-25S (■).

Results from Figure 2, show that sample U1F-25 is about 30% less active than sample USY-1 for n-heptane cracking. This result clearly shows that the sites associated to framework Al are not the only ones responsible for the cracking activity, and also that the differences in gasoil activity given in Figure 1a are related with the presence of the EFAL.

In the previous paper (14) we have shown that the $(\text{NH}_4)_2\text{SiF}_6$ treatment of relatively low temperature steamed samples produces an increase in the intensity of the HF and LF hydroxyls due to exchange of cationic species (AlO^+ , $\text{Al}(\text{OH})^{+2}$, etc...) by protons, as well as an increase in the Brönsted acidity measured by pyridine adsorption-desorption (Table 2). On the other hand, the $(\text{NH}_4)_2\text{SiF}_6$ treatment, removes not only the EFAL species giving non acidic OH groups at 3670 and 3610 cm^{-1} but also those species directly or indirectly responsible for the very strong acid hydroxyl groups at 3600 and 3525 cm^{-1} (14,19). After the acidity measurements (pyridine adsorption-desorption in Table 2), it becomes apparent that if only the acid sites associated to the HF and LF hydroxyls were active for cracking, the activity of sample U1F-25 should be higher than that of sample USY-1. Since the contrary is occurring, we have to claim an important role of those very strong Brönsted acid sites associated to hydroxyls appearing at 3600 and 3525 cm^{-1} , whose turnover number will be higher than that of the classical HF and LF hydroxyl bands associated to acid sites. The presence of those superacid sites has been related with the presence of EFAL species either as in the form of amorphous silica-alumina, and/or by interaction of cationic EFAL species and Brönsted (HF and LF) acid sites (14,19).

In any case, if a USY cracking catalyst is prepared by steam-calcination followed by an $(\text{NH}_4)_2\text{SiF}_6$ treatment to remove EFAL, the activity of the treated catalyst will be lower than that of the chemically untreated one.

When the chemical treatment is applied to a sample previously steamed at a higher temperature (725°C), which would simulate the zeolite in an equilibrium catalyst, only a very small, if any, decrease in activity is observed (Fig. 1b). The fact that when the steaming temperature is high ($\geq 700^\circ\text{C}$), the Brönsted sites of enhanced acidity (bands at 3600 and 3525 cm^{-1}) are not observed (8), and only the HF and LF bands are present (8), will explain the activity behaviour observed for samples USY-2 and U2F-35.

It remains one set of samples to be discussed, and this is the sample U1F-25 after steaming at 750°C (U1F-25S) and an USY sample of similar unit cell size (USY-3). This treatment would simulate the behaviour of a

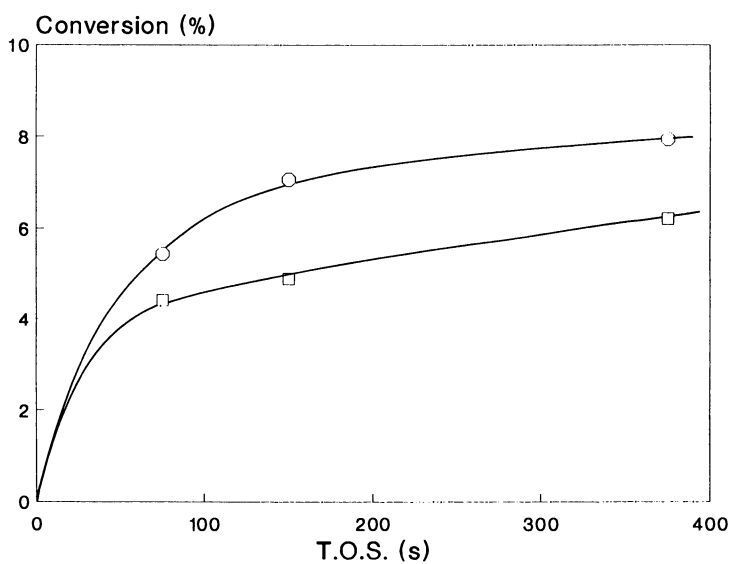


Figure 2. N-heptane cracking activity of samples USY-1 (○) and U1F-25 (□).

classical USY zeolite after chemical treatment to remove all EFAL and ulterior equilibrium in the unit. Results from Figure 1c, show that sample U1F-25S present a similar activity that USY-3.

Cracking Selectivity

In Figure 3 the yields for gases, gasoline, diesel and coke at different levels of conversion are given for samples USY-1 and U1F-25. It can be seen there that when extracting the EFAL of the lower temperature steam dealuminated sample (U1F-25), the selectivity to gases and coke increases while that to gasoline and diesel decreases. Since the $(\text{NH}_4)_2\text{SiF}_6$ treatment of sample USY-1 produces the disappearance of the strong Brönsted acid sites, and the increase of the intensity of the HF and LF hydroxyl bands, the net result of the chemical treatment is an increase in the density of classical framework acid sites. This, in turn, will make the sample more similar to one steamed at a lower temperature and therefore more similar to a sample with a unit cell size higher than 24.47 Å. Results from Figure 4 shows that when gasoil cracking is carried out on samples with high unit cell sizes ($> 24.47 \text{ Å}$) the selectivity to gases and coke increases when increasing unit cell size, while that to gasoline and diesel decreases. These results would suggest that Y zeolite catalysts with low acid strength, i.e. zeolite Y with high density of acid sites and low density of superacid sites (3600 and 3525 cm^{-1}), not only are less active for cracking, but the cracking selectivity behaviour will approximate more to that of samples steamed at low temperatures.

Then, we do not see any activity and selectivity benefit, from the point of view of the fresh catalyst by introducing, in fresh USY cracking catalyst a zeolite in which most of the EFAL has been removed.

In the case of the higher temperature steamed sample USY-2, the $(\text{NH}_4)_2\text{SiF}_6$ treatment does not produce big changes in selectivity but a small decrease in dry gases and diesel (Fig. 5). This indicates that the alumina type EFAL formed at high temperatures plays a positive role for cracking bottoms, but also produces more dry gases.

In the case of zeolite U1F-25S, the results from Figure 6 show that this sample produces less gases and coke and more gasoline than sample USY-3. These results would be in agreement with the hypothesis made above, that alumina type EFAL, while being active for bottoms conversion is less selective for gasoline and more selective for gases and coke.

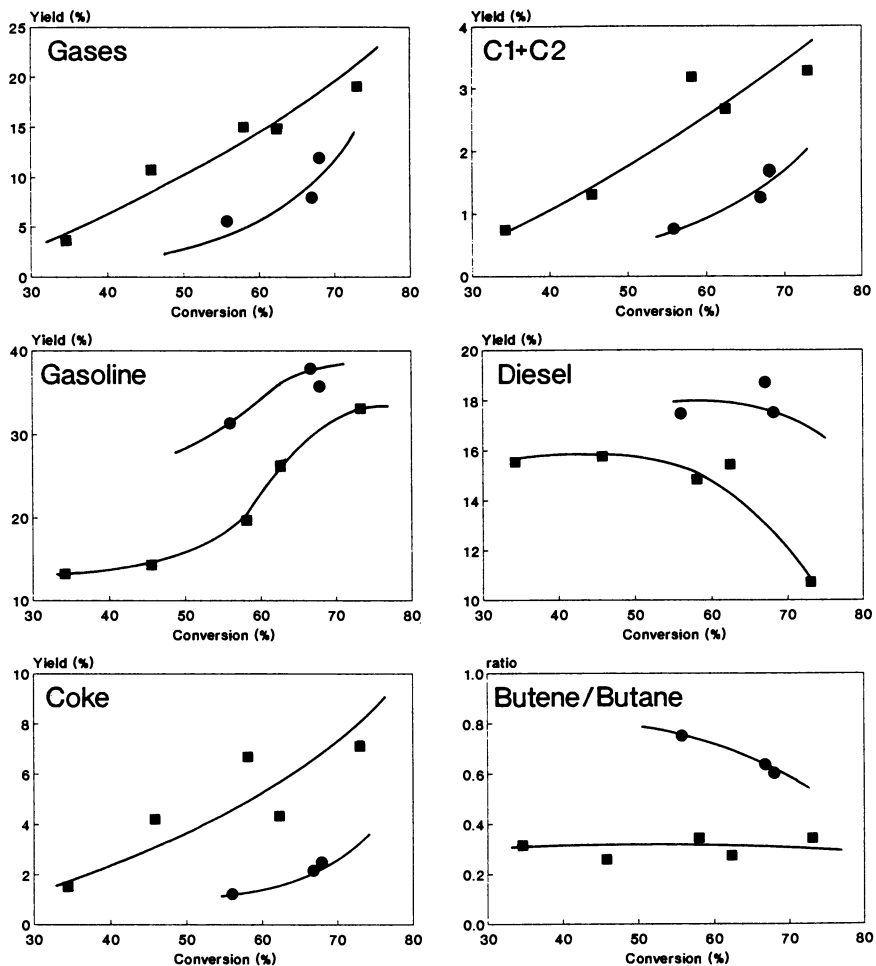


Figure 3. Selectivity to gases, C1 + C2, Gasoline, Diesel, Coke and Butene/Butane ratio of samples USY-1 (●) and U1F-25 (■) in gas-oil cracking.

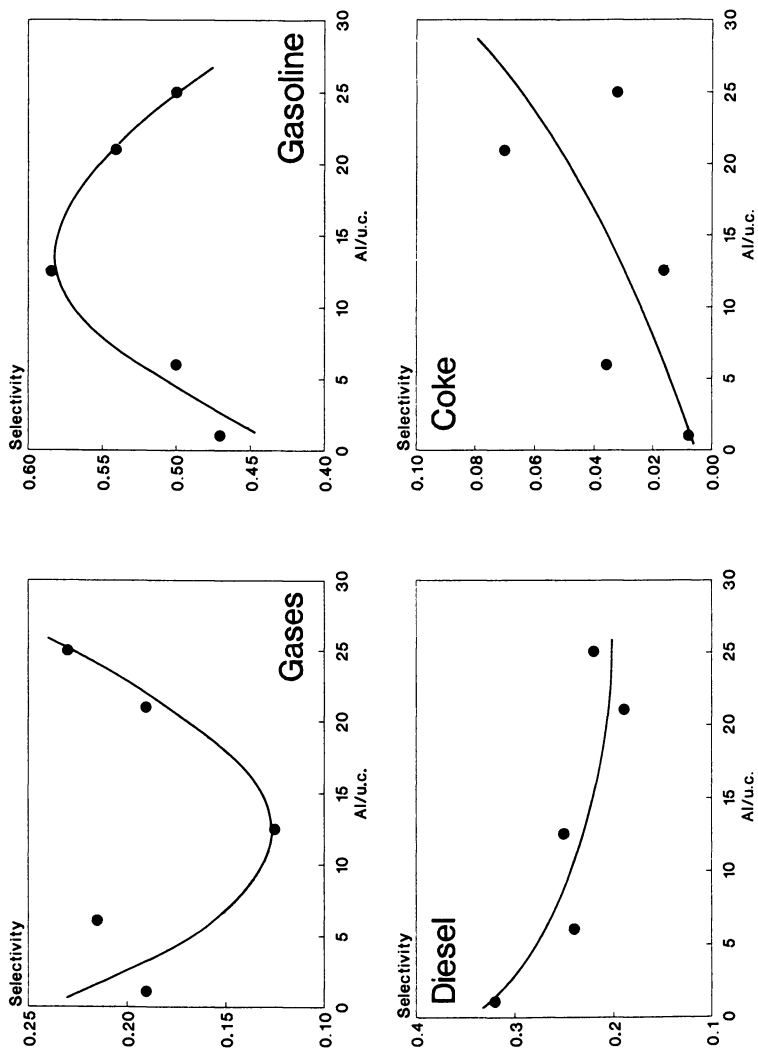


Figure 4. Selectivity to Gases, Gasoline, Diesel and Coke versus Al/u.c. of USY samples on gas-oil cracking at 60% conversion level.

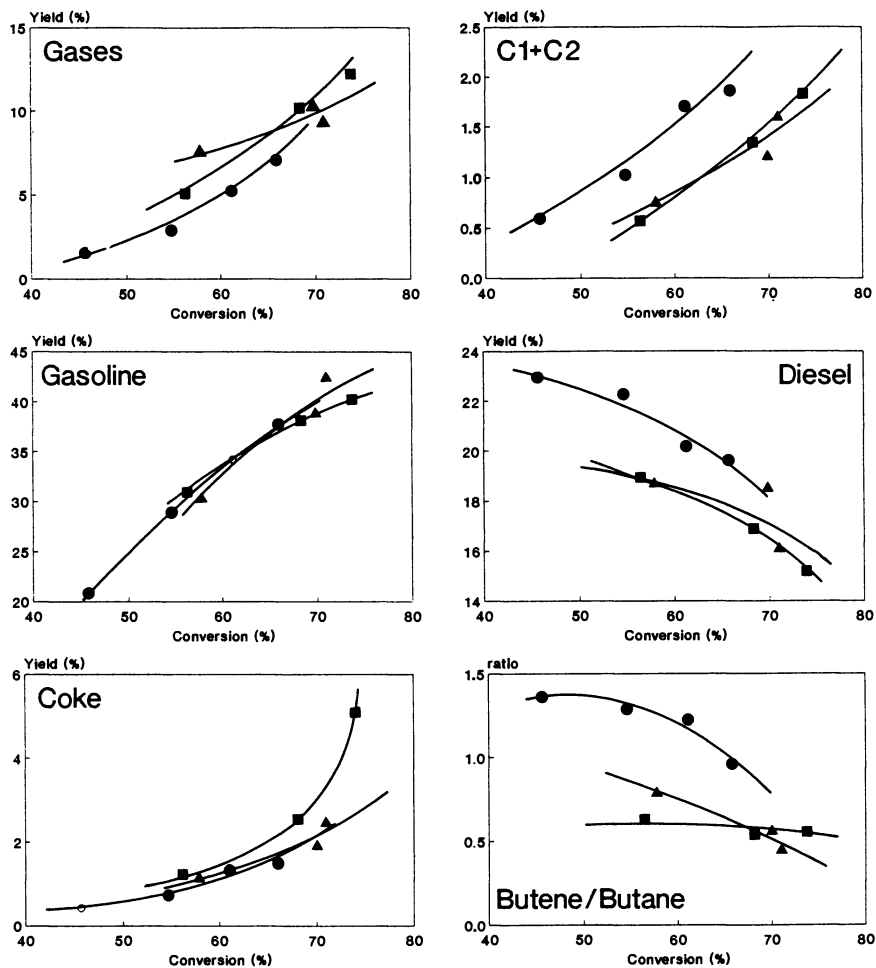


Figure 5. Selectivity to Gases, C1 + C2, Gasoline, Diesel, Coke and Butene/Butane ratio of samples USY-2 (●), U2F-15 (■) and U2F-35 (▲) in gas-oil cracking.

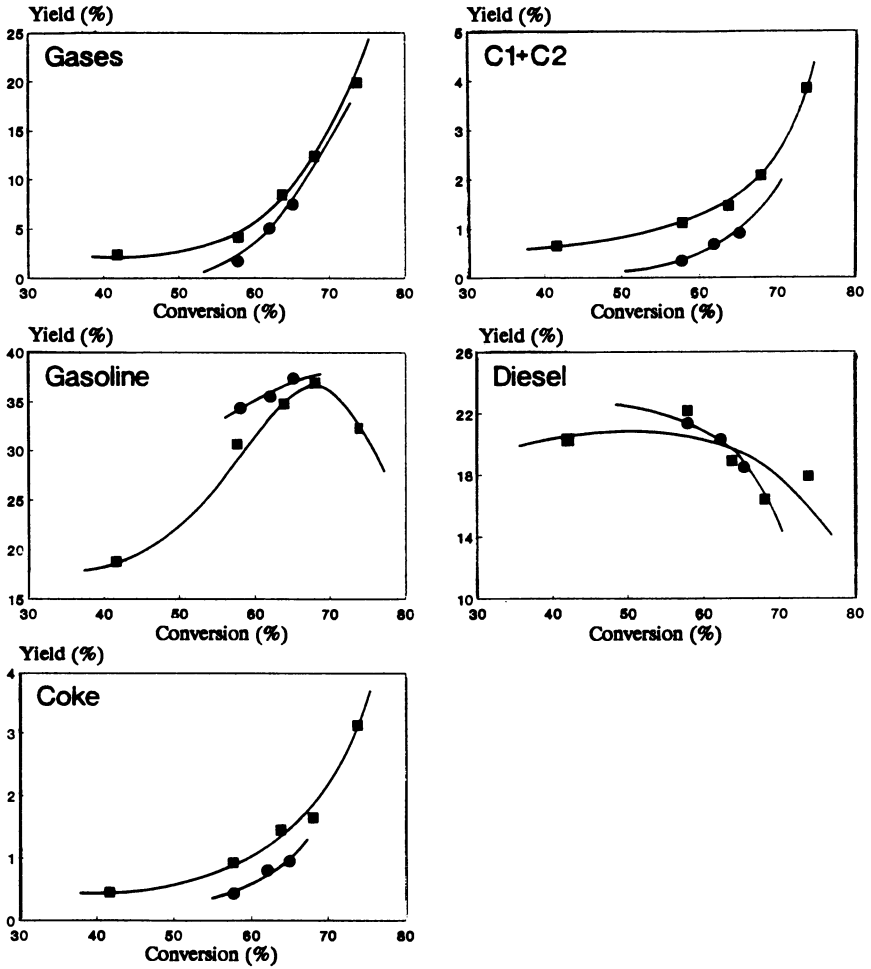


Figure 6. Selectivity to Gases, C1 + C2, Gasoline, Diesel and Coke for samples USY-3 (■) and U1F-25S (●) in gas-oil cracking.

Acknowledgments

Financial support by the CICYT (project MAT 88-0147) is gratefully acknowledged.

Literature Cited

1. McDaniel, C.V.; Maher, P.K. Zeolite Chemistry and Catalysis, Rabo, J.A., CS Monograph 171, Washington DC, 1976, p.285.
2. Ward, J.W. J. Catal. 1970 18, 348.
3. Beyer, H.K.; Belenkaja, I. Catalysis by Zeolites, Imelik B., Ed., Stud. Surf. Sci. Catal., Amsterdam, 1980, 5, p. 203.
4. Skeels, G.W.; Breck, D.W. Proc. 6th Inter. Zeol. Conf., Reno, Nevada, 1983.
5. Kerr, G.T. J. Phys. Chem. 1968, 72, 2594.
6. Scherzer, J. Catal. Rev. Sci. Eng. 1989, 31, 215.
7. Corma, A.; Fornés, V.; Martínez A.; Sanz, J. Fluid Catalytic Cracking. Role in Modern Refining, Occelli, M., Ed., ACS Symp. Ser., 375, Chap. 2, 1988, p. 17.
8. Corma, A.; Fornés, V.; Martínez, A.; Orchillés, A.V. Perspectives in Molecular Sieve Science, Flank, W.H.; Whyte Jr., T.E., Eds., ACS Symp. Ser. 368, Chap. 35, 1988, p. 542.
9. Relled, R.J.; Blackwell, C.S.; Rabo, J.A. J. Catal., 1988, 114, 71.
10. Beyerlein, R.A.; McVicker, G.B.; Yacullo, L.N.; Ziemiak, J.J. J. Phys. Chem., 1988, 92, 1967.
11. Corma, A., 8 IZC, Zeolites: Facts, Figures, Future, Jacobs, P.A.; van Santen, R.A., Eds., Stud. Surf. Sci. Catal., 1989, 49, p.49.
12. Garralón, G.; Fornés, V.; Corma, A. Zeolites, 1988, 8, 268.
13. Macedo, A.; Raatz, F.; Boulet, R.; Janin, A.; Lavalley, J.C. Innovation in Zeolite Materials Science, Grobet, P.J.; Mortier, N.J.; Vansant, E.F.; Schulz-Ekloff, G., Eds., Stud. Surf. Sci. Catal., Elsevier, Amsterdam, 1988, 37, p.375.
14. Corma, A.; Fornés, V.; Rey, F. Applied Catalysis 1990, 59, 267.
15. Hughes, T.R.; While, H.M. J. Phys. Chem. 1967, 71, 2191.
16. Corma, A.; Fornés, V.; Martínez, A.; Melo, F.; Pallota, O. Innovation in Zeolite Material Science, Grobet, P.J., Ed., Stud. Surf. Sci. Catal., 1988, 37, 495.
17. Dwyer, J.; Fitch, F.R.; Machado, F.; Quin, G.; Smyth, S.M.; Vickerman, J.C. J. Chem. Soc. Chem. Commun., 1981, 422.
18. Andérea, V.; Kubelková, L.; Nováková, J.; Vichterlová B.; Bednarová, S. Zeolites 1985, 5, 67.
19. Garralón, G.; Corma, A.; Fornés, V.; Zeolites 1988, 9, 84.

20. Fichtner-Schmittler, H.; Lohse, U.; Engelhard, G.; Patzelová, V. Crist. Res. Technol. 1984, 19, K1-K3, 1.
21. Sohn, J.R.; De Canio, S.J.; Lunsford, J.H.; O'Donnell, D.J. Zeolites, 1986, 6, 225.

RECEIVED June 8, 1990

Chapter 3

Characterization of Zeolite-Cracking Catalysts

G. T. Kokotailo, C. A. Fyfe, Y. Feng, and H. Grondey

Department of Chemistry, University of British Columbia,
Vancouver, British Columbia V6T 1Y6, Canada

The revolutionary zeolite cracking catalyst (synthetic Linde X and Y) was introduced commercially over 28 years ago, but considerable effort is still being expended on the improvement of its stability and catalytic properties. Decreasing the aluminum content of the zeolite framework and the replacing the rare-earth with the hydrogen form have greatly increased activity at the expense of stability. The thermal stability of the faujasites is fairly well understood, while the reasons for the increased catalytic activity are still not fully known.

The use of traditional and new techniques to elucidate the structure of synthetic faujasites with different silica alumina ratios, dealuminated by steaming and chemical treatment, and with and without faulting will be described. The migration and fixation of cations and the role of aluminum in the dealumination of the zeolite will be discussed.

Very clean and highly dealuminated samples have been prepared that have removed some of the variables in determining the state of the framework and extra-framework aluminum.

The replacement of amorphous silica alumina cracking catalysts with synthetic faujasites was a tremendous step forward and rapidly came to dominate the petroleum refining industry. The use of the rare-earth-exchanged form of synthetic faujasite (Linde X) in cracking catalysis resulted in a large increase in cracking activity and gasoline "make" while reducing gas and coke formation. Increases of up to 40% in yield were attained by 1962. Mobil's zeolite-based cracking catalyst, Durabead 5 (1), was in commercial use and provided the impetus for further research. The rare-earth form of

zeolite Y (REY) rapidly replaced the X form because Y offered improved chemical as well as hydrothermal stability. REY has since been replaced by ultrastable HY (USY). To compensate for some loss in hydrothermal stability, some REHY may be added.

Recently the effect of steaming on the presence of framework and extra-framework aluminium and its effect on catalytic activity has been the subject of a considerable research effort.

The Faujasite/ZSM-20 Family

Faujasite is a rare aluminosilicate mineral. Its synthetic high-alumina counterpart, Linde X, was synthesized by Milton (2), and Linde Y, a high-silica/alumina synthetic faujasite, was synthesized by Breck (3). The framework of faujasite-type zeolites has been well established by Bergerhoff et al. (4) and Broussard and Shoemaker (5).

The framework structure is shown in Fig. 1a. The basic building block is a sodalite cage. Layers formed by linking sodalite cages through double six-membered rings (D6MR) are linked also through D6MR to give a diamond-type structure, space group Fd3m, with four 12MR openings to each large cage. The layers are stacked in an ABS sequence. If every second layer is rotated so that the stacking of supercages along [111] cubic or [001] hexagonal is ABAB, a hexagonal framework results, with five 12MR openings to each supercage. The two openings to the cages in the 001 directions are planar, while those perpendicular to [001] are nonplanar and elliptical (Fig. 1b). These two frameworks are the end members of a family of structures with others varying only in the stacking sequence. The relationship of the lattice parameters of the two structures is given by

$$a_H = \frac{a}{\sqrt{2}} \quad \text{and} \quad c_H = \frac{2a}{\sqrt{3}} \quad (1)$$

The symmetry of the hexagonal form, ZSM-20, is $P6_3/mmc$.

When stacking faults are introduced in the cubic faujasite structure, the reflections with $H - K = 3N$ and $L = 3N'$ (where N and N' are integers) remain sharp, but the other reflections broaden and their maxima shift in opposite directions. Many of the line profiles in the faulted structures are asymmetric, with line broadening due to the size of the crystals and the domains. Ciric synthesized three members of this family: ZSM-20 (6), which is the hexagonal form with some stacking faults (7,8), is synthesized from aluminosilicate gels containing tetraethylammonium (TEA) cations; ZSM-3 (9), which has a nine-layer sequence and considerably more stacking faults (10), is synthesized in the $\text{Li}_2\text{O}-\text{Na}_2\text{O}-\text{Al}_2\text{O}_3-\text{SiO}_2-\text{H}_2\text{O}$ system; ZSM-2 (11) has a random stacking sequence, probably closer to faujasite and is also crystallized in a $\text{Li}_2\text{O}-\text{Na}_2\text{O}$ base. CSZ-1 is a distorted faujasite framework with rhombohedral rather than cubic symmetry (12) and is crystallized from aluminosilicate gels containing cesium.

Intergrowths and stacking faults in zeolite Y and ZSM-20 have been observed by lattice imaging using high-resolution electron-microscopy techniques. The supercages and their linkages are readily observed, providing direct information regarding local and

long-range ordering of building blocks or layers in zeolites. Recurring or random twinning may have an effect on ion exchange, the Si/Al ratio, and also ease of dealumination.

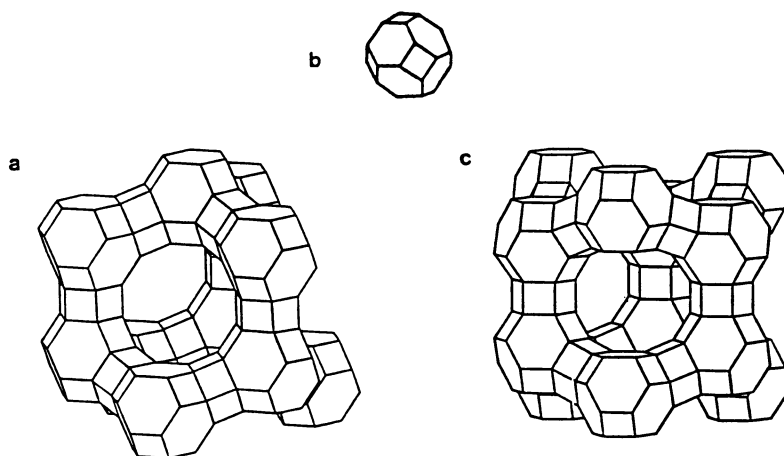
The occurrence of intergrowths of zeolite Y and ZSM-20, the cubic and hexagonal forms, is analogous to similar intergrowths in SiC and ZnS crystals. Intergrowths in zeolite Y and ZSM-20 do not block channels, as is the case in the erionite-offretite family, where rotation of cancrinite layers blocks the 12MR channels, but are more like intergrowths in the ZSM-5/ZSM-11 family, which modify the channel system.

Recent results have shown that HZSM-20 is a promising cracking catalyst with higher initial activity and thermal stability than HY (13). With CeH ZSM-20, the cracking activity increased with cerium exchange. This increase in activity is attributed to the formation of hydroxide bridge structures involving cerium cations (13). The difference is attributed to structural differences between zeolite Y and ZSM-20, with greater accessibility of the pore structure in ZSM-20 due to the linear alignment of the supercages.

Di- and Trivalent Exchange of Synthetic Faujasite

Cerium and lanthanum exchange of zeolite X resulted in some changes in the powder-X-ray-diffraction pattern. Calcination resulted in further changes that were not reversible on rehydration, indicating changes in the structure that were stabilized. Single-crystal analysis of cerium-exchanged faujasite (contacted with concentrated cerium nitrate for six months) and powder-diffraction analysis of lanthanum-exchanged Linde X (batch exchanged at 100°C for 13 days) indicated that room temperature exchange had little effect on the faujasite or Linde-X framework. The cation positions were established and the site designations used here are those introduced by Pickert et al. (14). SI is in the center of the hexagonal prism; SI' is adjacent to SI in the sodalite cage; SII' is in the sodalite cage and is adjacent to the supercage 6MR; SII is in the supercage adjacent to SII' (Fig. 1). Fully hydrated La and Ce cations were located in the center of the 12MR site designated SIII (15,16). On calcination, the framework changed very little, but the extra-framework atoms underwent a complete change in positions. The Ce(III) ions migrated to SI' and formed a tight Ce-O La-O complex (Fig. 2). The location of all Re ions in SI' is of particular interest, as all the cations are in the sodalite cage, leaving the supercage void of metal ions. The 3 or 4 La or Ce ions, 4 water oxygens, and 12 lattice oxygens form an extremely stable complex in the sodalite cage and cannot be back exchanged. This greatly contributed to the thermal and hydrothermal stability of the rare-earth synthetic faujasite catalysts.

Divalent cation (Ni, Ca, Sr) exchange and subsequent vacuum calcination of faujasite produces a loss of regularity in the zeolite framework (17,18). This loss is evident on comparison of bond lengths and angles of the divalent-cation-exchanged natural faujasite and the hydrated natural faujasite. There is a 10.5° average deviation from the mean value of the Si-O-Si angle for nickel faujasite compared to a 1.7° average deviation for hydrated faujasite. A similar loss in regularity is observed in dehydrated



Figures

Fig. 1: (a) Faujasite framework
 (b) Sodalite cage
 (c) Hexagonal faujasite ZSM-20

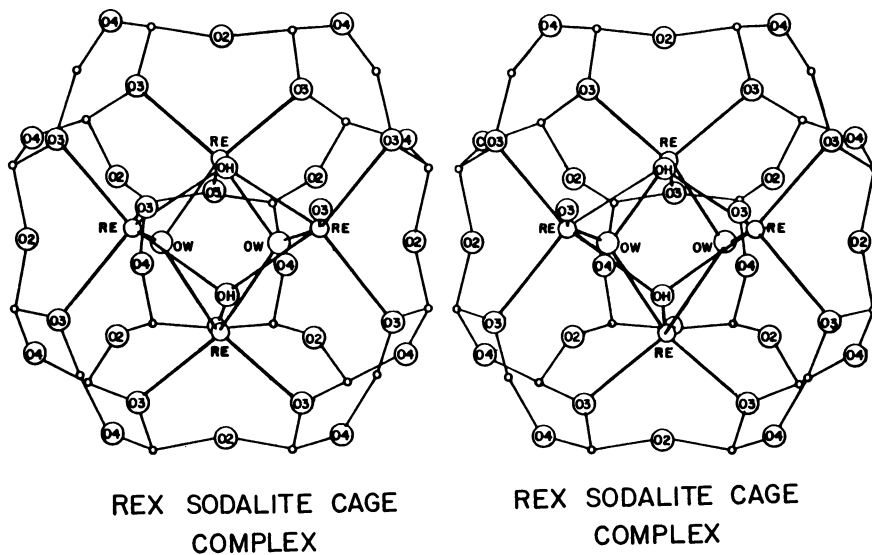


Fig. 2: Stereoscopic drawing of REX sodalite cage complex. Reproduced with permission from reference 15. (Copyright 1967 Macmillan)

CaX and SrX, but it is much more pronounced for nickel faujasite. The Ni(II) occupies two-thirds of the SI sites and attains near-perfect octahedral coordination with six framework oxygens, with all six oxygen atoms shifting .5 Å towards Ni (Fig. 3). The remaining Ni(II) ions are distributed in four unique positions, two in SI' sites and the other two in SII and SII' sites (Fig. 4).

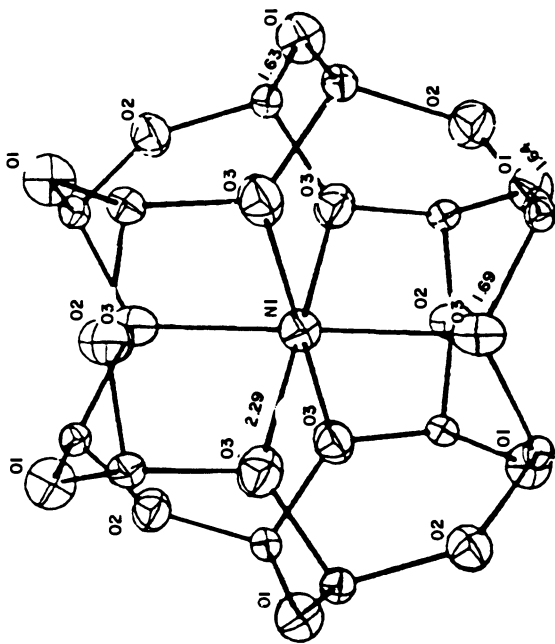
Cation Mobility

Similar effects were noticed in calcined Ca-exchanged erionite where Ca forced K out of the cancrinite cages and modified the cage structure (19). There is also evidence of reduced water absorp-tion in calcined Re-exchanged faujasite.

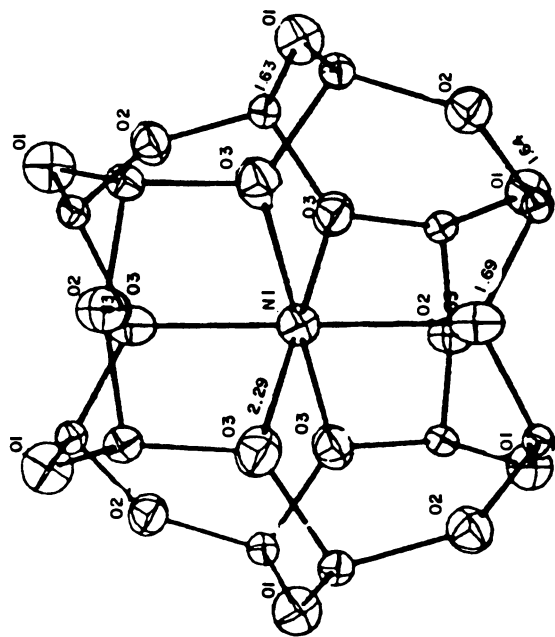
The mobility of cations in zeolites and their migration across contact boundaries between adjacent crystals may be studied using X-ray diffraction by measuring the rate of change of the lattice parameters. If the lattice parameters of two cationic forms such as Li and Na are considerably different, the inter- and intra-crystalline interchanges of cations can be readily tracked. A complete exchange due to mixing LiA and NaA was accomplished by mixing the powders for less than two minutes (20). A ^{29}Si -MAS-NMR spectrum of a mixture of LiA and NaA, prepared separately and mixed for less than 10 seconds with the spectrum recorded immediately after mixing, shows a single line spectrum for the mixed sample and two sharp resonances for LiA and NaA at $\delta = -85.1$ and -88.9 due to the two local silicon environments (21a). This indicates the rapid diffusion of Li^+ and Na^+ cations on physically mixing LiA and NaA powders. The rate of interchange is dependent on the amount of mechanical mixing, the crystallite size, and the degree of hydration. X-ray-diffraction patterns of LiX and NaX superimposed show a doublet pattern indicative of a two-phase system (20). When equal weights of LiX and NaX are mixed for less than two minutes, the X-ray diffraction indicates a single species with an intermediate lattice parameter. Precalcining and mixing the components while hot, then maintaining the mixture at 500°C for 14 hours, shows a trend towards a single species, indicating cation exchange even in a highly dehydrated system.

Dealuminated Synthetic Faujasite

With the phasing out of lead compounds as octane promoters, the REY cracking catalyst has been replaced by high-silica or ultrastable HY, which is attractive because of improved octane ratings. The mechanism of octane enhancement by USY proposed by Pine (21b) was believed to involve a reduction in the hydrogen-transfer reaction and an enhancement of the cracking reaction due to modification of acid-site characteristics. The high-silica HY is obtained by dealumination techniques. Various methods for dealumination lead to materials with a range of different structural and chemical features that affect the activity and selectivity of the cracking catalyst. The silica/alumina ratio is linearly related to the unit cell dimension (22a). Discontinuities in the linear relationship occur at 80, 64, and 52 Al atoms per unit cell (22b). These



NIY DOUBLE SIX RING



NIY DOUBLE SIX RING

Fig. 3: Stereoscopic view of hexagonal prism atom distribution in nickel faujasite. Reproduced with permission from reference 17. (Copyright 1968 American Chemical Society)

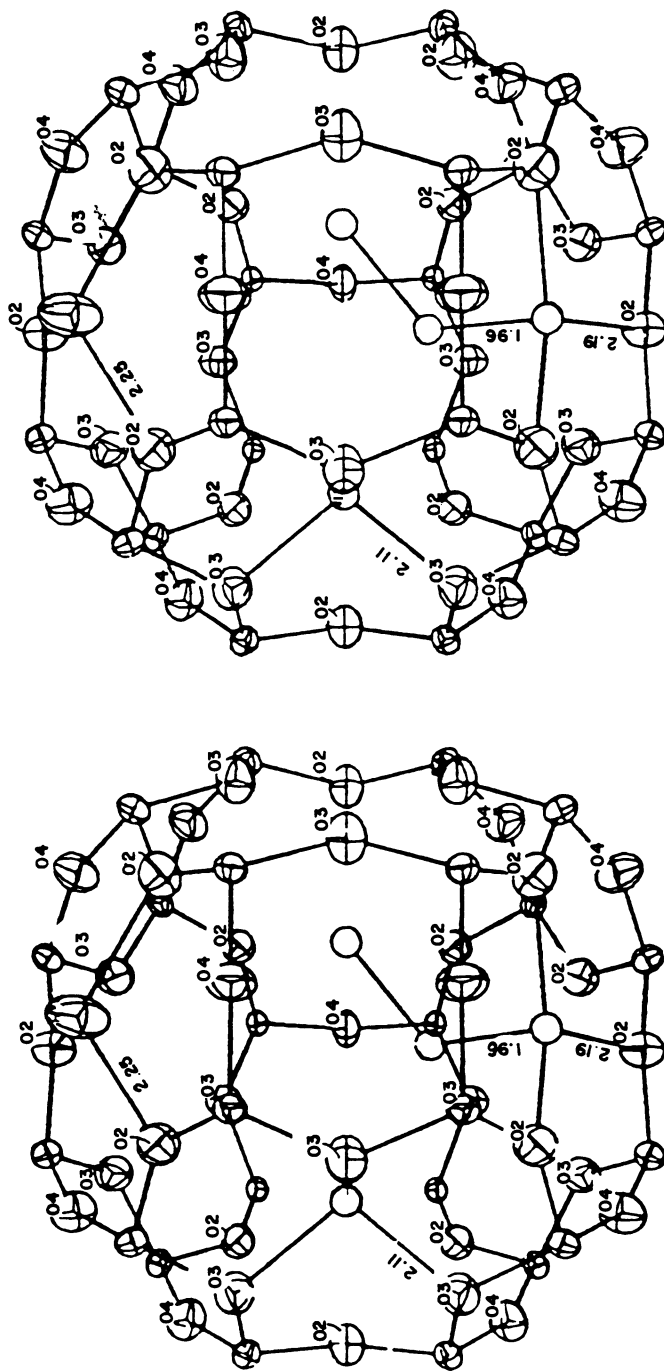


Fig. 4: Stereoscopic view of sodalite cage atom distribution of nickel faujasite. Reproduced with permission from reference 17. (Copyright 1968 American Chemical Society)

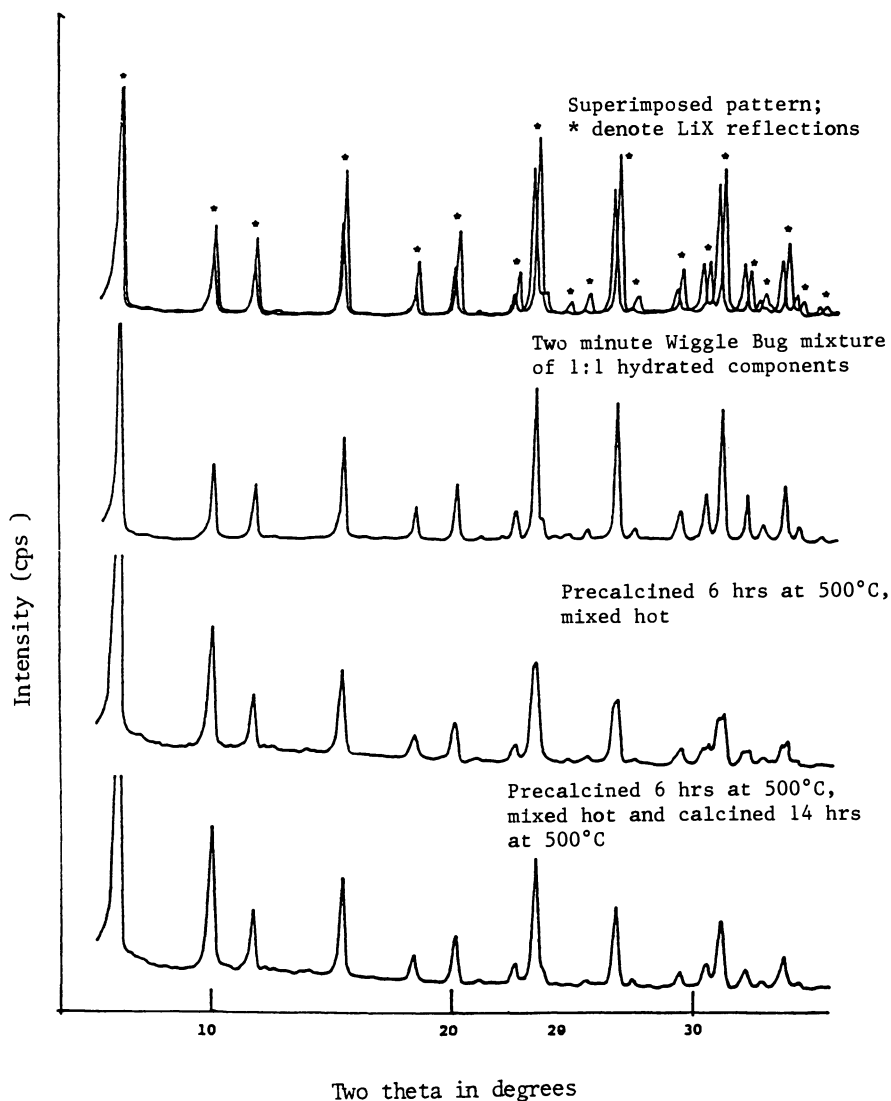


Fig. 5: X-ray diffraction patterns of the LiX-NaX system. Reproduced with permission from reference 20. (Copyright 1977 American Chemical Society)

results are supported by similar results for gallium-substituted zeolite Y (23), which shows discontinuities at 49 and 80 gallium ions per unit cell. Beyer et al. (24) showed that extrapolation to low-Al contents yields the relationship

$$a_o = 8.68 \times 10^{-4} N_{Al} + 2.425$$

In general the Si/Al ratio can be increased or the Al content decreased using using two treatments.

Chemical Extraction of Al. Barrer and Mikki (25) first reported the extraction of tetrahedrally coordinated Al from zeolites by acids; Kerr (25) used ethylenediaminetetracetic acid (EDTA), a chelating agent; Garwood et al. (26) used hydrated chromium(III) chloride; Skeels and Breck used ammonium hexafluorosilicate (AHF); and Beyer (24) used silicon tetrachloride.

The latter is the preferred chemical dealumination technique for zeolite Y, as it is a single-step method. An inert gas saturated with silicon tetrachloride is passed through a bed of dehydrated zeolite maintained at an elevated temperature (520°K). The Si/Al ratio can be varied by altering the temperature and duration of treatment. Part of the Al remains in the zeolite as $Na^+AlCl_4^-$, which is removed by water treatment, leaving a clean zeolite.

Hydrothermal Treatment. Heat treating ammonium-exchanged zeolite Y produces an ultrastable HY (26,29). ^{29}Si -MAS-NMR spectra of hydrothermally dealuminated NH_4Y indicate the presence of "NMR-invisible" Al (30). The framework Al can be determined for zeolite Y from the relationship

$$(Si/Al)_{NMR} = \frac{\sum_{n=0}^4 I_{Si(nAl)}}{\sum_{n=0}^4 \frac{n}{4} I_{Si(nAl)}}$$

as applied to the five-peak ^{29}Si -MAS-NMR spectrum of dealuminated NH_4Y .

The ^{29}Si -MAS-NMR spectra of a series of dealuminated samples Al-A8 are given in Fig. 6. The $NaNH_4Y$ sample was steamed for 2 hours at the indicated temperatures, ammonium exchanged after every steaming for 30 min at 80°C in a $(NH_4)_2SO_4$ solution, filtered, and washed. Sample A8 was steamed for 3 hours at 550°C, cooled, ammonium exchanged 3 times, then steamed for 3 hours at 800°C. All samples were dried at 100°C overnight. The spectra show a progressive decrease in the intensities of the Si(3Al), Si(2Al) and Si(1Al) peaks with respect to Si(0Al), which increases in intensity. The framework Al can also be determined from the ^{27}Al -MAS-NMR spectrum as a ratio of the octahedral signal to the total signal, although it is difficult to deconvolute the signals and the spinning side bands. The ^{27}Al -MAS-NMR spectra Al-A8 of the samples are given in Fig. 7. Thus there are three general types of Al in hydrothermally dealuminated NH_4Y : tetrahedrally coordinated framework Al; octahedrally coordinated extra-framework Al; and NMR-invisible Al. This latter Al could be present as $Al(OH)_3$, $Al(OH)_2^+$, Al_2O_3 , or some polymeric form of Al. Examination of the series of samples derived by hydrothermally dealuminating a starting NaY sample with Si/Al = 2.6 results in only a small amount of

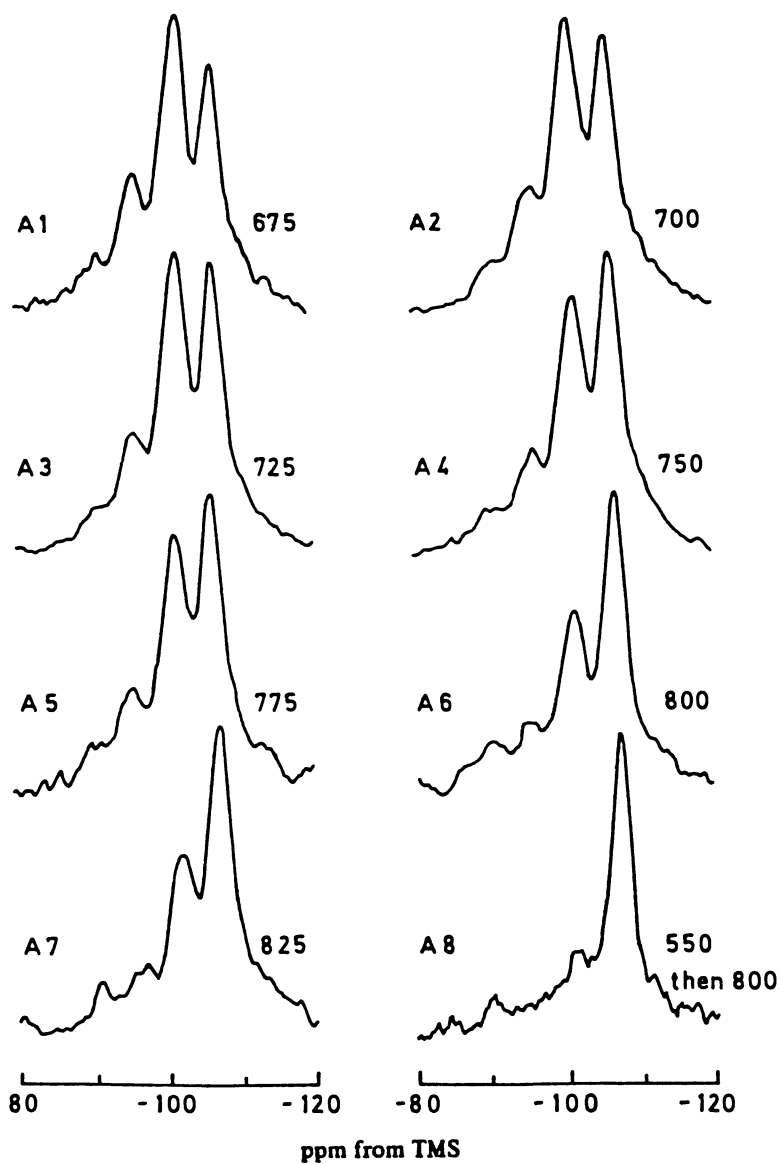


Fig. 6: ^{29}Si -MAS-NMR spectra of hydrothermally dealuminated samples. Temperatures in $^{\circ}\text{C}$. Reproduced with permission from reference 30a. (Copyright 1985 Royal Society of Chemistry)

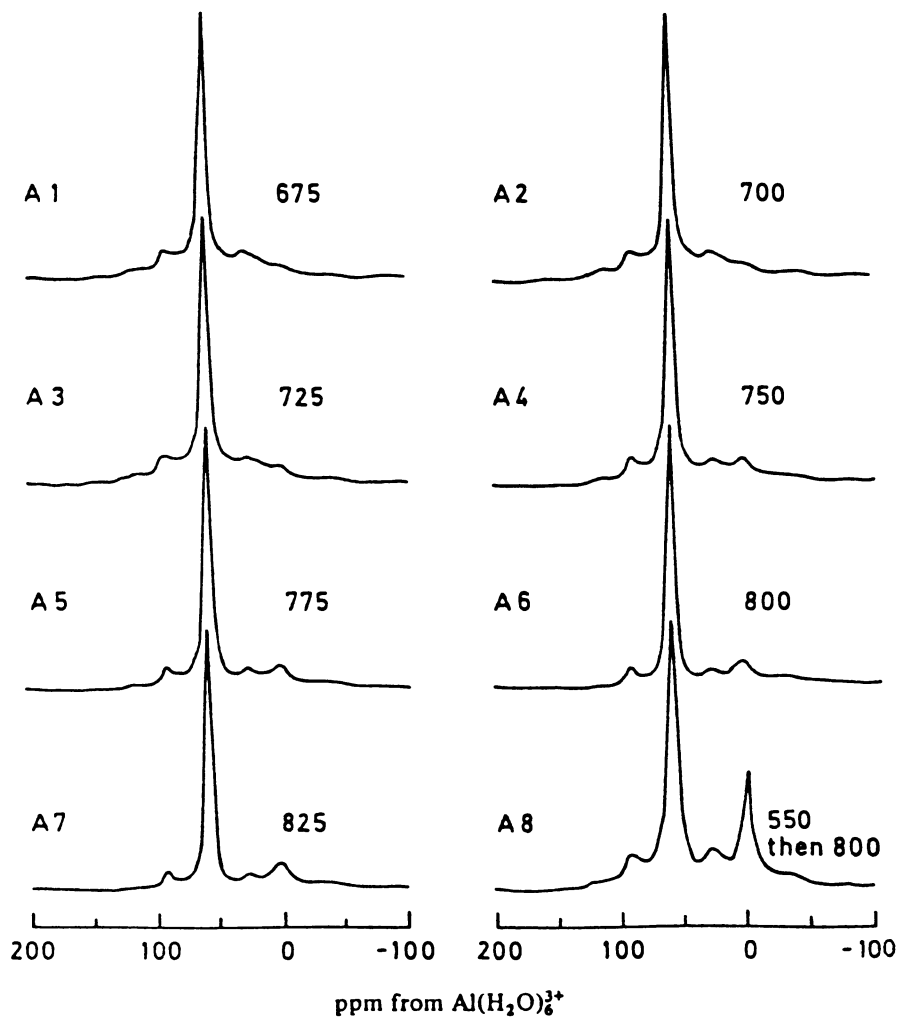


Fig. 7: ^{27}Al -MAS-NMR spectra of samples of hydrothermally dealuminated zeolite Y. Temperature in $^{\circ}\text{C}$. Reproduced with permission from reference 30a. (Copyright 1985 Royal Society of Chemistry)

Al being removed from the samples. Despite repeated ammonium exchange followed by hydrothermal treatments, the bulk of the Al, as much as 58.8% for A8, is still in the zeolite interstices. For all the samples the framework-Si/Al ratio as determined by NMR is considerably higher than the Si/Al ratio measured by elemental analysis, in agreement with the presence of extra-framework Al.

The ^{27}Al -MAS-NMR spectra of the hydrothermally treated samples consist of a sharp peak at ca. 61 ppm due to tetrahedrally coordinated Al in the zeolite framework and two signals due to octahedrally coordinated extra-framework Al, a very broad peak of ca. 100 ppm in half width, and in some samples a sharp peak at 0.35-3.5 ppm.

^{29}Si -MAS-NMR spectra of the synthetic faujasites indicate a much lower concentration of non-framework Al when dealuminated with SiCl_4 than in the case of the hydrothermally treated samples. The difference between the Si/Al ratio as obtained by ^{29}Si -MAS-NMR and elemental analysis is much smaller, indicating that much of the Al is completely removed from the lattice.

Parise and coworkers (30b) dealuminated samples of zeolite Y (LZ-Y82) using NH_3 /steam at 823°(10) K for 6 hours to a $\text{Si}/\text{Al}_F = 10.5$ and $\text{Si}/\text{Al} = 2.67$ (where Al_F is framework aluminum) with 16.7 framework and 35.6 extra-framework Al atoms per unit cell. If the sample is treated with a SiCl_4/Ar mixture at the same temperature and for the same time, the framework Al is essentially the same, 10.8 Al atoms/uc, but the extra-framework Al is considerably reduced, to 8.1. Using neutron-diffraction data and a combination of Reetveld refinement and difference-Fourier techniques, they (30b) determined the presence of tetrahedrally coordinated Al in the center of the sodalite cages in both dealuminated samples, but to a lesser extent in the SiCl_4/Ar -treated sample. No other types of aluminate species were detected, so that the octahedral species detected by Klenowski, Fyfe and Gobbi (30a) are disordered over the channel system of Y. The structural differences between the two samples are manifested in the T-O-T angle. The silicon atoms remain relatively fixed, but the oxygen atoms tend to move.

Meradotos and Barthomeuf (31) found enhanced activity in hydrothermally treated mordenites, which they accredited to bridging hydroxyl groups interacting with extra-framework Al. Lago et al. (32) found a large increase in the activity of HZSM-5 after mild steaming at 540°C, which they attributed to paired Al atoms.

Beyerlein et al. (33) studied the catalytic properties of a series of ultrastable synthetic faujasites dealuminated by steaming and by acid extraction to determine catalytic acidity as a function of framework characteristics. They found that carbonium-ion activity in isobutane conversion is proportional to framework-Al content, and comparing results obtained by using hydrothermally and AHF-dealuminated synthetic faujasite, they found that the steamed material, which contains extra-framework Al, gave a large increase in carbonium-ion activity compared with the AHF-treated material, which had a relatively clean framework. This indicates that strong acidity exhibited by mildly steamed synthetic faujasite, while directly related to framework-Al content, depends on a balance between framework and extra-framework Al, and that this extra-framework Al contributes greatly towards catalytic performance.

Cotterman et al. (34) showed that hexadecane-cracking activity of AFS and USY zeolites appeared to be a function of total Al content, independent of method of dealumination, implying that hexadecane cracking occurs over both framework- and extra-framework-acid sites. Hence, extra-framework material in mildly steamed synthetic faujasite, USY, makes a significant contribution to catalyst activity, as previously reported (33). Gasoline selectivity is influenced by both the method of dealumination and steam treatment, and depends on both framework-acid sites and the presence of extra-framework material.

Van Broekhoven et al. (35) measured the effect of dealumination of Y zeolites by steam AFS and SiCl_4 and showed that the Na_2O level during steaming has a strong effect on the level of framework dealumination. At 1.6% Na_2O , up to 18% of extra-framework Al is formed, while at 3.9% Na_2O only up to 11% is formed. Some of the extra-framework Al is removed along with Na_2O on washing. In the SiCl_4 and AFS treatments, only small amounts of extra-framework Al are present, and mainly of the NMR-visible type. XPS analysis shows that the surface concentration of extra-framework Al is high; also, steaming of the AFS-treated sample resulted in a strong framework dealumination.

Cruz et al. (36) also found that AFS preferentially dealuminates the surface of zeolite Y crystals to a depth of about 100 Å and produces an extra-framework-Al-free zeolite. They found that the activity for n-heptane cracking is the same as for a steamed dealuminated sample, while the gas oil cracking was lower, being controlled by the outer shell.

A method has been developed to characterize the NMR-invisible Al (37), which entails the complexing of non-framework Al with acetylacetone (acac) to form $\text{Al}(\text{acac})_3$ complexes. Because of their near-spherical Al symmetry, these complexes yield ^{27}Al -MAS-NMR spectra that can be used for more quantitative interpretation.

This method can be applied to zeolites dealuminated by various techniques. In steamed faujasites different extra-framework Al and Si species are observed. The dealuminated samples are soaked in a 38% acac-methanol solution at room temperature under a flow of dry air. After one hour the ethanol and excess acac are evaporated. In hydrothermally dealuminated faujasites additional ^{27}Al lines in the 50-30 ppm range appear, in addition to the tetrahedral and octahedral lines at 60 and 0 ppm. Gilson found a line at 34 ppm in zeolite Y with framework $\text{Si}/\text{Al} = 20$ by steaming at 760°C in 100% steam. Freude and coworkers (39,40) have described the use of ^1H - and ^{27}Al -MAS-NMR techniques to determine the dealumination mechanism in the hydrothermal and acid treatment of zeolite Y. They determined the framework aluminum from the equivalence of AlO_2^- anions in the framework and NH_4^+ cations using the Kjeldahl method to determine the amount of NH_3 in the zeolite.

The ^{27}Al -MAS-NMR spectra of dealuminated zeolite Y generally consist of three signals indicative of three types of aluminum, but the intensity does not account for all the aluminum in the sample. The authors ascribe the difference to NMR-invisible Al previously determined (30) from an analysis of the ^{29}Si -MAS-NMR data for dealuminated HY samples. The NMR resonance at 60 ppm for framework Al is relatively sharp. Octahedrally coordinated non-

framework Al also yields a sharp line at 0 ppm. The third species, a tetrahedrally coordinated extra-framework Al, gives a broad line at about 50 ppm and is clearly visible in zeolite hydrothermally dealuminated at 770°C to a framework Al of 7 atoms/uc. The authors(40) ascribe the two lines at 0 and 50 as due to extra-framework-Al complexes, $\text{Al}(\text{H}_2\text{O})_6^{3+}$ and $\text{Al}(\text{OOH})$. They propose that the $\text{Al}(\text{OOH})$ molecule is associated with two framework oxygens to give a tetrahedrally coordinated Al atom with a weakly interacting proton with a framework oxygen further away. They claim that the majority of extra-framework Al is a condensation of this species and has noncubic symmetry. These species are assumed to be NMR invisible and their concentration is determined by subtraction.

The total concentration of OH groups in dealuminated zeolite Y samples was determined using ^1H -NMR techniques described (40) and is in reasonable agreement with the concentration of tetrahedrally coordinated extra-framework Al. The concentration of SiOH groups does not change in hydrothermal dealumination, but increases on acid leaching due to removal of framework Al.

The number of bridging OH groups is equal to the number of framework-Al atoms.

Samosan (41) observed ^{27}Al signals at 50 and 30 ppm in zeolite Y dealuminated with 0.1 M Pa steam successively at 600°C and 850°C to give a framework Si/Al = 20. Weak peaks were also observed at 60 and 0 ppm. Gilson attributed the line at 30 ppm to penta-coordinated extra-frameowrk Al. Mobile, octahedral $\text{Al}(\text{H}_2\text{O})_6^{3+}$ complexes located in the zeolite channels give rise to 0-ppm signals (30). The sharp line at 0 ppm is caused by exchangeable cations (37). The 50-ppm signal decreases and the 30-ppm signal increases with increased steaming severity. The ^{27}Al spectra of acac-treated samples indicate that the NMR-invisible Al is complexed, resulting in an increase in the 0-ppm signal due to octahedral Al (37). The authors note that care should be exercised in the use of this procedure for quantification of extra-framework Al (37), as some may still not be observable.

Although many steaming procedures leave considerable quantities of extra-framework Al in the interstices, as described above, it should be possible to produce highly dealuminated, clean materials without defects or amorphous Si and Al complexes. Some progress has been made in this direction. Figures 8 and 9 show the corresponding Si and Al spectra of dealuminated faujasite with Si/Al ratios as indicated. The ^{29}Si spectra, obtained at 79.5 MHz on a Bruker MSL 400 spectrometer, indicate that all the material is highly crystalline with no amorphous silica present. The ^{27}Al spectra, obtained at 104.2 MHz on the same spectrometer, show only sharp peaks at 50 and 0 ppm, corresponding to tetrahedral-framework Al and octahedral Al. There is no evidence of broad resonance peaks due to amorphous alumina. The addition of acac does not increase the intensity of the octahedral peak.

Conclusions

Selectivities and activities of dealuminated zeolite Y are dependent on the method of dealumination and the "state" of the aluminum

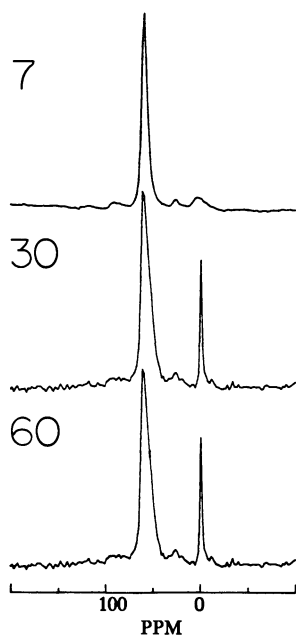


Fig. 8: ^{29}Si -MAS-NMR spectra of highly dealuminated zeolite Y samples. Si/Al ratios indicated.

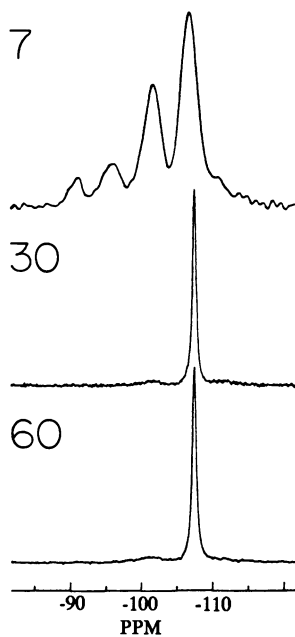


Fig. 9: ^{27}Al -MAS-NMR spectra of highly dealuminated zeolite Y samples. Si/Al ratios indicated.

species in the framework, the channels, or the surface of the zeolite component of the catalyst.

Improved NMR, XRD, neutron-diffraction, IR, and adsorption techniques are helping to sort out the physical properties of these various Al species in the dealuminated zeolite Y samples, and their relationship to catalytic activity.

Good crystalline samples are necessary, as well as the ability to prepare samples that isolate or concentrate the Al species generated by the various dealumination techniques in order that more structural information may be derived, which will give us further understanding of the catalytic activity due to these treatments and its relationship to structural features.

The formation of the Al-O complexes in the sodalite cages of zeolite Y is analogous to similar La-O complexes previously described (15,16). These phenomena are under study with neutron- and synchrotron-X-ray diffraction.

The NMR data on clean dealuminated samples of zeolite Y indicate that with good sample preparation and the advanced techniques for structural studies, it will be possible to elucidate further the relationship between structural features and catalytic properties.

Literature Cited

1. U.S. Patent 3 140 249, 1962.
2. Milton, R. M. U.S. Patent 2 882 244, 1959.
3. Breck, D. W. U.S. Patent 3 130 007, 1964.
4. Bergerhoff, G.; Baur, W. H.; Nowacki, W. Neues Jahrb. Mineral. Montash 1953, 193.
5. Broussard, L.; Shoemaker, D. P. JACS 1960, 82, 1041.
6. U.S. Patent 3 972 983, 1976.
7. Fulop, V.; Borbeley, G.; Beyer, H. K.; Ernst, S.; Weitkamp, J. J. J. Chem. Soc., Faraday Trans 1 1989, 85(8), 2127.
- 8a. Newsam, J. M.; Treacy, M. M.; Vaughan, D. E. W.; Strohmaier, K. G.; Mortier, W. J. J. Chem. Soc., Chem. Commun. 1989, 493.
- 8b. Thomas, J. M.; Millward, G. R.; Ramdas, S; Andier, M. ACS Symposium Series 218, Intrazeolite Chemistry 1983, 181.
9. U.S. Patent 3 145 736, 1968.
10. Kokotailo, G. T.; Ciric, J. Adv. in Chem. Series 1971, 101, 109.
11. U.S. Patent 3 411 874, 1968.
12. Treacy, M. M.; Newsam, J. M.; Beyerlein, R. A.; Leonowicz, M. E.; Vaughan, D. E. W. J. Chem. Soc., Chem. Commun. 1986, 1211.
13. Lemos, F.; Lopes, J. M.; Ribeiro, F. R; Derouane, E. Appl. Cat. 1989, 49, 175.
14. Pickert, P. E.; Rabo, J. A.; Dempsey, E.; Schomaker, V. Proc. 3rd Int. Congr. Catal., Amsterdam, 1965, 1, 714.
15. Olson, D. H.; Kokotailo, G. T.; Charnell, J. F. Nature 1967, 270, 5098.
16. Olson, D. H.; Kokotailo, G. T.; Charnell, J. F. J. Coll. and Interface Sci. 1968, 28, 305.
17. Olson, D. H. J. Phys. Chem. 1968, 72, 4366.

18. Olson, D. H., J. Phys. Chem. 1968, 72, 1400.
19. U.S. Patent 3 640 680, 1972.
20. Kokotailo, G. T.; Lawton, S. L.; Sawruk, S. ACS Symposium Series No. 40, Molecular Sieves II 1977, p. 439.
- 21a. Fyfe, C. A.; Kokotailo, G. T.; Graham, J. D.; Browning, C.; Gobbi, G. C.; Hyland M.; Kennedy, G. J.; DeSchutter, C. T. JACS 1986, 108, 522.
- 21b. Pine, L. A.; Maher, P. J.; Wachter, W. A. J. Catal. 1984, 85, 466.
- 22a. Breck, D. W.; Flanigin, E. M. In Molecular Sieves Society of Chem. Ind. London, 1968, 47.
- 22b. Dempsey, E.; Kuhl, G. H.; Olson, D. H. J. Phys. Chem. 1969, 73, 387.
23. Kuhl, G. H. J. Inorg. Nucl. Chem. 1971, 33, 3267.
24. Beyer, H. K.; Belenykaya, I. M.; Hange, F.; Tielen, M.; Grobet, P. J.; Jacobs P. A. J.C.S. Faraday Trans. 1985, 81, 2889.
25. Barrer, R. M.; Makki, M. B. Can. J. Chem. 1964, 42, 1481.
26. Kerr, G. T. J. Phys. Chem. 1968, 72, 2594.
27. Garwood, W. E.; Lucki, S. J.; Chen, N. Y.; Bailor, J. C. Inorg. Chem. 1978, 17, 610.
28. Skeels, G. W.; Breck, D. W. Proc. Sixth Int. Zeolite Conf., Reno, 1984, p. 87.
29. McDaniel, C. V.; Maher, P. K. In Molecular Sieves; Barrer, R.M., Ed.; Soc. of Chem. Ind.: London, 1968; p 186.
- 30a. Klinowski, J.; Fyfe, C. A.; Gobbi, G. C. J. Chem. Soc., Faraday Trans. 1 1985, 81, 3003.
- 30b. Parise, J. B.; Corbin, D. R.; Abrams, L. Acta Cryst. 1984, C40, 1493.
31. Miradatos, C.; Barthomeuf, D. J. Chem. Soc., Chem. Commun. 1981, 39.
32. Lago, R. M.; Haag, W. O.; Mikovsky, R. J.; Olson, D. H.; Hellring, S. D.; Schmidt, K. D; Kerr, G. T. Proc. 7th International Zeolite Conf., Tokyo; Elsevier: Amsterdam, 1986; p. 677.
33. Beyerlein, R. A.; McVicker, G. B.; Yacullo, L. N.; Ziemiak, J. J. Phys. Chem. 1988, 92, 1967.
34. Cotterman, R. L.; Hickson, D. A.; Shatlock, M. P. ACS Series 24, 1989.
35. Van Broekhoven, E. H.; Daamen, S.; Seink, R. G.; Wijngaards, M.; Nieman, J. In Zeolites, Facts, Figures, Future; Elsevier: Amsterdam 1981; p 1291.
36. Cruz, J. M.; Corma, A.; Fornes, V. Applied Catalysis 1989, 50, 287.
37. Grobet, P. J.; Geerts, H.; Tielen, M. Martens; J. A.; Jacobs, P. A. In Zeolites as Catalysts, Sorbents and Detergent Builders; Elsevier: Amsterdam, 1989; p 721.
38. Gilson, J. P.; Edwards, G. C.; Peters, A. W.; Rajagopalan, K.; Wormsbecher, R. F.; Roberie, T. G.; Shatlock, M. P. J. Chem. Soc., Chem. Commun. 1987, 91.
39. Freude, D.; Hunger, M.; Pfeiffer, H. Z. Phys. Chem. NF, 1987, 152, 171.

40. Freude, D.; Brunner, H.; Pfeiffer, H.; Prager, D.; Jerschkiwitz, H. G.; Lohse, U.; Oehlmaun, G. Chem. Phys. Letters 1987, 139, 325.
41. Samosan, A.; Lippmaa, E.; Engelhardt, G.; Lohse, U.; Jerschkevitc, H. C. Chem. Phys. Letters 1987, 134, 589.

RECEIVED July 20, 1990

Chapter 4

Increasing Motor Octanes by Using ZSM-5 in Catalytic Cracking

Riser Pilot Plant Gasoline Composition Analyses

D. A. Pappal¹ and P. H. Schipper²

¹Paulsboro Research Laboratory, Mobil Research and Development Corporation, Paulsboro, NJ 08066

²Engineering Department, Mobil Research and Development Corporation, Princeton, NJ 08543

This paper documents compositional analyses obtained for FCC gasolines produced over two commercially produced and available faujasite catalysts with and without the addition of ZSM-5 additive. These data indicate that ZSM-5 is effective at increasing the motor octane of the FCC gasolines produced. This is accomplished by increasing the iso to normal ratio of the aliphatic portion of the FCC gasoline.

ZSM-5, Mobil's propriety shape-selective zeolite, has been used commercially in synthetic fuels (methanol-to-gasoline), petrochemicals (xylene isomerization, toluene disproportionation, benzene alkylation) and in petroleum refining (lube and distillate dewaxing). Using these examples, Chen and Garwood(1) have demonstrated the shape selective behavior of this catalyst. In the dewaxing process, for example, ZSM-5 preferentially cracks the straight chain paraffins, substantially reducing the pour and cloud points while retaining high distillate yields.

Since 1983, ZSM-5 has been used in catalytic cracking to increase both the research and motor octanes and the production of light olefins. These olefins can then increase the yields of alkylate, MTBE and TAME. ZSM-5 accomplishes this by upgrading low octane components in the gasoline boiling range (C₇ - C₁₀ hydrocarbons) into light olefins (C₃, C₄, C₅). It also increases the concentration of C₄ and C₅ branched olefins, which are feed to MTBE and TAME units (2,3,4). Since its introduction in 1983, ZSM-5 has been in use in over 10% of the free world's cracking capacity.

In catalytic cracking applications, the ZSM-5 content in the unit has ranged up to three weight percent, the variations due primarily to variations in base octane, gasoline cut-point, catalyst make-up rate and regenerator temperature. It has been used primarily in the form of high concentration, separate particle additives since this method affords maximum flexibility to achieve the target octane increase in as little as one day of addition by accelerating the initial catalyst make-up rate. In contrast, octane catalysts containing Y zeolites with reduced unit cell size can generally take several months to boost octane, since they require significant turnover of the catalyst inventory.

Although the commercial benefits of ZSM-5 in catalytic cracking have frequently been discussed, there has not been significant discussion of the shape selective behavior of ZSM-5 in catalytic cracking. Rajagopalan et. al. (5) claim based on gas oil studies in a fixed bed reactor, that both the straight chain and mono-methyl branched paraffins have equivalent reactivity. Biswas et. al. (6) also report a large reduction in

branched paraffins with ZSM-5 blended with a USY zeolite catalyst. This work was done at very low oil partial pressures (less than 7 psia.). In both cases only small quantities of gasoline were produced, such that the all the liquids were evaluated by gas chromatography (GC) and the octanes calculated by correlations. Schipper et. al. (4) show that the compositional shifts which occur with ZSM-5 depend on the initial gasoline composition without ZSM-5; the olefin to paraffin ratio of the base gasoline was found to be a strong parameter in determining the compositional shifts. Pappal et. al. (7) reported, based on fixed fluidized bed data, that the iso to normal paraffin ratio increases with ZSM-5, and the olefin to paraffin ratio of the base gasoline determined the compositional shifts with ZSM-5. The authors suggested that these shifts could be responsible for the significant increase in FCC gasoline motor octane observed in riser pilot plant data.

In this paper we will discuss the detailed compositional analyses generated in riser pilot plant studies with and without ZSM-5. In particular, we note the relative yields of both the branched and normal paraffins and the iso and normal olefins as a function of carbon number and relate these to the increase in motor octane. Two different base catalysts were used in this study to provide a wide range in the base gasoline composition.

Experimental Procedure

Two conventional faujasite catalysts commercially produced and available were used in this study, catalyst A, which contains about three percent rare earth and catalyst B which contains almost zero rare earth and significantly more zeolite (as measured by X-ray crystallinity) than catalyst A.

The conventional faujasite catalysts were steamed at 1400 °F in 2 atmospheres steam at varying times in order to achieve the same activity as measured by our standard Fluid Activity Index (FAI). Table I summarizes the steaming conditions employed.

Table I.
Summary of Catalyst Steaming Conditions

Catalyst	A	B	ZSM-5 Additive
Time, Hours	20	4.5	10
Temperature, F	1400	1400	1450
Steam Partial Pressure, Atm.	2	2	0.45
Relative Catalyst Make-up to Achieve Constant Activity	Base	5 x Base	

Despite the increase in zeolite content, catalyst B deactivated faster than A requiring only four and a half hours to reach 66 FAI activity. Using our catalyst deactivation model which allows us to accurately translate laboratory catalyst deactivation to commercial make-up predictions (10), we estimate a much higher makeup rate is required for catalyst B to achieve the same activity as catalyst A (see Table I).

Physical and chemical properties of the two steamed catalysts are summarized in Table II.

Because of the low rare earth content and initially higher zeolitic silica/alumina ratio of catalyst B, its unit cell size after steaming is lower than that for catalyst A.

The ZSM-5 additive used in the study was commercially available and contains 25% ZSM-5 zeolite in an inert matrix. The ZSM-5 additive was steamed at conditions (8) chosen to simulate the activity of a commercially equilibrated REX cracking catalyst (Table I). Eight weight percent of the additive was then blended with each faujasite catalyst (two weight percent ZSM-5 zeolite).

These catalysts were evaluated in an isothermal, bench-scale, riser pilot plant at 1000°F average riser temperature, 5 seconds oil residence time (ORT) and at least four different catalyst to oil ratios varying from 4 to 10. The feedstock used was a Nigerian gas oil with properties as shown in Table III. Gases were analyzed by GC. The liquids were analyzed by a GC to give the carbon number isomer breakdown. In addition there was enough sample to analyze for mini-micro Motor octane which has a reported reproducibility of ± 0.75 octane for a single determination.

Results

Table IV shows the impact of ZSM-5 with respect to the overall yields/octanes for both catalysts A and B at 70 volume percent conversion.

The results on both catalysts A and B show the previously reported yield and octane shifts with ZSM-5 (2,3,4): an increase in gasoline motor octane, a reduction in the gasoline yield, an increase in C_3 and C_4 olefins, and isobutane, and no change in coke, C_2 , LCO or MCB yields. For both catalysts, the motor octane gain and also the motor octane gain per gasoline yield loss are essentially the same within experimental error. Note, that several motor octanes were determined to lend significance to the results.

The PONA composition of the gasoline as a percent of fresh feed (Table V) shows that the ZSM-5 is acting primarily on the C_7+ olefins and paraffins in the gasoline boiling range.

There is no increase in the naphthene or aromatic yields. Catalyst A which has a higher unit cell size and rare earth content, has increased hydrogen transfer reactivity resulting in a higher initial concentration of paraffins. Contrary to previous fixed fluidized bed data (7), adding ZSM-5 to catalyst A results in a decrease in the C_7+ olefin yield in a short contact time riser pilot plant. Catalyst B which has a much higher initial olefin concentration, because of lower hydrogen transfer reactivity, also shows a decrease in C_7+ olefins when ZSM-5 is added. The C_7+ paraffins decrease somewhat for both catalysts but for Catalyst A this decrease is much less than in the previous fixed fluidized bed data (7). The total paraffin yield is unchanged when ZSM-5 is used.

Table VI shows the detailed gasoline composition (as a per cent of fresh feed), particularly the breakdown of the straight chain and branched paraffins. The results show an increase in the ratio of the branched to straight chain paraffins for each carbon number when ZSM-5 is used. This is particularly striking in that the total paraffin yield is unchanged when ZSM-5 is added. Thus, although the total paraffin yield remains essentially unchanged, the iso/normal paraffin ratio increases for all carbon numbers. There is also a change in the paraffin carbon number distribution in that the C_8 and C_9 paraffin yields decrease and the C_5 and C_6 paraffin yield increases. The normal paraffins are decreasing at a faster rate than the isoparaffins despite the fact that their initial concentration is 5 to 10 times lower. In the C_7 carbon number, catalyst A shows an increase in the isoparaffins while catalyst B shows a decrease. The normal C_7 decreases for both catalysts.

The olefins (Tables VI and VII) show very similar shifts depending on the base catalyst.

Table II.
Summary of Catalyst Properties

Catalyst	A	B
<u>Steamed Catalyst Properties</u>		
Surface Area, m ² /gram	75	162
X-Ray Crystallinity, wt %	8	28
Total Rare Earth, wt %	3	0.2
Unit Cell Size, A	24.36	24.28
FAI Activity, %	66	66
<u>Fresh Catalyst Properties</u>		
Unit Cell Size, A	24.51	24.43
Surface Area, m ² /gram	221	202

Table III.
Summary of Feedstock Properties

Distillation Yields, Wt %	Total 100	650- 9.7
Physical Properties		
API Gravity		
Density at 70 °C	0.8920	0.8452
Distillation, D1160		
IBP, °F	460	
5 %	608	
10 %	676	
20 %	735	
30 %	778	
40 %	810	
50 %	832	
60 %	857	
70 %	882	
80 %	923	
90 %	993	
Aniline Point, °F	177	
Bromine Number	3.3	
Molecular Weight	390	239
CCR, Wt %	0.92	
Pour Point, °F	120	
Refractive index, 70 °C	1.4946	1.4680
Chemical Analysis		
Hydrogen, Wt %	12.6	
Sulfur, Wt %	0.24	0.18
Nitrogen, ppm	1400	
Basic Nitrogen, ppm	748	115
Nickel, ppm	2.2	
Vanadium, ppm	0.1	
Iron, ppm	2.3	
Molecular Composition, Wt %		
Paraffins		28.0
Naphthenes		41.2
Aromatics		30.8
C _A		17.0

Table IV.
Summary of Yields at 70 Vol % Conversion

Catalyst	A	A + ZSM-5	B	B + ZSM-5
Conversion, vol %	70	70	70	70
<u>Yields, wt %</u>				
Gasoline	46.2	45.5	47.4	46.8
LCO	27	27	27	27
MCB	6	6	6	6
C ₃ = + C ₄ =	7.4	8.2	8.7	9.3
C ₃ + nC ₄	2.1	2.0	1.6	1.6
iC ₄	3.0	3.1	2.0	2.3
C ₂ -	3.5	3.5	3.3	3.3
Coke	4.8	4.7	4.0	3.7
Gasoline M+0	81.5	82.0	81.2	81.6
Delta M+0/ Delta C ₅ + yield		0.7		0.6

Table V.
PONA Composition of Gasolines at 70 Vol% Conversion

Catalyst	A	A + ZSM-5	B	B + ZSM-5
<u>PONA, wt % FF</u>				
P				
C ₆ -	6.4	6.8	3.3	3.6
C ₇ +	4.3	4.1	2.6	2.2
O				
C ₆ -	5.2	5.1	8.3	8.7
C ₇	7.0	6.4	11.7	10.6
N	3.8	4.0	3.1	3.0
A	19.5	19.1	18.4	18.5
Total	46.2	45.5	47.4	46.8
Olefin/Paraffin	1.1	1.1	3.4	3.3

Table VI.

FCC Gasoline Composition

Catalyst	A	A + ZSM-5	B	B + ZSM-5
<u>Paraffins, wt % FF</u>				
nC ₅	0.40	0.40	0.29	0.29
iC ₅	3.02	3.33	1.76	1.95
I/N	7.55	8.33	6.07	6.72
nC ₆	0.29	0.27	0.16	0.14
mmC ₆	2.40	2.45	0.90	1.00
dmC ₆	0.30	0.35	0.15	0.17
I/N	9.31	10.37	6.56	8.36
nC ₇	0.22	0.19	0.17	0.13
mmC ₇	1.44	1.48	0.70	0.60
dmC ₇	0.29	0.31	0.18	0.20
I/N	7.86	9.42	5.18	6.15
nC ₈	0.20	0.18	0.10	0.08
mmC ₈	0.95	0.90	0.60	0.50
dmC ₈	0.10	0.12	0.08	0.07
I/N	5.25	5.67	6.80	7.13
nC ₉	0.10	0.09	0.09	0.07
mmC ₉	0.60	0.55	0.35	0.25
dmC ₉	0.38	0.30	0.38	0.35
I/N	9.80	9.40	8.11	8.57
<u>Olefins, wt % FF</u>				
C ₅ =	2.70	2.80	4.14	4.42
C ₆ =	2.50	2.35	4.13	4.43
C ₇ =	2.50	2.20	3.90	3.70
C ₈ =	3.40	2.90	5.00	4.60
C ₉ =	1.10	1.30	2.80	2.30
<u>Aromatics, wt % FF</u>				
C ₆	0.85	0.85	0.90	0.90
C ₇	1.78	1.83	1.70	1.85
C ₈	4.20	3.95	3.80	3.80
C ₉	4.5	4.20	4.00	4.00
C ₁₀ ⁺	8.20	8.20	8.00	8.00

Table VII.
Detailed C₅ and C₆ Olefin Composition

Catalyst	A	A+ B ZSM-5	B+	ZSM-5
C₅'s, wt %				
C ₅ =	2.70	2.80	4.14	4.42
C ₅ Linear =	1.25	1.10	1.72	1.47
C ₅ Iso =	1.45	1.70	2.42	2.95
C ₅ I/L =	1.15	1.53	1.41	2.00
C₆'s, wt %				
C ₆ =	2.5	2.35	4.13	4.43
C ₆ Linear =	0.80	0.67	1.35	1.3
C ₆ MM =	1.45	1.40	2.40	2.75
C ₆ DM =	0.25	0.28	0.38	0.38
C ₆ I/L =	2.12	2.51	2.06	2.41

Catalyst A shows a decrease in the C₆ through C₈ olefins while catalyst B shows a decrease in the C₇ through C₉ olefins. The respective lighter olefins increase for both catalysts. For both catalysts the iso to linear olefin ratio increases. In the C₅ carbon number range, the iso olefins increase and the linear olefins decrease for both catalysts. The increase in iso olefins results in increased TAME feedstock. In the C₆ carbon number range, both the linear and iso olefins decrease for catalyst A with the linear olefins decreasing faster. For catalyst B, the linear olefins decrease and the iso olefins increase.

Discussion

The componential yield shifts on a fresh feed basis provide an indication of the type of chemistry which occurs when ZSM-5 is used in catalytic cracking. Figure 1 indicates that ZSM-5 alters the distribution of olefin yields in the gasoline boiling range by decreasing the higher carbon number olefins (C₇+) and increasing the lower carbon number olefins (C₆-). In addition, the increase in the lower carbon number olefins is all in the branched olefins as illustrated below using Catalyst B as an example.

Olefin Shifts with ZSM-5 (wt % FF)

$$\begin{array}{l} \text{C}_6\text{- Olefins} \\ +0.58 \end{array} \quad \begin{array}{l} \text{C}_6\text{- Iso-Olefins} \\ +0.88 \end{array}$$

This example shows that ZSM-5 is still reacting the lower carbon number linear olefins and also is significantly increasing the formation of C₅ and C₆ iso-olefins.

Figure 1 also illustrates that a larger C₇+ olefin yield decrease occurs when ZSM-5 is blended with Catalyst B which produced the higher olefin content in the base gasoline. However, the C₇+ olefin conversion rate resulting from ZSM-5 is essentially the same for both catalysts, 8.5% for Catalyst A and 9.4% for Catalyst B. This result suggests that gasolines which initially contain a higher concentration of olefins will show a larger decrease in C₇+ olefin yields when ZSM-5 is added.

Figure 2 shows that the distribution of isoparaffins (on a fresh feed basis) is also altered with ZSM-5; the C₇+ isoparaffin yields are decreased and the C₆- isoparaffin yields are increased when ZSM-5 is added to either Catalyst A or B. The increase in the

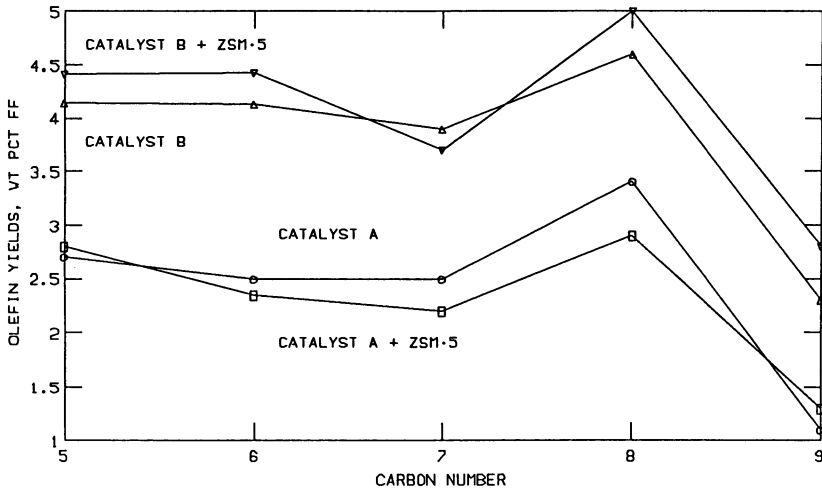


Figure 1. Olefin yields for the C_5 through C_9 carbon numbers for Catalysts A and B with and without ZSM-5.

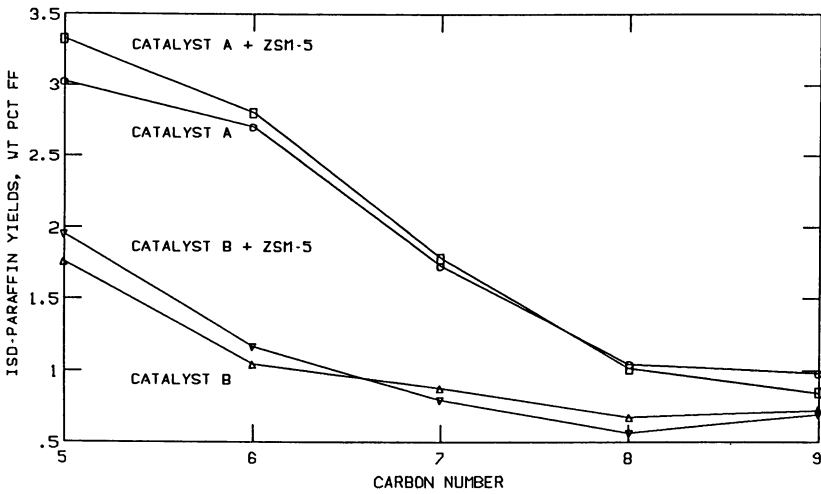


Figure 2. Iso-paraffin yields for the C_5 through C_9 carbon numbers for Catalysts A and B with and without ZSM-5.

lower carbon number isoparaffin is consistent with the increase in isobutane yield shown in Table IV and reported by others (2,4). Table VI shows that the addition of ZSM-5 also lowers the normal paraffin concentrations throughout the gasoline boiling range and increases the iso/normal paraffin ratio. Figure 3 shows that, in all cases, the iso/normal paraffin ratio is higher than that expected from equilibrium calculations.

Figure 3 also indicates that Catalyst B which has a lower unit cell size than Catalyst A also has a lower iso/normal paraffin ratio over the entire carbon number range. These lower unit cell size catalysts, which have been introduced into FCC units over the last 5 years have generally given higher research octane but very little (if any) increase in motor octane. Table IV and Figure 2 confirm this trend, showing that the motor octane of gasoline produced from Catalyst B is actually lower than that produced from Catalyst A, correlating with the lower iso/normal paraffin ratios. The iso/normal paraffin ratio for Catalyst B with ZSM-5 is close to that of Catalyst A, as is its motor octane.

The two previous papers which discussed the chemistry of ZSM-5 (5,6) have stated that ZSM-5 increases octane by mainly concentrating the aromatics in the gasoline due to non-selective cracking of the olefins and paraffins in the gasoline boiling range. However, the data presented here indicate that ZSM-5 is doing far more than just concentrating the gasoline aromatics. Table VIII illustrates the component shift on a gasoline yield basis. The gasoline aromatic content has increased similar to previous reports. However, ZSM-5 also increases the iso-olefins and isoparaffins (high octane components) and decreases the n-paraffins and the C₅ and C₆ straight chain olefins (low octane components). This data clearly illustrates the unique gasoline compositional shifts when ZSM-5 is used to increase the octane in catalytic cracking.

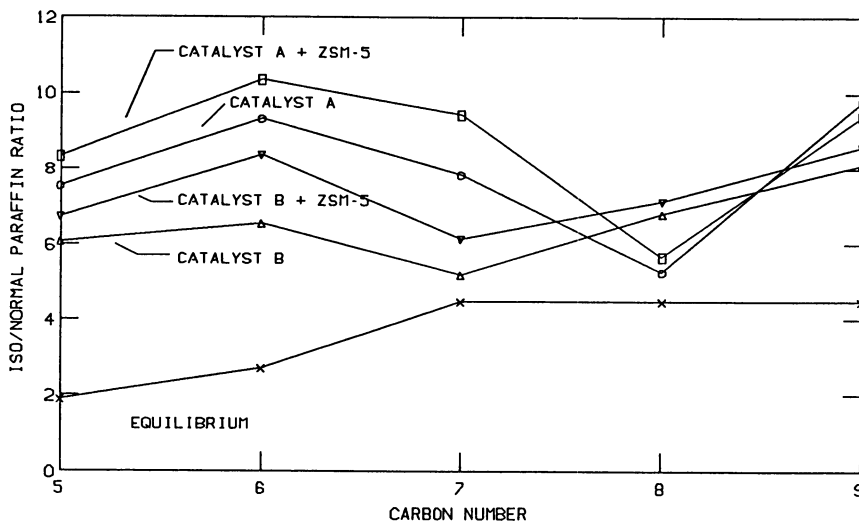


Figure 3. Iso to normal paraffin ratios for the C₅ through C₉ carbon numbers for Catalysts A and B with and without ZSM-5.

Table VIII.

Gasoline Composition Analysis

Catalyst Type	B	B+ZSM-5
Wt %, Gasoline		
Aromatics	38.8	39.5
Naphthenes	6.5	6.4
Olefins	42.2	41.2
iC ₅ i =	5.1	6.3
C ₅ Linear =	3.6	3.1
C ₆ =	5.9	6.6
C ₇	8.3	7.8
C ₈	10.6	9.7
C ₉	5.9	4.9
Paraffins	12.4	12.4
iC ₅	3.7	4.2
nC ₅	0.6	0.6
iC ₆	2.2	2.5
nC ₆	0.3	0.3
iC ₇	1.9	1.7
nC ₇	0.4	0.3
iC ₈	1.4	1.2
nC ₈	0.2	0.2
iC ₉	1.5	1.3
nC ₉	0.2	0.1

Acknowledgments

The authors would like to thank the many scientists and technicians within the laboratory whose efforts made this paper possible. Specifically, Rob Absil, Art Chester and Joe Herbst were particularly helpful.

Literature Cited

1. Chen, N. Y., Garwood, W. E., *Catalysis Reviews*, **28**, (2+3), 185.
2. Dwyer, F. G., Schipper, P. H., Gorra, F., NPRA Annual Meeting, March 29-31, 1987, San Antonio, Texas (AM-87-63)
3. Yanik, S. J., Campagna, R. J., Demmel, E. J.; Humphries, A. P., NPRA Annual Meeting, March 24-26, 1985, San Antonio, Texas, (AM-85-48)
4. Schipper, P. H., Dwyer, F. G., Donnelly, S. P., Huss, A. Jr., Sparrell, P. T., Mizrahi S., Herbst, J. A., ACS Meeting, Division of Petroleum Chemistry, August 30 - September 4, 1987.
5. Rajagopalan, K., and Young, G. W., ACS Preprints, Symposium on Advances in FCC, pg. 627.
6. Biswas, J., Maxwell, I. E., *Applied Catalysis*, **58**, pg. 1, 1990
7. Pappal, D. A., and Schipper, P. H., ACS Meeting, Division of Petroleum Chemistry, Chemistry of FCC Naphtha Formation, September 10-15, 1989, Miami Beach, Florida.
8. Sparrell, P. T., Donnelly, S. P. and Schipper, P. H., Tenth N. American Meeting of the Catalysis Society, March 1987, San Diego, California
9. Chester, A. W. and Stover, W. A., *Ind. Eng. Chem. Prod. Res. Dev.*, **16** #4, pg. 285, 1977.
10. Schipper, P. H., Sarli, M. S., Almgren, B. S., Krambeck, F. J., and Tanzio, M., Ninth N. American Meeting of the Catalysis Society, March 19, 1985, Houston, Texas.

RECEIVED June 8, 1990

Chapter 5

Modification of Fluid Catalytic Cracking Catalysis by the Addition of ZSM-5

Gasoline Over-Cracking Studies

D. J. Rawlence¹ and J. Dwyer²

¹Crosfield Catalysts, Warrington WA5 1AB, Cheshire, United Kingdom

²Department of Chemistry, University of Manchester Institute of Science and Technology, Sackville Street, Manchester, United Kingdom

Over-cracking of FCC gasoline with either ZSM-5 or REHY results, in both cases, in a preferential loss of heavier olefin components. The major differences between the two zeolites is the increased C3/C4 ratio with ZSM-5 which has been assigned to pore size effects, and enhanced bimolecular hydrogen transfer reactions with REHY, resulting in a higher paraffin/olefin ratio.

Typical carbenium ion reaction mechanisms are used to explain the general differences in yields obtained for the two zeolite structures.

Addition of ZSM-5 to the FCC circulating inventory results in a slight reduction in gasoline yield but an enhancement of gasoline quality in terms of octane rating [1]. In addition, increased yields of L.P.G. components are observed, notably propene and butenes which, subsequently, can be fed to alkylation reactors.

Typically, the ZSM-5 is contained in a separate microspheroidal particle which is physically blended with conventional zeolite Y based cracking catalysts prior to addition to the FCC unit. Concentration of the ZSM-5 crystal in the FCC unit can be regulated conveniently by this approach and is, generally, in the range 0.5-3.0 weight % of the total catalyst inventory.

The pore opening in ZSM-5 is smaller than for zeolite Y and access of the complex gas oil molecules into the pores will be restricted. As a result, ZSM-5 has little effect on the primary cracking of gas oil and, when allowance is made for the slight loss in conversion arising from dilution of the active zeolite Y concentration, there is no significant change in coke, bottoms, or light gas yields.

The major role of ZSM-5 is to react with converted products and, in particular, certain gasoline components. The shape selectivity of the zeolite allows only linear and mono-methyl paraffins and olefins ready access to active sites whilst other structures, such as aromatics and multi-branched paraffins, will be restricted [2]. Octane enhancement with ZSM-5 arises from this shape selectivity as the most accessible hydrocarbons are also octane depressants, whilst those structures precluded from the zeolite structure e.g. aromatics have high octane ratings. The gain in octane therefore results from the combined effect of reducing the concentration of low octane compounds together with the relative increase in concentration of desirable hydrocarbons as a result of the overall loss in gasoline yield. In addition, isomerisation of light linear olefins can occur, leading to further octane enhancement [3].

This paper examines the overall reaction between ZSM-5 and gasoline in more detail by comparing the compositional changes that arise after cracking of gasoline over a deactivated ZSM-5 catalyst. In addition, gasoline over-cracking over a REHY catalyst is studied in parallel tests, allowing comparisons to be made between the shape selectivity and hydrogen transfer properties of the respective zeolite structures.

EXPERIMENTAL

A conventional micro-activity (MAT) reactor was employed in these studies [4]. Reactor temperature was 516°C and operating conditions were set at 4.08 catalyst/feed ratio, 11.8 WHSV.

The feed used was an FCC gasoline sample obtained from a European refinery and was subsequently distilled to give an approximate boiling range of 35-190°C.

The gasoline feed was cracked over a fixed bed (4.69g) of the relevant catalyst and liquid and gaseous products were collected in conventional MAT receivers. Gaseous products were analysed on a dual-column Hewlett Packard 5890 gas chromatograph where hydrogen and nitrogen were quantified on a 13X column linked to the TCD detector. Individual hydrocarbons in the number range C1 - C7 were quantified on a 50m alumina-PLOT column carbon linked to an FID detector. The liquid fraction from each test was analysed directly on a PIONA analyser supplied by Analytical Control BV.

Results from both analyses were combined to give carbon distribution in the range 0-10 by several hydrocarbon types namely iso, normal and cyclo paraffins, iso, normal, and cyclo olefins, and mono-ring aromatics. For convenience these groups are abbreviated to IP, NP, CP, IO, NO, CO, and AR respectively, and suffixed by the relevant carbon number i.e. IP-5 equates to total C5 iso-paraffins.

Coke on catalyst was measured by a LECO 244 Carbon/Sulphur analyser.

Cracking reactions were duplicated and the results were averaged. In all cases, mass balances were in the range 98.0-100.5% and results were normalised to 100% using a feed weight correction.

The REHY catalyst employed was a commercial Quantum 2000 sample with a rare earth content of 1.27 wt%. The ZSM-5 catalyst was prepared on a pilot plant spray dryer from 25% wt% zeolite, 25% wt% silica sol, and 50 wt% kaolin clay. The ZSM-5 sample used in this study analysed at 30:1 silica-alumina ratio.

Both catalysts were elutriated, pre-heated at 538°C in air for 3 hours, and fluid bed steam deactivated at 816°C for 5 hours in 100% steam. After this treatment, the unit cell size of the REHY component in Quantum 2000 reduced from 2.453 nm to 2.427 nm.

EFFECT OF ZSM-5 ADDITION

Laboratory scale FCC evaluation studies are usually conducted in fixed bed reactors such as MAT, the results from which can provide a reliable and rapid means of ranking catalyst performance [4]. Depending upon the conditions employed, the effect of added ZSM-5 can also be predicted [5] and can give the same trends as those experienced in commercial reactors. For example, the effect of 2.5 wt% addition of ZSM-5 on gas oil cracking yields with Quantum 2000 is described in Table 1. In this example, a 4% reduction in gasoline yield occurs, predominantly from 105°C+ material. The L.P.G. composition indicates an enhancement of propene, butenes, and iso-butane, in agreement with commercial results and, furthermore, the relative increase in the individual butenes are similar to those reported by Schipper et al [1].

From detailed PIONA analyses of the gasoline fractions [5] it was apparent that iso-paraffins, particularly in the C7-C9 range, were the most reactive towards ZSM-5. However the gasoline composition produced from such reactors tends to be paraffin rich, and olefin deficient when compared to commercial samples.

Commercial FCC gasolines have, for example, a low concentration of n-paraffins which, although they can be easily cracked by ZSM-5, are unlikely to be the major source of propene and butenes as has been claimed [6]. However, such gasolines have much higher levels of n-olefins which also react readily with ZSM-5 [7] and could therefore contribute significantly to the overall effect on L.P.G./gasoline composition induced by ZSM-5. In order to investigate more fully the origins of the L.P.G. components and the changes in gasoline composition, a series of over-cracking studies were conducted using a commercial FCC gasoline as feed. By comparing the results obtained with ZSM-5

TABLE 1
EFFECT OF ZSM-5 ON GAS-OIL CRACKING

YIELD (Wt% Feed)	Q-2000	Q-2000/ZSM-5
Conversion (to 221°C)	68.00	68.00
Coke	2.10	2.13
350°C Bottoms	9.25	9.70
35-221°C Gasoline	49.45	45.40
105-221°C Gasoline	26.91	23.71
35-105°C Gasoline	22.54	20.69
L.P.G.	14.74	18.66
Dry Gas	1.73	1.84
H ₂ -C ₄ GAS YIELDS (Wt% Feed)		
Hydrogen	0.053	0.048
Methane	0.52	0.53
Ethane	0.52	0.54
Ethene	0.62	0.68
Propane	0.82	0.88
Propene	4.34	5.92
Iso-Butane	3.56	4.12
N-Butane	0.73	0.81
1-Butene	1.23	1.54
C-Butene-2	1.14	1.44
T-Butene-2	1.63	2.06
Iso-Butene	1.29	1.81
MAT CONDITIONS		
Feed	: Kuwait Waxy Distillate	
Catalyst/Feed	: 3.50	
WHSV	: 13.7	
Reactor Temperature	: 516°C	
Catalyst Deactivation	: 5 hours, 816°C, 100% Steam	

with those using REHY the relative effects of hydrogen transfer compared to shape selectivity could also be studied.

PARENT GASOLINE COMPOSITION

PIONA analysis by weight % of the parent gasoline is reported in Table 2A and includes the low level of C11+ material not completely analysed by PIONA. It is more convenient to eliminate this fraction and express the remainder as moles per 100 moles C10- feed (Table 2B) and, on this basis, the average molecular weight of the parent gasoline feed is computed at 101.8, with a calculated density of 0.7542 g/ml and a H/C atomic ratio of 1.88.

OVER-VIEW OF GASOLINE CRACKING

Results from the over-cracking of the parent gasoline over zeolites ZSM-5 and Y are summarised in Table 3.

It is evident that ZSM-5 is more active for gasoline cracking as 23.7 wt% L.P.G. + dry gas was produced compared with 18.2 wt% for REHY. As is commonly observed, a lower coke yield was also produced with ZSM-5.

The REHY catalyst produced more saturated light gas, most likely due to the slightly active matrix components, present in the commercial sample but absent from the experimental ZSM-5 catalyst. However, total dry gas yields were similar for both zeolites due to the enhanced ethene yields observed with ZSM-5.

Similarly, REHY produced more saturated L.P.G., notably iso-butane, possibly as a result of hydrogen transfer reactions involving olefins. Propene and total butenes also increase, but there is a relatively low gain in iso-butene. A considerable amount of propene is formed with ZSM-5, accounting for 40% of converted product, and whilst total butenes are higher than for REHY, the enhanced production of iso-butene is the major contributing factor. Again, with ZSM-5, the relative gains in the individual butenes is similar to those reported by Schipper et al [1].

The analysis of product gasoline indicates an increased aromatic content with the ZSM-5 but this arises solely from a concentration effect [1,6]. The gain in aromatics with REHY, however, is greater than can be explained by concentration alone and suggests additional aromatic formation from more extensive hydrogen transfer reactions.

In both cases, there is little reaction with cyclo-paraffins but cyclo-olefins virtually disappear with REHY. ZSM-5 also reacts with cyclo-olefins, and a similar result has been observed with gas-oil cracking [6].

TABLE 2

PARENT GASOLINE ANALYSIS

TABLE 2A - WEIGHT % OF HYDROCARBON TYPES

C#	PARAFFINS			OLEFINS			AROMATICS	TOTAL
	iso	n	cyclo	iso	n	cyclo		
0	0.00	0.00	0.00	0.00	0.00	0.00	0.00	0.00
1	0.00	0.00	0.00	0.00	0.00	0.00	0.00	0.00
2	0.00	0.00	0.00	0.00	0.00	0.00	0.00	0.00
3	0.00	0.00	0.00	0.00	0.00	0.00	0.00	0.00
4	0.22	0.34	0.00	0.33	1.37	0.00	0.00	2.26
5	4.01	0.81	0.13	3.23	3.72	0.00	0.00	11.01
6	3.87	1.00	1.86	4.26	3.35	2.13	0.42	17.78
7	2.78	0.57	2.32	4.82	1.18	2.79	4.46	18.93
8	2.03	0.39	1.81	3.72	0.43	2.14	6.75	17.26
9	1.71	0.30	1.08	2.74	0.33	0.84	6.57	13.58
10	1.42	0.25	0.52	2.08	0.34	0.28	10.91	15.80
TOT	16.04	3.66	7.72	21.18	10.72	8.18	29.11	96.62
Coke								0.00
Un-analysed C11+								3.38
								100.00

TABLE 2B - MOLES PER 100 MOLES FEED

C#	PARAFFINS			OLEFINS			AROMATICS	TOTAL
	iso	n	cyclo	iso	n	cyclo		
0	0.00	0.00	0.00	0.00	0.00	0.00	0.00	0.00
1	0.00	0.00	0.00	0.00	0.00	0.00	0.00	0.00
2	0.00	0.00	0.00	0.00	0.00	0.00	0.00	0.00
3	0.00	0.00	0.00	0.00	0.00	0.00	0.00	0.00
4	0.39	0.60	0.00	0.60	2.48	0.00	0.00	4.06
5	5.65	1.14	0.18	4.68	5.39	0.00	0.00	17.06
6	4.57	1.18	2.20	5.15	4.05	2.57	0.55	20.26
7	2.82	0.58	2.35	4.99	1.22	2.89	4.92	19.78
8	1.81	0.35	1.61	3.37	0.39	1.94	6.46	15.93
9	1.36	0.24	0.86	2.21	0.27	0.68	5.56	11.16
10	1.01	0.18	0.37	1.51	0.25	0.20	8.26	11.79
TOT	17.61	4.26	7.57	22.51	14.05	8.28	25.75	100.03

TABLE 3

SUMMARY OF GASOLINE OVER-CRACKING

YIELD (Wt% Feed)	PARENT	ZSM-5	ZEOLITE Y
C5-10 Gasoline	94.36	73.36	78.32
L.P.G.	2.26	22.45	16.92
Dry Gas	0.00	1.23	1.37
Coke	0.00	0.58	1.46
H2-C4 GAS COMPOSITION (Wt% Feed)			
Hydrogen	0.00	0.028	0.051
Methane	0.00	0.18	0.44
Ethane	0.00	0.13	0.38
Ethene	0.00	0.89	0.58
Propane	0.00	0.43	0.70
Propene	0.00	9.23	4.83
Iso-Butane	0.22	2.19	4.16
N-Butane	0.34	0.64	1.04
1-Butene	0.42	1.82	1.41
C-Butene-2	0.39	1.70	1.32
T-Butene-2	0.56	2.42	1.70
Iso-Butene	0.33	4.01	1.66
C5-C10 GASOLINE ANALYSIS (Wt% Gasoline)			
Average Mol.Wt	101.8	94.6	94.4
Total IP	16.8	26.7	36.3
Total NP	3.5	4.5	4.7
Total CP	8.2	9.8	8.2
Total IO	22.1	9.2	6.0
Total NO	9.9	8.6	4.9
Total CO	8.7	2.8	0.6
Total AR	30.9	38.4	39.3

RESULTS AND DISCUSSION

More detailed results of gasoline over-cracking with ZSM-5 or Y are given in Tables 4 and 5 where, for each hydrocarbon type and carbon number, the difference in moles i.e. moles product - moles (parent) are presented. From these, delta mole distributions for total hydrocarbon and for paraffins and olefins can be compared (Figures 1-5).

The impression from the total hydrocarbon distribution (Figure 1) is that both zeolites behave in a similar manner by producing C3-C5 products from C6+ hydrocarbons, the most significant difference being the ratio of C3/C4 yields. However, as is apparent from Figures 2-5, there are marked differences in paraffins and olefins for each zeolite.

Clearly the losses and gains of a particular species present in the product gasoline as compared to the parent feed gasoline can represent the balance of complex reactions. However, under the reaction conditions employed, it is not likely that there will be appreciable generation of C6+ hydrocarbons other than as intermediates, so that an examination of reactant losses in this region provides a reasonable comparison of reactant conversion over the two zeolites.

Figure 2 shows that there is a limited conversion of higher paraffins on either zeolite. There is some evidence to suggest that C7/C8 paraffin conversion is higher with ZSM-5 and C9/C10 with REHY. However, it would appear that ZSM-5 is not, under the present conditions, particularly effective in paraffin modification in the presence of a relatively high concentration of olefins.

REACTIONS OF OLEFINS

For both zeolites, the major reactants are the branched and linear C6+ olefins. The iso-olefins present in the FCC gasoline are considered to be predominantly mono-branched which, using C8 iso-olefin (IO-8) as an example, react typically as in Scheme 1. A previous report indicates that the conversion of IO-8 at 450°C gives mainly C4 products with little C3 + C5 [8]. This suggests that the increased rate of beta scission associated with the cracking of the C8 cation isomer (III, Scheme 1) is the preferred route to cracked products. This is in keeping with the accepted order of reactivity for cracking (A > B > C), and similar cracking schemes can be postulated for the other C6+ olefins. [8,9].

The major products, for both zeolites are C2-C5 olefins (Figures 3-5) and C1-C6 paraffins. Results show clearly the enhanced bimolecular hydrogen transfer with REHY as compared to ZSM-5 since individual C1-C7 paraffins are consistently higher

TABLE 4

GASOLINE OVER-CRACKING WITH ZSM-5DELTA MOLES PER 100 MOLES FEED

C#	PARAFFINS			OLEFINS			AROMATICS	TOTAL
	iso	n	cyclo	iso	n	cyclo		
0	+0.00	+1.62	+0.00	+0.00	+ 0.00	+0.00	+0.00	+ 1.62
1	+0.00	+1.14	+0.00	+0.00	+ 0.00	+0.00	+0.00	+ 1.14
2	+0.00	+0.44	+0.00	+0.00	+ 3.23	+0.00	+0.00	+ 3.67
3	+0.00	+0.99	+0.00	+0.00	+22.31	+0.00	+0.00	+23.30
4	+3.45	+0.53	+0.00	+6.67	+ 8.28	+0.00	+0.00	+18.93
5	+3.54	+0.17	-0.01	-0.14	+ 2.25	+0.00	+0.00	+ 5.80
6	+2.25	+0.13	-0.20	-1.40	- 3.05	-1.43	-0.21	- 3.90
7	+0.10	-0.07	+0.14	-4.63	- 1.15	-2.12	+1.11	- 6.62
8	-0.12	-0.05	-0.09	-3.24	- 0.32	-1.60	+0.87	- 4.54
9	-0.20	-0.04	-0.17	-2.21	- 0.23	-0.68	+0.03	- 3.49
10	-0.24	-0.04	-0.11	-1.51	-0.25	-0.20	-2.08	- 4.44
TOT	+8.78	+4.28	-0.44	-6.46	+31.08	-6.03	-0.28	31.47

TABLE 5

GASOLINE OVER-CRACKING WITH REHYDELTA MOLES PER 100 MOLES FEED

C#	PARAFFINS			OLEFINS			AROMATICS	TOTAL
	iso	n	cyclo	iso	n	cyclo		
0	+0.00	+2.44	+0.00	+0.00	+ 0.00	+0.00	+0.00	+ 2.44
1	+0.00	+2.79	+0.00	+0.00	+ 0.00	+0.00	+0.00	+ 2.79
2	+0.00	+1.01	+0.00	+0.00	+ 2.10	+0.00	+0.00	+ 3.12
3	+0.00	+1.61	+0.00	+0.00	+11.67	+0.00	+0.00	+13.29
4	+6.72	+1.23	+0.00	+2.41	+ 5.89	+0.00	+0.00	+16.25
5	+9.30	+0.51	+0.01	-1.33	- 0.94	+0.00	+0.00	+ 7.55
6	+5.88	+0.19	+0.11	-2.95	- 3.29	-2.25	-0.22	- 2.53
7	+1.37	+0.01	-0.08	-4.52	- 1.11	-2.76	+1.40	- 5.68
8	+0.32	-0.03	-0.41	-3.27	- 0.36	-1.91	+2.53	- 3.13
9	-0.17	-0.04	-0.41	-2.21	- 0.24	-0.68	+1.04	- 2.71
10	-0.35	-0.04	-0.24	-1.51	- 0.25	-0.20	-2.52	- 5.11
TOT	+23.07	+9.68	-1.02	-13.37	+13.48	-7.79	+2.23	+26.26

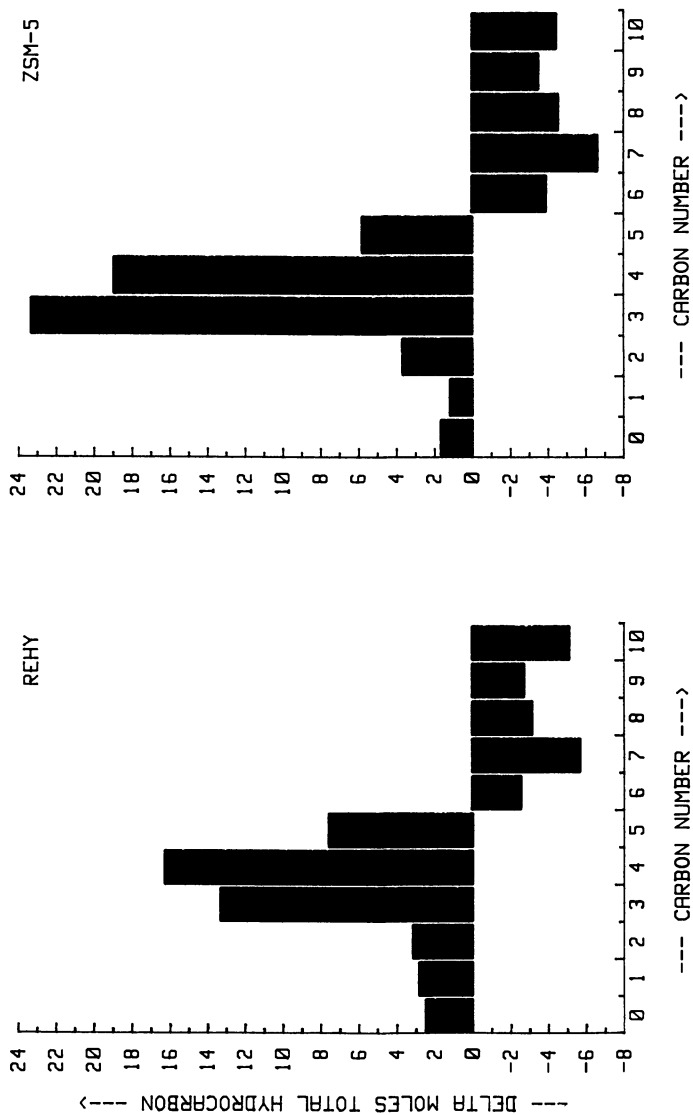


Figure 1 : Delta mole distributions for total hydrocarbons.

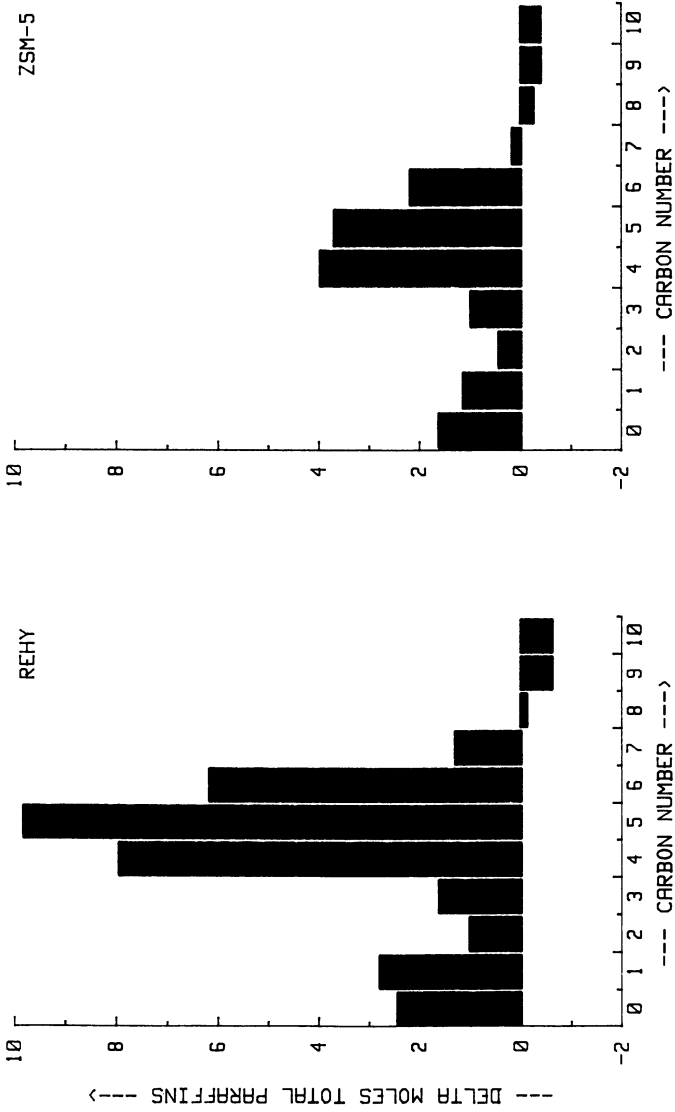


Figure 2 : Delta mole distributions for total paraffins.

Publication Date: January 23, 1991 | doi: 10.1021/bk-1991-0452.ch005

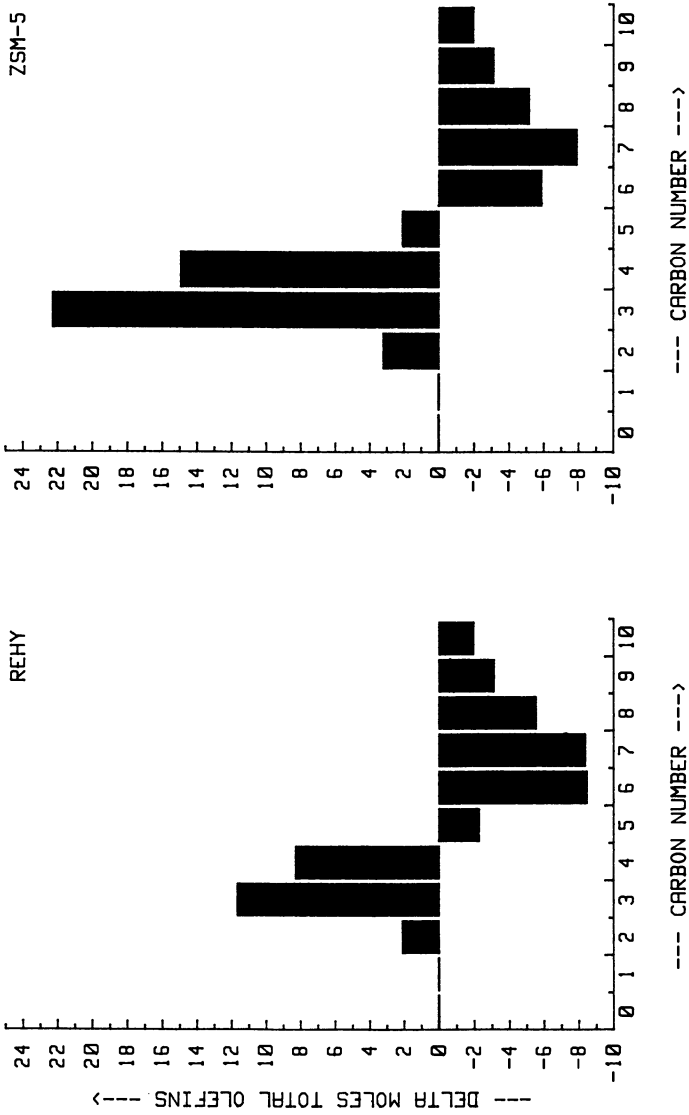


Figure 3 : Delta mole distributions for total olefins.

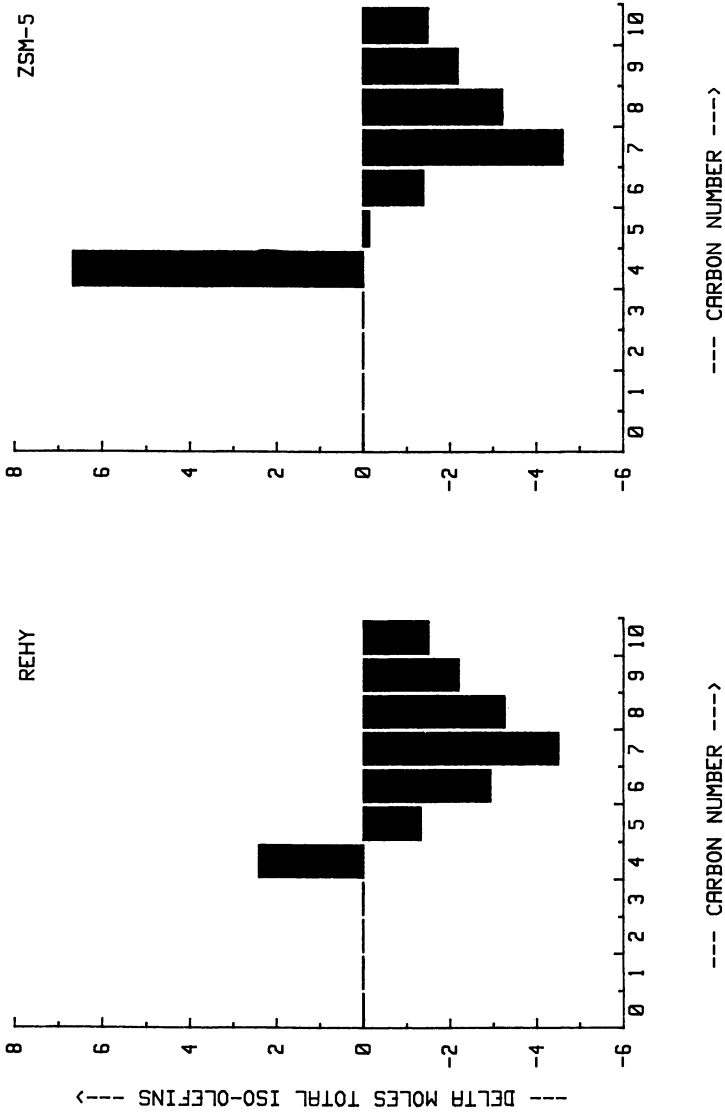


Figure 4 : Delta mole distributions for iso-olefins.

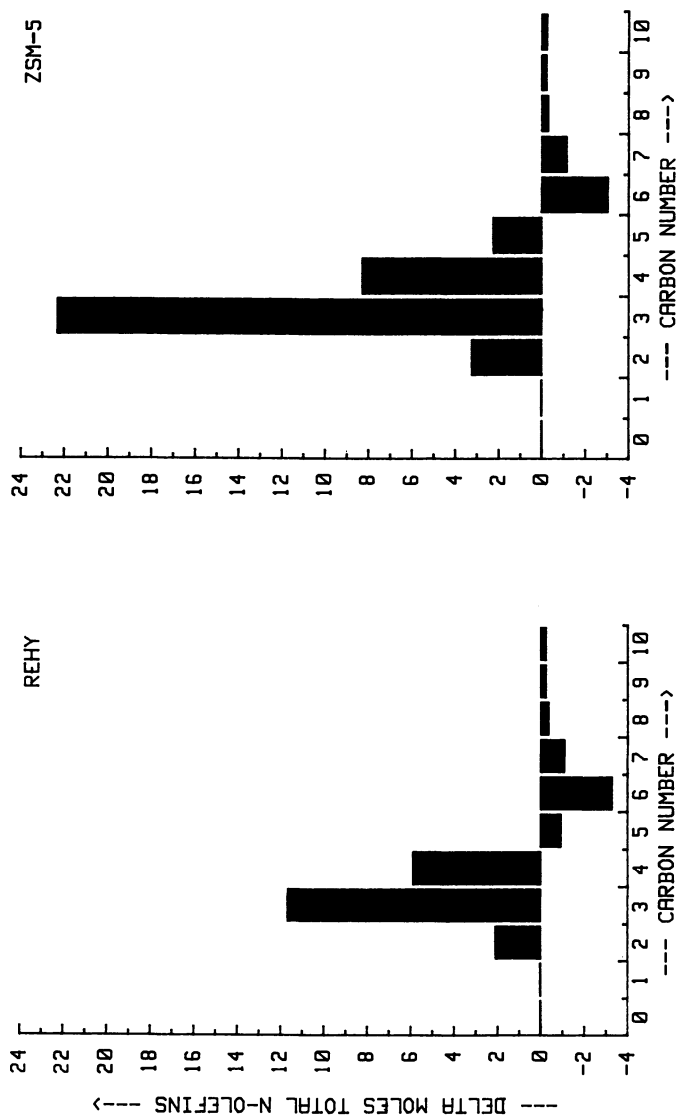
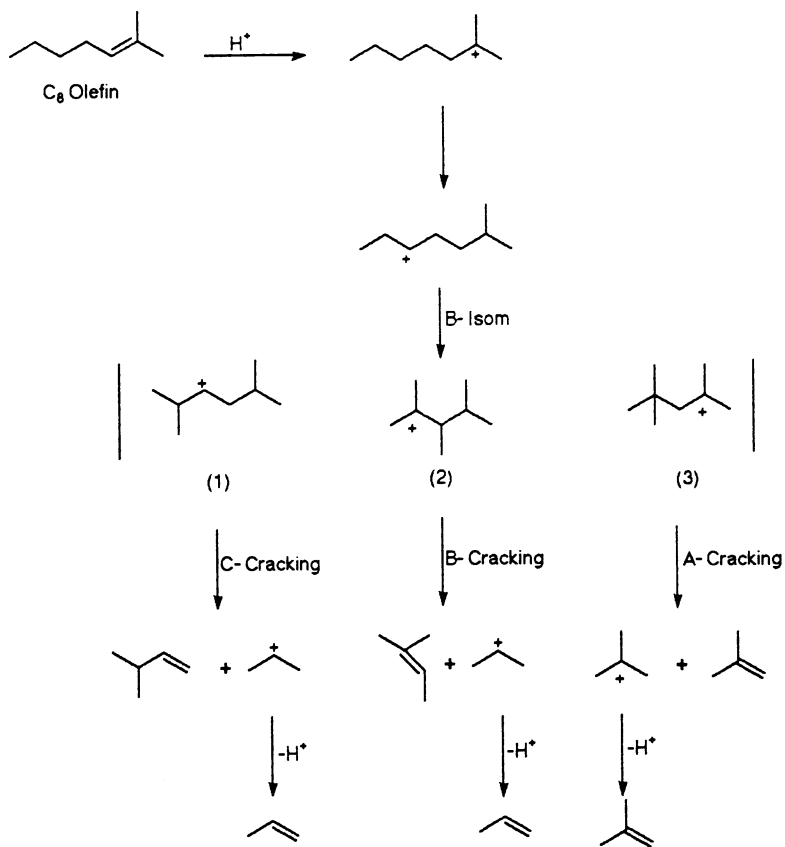


Figure 5 : Delta mole distributions for n-olefins.



Scheme (1)

for reactions over REHY, with the converse being true for olefins. The product distribution for ZSM-5 favours C3 hydrocarbons (23 moles) compared to 13 moles with REHY. This trend has also been observed in the cracking of several paraffins [10] and this is assigned to cage effects. This explanation may also apply here as the ratio of C3/C4 (1.00 for ZSM-5 and 0.65 for REHY) will ratio to 1.54, a value similar to that derived from the cracking of Cn hydrocarbons [10]. A structural as opposed to a compositional effect for the enhanced C3/C4 ratio in ZSM-5 is supported by results from a parallel series of tests on gasoline cracking using a US-Y of similar silica-alumina ratio to that of ZSM-5 described here [11]. The C3/C4 ratio from this study was identical to that observed for REHY.

Results for C4 products (Table 6) indicate that, whilst the total C4 yield is slightly higher with ZSM-5 (due to the greater conversion compared to REHY), the ratio of paraffins to olefins is significantly lower, and is particularly so with the iso compounds. This reflects the greater facility for hydrogen transfer in REHY, as opposed to ZSM-5, which can be explained in terms of the influence of site proximity [12], or the effects of sorption preference [13] both of which favour hydrogen transfer in more alumina-rich zeolites.

TABLE 6
YIELDS OF C4 products (Δ MOLES)

	ZSM-5		REHY	
	<u>iso</u>	<u>normal</u>	<u>iso</u>	<u>normal</u>
PARAFFINS	3.45	0.53	6.72	1.23
OLEFINS	6.67	8.28	2.41	5.89
TOTALS	10.12	8.81	9.13	7.12
TOTAL C4	18.93		16.25	
PARAFFIN/OLEFIN	0.27		0.96	
i-BUTANE/i BUTENE	0.52		2.79	

Size restrictions in ZSM-5 are expected to inhibit hydrogen transfer processes [14]. However, the yield of iso-butane shows that this process is not entirely excluded in ZSM-5 since alternative explanations for substantial yields of this product, for example direct attack of alkane chains by protonic hydrogen or by carbenium ions, seem less likely in view of the limited reaction of higher alkanes (Figure 2) under the present conditions. Size restrictions on bimolecular hydrogen transfer involving larger branched olefinic carbenium ions such as those generated from cyclo-olefins are expected to be more significant with ZSM-5, however, and will be discussed later.

Both normal and iso-butenes are formed largely from higher olefins but are not initially in thermodynamic equilibrium. In ZSM-5, equilibrium between the butenes is approximated but there is excess iso-butane over n-butane. Similarly for REHY, iso-butane is also in excess of equilibrium but there is a clear deficiency in iso-butene. Yields of iso-butene are very susceptible to the hydrogen transfer function of zeolite Y [11] and the present observation may be explained if it is assumed that hydrogen transfer involving the iso-C4 cation is relatively rapid compared to isomerisation. In this case iso-butene will be depleted with REHY but much less hydrogen transfer reaction will occur with ZSM-5. Excess iso-butane over equilibrium is observed for both zeolites and suggests that bimolecular hydrogen transfer involving nC4 cations is less rapid than for the iso-C4 cation. We are not aware of any detailed studies for these reactions but suggest, tentatively, that the greater stability of the iso-C4 cation may enhance its concentration and increase the rate of (bimolecular) hydrogen transfer as compared to the n-C4 cation which preferentially desorbs to olefins.

Reference to Figure 6 shows that, in addition to the greater yield of iso-paraffins over REHY, the distributions are different for the two zeolites. The larger C5-C7 iso-alkanes are relatively more abundant with REHY suggesting that hydrogen transfer in the larger pore zeolite can take place more readily with larger carbenium ions. In the smaller pore ZSM-5, the reduced rate of hydrogen transfer, discussed above, along with reduced space, for bimolecular reactions involving larger ions favours more scission of these larger ions to smaller ions where a limited amount of hydrogen transfer can then occur to produce light alkanes.

REACTIONS OF CYCLIC STRUCTURES

Cyclo-paraffins react more readily with REHY, presumably as a result of pore size differences between the 10 ring ZSM-5 and the 12 ring faujasite, resulting in size discrimination (reactant shape selectivity). Over both zeolites, C9-C10 cyclo-olefins are completely converted so that size discrimination is not observed. However, where conversion of cyclo-olefins is not complete (i.e. C6-C8) there is clear evidence for discrimination between the two zeolites (Figure 7). Presumably this high reactivity of C9/C10 cyclo-olefins over either zeolite can be explained by initial facile attack at outer surfaces.

Reactions of cyclo-olefins within the zeolites can generate aromatics by bi-molecular hydrogen transfer reactions. Such reactions are expected to be more favourable with REHY because of its greater framework aluminium content and because of restricted access to the inter-crystalline pores in ZSM-5. This is

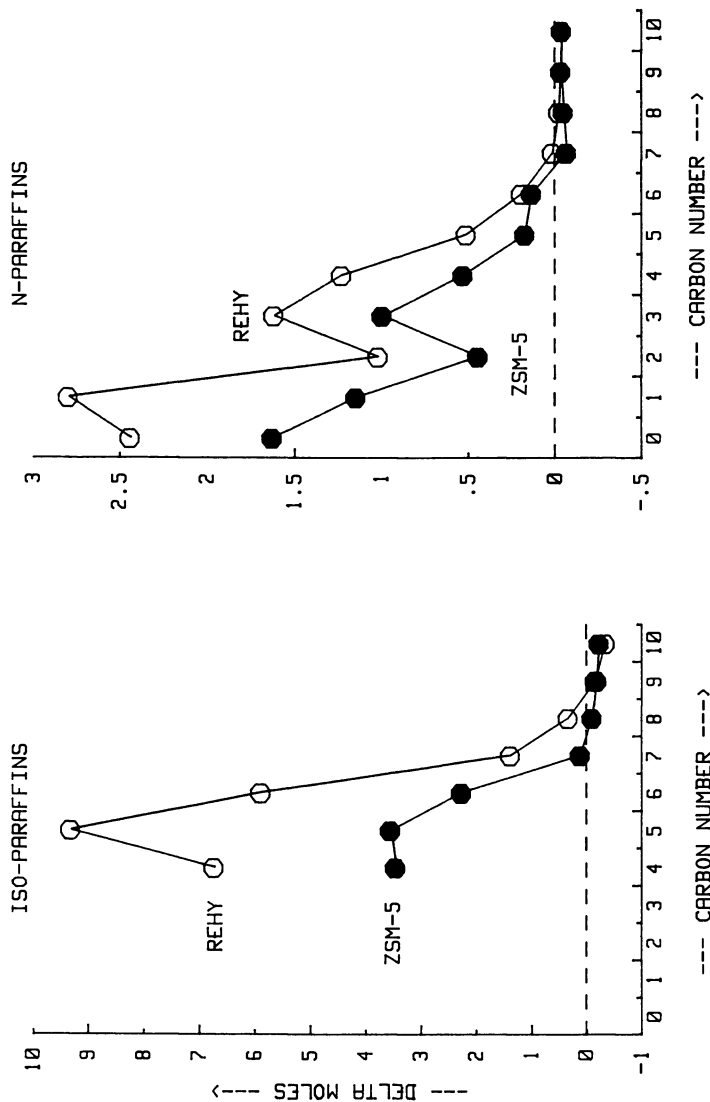


Figure 6 : Delta mole comparisons for iso/n paraffins.

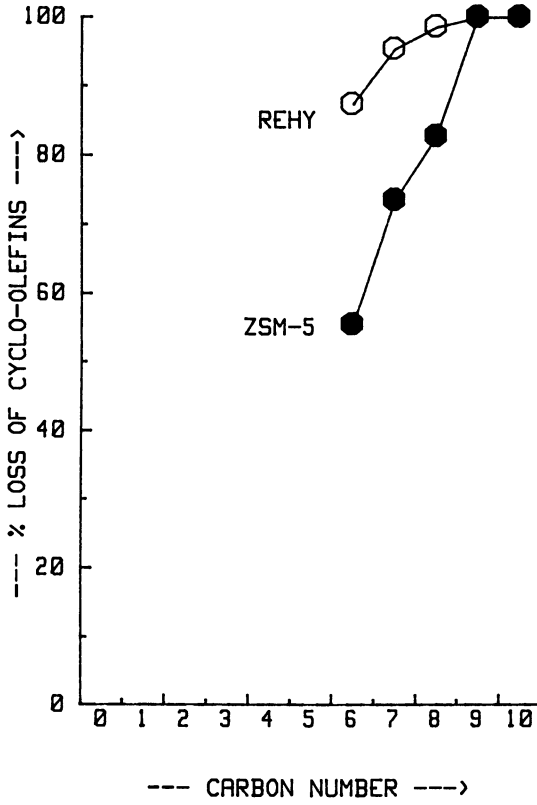
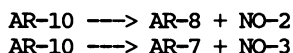


Figure 7 : Relative loss of cyclo-olefins.

supported by the increased total aromatics observed with REHY. There are changes in composition of the aromatics fraction in ZSM-5 but this is largely accounted for by the dealkylation of C10 aromatics to C7/C8 aromatics i.e.



As total number of aromatic rings remains constant for ZSM-5, the converted cyclo-hydrocarbons must largely be cracked to non-cyclic smaller molecules. To an extent, this must also be true for REHY since less aromatics are formed than total cyclo-hydrocarbons are lost.

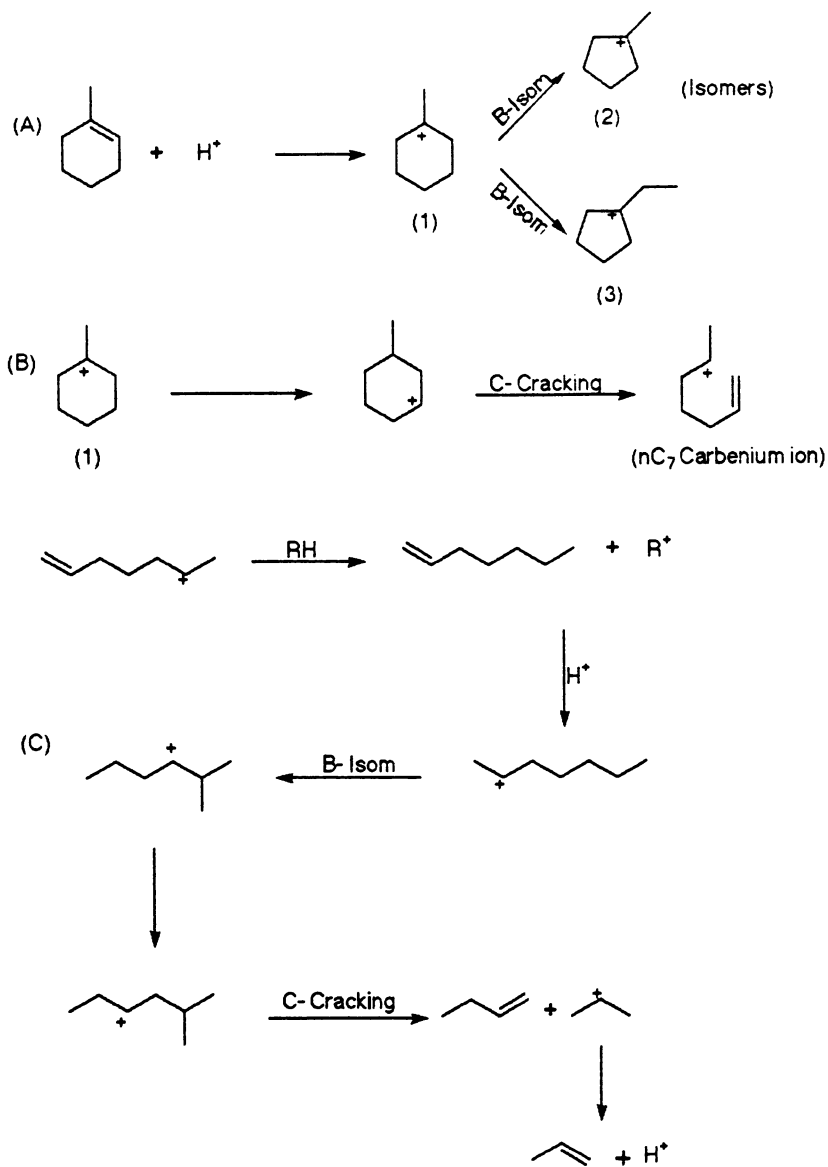
Cracking patterns for cyclo-paraffins over US-Y have recently been reported [9] where products from the conversion of methycyclohexane include C2-C6 compounds with C3 + C4 hydrocarbons as the major yields. The authors of this study have assumed that isomerisation of the initial carbenium ion is relatively facile and that a combination of hydrogen transfer, isomerisation, and beta scission generates the products. This is envisaged in Scheme 2 which uses the classification A, B, C for cracking, A, B for isomerisation [8,9] and which presumes that intramolecular hydrogen transfer is rapid [8].

Similar fates can be postulated for isomers II and III (Scheme 2A) and also for C8 - C10 cyclo-olefins which would generate C4+ olefins. C5 and C6 olefins are also presumed to arise from cracking of methylcyclopentane [8] by the interaction of small carbenium ions with olefins to form larger carbenium ions which can subsequently undergo beta scission. Such reactions can clearly modify product distributions in the present more complicated system.

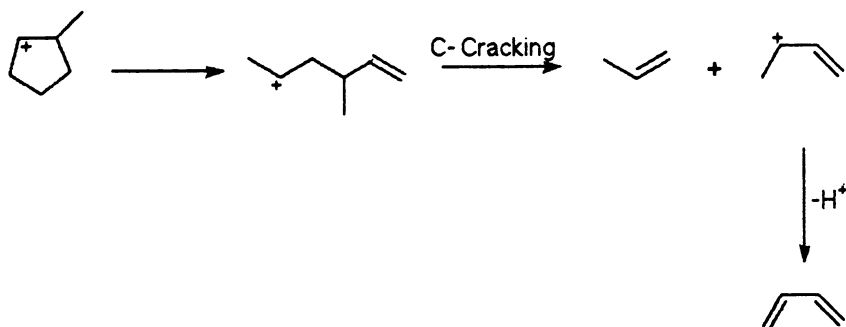
Scheme 2 suggests that the relatively large olefinic carbenium ions are involved in bimolecular hydrogen transfer reactions generating olefins which can then react further. This process is likely to be inhibited in the smaller pore ZSM-5 which could result in more conversion via intramolecular reaction paths to give allylic or di-olefinic intermediates, as in Scheme 3. Under the present conditions, involving long contact times and high conversion, dienes are not observed with either catalyst. Low yields of butadiene are observed during riser cracking with zeolite Y based catalysts; to date, however, there is no evidence for increased diene formation with ZSM-5.

CONCLUSIONS

From a study of gasoline over-cracking with either ZSM-5 or REHY, the resulting total hydrocarbon distributions by carbon number are grossly similar. In both cases, predominantly C2 - C5 products are formed from C6+ components. However, there are significant differences in detail, notably in hydrocarbon-type distributions.



Scheme (2)



Scheme (3)

The major effect of ZSM-5 is to convert higher molecular weight iso-olefins into C3/C4 olefins with no discernible change in aromatics other than some dealkylation of the C9+ fraction. Most of the enhanced LPG olefinicity arises from cracking of C7+ olefins and a pore size effect is thought to be responsible for the high C3/C4 ratio compared to REHY.

A major difference between the two zeolites concerns the extent of bimolecular hydrogen transfer. Whilst REHY is also very reactive with C7+ olefins, less total butenes are formed due to hydrogen transfer involving, in particular, iso-butene \rightarrow iso-butane. The more effective hydrogen transfer in REHY is also evident from the high paraffin/olefin ratio and from increased coke production.

ACKNOWLEDGMENTS

The authors wish to acknowledge Dr. G.J. Earl, Mr. A. Howard Monks, Mr. M.R. Butler, Miss C. de Prez, and Mr. M. Woodhouse of Crosfield Catalysts for the preparation and analyses of the catalysts and Dr. B. Booth of U.M.I.S.T. for helpful discussion.

LITERATURE CITED

1. Schipper P.H.; Dwyer F.G.; Sparrell P.T.; Mizrahi S; Herbst J.A. In Fluid Catalytic Cracking : Role in Modern Refining : American Chemical Society, 1988, P.65.
2. Chen N.Y.; Garwood W.E., J. Catal. 1978, 58, p.453.
3. Scherzer J. Catal.Rev.-Sci.Eng., 1989, 31(3), p.215
4. Rawlence D.J.; Gosling K. Appl.Catal., 1988, 43, p.213
5. Rawlence D.J.; Dwyer J., In preparation.
6. Biswas J.; Maxwell I.E. In Zeolites : Facts, Figures, Future; Elsevier 1989, p.1263.
7. Wojciechowski B.J.; Corma A. Catalytic Cracking; Marcel Dekker Inc., 1986, p.154.
8. Lin L.; Gnep N.S.; Guisnet M.R. Symposium on the Hydrocarbon Chemistry of Naphtha Formation, ACS Div. Pet. Chem.Inc, American Chemical Society Miami, Sept. 1989, p.687.
9. Weitkamp J.; Jacobs P.; Martens P.A. Appl. Catal., 1983, 8, p.123.
10. Barthomuef D.; Merodatos C. Reference 8, p.714.
11. Rawlence D.J. Unpublished results.
12. Pine L.; Mather P.J.; Wachter W.A. J. Catal. 1984, 85, p.466.
13. Corma A.; Faraldos M.; Mifsud A. Appl. Catal. 1989, 47, p.125.
14. Haag W.O.; Weiss P.B. Chem. Soc. Faraday Disc. 1981, p.317

RECEIVED October 5, 1990

Chapter 6

Hydrothermal Stability and Cracking Behavior of Silicoaluminophosphate Molecular Sieve-37 with Different Silicon Contents

A. Corma, V. Fornés, M. J. Franco, F. A. Mocholí, and J. Pérez-Pariente

Instituto de Tecnología Química, UPV-CSIC, Universidad Politécnica de Valencia, Camino de Vera S/N, 46071 Valencia, Spain

The decomposition of organic templates in SAPO-37 and the evolution of the hydroxyl groups upon calcination as well as the stability of the framework have been followed by IR spectroscopy. Moreover, activity and selectivity to n-heptane and gas-oil cracking allow us to discuss the acidity character of SAPO-37 as compared to USY zeolites.

The main objective in FCC catalyst design is to prepare cracking catalyst compositions which are active and selective for the conversion of gas-oil into high octane gasoline fraction. From the point of view of the zeolitic component, most of the present advances in octane enhancement have been achieved by introducing low unit cell size ultrastable zeolites (1) and by inclusion of about 1-2% of ZSM-5 zeolite in the final catalyst formulation (2). With these formulations, it is possible to increase the Research Octane Number (RON) of the gasoline, while only a minor increase in the Motor Octane Number (MON) has been obtained. Other materials such as mixed oxides and PILCS (3,4) have been studied as possible components, but there are selectivity limitations which must be overcome.

The actual research is focused on finding new types of zeolites or modifying already known ones (5), to selectively catalyze branching isomerization and self alkylation reactions in the gasoline fraction, while minimizing overcracking. Efforts have also been devoted to development of new active and selective matrices.

In the first line of research, large pore high silica to alumina ratio zeolites obtained by synthesis,

such as Beta and ZSM-20, have been studied for catalytic cracking (6-9). Beta zeolites produce gasoline with a higher RON than USY, but at the same time give more gases and less gasoline. ZSM-20 zeolite shows a similar cracking behavior to faujasite (10), which is not surprising taking into account that it is a faujasite type structure crystallized with cubic and hexagonal symmetry (11).

The synthesis of a new type of molecular sieves containing silicon, aluminum and phosphorous in the framework (SAPOS) (12), has opened new possibilities for increasing the RON and MON of the gasoline obtained in FCC. The possibility of using different SAPO structures as components in FCC catalysts has also recently appeared in the patent literature (12-20). SAPO-37, with a faujasite structure, looks especially promising and deserves further studies. SAPO-37 has low stability in the presence of water at room temperature after high temperature activation (12,22). This complicates the use of structural reasons to give a chemical interpretation of SAPO-37 cracking behavior.

In the present work, samples of SAPO-37 with different silicon content have been synthesized, and studied from the point of view of their stability, physicochemical and texture characteristics. Finally their behavior as cracking catalysts has allowed us to formulate a hypothesis on the parameters which control activity and selectivity in SAPOS.

Experimental Materials

The SAPO-37 samples were synthesized following a procedure similar to that described by Saldarriaga et al. (21). H_3PO_4 (85%), Al_2O_3 (pseudoboehmite), tetrapropylammonium hydroxide (40% TPAOH, Alfa products with $K+Na=340$ ppm), tetramethyl ammonium hydroxide pentahydrate ($TMAOH \cdot 5H_2O$, from Aldrich) and Aerosil-200 were used as starting materials.

Gels of the following oxide molar composition: $0.025(TMA)_2O:(TPA)_2O:Al_2O_3:P_2O_5:xSiO_2 \cdot 52H_2O$ (x being 0.5, 1.0 and 1.5 for samples S37-1, S37-2 and S37-3) were prepared by adding a solution B into a solution A with vigorous stirring, and kept at 293 K for 24 hours in a closed system. Solution A was prepared by adding the pseudoboehmite into the phosphoric acid solution with vigorous stirring; the viscous mixture was stirred for 8 hours in order to obtain complete homogeneity. Solution B was prepared by adding, while stirring, the TMAOH to the TPAOH until it was dissolved. The silica was then added and stirred for one hour until the solution was homogeneous. The crystallization reaction was carried out at 473 K during 22-26 hours in a static system by using stainless steel autoclaves of 60 cm³ provided with teflon liners. After crystallization the SAPO was washed, centrifuged and, finally, dried at 353

K. Chemical composition of the final products are given in Table I. Minor amounts of unreacted pseudoboehmite were detected by XRD in all samples.

Table I. Chemical composition of samples

SAMPLE	Molar oxide composition (TO ₂ formula)	Si/u.c.
S37-1	(Al _{0.60} P _{0.21} Si _{0.19}) ₀₂	36
S37-2	(Al _{0.55} P _{0.22} Si _{0.23}) ₀₂	44
S37-3	(Al _{0.51} P _{0.20} Si _{0.28}) ₀₂	54

Procedures

X-ray powder diffraction was performed on a Phillips diffractometer using CuK α radiation. IR spectroscopy measurements were carried out in a conventional greaseless cell. Wafers of 10 mg.cm⁻² were pretreated under different conditions of temperature and vacuum; the spectra in the 4000-1300 cm⁻¹ region were recorded at room temperature.

The cracking catalysts were prepared by diluting SAPO-37 samples in a silica matrix. The cracking experiments were carried out in a quartz fixed bed tubular reactor after "in situ" activation. The activation was performed by increasing the temperature up to 823 K at 2K.min⁻¹, under N₂ flow (240 ml.min⁻¹). These conditions were maintained for 4 hours, and then N₂ was changed to dry air (240 ml.min⁻¹) for 1 hour. At this point, the temperature was raised (2K.min⁻¹) up to 923 K and maintained overnight. After this treatment all the organic template was removed from SAPO crystals.

Table II. Characteristics of vacuum gas-oil

Density (g/ c)	0.873	Conradson carbon (wt.%)	0.03
API gravity	30.6 ^o	MeABP (°C)	366
Nitrogen (ppm)	370	K-UOP	12.00
Sulfur (%)	1.65	Viscosity (c.s.at 50°C)	8.249

Distillation Curve (°C)

IBP	5	10	20	30	40	50	60	70	80	90	FBP
167	245	281	304	328	345	363	380	401	425	450	551

A vacuum gas-oil (characteristics given in Table II) was cracked at 755 K. The catalyst to oil ratio (g.SAPO/g.gas-oil) was varied between 0.20 and 0.84 g.g⁻¹ in order to obtain different levels of conversion,

while the time on stream was always 60 seconds. In this way it is possible to obtain the yields of gasoline, diesel, gases and coke at different conversions. Conversion is defined here as the sum of gases, coke, gasoline (483 K⁻) and diesel (593 K⁻). The catalyst was regenerated "in situ" after each experiment, by passing 100 ml.min⁻¹ of air through the reactor at 803 K for 5 hours.

Gases were analyzed by GC and separated by a Porapak-Q plus silica column. Liquids were analyzed by simulated distillation.

Results and Discussion

Thermal and hydrothermal stability

It has been shown (13,22) that SAPO-37 is a highly thermal and hydrothermal stable material. More specifically, SAPO-37 free of organic templates is stable in the presence of water vapor at temperatures above 345 K. The crystallinity in the presence of water decreases only if the contact occurs at temperatures below 345±15 K (22). One hypothesis which would explain this observation is the formation of P-O-P bonds in SAPO-37 during treatments, which would hydrolyze at room temperature in the presence of water causing the breaking of the P-O-P bonds, while producing the acid attack of the Si-O-Al bonds. If this is the reason, it becomes apparent that the formation of P-O-P bonds would occur as a consequence of the activation procedure, since in our original materials, ³¹P MAS NMR spectroscopy only shows the signal corresponding to P coordinated with four Al. In order to produce P-O-P bonds during activation, some dealumination and/or breaking of some parts of the structure should occur. Treating the SAPO-37 in a Guinier-Lenné camera (22) indicates a small dealumination, since the unit cell size decreases from 2.469 to 2.465 nm.

When the sample S37-1 is treated at 923 K in air, and then cooled down at room temperature into a sealed jar, the zeolite is still highly crystalline if the X-ray diffraction is carried out rightaway when taking the sample from the sealed jar (22). However, most of the crystallinity is lost after 40 minutes in contact with moisture. This is a clear indication that the structure is not destroyed by the thermal treatment, but takes place during exposure to moisture at room temperature. Nevertheless, when the sample was first heated in the presence of N₂ at 753 K, for 4 hours and then calcined at 803 K in dry air (100 ml.min⁻¹) overnight, it retains 75% of the crystallinity after exposure to the moisture at room temperature for several hours. After this treatment all the TPA⁺ has been removed, but most of the TMA⁺ remained in the structure. If the calcination temperature is increased to 823 K, the

crystallinity (after exposure to moisture) is only 55% of the original value. After the corresponding treatment at 873 K, crystallinity retention is only 20%. Since all the TMA⁺ has also been removed (see below) at 873 K, one is tempted to relate the final effect observed to a modification of the SAPO-37 structure produced when the TMA⁺ (which is the counteraction in the sodalite cages) is decomposed. This can be due either to a modification of bond angles (22) or to the formation of P-O-P bonds due to local breaking of the structure.

In order to better discuss the influence of the decomposition of the organic templates, the changes observed in the zeolite (and the nature of the remaining products when heated) were followed "in situ" by IR spectroscopy using a quartz cell.

In the IR spectra of Figure 1, it can be seen that vacuum treatment at 373 K and $1.33 \cdot 10^{-2}$ Pa of S37-1 removes most of the water present in the solid (see 1640 cm^{-1} band). The bands corresponding to the stretching vibrations of CH₃- and CH₂- groups of the templates appear in the 2800-2900 cm^{-1} region. The study in the bending region allows more precision on the origin of the bands, and following Bellamy (23), a tentative assignment could be made:

1491 cm^{-1}	-----	-CH ₃	(TMA ⁺)
1484 "	-----	-CH ₃	(TPA ⁺)
1474-1462 "	-----	-CH ₂ -	(TPA ⁺)
1386,1377 "	-----	-CH ₃	(TMA ⁺ , TPA ⁺)

When the sample is heated in vacuum at increasing temperatures, the following changes are observed in the spectra (Fig. 1). First, at 523 K, the 1484 cm^{-1} band decreases while a new band at 1600-1610 cm^{-1} appears which can be assigned to the RNH₃⁺ group of a protonated amine. This indicates that the TPA⁺ is the first organic decomposing, and that decomposition takes place through a mechanism involving aliphatic amine intermediates, as has been proposed in the literature (24). At 573 K, the IR spectrum shows the presence of, at least, six types of hydroxyl groups, whose assignment could be as follows:

3745 cm^{-1}	-----	SiO-H	external
3675 "	-----	PO-H	external
3632 "	-----	Si-O-Al	directed to the supercavity, high frequency hydroxyls (HF)
3573 "	-----	Si-O-Al	directed to sodalite cages, low frequency hydroxyls (LF)
3612 & 3530 "	-----	Assigned, in principle, to HF & LF hydroxyls shifted by interaction with organics.	

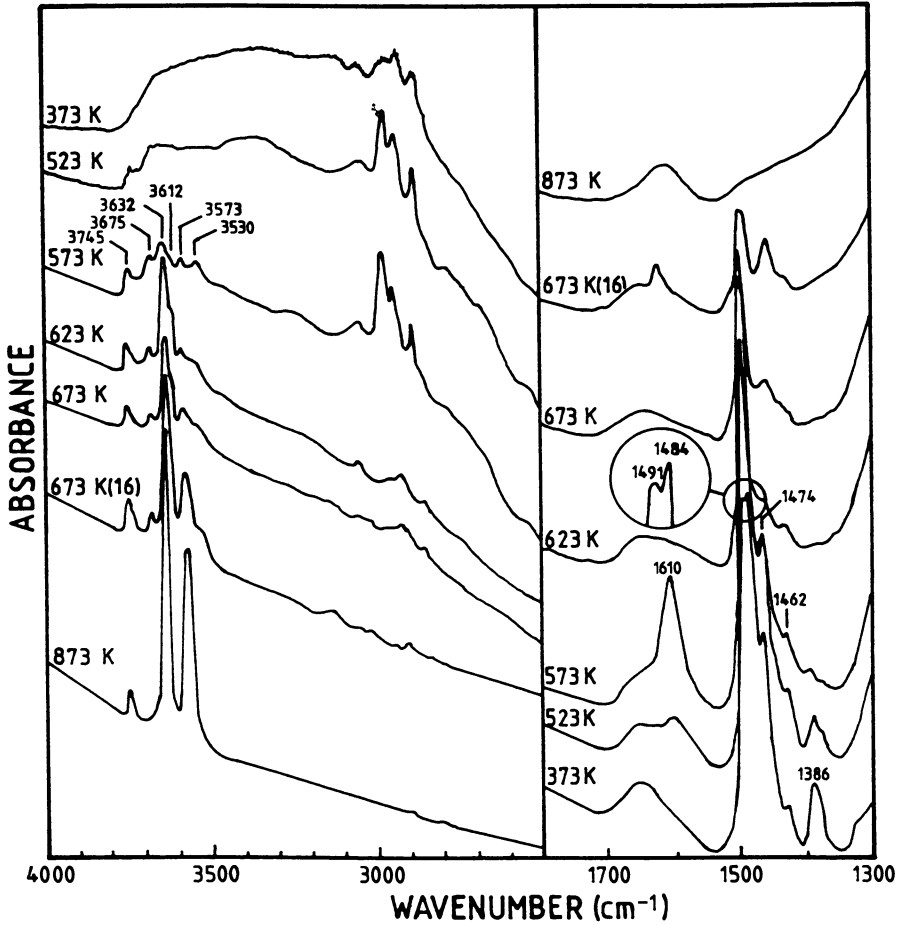


Figure 1. IR spectra of sample S37-1 treated in vacuum at increasing temperature.

At 623 K, the ratio of the HF to LF hydroxyls is very high, while the 1482, 1462 and 1386 cm^{-1} bands, all assigned to TPA^+ , have practically disappeared. On the other hand, the 1491 cm^{-1} band associated with TMA^+ has slightly decreased. When the sample is heated at 673 K, the 1491 cm^{-1} band decreases, while the OH population slightly increases. If the treatment at 673 K is maintained for 16 hours, a strong increase in both HF and LF hydroxyl groups is observed, the increase of the LF being proportionally bigger. This treatment strongly decreases the intensity of the 1491 cm^{-1} band. This result indicates that the elimination of the TMA^+ located in the sodalite cages is strongly controlled by diffusion.

In order to completely eliminate the organics, the temperature was raised to 873 K (Fig. 1) and maintained for 1 hour. Under these conditions, no bands associated with organic materials were detected, while a strong increase in the intensity of the HF and LF hydroxyl bands was observed. From this spectrum two points have to be remarked:

- A decrease in the intensity of the bands at 3745 (SiO-H) and 3678 cm^{-1} (PO-H).
- The disappearance of the 3612 and 3530 cm^{-1} bands.

The first observation could be explained by assuming that at 873 K there is a condensation of some M-OH, M being either Si or P, forming Si-O-Si or P-O-P bonds. The second observation agrees with the hypothesis made above, considering that these two bands correspond to the HF and LF hydroxyls, shifted to lower frequencies due to their interaction with the organic molecules in the crystals. When organic molecules are removed, the interaction disappears and, correspondingly, the hydroxyl band associated with this interaction also disappears.

In order to study the influence of the decomposition of the TPA^+ and TMA^+ on the stability of the final material, a sample heated at 673 K and $1.33 \cdot 10^{-2}$ Pa (in which TMA^+ was still present) was exposed to moisture at room temperature for two hours. After this treatment, the IR spectrum shows the presence of a strong band at 1640 cm^{-1} characteristic of molecular water, which interacts with the hydroxyl groups of the SAPO (Fig. 2). The presence of species $[\text{H}_2\text{O}_5]^+$ (2500 cm^{-1}) which have also been observed in HY zeolites should be noted (25). When the sample was dehydrated at 673 K in vacuum, the original spectrum was restored, indicating that the structure was maintained. However, if the same experiment is carried out at 873 K (Fig. 3), the subsequent exposure to moisture at room temperature results in the disappearance of the structural hydroxyl groups. The disappearance of these bands can be due

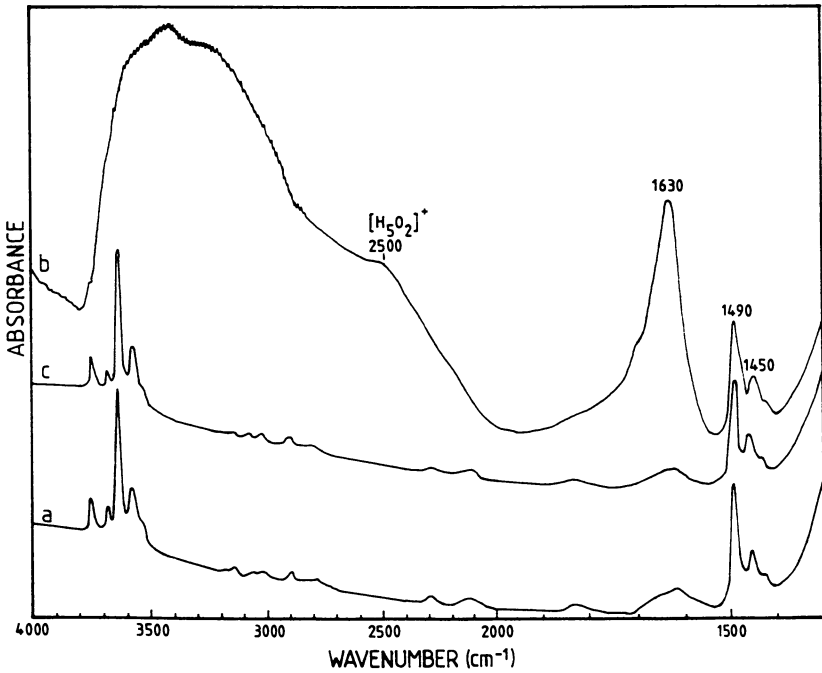


Figure 2. IR spectra of sample S37-1 treated at several conditions: a) vacuum at 673 K. b) after exposition to atmospheric moisture at room temperature. c) Sample b) heated again at 673 K.

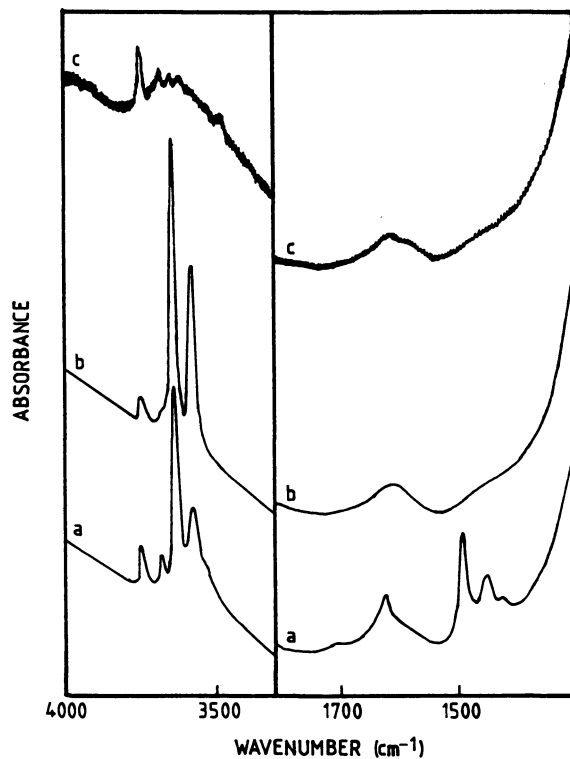


Figure 3. IR spectra of sample S37-1 treated at several conditions: a) vacuum at 673 K. b) vacuum at 873 K. c) after exposition of sample b) to atmospheric moisture and heated again at 673 K in vacuum.

either to a collapse of the structure or to a breaking of Si-O-Al bonds and to the compensation of the remaining negative framework charge by positively charged extra-framework aluminum species. These species could be formed by partial dealumination of the zeolite.

From all these experiments we can propose one hypothesis to explain the stability of H-SAPO-37 molecular sieve. The elimination of TMA⁺ from the sodalite units by thermal treatment and the exit of the decomposition products through the six member ring windows produces the breaking of some T-O-T bonds and the formation of T-OH groups. If the temperature is high enough, some of these groups can condense forming Si-O-Si or P-O-P bonds. The facility of hydrolysis of the P-O-P bonds in the presence of liquid water and the formation of very strong acidic species (which would attack the structure, preferentially Si-O-Al bonds) would be responsible for the breakdown of the structure, and, at least, for the loss of the bridged hydroxyl groups. This effect could be stronger with higher activation temperatures, and could also be influenced by the atmosphere in contact with the sample during the activation treatment. In Figure 4a it can be seen that for samples treated previously in N₂ and then in air, the higher the activation temperature in air, the lower the crystallinity after exposure to moisture at room temperature. Nevertheless, all the organic has been removed after calcination at T>823 K (Fig. 4b), which might suggest that the concentration of P-O-P bonds increases with the activation temperature. In contrast with the behavior of samples activated in vacuum, no hydroxyl groups are visible after the N₂-air activation, (and subsequent exposure to moisture at room temperature) despite the fact that the crystallinity is more than 55%. This observation would be in favor of the breaking of Si-O-Al bonds by the strongly acidic species formed during hydrolysis of P-O-P bonds.

Cracking activity

It can be seen in Figure 5 that when the amount of silicon in SAPO-37 is increased, the conversion increases up to 44 Si/unit cell and then decreases. In order to avoid the possible contribution of the free alumina (Table I), present in minor amounts in these samples, the first order kinetic rate constant per unit of BET surface area (calculated at cat/oil = 0.4) has been plotted as a function of the silicon content, Figure 6. The same behavior is observed. This behavior can be explained in an analogous way as in the case of zeolites, but considering that the acid sites in SAPO are related to the introduction of silicon. Therefore, in SAPO, the number and density of acid sites will be related to the number of silicon atoms. Consequently,

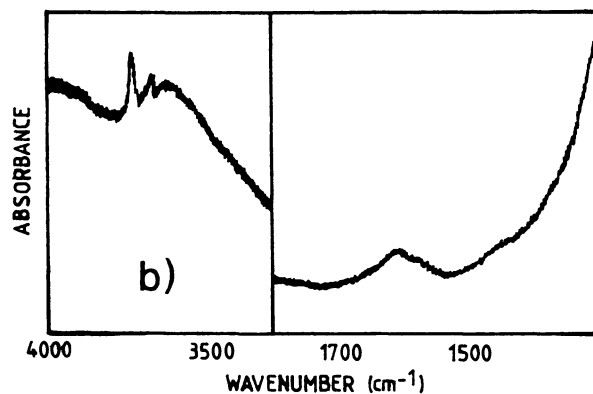
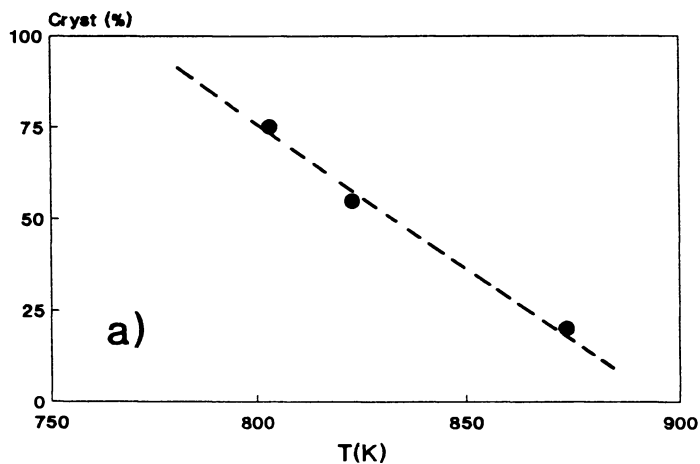


Figure 4. a) Variation of crystallinity with activation temperature in nitrogen/dry-air atmosphere. b) IR spectrum of sample S37-1 activated in nitrogen/dry-air atmosphere.

the density of acid sites and, therefore, the acid strength of these sites will depend on the number of silicon atoms in the next nearest neighbors of a given silicon atom. This concept could be directly applied to those samples in which most of the Si substitution takes place through a mechanism 2 (26), i.e. silicon replacing phosphorus. In the cases where Si substitution takes place by a mechanism 2, and also by a mechanism 3 (i.e. two Si replace one Al-P pair), the behavior would be the same but with the maximum probably shifted to samples with lower silicon content. It has recently been proposed (27) that in SAPO-37, silicon insertion takes place by both mechanisms 2 and 3. The contribution of mechanism 3 increases when the silicon content increases. In any case, the contribution of mechanism 3 to the total silicon substitution in samples with an overall Si/Si+Al+P ratio 0.16 is below 10%, being in the order of 20% for samples with a ratio of 0.21. This result indicates that one can assume relatively safely, that a maximum in activity for carbonium ion reactions needing strong acid sites, will be found in SAPO-37 containing 20-30 Si per unit cell. So far, our gas oil cracking results indicate that maximum activity is achieved with samples containing between 40 and 50 Si/u.c. which should correspond, following our model, to acid sites of medium strength. Moreover, this behavior could suggest that the difference in acid strength between the several types of acid sites would not be very high.

When the cracking activity of SAPO-37 is compared with that of an USY with unit cell size of 2.447 nm (Fig. 5), which would be equivalent to the stabilized zeolite compared in the patent literature (13,14), the activity of the SAPO 37-2 is higher.

The lower acid strength of SAPO compared to USY has been checked by n-heptane cracking at 743 K, and the activity of S37-2 has been found to be ten times lower than that of USY. This result seems to indicate (in contrast to what is currently believed), that strong acid sites are not necessarily required to obtain high activity during gas-oil cracking. Materials like SAPO-37, having very high concentrations of acid sites of medium strength, can also be very effective in cracking long-chain hydrocarbons. Moreover, the lower acid strength shown by SAPO-37 with respect to zeolite Y cannot be related to Sanderson's electronegativity, since SAPO-37 has equal or higher χ than Y zeolites (28).

In order to properly compare the catalytic activity of these two types of materials, a sample of SAPO-37 free of amorphous alumina (S37-4) with 35 Si/u.c., has been prepared. Its catalytic activity is compared in Figure 7 with that of a USY zeolite with unit cell of 2.442 nm described in previous studies (29). The sample

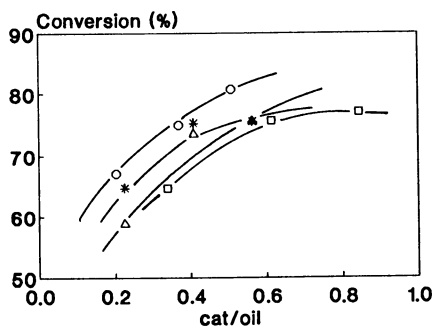


Figure 5. Gas-oil cracking activity of samples S37-1 (\square), S37-2 (\circ), S37-3 (Δ) and USY ($a=2.447$ nm) (*).

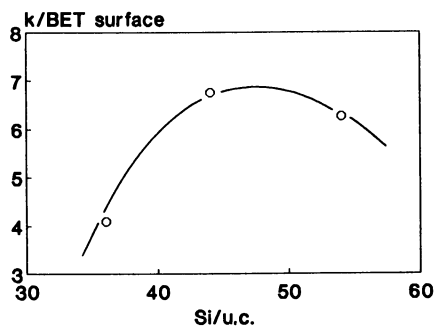


Figure 6. Variation of activity per unit of BET surface with Si content in SAPO-37 samples.

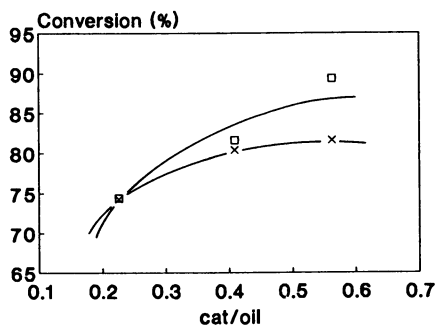


Figure 7. Gas-oil cracking activity of samples S37-4 (\square) and USY ($a=2.442$ nm) (x).

of SAPO-37 is shown to be more active than the one with a similar silicon content because of the higher crystallinity of the former. Meanwhile, it is also more active than the USY zeolite. From the viewpoint of selectivity, it can be seen in Figure 8 that the SAPO-37 gives less gases and coke and more gasoline and diesel than the USY zeolite. The differences observed in Butene/Butane ratio are remarkable, being much higher in SAPO-37 than in USY. This indicates that the extent of hydrogen transfer reactions are lower in the former. This effect can hardly be explained by considering the density of acid sites, or the framework Al content, as the only factor controlling hydrogen transfer. Indeed, if the density of acid sites were the only factor, hydrogen transfer should be higher in the case of SAPO-37 with ~ 40 Si/u.c. than on a USY with ~ 20 Al/u.c.

It has been presented that in Y zeolites, the relative rate of cracking versus hydrogen transfer is related to differences in adsorption capacity and adsorption selectivities. Changes in zeolite composition modify the electrostatic fields, changing the hydrophilic-hydrophobic character and, consequently, the adsorption properties of the zeolites. If this is so, the higher cracking to hydrogen transfer ratio shown by SAPO-37 with respect to Y zeolites, could be related to its less polar character (less pronounced electrostatic fields in the pore system) with respect to Y zeolites (30). This would imply a relative lower olefin to paraffin adsorption ratio on the SAPO-37, and, consequently, a lower hydrogen transfer.

Conclusions

It has been shown that stability of SAPO-37 can be improved if calcination is made in the presence of N_2 . However, the exit of TMA^+ makes the crystallinity of the sample fall to $<20\%$.

IR spectroscopy allow us to conclude that TPA^+ are removed first, through the formation of amines. At 623 K, TMA^+ starts to desorb, and at 873 K, all organic materials are removed.

Besides from the non-acidic SiOH and POH and the acidic HF and LF hydroxyls, the presence of two bands at 3612 and 3530 cm^{-1} has been related to the presence of organic templates interacting with HF and LF framework hydroxyls respectively.

An hypothesis to explain the collapse of SAPO-37 after high temperature calcination followed by exposure to moisture at room temperature, is the breaking of T-O-T bonds due to the exit of TMA^+ . This is followed by the formation of T-OH that, at relatively high temperature condenses, forming Si-O-Si and P-O-P bonds. The presence of liquid water hydrolyzes the P-O-P bonds forming $P(OH)_n$ species, acidic enough to attack the Si-O-Al

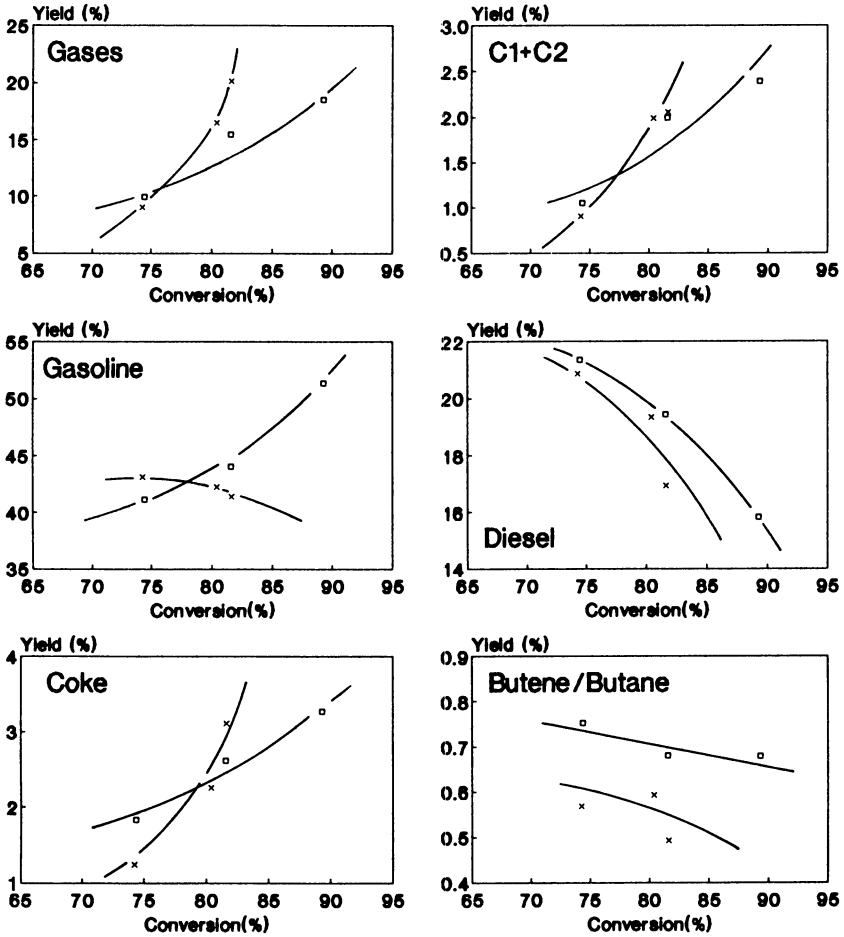


Figure 8. Selectivity to diverse products from gas-oil cracking using samples S37-4 (\square) and USY ($a=2.442$ nm) (\times).

bonds.

It appears from short chain alkane cracking experiments that SAPO-37 shows a weaker acidity than USY zeolites, regardless of the higher Sanderson's electronegativity of the former structure (28). A maximum in gas-oil cracking activity is found for SAPO-37 with 40-50 Si per unit cell. Gas-oil cracking activity is higher for SAPO-37 than for USY zeolites, and therefore strong acid sites as well as sites with medium strength seems to be active for gas oil cracking.

SAPO-37 produces more liquid distillates and less gases and coke than USY zeolites with 20 Al/u.c. (2.442 nm). Meanwhile the hydrogen transfer is lower in SAPO-37, than in USY samples with lower density of acid sites. The high ratio of cracking to hydrogen transfer is related to the less polar character (less pronounced electrostatic fields) of SAPO-37 with respect to USY zeolites.

Acknowledgments

Financial support by the CICYT (project MAT 88-0147) is gratefully acknowledged.

Literature Cited

1. Pine, L.A.; Maher, P.J.; Wachter, W.A. J. Catal. 1984, **85**, 466.
2. Yanik, S.J.; Demmel, F.J.; Hummthries, A.C.; Campagna, R.J. Oil Gas J. 1985, May **13**, 108.
3. Esterte, J.; J. Prep. Div. Petr. Chem. 1989, **34**, 489.
4. McCouley, J.R.; PCT Int. Appl. WO 8806, 488, 1988.
5. Scherzer, J. Catalytic Materials: Relationship between structure and reactivity, Whyte Jr., C.E.; Talla Betta, R.A.; Derouane, E.G.; Baker, R.T.H., Eds., A.C.S. Symp. Ser., 1984, **248**, 157.
6. LaPierre, R.B.; Partridge, R.D., Eur. Pat. Appl. EP 94 827, 1983.
7. Corma, A.; Fornés, V.; Melo, F.; Perez-Pariente, J. ACS Symp. Ser., 1988, **375**, 49.
8. Ćirić, J., U.S. Patent 4 021 331, (to Mobil Oil Corp.) 1977.
9. Dessau, R.M., U.S. Patent 4 384 153 (to Mobil Oil Corp.) 1983.
10. Dwyer, J.; Millward, D.; J.O'Malley, P.; Araya, A.; Corma, A.; Fornés, V.; Martínez, A. J. Chem. Soc. Far. Trans. I, 1990 **86**, 1001.
11. Vaughan, D.E.W.; Tracey, M.M.J.; Newsam, J.H.; Strohmaier, K.G.; Mortier, W.J. A.C.S. Symp. Ser. 1989, **398**, 546.
12. Lok, B.M.; Messina, C.A.; Patton, R.L.; Gajek, R.T.; Cannan, T.R.; Flanigen, E.M., U.S. Patent 4 440 871, 1984.

13. Edwards, G.C.; Gilson, J.P.; McDaniel, C.V., U.S. Patent 4 681 864, 1987.
14. Edwards, G.C.; Gilson, J.P.; McDaniel, C.V., U.S. Patent 4 764 269, 1988.
15. Pellet, R.J.; Coughlin, P.K.; Staniulis, M.T.; Long, G.N.; Rabo, J.A., U.S. Patent 4 734 185, 1988.
16. Herbst, J.A.; Dwyer, F.G.; Huss, A.Jr., Eur Pat. Appl. O 208 409, 1987.
17. Pellet, R.J.; Coughlin, P.K.; Staniulis, M.T.; Long, G.N.; Rabo, J.A., U.S. Patent 4 791 083, 1988.
18. Pellet, R.J.; Coughlin, P.K.; Staniulis, M.T.; Long, G.N.; Rabo, J.A., U.S. Patent 4 842 714, 1989.
19. Edwards, G.C.; Gilson, J.P.; McDaniel, C.V., Eur. Pat. Appl. O 209 793, 1987.
20. Maselli, J.M.; Gilson, J.P.; Edwards, G.C., Eur. Pat. Appl. O 230 005, 1987.
21. Sierra de Saldarriaga, L.; Saldarriaga, C.; Davis, M.E. J. Am. Chem. Soc., 1987, 109, 2686.
22. Briend, M.; Shikholeslami, A.; Peltre, M.J.; Delafosse, D.; Barthomeuf, D. J. Chem. Soc. Dalton Trans. 1989, 1361.
23. Bellamy, L.J. Infrared Spectra of Complex Molecules, Chapman and Hall, London (1975).
24. Parker, L.M.; Bibby, D.M.; Patterson, J.E. Zeolites 1984, 4, 168.
25. Corma, A.; Lopez-Agudo, A.; Fornés, V. J. Chem. Soc. Chem. Commun. 1983, 942.
26. Flanigen, E.M.; Patton, R.L.; Wilson, S.T. Innovations in zeolites materials science, Grobet, P.J.; Jacobs, P.A., Eds., Stud. Surf. Sci. Catal. 1988, 37, 13.
27. Martens, J.; Janssens, C.; Grobet, P.J.; Beyer, H.K.; Jacobs, P.A. Zeolites: Facts, Figures, Future, Jacobs, P.A.; Van Santen, R.A., Eds., Stud. Surf. Sci. Catal., 1988, 49, 13.
28. Uytterhoeven, L.; Mortier, W.J.; Geerlings, P. Phys. Chem. Solids 1989, 50, 479.
29. Corma, A.; Fornés, V.; Martínez, A.; Orchillés, A.V. Perspectives in Molecular Sieve Science, Flank, W.H.; Whyte Jr., T.E., Eds., ACS Symp. Ser. 1988, 368, 542.
30. Corma, A.; Faraldos, M.; Martínez, A.; Mifsud, A. J. Catal. 1990, 122, 230.

RECEIVED October 5, 1990

Chapter 7

Octane Enhancement in Catalytic Cracking by Using High-Silica Zeolites

S. J. Miller and C. R. Hsieh

Chevron Research and Technology Company, P.O. Box 1627,
Richmond, CA 94802-0627

The effect of ZSM-5 as an octane additive to a cracking catalyst was studied in both a small fixed-bed reactor and a fluidized-bed pilot plant. Analyses of the products of these tests were used to determine the reaction chemistry. It was found that by maximizing the ratio of isomerization activity to hydrogen transfer activity, gasoline octane was increased with a minimum of yield loss. This could be accomplished by increasing the silica-to-alumina ratio of the additive zeolite.

Approximately 40% of the gasoline produced in the United States is made by fluid catalytic cracking. Because of the need for higher gasoline octane, refiners are looking for economical ways of improving octane in their FCC units, either by changing operating conditions or cracking catalyst. The latter has primarily involved the use of catalysts containing low unit cell size ultrastable-Y zeolite (USY) which produces fewer paraffins and more olefins than conventional rare earth catalysts (1). A second catalytic option, which may be used in conjunction with USY, is the introduction of a minor amount of a catalyst designed to improve gasoline octane.

Anderson et al. (2) and Donnelly et al. (3) have reported on the use of the zeolite ZSM-5 as an additive catalyst for increasing the octane of FCC gasoline. This zeolite has been reported by workers at Mobil (4) to increase octane by cracking out low octane straight-chain paraffins and olefins in the heavy gasoline product and by olefin isomerization. Rajagopalan and Young (5) have proposed that the ZSM-5 prevents paraffin formation by cracking carbonium ions or olefin intermediates to light products. In either case, C₃ and C₄ olefins increase while gasoline yield decreases. Chevron researchers (6,7) have shown that gasoline loss can be reduced by using a ZSM-5 type additive of high silica to alumina ratio, in particular one of SiO₂/Al₂O₃ molar ratio greater than 500.

In this report we examine the effect of SiO₂/Al₂O₃ ratio on the selectivity of ZSM-5 type additives and discuss the chemistry involved.

EXPERIMENTAL

CATALYST PREPARATION ZSM-5 was prepared according to procedures discussed in the literature (8,9) and identified as such by X-ray diffraction analysis. Ultrastable Y zeolite was obtained from the

Union Carbide Corporation. Dealuminated H-mordenite was prepared by acid extraction of H-mordenite obtained from the Norton Company.

Octane additives were composed of 25 wt % zeolite in a silica-alumina binder, spray-dried to conventional FCC catalyst size, and treated at 1450°F in 100% steam at 1 atm for five hours before testing.

An equilibrium cracking catalyst containing approximately 25 wt % zeolite was used as the base catalyst for all additives.

FIXED-BED AND FLUIDIZED-BED TESTS In the fixed-bed test, a sample of cracking catalyst was contacted with an FCC feed in a manner similar to the standard microactivity test (MAT) prescribed by ASTM (10). One major difference was that the reactor temperature was increased from 900°F to 960°F to better simulate current commercial operations.

The fluidized-bed tests were conducted in a 0.5 BPD circulating pilot plant equipped with a 50-ft riser reactor and an on-line debutanizer. The total liquid product from each test period was distilled externally, and the individual cuts were submitted for inspections.

In both types of tests, additives were admixed with the equilibrium catalyst prior to testing.

HYDROGEN TRANSFER INDEX (HTI) TEST In this test, 0.5 μL pulses of 1-hexene feed were carried from a heated sampling valve into a fixed-catalyst bed in a stainless steel reactor by a nitrogen carrier stream at 800 mL/min. (at STP). The catalyst was -250 mesh and diluted with alumina of the same mesh size plus 80-100 mesh acid-washed Alundum. Reactor pressure was controlled by an Annin valve. The effluent stream went to the injector splitter of a gas chromatograph. The reactor conditions included a catalyst temperature of 221°C and 3.45 MPa total pressure.

The HTI was calculated from the product ratio of 3-methylpentenes to 3-methylpentane at a linear hexene conversion of 30-70%.

RESULTS

MICROACTIVITY TESTING

Selectivity to C₅-Plus Versus SiO₂/Al₂O₃ Ratio

An additive containing a sieve of 40 S/A (SiO₂/Al₂O₃) was compared with one of 525 S/A. Figure 1 shows the C₅-plus gasoline yield using the 525 S/A sieve was less than with the base catalyst alone, but substantially higher than when using the 40 S/A sieve at equal conversion. Furthermore, the C₄ olefinicity (Figure 2), generally an indicator of light gasoline research octane, showed about the same improvement relative to the base for both additives.

Using another binder which was higher in silica, the 525 S/A was compared with a sieve of 1000 S/A. Figure 3 shows a continued increase in C₅-plus yield up to 1000 S/A. Again, all additives produced about the same C₄ olefinicity (Figure 4), above that for the base catalyst as well as the base plus additive with no zeolite.

Effect of Additives on Selected Hydrocarbon Types

The effect of the 40 S/A and 525 S/A additives on certain hydrocarbon types was examined by adding to the test feed either an n-paraffin (n-nonane) in the higher boiling range of gasoline or a 1-olefin (1-pentene) in the lower boiling range. A high amount of additive (10%) was used.

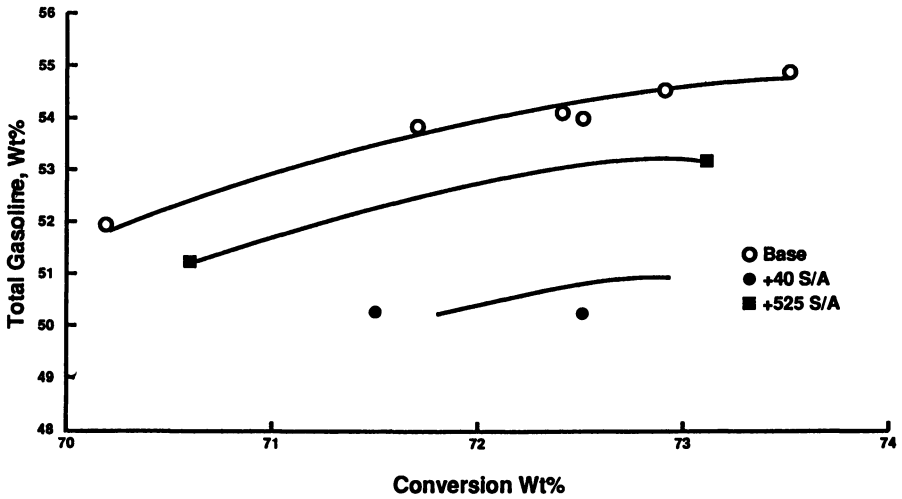


Figure 1. Effect of zeolite SiO₂/Al₂O₃ ratio on gasoline selectivity in MAT.

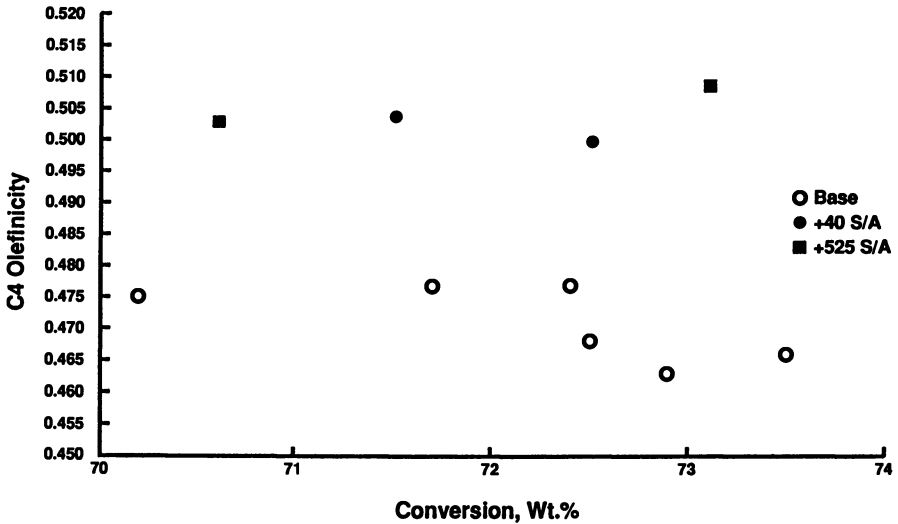


Figure 2. Effect of zeolite SiO₂/Al₂O₃ ratio on C₄ olefinicity in MAT.

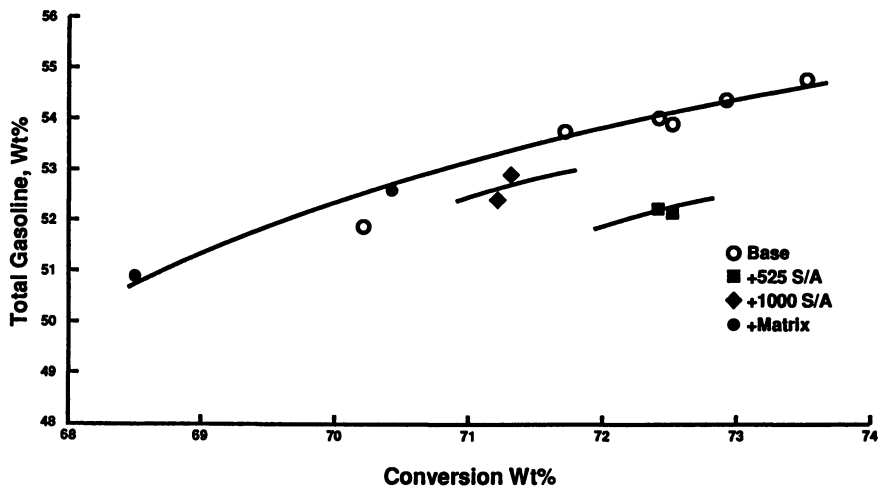


Figure 3. Effect of zeolite $\text{SiO}_2/\text{Al}_2\text{O}_3$ ratio on gasoline selectivity in MAT.

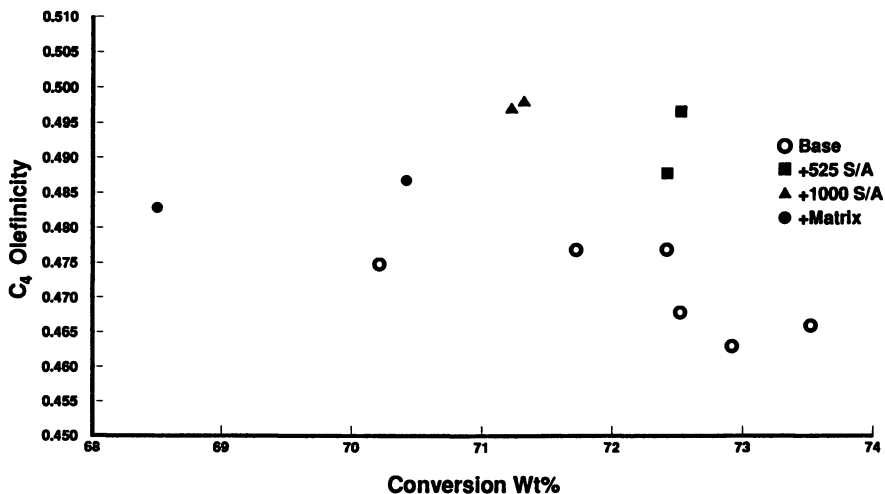


Figure 4. Effect of zeolite $\text{SiO}_2/\text{Al}_2\text{O}_3$ ratio on C_4 olefinicity in MAT.

With 5% nC₉ in feed, conversion of the nonane was less than 5% with either the 40 S/A or 525 S/A additives. If less than 10% additive had been used, the conversion of nC₉ due to the additive would have been almost undetectable. Since the rate of cracking of lower boiling paraffins is likely to be lower than that of nC₉, those components should also be unaffected. This suggests that any octane enhancement observed with the additives has little to do with cracking of n-paraffins.

With 1% 1-pentene in feed, and using the 525 S/A additive, there was an increase in C₅ branched olefins and paraffins, as well as an increase in C₅ normal olefins and paraffins. Other carbon numbers remained unaffected (Table I).

Table I. Relative Yields of C₅-C₆ Paraffins and Olefins Upon Addition of 1% 1-Pentene to Feed in MAT

iC ₅	1.2
nC ₅	1.2
1-C ₅ =	1.1
t and C-2-C ₅ =	1.1
iso-C ₅ =	1.1
iC ₆	1.0
nC ₆	1.0
n-C ₆ =	1.0
iso-C ₆ =	1.0

Effect of Additives on Iso/Normal Paraffin Composition

The effect of 40 S/A and 525 S/A additives on the iso/normal paraffin ratios of the product gasoline was studied using both fresh and steam-deactivated samples.

Iso/normal C₄-C₇ paraffin ratios versus carbon number are shown in Figure 5. If a major function of the additive is to crack away n-paraffins, then one would expect the iso/normal ratio to be higher with additive than in the base case. While this is found for C₄ and C₅, with fresh additive the opposite was observed with C₆ and C₇. Since C₆ and C₇ paraffins are more prone to crack than C₄ and C₅, it is unlikely that an n-paraffin mechanism is involved in increasing iso/normal ratios.

HYDROGEN TRANSFER INDEX TEST

Relative hydrogen transfer activity can be determined using an HTI test (11), where the index is a measure of the degree of saturation in the reaction product. The test determines the product ratio of 3-methylpentenes to 3-methylpentane derived from a 1-hexene feed. While the branched products come mainly from oligomerization followed by cracking, the results should be relevant here as well. The higher the index, the lower the relative hydrogen transfer activity.

Figure 6 shows the HTI values for a number of catalysts as a function of linear hexene conversion. Ultrastable Y was very active for H-transfer, with dealuminated H-mordenite somewhat less. Although its SiO₂/Al₂O₃ ratio was near that of the mordenite, ZSM-5 of 78 S/A catalyzed even less H-transfer, possibly resulting from the limited space in the ZSM-5 cavities for forming the bimolecular

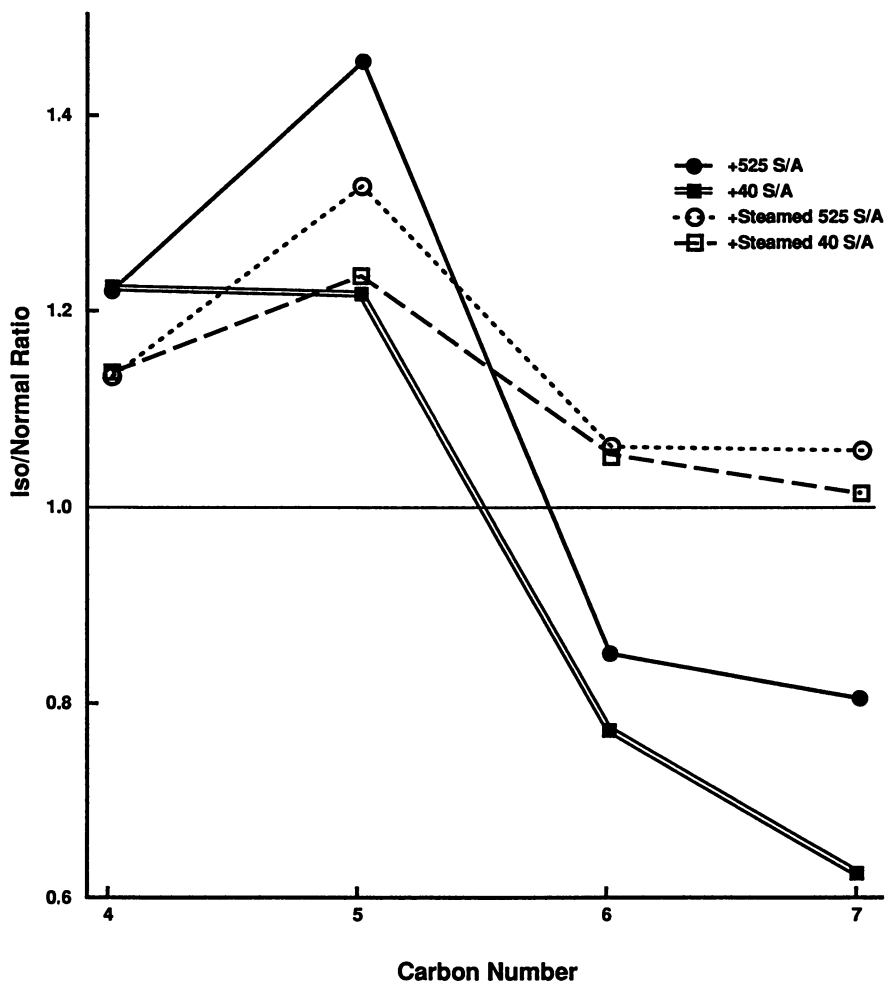


Figure 5. Iso/normal ratio of paraffins relative to base.

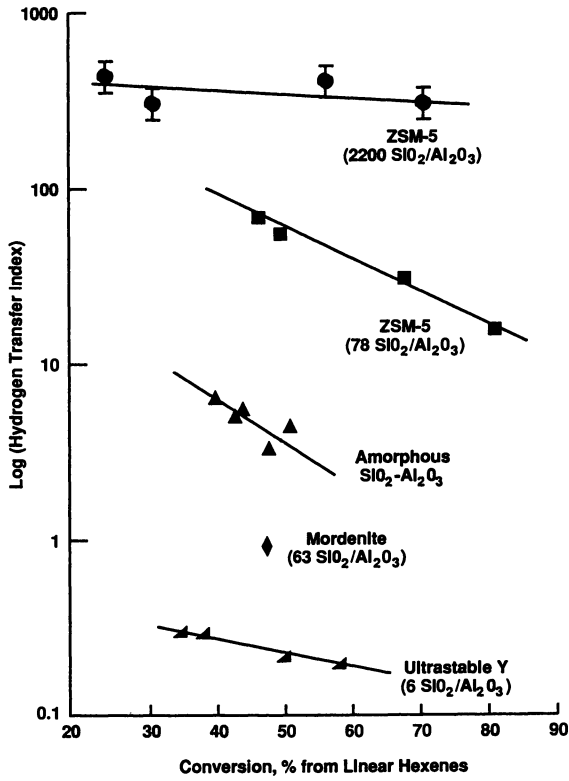


Figure 6. Hydrogen transfer index test results.

H-transfer reaction complex (12). ZSM-5 of 2200 S/A had the highest index with very little H-transfer even at high conversion.

PILOT PLANT TEST

Comparisons were made using a circulating pilot plant for the following cases:

- a. Base case (equilibrium cracking catalyst).
- b. Base plus 40 S/A.
- c. Base plus 525 S/A.

Reactor conditions were 950°F and 5 catalyst/oil. The conversion below 430°F was 60 wt %. Before use, the additives were steam deactivated for five hours at 1450°F in 100% steam.

The incremental differences in yield and measured octanes produced by the additives are shown graphically in Figures 7 and 8, respectively. These show that both additives reduced gasoline yield, mainly 265-430°F, with 525 S/A giving the least reduction. Most of the yield loss in both cases was accompanied by gains in C₃-C₄ olefins. These also show an octane gain/wt % yield loss in the C₅-430°F gasoline of 0.6 (1.0/1.7) for 40 S/A and 1.0 (0.9/0.9) for 525 S/A.

Compositional information on the product C₃-C₇ fractions and calculated research octanes are given in Table II. The C₄-C₇ fractions all show higher iso/normal paraffin ratios with the additives than in the base case. The additives also give higher olefinicity, particularly in the C₃-C₅ range, and higher iso/normal olefin ratios with reduction especially in the relative amounts of normal 1-olefins. These factors all result in higher octanes.

Table II. Product Inspections at 60% Conversion and 950°F

	Base	+40 S/A	+525 S/A
C ₃ =/C ₃ P	4.18	5.05	4.89
C ₄ =/C ₄ P	1.56	1.92	1.83
1-C ₄ =/C ₄ =	0.23	0.21	0.22
I-C ₄ =/C ₄ =	0.24	0.28	0.27
I-C ₄ /nC ₄	3.83	4.06	4.08
C ₅ =/C ₅ P	1.44	1.72	1.59
1-C ₅ =/C ₅ =	0.11	0.085	0.089
IC ₅ =/C ₅ =	0.54	0.62	0.60
IC ₅ /nC ₅	6.97	7.39	7.78
C ₅ P RON	88.4	88.6	88.8
C ₅ = RON	98.8	98.9	98.9
C ₆ =/C ₆ P	1.01	1.07	1.11
1-C ₆ =/C ₆ =	0.067	0.049	0.050
IC ₆ =/C ₆ =	0.49	0.58	0.57
IC ₆ /nC ₆	6.06	6.41	6.72
C ₆ P RON	70.0	70.1	70.4
C ₆ = RON	93.9	94.5	94.5
C ₇ =/C ₇ P	0.90	0.92	0.91
1-C ₇ =/C ₇ =	0.074	0.073	0.069
IC ₇ =/C ₇ =	0.597	0.685	0.680
IC ₇ /nC ₇	9.6	10.8	12.0
C ₇ A/C ₇	0.225	0.232	0.223
C ₇ P RON	53.1	54.0	54.7
C ₇ = RON	84.6	85.1	85.6

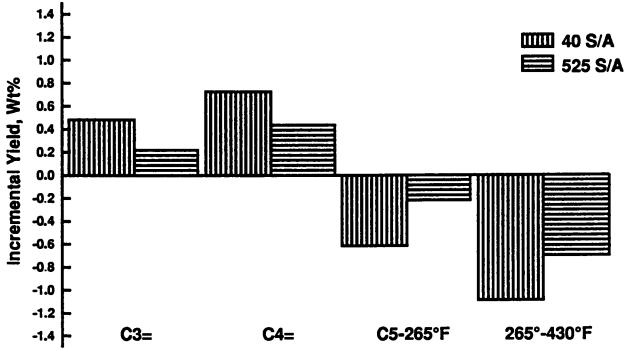


Figure 7. Incremental pilot plant yields at 950°F and 60% conversion.

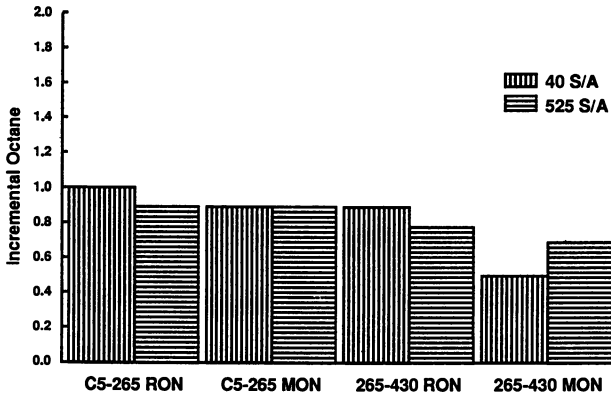


Figure 8. Incremental pilot plant octanes at 950°F and 60% conversion.

Looking at what happens within each carbon number group, one finds that for 40 S/A, the main contributor to octane enhancement in the C₅'s is increased olefinicity. While the olefinicity also increases with 525 S/A, nearly half the C₅ octane increase with that additive comes from a higher iso/normal paraffin ratio. The olefinicity enhancement is of a lesser degree in the C₆'s and essentially nil in the C₇'s. Nevertheless, higher iso/normal ratios contribute to octane improvement in both carbon number fractions.

Relative yields per volume of feed versus the base case are shown for each carbon number in the C₅-265°F gasoline in Figure 9. This shows that the 40 S/A additive increases C₅ while reducing C₆-C₈. With 525 S/A, the C₅-C₇ stays about the same, with some reduction in C₈.

Because the octane rating in the C₅-265°F gasoline decreases with an increase in carbon number, increasing C₅'s at the expense of higher boiling components increases octane even without a change in the octane within an individual carbon number group. For the 40 S/A additive, in fact, about half the octane increase comes from this effect. Producing this shift, however, also involves a yield loss.

Most of the total gasoline yield loss, both for 40 S/A and 525 S/A, is found in the heavy gasoline (265-430°F). Table III shows this loss to be spread throughout the carbon number range of this fraction, due in large part to a reduction in paraffins as indicated by a higher ratio of aromatics to paraffins. This increased aromaticity contributes to higher octane.

Table III. 265-430°F Gasoline Composition

Additive	40 S/A	525 S/A
Carbon No. Relative to Base		
C ₈	0.950	0.966
C ₉	0.956	0.965
C ₁₀ +	0.930	0.946
Wt Aromatics/Paraffins Relative to Base		
C ₈ *	1.12	1.04
C ₉	1.14	1.06
C ₁₀	1.22	1.18

*Includes C₈ in C₅-265°F fraction.

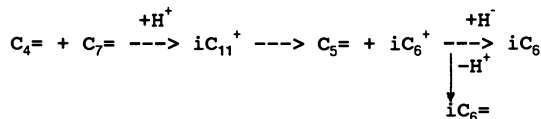
DISCUSSION

Based on the findings that the ZSM-5 additives do not catalyze much conversion of gasoline range paraffins, we conclude that they primarily work on olefins produced by the large-pore cracking catalyst. We can divide these olefins into two main groups, those that are so small, e.g., C₄-C₅, that further cracking can be neglected, and larger olefins where further cracking is significant. In looking at the first case for a C₅ olefin, for example, we consider the main reactions that can occur to the normal olefin once it has been protonated at a Bronsted site to form a normal carbenium ion.

As shown in Figure 10, one reaction is the isomerization of the normal carbenium ion. We can neglect the reverse reaction since the iso/normal olefin ratio produced over the cracking catalyst is usually well below the thermodynamic equilibrium value, due in part to depletion of the isoolefins by hydrogen transfer.

A second reaction is oligomerization with another olefin to produce a larger branched carbenium ion. Earlier work on normal

alphaolefin oligomerization over ZSM-5 type catalyst at lower temperature showed very little skeletal isomerization of the unconverted feed olefin, but substantial production of isomerized species through oligomerization and cracking (11). If the carbenium ion formed by oligomerization is larger than C_5^+ , it can then crack to form a different olefin and a branched carbenium ion, e.g.:



The MAT test with 1-pentene spiked feed did not show an increase in carbon numbers other than C_5 , leading to the conclusion that isomerization predominates over oligomerization at high temperatures, so that isoolefins come mainly from isomerization, and from cracking of larger olefins which are not products of oligomerization.

The main competing reaction to isomerization of the n-carbenium ion is its hydrogen transfer to the n-paraffin which should then be relatively unreactive. By maximizing the relative rates of isomerization to hydrogen transfer (k_i/k_H), the yield of branched products, especially branched olefins, should also be maximized.

The situation is more complex with a larger carbenium ion, for example, a C_7^+ (Figure 11). In this case, we consider not only isomerization and hydrogen transfer, but cracking as well, particularly of the iso carbenium ion to form a smaller carbenium ion and an olefin. Where the ratio of cracking rate to hydrogen transfer rate is high, the yield of branched C_7 products will be reduced, rather than enhanced, due to conversion of iC_7^+ to lower molecular weight species.

The low iso/normal C_6 - C_7 paraffin ratios observed in the MAT testing with fresh additive is then the result of iso- C_6 and - C_7 carbenium ion cracking, reducing the amount of these species available for conversion to isoparaffins by H-transfer. C_4 and C_5 carbenium ions are too small to crack, requiring the formation of a primary ion, so that C_4 and C_5 isoparaffins increase due to cracking of C_7 -plus ions. For deactivated additive, the C_6 - C_7 iso/normal ratios are higher than for the base catalyst, since the cracking activity of the additive is reduced, and since H-transfer activity for, e.g., $nC_7^+ \rightarrow nC_7$ is lower than for the base, the 525 S/A additive having less H-transfer activity than the 40 S/A.

Minimizing hydrogen transfer minimizes the formation of low octane n-paraffins. For optimum selectivity, therefore, an additive catalyst should have a high ratio of isomerization activity compared to hydrogen transfer activity. The high HTI of ZSM-5 type zeolites compared to larger pore zeolites confirms the usefulness of these zeolites as octane additives. Assuming that isomerization of the normal carbenium ion is a unimolecular reaction while H-transfer is bimolecular (13) would explain why the HTI increases with the SiO_2/Al_2O_3 ratio of the ZSM-5 type sieve.

In improving gasoline octane, cracking such as:



can improve octane, mostly by producing higher octane, lower molecular weight isoolefins, and by concentrating more refractory high octane components (i.e., aromatics) in the C_7 -plus fraction. This mechanism has the drawback, however, of reducing the liquid C_3 -plus yield. As the additive ages, this effect should diminish, particularly involving the cracking of smaller species such as C_7^+ .

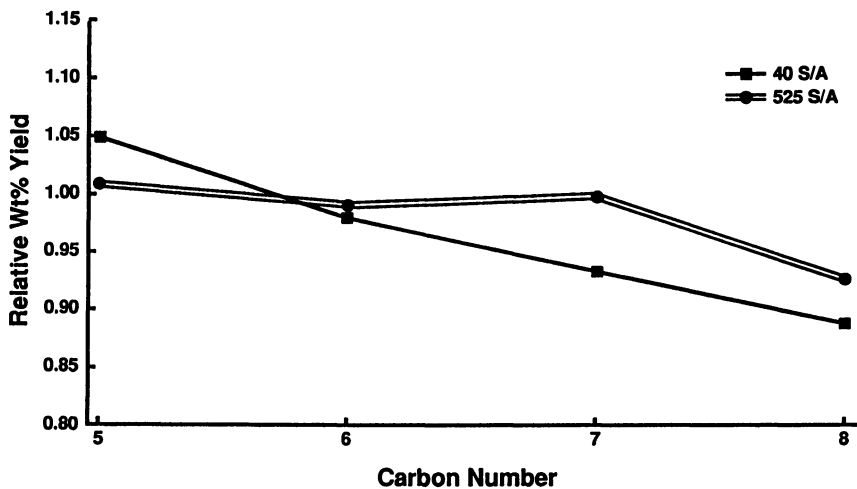


Figure 9. Relative carbon number yields in C₅-265°F gasoline versus base case in pilot plant test.

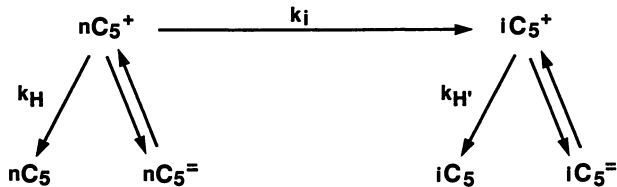


Figure 10. Normal C₅ carbenium ion reactions.

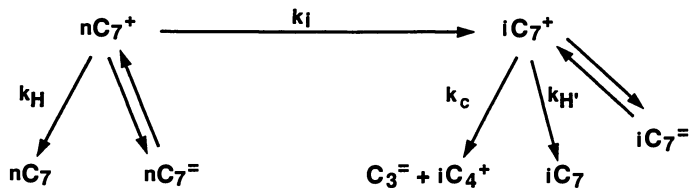


Figure 11. Normal C₇ carbenium ion reactions.

The octane upgrade will not be as great as with fresh catalyst, since a substantial fraction of the iC_7 carbenium ions will undergo H-transfer to form C_7 isoparaffins which have octane numbers lower than the rest of the gasoline. Isomerization activity will also decline during aging, but not as fast as cracking, so that there will still be formation of branched products. Since this involves no yield loss, and since the isoparaffins and isoolefins have higher octanes than their respective normals, the delta octane/% yield loss will be greater than with fresh additive.

Since the ratio of isomerization activity to H-transfer activity increases with SiO_2/Al_2O_3 ratio, the selectivity for octane enhancement will improve at higher ratios. The total octane gain per unit of additive will drop at very high SiO_2/Al_2O_3 , however, due to reduced cracking of lower octane C_7 -plus species. This factor may be offset by increasing additive concentration.

SUMMARY

FCC additives of the ZSM-5 type are effective for increasing gasoline octane due to their low activity for hydrogen transfer. Octane is increased by the cracking and isomerization of olefins produced by the base cracking catalyst. Cracking converts low octane components in the C_7 -plus gasoline partly to higher octane components of lower molecular weight, and to C_4 -minus, reducing gasoline yield. Isomerization increases the concentration of isoolefins and isoparaffins, increasing octane without yield loss. Isomerization is maximized and, therefore, yield loss minimized, as the zeolite SiO_2/Al_2O_3 ratio increases. While catalyst deactivation also improves selectivity, the advantage for a high SiO_2/Al_2O_3 ratio is retained.

Literature Cited

1. Pine, L. A., Maher, P. J., and Wachter, W. A., J. Catal., **85**, 466 (1984).
2. Anderson, C. D., Dwyer, F. G., Koch, G., and Niiranen, P., Proc. Ninth Iberoam. Symp. Catal., 247 (1984).
3. Donnelly, S. P., Mizrahi, S., Sparrell, P. T., Huss, Jr., A., Schipper, P. H., and Herbst, J. A., PREPRINTS, Div. of Petrol. Chem., ACS, **32** (3), 621 (1987).
4. Dwyer, F. G., Schipper, P. H., and Gorra, F., NPRA Ann. Mtg., March (1987).
5. Rajagopalan, K., and Young, G. W., PREPRINTS, Div. of Petrol. Chem., ACS, **32** (3), 627 (1987).
6. Miller, S. J., and Bishop, K. C. III, U.S. Patent 4,340,465 (1982).
7. Miller, S. J., U.S. Patent 4,309,276 (1982).
8. Argauer, R. J., and Landolt, G. R., U.S. Patent 3,702,886 (1972).
9. Grose, R. W., and Flanigan, E. M., U.S. Patent 4,061,724 (1977).
10. ASTM, D 3907-87, Annual Book of ASTM Standards, **503**, 733 (1989).
11. Miller, S. J., Stud. Surf. Sci. Catal., **38**, 187 (1987).
12. Haag, W. O., Lago, R. M., and Weisz, P. B., Faraday Disc., **72**, 317 (1982).
13. Chen, N. Y., and Haag, W. O., in Hydrogen Effects in Catalysis Fundamentals and Practices; Paal, Z., and Menon, P. G., Eds; Dekker: New York, p 695 (1988).

RECEIVED June 8, 1990

Chapter 8

Monitoring Fluid Cracking Catalyst Deactivation Profile by Equilibrium Catalyst Separation

R. A. Beyerlein, G. A. Tamborski, C. L. Marshall, B. L. Meyers, J. B. Hall,
and B. J. Huggins

Amoco Corporation, Naperville, IL 60566

Successful separation of a precoked, equilibrium USY cracking catalyst into fractions of increasing age reveals a deactivation profile that is largely controlled by zeolite dealumination. Precoking is found to aid the density/age separation only for the youngest fractions. The observed change in Ni/V ratio with increasing "Ni age" is indicative of vanadium migration.

Catalytic activity, assessed by cumene cracking on separated fractions and also by analysis of residual coke on catalyst fractions, shows a sharp decline with increasing density (age). This rapid loss of initial activity coincides with zeolite dealumination which is largely completed as a slow rate of zeolite destruction is established. Subsequent loss of crystallinity has little additional effect on activity. The associated loss of microporosity leads to an apparent increase in skeletal density with increasing age.

Lattice imaging studies by TEM on a "young" fraction showed extensive regions of crystallinity with minimal evidence of crystallite fracturing. By contrast, similar investigations of an "old" fraction, combined with *in situ* compositional analysis, revealed small "islands" of crystallinity within a "sea" of disordered material that was once crystalline. Fracture lines at crystallite boundaries are absent. Instead, the small USY crystallites within the "old" fraction are in intimate mixture with the collapsed zeolite.

Laboratory evaluation of fluidized-bed catalytic cracking (FCC) catalysts is critically dependent upon the method chosen to simulate catalyst deactivation in the commercial FCU.

Conventional laboratory deactivations (high-temperature steam

treatment) are typically designed to simulate only the irreversible loss of activity that results from hydrothermal deactivation of the zeolitic component in the FCC regenerator. The combination of high temperature and steam in the regenerator causes framework dealumination (rapid) and crystalline zeolite destruction (slower). Dealumination both lowers activity and produces important changes in selectivity, while zeolite destruction leads primarily to a loss in activity.

Zeolite destruction is slower for dealuminated zeolites which have increased hydrothermal stability, but is accelerated by deposition of metals, particularly vanadium and sodium from the feed. In addition, these metals are powerful poisons which neutralize acid sites, thereby reducing activity and compromising selectivity. Nickel species, which accompany vanadium as feed contaminants, are powerful dehydrogenation catalysts and lead to increased production of hydrogen and coke with reduced gasoline yields. All of this is complicated by the fact that the circulating equilibrium catalyst inventory in the FCU contains a wide spectrum of ages and levels of deactivation, owing to the 1% to 3% daily fresh catalyst make-up rate.

Laboratory steam deactivations represent a significant compromise in the effort to simulate equilibrium catalyst. Since hydrothermal deactivation of FCC catalysts is not rapid in commercial practice, deactivation of the fresh catalyst in the laboratory requires accelerated techniques. The associated temperatures and steam partial pressures are often in substantial excess of those encountered in commercial units. In some instances, the effect of contaminant metals is measured by an independent test not affiliated with steam deactivation. In subsequent yields testing, interactions between different modes of deactivation may be overlooked. Finally, single mode deactivation procedures can not reproduce the complex profile of ages and levels of deactivation present in equilibrium catalyst.

Density Separation of Precoked Catalyst. In order to monitor and understand catalyst deactivation in the commercial unit and to supply guidance for developing improved laboratory deactivation procedures, we have carried out a separation by density of equilibrium cracking catalyst from an Amoco FCU. The density separation is based, in part, on the activity of the equilibrium catalyst for coke deposition from isobutene. Each catalyst particle develops a coke level proportional to its intrinsic activity level. The coked catalyst particles are then separated into fractions by immersion in progressively more dense mixtures of carbon tetrachloride and tetrabromoethane. Since coked particles exhibit lower skeletal density, the higher activity and presumably younger catalyst particles are sequestered into the lighter fractions. A recent report (1) indicates that this separation method produces fractions of increasing age, the heaviest fractions being the oldest. In the present work, it is found that the separation by density is based only in part on differences in coking activity.

Measured Ni levels on catalyst are expected to supply an independent age marker, as it has been shown that Ni tends not to migrate following deposition on the catalyst (2). In fact, metals (Ni and V) deposition from the feed onto the catalyst is expected to assist the separation by density/age/activity as older catalyst particles exhibit higher metals levels which contribute to an increase in density. Except for the oldest fractions, which contain the highest metals levels, the older portion of catalyst tends to make less coke as the increase in activity due to increasing metals content is overwhelmed by the loss of activity due to crystalline zeolite destruction (1).

The present study shows that only the youngest, most active fractions are density-separated on the basis of activity for coking from isobutene. For the majority of the separated fractions, the gradual increase in skeletal density with increasing age (Ni level) appears to be associated with the gradual loss of zeolite crystallinity that occurs with increasing time in the unit.

Catalyst History

Catalyst Changeover, Metals Content. The equilibrium sample of a USY octane catalyst, Catalyst A, was withdrawn from an Amoco FCU. Results of metals analyses on the equilibrium catalyst and on its parent are given in Table I. Catalyst A was introduced to the unit during a five-month period over Catalyst B, which was identical to Catalyst A in all respects, except for a low level of contaminant rare earth. Catalyst B had, in turn, been introduced over a rare earth-containing catalyst, Catalyst C, eight months prior to withdrawal of the equilibrium sample. Catalyst history and rare earth contents are summarized in Table II.

Table I. Equilibrium and Fresh USY Catalyst Inspections*

Elemental		Fresh Catalyst A	Equilibrium Catalyst A
Ni, ppm	(XRF)	30	570
Fe	(XRF)	2140	3110
V	(XRF)	<200	440
Sb	(XRF)	<30	80
Nd	(XRF)	<300	310
Ce	(XRF)	<100	360
La	(XRF)	<100	740
Rare Earth	(XRF)	<500	1410
Ti	(XRF)	4900	5600
Na, ppm	(AA)	1360	1430
Si, wt%		29.8	30.4
Al, wt%		15.3	20.4

*All catalysts calcined at 538°C for five hours.

The unit cell dimension of fresh Catalyst A is 24.40 Å.

Table II. Rare Earth Material Balance and Feedstock Contaminant Metals Material Balance on Equilibrium Catalyst

From	To	Rare Earth on Equil., Wt%
Catalyst B	Catalyst A	0.55
Catalyst C	Catalyst B	0.85

Catalyst A--USY octane catalyst.

Catalyst B--USY octane catalyst with low levels of rare earth contamination (0.5 wt%).

Catalyst C--Rare-earth-containing (REY) catalyst.

Estimated changeover based on rare earth material balance = 88%

Fresh Catalyst Addition Rate (see text): 2% of inventory/day

Contaminant Metals on Feedstock:

Metals in Feedstock, ppm: Ni = 0.7
V = 0.5
Fe = 1.2

Metals Laydown, lb/day: Ni = 5.57
V = 3.98
Fe = 8.76

Metals on Catalyst/Day, ppm: Ni = 11.1
V = 8.0
Fe = 17.4

During the five months of operation with the zero rare earth octane catalyst, the effective fresh catalyst addition rate, after correction for catalyst loss from the unit as fines, was about 5 tons/day. Based on a rare earth material balance (Table II) that was used to give the best estimate of pedigree, the equilibrium sample consists of 88% USY octane catalyst. The remaining 12% should be a mixture of the prior two catalysts, the first of which contains a contaminant rare earth level of 0.5 wt% versus 0.1 wt% for the octane catalyst. The balance of this mixture is the rare earth-Y catalyst from the previous changeover which exhibits a rare earth level of 0.85 wt% (Table II).

Feedstock Metals, Catalyst Age. Monthly FCU operating reports for the FCU indicate that average unit throughput during Catalyst A usage was fairly constant. Feedstock metals levels averaged 1.2 ppm Fe, 0.7 ppm Ni, and 0.5 ppm V during the two months preceding withdrawal of the equilibrium sample. From these data a metals balance can be constructed, as shown in Table II.

The utilization of nickel level on catalyst as an age marker is based on previous evidence that nickel deposits uniformly on the circulating catalyst inventory, independent of catalyst activity (1.2). In contrast to the case for nickel, vanadium

migration is known to occur at regenerator conditions (1,2). Therefore, the vanadium level cannot be used as an age marker. Nickel deposition rate was, on average, 5.57 lb/day or 11.1 ppm on catalyst/day. Observing that the overall nickel level on catalyst is 570 ppm (Table I), the average inventory age is about 50 days.

Experimental Method

Coking of Equilibrium Catalyst. A 200 g portion of equilibrium USY octane catalyst (Catalyst A) was precoked in a fluidized bed using a stream of isobutene diluted with nitrogen gas (400 ml/min) at 510°C. The catalyst was held in a 2-inch diameter quartz tube while 27.8 g of isobutene gas was passed upflow through it at atmospheric pressure over a period of 25 minutes. The net amount of carbon deposited on catalyst was determined to be 0.55 wt%.

Separation Method. Trial experiments with small portions of the coked catalyst in progressively more dense mixtures of carbon tetrachloride ($d = 1.594$ g/cc) and 1,1,2,2-tetrabromoethane ($d = 2.967$ g/cc) showed that the lightest catalyst fractions exhibited a density of about 2.3 g/cc. A solvent mixture with $d = 2.33$ g/cc was prepared from a mixture of 46.4 ml of carbon tetrachloride and 53.6 ml of tetrabromoethane. A 20 g portion of coked catalyst was placed in a 120 ml quantity of this solvent mixture in a 250 ml Teflon centrifuge bottle. The mixture was thoroughly agitated for several minutes and then placed in a centrifuge at 3,600 rpm for 30 minutes. Upon removal from the centrifuge, the mixture was allowed to stand for several hours in order to obtain well-defined float and sink fractions. Apparently, the catalyst was redispersed to some extent by the slowing and braking of the centrifuge. In these procedures, the centrifuge is viewed merely as an additional means to obtain equilibrium of the catalyst with the solvent. Each float fraction was removed in several installments using a vacuum pipette. Introduction of the vacuum pipette dispersed some of the float fraction into the solvent. Complete removal of a float fraction required two to four installments separated by 30 to 60 minutes to allow gravity separation. Following removal of a float fraction, a 10 ml quantity of solvent was withdrawn by syringe in order to determine the solvent density by pycnometer. At least two pycnometer measurements were made in each case. Net solvent loss was determined by comparing centrifuge bottle mass before and after float fraction withdrawal. Using a 10 ml syringe and a precision balance, an equivalent mass solvent mixture was prepared at a density chosen so that, upon addition to the catalyst/solvent slurry, a net increase in solvent density of $\Delta d \approx 0.02$ g/ml was obtained. (The incremental change in density was increased for the later (heavier) fractions, which exhibited less pronounced density gradients.) The centrifuge bottle remained capped except for float fraction withdrawal and solvent addition in order to avoid

preferential loss of carbon tetrachloride by evaporation. The above procedures were repeated to obtain a total of seven float fractions and a final sink fraction within an overall density range of 2.3 to 2.6 g/ml.

Residual solvent was washed from each float fraction by soxhlet extraction with methanol for a period of one to two hours. Each catalyst fraction was then dried in a 50°C vacuum oven for at least three hours. Except for the smallest float fractions, fresh methanol was used for each fraction to avoid contamination of the rinse with high levels of the tetrabromoethane/carbon tetrachloride mixture. The separation procedures just described were also applied to fresh Catalyst A and to a portion of this catalyst which had been steam deactivated at 815°C. No precoking was carried out for these materials.

Analysis of Fractions. Surface areas and pore size distributions for both coked and regenerated catalyst fractions were determined by low temperature (Digisorb) N₂ adsorption isotherms. Relative zeolite (micropore volume) and matrix (external surface area) contributions to the BET surface area were determined by t-plot analyses (3). Carbon and hydrogen on catalyst were determined using a Perkin Elmer 240 C instrument. Unit cell size and crystallinity for the molecular zeolite component were determined for coked and for regenerated catalyst fractions by x-ray diffraction. Elemental compositions for Ni, Fe, and V on each fraction were determined by ICP. Regeneration of coked catalyst fractions was accomplished in an air muffle furnace heated to 538°C at 2.8°C/min and held at that temperature for 6 hr.

Cumene Cracking Reactions on Separated Fractions. Cumene cracking reactions were tested on a gravimetric setup; the basic flow diagram for the reactor system is shown in Figure 1. The reactor determines both the activity of the catalyst (cracking of cumene to benzene and propylene) and the instantaneous rate at which coke is deposited on the catalyst (polymerization of the propylene). Conversion of the cumene is adjusted to exclude the amount of cumene disproportionation which yields benzene and diisopropyl benzene.

Correlation of Equilibrium Catalyst Fraction Properties with Fraction Density/Age

Coke Deposition. The properties of catalyst fractions separated in coked condition from spent equilibrium catalyst are summarized in Tables III and IV. The distribution of catalyst fractions along with the percent carbon found on each coked fraction is given in Figure 2. The activity for coke deposition falls off sharply with increase in density. Only the three lightest fractions show a coke make that is significantly above the minimum coke make exhibited by the heavier fractions. The fact that the lightest fractions are the most active is consistent with the notion that they are the youngest. The distribution of catalyst

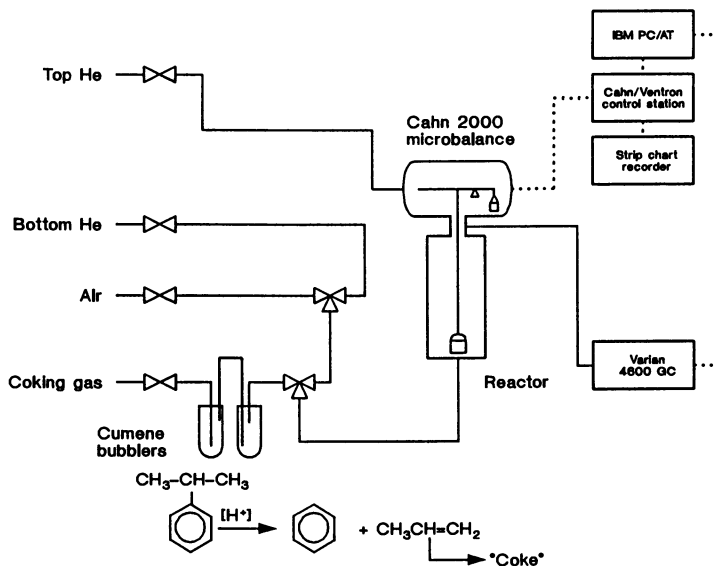


Figure 1. Gravimetric reactor used in cumene cracking studies.

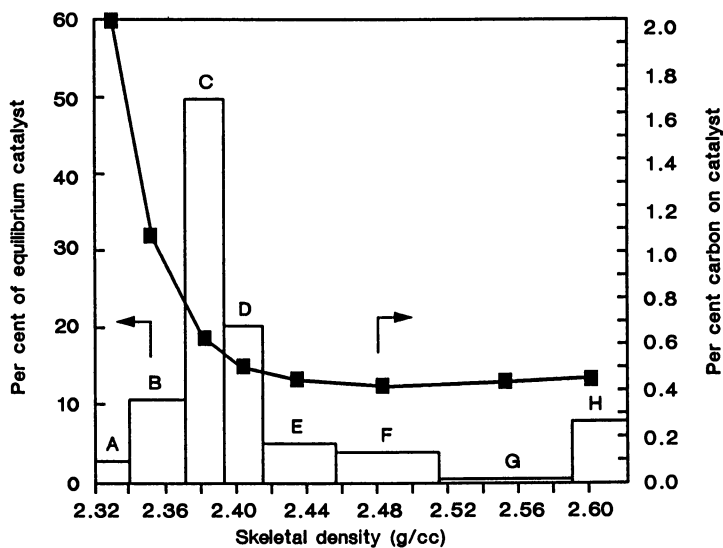


Figure 2. Distribution of catalyst fractions--carbon content on coked fractions.

Table III. Properties of Equilibrium Catalyst Fractions

Catalyst Fraction	Density Limit, g/cc	Median Density, g/cc	% of Total	% C	ppm Ni	ppm V	ppm Fe
Float A	<2.340	2.330	2.6	2.00	161	206	3070
Float B	<2.371	2.355	10.3	1.06	188	234	2680
Float C	<2.393	2.382	50.0	0.62	330	339	2340
Float D	<2.415	2.404	20.2	0.49	670	434	2950
Float E	<2.457	2.436	4.8	0.43	992	612	3560
Float F	<2.514	2.486	3.8	0.41	905	612	5520
Float G	<2.588	2.551	0.7	0.42	.	.	.
Sink H	>2.588	2.604	8.1	0.44	1910	1180	7000

	ppm Ti	ppm RE	ppm Na	BET S.A. (coked)	BET S.A. (regen)	Unit Cell Å	% Cryst. micropore volume	% Cryst. XRD
Flt. A	5060	.	1710	181	213	24.31	28.0	24
Flt. B	3850	232	1680	207	219	24.27	27.0	26
Flt. C	5200	455	1320	206	208	24.26	25.0	25
Flt. D	4750	975	1530	190	192	24.24	22.0	23
Flt. E	6580	232	1710	162	160	24.26	18.0	16
Flt. F	6050	1551	1730	117	118	24.28	13.0	13
Flt. G	.	.	.	95	92	24.33	10.0	7
Sink H	11380	6790	1040	83	82	.	2.6	5

fractions is sharply peaked about a density $d = 2.38$ g/cc, with 80% of the catalyst occupying a density range 2.34 to 2.42 g/cc.

Cumene Cracking Activity. Portions of each of the first five separated fractions were regenerated and subjected to cumene cracking investigations in order to determine relative acidity and coke selectivity trends. The catalyst within the thermogravimetric reactor was exposed to a constant flow of cumene vapor at 400°C. Coke buildup on catalyst was continuously monitored by gravimetry, while converted products in the effluent stream were analyzed at regular intervals by gas chromatography (Figure 1). The results for net coke on catalyst at constant conversion (25%) given in Table V-A show a steady decrease in coke on catalyst for increasingly dense fractions. These results are consistent with those for residual carbon on catalyst just discussed. The lighter fractions prove to be the most active ones, while the heavier, less active fractions make proportionally less coke. "Coke selectivity", defined as the ratio conversion/coking, increases with increasing density in agreement with the expected trend for USY catalyst fractions of increasing age.

Table IV. Digisorb Analyses of Coked and Regenerated Equilibrium Catalyst Fractions

Catalyst Fraction	Density Limit, g/cc	Median Density, g/cc	% of Total	BET SA m ² /g	Cum Por Vol., cc/g	Avg Pore Radius, Å	Micropore Volume, cc/g	Micropore Area, m ² /g	Micropore Matrix Area, m ² /g
Float A	<2.340	2.330	2.6	181	0.13	64	0.060	125	56
Regen A	<2.340	2.330	2.6	213	0.13	66	0.075	156	56
Float B	<2.371	2.355	10.3	207	0.14	55	0.069	144	63
Regen B	<2.371	2.355	10.3	219	0.14	56	0.073	151	68
Float C	<2.393	2.382	50.0	206	0.14	55	0.067	138	68
Regen C	<2.393	2.382	50.0	208	0.12	45	0.067	138	69
Float D	<2.415	2.404	20.2	190	0.14	62	0.060	124	66
Regen D	<2.415	2.404	20.2	192	0.15	71	0.060	124	68
Float E	<2.457	2.436	4.8	162	0.15	110	0.049	102	59
Regen E	<2.457	2.436	4.8	160	0.15	111	0.048	99	62
Float F	<2.514	2.486	3.8	117	0.13	154	0.036	75	42
Regen F	<2.514	2.486	3.8	118	0.14	148	0.035	72	46
Float G	<2.588	2.551	0.7	95	0.09	154	0.030	62	33
Regen G	<2.588	2.551	0.7	92	0.09	104	0.026	53	39
Sink H	>2.588	2.604	8.1	83	0.19	91	0.009	19	64
Regen H	>2.588	2.604	8.1	82	0.19	84	0.007	15	67

Float = Coked

Table V. Cumene Cracking Results on Equilibrium Catalyst Fractions^a

<u>A. Net Coke Content and Coke Selectivity at Constant Conversion (25%)</u>		
Catalyst Fraction	Corrected ^b Wt% Coke (wt%)	"Coke" ^c Selectivity" (conv/coke)
Float A	1.50	17
Float B	1.15	22
Float C	0.26	96
Float D	0.25	100
Float E	0.0	--

B. Conversion at Constant Coke (0.25 wt%)

<u>Catalyst Fraction</u>	<u>Conversion (%)</u>
Float A	45
Float B	43
Float C	25
Float D	25
Float E	7

^a Conditions 400°C, 50 mg catalyst.

^b Corrected wt% coke on catalyst = (wt% coke at time t) - (wt% coke at t = 15 minutes)

^c An increase in "coke selectivity" implies a reduced tendency for coking.

The difference in activity among the separated fractions is demonstrated by the steady drop in coke make at constant conversion with increasing density/age (Table V-A). The anticipated drop in activity with age is demonstrated from a complementary way of presenting the cumene cracking data, specifically, the results for conversion at constant coke make (0.25 wt%) given in Table V-B. The conversion level shows a steady decrease from a maximum of 45% for the first (youngest) fraction (A) to only 7% for the fifth fraction (E).

Metals Deposition/Catalyst Age. The metals on catalyst results given in Figure 3a indicate that the separation by density is equivalent to a separation by age. The nickel level on each catalyst fraction exhibits a monotonic increase with increasing density. The dramatic decrease exhibited by the ratio V/Ni with increasing catalyst density/age (Figure 3b) comprises indirect evidence for interparticle vanadium migration. The ratio V/Ni (ppm on catalyst) is highest for the younger (lighter) particles due to a net migration of vanadium from the older particles with

high metals levels. The oldest particles exhibit a metals ratio $V/Ni = 0.65$, which is comparable to but slightly lower than that characteristic of the feed, $V/Ni = 0.71$ (Table II). Indirect evidence for interparticle vanadium migration in the steam regenerator has been cited previously (1,2).

Inspection of the feed records for the FCU from which Catalyst A was removed shows no significant variation of the nickel content in the feed during the period of catalyst residence. Therefore, the nickel content on each catalyst fraction can be used to estimate a fraction age. Application of a linear regression analysis to the Ni content data given in Figure 3a (Fractions A-F) shows that the trend for increasing nickel content with increasing density is given by:

$$Ni \text{ (ppm)} = (d_m - 2.32) \times 6470 + 30 \quad (1)$$

where d_m is the median density (g/cc) for each fraction (Tables III and IV). Since the low density limit of the first fraction, A, is 2.32 g/cc, and the Ni content of fresh catalyst is 30 ppm (Table I), the linear regression analysis was constrained to pass through $Ni \text{ (ppm)} = 30$ at $d_m = 2.32$ g/cc. The quantity $(Ni \text{ (ppm)} - 30 \text{ ppm})$ determined from Equation 1 represents the accumulated Ni level on catalyst due to deposition from the feed. The estimated age distribution which results upon division of this quantity by the rate of Ni deposition on catalyst, 11.1 ppm/day (Table II), is as follows:

Fraction A -- 6 days
 Fraction B -- 26 days
 Fraction C -- 36 days
 Fraction D -- 49 days
 Fraction E -- 68 days
 Fraction F -- 97 days
 (Sink) Fraction H -- 169 days

Surface Area/Micropore Volume Loss for Equilibrium Catalyst: Comparison with Results of Surface Area, Micropore Volume Loss During Catalyst Deactivation. The total BET surface areas and the micropore areas are given for coked and for regenerated catalyst fractions in Figure 4 and Table IV (total BET surface area equals micropore surface area plus matrix surface area). The surface area values for coked fractions differ significantly from those for regenerated fractions only for the first two fractions, consistent with the carbon on catalyst results given in Figure 2. For the second and succeeding fractions, there is a systematic decrease in micropore area with increasing density. In consideration of the evidence just discussed for an association of increasing density with increasing fraction age, this result reflects the occurrence of increasing destruction of the crystalline zeolite with increasing time in the unit. For comparison, results of XRD, porosity, and surface area analyses for the fresh parent of Catalyst A, and for portions of this

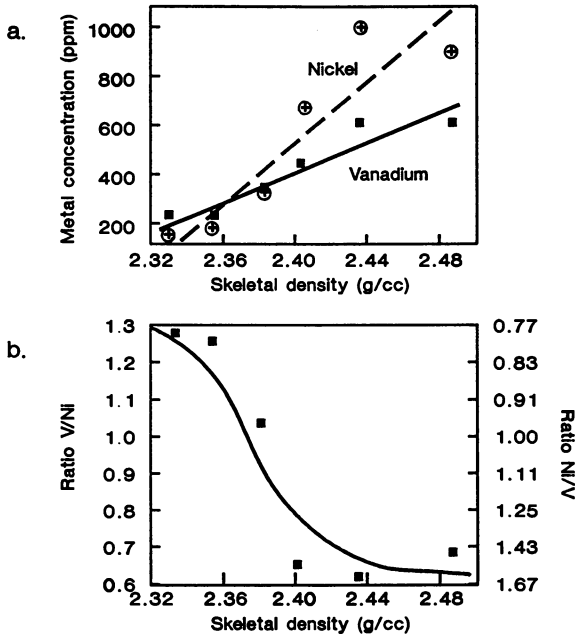


Figure 3. (a) Nickel and vanadium concentrations on separated catalyst fractions, and (b) V/Ni ratio for separated catalyst fractions.

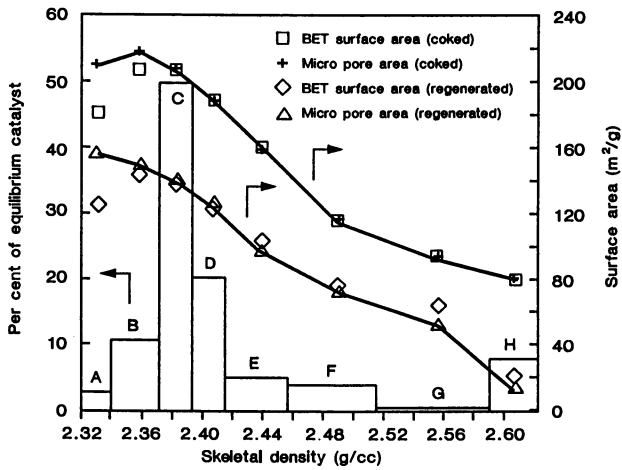


Figure 4. BET and micropore surface areas for coked and regenerated catalyst fractions shown together with distribution of catalyst fractions versus density.

catalyst that have been steam deactivated for different times at temperatures in the range 700°C-815°C are given in Table VI. The materials steamed at temperatures in the range 760°C to 815°C show a change in physical properties similar to those exhibited by Fractions A-D of the equilibrium catalyst (Table VII). XRD unit cell sizes, micropore and matrix surface areas, and total pore volumes are comparable, and a decrease in micropore volume/area of about 20% is observed for each set of materials. These results indicate that single mode deactivation provides a poor simulation of catalyst aging in the FCU.

The fact that the micropore area for regenerated catalyst fractions decreases monotonically with increase in density supplies an additional clue about the nature of this separation. Except for equilibrium catalyst fractions A, B, and C, for which residual coke on catalyst changes with density (Figure 2), the separation by density cannot be associated with activity for coke formation from isobutene. For Fraction C and succeeding fractions, the increase in catalyst density is strongly correlated with a decrease in the crystalline, microporous zeolite component (Figure 4, Table IV). The loss of micropore volume dominates the decrease in total surface area with increasing time in the unit. The external or matrix surface area shows no significant decrease until after the fourth fraction and then exhibits only a slow decrease in comparison to the rate of loss of micropore area/volume (Figure 4 and Table IV).

Density of Steam Deactivated vs. Fresh Catalyst. The results of density measurements on the fresh parent of Catalyst A and on a portion of this catalyst that has been steam deactivated at 815°C for five hours (Table VIII) indicate a direct connection between the loss of crystalline microporous zeolite and increase in catalyst density. The major portion (67%) of the fresh catalyst is found in the density range $2.330 \leq d \leq 2.355$ g/cc. By contrast, the major portion (87%) of the steam deactivated catalyst is found in the density range 2.372 to 2.394 g/cc.

Table VI. Properties of Fresh and Steam Deactivated Catalyst A

Steam Treatment	Unit		% Cryst XRD	% Cryst micropore volume	BET SA m ² /g	Cum Pore Volume cc/g
	Cell Å	% Cryst				
Fresh	24.40	35	34	281	0.15	
704°C, 2-hr	24.33	31	30	249	0.15	
760°C, 2-hr	24.30	31	30	236	0.14	
788°C, 5-hr	24.26	28	28	224	0.15	
815°C, 5-hr	24.21	25	24	199	0.14	
815°C, 24-hr	24.24	20	21	169	0.15	

Steam Treatment	Avg. Pore Radius, Å	Micropore Volume cc/g	Micropore Area m ² /g	Matrix Area m ² /g
Fresh	33	0.091	188	93
704°C, 2-hr	44	0.082	170	79
760°C, 2-hr	51	0.080	164	71
788°C, 5-hr	58	0.076	157	67
815°C, 5-hr	71	0.066	138	61
815°C, 24-hr	51	0.057	117	52

Table VII. Comparison of Lab-Steamed Catalyst with Equilibrium Fractions

Lab-Steamed Catalyst; Steam-Treat Conditions	Unit Cell \AA	Micropore area m^2/g	Matrix area m^2/g	% Cryst* Relative to Fresh
760°C, 2-hr	24.30	164	71	87
788°C, 5-hr	24.26	157	67	84
815°C, 5-hr	24.21	138	61	73
815°C, 12-hr	24.24	130	60	69
815°C, 24-hr	24.24	117	52	62

Equilibrium Catalyst Fraction	Unit Cell \AA	Micropore area m^2/g	Matrix area m^2/g	% Cryst* Relative to Fresh
A	24.31	156	56	83
B	24.27	151	68	80
C	24.26	138	69	73
D	24.24	124	68	66
E	24.26	99	62	53
F	24.28	72	46	38

*On the basis of micropore volumes

Table VIII. Density Separation of Fresh (F) and 815°C Steamed (S) Catalyst A: Properties of Separated Catalyst Fractions

Catalyst Fraction	Density Limit, g/cc	Median Density, g/cc	% of Total	Unit Cell Å	% Cryst XRD
F, Float A	<2.320	2.330	33.0	24.41	37
F, Float B	<2.355	2.342	67.0	24.40	35
S, Float A	<2.372	2.362	8.1	24.23	26
S, Float B	<2.394	2.383	87.0	24.23	22

Catalyst Fraction	BET SA, m ² /g	Cum Pore Volume, cc/g	Avg Pore Radius, Å	Micropore Volume, cc/g	Micropore Area, m ² /g	Matrix Area, m ² /g
F, Flt A	270	0.14	32	0.087	179	91
F, Flt B	268	0.14	30	0.082	169	99
S, Flt A	204	0.13	76	0.071	146	58
S, Flt B	204	0.18	59	0.058	119	85

It is observed (Table VI) that a reduction in micropore volume of more than 27% occurs as a result of steam deactivation at 815°C for five hours. In the discussion which follows, it is shown how destruction of crystalline zeolite with the concomitant loss in micropore volume leads to increased accessibility by the solvent, which manifests itself as an effective increase in skeletal density.

The heavier portion of the fresh and laboratory steamed catalyst (Float B) exhibits a decreased micropore volume with respect to the lighter portion (Float A), suggesting that the density fractionation within each catalyst reflects the presence of a finite range of zeolite crystallinities. Particularly for the fresh catalyst, this inhomogeneity is small (Table VIII).

Solvent Accessibility in Zeolitic Portion-Influence of Excluded Volume

Micropore Structure and Solvent Accessibility. Loss of micropore volume is expected to lead to an increase in measured catalyst density owing to excluded volume effects and to imperfect packing of the two solvent molecules, particularly tetrabromoethane, inside the zeolite cages. The micropore volume associated with the faujasitic zeolite component of the catalyst is composed of a three-dimensionally connected system of large cages (supercages) and small cages (sodalite units and double six-ring prisms), as shown in Figure 5a.

The large cages (supercages) are accessed through 12-membered oxygen rings which define a pore opening of about 7.6 Å. Carbon tetrachloride with an effective diameter of about 5.8 Å (4) is readily admitted. Using molecular modeling (5), the effective

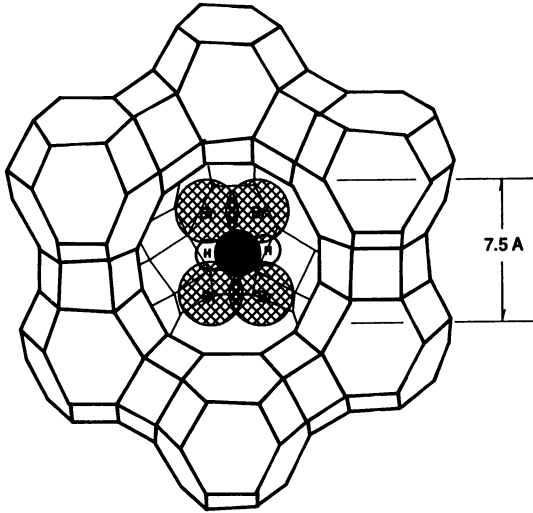


Figure 5a. Three-dimensionally connected system of large and small cages in zeolite Y (faujasite) showing 1,1,2,2-tetrabromoethane inside a large cage.

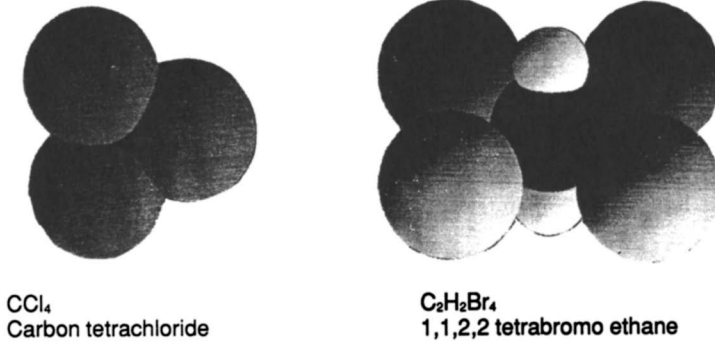


Figure 5b. Molecular graphics representation of carbon tetrachloride and of 1,1,2,2-tetrabromoethane.

diameter of 1,1,2,2-tetrabromoethane was estimated to be about 7.5 Å (see Figure 5b), roughly equivalent to the size of the window opening. Any constriction of these apertures associated with occluded alumina or with metals deposition might lead to a partial or total exclusion of tetrabromoethane. More pronounced pore plugging could lead to exclusion of carbon tetrachloride as well.

The small cages are accessed through six-membered rings with an effective pore opening of only about 2.8 Å and are inaccessible, not only to both solvent molecules, but also to N₂ molecules (4) during collection of the low temperature nitrogen isotherm data that is used to determine micropore volume. These small cages do admit small polar molecules such as H₂O and NH₃. Comparison of water uptake with uptake of nitrogen or normal paraffins shows that these small cages comprise about 12% of the total micropore volume (6).

Factors Leading to Density Variation. Summarizing, the factors which lead to an increase in measured catalyst density with increasing age are categorized as follows: 1) decreased activity for coke deposition, 2) increasing metals deposition, 3) excluded volume associated with the small zeolite cages, 4) excluded volume associated with imperfect packing of tetrabromoethane and of carbon tetrachloride in the supercages, 5) preferential adsorption of carbon tetrachloride associated with imperfect packing of the bulky tetrabromoethane molecule inside the supercages, and 6) pore mouth constrictions that lead to partial or complete pore mouth plugging. The size of Factors 1 and 2 may be readily estimated from the analytical data given in Tables III and IV. The contribution from the excluded volume associated with the small cages, Factor 3, is also readily estimated. An effective contribution from Factors 4 and 5, modeled as an excluded volume effect, can be estimated on the basis of the observed density difference between fresh and steamed catalyst (Table VIII).

Quantitative Estimates of Density Variations. Quantitative estimates of the relative contribution of Factors 1-5 to changes in catalyst density are given in Table IX. In carrying out these calculations, the average skeletal density of coke on catalyst was taken to be 1.2 g/cc (Appendix A). Nickel, vanadium, and rare earth were assumed to be present as the oxides NiO, V₂O₄, and RE₂O₃ with densities of 6.7, 4.3, and 6.9, respectively. Similar assumptions were made for iron and titanium (Appendix A), but the effect of Fe and Ti was included only for the heavier Fractions E, F, and H, which exhibited increased levels of these two metals (Table III). For the float Fractions A-F, this approach, based on bulk oxide densities, is expected to overestimate the density increase due to metals that are present as well-dispersed species.

However, the contribution to density increase from metals tends to be small for these fractions (Table IX). For the sink Fraction H, which has low surface area, low zeolite content, and high metals levels (Tables III and IX), high metals dispersion, particularly for Fe, Ti, and RE, is unlikely.

Table IX. Estimate of Relative Contribution of Factors Affecting Density Change

Catalyst Fraction	Micropore Volume cc/g	Δ (Mpore Volume) cc/g	Δ (Ni+V) ppm	Δ RE ppm	Δ Carbon wt%
Regen A	0.075			.	
Regen B	0.073	-0.002	55	.	-0.94
Regen C	0.067	-0.006	247	223	-0.44
Regen D	0.060	-0.007	435	520	-0.13
Regen E	0.048	-0.012	500	.	-0.06
Regen F	0.035	-0.013	-87	576	
Regen G	0.026	-0.011		.	
Sink H	0.007	-0.019	1530	5239	

Catalyst Fraction	Ad Contribution x 100				Net Δd g/cc
	Δ Mpore excl vol	Δ (Ni+V)	Δ RE	Δ C	
Regen A
Regen B	0.30	0.01	.	2.24	0.026
Regen C	0.90	0.05	0.04	1.05	0.020
Regen D	1.05	0.08	0.10	0.31	0.015
Regen E	1.79	0.10	.	0.14	0.024(a)
Regen F	1.94	.	0.11	.	0.024(b)
Regen G	1.64
Sink H	2.84	0.29	0.96	.	0.051(c)

From the data given in Table III,

- (a) Float E exhibits an Fe concentration that is 800 ppm greater than the average for A-D. The resultant contributions to density are $\Delta d(\text{Fe}) + \Delta d(\text{Ti}) = 0.0015 + 0.0024 = 0.0039$ g/cc. For Fraction E, the net $\Delta d(\text{E}) = 0.0179 + 0.001 + 0.0014 + 0.0039 = 0.024$ g/cc.
- (b) Similarly, for Float F, $\Delta d(\text{Fe}) + \Delta d(\text{Ti}) = 0.0037 + 0$, and $\Delta d(\text{F}) = 0.0205 + 0.0037 = 0.024$ g/cc.
- (c) Similarly, for Sink H, $\Delta d(\text{Fe}) + \Delta d(\text{Ti}) = 0.0028 + 0.0069$, and $\Delta d(\text{H}) = 0.041 + 0.012 = 0.051$ g/cc.

In order to estimate the density increase associated with loss of micropore volume, the contribution from the large cages was "calibrated" using the comparative data on fresh and steamed catalyst given in Tables VI and VIII. Steam treatment of the fresh catalyst at 815°C for five hours resulted in an increase in

average density of $\Delta d \approx 0.04$ g/cc and an associated decrease in (large cage) micropore volume from 0.091 to 0.066 cc/g. Calculations given in Appendix A show that about 30% of the measured density increase is contributed by Factor 3, the excluded volume associated with the small cages. The large cage packing fraction that is required to account for the balance of the density increase is found to be 67%, or equivalently, a 33% excluded volume. It is shown in Appendix A that, for a given packing fraction, selective adsorption of the lighter component, carbon tetrachloride, would lead to a decrease in this estimated packing fraction with a parallel increase in the size of the excluded volume.

For the first six catalyst fractions (A-F), the estimated net change in density (net Δd (est)) ≈ 0.11 g/cc, Table IX) is 70% of that actually observed ($\Delta d \approx 0.16$ g/cc, Table III and Figure 1). The estimated Δd 's given in Table IX indicate that coke on catalyst dominates the density separation only in the case of the separation of Fraction A from Fraction B. For separation of Fraction B from Fraction C, the effect of loss of micropore volume is comparable to that of decreased coke make, while for succeeding fractions, density increase is due primarily to the combined effects of loss of micropore volume and increasing metals levels.

The estimates in Table IX represent the minimum effect of the loss of micropore volume. Pore-mouth constrictions which lead to partial or complete micropore plugging would serve to increase the contribution of loss of micropore volume to density change. No such pore plugging is expected to occur in the (mesoporous) catalyst matrix or in the mesoporous material that is generated during crystalline zeolite destruction.

It is possible to attribute the net difference between the calculated and the observed density range to micropore plugging. Recasting the calculations given in Appendix A show that this would require reducing the overall packing fraction for the large cages from 67% to 31%. This result suggests a tendency for the zeolite to selectively adsorb the lighter component, carbon tetrachloride, which would result in smaller estimated packing fractions.

Density Variations for the Heaviest Fractions--Remnant Rare Earth Catalyst. The estimated density variations given in Table IX show that the relatively high density exhibited by the sink Fraction H is associated with the high concentrations of metals present in this fraction (Table III). The high concentration of rare earth in Fraction H, 0.68 wt%, indicates that it is composed entirely of the old catalyst(s) present in the unit at changeover (see Table II). By comparison, float Fraction F, with a rare earth content of 0.16 wt%, includes an admixture of about 20% of the prior catalyst(s). The presence of the prior rare earth-containing catalyst (Catalyst C, Table II) in the heaviest Fractions F, G, and H is also indicated by the increase in unit cell size exhibited by these fractions (Table III). Recalling that the changeover for the equilibrium catalyst of this study is

88% complete (Table II), these results show that the major portion of the remnant rare earth-containing catalyst(s) is sequestered into the heaviest fractions G and H.

Deactivation Profile

Rate of Dealumination Compared with Rate of Zeolite Destruction.

The results developed earlier for the nickel age of each catalyst fraction can be used to quantify and compare the rate of zeolite dealumination with that for zeolite destruction. Upon introduction of the catalyst to the FCU unit, the unit cell dimension decreases from 24.40 angstroms to 24.31 angstroms (Fraction A), indicating that about half of the original framework aluminum content (Z) is lost in the first six days. Dealumination is largely complete for Fraction B (26 days residence), with $a_0 = 24.27$ angstroms representing retention of about 20% of the original framework aluminum content (Z). Framework aluminum loss continues at a slower rate for the third and fourth fractions, which exhibit unit cell dimensions of 24.26 and 24.24 angstroms, indicating that almost 90% of the original framework aluminum content has been lost (Z).

Loss of micropore area/zeolite crystallinity is a slow process in comparison with dealumination. Following an initial decline in micropore area of 17% upon catalyst addition (Tables IV, VI), zeolite micropore area/crystallinity decreases by only an additional 3% over the next 26 days (Fraction B, Table IV, Figure 4), by which time dealumination is largely complete. There follows a steady rate of zeolite destruction which results in an additional 42% loss of crystalline zeolite (relative to fresh catalyst) over the next 80 days (see Figure 4, Fractions B-F). Fraction F, representing the end point of the USY catalyst distribution, retains only 38% of the crystallinity characteristic of fresh catalyst. Fractions A-D, representing the major portion of this equilibrium catalyst, exhibit relative crystallinity retentions ranging from 83 to 66%.

Comparison with Lab Steam Deactivations. Catalyst fractions which exhibit 50% or greater loss in micropore volume/crystallinity comprise less than 15% of equilibrium catalyst. The major portion of this particular equilibrium catalyst is remarkably similar to the material which results from increasingly severe laboratory steam deactivations at 815°C or less (Tables VI and VII). Dealumination is rapid, the associated crystallinity loss is small, and the matrix surface area shows little change. Crystallinity retention falls below 70% only after dealumination is complete.

The comparison of physical properties of laboratory-steamed catalyst with those of equilibrium catalyst fractions given in Table VII indicates that a wide range of steaming temperatures is necessary to reproduce the equilibrium catalyst deactivation profile for lab steaming times of one day or less. These results indicate that an improved catalyst aging procedure for simulating

FCC conditions will involve a program of steam treatments at different temperatures as contrasted with a recent suggestion that steam treatment be carried out at constant temperature for varying times (8).

It is evident from the results presented in Table VII that steaming temperatures of 850°C or even higher are required in order to match the physical properties of the oldest Fraction F, which retains only 38% of the crystallinity exhibited by fresh catalyst. This does not necessarily suggest the presence of local hot spots in the regenerator, which actually operates at relatively mild conditions. The net 60% loss in crystallinity displayed by Fraction F is more probably the result of steaming at 680°C to 705°C for long times. Since the catalyst resides in the regenerator most of the time, it is estimated that Fraction F has been subjected to high-temperature steam treatment for 80 days or more.

Activity Profile for Increasingly Severe Lab Deactivations.

Determination of the activity/selectivity profile exhibited by separated fractions for a full range gas oil awaits larger-scale separation. In the meantime, measurements have been made at a microcracking yields unit (MYU) on each of the laboratory steamed catalysts represented in Table VII, which exhibited physical properties similar to those of the separated equilibrium Fractions A-D. Results for conversion and for individual yields of gasoline, light gas, and coke, are given in Figure 6. For the early portion of the deactivation profile represented by these investigations, conversion and gasoline yield decrease linearly with the fraction of crystalline zeolite retained. Thus, within this region, losses in cracking activity and in gasoline selectivity can be directly attributed to zeolite destruction. Observing that both thermal cracking activity and residual matrix activity contribute to conversion and to gasoline yield, it is clear that the linear relationships shown in Figure 6 cannot be maintained into the region where the zeolite destruction approaches completion. Accordingly, both conversion and gasoline yield are expected to show increasingly less dependence on zeolite destruction in the later stages of deactivation. This expectation is borne out by the plot shown in Figure 6a for the pseudo second-order parameter, kinetics conversion ($\text{wt}\% \text{ conversion}/100 - \text{wt}\% \text{ conversion}$), which indicates minimal dependence on zeolite content as crystallinity retention falls below 60%.

The results for residual carbon on equilibrium catalyst fractions (Figure 2) and for cumene cracking on regenerated equilibrium fractions (Table V) also indicate that cracking activity shows little dependence on zeolite content following completion of framework dealumination (minimum unit cell size). At this point, the 60 to 70% of crystalline zeolite that remains contains a diminishingly small number of acid sites, and further zeolite destruction has little effect on cracking activity.

Except for the highest conversion where overcracking is presumed to be more significant, the light gas yields (TC2⁻,

Deactivation Profile for Lab-Steamed Catalyst

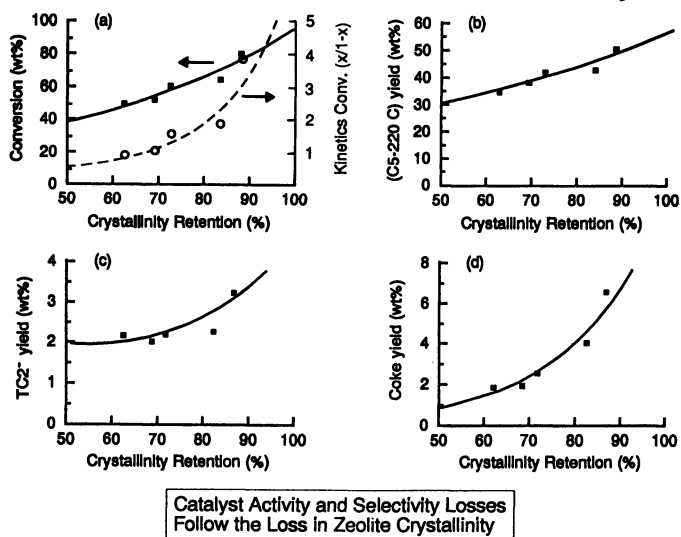


Figure 6. (a) Conversion, (b) Gasoline Yield (C₅-220°C), (c) Light Gas (TC2-) Yield, and (d) Coke Yield, each plotted vs. Fraction of Zeolite Crystallinity that is retained.

Figure 6c), show little dependence on zeolite content. This result is consistent with the role of C_2^- as a marker of thermal cracking. Initially, coke yields (Figure 6d) drop sharply with crystalline zeolite content, but level off as crystallinity retention falls below about 70%, a behavior similar to that displayed by the plot of the pseudo second-order rate constant, kinetics conversion, given in Figure 6a. Accordingly, the coke yields plotted in Figure 6d must represent "catalytic coke" (9) and, of themselves, comprise a reliable measure of the deactivation profile associated with these increasingly severe laboratory deactivations. The close comparison of the results for coke yields versus crystallinity retention plotted in Figure 6d, with the analogous results for residual carbon on equilibrium catalyst given in Figure 2 and Table III, further demonstrate the similarity between the associated catalyst deactivation profiles.

Analytical Electron Microscopy Investigations of Equilibrium Catalyst Fractions

Young Fraction-Extensive Zeolite Crystallites. Analytical electron microscopy (AEM) was used to track zeolite destruction with increasing time in the unit. In these investigations, the USY crystallites embedded in each microspheroidal spray-dried catalyst particle could be distinguished on the basis of a combination of lattice imaging, Si/Al ratio, and morphology. A lattice image from a USY crystallite (FAU material) in a catalyst particle from Fraction B is shown in Figure 7b. The extent of the lattice lines indicate that the crystallite is at least 0.4 microns in spatial extent. Catalyst morphology in this region is shown in the inset, Figure 7a. Lattice imaging together with compositional analysis (energy dispersive X-ray, EDX) was used to demonstrate that the zeolite crystallites exhibited higher Si/Al than the surrounding matrix, as shown by the micrographs in Figure 8, and the compositional analysis spectra in Figure 9 for Fraction F. The particular lattice image shown in Figure 8b originates from an isolated, small region of crystalline FAU material as shown in the inset, Figure 8a. Results of compositional analyses show that the FAU material exhibits a significantly higher Si/Al than does the surrounding matrix (Figure 9).

Old Fraction-Intimate Mixture of Crystalline and Collapsed Zeolite. Fraction F exhibits a characteristic morphology feature (note the region just below and to the right of center in Figure 10a) not observed in Fraction B. This structure is indicative of amorphous material, but with an Si/Al that is characteristic of USY zeolite. Further examination of this largely amorphous region reveals lattice images from small regions of crystalline FAU material, as shown in Figure 10b. Apparently, these particular largely amorphous regions in Fraction F represent what was once extensive crystalline FAU material which, after long residence time (about 100 days for F in comparison with 20 days for B) in

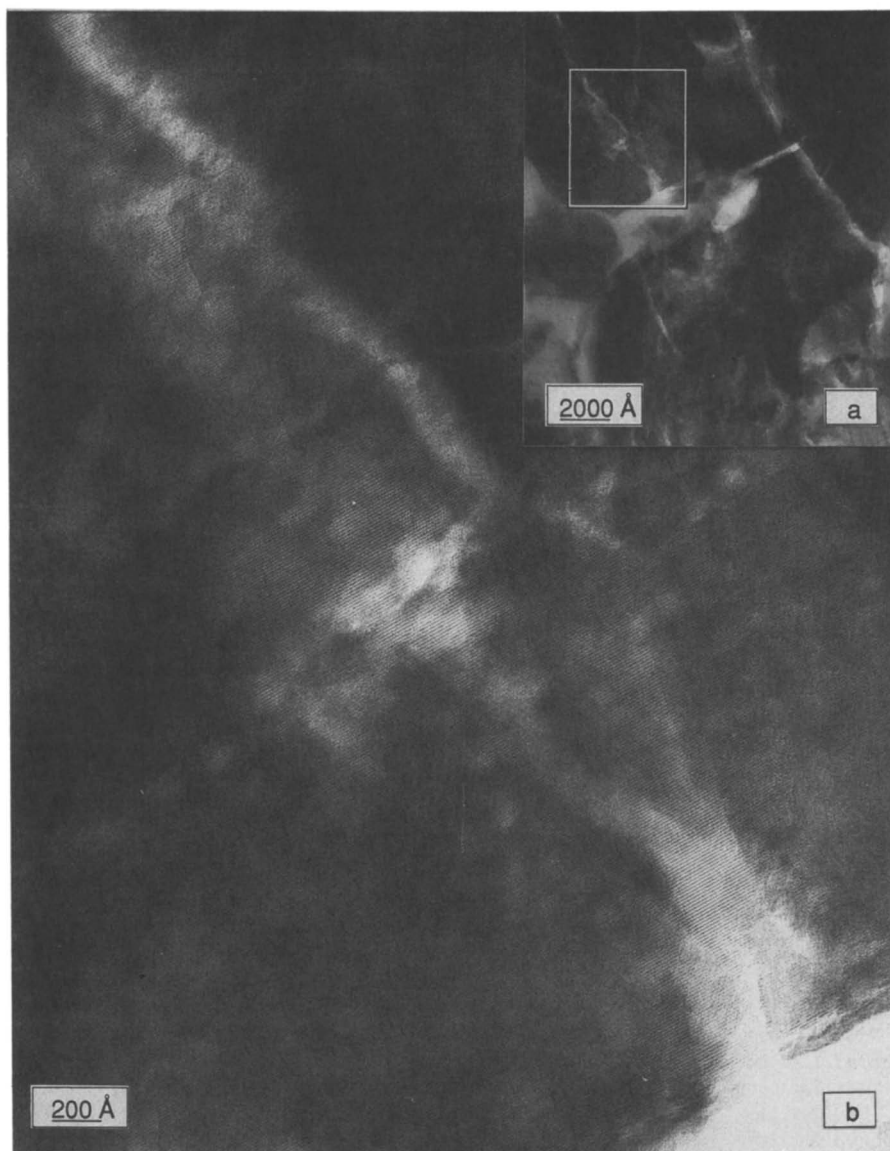


Figure 7. (a) Catalyst morphology (Fraction B) in region of USY crystallite, and (b) Lattice image of USY crystallite (FAU material).



Figure 8. (a) Isolated USY crystallite within Fraction F, and (b) Lattice image of USY crystallite within Fraction F.

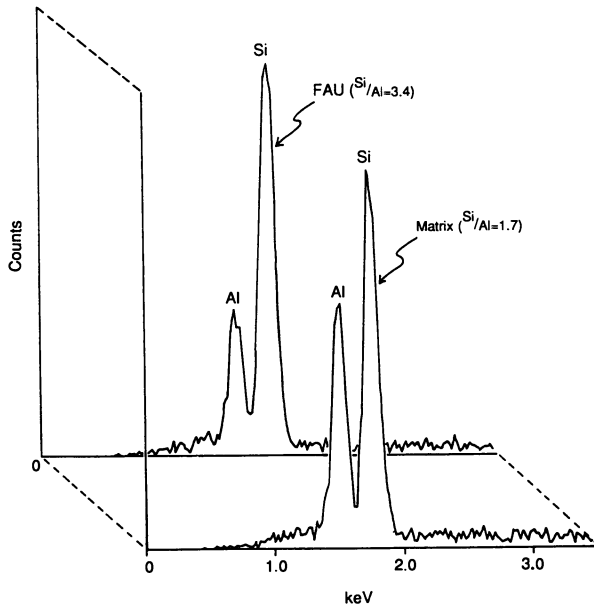


Figure 9. Comparison of compositional analysis data for FAU and matrix.

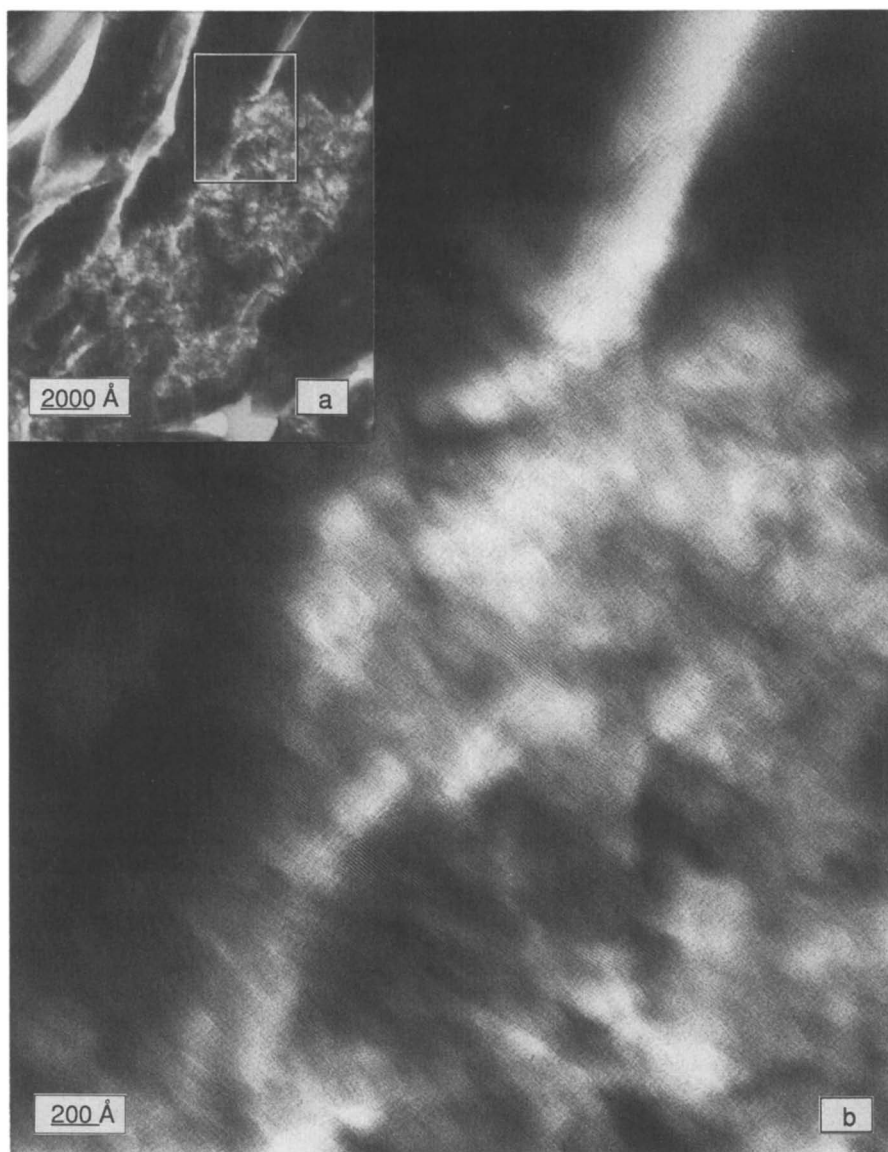


Figure 10. (a) Characteristic "amorphous" morphology feature observed in Fraction F, and (b) Lattice image of FAU crystallites within an "amorphous" region of Fraction F.

the FCU, has become an intimate mixture of crystalline FAU material and collapsed zeolite. The collapsed or destroyed zeolite does not produce a lattice image. Instead, it displays a finely divided amorphous structure.

The observed zeolite destruction is almost certainly caused by exposure to high-temperature steam in the regenerator since USY zeolite is thermally stable in dry air to temperatures in excess of 1000°C (10). It is unlikely that the steam-induced collapse of crystalline zeolite in this USY catalyst is much affected by the presence of a low concentration of vanadium (612 ppm V, Table III). Recent work by Occelli and Stencel (11), and by Mauge et al. (12) on both USY crystals and calcined rare earth-exchanged Y (CREY) crystals, show that, in the presence of high-temperature steam (760°C), vanadium has little effect on USY crystallinity up to about 0.6 wt% V, while with only 0.2-0.4 wt% V, CREY becomes essentially amorphous.

The intimate mixture of FAU material and amorphous regions seen in Figures 8 and 10 indicates that high temperature steam destruction of zeolite in the FCU is accompanied by extensive crystallite fracturing. This observation is further supported by the results of x-ray line broadening (increased x-ray line broadening is observed for Fraction F in comparison with Fraction B) and by the fact that the crystalline regions are much more extensive in the younger fraction (B). The latter point is demonstrated by the comparison given in Figure 11 of lattice images from FAU crystallites in Fraction B (top) and F (bottom), respectively. While high temperature steam destruction of USY zeolite in the FCU is well known, we believe that this is the first reported direct observation of this phenomenon on equilibrium catalyst by electron microscopy. Similar measurements have been carried out on laboratory steamed (800°C, 5-hour) La-Y crystals (12) and on a steamed (770°C, 15-hour) industrial FCC catalyst (13) with markedly different results. For these two cases, lattice images contained low contrast zones or holes within the zeolite grain which were attributed to amorphous material in the former case (12) and to mesopores in the latter (13).

Conclusions

A successful separation by density into fractions of increasing age has been obtained for the USY equilibrium catalyst of this study. The nickel level on each catalyst fraction, which is expected to furnish a stable age marker, increases with increasing density/age. The observed decrease in the V/Ni ratio with increasing age is indicative of interparticle vanadium migration. The trend of increasing Ni level with increasing density has been used to correlate increases in density with "Ni days" in the unit.

Both the results of cumene cracking investigations on regenerated fractions and of residual coke determinations on precoked fractions indicate that relatively high activity is exhibited by only the lightest/youngest fractions. It follows that a disproportionate share of catalyst activity is associated

a



b

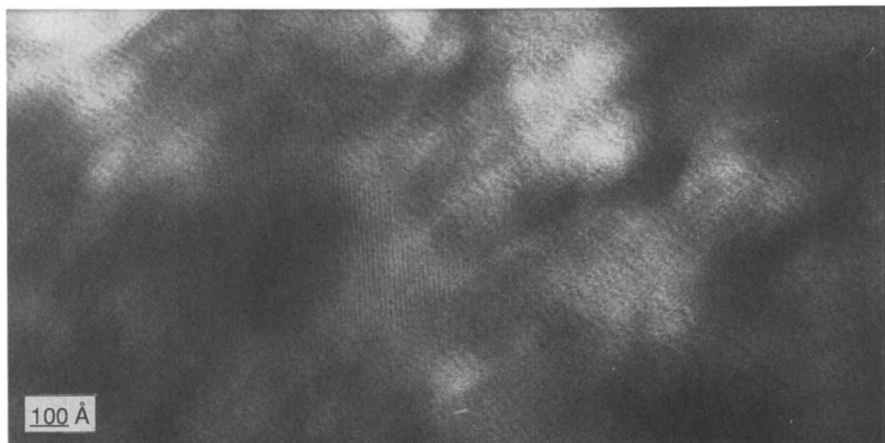


Figure 11. (a) Lattice image showing extent of a FAU crystallite in Fraction B, and (b) Intimate mixture of small FAU crystallites and collapsed zeolite in Fraction F.

with the youngest 15% of the catalyst inventory. The initial rapid decline in catalyst activity coincides with zeolite dealumination which is largely completed during the first 36 days of catalyst residence. Results of microcracking yields tests on a series of laboratory steamed catalysts are in qualitative agreement with this picture. Further corroboration, based on similar investigations of equilibrium catalyst fractions, awaits larger-scale separations.

The deactivation profile exhibited by the majority of this equilibrium catalyst is remarkably similar to that resulting from increasingly severe laboratory steam deactivations. Dealumination is rapid, crystallinity retention is 70% or more, and there is little loss of matrix surface area. The wide range of steaming temperatures necessary to reproduce the equilibrium catalyst deactivation profile indicates that improved aging procedures will involve the blending of catalyst portions steamed at different temperatures. Accordingly, the present study suggests that efforts to achieve improved catalyst aging procedures which rely on single mode deactivation or on steam treatment at a single temperature for varying times will be less successful.

Lattice imaging studies by TEM on a "young" fraction showed extensive regions of crystallinity with minimal evidence of crystallite fracturing. By contrast, similar investigations of an "old" fraction, combined with in situ compositional analysis, revealed small "islands" of crystallinity within a "sea" of disordered material that was *once* crystalline. Fracture lines at crystallite boundaries are absent. Instead, the small USY crystallites within the "old" fraction are in intimate mixture with the collapsed zeolite.

A "remnant" rare earth catalyst found in the high-density tail of the distribution is associated with incomplete changeover (88%) of this USY catalyst. This result indicates that density separation may not yield a good age profile in those cases where a rare earth catalyst has been introduced over a zero rare earth USY catalyst. Significant inhomogeneity within the parent (fresh) catalyst will also compromise the age/density correlation.

The result that only the youngest (most active) fractions are density-separated on the basis of activity for coking from isobutene has led to new insight which provides a sound basis for future application of float-sink density separation techniques on equilibrium catalysts containing high proportions of zeolite. For the majority of separated fractions, the gradual increase in skeletal density with increasing age appears to be associated with the apparent loss of microporosity (zeolite destruction) which occurs with increasing time in the unit. Provided that the parent catalyst does not itself exhibit marked inhomogeneity, the techniques described here can be used to construct a density/age correlation for "high changeover" equilibrium catalyst.

Appendix A: Factors Contributing to Catalyst Density Change

The analytical data on separated catalyst fractions given in Tables III, IV, VI, and VII can be used to estimate the contribution to catalyst density change from 1) decreased activity for coke deposition, 2) increasing metals deposition, and 3) excluded volume associated with both the small and large zeolite cages.

Estimates of the contribution to catalyst density associated with each of the above factors are carried out by identifying the density d_f ($f = A, B, C, \dots$) of an individual catalyst fraction with net catalyst density d_{ave} defined as follows:

$$d_{ave} = \frac{\sum_{i=1}^n d_i v_i}{\sum_{i=1}^n v_i} \quad (2)$$

where d_i , v_i are, respectively, the density and volume associated with the i th component of the catalyst. Observing that $v_i = w_i/d_i$, where w_i = weight of the i th component, it follows from Equation 2 that

$$d_{ave} = \frac{\sum_{i=1}^n w_i}{\sum_{i=1}^n v_i} = \frac{W}{V} \quad (3)$$

where W , V are, respectively, the net system weight and the net system volume.

Incremental Addition of Heteroatom Species

The effect of incremental addition of heteroatom species as coke or metals is estimated using Equation 3:

$$\sum_{i=1}^n v_i = \sum_{i=1}^n \frac{w_i}{d_i} = V = \frac{W}{d_{ave}} \quad (4)$$

where $i=1$ is now associated with the base catalyst, and $i = 2, 3, 4, \dots$ is associated with incremental addition of heteroatom species. Since the incremental effect on density of

each heteroatom species is expected to be small, each species can be treated individually according to the approximation

$$\frac{w_1/100}{d_1} + \frac{w_2/100}{d_2} = \frac{1}{d_{ave}} \quad (5)$$

For convenience, the net system weight W has been set equal to 100 g.

Effect of Carbon on Catalyst. Observing that the average H/C mole ratio for coke on catalyst is >1 and that condensed polyaromatics with similar H/C (e.g., phenanthrene, anthracene) exhibit densities in the range 1 to 1.3, a skeletal density of 1.2 g/cc is assumed for coke on catalyst (14, 15). Then for each 1% addition in coke, for a nominal catalyst density of 2.4,

$$\frac{0.99}{2.4} + \frac{0.01}{1.2} = \frac{1}{d_{ave}}$$

or $d_{ave} = 2.3162$

and $\Delta d = -0.0238$ g/cc for addition of 1 wt% coke.

Effect of Metals on Catalyst. Nickel and vanadium are assumed to be present as the oxides NiO and V_2O_4 with densities of 6.7 and 4.4 g/cc. For a nominal catalyst density of 2.5, the estimated density for a 0.1% change in V concentration is

$$\frac{(1 - 0.001 \times 1.63)}{2.5} + \frac{(0.001 \times 1.63)}{4.4} = \frac{1}{d_{ave}}$$

or $d_{ave} = 2.50176$ and $\Delta d = 0.0018$ g/cc for a 1000 ppm change in V concentration. The factor 1.63 accounts for the vanadium oxide/vanadium weight ratio. Similarly, for a 0.1% change in Ni concentration,

$$\frac{(1 - 0.001 \times 1.27)}{2.5} + \frac{(0.001 \times 1.27)}{6.7} = \frac{1}{d_{ave}}$$

or $d_{ave} = 2.50199$ and $\Delta d = 0.0020$ g/cc for a 1000 ppm change in Ni concentration. The factor 1.27 accounts for the nickel oxide/nickel weight ratio. Then for an increase in metals content

Δ (Ni + V) = 1000 ppm, the net density increase is estimated as $\Delta d = 0.0019$ for Δ (Ni+V) = 1000 ppm.

Similarly, if the effect of rare earth is modeled as if rare earth were present as RE_2O_3 , the estimated density change for a 0.5% change in RE content is

$$\frac{1 - 0.005 \times 1.17}{2.5} + \frac{0.005 \times 1.17}{6.75} = \frac{1}{d_{ave}}$$

or $d_{ave} = 2.50924$

and $\Delta d = 0.0092$ g/cc for a 0.5% increase in rare earth content. Similar calculations show that if iron and titanium are assumed to be present as the oxides α -Fe₂O₃ and TiO₂, with densities of 5.24 g/cc and 4.2 g/cc, respectively, the estimated Δd 's are

$$\begin{aligned} \Delta d_{Fe} \quad (5000 \text{ ppm}) &= 0.0094 \text{ g/cc} \\ \Delta d_{Ti} \quad (5000 \text{ ppm}) &= 0.0068 \text{ g/cc} \end{aligned}$$

Effect of Excluded Volume

As discussed in the text, about 12.5% of the total micropore volume of zeolite Y, 0.36 cc/g, is associated with the small cages. Assume that the same proportion holds for ultrastable Y which, due to occluded material in the micropore, typically shows a measured micropore volume of about 0.27 cc/g. Accounting for the excluded volume in the (inaccessible) small cages, the total micropore volume is $0.27/0.875 = 0.31$ cc/g. Observing that the X-ray density of ultrastable Y is about 1.3 g/cc, the net void volume is $0.31 \text{ cc/g} \times 1.3 \text{ g/cc} \approx 0.40 \text{ cc/cc}$. Assuming that the small cages of crystalline zeolite are never filled and that the excluded volume in the large cages is given by $(1-F)$ where F is a packing fraction, the observed density before zeolite destruction

$$d_f^B = 2 \times 4 (0.125 \times 0 + 0.875 \bullet F) \times 0.40 \text{ g/cc} + 1.3 \times 0.60 \text{ g/cc}$$

where the solvent medium density $d_m = 2.4$ g/cc. The observed density of the mesoporous material that results following zeolite destruction is

$$d_f^A = 2.4 (0.125 + 0.875) 0.40 \text{ g/cc} + 1.3 \times 0.60 \text{ g/cc}$$

The catalyst density increase, Δd_x^d , associated with the effect of excluded volume, is

$$\Delta d_x = R_x (d_f^A - d_f^B) = 2.4 R_x (0.125 + (1-F) \times 0.875) \times 0.40 \text{ g/cc}$$

where R_x = fraction of catalyst crystallinity destroyed.

Upon steam treatment at 815°C for 5 hours, the crystallinity of the fresh catalyst, as determined from micropore volume, decreases from 34 to 24% (Table VI). This requires $R_x = 0.1$. The associated measured density increase is 0.04 g/cc. Setting $\Delta d_x = 0.04$ g/cc gives the result $F = 0.67$. In other words, a packing fraction of 67% in the large cages accounts for the density increase that was observed upon steam treatment of the fresh catalyst.

The above estimate for packing fraction/excluded volume in the large cages is based on non-selective adsorption. The estimated value is decreased if, for a given packing fraction, there is selective adsorption by the zeolite of the lighter component, carbon tetrachloride.

Selective sorption gives rise to ambiguity within the model just described. For example, suppose that the density of the solvent medium is 2.4 g/cc. It is not possible to differentiate between an actual large-cage packing fraction of unity in combination with a selectively adsorbed solvent density of 1.61 g/cc and an actual packing fraction of 0.67, together with a non-selectively adsorbed solvent density of 2.4 g/cc.

Assuming non-selective adsorption and observing that the equilibrium catalyst Fraction A exhibits a crystallinity of 28% with a micropore volume of 0.075 cc/g, the expected increase in density due to a given change in micropore volume, Δmpore , is:

$$\Delta d = \left(\frac{\% \text{ crystallinity reduction}}{100} \right) \frac{0.04}{R_x} \text{ g/cc}$$

or

$$\Delta d = \frac{\Delta \text{mpore}}{0.075} \times 0.28 \text{ (0.4)}$$

$$= \frac{\Delta \text{mpore}}{0.075} \times 0.112 \text{ g/cc}$$

where the quantity $\frac{0.04}{R_x} = 0.4$ g/cc represents the density increase that would occur upon complete destruction of the neat zeolite.

Acknowledgments

The authors gratefully acknowledge John F. Newbury for performing the steam treatments on fresh catalyst, John P. Companik for collecting the data on cumene cracking, Frank S. Modica and Dr. Eugene H. Hirschberg for many helpful discussions, and Dr. James A. Kaduk for generous assistance and many helpful discussions concerning the X-ray diffraction analyses.

REFERENCES

1. Palmer, J. L.; Cornelius, E. B. Applied Catalysis 1987, 35, 217-35.
2. Kugler, E. L.; Leta, D. P. J. Catal. 1988, 109, 387-395.
3. Johnson, M. F. I. J. Catal. 1978, 52, 425-31.
4. Breck, D. W. Zeolite Molecular Sieves; R. E. Krieger: Malabar, Florida, 1984; p 637.
5. The effective size of 1,1,2,2-tetrabromoethane was determined using CHEM-X molecular modeling.
6. Barrer, R. M. In Zeolites and Clay Minerals as Sorbents and Molecular Sieves, Academic Press: London, 1978; p 121.
7. Kerr, G. T. Zeolites 1989, 9, 350-51.
8. Keyworth, D. A.; Turner, W. J.; Reid, T. A. Oil & Gas J. 1988, 86 (11) 65-8.
9. Rawlence, D. J.; Gosling, K. Applied Catalysis 1988, 43, 213-37.
10. McDaniel, C. V.; Maher, P. K. In Zeolite Chemistry and Catalysis; Rabo, J. A., Ed.; ACS Monograph 171; American Chemical Society: Washington, DC, 1976; p 323.
11. Ocelli, M. L.; Stencel, J. M. "Surface-Metals Interaction in Fluid Cracking Catalysts During the Upgrading of Vanadium-Contaminated Gas Oils," in Proceedings of the International Zeolite Conference, Wurzburg, Germany, September 1988.
12. Mauge, F.; Courcelle, J. C.; Engelhard, Ph.; Gallezot, P.; Grosmanin, J. In New Developments in Zeolite Science and Technology; Murikami, Y.; Iijima, A.; Ward, J. W., Eds.; Stud. Surf. Sci. Catal. 28; Kodansha, Tokyo; Elsevier, Amsterdam, 1986; pp 803-9.
13. Gallezot, P.; Feron, B.; Bourgogne, M.; Engelhard, Ph. Zeolites: Facts, Figures, Future; Jacobs, P. A.; van Santen, R. A., Eds.; Stud. Surf. Sci. Catal. 49; Elsevier, Amsterdam, 1989; pp. 1281-90.
14. Guisnet, M.; Magnoux, P.; Canaff, C. New Developments in Zeolite Science and Technology; Murikami, Y.; Iijima, A.; Ward, J. W., Eds.; Stud. Surf. Sci. Catal. 28; Kodansha, Tokyo; Elsevier, Amsterdam, 1986; pp 701-07.
15. Magnoux, P.; Cartraud, P.; Mignard, S.; Guisnet, M. J. Catal. 1987; 106, pp 235-41.

RECEIVED June 8, 1990

Chapter 9

Translation of Laboratory Fluid Cracking Catalyst Characterization Tests to Riser Reactors

A. V. Sapre and T. M. Leib

Paulsboro Research Laboratory, Mobil Research and Development Corporation, Paulsboro, NJ 08066

A theory has been developed which translates observed coke-conversion selectivity, or dynamic activity, from widely-used MAT or fixed fluidized bed laboratory catalyst characterization tests to steady state risers. The analysis accounts for nonsteady state reactor operation and poor gas-phase hydrodynamics typical of small fluid bed reactors as well as the nonisothermal nature of the MAT test. Variations in catalyst type (e.g. REY versus USY) are accounted for by postulating different coke deactivation rates, activation energies and heats of reaction. For accurate translation, these parameters must be determined from independent experiments.

This work provides conclusive evidence that transient catalyst characterization tests can result in erroneous catalyst ranking. For example, USY catalysts show higher activity than REY catalysts in the laboratory tests but lower activity in a steady state riser. Although emphasis in this paper is placed mainly on the coke-conversion selectivity, the analysis is also extended to yields of other FCC products.

While most catalyst vendors rely on fixed bed microactivity (MAT) tests, fixed fluid bed (FFB) reactor experiments are widely used within Mobil to characterize FCC catalysts. The amount of catalyst used is constant for each test, and products are collected for a known period of time. In MAT experiments, catalyst bed is fixed while in FFB test the catalyst bed is fluidized. As products are collected over the decay cycle of the catalyst, the resulting conversion and coke yields are strongly influenced by catalyst deactivation. Systematic differences exist between the measured conversion or catalyst activity and coke yields for the MAT and FFB tests. The magnitude of these differences varies depending on the type of catalyst being tested (REY or USY). Experimental data in Figure 1 clearly show that FFB conversion is higher than MAT conversion for USY catalysts. On the other hand, FFB conversion is lower than MAT conversion for REY catalysts. Furthermore, the quantitative

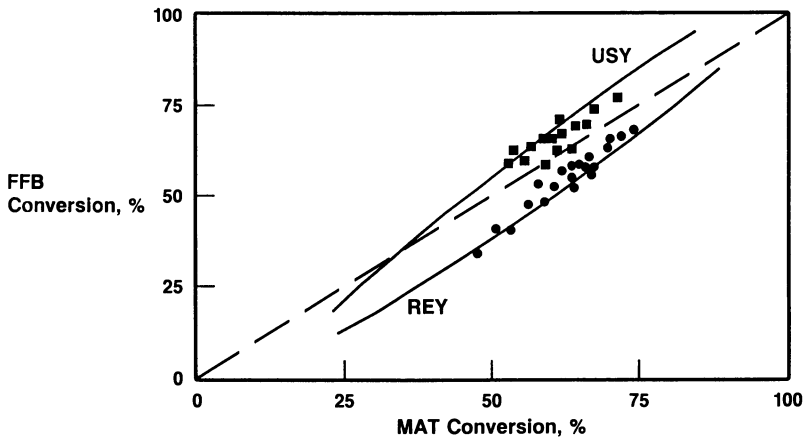


Figure 1: Comparison of MAT and FFB conversions. Lines correspond to model predictions.

translation of the catalyst performance from these laboratory tests to steady state riser is a strong function of catalyst type. Therefore, we recognized that a fundamental approach relating laboratory catalyst screening tests to riser performance is needed. In this paper we summarize a theory which quantitatively accounts for these differences and give insights into interpreting laboratory test data.

Potential pitfalls exist in ranking catalysts based solely on correlations of laboratory tests (MAT or FFB) to riser performance when catalysts decay at significantly different rates. Weekman first pointed out the erroneous conversion ranking of decaying catalysts in fixed bed and moving bed isothermal reactors (1-3). Phenomena such as axial dispersion in the FFB reactor, the nonisothermal nature of the MAT test, and feedstock differences further complicate the catalyst characterization. In addition, differences between REY, USY and RE-USY catalyst types exist due to differences in coke deactivation rates, heats of reaction, activation energies and intrinsic activities.

In this paper, we will first illustrate the mathematical models used to describe the coke-conversion selectivity for FFB, MAT and riser reactors. The models also include matrix and zeolite contributions. Intrinsic activity parameters estimated from a small isothermal riser will then be used to predict the FFB and MAT data. The inverse problem of predicting riser performance from FFB and MAT data is straightforward based on the proposed theory. A parametric study is performed to show the sensitivity to changes in coke selectivity and heat of reaction which are affected by catalyst type. We will highlight the quantitative differences in observed conversion and coke-conversion selectivity of various reactors.

Theory

Coke-Conversion Kinetics. Coke formation kinetics and gas oil conversion are represented by the following irreversible reactions (cracking and coking):



Based on Voorhies time-on-stream theory (4), catalytic coke is a function of catalyst contact time:

$$\Delta c = A t_c^n \quad (2)$$

and the coke yield on fresh feed is given by:

$$\text{coke} = \text{CCR} + \Delta c [\text{C/O}] \quad (3)$$

Typically less than 100% of the feed CCR goes to coke depending on the feedstock and operating conditions. In Equation 3, however, for simplicity we assume that 100% of the feed CCR is deposited as coke on catalyst.

The reaction rate per unit volume for gas oil cracking is given by:

$$r = r_0 \phi(t) \quad (4)$$

where r_0 is the initial cracking rate, and $\phi(t)$ is the catalyst deactivation function. We assume that the catalyst deactivates due to coke formation, and the cracking activity declines in direct proportion to the rate of coke formation. The deactivation function therefore may be written as:

$$\phi(t) = d\Delta c/dt \quad (5)$$

Similar dependence of catalyst deactivation on coke or catalyst residence time is suggested by Corella et al. (5-7). The authors give details on possible mechanisms of catalyst deactivation by coke, and also suggest, based on their data, that the deactivation order n may not be a constant. For our analysis, however, we will assume that n is constant and a function of catalyst type. Further theoretical treatment of catalyst decay is given by Wojciechowski (8,9).

The effect of feedstock quality and oil partial pressure on coking is given by:

$$\Delta c = A t_c^n (a + k_A \dot{C}_A) P_{oil}^b \quad (6)$$

Blanding (10) first proposed the second order cracking kinetics for FCC. Krambeck (11) theoretically demonstrated that conversion in systems with a large number of parallel reactions can be approximated by simple second order kinetics. More recently, Ho and Aris (12) have developed a further mathematical treatment of this concept. An inhibition term was incorporated into the second order cracking kinetics for gas oil conversion to account for competitive adsorption. The initial cracking rate is then given by:

$$r_0 = k \rho_b C_A^2 / (1 + k_{HA} C_A) \quad (7)$$

Differences between various zeolites and matrix components of the catalyst have been accounted for by fitting coke deactivation rates (exponent n), coking and cracking activities (A and k), and adsorption coefficients (k_A and k_{HA}). Similar ideas on deactivation of a composite cracking catalyst have been presented by Dean and Dadyburjor (13). Coke on catalyst then becomes the sum of the coke on the matrix and the coke on the zeolite:

$$\Delta c = \Sigma \Delta c_i z_i \quad (8)$$

Here Z_i is the mass fraction of zeolite or matrix components.

And the deactivation functions become:

$$d\Delta c_i/dt = \phi_i(t) (a + k_{A_i} C_A) P_{oil}^b \quad (9)$$

$$\phi_i(t) = d\Delta c_i/dt \quad (10)$$

Similarly, the cracking reaction will be composed of the reactions occurring on the

matrix and zeolite:

$$r = \sum r_i \quad (11)$$

where

$$r_i = k_i \phi_i z_i C_A^2 \rho_b / (1 + k_{HAi} C_A) \quad (12)$$

Although the theory includes the impact of matrix contribution, we will restrict our discussions primarily to low matrix activity catalysts, and highlight the differences in zeolite type.

FFB Model. Use of FFB units in the industry for catalyst characterization is primarily due to excellent temperature control and resulting isothermal reactor temperature. The operating conditions of the FFB activity unit used in our study are given in Table I. The material balance using a pseudo steady state assumption (at any given instant the vapor is in contact with catalyst of almost uniform activity) gives:

$$\epsilon D_A d^2 C_A / dz^2 - d(u C_A) / dz = \sum r_i(C_A, t) \quad (13)$$

where r_i is given by Equation 12. In the above equation, the hydrodynamics of FFB reactors are represented by an axial dispersion model. The degree of bubbling, and hence, the bypassing are reflected in the dispersion coefficient. The superficial gas velocity u changes along the reactor due to molar expansion. Assuming u varies linearly with conversion:

$$u = u_0(1 + \alpha y_{A0} X) \quad (14)$$

Where conversion X is given by

$$X = 1 - u C_A / (u_0 C_{A0}) \quad (15)$$

Danckwert's boundary conditions give:

$$@ z = 0 \quad u(C_{A0} - C_A) = -\epsilon D_A dC_A / dz \quad (16)$$

$$@ z = L \quad dC_A / dz = 0 \quad (17)$$

Equations 13-17 expressed in dimensionless form give:

$$Pe^{-1} d^2 y / dx^2 - d(v y) / dx = y^2 \sum f_i(\theta) \quad (18)$$

$$v = 1 + \alpha y_{A0} X \quad (19)$$

$$X = 1 - v y \quad (20)$$

$$@ x = 0 \quad v(1 - y) = -Pe^{-1} dy / dx \quad (21)$$

$$@ x = 1 \quad dy / dx = 0 \quad (22)$$

Here,

$$f_i = \omega_i \eta_i \theta^{\eta_i - 1}; \quad \omega_i = k_i A_i n_i z_i M_A C_{A0}^2 / (S_V (1 + k_{HAi} C_{Ai}))$$

$$\eta_i = t^{\eta_i - 1}; \quad Pe = L u_0 / (\epsilon D_A)$$

$$y = C_A / C_{A0}; \quad x = z/L$$

$$v = u/u_0; \quad \theta = t/t_C$$

$$S_V = (t_C [C/O])^{-1}$$

Solution of Equations 18 to 22 gives the instantaneous outlet concentration y , which when integrated over the run length gives the average conversion (\underline{X}):

$$\underline{X} = 1 - \int_0^1 v y \, d\theta \tag{23}$$

The crackability (Cr), or the second order conversion is given by:

$$Cr = \underline{X} / (1 - \underline{X}) \tag{24}$$

A parameter k_C representing coke-conversion selectivity, is defined as:

$$k_C = \text{coke} / Cr \tag{25}$$

The use of k_C in analyzing data from pilot units was proposed by Krambeck in the early 1970's and has been used in Mobil since then. More recently, the same concept has been published in the open literature, and the reciprocal of k_C is defined as UOP "dynamic activity" (14). The dynamic activity is now popularly used in the FCC literature, and is even used to correlate catalyst performance with fundamental catalyst parameters such as unit cell size (15). In this paper, however, we will use the Mobil defined k_C parameter.

Table I. FFB, MAT and Riser Operating Conditions

Reactor	FFB	MAT (Davison) Fixed Bed	Steady State Riser
T, °F	850	930	1000
C/O, wt/wt	2	3	5
t _C , s	300	75	3
Poil, psia	10	15	35
	Light East		
Gas Oil	Texas	<-----W. Texas----->	
C _A , wt %	10	18	18
CCR, wt %	.01	.40	.40
M _A	233	400	400

MAT Model. The operating conditions of Davison's MAT unit (16) are given in Table I. These conditions correspond to testing prior to the change in November 1988. The material and energy balances, using pseudo steady state and adiabatic plug flow assumptions give:

$$-d(u C_A)/dz = \Sigma r_i(C_A, T, t) \quad (26)$$

$$w_c c_{pc} \partial T / \partial t + m_A c_{pA} L \partial T / \partial z = -M_A V \Sigma \Delta H_i r_i(C_A, T, t) \quad (27)$$

The inlet conditions are:

$$@ z = 0 \quad C_A = C_{A0}, \quad T = T_0 \quad (28)$$

The partial differential Equation 27 can be simplified to an ordinary differential equation in the independent variable z , by the following approximation: For typical FCC catalysts and feedstocks, $c_{pA} \sim 3 \times c_{pc}$, and for the MAT test, $[C/O]$ is 3 (Table I). Hence, if we assume that the catalyst and oil temperatures are identical (no heat transfer resistance between oil and catalyst), then as a first approximation, the change in the energy content of the oil and of the catalyst are roughly the same over the length of the run. Thus, the two terms on the left hand side of Equation 27 are approximately the same magnitude. Therefore, the time derivative of T can be lumped with the distance derivative. The right hand side of Equation 27 is divided by 2, and it becomes:

$$m_A c_{pA} L dT/dz = -M_A V \Sigma (\Delta H_i / 2) r_i(C_A, T, t) \quad (29)$$

This approximation of the energy balance may lead to inaccurate prediction of the temperature profile as a function of time on stream. Thus, at short contact times it may underpredict the temperature, while at long contact times it may overpredict the actual temperature profiles. However, on the average, the model predictions are good, as seen from the comparisons with data in subsequent sections. In our opinion, the above simplifications are reasonable, especially since the reproducibility of the MAT test is somewhat poor.

Normalizing Equations 27-29 gives:

$$-d(y) / dx = y^2 \Sigma f_i(\theta) \quad (30)$$

$$ds/dx = y^2 \Sigma \beta_i f_i(\theta) \exp(-\epsilon_i/s) \quad (31)$$

$$@ x = 0 \quad y = s = 1 \quad (32)$$

Here,

$$s = T/T_0 \quad \beta_i = \Delta H_i / (2c_{pA} T_0)$$

$$\epsilon_i = E_i / (R T_0) \quad \hat{f}_i = f_i / \exp(-\epsilon_i / s)$$

The other parameters are the same as for the FFB model. Similar to the FFB model, Equations 30-32 give the instantaneous conversion; to obtain time averaged values, integration is required for \underline{X} (Equation 23) and \underline{T} :

$$\underline{T} = \int_0^1 T \, d\theta \quad (33)$$

Forissier and Bernard (17), also give a model for the MAT test. However, since they did not attempt to translate product selectivities from the MAT test to a steady state riser, it is somewhat less complex.

Riser Model. The riser is represented by a steady state adiabatic plug flow model with no slip between oil and catalyst (18). The material and energy balances give:

$$-d(u C_A)/dz = \Sigma r_i(C_A, T) \quad (34)$$

$$(m_c c_{pC} + m_A c_{pA}) L dT/dz = -M_A V \Sigma \Delta H_i f_i(C_A, T) \quad (35)$$

The inlet conditions are identical to Equation 28. Equations 28, 34 and 35 can be written in dimensionless form similar to Equations 30-32. The definition of the dimensionless variables is identical to those of the MAT model, except for β_i :

$$\beta_i = \Delta H_i / (c_{pA} T_0 (1 + m_c c_{pC} / (m_A c_{pA})))$$

Since the riser operates at steady state no time averaging is required.

Numerical Method. Both the isothermal FFB and the adiabatic MAT models are very stiff due to the coke deactivation terms ϕ_i . The spline orthogonal collocation technique was used to solve the above models (19). Typically, the distance x was divided into two regions ($0 < x < \gamma$ and $\gamma < x < 1$, $\gamma < 1$), with 6-8 collocation points in each region. At the interface between the two regions, both the concentration and the mass flux were taken as continuous. The value of γ varied with the degree of stiffness.

Comparison of Model Predictions and Experimental Data

Potential Erroneous Ranking of Catalysts. We ran a series of tests on equilibrium REY [A], USY [B] and RE-USY [C] catalysts in an isothermal riser, an FFB and a MAT unit. The experimental data are summarized in Table II:

Table II. Catalyst Ranking Based on Experimental Data

	FFB Test		MAT Test		Riser Results*	
	Conv., %	k_c	Conv., %	k_c	Conv., %	k_c
Catalyst [A]	63	0.53	66	1.39	70	1.47
Catalyst [B]	65	0.38	62	0.98	64	1.20
Catalyst [C]	68	0.42	67	1.04	67	1.33

	Ranking for Activity			Ranking for Coke Selectivity		
	FFB Ranking	C	B	A	B	C
MAT Ranking	C	A	B	B	C	A
Riser Ranking	A	C	B	B	C	A

$$k_c = \frac{\text{coke}}{\text{crackability}}$$

Catalyst A - REY

Catalyst B - USY

Catalyst C - RE-USY

* At [C/O] of 5 and constant catalyst contact time and temperature.

For each test, the first column represents the observed catalyst activity and the second column represents coke conversion selectivity given by Equation 25.

From the above table, the FFB test would rank the catalysts with respect to decreasing catalyst activity in the order C, B, A. The MAT test on the other hand would rank them in the order C, A, B. However, the true ranking, as seen in the riser test, is A, C, B. Thus, both MAT and FFB rank the catalysts incorrectly with respect to catalyst activity. Although the relative magnitude of k_c parameters is different, the rankings by coke conversion selectivity is correct for all tests. These results are not unexpected and can be explained by the mathematical model presented above.

Quantitative Predictions. In this section we use the riser data to determine intrinsic activity and coking parameters (k_i , A_i) in the model, and then predict MAT and FFB conversion and coke yields. Typically, we will have either the MAT or FFB activity and coke information and the task is to predict the riser performance. As the models use intrinsic parameters, it is immaterial which test information is available. The intrinsic parameters can be easily extracted by fitting the data to the appropriate reactor model. We will use the riser data as it gives the intrinsic information directly. The fitted rate parameters are summarized in Table III. The other model parameters, such as the activation energies, heats of reaction, the coke deactivation exponent, n , (also given in Table III), were estimated independently. The details of parameter estimates are described in the Appendix.

Table III.(1) Key Rate Parameters for Three Types of Catalysts

	(REY) [A]	(USY) [B]	(RE-USY) [C]
Model Parameters			
E_1 Btu/lb mole	19,800	27,000	23,400
ΔH_1 , Btu/lb	130	200	180
n_1	0.2	0.4	0.4
$k_{10} \times 10^{-6} \left(\frac{\text{ft}^3}{\text{lbmol}} \right)^2 \frac{\text{lbmol}}{\text{lbcoke}}$	9.6	96.0	16.0
$A_1 \times 10^8 \text{ s}^{-n} \frac{\text{lbcoke}}{\text{lbcat}}$	6.4	2.4	3.3

(1) k_{10} and A_1 are relative to k_{HA1} of Table V.

Comparison of predicted and experimental FFB and MAT conversions and coke yields is given in Table IV.

Table IV. Comparison Between Predicted and Observed Test Data

	Catalyst A		Catalyst B		Catalyst C	
	Obs	Pred	Obs	Pred	Obs	Pred
FFB Conversion, vol %	63	62	65	65	68	66
Coke, wt %	0.9	0.8	0.7	0.8	0.9	1.1
MAT Conversion, vol %	66	66	62	62	67	65
Coke, wt %	2.7	2.7	1.6	1.8	2.1	2.3

The conversions are predicted quite accurately over a wide range of coke levels (from 0.7 to 2.7 wt %). There are some minor discrepancies in the coke predictions. However, these predictions are within the experimental accuracies of the tests. The FFB conversions are reproducible within ± 2 numbers, with $\pm 20\%$ accuracy for coke yields. Similarly, the MAT data are reproducible within ± 3 numbers with $\pm 30\%$ accuracy for coke yields. These comparisons suggest that the models could be used to fit the catalyst intrinsic parameters (k_i , A_i) from the transient tests and then predict the steady state riser performance. Indeed, we have done this exercise and we predict a reverse ranking for catalysts A and C in going from transient tests to the riser performance, as observed in the riser experimental data.

Parametric Studies. To provide a feel for the relative importance of some of the model parameters, and to understand observed differences in performance between REY and USY catalysts (Figure 1), key parameters such as the cracking and coking intrinsic constants k_i and A_i , the heats of reaction ΔH_i , and the order of coke deactivation, n_i , were varied. The base case model parameters and the rate

constants for an REY catalyst (Catalyst D) were estimated from Mobil's precision test runs and are summarized in Table V.

Table V. Estimated Relative Rate Constants and Parameters
For REY Catalysts
(Catalyst D)

<u>Parameters</u>		<u>Estimated Rate Constants⁽¹⁾</u>	
Pe	5	k_{A1} , ft ³ /lbmol	3.8
z ₁	0.3	k_{HA1} , ft ³ /lbmol	1
E ₁ , Btu/lbmol	19,800	$k_{10} \left(\frac{\text{ft}^3}{\text{lbmol}} \right)^2 \frac{\text{lbmol}}{\text{lbcoke}}$	8.4x10 ⁶
ΔH ₁ , Btu/lb	130		
C _{PA} , Btu/(lb °F)	0.75	A_1 , s ⁻ⁿ $\frac{\text{lbcoke}}{\text{lbcat}}$	1.6x10 ⁻⁸
C _{PC} , Btu/(lb °F)	0.29	n ₁	0.2

(1) Relative to the magnitude of k_{HA1}

REY Catalysts. REY catalysts always give lower FFB conversions than MAT conversions (Figure 1). To simulate the observed conversion differences in the MAT and FFB units for REY catalysts, the intrinsic cracking activity k_i is increased at constant coking activity A_i . This choice of parameters is a first order approximation for the activity and coke-conversion selectivity variation of equilibrium catalysts. Parameters summarized in Table V are used as the initial starting point.

The results of the simulation are shown by the curve marked REY in Figure 1, and the curves of Figure 2. The results of Figure 1 agree with our experimental observations, showing that the MAT conversion is always higher than the FFB conversion for REY catalysts.

The lower FFB conversions in Figure 1 can be rationalized based on the following nonidealities of the FFB test relative to MAT:

- Backmixing (low Peclet No.).
- Longer contact time resulting in lower time averaged conversion.
- Lower temperature.

At high conversions, the adiabatic nature of the MAT reactor compensates somewhat for the FFB nonidealities; thus, decreasing the difference between the MAT and FFB conversions. Temperature drops of 60-150 °F are not uncommon in MAT units, Cronkright et al (20). Early on stream, the catalyst is very active resulting in large endotherm (~100 °F). As the catalyst deactivates, however, the temperature profile is less steep and results in lower endotherm corresponding to lower

conversions at the end of the run. As mentioned before, MAT activity is a time averaged conversion corresponding to the temperature history of the run.

In Figure 2, we compare the coke-conversion selectivity behavior as a function of activity for MAT, FFB and riser reactors. The k_c is relatively flat for the FFB test, with correspondingly higher negative slopes for MAT and steady state risers. The riser results show the steepest slope indicating that even though the k_c observed in the FFB test is relatively independent of activity, the coke selectivity improves with activity in a riser.

An important conclusion from these simulations is that neither the FFB nor the MAT test simulates riser behavior, since neither of these tests reflects the intrinsic catalyst activity and decay. These intrinsic parameters are masked by backmixing in the FFB test and by a high temperature drop in the adiabatic MAT unit. In addition, the time averaged values of the long contact time FFB and MAT tests over-emphasize the low catalyst activity at long contact times, while the short contact time riser is only exposed to initial activity and catalyst decay.

USY Catalysts. USY catalysts are advertised by catalyst vendors, as low coke/high octane catalysts. This behavior results from the smaller zeolite unit cell size due to dealumination (21,22). The controlled dealumination leads to fewer but stronger acid sites resulting in increased cracking relative to H-transfer. The decrease in the extent of the exothermic H-transfer reactions also results in net increase in the endothermic heat of cracking for USY catalysts (21).

USY catalysts generally show higher FFB conversions than MAT conversions (Figure 1). This trend is opposite of what was shown before for the REY catalysts. We postulate that USY catalysts have lower coke deactivation rates and lower initial activity than REY catalysts, as shown schematically in Figure 3. As mentioned above, USY catalysts also exhibit higher heat of reaction (21), which results in a larger temperature drop in the adiabatic MAT unit, and hence, in lower conversion. Similarly, the lower deactivation rate benefits the longer contact time FFB unit relative to the shorter contact time MAT unit. These two effects can compensate for the FFB activity nonidealities listed before and effectively give higher conversion in the FFB test relative to MAT.

Figures 4 and 5 show the effects of varying deactivation order, n and endotherm ΔH , respectively, on the FFB and MAT conversions. In Figure 4, ΔH was kept at the base value of 130 Btu/lb and only n was varied. As expected, with increasing n , i.e. lower deactivation rate, the longer time on stream FFB test shows higher conversion relative to MAT. In this specific simulation, for values of $n > 0.3$, FFB conversion is higher than MAT conversion. Similarly, at constant n of 0.2, ΔH is varied in Figure 5. Here again, at high values of endotherm a lower average temperature in the MAT tests results in lower MAT conversion relative to the FFB test. From Figure 5, a 50% increase in the endotherm from 130 Btu/lb to 200 Btu/lb would result in lower MAT conversions than FFB conversions. Thus, both a higher n and ΔH for USY catalysts relative to REY catalysts would account for higher observed FFB conversions than MAT conversions. We estimated values of $n = 0.4$ and $\Delta H = 200$ Btu/lb for USY catalysts based on literature and Mobil data. The simulated results are shown by the curve marked USY in Figure 1. Here again, simulations match experimental observations quite well.

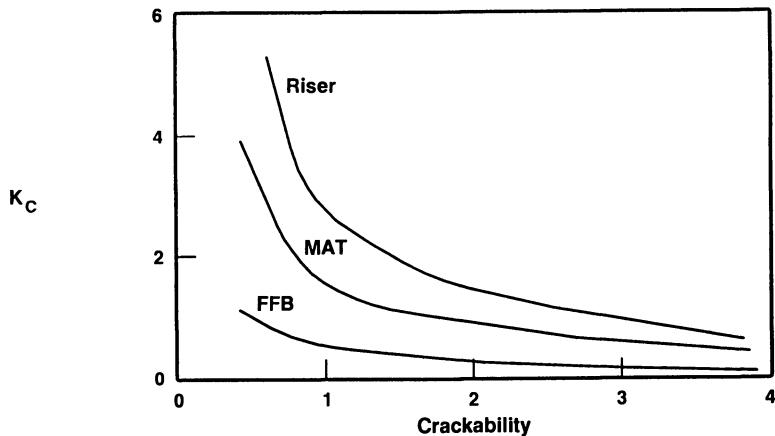


Figure 2: Predicted coke-conversion selectivity as a function of catalyst activity (crackability) for REY catalysts.

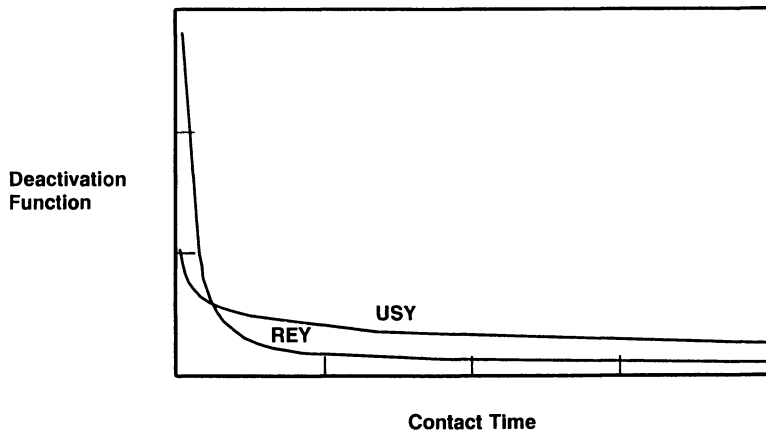


Figure 3: A schematic representation of catalyst deactivation functions for REY and USY catalysts.

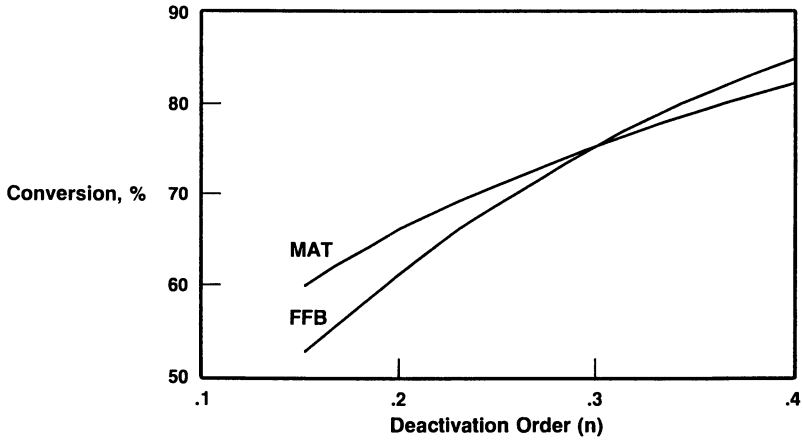


Figure 4: Impact of catalyst deactivation rate on predicted MAT and FFB conversions.

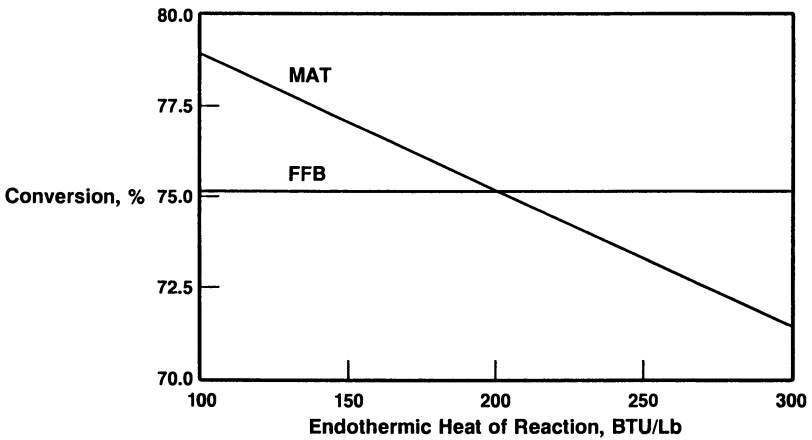


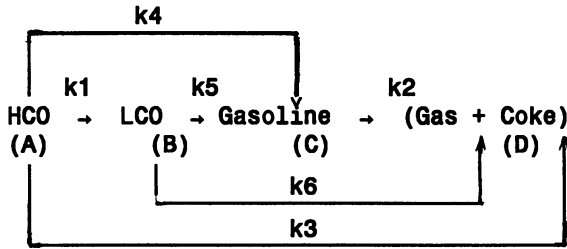
Figure 5: Impact of heat of reaction on predicted MAT and FFB conversions.

In Figure 6, we show the results of a simulation in which the cracking activity k_i was varied while keeping the coking activity A_i constant (similar to the simulation above for REY catalysts). It is interesting to note that for the choice of the parameters noted above, k_c values in MAT and riser closely trace each other. On the other hand, FFB coke-conversion selectivity, k_c , has somewhat lower slope.

Other Product Selectivities

In the preceding sections we concentrated mainly on the coke-conversion selectivity aspects of various reactors. In this section we will briefly discuss the selectivities of major FCC products: gasoline, LCO, HCO, and light gases in both transient and steady state reactors. Weekman (1-3) has looked at steady state and transient reactors for gasoline selectivity shifts. However, he did not include axial dispersion effects in his analysis which are important for laboratory FFB reactors, and are accounted for here.

Consider the following reaction network for gas oil cracking.



Each reaction in the above network is assumed to be a second order in the reactant, and coking is assumed to deactivate all reactions identically. The dimensionless continuity equations for each component, similar to Equation 18, are:

$$\frac{1}{Pe} \frac{d^2 y_A}{dx^2} - \frac{dy_A}{dx} = (f_1 + f_3 + f_4) y_A^2$$

$$\frac{1}{Pe} \frac{d^2 y_B}{dx^2} - \frac{dy_B}{dx} = (f_5 + f_6) y_B^2 - f_1 y_A^2$$

$$\frac{1}{Pe} \frac{d^2 y_C}{dx^2} - \frac{dy_C}{dx} = f_2 y_C^2 - (f_4 y_A^2 + f_5 y_B^2)$$

$$y_D = 1 - (y_A + y_B + y_C)$$

$$\text{B.C.: } @ \quad x = 0 \quad (1 - y_A) = - \frac{1}{Pe} \frac{dy_A}{dx} \tag{36}$$

$$y_B = \frac{1}{Pe} \frac{dy_B}{dx} ; \quad y_C = \frac{1}{Pe} \frac{dy_C}{dx}$$

$$@ \quad x = 1 \quad \frac{dy_A}{dx} = \frac{dy_B}{dx} = \frac{dy_C}{dx} = 0$$

$$\text{where, } f_i = w_i \eta \theta^{n-1} \quad w_i = \frac{k_i An}{Sv}$$

y_A, y_B, y_C, y_D - normalized concentrations of A,B,C,D, respectively.

The time averaging equations are straightforward and will not be shown here. A steady state equivalent of Equations (36) for the ideal plug flow riser reactor, $Pe \rightarrow \infty$, can be easily derived, and also will not be shown here. Equations (36) were solved numerically using the spline collocation technique discussed before. The product selectivities in various reactors for the following relative rates, $k_4/k_1 = 0.5$; $k_5/k_1 = 0.7$; $k_2/k_1 = 0.1$ $k_3/k_1 = 0.05$; $k_6/k_1 = 0.035$ are shown in Figure 7.

The product yields in Figure 7 correspond to steady state riser ($Pe \rightarrow \infty$), isothermal MAT ($Pe \rightarrow \infty$), and FFB ($Pe \rightarrow 1$) reactors. The yields of desirable products, gasoline and LCO are always lower in transient units due to time averaging. The axial dispersion causes further decline in product selectivity. In Figure 7, the maximum in gasoline yield occurs much earlier in the FFB reactor compared to MAT, or steady state riser reactors. There are sufficient data in the literature to verify that overcracking of gasoline occurs earlier in laboratory fluid bed reactors than in risers [23,24]. Thus, if laboratory reactors are used to rank catalysts based on product selectivities, one should consider the above differences. Furthermore, at conversions above those which give maximum gasoline yields, there is a sharp increase in the light hydrocarbon yields and increased gasoline octanes. The product qualities from the laboratory transient reactors, like octane for example, should therefore be interpreted cautiously. At the same conversion level, Research Octane numbers of the gasoline obtained from a transient laboratory reactor could be higher than those of steady state risers.

The effect of time averaging on yields in transient tests can be minimized by shortening the duration of the test. Also, a fixed bed test is superior to an FFB activity test in that backmixing is minimized. Furthermore, an isothermal fixed bed test would be easier to interpret than the adiabatic MAT test. This work shows that from the point of view of a catalyst characterization test, a small steady state riser will give the most direct information for catalyst performance in a commercial riser.

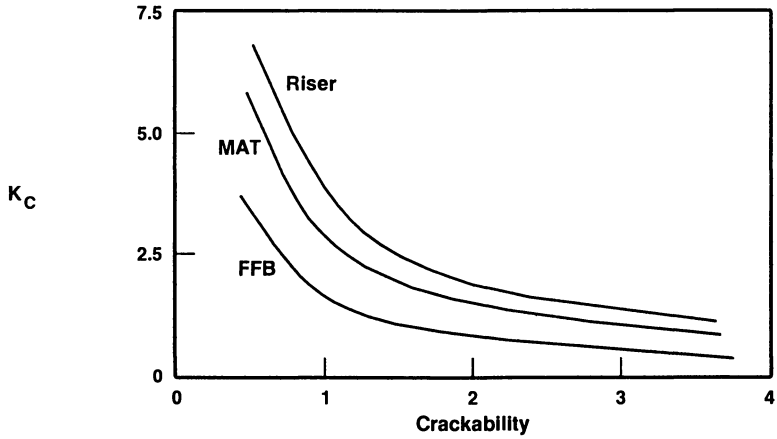


Figure 6: Predicted coke-conversion selectivity as a function of catalyst activity (crackability) for USY catalysts.

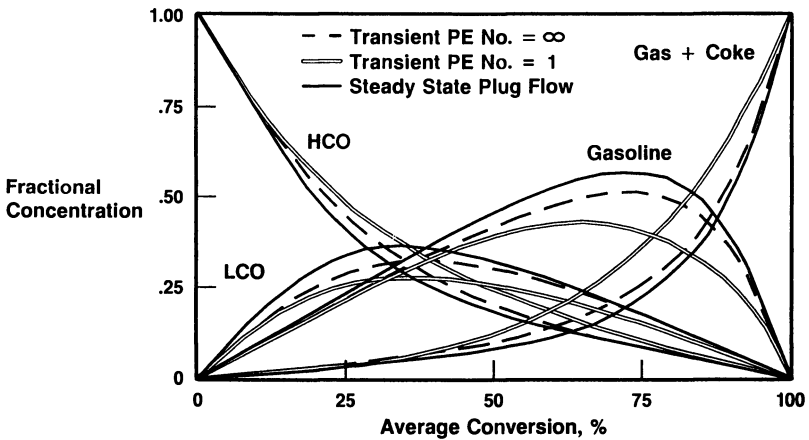


Figure 7: Predicted product selectivities as a function of conversion for three different laboratory catalyst characterization test units.

Summary

FCC catalyst testing prior to use in commercial reactors is essential for assuring acceptable performance. Purely correlative relations for ranking catalysts based on laboratory tests, however, can be erroneous because of the complex interaction of the hydrodynamics in the test equipment with the cracking kinetics. This paper shows how the catalyst activity, coke-conversion selectivity and other product selectivities can be translated from transient laboratory tests to steady state risers. Mathematical models are described which allow this translation from FFB and MAT tests. The model predictions are in good agreement with experimental data on identical catalysts run in the FFB, MAT and a laboratory riser.

Legend of Symbols

A	Intrinsic coking kinetic constant
c_p	Heat capacity at constant pressure
C_A	Volumetric concentration of gas oil
C_A	Total carbon in aromatics
CCR	Conradson carbon residue
Cr	Crackability
C/O	Catalyst/oil ratio, wt/wt
D_A	Axial dispersion coefficient
f	Dimensionless reaction parameter for FAI
\bar{f}	Dimensionless reaction parameter for MAT and riser
f_i	Dimensionless constants in Equation (36)
k	Ratio of cracking to coking rate constants
k_A	Intrinsic coking reaction constant
k_C	Coke-conversion selectivity
k_{HA}	Adsorption constant
k_O	Exponential factor of k
L	Reactor height
m	Mass flow rate
M_A	Oil molecular weight
n	Voorhies parameter
Pe	Axial Peclet number
r	Reaction rate per reactor volume
s	Dimensionless temperature
S_v	Space velocity
t	Time
t_c	Catalyst contact time
T	Temperature
u	Superficial vapor velocity
v	Dimensionless vapor superficial velocity
V	Reactor volume
w_c	Catalyst holdup in reactor
x	Dimensionless axial distance

X	Conversion
y	Dimensionless volumetric concentration
Y _A	Fraction of oil in feed, mol/mol
Y _B	Dimensionless concentration of LCO
Y _C	Dimensionless concentration of gasoline
Y _D	Dimensionless concentration of gas
z	Axial distance; fraction of zeolite in catalyst, wt/wt

Greek Letters

α	Axial molar expansion coefficient
β	Dimensionless heat of reaction
ϵ	Dimensionless activation energy
ΔH	Heat of reaction
Δc	Δ Coke on catalyst
θ	Dimensionless time
ω	Dimensionless reaction parameter
η	Dimensionless reaction parameter
γ	Spline point
ϕ	Coke deactivation function

Subscripts

A	Oil
c	Catalyst
i	1=zeolite, 2=matrix
o	feed

Appendix

Estimates of Model Parameters. The reactor models for FFB, MAT and riser include important features for translating the MAT and FFB data to steady state riser performance. A series of key parameters specific to a given zeolite and matrix component are needed for a given catalyst. Such key parameters are intrinsic cracking and coking activities (k_i , A_i), activation energies and heats of reaction (E_i , ΔH_i), coke deactivation rate (exponents n_i), and axial dispersion in the FFB unit (D_A). Other feedstock dependent parameters include the inhibition constants ($k_{H_{A_i}}$), the coking constants (K_{A_i}), and the axial molar expansion factor (α).

It is the objective of the FFB or the MAT test to determine cracking and coking activities of the catalyst (k_i , A_i). Therefore, all other parameters should be known from independent experiments or estimated prior to determining these intrinsic catalyst parameters. These other parameter estimates are described below.

It can be shown, that the molar expansion parameter α is a function of the charge stock and product molecular weights:

$$\alpha = \frac{M_o}{M} - 1$$

M_o is the molecular weight of the charge stock, and M is the average molecular weight of the product. The value of α varied from 2 to 6 in this study.

An axial Pe number of 5 was estimated for the FFB unit, corresponding to a D_A of $\sim 30 \text{ cm}^2/\text{s}$. This estimate was based on dispersion data reported by Zenz (25) on Geldart's Group A powders.

The coke deactivation exponent n , is typically estimated from riser pilot plant experiments at varying catalyst contact time for different catalyst types. A value of n of 0.2 was found for REY catalyst data base. For USY and RE-USY catalysts n was estimated to be 0.4.

Heats of reactions were estimated from heats of formations and chemical compositions of feed and product using standard procedures. For REY catalysts, we estimated approximately 130 Btu/lb heat of reaction. The heat of reaction was close to 200 Btu/lb for USY catalysts. These values are in close agreement with reported data (21). The activation energies for different catalyst types were estimated from our extensive pilot plant data base, and found to be a weak function of catalyst type. The adsorption constants and other kinetic parameters used in these simulations were fitted to a large in-house data base. Typical parameter values are reported in Tables III and V. The kinetic parameters (k_i and A_i) are a strong function of catalyst used, whereas the adsorption parameters were found to be relatively insensitive. One could estimate these parameters even from a limited data base as illustrated below for Catalyst D.

Table VI. Commercial Equilibrium REY Catalyst
(Catalyst D)

FFB Test		MAT Test	
Conversion	Coke	Conversion	Coke
wt %	wt %	wt %	wt %
63	0.43	66	1.56
63	0.44	68	1.51
64	0.47	69	1.59
64	0.49	71	1.51
64	0.50	71	1.51
65	0.51	72	1.85
66	0.55	72	1.59

A set of MAT and FFB data on a low metals equilibrium commercial REY catalyst with a low matrix activity (Catalyst D) is summarized in Table VI. The range of activities indicates varying steam deactivation levels in the commercial unit. These data could be used to estimate the following four parameters: intrinsic cracking and coking activities (k_i , A_i) and feedstock parameters (k_{HA} , k_A). The feedstock differences between Light East Texas Gas Oil (LETGO) and West Texas Gas Oil used in the FFB and MAT tests, respectively, allows the determination of k_{HA} and k_A . A modified Marquardt algorithm was used for parameter estimation. The fit was meaningful at a 95% confidence level, and the correlation coefficient was 0.93. These parameters are summarized in Table V. These parameter values were in close agreement with other REY catalysts, for example Catalyst A in Table III.

Acknowledgments

Useful discussions with F. J. Krambeck are sincerely appreciated. We thank D. M. Nace for obtaining the experimental data. Also, D. H. Anderson's effort in programming the spline orthogonal collocation technique is appreciated.

Literature Cited

1. Weekman, Jr. V. W. I&EC Proc. Des. & Dev. 1968, 7, (1), 90.
2. Weekman, Jr. V. W. I&EC Proc. Des. & Dev. 1969, 8, (3), 385.
3. Weekman, Jr. V. W. and Nace, D. M. AIChE J. 1970, 16, (3), 397.
4. Voorhies, A. I&EC 1945, 37, 318.
5. Corella, J. and Menendez, M. CES, 1986, 41, 1817.
6. Corella, J., Bilbao, K., Molina, J. A. and Artigas, A. I&EC Proc. Res. Dev., 1985, 24, 625.
7. Corella, J., Fernandez, A. and Vidal, J. M. I&EC Prod. Res. Dev., 1986, 25, 554.
8. Wojciechowski, B. W. Can. J. Chem. Eng. 1968, 46, 48.
9. Wojciechowski, B. W. Cat. Rev. Sci. Eng. 1974, 9(1), 79.
10. Blanding, F. H. I&EC, 1953, 45, 1186.
11. Krambeck, F. J. Int. Chem. E. Symp. Ser., (ISCRE-8), 1984, 733.
12. Ho, T. C. and Aris, R. AIChE J., 1987, 33, (6), 1030.
13. Dean, J. W. and Dadyburjor, D. B. Ind. Eng. Chem. Res., 1989, 28, 271.
14. Moh, R. W. Oil & Gas Journal, 1987, January 26, 73.
15. Rajagopalan, K. and Peters A. W. Journal of Catalysis, 1982, 106, 410.
16. Davison Catalagram, 1988 Nov. 1.
17. Forissier, M. and Bernard, J. R. AIChE Spring Meeting, 1989, Houston, April 2-6, Paper 84d.
18. Yen, L. C., AIChE Spring Meeting, 1989, Houston, April 2-6, Paper 84b.
19. Villadsen, J. and Michelsen, M. L. Solution of Differential Equation Models by Polynomial Approximations, Prentice Hall, Inc., Englewood Cliffs, NJ, 1978.
20. Cronkright, W. A., Butler, M. M. and Harter, D. A. Ketjen Catalyst Symposium, Kurhaus, The Netherlands, 1986, May 25-28.
21. Leuenerger, E. L. and Wilbert, L. J. Oil & Gas Journal, 1987, May 25, 38.
22. Desai, P. H. Oil & Gas Journal, 1986, September 22, 42.
23. Creighton, J. E. and Young, G. W. ACS National Meeting, Philadelphia, 1984.
24. Gross, B., Nace, D. M. and Voltz, S. E. I&EC Proc. Des. & Dev., 1974, 13, (3), 199.
25. Zenz, F. A. and Othmer, D. F. Fluidization and Fluid Particle Systems, Reinhold Publishing Co., New York, 1960, 300.

RECEIVED June 8, 1990

Chapter 10

Analysis of the Riser Reactor of a Fluid Cracking Unit

Model Based on Kinetics of Cracking and Deactivation from Laboratory Tests

J. Corella and E. Francés

Department of Chemical Engineering, University of Zaragoza,
50009 Zaragoza, Spain

A model for the riser reactor of commercial fluid catalytic cracking units (FCCU) and pilot plants is developed. This model is for real reactors and feedstocks and for commercial FCC catalysts. It is based on hydrodynamic considerations and on the kinetics of cracking and deactivation. The microkinetic model used has five lumps with eight kinetic constants for cracking and two for the catalyst deactivation. These 10 kinetic constants have to be previously determined in laboratory tests for the feedstock-catalyst considered. The model predicts quite well the product distribution at the riser exit. It allows the study of the effect of several operational parameters and of riser revampings.

Fluid catalytic cracking (FCC) of heavy oil fractions is a well-known process in oil refineries. Numerous books (e.g., 1–3) and publications about the different aspects of this subject are available. This chapter is concerned with the modeling of the transfer line or riser reactor of an FCC unit (FCCU) or of a pilot plant. The riser reactor in FCCUs is a vertical pipe about 1 m in diameter and 10–30 m in height. The hot catalyst coming from the regenerator at about 710 °C first comes in contact with steam and is fluidized. Then, at a height of some meters above, the catalyst is mixed with the preheated feedstock at about 300 °C.

The first oil-catalyst contact is essential. The mixing temperature (about 530–600 °C) is very difficult to measure and is about 20–80 °C higher than the riser exit temperature (4, 5). The superficial gas velocity at the inlet is several meters per second, much higher than the terminal velocity of the catalyst, which is about 0.20 m/s. The catalyst and the gas are transported upwards together but at a different superficial velocity, u (6). These two velocities are related by the slip velocity (sv), defined as follows:

$$\text{slip velocity (sv)} = \frac{u_{\text{gas}}}{u_{\text{catalyst}}} = \frac{t_c}{t_g} \quad (1)$$

The value of sv in the riser makes the residence time or, better, the space time different for the gas (t_g) and the catalyst (t_c).

The riser reactor seems to be a very easy reactor. Its hydrodynamics seems quite simple, and it could be studied with a simple piston-flow consideration. But when the hundreds of cracking and coke-formation reactions are considered with their very difficult kinetics and when the injection or feeding point is studied in detail, this reactor becomes impossible to model with 100% accuracy, at least today.

For these and other reasons, only a few papers have been devoted to the modeling of FCC risers. The great economic importance of the FCC process, the competition between companies, and the high cost of good research on FCC have given rise to a lot of confidentiality in this field, and thus many studies do not appear in the open literature.

Previous Models of FCC Risers

The best-known model for FCC risers may be that of Paraskos et al. (8) and Shah et al. (8), although their valuable work is already a little old (published in 1976–1977). They considered the riser to be isothermal (7) and adiabatic (8). Besides piston flow in the riser, they assumed a deactivation order (d) of 1, which is, for us, an important error, and a slip velocity of unity (in reality they only mention one time, their η).

Other models are presented in references 9–14. Gates et al. (9) also considered piston flow and $d = 1$. Van der Baan (10) considered piston flow but with d undetermined. One patent (14) is based on piston flow, $sv = 1$, $d = 2.3$ ($\Theta = 0.76$), and some corrective “scale factors.” In our previous work on the subject (11), we considered piston flow, $sv = 1$, and $d = 3$. The recent work of Bernard et al. (12) points to the necessity of taking into account radial velocity profiles. Finally, in an earlier work, Wollaston et al. (13) used only an empirical equation relating conversion at the riser exit and process severity.

All the works just cited have an important and common assumption: the well-known, three-lump Weekman model with three kinetic constants. This three-lump model was a significant achievement, but it lumps together gas and coke, which are clearly different. Therefore, we consider it absolutely necessary to expand this model by using a five-lump model with eight cracking constants and the following definitions: A = feedstock (bp > 350 °C), O = gas oil (bp 221–350 °C), E = gasoline (bp 36–221 °C), G = gas (bp < 36 °C), and C = coke (by combustion).

To our knowledge, the control of most FCCUs in refineries is based today on a 10- or 11-lump model (14, 15) with 20 kinetic cracking constants. We think that these 20 kinetic constants cannot be calculated with precision from kinetic tests and that they are only empirical parameters

used to adjust the operation of the FCCU. Besides, these models use scale factors (14) or installation factors (15) to adjust the real yields at the FCCU exit. So we prefer a model with only 5 lumps for which we can calculate with accuracy and from laboratory tests the eight kinetic cracking constants. Nevertheless, the optimal number of lumps to be used is a question open to discussion and to more sophisticated kinetic techniques.

All the previously cited models and works also consider, and some explicitly cite, this assumption—that the catalyst activity varies with time-on-stream (or with coke concentration [12]) in the same manner or with the same deactivation function (ψ) for all reactions in the network. That is, a nonselective deactivation model is always used. Corella et al. (16) have recently demonstrated that in the FCC process this assumption is not true and that it would be better to use a selective deactivation model. Another work (17) also shows how this consideration, when applied to catalytic cracking, influences the yield–conversion curves. Nevertheless, to avoid an additional complication, we will use in this chapter a nonselective deactivation model with the same $a-t_c$ kinetic equation and deactivation function (ψ) for all the cracking reactions of the network.

The radial catalyst density profiles or piston-flow deviations in FCC risers have also been studied (9, 12, 18, 19, 20). The catalyst density is low in the center and high near the wall, with gas velocities high at the center and lower close to the wall. This factor could be modeled by using an axial dispersion coefficient (9, 19), but in our opinion, the use of this coefficient is not clear and important. So we will use piston flow. After comparing results from this model with some plant data, we think that this assumption is acceptable.

Assumptions of the Model

The following assumptions or considerations are made in the derivation of the mathematical model:

1. Piston flow for gas and solid with a slip velocity that can vary with the height of the riser.
2. Adiabatic riser with temperature (T) that varies with height. In each height interval (three or four intervals throughout the riser), different temperatures and kinetic constants can be used.
3. Temperature of the liquid–vapor the same as that of the catalyst. This assumption is not true (21) particularly in the first meter of the riser. This error is compensated if the kinetic constants have been calculated under the same or similar conditions or with a scale factor.
4. Good and instantaneous vaporization of the charge. In our opinion, assumptions 3 and 4, which are due to the difficulty in modeling the first meter or the first catalyst–feed contact, are the most important ones.

5. Five-lump model with eight kinetic cracking constants (k_i) and two kinetic deactivation constants (ψ and d) (Scheme 1). These 10 constants must be known beforehand and with accuracy for each catalyst–feedstock used. One of the most important feature of our model is that the k_i values used come from modified MAT or laboratory tests and they are not simply empirical parameters obtained by adjusting the FCCU data, as is commonly done in actual control models (22). These k_i , ψ , and d kinetic parameters clearly depend on the catalyst–feedstock used. Details of how these kinetic parameters (k_i , ψ , and d) are obtained have been previously shown (23). Of course, there are more complex models for the stoichiometry of catalytic cracking (24), but we do not know how the more than 100 cracking kinetic constants needed can be calculated simultaneously and with precision from a laboratory kinetic test. For us, the work of Liguras and Allen (24) is good in stoichiometry but weak in the kinetic aspects.
6. Selective deactivation model ($a_A = a_O = a_E = \dots a$ [catalyst activity], or $\psi_A = \psi_O = \psi_E \dots = \psi$; $d_A = d_O = d_E \dots = d$).
7. Microkinetic cracking model for A:

$$(-r_A) = k_A Y_A^2 a \quad (2)$$

where

$$k_A = k_1 + k_2 + k_3 + k_7 \quad (3)$$

8. Riser height divided into zones. In each zone, the parameters (k_i , ψ , ϵ_A [expansion factor defined by equation 6], sv, \dots) and the diameter or cross section (S) will have a constant value. These values can vary from one zone to the other. If enough information is available about the variation of these parameters with height, new equations relating these variables with height could be introduced and an integration of the equations along the riser height could be made. But, in our opinion, with the present knowledge on these aspects, only some discrete (not continuous) values can be used. In any case, the use of more intervals does not offer mathematical problems. The change of S from one zone to other will change the superficial velocity of the gas (u), a very important parameter.
9. No lateral or secondary feed injections downstream of the feeding point. This limitation and a constant cross section will be eliminated in a forthcoming paper dealing with riser revamping with the model presented in this chapter.

Other Considerations

Expansion Factor: Flow Increase along Riser Height. Because of cracking, the flow rate, the volume, and the superficial velocity of the gas increase. For mean molecular sizes, the following values can be used: A, 40; O, 20; E, 9; and G, 3 (21). Then, for a given weight of feed (*A*), the volumetric flow rate (*Q*) will be inversely proportional to these mean molecular sizes. Thus:

$$Q_o \propto \frac{\dot{A}}{40} \tag{4}$$

$$Q \text{ (at } X_A) \propto \dot{A} \left(\frac{Y_A}{40} + \frac{Y_O}{20} + \frac{Y_E}{9} + \frac{Y_G}{3} \right) \tag{5}$$

Thus, the flow rate is not directly proportional to the conversion $X_A = (1 - Y_A)$, but the influence of the other products (Y_O , Y_E , and Y_G) is clear. As a result, the expansion will not be linear, as Figure 1 indicates. To approximate this situation, we can consider several zones along the riser height. For each zone, equation 6 applies:

$$Q = Q_o(1 + \epsilon_A X_A) = Q_o + Q_o \epsilon_A X_A \tag{6}$$

ϵ_A can vary with X_A because of the cracking mechanism; therefore, for each zone we can use a different ϵ_A , a low value for the first zone and about 4 for the last zone.

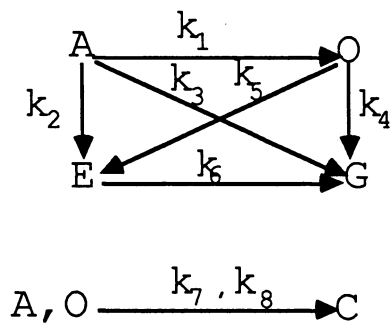
When the proposed model is solved for each zone, the product distribution at the exit of the zone is calculated, and a better value for ϵ_A can be then calculated. For simplicity, we suggest using initially equation 6, with only one or two values of ϵ_A for the whole length of the riser. When the model is well understood and managed, a new value for ϵ_A can be calculated and used for each zone. For this purpose, equation 7 applies:

$$Q = Q_{H_2} + Q_{H_2S} + Q_{\text{steam}} + Q_{C_1} + Q_{C_2} + Q_{C_3} \dots + \tag{7}$$

$$+ Q_E + Q_O + Q_A \text{ (nonconverted)}$$

These flow rates can be calculated if Q_o and X_A and Y_i at different riser heights are known. ϵ_A can also vary from one feedstock to another.

Mean Molecular Weight of Feedstock. The mean molecular weight (MW) affects at least two factors: (1) the kinetic constants k_i and ψ (usually, when MW increases, k_i decreases) and (2) the number of moles and the flow rate



Scheme 1

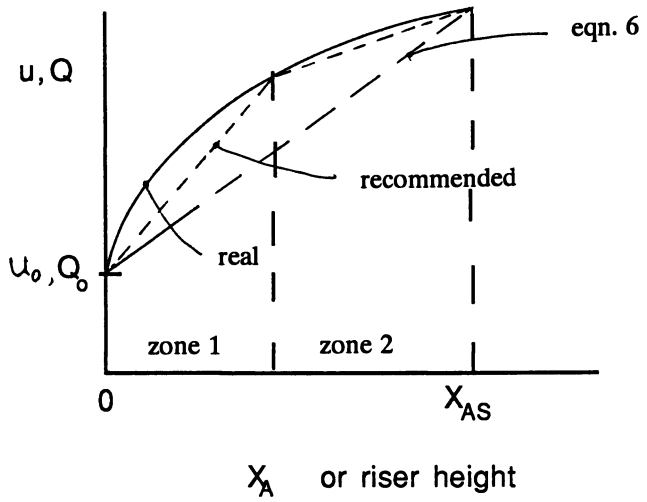


Figure 1. Variation of flow rate with riser height.

Publication Date: January 23, 1991 | doi: 10.1021/bk-1991-0452.ch010

(14). For a given flow (in tons per day) of feedstock to be processed, if MW increases, the number of moles decreases, the superficial velocity of the gas decreases, and the residence time of the gas in the riser increases. These two effects are then opposed: the first decreases X_A and the second increases it. In any case, the MW of the feedstock must be known or estimated.

Temperature along the Riser Height. Temperature (T) affects the cracking (k_i) and deactivation (ψ) constants (or functions). It also influences the gas density and, as a consequence, the flow rates, the superficial velocities, and the residence time of the gas in the riser. Its effect on k_i makes the product distribution (gas, coke, etc.) dependent on T .

The riser could be considered isothermal, but if the values for E , E_d , ΔH_r , etc., are known, it is better to use a nearly adiabatic regime. A rigorous calculation of the temperature profile in the riser (indicated, for instance, in Figure 2 of reference 4) is in reality quite difficult and may be impossible. In the riser, a temperature difference of 20–60 °C between the mixing point and the top has to be considered. Our solution is to divide the riser into several zones (four or five zones are recommended). In each zone, T will be different. Thus, different values of k_A , ψ , and k_i will have to be used. Then by calculating the ΔX_A in each zone and by assuming an adiabatic regime, ΔT can be calculated. Thus, the estimated T of the zone can be checked.

The initial basis will be that T at the top is known (515 °C for instance) and that at the feed injection point the mix temperature is 560–570 °C (this T can also be calculated by a heat balance).

Residence Time of the Catalyst in the Riser. The residence time of the catalyst in the riser, t_c , can be calculated from equations 8 and 9

$$t_c = \frac{W_c}{C} \quad (8)$$

$$dW_c = C dt_c \quad (9)$$

in which C is the flow rate of catalyst (in kilograms per second) and W_c is the weight of catalyst in the riser. Because it is difficult to determine W_c , t_c is calculated from equation 10:

$$t_c = sv \cdot t_g = sv \cdot \frac{L}{u_g} = sv \cdot \frac{L}{u_{A,0}(1 + \epsilon_A X_A) + \frac{Q_{\text{steam}}}{S}} \quad (10)$$

According to reference 6, sv can have values between 1.05 and 1.15.

Kinetics of deactivation. On the basis of findings of Corella et al. (25) and Espinosa et al. (26), we are convinced that

$$-\frac{da}{dt_c} = \psi a^d \quad (11)$$

or, in integrated form for $d \neq 1$

$$a = \frac{1}{\left[a_0^{1-d} + (d-1)\psi t_c \right]^{1/(d-1)}} \quad (12)$$

Equation 12 is equivalent to equation 13

$$a = \frac{1}{(1 + Gt)^j} \quad (13)$$

commonly used by Wojciechowski (27) and in some FCC control models. As written in equation 12, ψ and d have a clear physicochemical significance and their values can be interpreted and discussed. In equation 13, G and j only have empirical significance.

Calculation of Product Distribution from X_A . The kinetic equations of the network allow Y_O , Y_E , and Y_G to be calculated versus X_A ($= 1 - Y_A$) or versus riser height.

Flow Rates at Riser Inlet. If the ideal gas law can be applied, the flow rates of feedstock (Q_{Ao}) and steam (Q_{Vo}) and the total flow rate (Q_o ; in cubic meters per second) are easily calculated from equations 14–16.

$$Q_{Ao} = \frac{O \text{ (ton/day)} \cdot 10^3 / 24 \cdot 3600}{MW} \frac{RT}{P} \quad (= \text{m}^3/\text{s}) \quad (14)$$

$$Q_{Vo} = \frac{m_v \text{ (ton/day)} \cdot 10^3 / 24 \cdot 3600}{18} \frac{RT}{P} \quad (= \text{m}^3/\text{s}) \quad (15)$$

$$Q_o = Q_{Ao} + Q_{\text{steam}} \quad (16)$$

The superficial velocity of the gas at the inlet is given by equation 17:

$$u_o = \frac{(Q_{Ao} + Q_{Vo})}{S} \quad (17)$$

Weight Fraction of A at the Inlet. The weight fraction of A at the inlet, Y_{A0} , is defined by equation 18:

$$Y_{A0} = \frac{O}{(O + m_v)} \quad (18)$$

Because steam is introduced at the bottom (m_v), $Y_{A0} \neq 1$.

For the catalyst activity at the riser inlet (a_0), it will be supposed that $a_0 = 1$.

The conversion (X_A) is defined by equation 19:

$$X_A = \frac{Y_{A0} - Y_A}{Y_{A0}} = 1 - \frac{Y_A}{Y_{A0}} \quad (19)$$

Modeling the Riser

Mass Balance for A in dL . With an assumed piston flow (Figure 2), a mass balance for A in dL (in which there is a catalyst of weight dW_c) gives equation 20:

$$-O dY_A = (k_A Y_A^2 a) \cdot dW_c \quad (20)$$

By substituting equation 12 in equation 20 and separating variables, equation 21 is obtained:

$$-\frac{dY_A}{Y_A^2} = k_A \frac{1}{O} \frac{dW_c}{\left[a_0^{(1-d)} + (d-1)\psi t_c \right]^{1/(d-1)}} \quad (21)$$

By substituting the value of dW_c given by equation 9 and integrating equation 21, equation 22 is obtained:

$$\frac{1}{Y_{As}} - \frac{1}{Y_{A0}} = k_A \frac{(C/O)}{(d-2)\psi} \quad (22)$$

$$\left[\frac{1}{(a_0^{(1-d)} + (d-1)\psi t_c)^{(2-d)/(d-1)}} - \frac{1}{u_0^{(d-2)}} \right]$$

(valid for $d \neq 1$ and $d \neq 2$)

From this basic equation, Y_{As} (and then X_{As}) is calculated. To do this, it is necessary to know a_0 , Y_{A0} , kinetic parameters for the

catalyst–feedstock system used (ψ , d , and k_A), C/O , and t_c (which implies knowing ϵ_A , equation 10). It is also necessary to know the cross section (S) and height (L) of the riser.

Method

The riser will be considered as divided into zones that can be represented by a battery of piston-flow reactors in series (Figure 3). Each zone will have a length of L_1 , L_2 , L_3 , etc. The following relations will apply:

- Zone 1, ϵ_{A1} (small), T_1 , (k_A , k_1, \dots, ψ) at T_1
- Zone 2, ϵ_{A2} (bigger), T_2 , (k_A , k_1, \dots, ψ) at T_2 , etc.

Zone 1. The inlet conditions are given by equations 14–18. To calculate Y_A at the exit of zone 1 (Y_{Am}) with equation 22, \bar{u}_1 , the mean superficial gas velocity at zone 1, has to be estimated. As a first trial we propose using equation 23:

$$(\bar{u}_1)_e = 1.2 u_o \quad (23)$$

With equation 10, the mean residence time of the catalyst in zone 1 ($t_{c,1}$) is calculated by using equation 24:

$$t_{c,1} = sv_1 \frac{L_1}{(\bar{u}_1)_e} \quad (24)$$

With this value and equation 17, Y_A (and X_{Am}) and a at point m are calculated with equations 22 and 12, respectively. The superficial velocity of the gas at point m (u_m) and the mean velocity in zone 1 (\bar{u}_1) can be calculated by using equations 25–27:

$$u_m = u_{A,o}(1 + \epsilon_{A1}X_{Am}) + \frac{Qv}{S} \quad (25)$$

$$\bar{u}_1 = u_{A,o}(1 + \epsilon_{A1} \cdot \bar{X}_{A1}) + \frac{Qv}{S} \quad (26)$$

when

$$\bar{X}_{A1} = \frac{X_{Am}}{2} \quad (27)$$

given that $X_{Ao} = 0$.

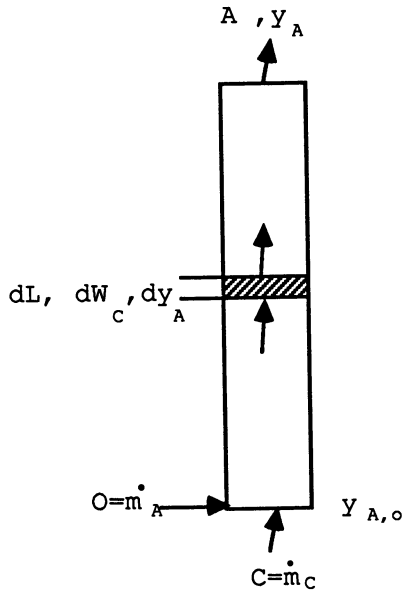


Figure 2. Scheme of the riser.

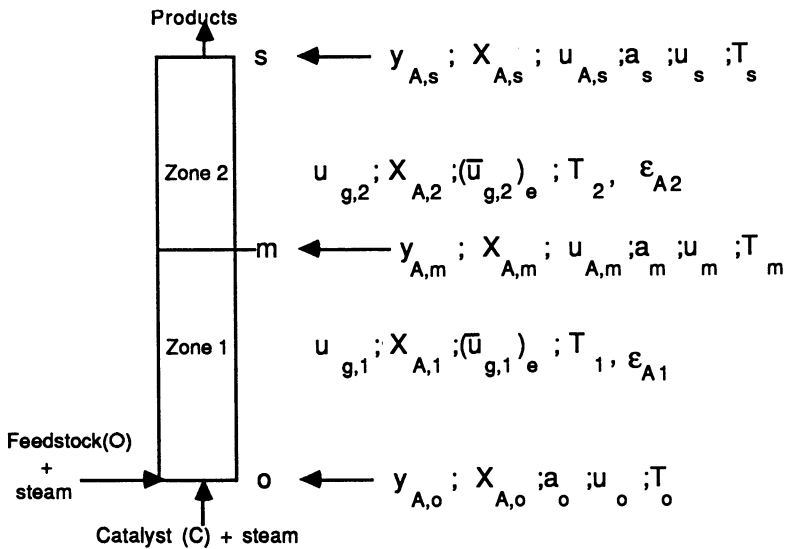


Figure 3. Nomenclature for the riser (only two zones are shown).

The calculated \bar{u}_1 value from equation 26 and the assumed (or estimated) value, $(\bar{u}_1)_e$ are now compared. If they are the same, the assumption was correct and the calculation passes to zone 2. If $\bar{u}_1 \neq (\bar{u}_1)_e$ the calculation is repeated by using equation 24 with a new value for $(\bar{u}_1)_e$, the calculated \bar{u}_1 . This iterative method is continued until two consecutive values appear to be the same.

With the calculated correct or definitive X_{Am} , a simple heat balance, and the known ΔH_r , ΔT in zone 1 is calculated. ΔT is obtained from $T_m = T_o - \Delta T$.

Zone 2. The inlet conditions of zone 2 are those of point m (exit of zone 1). The calculation for this case is the same. The values for ϵ_A , k_A , k_i , ψ , sv , etc., are those corresponding to T_2 .

The superficial velocity of the gas at the exit of zone 2 (u_s) and the mean velocity in zone 2 (\bar{u}_2) are given by equations 28 and 29:

$$u_s = u_{Ao} \left[1 + \epsilon_{A1} X_{Am} + \epsilon_{A2} (X_{As} - X_{Am}) \right] + \frac{Q_v}{S} \quad (28)$$

$$\bar{u}_2 = u_{Ao} \left[1 + \epsilon_{A1} X_{Am} + \epsilon_{A2} (X_{A2} - X_{Am}) \right] + \frac{Q_v}{S} \quad (29)$$

where

$$X_{A2} = \frac{X_{As} + X_{Am}}{2} \quad (30)$$

The first estimate of the mean superficial velocity of the gas in zone 2, $(\bar{u}_2)_e$, is determined as for zone 1 (equation 31):

$$(\bar{u}_2)_e = 1.2 u_m \quad (31)$$

With the value of $t_{c,2}$ (equation 32)

$$t_{c,2} = sv_2 \frac{L_2}{(\bar{u}_2)_e} \quad (32)$$

and equation 22 and with $Y_{Ao} = Y_{Am}$, Y_{As} is calculated. With Y_{As} , X_{As} is obtained. With this value and equations 29 and 30, \bar{u}_2 is calculated and compared with $(\bar{u}_2)_e$. If $\bar{u}_2 \neq (\bar{u}_2)_e$, the calculation is repeated, with $\bar{u}_2 = (\bar{u}_2)_e$ and equation 22.

Zones 3, 4, 5,... If we prefer to use several more zones, the calculation is repeated. For each zone, a different T with different values of k_A , k_i ,

$k_2, \dots, \psi, \epsilon_A$, and sv must be used. The X_A at the exit of the last zone considered is X_{As} at the riser exit (X_{As}).

Product Distribution at the Riser Exit. With X_{As} or Y_{As} calculated, Y_O, Y_E, Y_C and Y_G at the riser exit must be now be computed. This can be done by integrating the kinetic equations by numerical methods with the following boundary conditions: $Y_A = Y_{Ao}$ and $Y_O = Y_E = Y_G = Y_C = 0$.

The integration, between $Y_A = Y_{Ao}$ and $Y_A = Y_{As}$, can be carried out by the Runge–Kutta–Merson method. For good accuracy, the intervals have to be very small. For this calculation, the correct values of k_1 – k_8 must be known. If periodic deviations are obtained between the experimental (from the FCCU) yields and the yields predicted by this model, a corrective factor in these k_i values can be introduced.

Data Input to the Program or Model

To the program or model it is necessary to give the following data:

- Operating parameters
 1. u_o — superficial velocity of the gas at the bottom of the riser (feedstock injection point)
 2. Q_{steam}, Q_N — steam or N_2 flow rates at the bottom of the riser
 3. p — total pressure
 4. CATOIL or C/O — ratio of catalyst to oil flow rates
- Feedstock–catalyst parameters
 1. k_A, k_1 – k_8 — values of the cracking kinetic constants
 2. ψ — value of the deactivation kinetic constant
 3. d — deactivation order
- Dimensions of the riser
 1. S — section
 2. L — height
- Hydrodynamic parameters
 1. ϵ_A — expansion factor
 2. sv — slip velocity

Example

Input File. The following data are used with the program.

- Mass flow rate of the distillate or feedstock (A) in the inlet = 3358 tons per day

- Flow rate of steam in the inlet = 150.4 tons per day
- CATOIL or C/O = 5.9
- Average molecular weight of distillate (MW) = 450 g/mol
- Pressure in the riser = 3.09 bar
- Average temperature in each zone = 814, 792, 790, 789, and 789 K.
- Deactivation kinetic constant (ψ) in each zone = 0.50/s
- Slip velocity in each zone = 1.02, 1.04, 1.06, 1.08, and 1.1
- Expansion factor (ϵ) in each zone = 4.17
- Cracking order for distillate = 2
- Allowed error = 0.00001

Output File. The output is given in Table 1.

These results agree quite well with the experimental values from an FCCU.

Another Example

The model can be used to study, for instance, the influence of the total pressure. For the same conditions used for the first example, Figure 4 shows this influence in the conversion at the riser exit.

Table 1. Output from Model

<i>Variable</i>	<i>Zone 1</i>	<i>Zone 2</i>	<i>Zone 3</i>	<i>Zone 4</i>	<i>Zone 5</i>
Riser height	1.0	5.0	10.0	19.0	28.0
a_{outlet}	0.959	0.834	0.723	0.571	0.478
u_{outlet} (meters per second)	9.52	12.27	13.71	14.40	14.37
t_g in each zone (second)	0.131	0.367	0.385	0.698	0.603
t_c (second)	0.132	0.382	0.408	0.753	0.664
t_g total (second)	0.131	0.498	0.883	1.581	2.184
Y_A	0.665	0.397	0.291	0.207	0.172
Y_O	0.083	0.144	0.162	0.170	0.169
Y_E	0.200	0.358	0.417	0.462	0.478
Y_G	0.048	0.094	0.119	0.149	0.168
Y_C	0.006	0.017	0.025	0.037	0.044

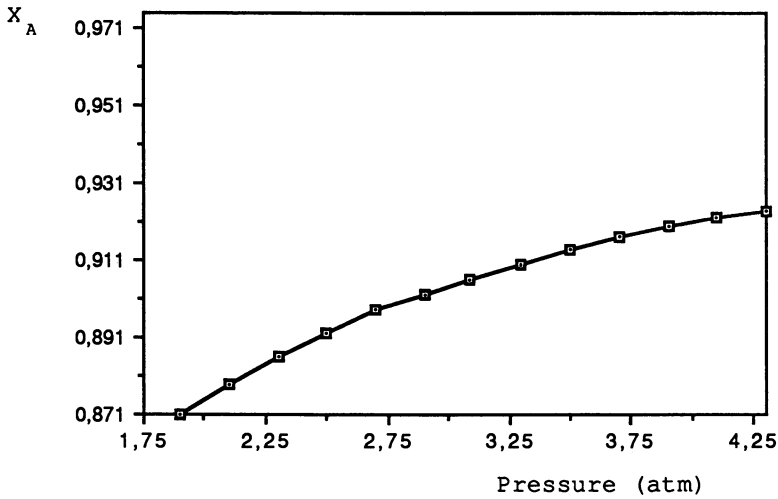


Figure 4. Influence of the total pressure in the riser in the conversion at the exit for a give mass flow rate of A.

Nomenclature

\dot{A}	mass flow rate of A, in kilograms per second
a	catalyst activity at some riser height, defined by $r_A/(r_A)_0$
a_0	catalyst activity at bottom of riser or feedstock inlet
a_A, a_O, a_E	catalyst activities for the cracking reactions of A, O, and E, respectively
d	deactivation order, defined by equation 11
d_A, d_O, d_E	deactivation orders for the cracking reactions of A, O, and E, respectively
E	activation energy according to Arrhenius law for the disappearance (cracking) of A, in kilocalories per mole
E_d	deactivation energy, in kilocalories per mole
G, j	empirical parameters of equation 13
k_1, k_8, k_i	kinetic cracking constants for reactions 1, 8, and i , respectively, in reciprocal second
k_A	overall kinetic cracking constant for the cracking of A, in reciprocal second
L	height from the feedstock injection point (m) in the riser

Q	total volumetric flow rate, in cubic meters per second
Q_0	total volumetric flow rate at feedstock inlet, in cubic meters per second
Q_A, Q_V, Q_{V_0}	total volumetric flow rates of A, of steam, and of steam at feedstock inlet, respectively, in cubic meters per second
r_A	reaction rate of A, in kilograms of A per kilogram of catalyst per second
t_c, t_g	residence times in the riser of the catalyst and the gas, respectively, in seconds
u	superficial velocity, in meters per second
X_A	feedstock conversion
Y_A, Y_O, Y_E, Y_G	weight fractions of unreacted A, gas oil, gasoline, and gas, respectively
Y_{A_0}	weight fraction of unreacted A at the feedstock inlet
Y_{A_s}	weight fraction of unreacted A at the riser exit
ϵ_A	expansion factor, defined by equation 6
ψ	deactivation kinetic constant or function, defined by equation 11, in reciprocal second
ψ_A, ψ_O, ψ_E	deactivation kinetic constants for the cracking reactions of A, O, and E, respectively, in reciprocal second
η, θ	parameters described in references

Acknowledgments

We thank our colleagues from the CRAL of BP France at Lavéra (France), whose friendship encouraged us to write this chapter. The discussions with P. Vernet, M. Provost, A. Espinosa, and A. Priou were particularly stimulating.

Literature Cited

1. Venuto, P. B.; Habib, E. T. *Fluid Catalytic Cracking with Zeolite Catalysts*; Marcel Dekker, New York, 1979.
2. *Fluid Catalytic Cracking: Role in Modern Refining*; Occelli, M. L., Ed.; ACS Symposium Series 375; American Chemical Society: Washington, DC, 1988.

3. Gates, B. C.; Katzer, J. R.; Schuit, G. C. A. *Chemistry of Catalytic Processes*; McGraw-Hill, New York, 1989; Chapter 1.
4. Mauleon, J. L.; Sigaud, J. B. *Proc. 12th World Petroleum Congress, 1987*, 4, 71–81.
5. O'Connor, P.; Hartkamp, M. B. (Akzo Chemical Division, The Netherlands), personal communication.
6. Whittington, E. L.; Murphy, J. R.; Lutz, I. H. *Book of Abstracts, Symposium on Advances in Gasoline Technology* (ACS National Meeting, New York), 1972, pp B66–B82.
7. Paraskos, J. A.; Shah, Y. T.; McKinney, J. D.; Carr, N. L. *Ind. Eng. Chem. Process Des. Dev.* 1976, 15(1), 165–169.
8. Shah, Y. T.; Huling, G. P.; Paraskos, J. A.; McKinney, J. D. *Ind. Eng. Chem. Process Des. Dev.* 1977, 16(1), 89–94.
9. Gates, B. C.; Katzer, J. R.; Schuit, G. C. A. *Chemistry of Catalytic Processes*; McGraw-Hill, New York, 1989; pp 90–99.
10. Van der Baan, H. S. In *Chemistry and Chemical Engineering of Catalytic Processes*; Prins, R. and Schuit, G. C. A., Eds.; Sijthoff and Noordhoff: The Netherlands, 1980; pp 217–233.
11. Corella, J.; Fernandez, A.; Vidal, J. M. *Ind. Eng. Chem. Product Res. Dev.* 1986, 25, 554–562.
12. Turlier, P.; Forissier, M.; Bernard, J. R. (ELF France); work presented at the CCRE meeting in Lyon, June 1989 and at the AIChE meeting in Houston.
13. Wollaston, G.; Haflin, W. J.; Ford, W. D.; D'Souza, G. J. *Hydrocarbon Proc.* 1975, September, 93–100.
14. Gross, B.; Jacob, S. M.; Nace, D. M.; Volz, S. E. U.S. Patent 3 960 707, June 1976.
15. Xinjun, M.; Shunsheng, W.; Huixin, W. *J. East China Inst. Chem. Tech.* 1988, 14(4), 409–417.
16. Corella, J.; Morales, F. G.; Provost, M.; Espinosa, A.; Serrano, J. In *Recent Advances in Chemical Engineering*; Saraf, D. N. and Kunzru, D., Eds.; Tata McGraw-Hill: New Delhi, 1989; pp 192–210.
17. Shaikh, A. A.; Carberry, J. J. *Chem. Eng. Res. Dev.* 1984, 62, 387–390.
18. Shuurmans, H. J. A. *Ind. Eng. Chem. Process Des. Dev.* 1980, 19, 267–271.
19. Dry, R. J.; White, C. C. *Powder Tech.* 1989, 58, 17–23.
20. Saxton, A. L.; Warley, A. C. *Oil Gas J.*, 1979, October, 71–82.
21. O'Connor, P.; Gevers, A. W. (Akzo Chemical Division, The Netherlands), private communication.
22. Bartholomew, K. D.; Soudek, A. *Oil Gas J.* 1989, October, 57.
23. Corella, J.; Provost, M.; Espinosa, A.; Gutierrez-Morales, F. In *Proceedings, XI Iberoamerican Symposium on Catalysis*, Guajanato, Mexico; Cossio, F. et al., Eds.; IMP Mexico: Mexico, 1988; pp 415–421.

24. Liguras, D. K.; Allen, D. T. *Ind. Eng. Chem. Res.* 1989, 26, 665.
25. Corella, J.; Bilbao, R.; Molina, J. A.; Artigas, A. *Ind. Eng. Chem. Process Des. Dev.* 1985, 24, 625–636.
26. Espinosa, A.; Provost, M.; Corella, J.; Francés, E. (BP France, Lavéra), private communication, 1989.
27. Wojciechowski, B. W. *Canad. J. Chem. Eng.* 1968, 46, 48.

RECEIVED March 12, 1990

Chapter 11

Fluid Cracking Catalyst Metals Passivation

Development and Application

Robert W. Bohmer, Dwight L. McKay, and Kelly G. Knopp

Phillips Petroleum Company, Bartleville, OK 74004

Passivation of metals on equilibrium catalytic cracking catalyst is widely and successfully applied operating practice within the refining industry. The technology is effective over a broad range of catalysts metals concentrations, oil feed compositions, operating conditions and types of catalytic cracking units. Practice of antimony metals passivation technology increases FCC unit oil feed capacity, significantly decreases the yields of hydrogen and coke and increases the yield of gasoline. Lower quality oil feedstocks can be cracked. Options for maximizing metals passivation benefits are illustrated with examples from refinery units.

The use of metals passivation to reduce the undesired effects of nickel and vanadium on fluid catalytic cracking catalysts has become an established operating practice within the refining industry. Several operating trends within the industry, such as increased resid cracking and higher regenerator temperature operation, are related to the benefits provided by metals passivation (1). Over the 14 years since it was first commercially introduced, metals passivation has played a key role in allowing refiners to maximize profits while cracking resid.

Phillips Petroleum Company discovered and developed the antimony metals passivation process in the early 1970's, and successfully applied the process at its Borger, Texas heavy oil cracker (HOC) in 1976 (2). For catalytic cracking units with contaminant metals problems, metals passivation with antimony significantly decreases the yields of hydrogen and coke, and increases the yield of gasoline. For a unit operating against a limited gas compressor or regenerator air blower, decreases in yields of hydrogen and coke allow for any of the following

benefits: increased throughput, increased conversion, or substitution of low value resid for some gas oil feed. With these performance benefits, metals passivation is widely used and accepted.

Optimizing passivation performance is an important consideration as refiners maximize throughput to catalytic cracking units and charge greater quantities of resid. Metals passivation should now be integrated into overall refining optimization models. Models used to predict catalytic cracking yields based on feedstock properties and operational parameters can be used effectively to evaluate the real benefits of additives and methods for enhancing the performance of metals passivation. Models are being used as well as advanced laboratory methods to develop techniques for improving the commercial performance of metals passivation.

Specific commercial performance benefits obtained with the antimony metals passivation process and methods used for evaluating potential benefits are discussed. Options for maximizing benefits are also presented.

Early Development and Initial Application

Research and Development. Research studies were carried out in laboratory units designed to meet particular needs in the area of heavy oil cracking and contaminant metals on cracking catalysts. These reactor systems were described in early papers (3-5). Metals passivation agents were evaluated in screening tests. Commercial equilibrium catalysts and catalysts contaminated with nickel and vanadium in the laboratory were used to crack gas oils or resids. The passivation agents were primarily organo metal compounds or oxides of the elements studied. The effectiveness of several elements for the reduction of the yield of hydrogen is shown in Table I. Antimony containing compounds were the most effective metals passivation agents. Although not discussed in this paper, metals passivation studies have been made using combinations of elements.

Equilibrium catalyst from a heavy oil catalytic cracker was used to crack 20 API gravity West Texas Long Resid. The catalyst contained 3100 ppm nickel and 4500 ppm vanadium; the concentration of antimony was varied. Evaluation results for 75 volume percent conversion are illustrated in Figure 1. The distribution of cracked products improved as antimony on the catalyst increased. Addition of 0.25 weight percent antimony reduced the yield of hydrogen about 50 percent, reduced the yield of coke about 20 percent, and the yield of gasoline increased 10 percent. Larger scale tests in a transfer line catalytic cracking pilot plant confirmed the outstanding response when the metals on the catalyst were passivated with a compound containing antimony.

A plan aimed at commercial application of metals passivation technology was implemented. Toxicology, industrial hygiene, and environmental questions relative to the use of antimony or passivation of metals on catalyst in FCC units were addressed. Procedures for injection of antimony compounds into FCC units were

**Table I. Passivation of Metals on FCC Catalysts
Ranking of Elements for Reduction of Hydrogen**

<u>Element</u>	<u>Hydrogen Reduction Relative To Antimony Passivation</u>
Sb	1.0
Tl	.8
Bi	.7
P	.6
Sn	.5
In	.4
Ca	.4
Te	.3
Ba	.3
Ge	.2
Al	.2
Si	.2

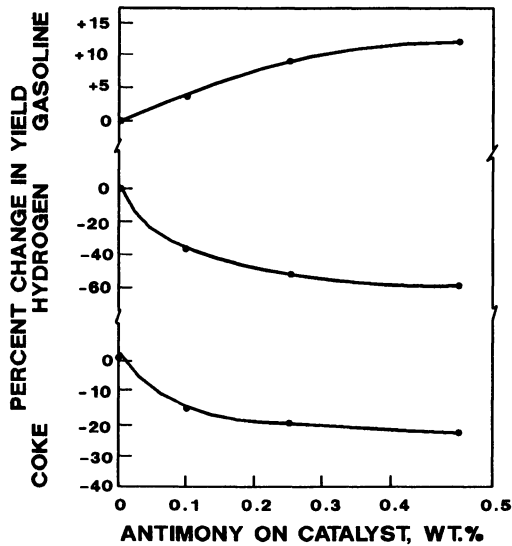


Figure 1. 75 Vol % conversion in pilot plant operation.
(Reproduced with permission from ref. 2. Copyright 1977 Gulf Publishing Co.)

developed, and extended pilot plant tests demonstrated operability. Assessment of all information indicated that, when applied properly, metals passivation with antimony could be carried out safely in refinery FCC units. The potential economic benefits were large, so a commercial test in a heavy oil catalytic cracker was undertaken. A project team prepared the commercial test plan, participated in conduction of tests, and evaluated the test information.

Commercial Application. The commercial test showed outstanding benefits. Comparison of information from the heavy oil cracker for several months before and after passivation of the metals on the catalyst demonstrated long term, trouble-free application of metals passivation technology. Passivation of the metals on the catalyst with antimony improved catalyst selectivity to gasoline, and reduced production of gas and coke. Many details of the test program and the demonstrated benefits achieved have been reported (2, 6-8). Commercial benefits of metals passivation were similar to the benefits predicted from research and development information.

Effects on Environment, Industrial Hygiene, and Metallurgy. The effects of metals passivation with antimony on the environment, industrial hygiene and metallurgy were studied by Phillips Petroleum Company and by independent testing laboratories. The toxicological and environmental information related to antimony metals passivation has been studied by specialists representing over seventy refineries. The guidelines for safe practice of metals passivation with antimony have been demonstrated in commercial experience. (6, 9).

Mechanism. The interaction of antimony with supported nickel particles was studied with X-ray diffraction (XRD) (10). These studies suggested that a high level of antimony is present on the surface of Ni-Sb alloys. Further studies of the Ni-Sb alloy, using X-ray photoelectron spectroscopy (XPS) and Auger electron spectroscopy (AES), confirmed the presence of an antimony enriched surface (11). The surface enrichment of antimony on the Ni-Sb alloy would be expected to significantly alter the catalytic activity of nickel, as indeed occurs when antimony is added to nickel laden cracking catalysts.

Effect of Antimony on CO Combustion Promoters and SO_x Catalysts. Partial passivation of CO combustion catalyst may occur when antimony-containing metals passivation agents are injected into catalytic cracking units. A decrease in CO combustion may be most noticeable during the front end loading period of high antimony injection (12). Technology has been developed to overcome the decreased activity of the combustion catalysts. Passivation of metals on catalyst with antimony is routinely practiced in catalytic cracking units using CO combustion catalyst for complete

or partial CO combustion. Passivation of metals with antimony does not affect the performance of the SO_x reduction catalysts (13).

Industry Wide Acceptance

Antimony metals passivation technology has been utilized in a variety of FCC unit designs, with a wide range of FCC catalysts (14, 9). In addition, antimony metals passivation has been commercially proven over a broad range of catalyst metals concentrations. As the catalyst metals level increases, the passivation performance improves. A study of over 25 commercial trials revealed that the average hydrogen reduction improved from 35% to 45% as the metals levels increased from less than 6000 ppm (4Ni+V) to over 9000 ppm (4Ni+V), Figure 2.

Metals passivation compliments the latest generations of FCC catalysts: octane catalysts based on USY zeolite technology and chemical dealumination. Octane catalysts equilibrate at lower unit cell sizes, resulting in minimization of hydrogen transfer reactions (15). Commercial tests have demonstrated that antimony does not affect the zeolite unit cell size (9).

Case Studies. As shown in Figure 2, metals passivation is utilized effectively with 4Ni+V concentrations less than 6000 ppm. Specific benefits of antimony metals passivation for two refinery FCC units operating at less than 6000 ppm 4Ni+V are discussed below.

The first example is a FCC unit operating against its wet gas compressor constraint. The FCC catalyst contained 900 ppm nickel and 600 ppm vanadium; these metals catalyzed a significant production of hydrogen. Introduction of antimony dramatically improved the unit performance. Hydrogen production decreased 31%, yield of coke decreased 5%, and yield of gasoline increased 1.5%. The decrease in hydrogen production unloaded the wet gas compressor, and enabled substitution of 2.5% of the gas oil feed with lower value resid. The benefit to cost ratio of these improvements was greater than 30.

Table II, the second example, shows the benefits of metals passivation at a FCCU in a refinery operating to maximize throughput. The FCC catalyst contained 490 ppm nickel and 1200 ppm vanadium, and the unit was operating against both its air blower and gas compressor limits. Hydrogen production was 92 SCF per barrel of FCCU feed; with this amount of hydrogen in the gas to the compressor, it was difficult to maintain the compressor governor on control. The high concentration of hydrogen in the fuel gas also affected the steady state operation of the heat control of other processing units.

When antimony was injected, hydrogen production decreased to 58 SCF/BFF, and the load on the compressor was eased. Coke production decreased as evidenced by a decreased load on the air blower and the 17°F decrease in regenerator temperature. As the load on the compressor was eased, the compressor speed controller was effective, and this stabilized the refinery steam balance. Overall, the unit operated closer to steady state, and this helped

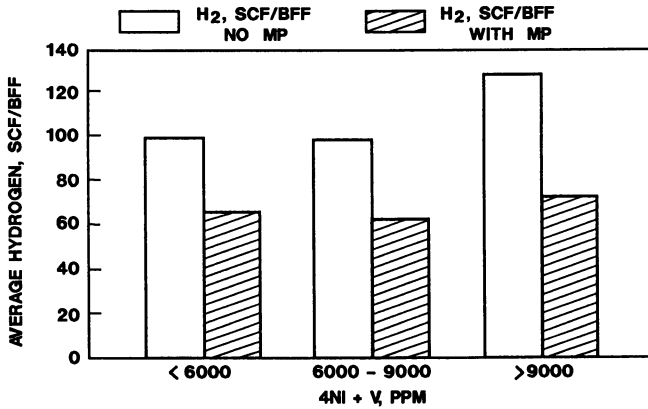


Figure 2. Hydrogen make with metals passivation.

Table II. Antimony Metals Passivation Effects on Charge Rate

	<u>Before</u>	<u>After Passivation</u>
Charge, B/D	30,774	32,943
Feed API Gravity	28.2	27.5
Feed Carbon Residue, Wt%	0.38	0.63
Regenerator Bed, F	1302	1285
Metals on Catalyst, PPM		
Nickel	489	611
Vanadium	1203	1585
Hydrogen, SCF/BFF	92	58
C ₂ & Lighter, LB/BFF	14.3	14.7
C ₃ & C ₄ Olefins, LV%FF	12.8	13.2
IC ₄ , LV%FF	3.1	2.9
Gasoline, LV%FF	56.2	54.3*
LCO, LV%FF	24.3	26.5
Coke, LB/BFF	19.7	18.3

*Separations conditions were changed to increase the yield of LCO during the late fall and winter months.

smooth out the overall refinery operations. With the decreased load on the compressor, the charge was increased from 31,000 BPD to 33,000 BPD. The refinery was also able to charge a poorer quality feed to the unit; the metals in the feed increased as did the metals on the catalyst. The yield of gasoline was less after the addition of antimony to the unit, due primarily to a change in fractionation of liquid products.

Metals passivation allows refiners to maximize the charge of lower value feeds. Injection of antimony into the Phillips Sweeny, Texas HOC decreased unit hydrogen production and decreased the process gas compressor speed about 500 rpm. This enabled the refinery to increase throughput 10% and process a more difficult to crack feedstock (14). Fifteen percent of Oriente crude from Ecuador was blended into the Phillips Borger, Texas refinery crude slate with the use of metals passivation at its HOC. Metals in the HOC feed and on the HOC catalyst increased significantly, but yield of hydrogen was still less than it had been prior to metals passivation (6).

Metals passivation also allows refiners to increase reactor severity to increase FCCU conversion. One refinery increased C₄ production (valuable alkylation feed) 17.2% by increasing conversion with the injection of antimony. Another refiner was able to increase the FCCU riser outlet temperature 8°F through decreased dry gas production with metals passivation. Yield of gasoline increased, and gasoline RON clear increased 0.7.

Other types of operations where metals passivation has been successful are FCC units that operate to maximize distillate production and Thermoform Catalytic Cracking Units (TCCU). A refiner operating a FCCU at conversions less than 60 liquid volume percent of the oil feed observed a 56% decrease in hydrogen production with metals passivation. Yields of liquid products increased. In a TCCU application, injection of antimony decreased yield of coke, as evidenced by a 70°F decrease in regeneration temperature, and decreased the H₂/CH₄ mole ratio in the off gas 13.7%.

Catalyst V/Ni Ratio Effects on Hydrogen Generation. Much of the literature on antimony metals passivation focuses on the effect of antimony on nickel. Little is mentioned about the interaction of antimony and vanadium. Vanadium has been shown to stabilize nickel coking activity to mild steam deactivation. Evidence for this interaction came from coking experiments, X-ray diffraction, and temperature-programmed reduction studies (16). Stabilization of nickel by vanadium suggests that in addition to the direct effect of antimony on vanadium, the presence of vanadium will influence the interaction of antimony and nickel. Figure 3 shows the percentage hydrogen decrease with antimony metals passivation in commercial units vs. FCC catalyst vanadium to nickel ratios. The data indicate that the ratio of vanadium to nickel on the catalyst is not a significant controlling factor in the performance of antimony metals passivation.

A study of the vanadium catalyzed dehydrogenation reaction showed antimony interacts with vanadium and decreases its dehydrogenation activity. Cracking catalyst was contaminated with vanadium in the laboratory. A portion of this contaminated catalyst was then treated with an antimony containing compound to passivate vanadium. The catalysts were evaluated by cracking gas oil. The yield of hydrogen for passivated catalyst averaged fifteen percent less than for the unpassivated catalyst.

Technology is Effectively Transferred to Commercial Use

Based on pilot plant and commercial metals passivation evaluations, a procedure was developed for estimating potential commercial benefits of the process. The estimation procedure utilizes plant data such as catalyst metals concentrations, FCCU hydrogen production, feed type, and reactor severity to determine potential economic benefits (17).

Figure 4 shows that the magnitude of benefits observed in commercial operations is close to the magnitude of benefits observed in the pilot plant and the magnitude of benefits predicted. In case 1, the commercial hydrogen production decrease with metals passivation was 42%, and the pilot plant predicted decrease was 35%. In case 2, the commercial, pilot plant, and predicted decreases in hydrogen production were 36%, 41% and 39% respectively. In case 3, the commercial and pilot plant decreases in the yield of hydrogen were 46% and 28% respectively. In case 4 the commercial, pilot plant, and predicted decreases in hydrogen production were 34%, 38% and 36% respectively. Estimations of changes in yield of coke were acceptable. Changes in yields of other products were difficult to estimate.

Optimization of Metals Passivation Benefits

Maintenance of Proper Antimony Concentration. Close monitoring of the antimony concentration on the catalyst will assure that maximum benefits are derived from a metals passivation program. The antimony-to-nickel ratio on the equilibrium catalyst has been correlated with hydrogen production in commercial operations (Figure 5). The non-linear shape of the hydrogen production curve has been confirmed in pilot plant tests (Figure 1). The recommended antimony concentration corresponds to a point beyond the breakpoint of the curve. A "cushion" is desired to allow fluctuations in the system without major increases in the yields of hydrogen and coke.

Type of Antimony. The type of antimony additive selected will affect the performance of a metals passivation program. Antimony additives are generally categorized as organic or inorganic. Gall, et. al. compared the passivation performance of an organo-antimony additive, antimony trisdipropyldithiophosphate, with antimony pentoxide in a fluidized pilot plant (14). The organo-antimony gave better passivation performance benefits than the inorganic

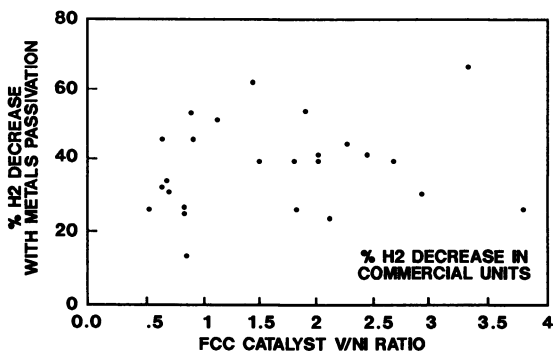


Figure 3. Catalyst V/Ni effects on hydrogen generation.

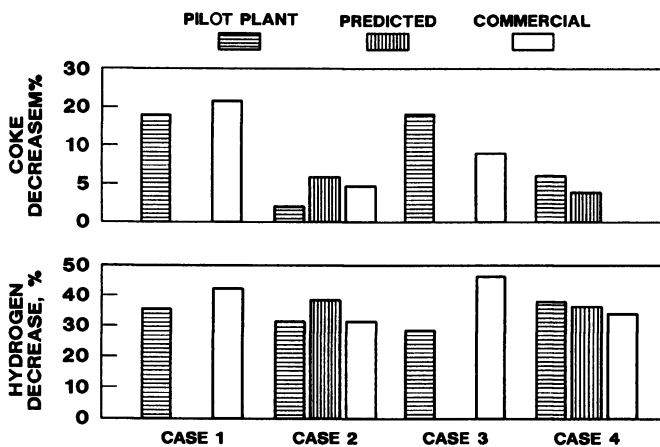


Figure 4. Comparison of pilot plant, predicted, and commercial benefits.

compound. It has been suggested that organo-antimony additives lay down on the catalyst more effectively than the inorganic compounds. Miller, et. al. presented commercial comparisons of antimony pentoxide and an organo-antimony additive (18). The data showed a significant improvement in lay-down efficiency for the organo-antimony compound, but the authors concluded that the antimony pentoxide was preferred due to lower additive costs. Phillips uses organo-antimony additives in its commercial applications based on a cost/benefit economic optimization.

Commercial Metals Passivation Systems

Metals passivation is an area of active research and development, and several passivation systems have been commercialized. Commercialized systems include addition of elements and combinations of elements to FCC catalysts, such as antimony, antimony plus phosphorus (6, 14), antimony plus phosphorus plus tin, antimony plus tin, tin (19-21), and bismuth (22, 23). Other commercialized systems include process changes or catalyst changes such as the use of steam or light hydrocarbons as diluents in the reactor (24) and vanadium traps (25). Antimony has been used successfully in conjunction with these systems. Another metals passivation additive, containing ingredients that are proprietary, has also been introduced commercially (26).

The combination of antimony and tin reduces the yield of hydrogen and coke, and increases the yield of gasoline when compared with the use of antimony alone. The resistance of the catalyst to deactivation by vanadium may also be improved. The combination of antimony and tin helped maintain catalyst activity for several commercial cases. With comparable feedstock and process conditions, the conversion increased up to three percent, the yield of gasoline increased up to 2.4 percent, and the yield of coke decreased up to 0.5 weight percent.

Future Application and Development

Economic pressures for higher gasoline octane and increased throughput assure that passivation of metals on cracking catalysts will remain an important technology in the refining industry. Work continues on improvements to the passivation process. The dichotomy at high antimony concentration levels between increasing benefits and decreasing laydown efficiency has been documented (27). Methods to improve the retention of antimony on the catalyst would result in the shifting of the economic optimum to a higher antimony concentration. The dynamics between the antimony laydown mechanisms and the unit operations must be considered. Improvements in antimony laydown efficiency of 35 to 40 percent have been observed in tests of new antimony containing additive systems.

Studies which apply surface science technology are being utilized to develop a better understanding of metals passivation mechanisms. Transport experiments in the lab have shown that

during steam-aging intraparticle transfer of V occurs and that migrating V can be irreversibly sorbed by a metal trap such as sepiolite in the form of a heat stable vanadate. The mechanism of V passivation and the nature of the compound formed during V-catalyst interaction has been studied by XRD, XPS and laser Raman spectroscopy (28-31). Lea and Kugler (32) studied equilibrium FCC catalysts by imaging secondary ion mass spectrometry (SIMS). In Agreement with lab results of Occelli (28) vanadium was found to be partially free to move from particle to particle as well as within a particle. Woolery, et. al. investigated the oxidation state and local structure of vanadium and nickel in FCC catalyst (33). Their data suggest that oxidation of V to V+5 is not a sufficient condition for catalyst deactivation. Other factors such as vanadium location and mobility play a role in the deactivation of catalyst by vanadium (28).

As market demands shift the desired FCC yield slate, the economics of a metals passivation program also change. Industry trends include higher reactor temperatures (greater than 1000°F) to maximize C₂-C₄ olefins, higher throughput, and lower quality feedstocks. Metals passivation technology can be used to improve the light end product quality at high reactor temperatures. Pilot plant tests at 1050°F reactor temperature with catalyst containing 10,000 ppm metals revealed that, in addition to reductions in yields of hydrogen and coke, a passivation agent reduced the butadiene yield 90%, increased the propylene yield 20%, and total butylenes increased 10%. A variety of passivation techniques may be used to customize the total product slate for a particular unit configuration.

The Modeling of Metals Passivation Effects

Models have been developed to predict cat cracker yields based on operating parameters and feedstock properties (34). These have aided in application and evaluation of metals passivation benefits. Miller and Pawloski (35) reported the use of mathematical models to calculate the benefits of vanadium passivation, and Teran (27) reported the need for FCCU hydrogen modeling and metals tracking to optimize passivation benefits.

In instances where refiners maximize charge of lower quality feed, observed selectivity changes with passivation are sometimes not as expected. In one commercial application, hydrogen production decreased 34% with the addition of antimony, but the yield of coke increased 5.6%, not an expected result. The decreased hydrogen production removed the FCCU gas compressor restraint, allowing the refinery to increase FCCU conversion and charge a lower quality feed. These operational changes influenced yields significantly. Models were used to project what the yields would have been with the change in feedstock, had there been no injection of antimony. The second column of Table III compares the actual yields with metals passivation, to the yields projected by the model had there been no metals passivation. This shows that metals passivation benefits were greater when the lower quality

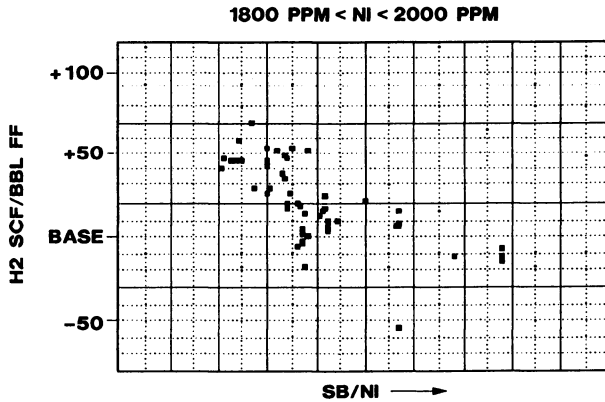


Figure 5. Commercial response of hydrogen production to variations in catalyst Sb/Ni ratio.

Table III. The Effects of Feedstock Quality on Passivation

	<u>Percent Change With Metals Passivation</u>	<u>Percent Change With Metals Passivation Considering Feed Quality Changes</u>
Gasoline	+1.3	+3.8
C ₄ LPG Gas	+17.2	+9.6
Coke	+5.6	-8.9
LCO	-13.6	+7.1
H ₂	-33.6	-33.6
Benefits/Costs	6.4	17.9

feed was considered. The benefit to cost ratio of metals passivation was better, 17.9 vs. 6.4, when accounting for operational and feed changes.

Similar models were used to aid in evaluating the benefits of antimony and tin compared with antimony alone. In one commercial trial, additional benefits achieved with the antimony-tin system included 2.9 percent higher conversion, 2.2 percent increase in the yield of gasoline with only a 0.2 percent increase in the yield of coke. When variations in fresh feed properties, slurry recycle and other processing conditions were included in data evaluated with the model, benefits with the antimony-tin system improved to 4.4 percent higher conversion, 2.6 percent increase in yield of gasoline, and the yield of coke only increased 0.3 weight percent. Incorporation of metals passivation technology into plant FCC unit operation models and into overall refinery economics models is expected to significantly extend the documented benefits of metals passivation.

Summary

Passivation of metals on equilibrium catalytic cracking catalyst is an established operating practice within the refining industry. The technology is effective over a broad range of catalyst contaminant metals concentrations, process operating conditions and types of catalytic cracking units. Practice of antimony metals passivation technology increases FCC unit oil feed capacity, decreases the yields of hydrogen and coke and increases the yield of gasoline. Lower quality oil feedstocks can be cracked. Commercial benefits obtained with the practice of metals passivation technology and the application of models for maximizing metals passivation benefits are illustrated with examples from refinery units.

Literature Cited

1. Stokes, G. M., Davison Catalog No. 77 (1988).
2. Dale, G. H., and McKay, D. L., Hydrocarbon Processing, **56** (9), 97-102 (1977).
3. McKay, D. L., and Bertus, B. J., PREPRINTS, Div. of Petrol. Chem., ACS, **24** (2), 645 (1979).
4. McKay, D. L., Schaffer, A. M., and Bertus, B. J., Southwest Catalysis Society Symposium, Fall 1980 Meeting, Houston, TX.
5. Lee, F. M., Ind. Eng. Chem. Res., **28**, 920-925 (1989).
6. Dale, G. H., Rogers, C. L., Nielsen, R. H., McKay, D. L., and Davis, E. D., API 43rd Midyear Meeting, Toronto, Canada, May 8-11, 1978, Proceedings-Refining Department, **57**, 432-438 (1978).
7. Rush, J. B., Chemical Engineering Progress, **77** (12), 29-32 (1981).
8. Rush, J. B., AM-81-43, NPRA Annual Meeting, March 29-31, 1981, San Antonio, TX.

9. Bohmer, R. W., McKay, D. L., and Knopp, K. G., AM-89-51, NPRA Annual Meeting, March 19-21, 1989, San Francisco, CA.
10. Dreiling, M. J., and Schaffer, A. M., J. Catal., **56**, 130-133 (1979).
11. Parks, G. D., Applications of Surface Science, **5**, 92-97 (1980).
12. Transcript of NPRA Question and Answer Session on Refining and Petrochemical Technology, 40-41 (1980), 50-51 (1982), 68 (1984), 62 (1987).
13. Pettersen, F. A., and Blanton, W. A., Paper 37e, AICHE, Summer National Meeting, 1986, Boston, MA
14. Gall, J. W., Nielsen, R. H., McKay, D. L., and Mitchell, N. W., AM-82-50, NPRA Annual Meeting, March 21-23, 1982, San Antonio, TX.
15. Pine, L. A., Maher, P. J. and Wachter, W. A., J. Catal., **85**, 466-476.
16. Tatterson, D. F., and Mieville, R. L., Ind. Eng. Chem. Res., **27**, 1595-1599 (1988).
17. McCarthy, W. C., Hutson, T. Jr., and Mann, J. W., Katalistiks 3rd Annual Fluid Cat Cracking Symposium, May 1982, Amsterdam, The Netherlands.
18. Miller, R. F., Blaschke, M. W., and Pawloski, J. N., AM-88-72, NPRA Annual Meeting, March 20-22, 1988, San Antonio, TX.
19. Denison, F. W. III, Hohnholt, J. F., English, A. R., and Krishna, A. S., AM-86-51, NPRA Annual Meeting, March 23-25, 1986, Los Angeles, CA.
20. English, A. R., and Kowalczych, D. C., Oil and Gas J., 127-128, (July 16, 1984).
21. Anderson, M. W., Ocelli, M. L., and Suib, S. L., J. Catal., **118**, 31-42 (1989).
22. Ramamoorthy, P., English, A. R., Kennedy, J. V., Lossens, L. W., and Krishna, A. S., AM-88-50, NPRA Annual Meeting, March 20-22, 1988, San Antonio, TX.
23. Kennedy, J. V., and Jossens, L. W., Paper 60a, AICHE, Spring National Meeting, 1990, Orlando, FL.
24. Cabrera, C. A., Helmer, C. L., and Davis, J. P., Paper 14, Katalistiks 8th Annual Fluid Cat Cracking Symposium, June 1-4, 1987, Budapest, Hungary.
25. Upson, L. L., Paper 18, Katalistiks 8th Annual Fluid Cat Cracking Symposium, June 1-4, 1987, Budapest, Hungary.
26. Barlow, R. C., and Lipinski, J. J., AM-89-17, NPRA Annual Meeting, March 19-21, 1989, San Francisco, CA.
27. Teran, C. K., AM-88-70, NPRA Annual Meeting, March 20-22, 1988, San Antonio, TX.
28. Ocelli, M. L., in "Fluid Catalytic Cracking: Role in Modern Refining," ACS Symposium Series, Vol. 375: M. L. Ocelli, Ed., ACS, Washington, D. C., p. 162 (1989).
29. Ocelli, M. L. and Stencel, J. M. in "Fluid Catalytic Cracking: Role in Modern Refining," ACS Symposium Series, Vol. 375: M. L. Ocelli, Ed., ACS, Washington, D. C., p. 195 (1989).

30. Ocelli, M. L. and Stencel, J. M. in "Zeolites as Catalysts, Sorbents and Detergent Builders," H. G. Karge and J. Weitkamp Eds.; Elsevier, p. 127 (1989).
31. Ocelli, M. L. and Stencel, J. M. in "Zeolites, Facts, Figures, Future," P. A. Jacobs, P. A. Vanjarter, Eds., Elsevier, Part B, p. 1311, 1989.
32. Leta, D. P., and Kugler, E. L., PREPRINTS, Div. of Petrol. Chem., ACS, 33 (4), 636-641 (1988).
33. Woolery, G. L., Chin, A. A., Kirker, G. W., Huss, A. Jr., and Chester, A. W., PREPRINTS, Div. of Petrol. Chem., ACS, 33 (4), 648.
34. Wenig, R. W., White, M. G., and McKay, D. L., PREPRINTS, Div. of Petrol. Chem., ACS, 28 (4), 909-919 (1983).
35. Miller, R. F. and Pawloski, J. N., Paper 18b, AIChE., Spring National Meeting, 1988, New Orleans, LA.

RECEIVED June 8, 1990

Chapter 12

Selectivity of Silica–Alumina Matrices

W.-C. Cheng and K. Rajagopalan

Davison Chemical Division, W. R. Grace and Company–Conn.,
Columbia, MD 21044

Amorphous silica-aluminas containing 13, 27 and 59 wt% Al_2O_3 were prepared by precipitating alumina onto silica gel, followed by hydrothermal treatment. These materials were characterized by ^{27}Al NMR and ESCA and evaluated in gas oil cracking. NMR revealed the presence of tetrahedral, pentacoordinated and octahedral Al species in the steamed SiO_2 - Al_2O_3 samples with 27 and 13% Al_2O_3 . The sample containing 59% Al_2O_3 , however, showed the presence of only tetrahedral and octahedral Al species and a 3-fold enrichment of Al at the surface. In gas oil cracking, the activity of the catalyst per unit surface area increased with increasing Al_2O_3 content. NMR analysis indicated that different types of Al species (eg., tetrahedral, octahedral) played a role in gas oil cracking. The catalysts with 13 and 27% Al_2O_3 showed equivalent selectivity while the catalyst with 59% Al_2O_3 yielded higher coke, H_2 , gasoline and LCO and lower C_3 and C_4 olefins at constant conversion. The differences in activity and selectivity can be attributed to increase in acid site density with increase in alumina content of these catalysts.

Commercial fluid cracking catalysts are comprised of faujasite zeolite dispersed in an inorganic mixed oxide matrix (1). X-ray amorphous silica-aluminas are generally used as matrix components. Cracking of large molecules present in a resid feed is limited by diffusion within a zeolite crystallite. As a result, the amorphous silica-alumina matrix plays a major role in cracking of these feed components (2). Cracking activity of amorphous silica-alumina is related to its acidity (3). Acidity and hydrocarbon cracking activity of amorphous silica-alumina catalysts of varying composition and preparation methods have been reported (4 - 7). Hydrothermal pretreatment of cracking catalysts has been employed as a

method to simulate aging in a commercial FCC unit (1). The objective of this work is to determine gas oil cracking activity and selectivity for silica-aluminas of varying composition. Hydrothermal pretreatment under varying conditions was employed to generate catalysts of the same composition with varying surface area. NMR and ESCA characterization of the silica-aluminas were employed to elucidate the nature of active site for gas oil cracking and determine catalyst structural properties that influence selectivity.

Experimental Methods

Amorphous silica-alumina catalysts of varying composition (13 to 59 wt% Al₂O₃) were prepared following the method described by Magee and Blazek (8). Catalysts are designated by their alumina content as SA-13, SA-27 and SA-59. The catalysts were washed free of soluble salts and spray dried. Properties of the fresh catalysts are described in Table I. Catalysts were hydrothermally pretreated at 1090°K with 100% steam for varying periods (2 to 16 hours). The pretreated catalysts were characterized by ESCA and solid state NMR. ESCA analyses were carried out on a PHI 5400 XPS with a Mg K α X-ray source. The surface Al/Si was taken as the ratio of the peak areas of the Al 2P and Si 2P peaks. Solid state ²⁷Al NMR analyses were performed using a Bruker AM-400 spectrometer (²⁷Al frequency, 104.25 MHz). About 1000 scans were accumulated before Fourier transformation. A line broadening of 100 Hz was used to eliminate the high frequency noise without affecting peak widths. A 2 μ s pulse (10 degree) was used with a repetition time of 0.1 s between pulses. Chemical shift was referenced to hexaquo aluminum ion. Solid state ²⁹Si NMR was carried out on a Bruker MSL-200 spectrometer (²⁹Si frequency, 39.76 MHz). An average of 1600 scans were collected. A line broadening of 50 Hz was used. Chemical shift was referenced to tetramethylsilane. In all experiments, the samples were equilibrated with a 50% relative humidity atmosphere for 16 hours and spun at the magic angle at a frequency between 4 - 8 kHz.

Table I: Properties of Catalysts

Description	:	SA-13	SA-27	SA-59
wt% Na ₂ O	:	.08	.04	.02
wt% SO ₄	:	.07	.16	.70
wt% Al ₂ O ₃	:	12.7	27.1	58.6
BET Surface Area ¹ (m ² g ⁻¹)	:	417	320	504

¹Measured after activating the catalyst for 3 hours at 810°K.

A fixed bed reactor described by ASTM Method No. D3907 was employed for catalytic testing. A sour, imported heavy gas oil with properties described in Table II was used as the feedstock. Experiments were carried out at a reactor temperature of 800°K and catalyst residence time ($\bar{\theta}$) of 30 seconds. Liquid and gaseous products were analyzed with gas chromatographs. Carbonaceous deposit on the catalyst was analyzed by Carbon Determinator WR-12 (Leco Corp., St. Joseph, MI). The Weight Hourly Space Velocity (WHSV) was varied at constant catalyst contact time to generate selectivity data of various products as a function of conversion. For certain experiments, conversion was also varied by varying the catalyst pretreatment conditions.

Table II: Properties of Sour, Imported Heavy Gas Oil

API gravity at 16°C	:	22.5
Sulfur (wt%)	:	2.6
Nitrogen (wt%)	:	.086
Conradson Carbon (wt%)	:	.25
Aniline Point (°C)	:	73
K Factor	:	11.6
D-1160 (°C)		
IBP	:	217
5	:	307
10	:	324
20	:	343
40	:	382
60	:	423
80	:	472
90	:	500
95	:	524

Results and Discussion

NMR and ESCA Characterization. Increasing the duration of hydrothermal pretreatment reduced the surface area of the silica-alumina catalysts (Figure 1). By varying the duration of pretreatment, catalysts of varying surface area were obtained for characterization and evaluation. Twelve catalysts of varying composition and surface area were analyzed (Table III). For the purpose of illustration, ^{27}Al and ^{29}Si NMR spectra of three of those catalysts are shown as Figures 2 and 3. ^{27}Al NMR analyses (Figure 2) indicated the presence of three lines for the pretreated SA-13 and SA-27 catalysts. The approximate chemical shift values for the lines were 0, 30 and 60 ppm. These lines were attributed to octahedral, pentacoordinated and tetrahedral Al respectively (10). The SA-59 catalyst exhibited only two

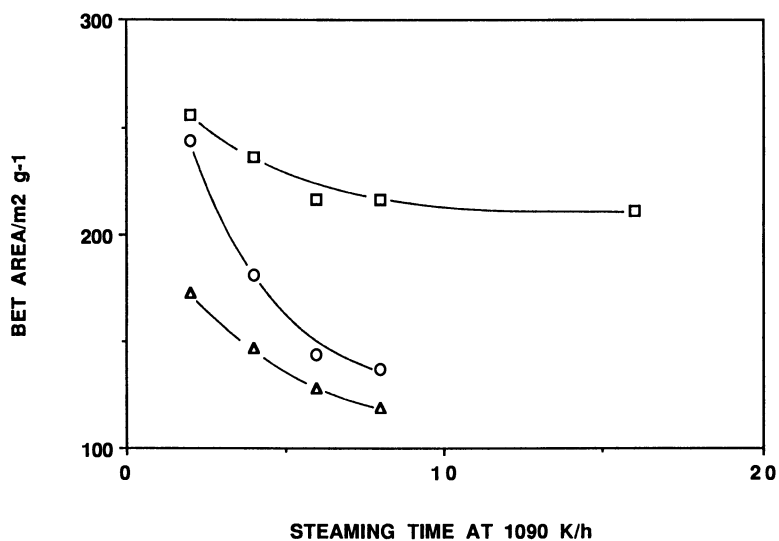


Figure 1. Effect of the time of pretreatment on surface area of catalysts.
△ SA-13; ○ SA-27; □ SA-59

lines near 70 ppm and 0 ppm (Figure 2). The chemical shift of about 70 ppm observed in SA-59 is characteristic of tetrahedral Al observed in γ -Al₂O₃ (11), indicative of Al-O-Al species, while the chemical shift of about 60 ppm observed in SA-13 and SA-27 is characteristic of tetrahedral Al present in zeolites, indicative of Al-O-Si species. These results imply that the pentacoordinated Al is not present in the pretreated SA-59 catalyst. Integrated line intensities for the NMR peaks for the catalysts after various pretreatments are summarized in Table III. These intensities are designed to be a qualitative measure of changes in the type of Al species as a function of composition and pretreatment. The results indicate that the distribution of Al species in SA-13 and SA-27 catalysts changed significantly with changes in pretreatment conditions. For example, increasing the duration of hydrothermal treatment of SA-13 increased pentacoordinated Al at the expense of tetrahedral Al. However, the surface composition of the catalysts, as measured by ESCA, did not change significantly with changes in pretreatment conditions.

Table III: Characterization of Steamed Silica-Alumina Catalysts

Description	ESCA Al/Si	Relative Intensities - ²⁷ Al NMR		
		Tetrahedral	Pentacoordinated	Octahedral
SA - 13 - 2 hrs.	.17	.67	.06	.27
SA - 13 - 4 hrs.	.18	.33	.31	.36
SA - 13 - 8 hrs.	.19	.32	.41	.27
SA - 27 - 2 hrs.	.68	.35	.42	.23
SA - 27 - 4 hrs.	.67	.33	.39	.28
SA - 27 - 8 hrs.	.75	.36	.37	.27
SA - 59 - 2 hrs.	4.5	.31	0	.69
SA - 59 - 4 hrs.	4.2	.27	0	.73
SA - 59 - 8 hrs.	4.6	.29	0	.71

The ²⁹Si NMR Spectra (Figure 3) for SA-13 and SA-27 exhibited a broad peak at a chemical shift of - 110 ppm, indicative of silicon species with zero nearest Al neighbors, Si(OAl)₀ (12). Shoulders at a chemical shift of 100 to 105 ppm suggest that a small amount of Si(OAl)₁ species are also present. The SA-59 sample, exhibited the peak at 110 ppm and several other broad peaks up to a chemical shift of 82 ppm, suggesting that this sample contained the full range of structures from Si(OAl)₀ to Si(OAl)₄. The higher alumina content of SA-59 apparently resulted in the presence of significant concentrations of Si(OAl)₂, Si(OAl)₃ and Si(OAl)₄ species.

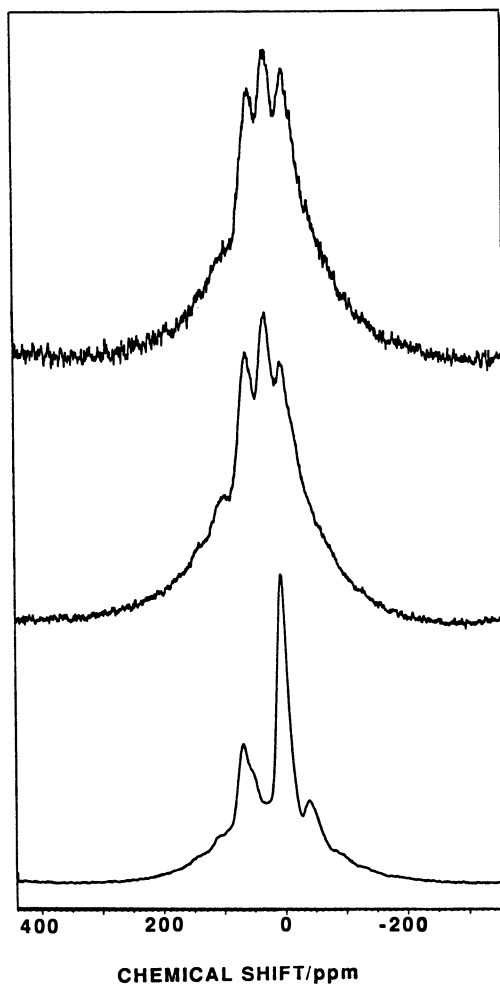


Figure 2. ^{27}Al NMR spectra for hydrothermally pretreated (1090° K) catalysts, SA-13 (above), SA-27 (middle) and SA-55 (below).

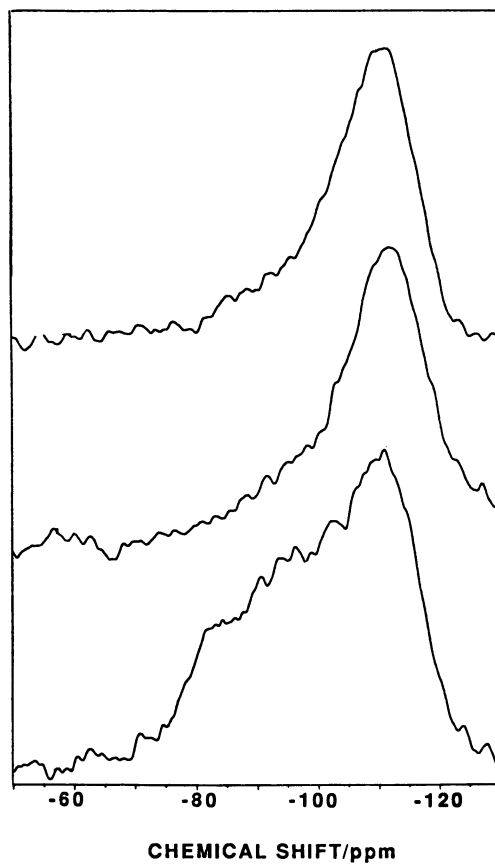


Figure 3. ^{29}Si NMR spectra for hydrothermally pretreated (1090°K) catalysts. SA-13 (above), SA-27 (middle) and SA-55 (below).

Activity per Unit Surface Area for Gas Oil Cracking. A second order kinetic conversion parameter (conversion + 100 - conversion) was used (13) to monitor gas oil cracking activity. The activity relationship as a function of surface area and catalyst composition is described in Figure 4. As expected, activity increased linearly with surface area. Activity per unit surface area depended on composition and increased with increasing alumina content. A catalyst with 27 wt% Al₂O₃ was more active for cumene cracking than a catalyst with 13 wt% Al₂O₃ (6). An activity maximum at 30 wt% Al₂O₃ was reported with thermally pretreated, cogelled silica-alumina catalysts for n-octane cracking and propylene polymerization (4). Propylene polymerization and n-octane cracking activity declined at higher alumina content. In the current work with hydrothermally pretreated catalysts, we observe the highest gas oil cracking activity per unit surface area at the highest (59 wt%) alumina content that was examined. Differences in catalyst preparation methods between the current and previous (4) work (cogellation or impregnation), could have influenced the activity - composition relationship.

For a given composition, when the catalyst surface area was varied by varying the pretreatment conditions, the distribution of Al species within the catalyst (tetrahedral, pentacoordinated, octahedral) varied significantly (Table III) without a significant change in activity per unit surface area (Figure 4). Cracking activity in amorphous silica-alumina has been attributed to tetrahedrally coordinated Al (14). The above NMR and activity results indicate that activity does not correlate with concentration of Al species of any particular coordination. This implies that Al that is not tetrahedrally coordinated in the catalyst also plays a role in gas oil cracking.

Effect of Composition and Pretreatment on Coke and H₂ Selectivity. We examined the effect of catalyst composition and pretreatment on the selectivity for coke and H₂. Results (Figures 5 and 6) indicate higher yields of coke and H₂ at constant conversion for SA-59 relative to catalysts with lower alumina content. Pretreatment conditions influenced coke, H₂ yields indirectly by influencing surface area and gas oil conversion. Thus, coke and H₂ selectivity was not influenced by pretreatment conditions. We conclude that coke and H₂ selectivity does not correlate with the concentration of Al species of a particular coordination (eg., tetrahedral).

The activity per unit surface area as well as selectivity for coke and H₂ were higher for SA-59 relative to catalysts of lower alumina content. Coke selectivity of various Y-faujasite catalysts has been related to density of acid sites (13). Perhaps the density of acid sites per unit surface area in these amorphous silica-alumina catalysts increase with Al₂O₃ concentration. The higher density of sites in SA-59 can explain its higher activity per unit surface area as well as higher coke yields at constant conversion. Increasing site density in faujasite catalyst resulted in lower selectivity for light olefins (eg., butylene) and higher selectivity for gasoline (15). Hence, we examined the detailed selectivity for all the cracked products with the amorphous silica-alumina catalysts.

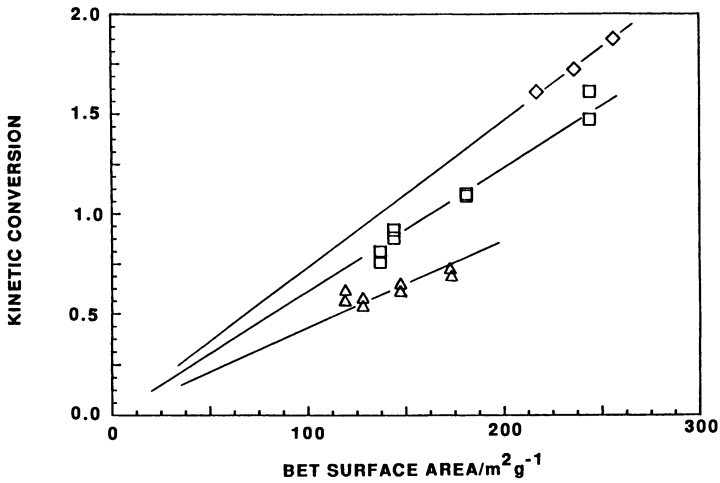


Figure 4. Activity of catalysts of varying surface area. Surface area was varied by varying the duration of hydrothermal pretreatment. \triangle SA-13; \square SA-27; \diamond SA-59

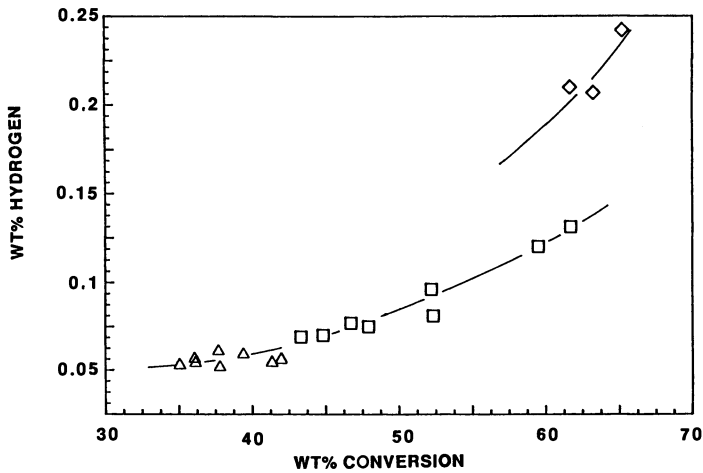


Figure 5. Hydrogen selectivity of catalysts. Conversion was varied by varying the duration of hydrothermal pretreatment \triangle SA-13; \square SA-27; \diamond SA-59

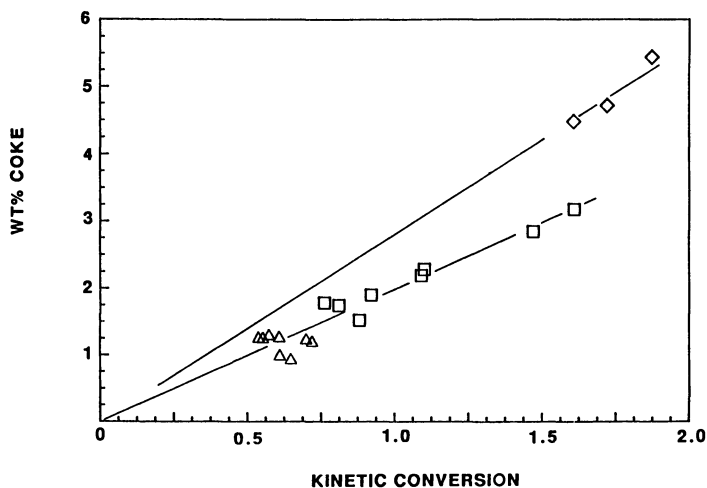


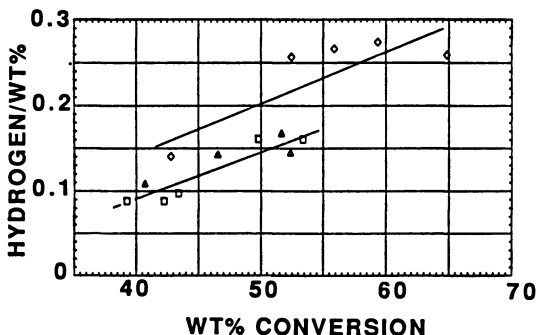
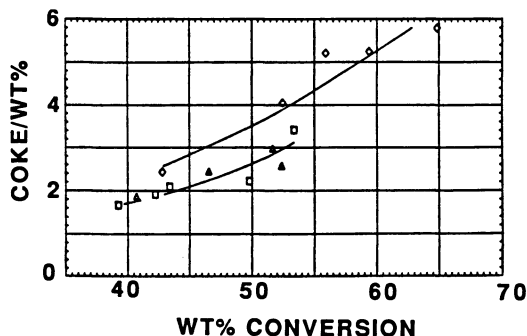
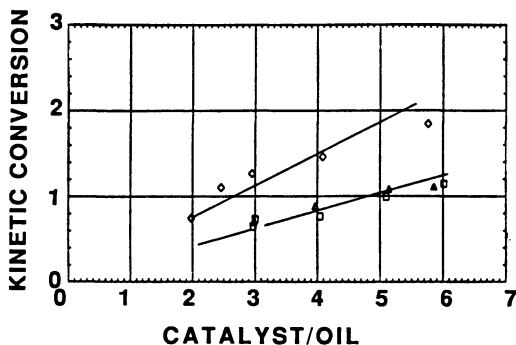
Figure 6. Coke selectivity of catalysts. Conversion was varied by varying the duration of hydrothermal pretreatment.
△SA-13; □SA-27; ◇SA-59

Product Distribution as a Function of Composition. Pretreatment conditions for the catalysts of varying composition were adjusted to achieve catalysts of comparable activity. Thus, the more active SA-59 catalyst was pretreated longer (16 hrs.) than the less active SA-13 catalyst (2 hrs.). This was considered acceptable as results reported earlier indicate that activity per unit surface area and coke, H₂ selectivity are not influenced by the pretreatment conditions. Gas oil conversion was varied by varying the space velocity. Results summarized in Figures 7 and 8 indicate that SA-59 yielded more coke, H₂, gasoline and light cycle oil (LCO) at constant conversion than SA-13 and SA-27. SA-13 and SA-27 were more selective for propylenes and butylenes relative to SA-59. Selectivity for C₂-hydrocarbons of all the catalysts were equivalent. The selectivity of SA-59 for gasoline at the expense of propylenes and butylenes is consistent with the hypothesis of higher acid site density in SA-59. With high acid site density bimolecular hydrogen transfer reactions compete with unimolecular cracking reactions (15) resulting in increased yield of intermediate cracked products like gasoline and LCO at the expense of fully cracked products like propylenes and butylenes. The high site density also favors bimolecular reactions that facilitate formation of coke precursors (13).

Conclusions

The distribution of Al species of varying coordination (tetrahedral, pentacoordinated and octahedral) can be influenced by changing the conditions of hydrothermal pretreatment of amorphous silica-alumina catalysts. However, for a given composition, activity per unit surface area and selectivity were independent of pretreatment conditions. Thus, gas oil cracking activity and selectivity in amorphous silica-alumina cannot be

ascribed to Al species of a particular coordination (eg., tetrahedral). Al that is not tetrahedrally coordinated in the catalyst also plays a role in gas oil cracking. Activity per unit surface area and selectivity for the production coke, gasoline, LCO and light olefins were influenced by the composition (alumina content) of the catalyst. The activity and selectivity results can be explained by suggesting that the catalyst with the highest alumina content (SA-59) has the highest density of acid sites. Higher site density resulted in increased selectivity for gasoline, LCO and coke at the expense of light (C₃, C₄) olefins. The selectivity trends are consistent with reported effects of site density on selectivity in faujasite.



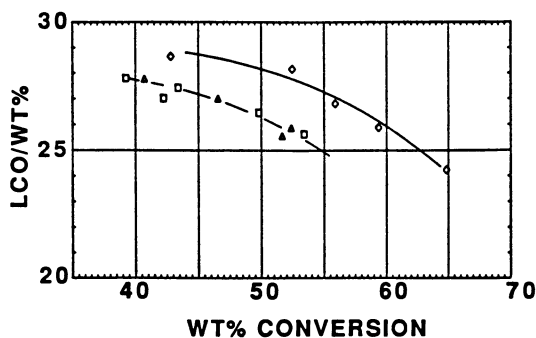
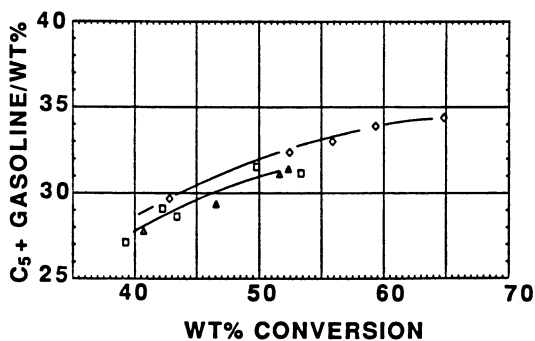
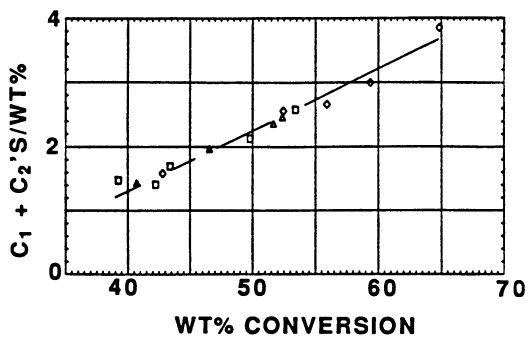
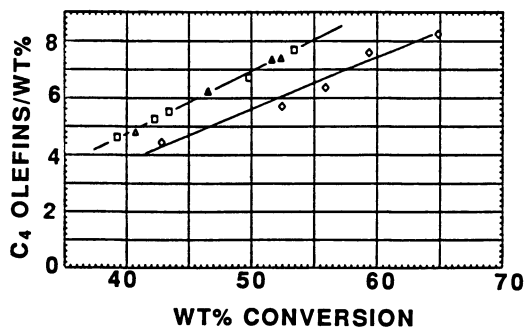
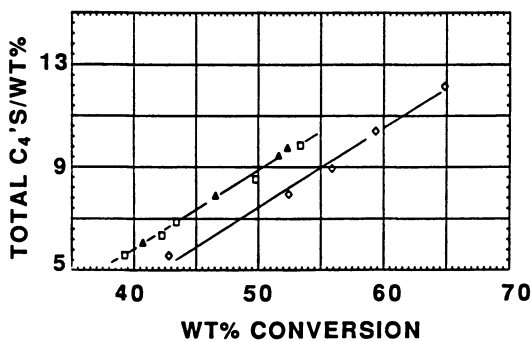
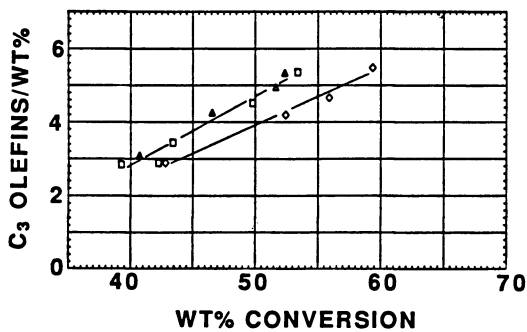
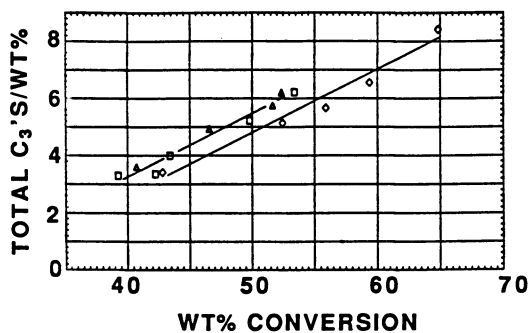


Figure 7. Activity and selectivity of hydrothermally pretreated (1090°K) catalysts. Conversion was varied by varying weight hourly space velocity.

△SA-13 (2 hrs.); □SA-27 (8 hrs.); ◇SA-59 (16 hrs.)



(Figure continued)



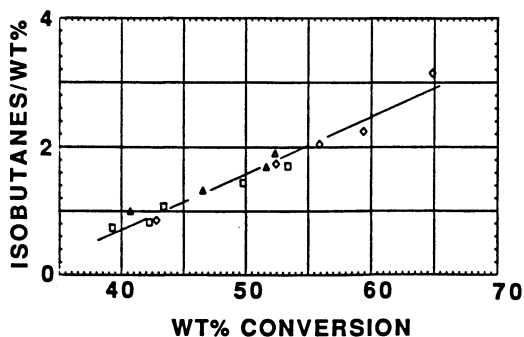


Figure 8. Light hydrocarbon selectivity of hydrothermally pretreated (1090°K) catalysts. Conversion was varied by varying weight hourly space velocity.

△SA-13 (2 hrs.); □SA-27 (8 hrs.); ◇SA-59 (16 hrs.)

Acknowledgments

The authors are grateful to M. P. Shatlock for the solid state NMR spectra, B. J. Rees for the ESCA work and to the Davison Chemical Division of W. R. Grace & Co.-Conn. for permission to publish this work.

Literature Cited

1. Venuto, P. B.; Habib, Jr., E. T. Fluid Catalytic Cracking with zeolite Catalysts; Marcel Dekker, Inc.: New York, 1979.
2. Young, G. W.; Rajagopalan, K. Ind. Eng. Chem. Proc. Des. Dev. 1985, **24**, 995.
3. Tamele, M. W. Disc. Faraday. Soc. 1950, **8**, 270.
4. Holm, V. C. F.; Clark, A. J. Catal. 1963, **2**, 16.
5. Holm, V. C. F.; Baily, G. C.; Clark, A. J. Phys. Chem. 1959, **63**, 129.
6. Marczewski, M.; Wojciechowski, B. W. Can. J. Chem. Eng. 1982, **60**, 617.
7. Murrell, L. L.; Dispenziere, N. C. J. Catal. 1989, **117**, 275.
8. Magee, J. S.; Blazek, J. J. Preparation and Performance of Zeolite Cracking Catalysts in "Zeolite Chemistry and Catalysis" J. A. Rabo, Ed. ACS Monograph, ACS, Washington, D.C. 1976, **171**, 615.
9. Weekman, Jr., V. W. Ind. Eng. Chem. Proc. Des. Dev. 1968, **7**, 90.
10. Gilson, J-P.; Edwards, G. C.; Peters, A. W.; Rajagopalan, K.; Wormsbecher, R. F.; Roberie, T. G.; Shatlock, M. P. J. Chem. Soc. Chem. Comm. 1987, 91.
11. John, C. S.; Alma, N. C. M.; Hays, G. R. Appl. Catal. 1983, **6**, 341.
12. Klinowski, J.; Thomas, J. M.; Fyfe, C. A.; Hartman, J. S. J. Phys. Chem. 1981, **85**, 2590.
13. Rajagopalan, K.; Peters, A. W. J. Catal. 1987, **106**, 410.
14. Thomas, C. L. Ind. Eng. Chem. 1949, **41**, 2564.
15. Pine, L. A.; Maher, P. J.; Wachter, W. A. J. Catal. 1984, **85**, 466.

RECEIVED June 8, 1990

Chapter 13

Solid–Solid Reaction Between Y-Zeolite and Vanadium Pentoxide

C. Marchal, J. Thoret, M. Gruia, C. Dorémieux-Morin, and J. Fraissard

Laboratoire de Chimie des Surfaces, associé au Centre National de la Recherche Scientifique, URA 870, Université Pierre et Marie Curie, 4 Place Jussieu, 75252 Cedex 05, Paris, France

X-ray diffractometry, spectrometric techniques (^{29}Si high-resolution NMR, adsorbed ^{129}Xe NMR, and electron paramagnetic resonance), and transmission electron microscopy (TEM) have been used to study solid-state reactions occurring between NaY zeolite and V_2O_5 at 700 K. When the ratio R (V atom number/[Al + Si] atom number) is 0.2, the zeolite lattice collapses. However, when $R \sim 0.05$, the lattice remains. The interaction is interpreted in terms of sodium vanadate (containing V^{V} and V^{IV} atoms) formation.

Zeolite modifications have been the subject of extensive studies. Some research deals with the replacement of lattice silicon or aluminum by another element (1–8). The motivation for such studies is that, even for a low substitution ratio, the modified zeolites would acquire specific catalytic properties. In fact, the location of the heteroatoms is generally uncertain, a fact bringing to question whether the heteroatoms really enter the lattice or lie in cavities or channels to generate compounds of potential interest to industries.

In his monograph (9), Rabo reported the first studies of solid-state reactions between zeolites, mainly Y zeolite, and some salts. These studies revealed either ion exchange or more or less reversible occlusion of the salt. In cases of occlusion, the salt anion (halide, nitrate, or oxygenated chlorine anions) was usually located in sodalite cavities.

Recently, Karge et al. reported results of solid-state ion exchange between alkaline chlorides and HZSM-5 (or $\text{NH}_4\text{ZSM-5}$) (10) and between alkaline earth chlorides and mordenite (11). They used IR spectroscopy (to monitor OH groups), thermogravimetric analysis, titration of the evolved gases, and mass spectrometry associated with temperature-programmed gas evolution. The mass spectrometric technique enabled them to distinguish between low- and high-temperature exchange reactions. Subsequently, they

studied the solid-state interaction of HZSM-5 with several oxides (MnO, Cu₂O, CuO, and NiO) and chlorides of the same metals (12). The degrees of exchange of zeolite protons with the oxides were considerably lower than those for the corresponding chlorides.

Kucherov and Slinkin reported solid-state reactions of H-mordenite and HZSM-5 zeolites with metallic oxides such as CuO (13), Cr₂O₃, MoO₃, and V₂O₅ (14–17). The resulting samples were studied by EPR (electron paramagnetic resonance) spectrometry. The authors have shown that the metal cations migrate to cationic sites, where they are coordinately unsaturated.

When V₂O₅ is used, vanadyl ions (VO²⁺) that are formed interact strongly with lattice aluminum atoms located in acidic site vacancies of the ZSM-5 lattice (14, 16).

In this chapter, we report the results of some solid-state experiments on NaY zeolite and vanadium pentoxide, V₂O₅ (18).

Experimental Procedures

NaY zeolite (LZY-52 from Union Carbide Corporation) and V₂O₅ (from Prolabo) were used. Mixtures were prepared by using ratios calculated as follows

$$R = \frac{\text{V atom number}}{(\text{Al} + \text{Si}) \text{ atom number}}$$

for the same NaY zeolite unit (for example, the unit cell).

Samples weighing 2 g were prepared each time. The samples were ground by hand in an agate mortar for 15 min and then heated in air (at 150 K/h) in a refractory nacelle to 690–750 K. The materials were kept at this temperature for 16 h. The samples were then allowed to remain at ambient temperature in air to rehydrate freely.

X-ray diffractograms were obtained with a Philips NP 760 apparatus using the K_α radiation of cobalt or copper. The value of the cubic-unit-cell parameter was determined from an internal silicon standard.

The pretreatment temperature of the sample submitted to xenon adsorption and NMR experiments was low enough (393 K) to prevent any hydrolysis. Evacuation to 10⁻⁴ torr (1 torr = 133.322 Pa) for 15 h at this temperature ensures the elimination of most of the water of hydration. Moreover, Gédéon et al. (19) showed that when NaY is less than 15% hydrated the remaining water molecules are in the sodalite cages. Such a small amount of water cannot affect xenon adsorption, which occurs only in the supercages.

Measurements of xenon gas adsorption isotherms were performed at temperatures between 273 and 299.5 K (this latter temperature being that of the ¹²⁹Xe NMR probe).

^{129}Xe NMR experiments were performed according to previously described methods (19) on a Bruker CXP 100 apparatus at 24.3 MHz. The chemical shift (δ) of adsorbed xenon is given relative to the value for gaseous ^{129}Xe extrapolated to zero pressure.

^{29}Si magic-angle-spinning (MAS) solid-state NMR spectra were obtained with a Bruker MSL 400 apparatus at 79.5 MHz. The Si/Al ratios were calculated by the usual method (20) after simulation of the experimental spectra.

EPR spectra were obtained with a Varian CSE 109 apparatus at 9.277 GHz. The g reference value was 2.0037 for DP. Commercial NaY zeolite could not be used because it contains too much iron, and so the experiments were performed with a noncommercial zeolite containing only 28 ppm of iron.

TEM results were collected on a Jeol JEM 100 CXII high-resolution apparatus with an acceleration voltage of 100 kV. The samples were prepared on a copper grid from an aqueous suspension. The magnification varied from 3×10^5 to 9×10^5 .

Results and Discussion

The X-ray spectra of the heated samples (Figures 1 and 2 and Tables I and II) show different results depending on R . For samples with $R \leq 0.05$, the spectrum contains the characteristic lines of the NaY zeolite and no additional lines. In particular, no lines characteristic of V_2O_5 are observed. The cubic-unit-cell parameter rises from 2.4639 ± 0.0005 nm for NaY zeolite to 2.4673 ± 0.0015 nm for the sample with $R = 0.05$.

For $0.05 < R < 0.2$, the structure of NaY zeolite is almost retained, but some weak lines of V_2O_5 can be identified in the spectrum.

For $0.2 \leq R \leq 0.6$, the NaY zeolite lines are weak, and V_2O_5 is still visible; an amorphous phase exists, and the lines of the sodium vanadate $\text{Na}_5\text{V}_5\text{V}^{\text{IV}}\text{O}_{15}$ containing some tetravalent V^{IV} are detected. When the sample with $R = 0.6$ is heated to 810 K again for 9 h, a new sodium vanadate, $\text{Na}_5\text{V}_{11}\text{V}^{\text{IV}}\text{O}_{32}$, crystallizes. X-ray spectroscopy clearly attests to a chemical interaction between NaY zeolite and V_2O_5 .

The ^{29}Si NMR spectrum determined that the Si/Al ratio for NaY zeolite is 2.45 ± 0.12 . Because of this experimental error, no significant modification of this ratio can be observed for the sample with $R = 0.05$. For treated samples containing an amorphous phase, the ^{29}Si NMR signal cannot be used for two reasons: the resolution is reduced and the interpretation is not clear.

Because it would be difficult to compare isothermal adsorption results for multiphase samples, the studies were restricted to NaY zeolite and the compound for which $R = 0.05$. For both solids, the logarithmic representations for the relation $\log N = f(\log P)$, where N is the number of adsorbed xenon atoms per gram of dehydrated zeolite and P is the xenon equilibrium pressure, are straight lines. The line for the sample with $R = 0.05$ is below that of NaY zeolite (Figure 3). The $\log N$ value extrapolated to zero abscissa is smaller, and the slope is only a little larger.

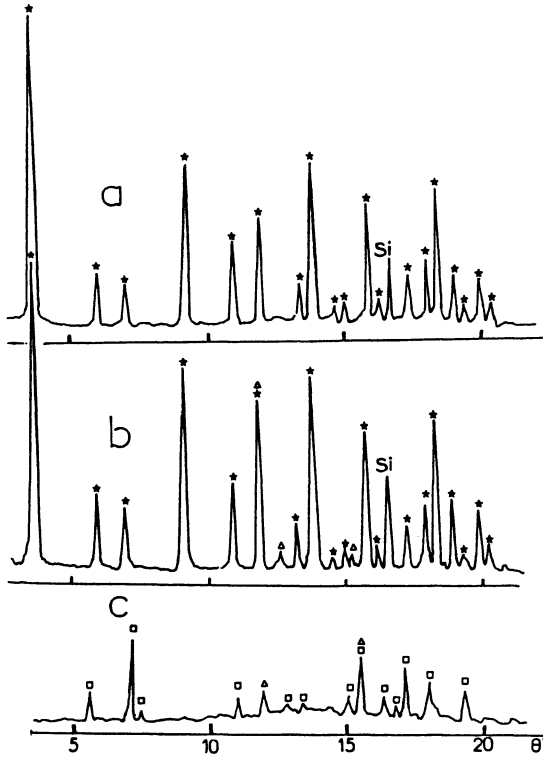


Figure 1. X-ray data for NaY zeolite- V_2O_5 : (a) sample with $R = 0.05$, (b) sample with $R = 0.10$, and (c) sample with $R = 0.60$. For all samples, $Co K_{\alpha}$ radiation was used. Symbols are defined as follows: *, NaY zeolite; Δ , V_2O_5 ; and \square , NaV_6O_{15} .

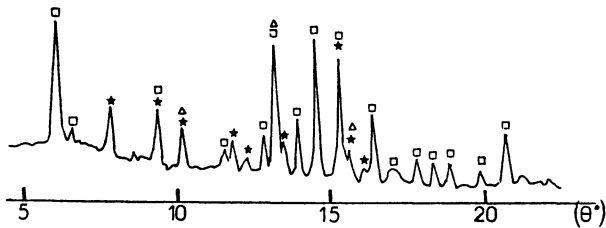


Figure 2. X-Ray data for NaY zeolite- V_2O_5 ($R = 0.50$, $Cu K_{\alpha}$ radiation). Symbols are defined as follows: *, NaY zeolite; Δ , V_2O_5 ; and \square , NaV_6O_{15} .

Table I. X-Ray data

Samples	θ	Intensities	$d_{h,k,l}$ (Å)	NaY	New	V_2O_5
				h, k, l	phase	h, k, l
NaY- V_2O_5 R=0.05 Co K_{α} radiation	3.57	TF	14.364	111		
	5.89	m	8.716	220		
	6.91	m	7.434	311		
	9.07	F	5.688	331		
	10.86	m	4.747	511		
	11.84	F	4.359	440		
	13.26	m	3.899	620		
	13.74	F	3.766	533		
	14.58	f	3.553	444		
	15.02	f	3.451	551		
	15.74	F	3.294	642		
	16.18	f	3.209	731		
	17.28	m	3.011	733		
	17.92	m	2.906	660		
	18.29	F	2.850	555		
	18.92	m	2.758	840		
	19.29	f	2.706	911		
19.89	m	2.630	664			
NaY- V_2O_5 R=0.10 Co K_{α} radiation	3.57	TF	14.364	111		
	5.91	m	8.687	220		
	6.93	m	7.413	311		
	9.10	F	5.655	331		
	10.87	m	4.743	511		
	11.84	F	4.358	440		001
	12.65	m	4.080			101
	13.27	m	3.896	620		
	13.76	F	3.760	533		
	14.57	f	3.555	444		
	15.01	f	3.453	551		
	15.22	f	3.407			110
	15.75	F	3.295	642		
	16.175	f	3.2108	731		
	17.275	m	3.012	733		
	17.194	m	2.9038	660		
	18.31	F	2.846	555		
18.93	m	2.757	840			
19.32	f	2.703	911			
19.90	m	2.627	664			

Table II. X-Ray data

Samples	θ	Intensities	$d_{h,k,l}$ (Å)	NaY	New	V_2O_5
				phase	phase	phase
				h, k, l	h, k, l	h, k, l
	6.06	F	7.292		002	
	6.22	f	7.013		$10\bar{2}$	
	7.76	m	5.702	331		
	9.30	m	4.762	511	200	
	10.10	m	4.371	440		001
	11.50	f	3.867		$10\bar{4}$	
	11.70	m	3.76	533		
	12.20	f	3.643		004	
	12.78	m	3.482		202	
	13.12	F	3.391		$11\bar{1}$	110
NaY- V_2O_5 R=0.5	13.40	m	3.305	642		
	13.88	m	3.20		111	
	14.50	F	3.07		104	
Cu K_α radiation	15.25	F	2.928		$30\bar{4}$	
	15.55	m	2.87	555		400
	16.17	f	2.76	840		
	16.37	m	2.73		$21\bar{3}$	
	17.20	f	2.63		113	
	17.78	m	2.52		$10\bar{6}$	
	18.30	m	2.45		$31\bar{1}$	
	18.88	m	2.38		$40\bar{4}$	
	19.82	m	2.271		311	
	20.70	F	2.18		106	
	5.42	f	9.48		100	
	7.09	m	7.25		002	
	7.40	f	6.97		$10\bar{2}$	
	10.86	f	4.75		200	
	11.85	f	4.35			001
NaY- V_2O_5 R=0.6	13.30	f	3.88		$10\bar{4}$	
	14.30	f	3.64		004	
	15.00	f	3.46		202	
Co K_α radiation	15.35	m	3.38		$11\bar{1}$	110
	16.25	f	3.25		111	
	16.50	f	3.16		300	
	17.02	m	3.06		104	
	17.25	m	2.90		$30\bar{4}$	
	19.25	m	2.72		$21\bar{3}$	

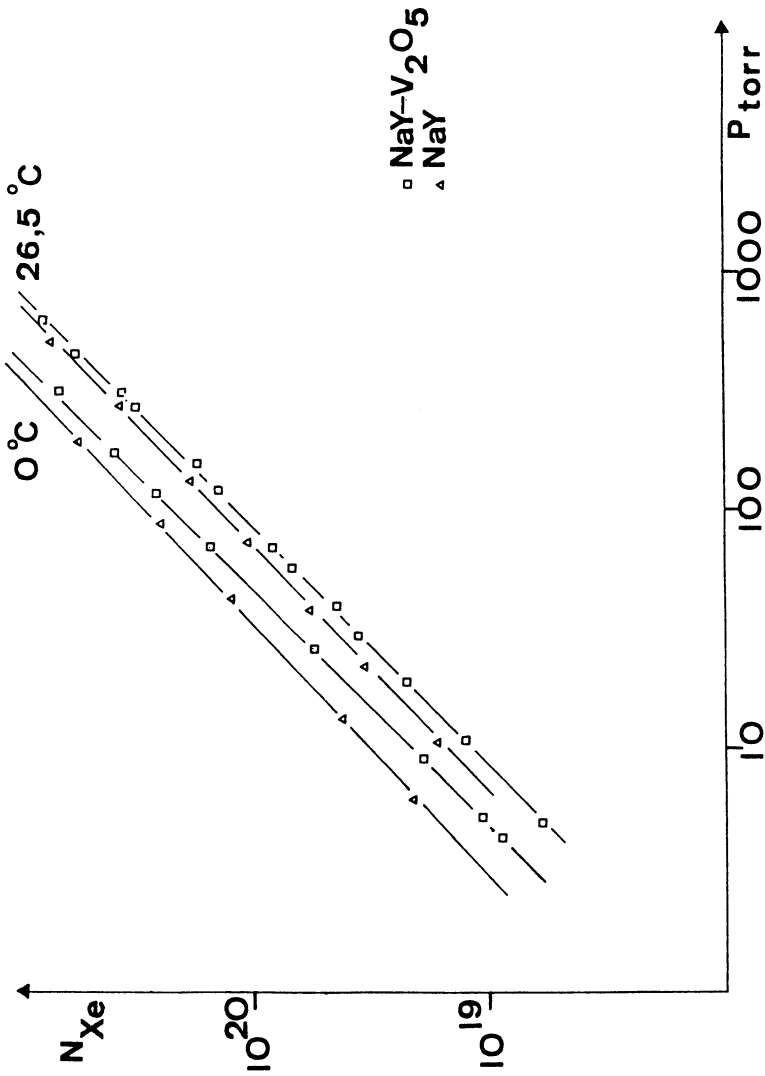


Figure 3. Adsorption isotherm curves for xenon on NaY zeolite and NaY zeolite-V₂O₅ at 273 and 299.5 K.

These results would mean that part of the zeolite lattice is damaged, that some of the lattice cavities are blocked, or that the diameter of the cavities is reduced.

One observes also the smaller absolute initial adsorption energy value for the NaY zeolite- V_2O_5 product (12.1 ± 0.8 kJ/mol) compared with that for NaY zeolite (18.8 ± 0.2 kJ/mol) at 273–299.5 K.

The adsorbed- ^{129}Xe NMR spectrum allows us to choose between these interpretations. The chemical shifts extrapolated to $N = 0$, (δ_s), are 59.6 and 58.0 ± 0.5 ppm for NaY zeolite and NaY zeolite- V_2O_5 ($R = 0.05$), respectively. Although the difference between these values is small, it may be associated with a difference in the Na^+ concentration (19). However, according to the relationship between δ_s and the pore free space (19), this result proves that the size of cavities where xenon is adsorbed remains unchanged. On the other hand, the variation of δ with N ($\delta = f[N]$) is rectilinear, with good correlation coefficients (0.9998; δ) for NaY zeolite and the sample with $R = 0.05$ (Figure 4).

The slope of these straight lines is significantly larger for the treated zeolite (4.52×10^{-20} ppm/atom) than for NaY zeolite (3.51×10^{-20} ppm/atom). Because the xenon chemical shift change is due mainly to Xe–Xe interaction (19), the xenon density inside any supercage cavity must be higher. Consequently, the number of these undamaged cavities per gram is lower (much lower than would result from the small reduction of zeolite mass because of the introduction of V_2O_5). The porosity of bulk V_2O_5 would possibly give another distinct ^{129}Xe signal, which, however, is not detected here.

The samples corresponding to $R = 0.05$ and 0.005 were studied by EPR spectrometry. For both mixtures, an isotropic signal with a g value of 1.973 and a width (ΔH) of 75 gauss observed before heating indicates the usual V^{IV} impurities in V_2O_5 crystals (21). The corresponding hyperfine structure would be detected at low temperature. After being heated, the sample with $R = 0.05$ gives a room-temperature spectrum showing a hyperfine structure that is hardly visible because of strong interactions between the neighboring tetravalent V atoms (less than 1 nm distant) (21). For this reason, a much more dilute vanadium sample was needed.

Under the same experimental conditions, the spectrum of the sample with $R = 0.005$ gave a better resolved hyperfine structure because of the relative decrease in the dipolar interaction. The 77-K spectrum of this sample shows enhanced hyperfine structure (Figure 5). However, with nine lines, the spectrum demonstrates that the V^{IV} atoms have axial symmetry. The spectrum, looks qualitatively like that obtained by Kucherov and Slinkin (16) (although less resolved) for the sample obtained by HZSM-5 and V_2O_5 interaction. The similarity confirms this symmetry, but a quantitative interpretation of our spectrum would not give the same characteristic values as Kucherov and Slinkin's. The vanadium atom environment is different. This interpretation would require spectrum simulation and will not be given in this discussion.

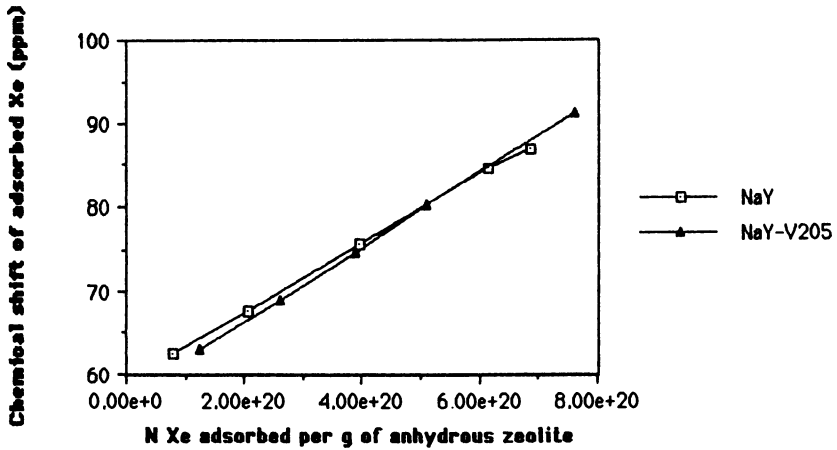


Figure 4. ^{129}Xe chemical shift versus the number of adsorbed xenon atoms per gram of anhydrous zeolite N.

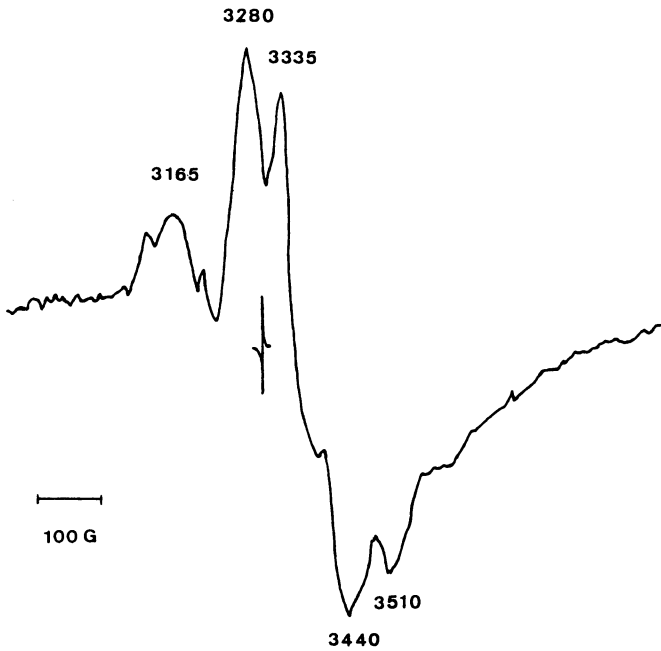


Figure 5. EPR spectrum at 77 K for NaY zeolite- V_2O_5 , $R = 0.005$.

In conclusion, the EPR results demonstrate the presence of tetravalent vanadium atoms in some sites of the sample. The V^{IV} atoms could be included in a new compound, as in the $NaV_5V^{IV}O_{15}$ vanadate identified in the sample by X-ray spectroscopy. They could also interact with the zeolite surface as reported for V_2O_5 supported on silica or γ alumina (22) and titania surfaces (23).

TEM photographs of the modified zeolite with $R = 0.05$ have been studied. The zeolitic lattice is visible at the beginning of the experiment, but later on, it is destroyed by the electron beam (24). In some cases, crystals with different morphologies appear with no zeolitic particles because they are too large to be inserted in the zeolite lattice. They could contain part or all of the vanadium atoms, which would then be outside the lattice.

Conclusions

NaY zeolite and V_2O_5 react at temperatures as low as 700 K, although both compounds are stable at this temperature. For low R values, the V_2O_5 structure disappears, whereas that of the zeolite does not seem to be damaged nor is the cavity size reduced. However some cavity entrances are blocked by a compound containing vanadium atoms and, in particular, a few tetravalent vanadium atoms. Some tetravalent vanadium atoms have also been observed by Occelli and Stencel (25, 26) in much more complex reaction mixtures.

We have not determined the number of V^{IV} species. We assume that they come from two distinct sources. Some of them may already be present in the V_2O_5 samples (21). Most of them come from a reaction between V_2O_5 and Na^+ of NaY zeolite crystals giving vanadium bronze phases (27–29) among which two crystalline phases were identified: $NaV_5V^{IV}O_{15}$ and $Na_5V_{11}V^{IV}O_{32}$.

We therefore propose the following simplified reaction process: V_2O_5 reacts as an acidic medium with the zeolite to give sodium vanadates. For $R = 0.05$, about 1.6 Na^+ of the 56 in the zeolite lattice unit would be used to transform all V_2O_5 into $NaV_5V^{IV}O_{15}$. The small difference obtained for the δ_s values is in agreement with this process. The growth of the hydrated zeolite cubic lattice parameter (0.14%) may be associated with two phenomena: the change in the Na^+ content of the zeolite, these ions being replaced by protons during the free rehydration, or $Si^{IV}-V^{IV}$ substitution in the zeolite framework. However, we have no experimental support for such a substitution. When the R value is higher, the zeolite lattice is no longer in electrostatic equilibrium, and partial breakdown occurs.

Literature Cited

1. Flanigen, E. M.; Lok, B. M.; Patton, R. L.; Wilson, S. T. In *New Developments in Zeolite Science and Technology*; Studies in Surface Science and Catalysis, Vol. 28; Proc. 7th Int. Zeolite Conf.; Murakami, Y.; Iijima, A.; Ward, K. W., Eds.; Elsevier: Amsterdam, 1986; p 103.

2. Guth, J. L.; Kessler, M.; Wey, R. In *New Developments in Zeolite Science and Technology*; Studies in Surface Science and Catalysis, Vol. 28; Proc. 7th Int. Zeolite Conf.; Murakami, Y.; Iijima, A.; Ward, K. W., Eds.; Elsevier: Amsterdam, 1986; p 121.
3. Coudurier, G.; Védrine, J. C. In *New Developments in Zeolite Science and Technology*; Studies in Surface Science and Catalysis, Vol. 28; Proc. 7th Int. Zeolite Conf.; Murakami, Y.; Iijima, A.; Ward, K. W., Eds.; Elsevier: Amsterdam, 1986; p 643.
4. Newsam, J. M.; Vaughan, D. E. W. In *New Developments in Zeolite Science and Technology*; Studies in Surface Science and Catalysis, Vol. 28; Proc. 7th Int. Zeolite Conf.; Murakami, Y.; Iijima, A.; Ward, K. W., Eds.; Elsevier: Amsterdam, 1986; p 457.
5. Inui, I.; Miyamoto, A.; Matsuda, H.; Nagata, H.; Makino, Y.; Fukuda, K.; Okazumi F. In *New Developments in Zeolite Science and Technology*; Studies in Surface Science and Catalysis, Vol. 28; Proc. 7th Int. Zeolite Conf.; Murakami, Y.; Iijima, A.; Ward, K. W., Eds.; Elsevier: Amsterdam, 1986; p 859.
6. Mostowicz, R.; Dabrowski, A. J.; Jabonski, J. M. In *Zeolites: Facts, Figures, Future*; Studies in Surface Science and Catalysis, Vol. 49; Proc. 8th Int. Zeolite Conf.; Jacobs, P. A.; van Santen, R. A., Eds.; Elsevier: Amsterdam, 1989; p 249.
7. Skeels, G. W.; Flaningen, E. M. In *Zeolites: Facts, Figures, Future*; Studies in Surface Science and Catalysis, Vol. 49; Proc. 8th Int. Zeolite Conf.; Jacobs, P. A.; van Santen, R. A., Eds.; Elsevier: Amsterdam, 1989; p 331.
8. Davies, M. E.; Montes, C.; Hathaway, P. E.; Garces, J. M. In *Zeolites: Facts, Figures, Future*; Studies in Surface Science and Catalysis, Vol. 49; Proc. 8th Int. Zeolite Conf.; Jacobs, P. A.; van Santen, R. A., Eds.; Elsevier: Amsterdam, 1989; p 199.
9. Rabo, J. A. In *Zeolite Chemistry and Catalysis*; Rabo, J. A., Ed.; ACS Monograph 171; American Chemical Society: Washington, DC, 1976; pp 332–349.
10. Beyer, H. K.; Karge, H. G.; Borbély, G. *Zeolites* **1988**, 8, 89.
11. Karge, H. G.; Beyer, H. K.; Borbély, G. *Catalysis Today* **1988**, 3, 41.
12. Wicherlova, B.; Beran, S.; Karge, H. G. In *Zeolites for the Nineties: Recent Research Reports; presented during the 8th Int. Zeolite Conf., Amsterdam, 1989*; Jansen, J. C.; Moscou, L.; Post, M. F. M., Eds.; Amsterdam, 1989; p 87.
13. Kucherov, A. V.; Slinkin, A. A. *Zeolites* **1986**, 6, 175.
14. Kucherov, A. V.; Slinkin, A. A. *Zeolites* **1987**, 7, 38.
15. Kucherov, A. V.; Slinkin, A. A. *Zeolites* **1987**, 7, 43.
16. Kucherov, A. V.; Slinkin, A. A. *Zeolites* **1987**, 7, 583.
17. Kucherov, A. V.; Slinkin, A. A.; Beyer, G. K.; Borbély, G. In *Zeolites for the Nineties, Recent Research Reports*; presented during the 8th Int. Zeolite Conf., Amsterdam, 1989; Jansen, J. C.; Moscou, L.; Post, M. F. M., Eds.; Amsterdam, 1989; p 89.

18. Dorémieux-Morin, C.; Fraissard, J.; Gruia, M.; Marchal, C.; Rafaraharimbola, J.; Thoret, J.; 4th Meeting of the French Zeolite Group (Eveux, France), 1988.
19. Fraissard, J.; Ito, T. *Zeolites* **1988**, *8*, 350 and references therein.
20. Engelhardt, G.; Lohse, U.; Lippma, E.; Tarmak, M.; Mägi, M. *Z. Anorg. Allg. Chem.* **1981**, *482*, 49.
21. Gillis, E.; Boesman, E. *Phys. Status Solidi* **1966**, *14*, 337.
22. Taouk, M. B. Ph. D. Thesis, Lille-Flandre-Artois University, France, 1988.
23. Jammul, N. Ph. D. Thesis, Pierre and Marie Curie University, Paris, 1989.
24. Bursill, L. A.; Lodge, E. A.; Thomas, J. M. *Nature (London)* **1980**, *286*, 111.
25. Occelli, M. L.; Stencel, J. M. In *Zeolites: Facts, Figures, Future*; Studies in Surface Science and Catalysis, Vol. 49; Proc. 8th Int. Zeolite Conf.; Jacobs, P. A.; van Santen, R. A., Eds.; Elsevier: Amsterdam, 1989; p 1311.
26. Occelli, M. L.; Stencel, J. M. In *Zeolites as Catalysts, Sorbents, and Detergent Builders*; Studies in Surface Science and Technology, Vol. 46; Applications and Innovations, proceedings of an international symposium; Karge, H. G.; Weitkamp, J., Eds.; Elsevier, Amsterdam, 1989; p 127.
27. Hardy, A.; Galy, J.; Casalot, A.; Pouchard, M. *Bull. Soc. Chim. Fr.* **1965**, 1056.
28. Perlstein, J.; Sienko, M. J. *J. Chem. Phys.* **1968**, *48*, 174.
29. Chakrabarty, D. K.; Dipak G.; Bismas, A. B. *J. Mater. Sci* **1976**, *11*, 1347.

RECEIVED June 8, 1990

Chapter 14

Luminescence as a Probe of Metal Effects in Fluidized Cracking Catalysts

L. K. Kurihara¹, M. L. Occelli², and S. L. Suib¹

¹Department of Chemistry, U-60, University of Connecticut,
Storrs, CT 06269-3060

²Science and Technology Division, Unocal Corporation, Brea, CA 92621

Naphthenate, phthalocyanine and porphyrin ligands have been used to represent vanadium contaminants in petroleum feedstocks. Lanthanum HY zeolites were then V-loaded with each of these species and the vanadium deposited was passivated with tetraphenyl tin. Materials were studied by luminescence emission and lifetime measurements after drying, calcination and steam aging. Results suggest that naphthenates are degraded most readily followed by phthalocyanines and by porphyrins. Vanadium, after the oxidative decomposition (in air) of naphthenate and phthalocyanine ligands, forms V_2O_5 . When vanadyl mesotetraphenyl porphyrin was used to metal load LaY crystals, V_2O_5 formation was observed only after steam-aging. Tin addition prevents (minimizes) vanadia formation irrespective of the vanadium contaminant used. Luminescence can detect V_2O_5 formation when LRS (and XRD) cannot.

In fluid catalytic cracking, the high boiling components of crude oils are cracked into gasoline and other light hydrocarbon fuels. The fluidized cracking of petroleum fractions is still the main process for large-scale gasoline production and it represents the main commercial use of zeolites. In fact, 95% of all refineries use zeolite-containing catalysts in their fluidized cracking units. The savings in petroleum resources in the U.S. through the use of zeolite catalysts over the last 15 years has been estimated at three billion barrels (1).

During the 1970's, the limited availability of crude oil led to the refining of heavier fractions (resids); today, economic incentives have kept the petroleum engineer's interest in cracking metal-contaminated crudes. When cracking resids, metals (such as Ni, V, Cu, Fe) are continuously deposited on fluid cracking catalysts (FCC). These metals can increase hydrogen and coke production in the cracking unit. Furthermore, vanadium irreversibly destroys the zeolite thus eliminating the FCC cracking activity. Techniques to avoid metal effects on FCC selectivities and

activity properties include varying process conditions (2-4), modifying the catalyst composition (5-10), feed pretreatment (11,12,13,14), and the use of passivating agents (15-21). Recently, it has been shown that at microactivity test conditions addition of diluents capable of selectively sorbing metal contaminants from gas oils, can form dual function cracking catalysts (DFCC) that retain most of their useful cracking activity even in the presence of 1.0-1.5% V (22-25).

Modern spectroscopic techniques have been proven particularly useful in studying metal-FCC interactions. In fact, Tin-119 Mossbauer spectroscopy has indicated that Sn-V interactions take place only during steam-aging (26). EPR data have shown that tin seems to promote the oxidation of VO^{+2} to V^{+5} during steam aging, forming complexes that minimize V-zeolite interactions (27). Luminescence emission and lifetime experiments have been used in determining the identity of metal contaminants, quenching effects on rare earth zeolite Y emission and as indicators of degradation of initial cracking activity (28). Luminescence can provide useful information on the environment of the rare earth cations present in the zeolite and it can be used to monitor V-migration between the zeolite and the catalyst matrix (29).

It is the purpose of this paper to investigate and report the use of luminescence techniques to follow the mechanism of metals deposition and passivation in a zeolite when the three vanadium precursors shown in Figure 1 are used.

Experimental

Catalyst Preparation. Ammonium zeolite Y (Linde LZV-62) was exchanged with La^{3+} cations by stirring 3.0g of zeolite in 300 mL of 0.1 M $La(NO_3)_3 \cdot 6H_2O$ at room temperature for 24 hours. After the exchange, the zeolite was washed with 3 x 25 ml of distilled deionized water to remove excess nitrates and dried in a 60°C oven for 20 hours. Vanadyl naphthenate (3%; K & Labs), Vanadyl phthalocyanine (Kodak) and vanadyl mesotetraphenyl porphyrins were dissolved in a minimum amount of hot benzene and added to LaY via incipient wetness. Excess benzene was removed under reduced pressure. The metal loaded zeolite contained about 2.3% V_2O_5 , 17.7% La_2O_3 and a residual 1.76% Na_2O . The LaY was loaded with 1 wt% Sn using a hot solution of tetraphenyl tin (Alfa) in benzene. Calcination was at 540°C for 10 hours in flowing air. Steam deactivation was performed at 730°C for 10hr with 95% steam/5% nitrogen at a flow of 4 mL liquid water per hour.

Laser Raman spectroscopy (LRS) measurements were performed on a Spex Ramalog 1403 spectrometer described in detail elsewhere (23). Powder diffraction measurements were obtained with a Siemens D-500 diffractometer at a scan rate of 1°/min using monochromatic $Cu-K\alpha$ radiation.

Luminescence. Both excitation and emission spectra were recorded using a Spex Fluorolog 202 B double monochromator fluorescence spectrometer. The spectrometer was operated in the front face mode with bandpass slits of 1.0 nm.

Excitation spectra were recorded using a Rhodamine B solution as a reference to correct for variations in the arc lamp intensity. All samples were sealed in evacuated quartz tubes.

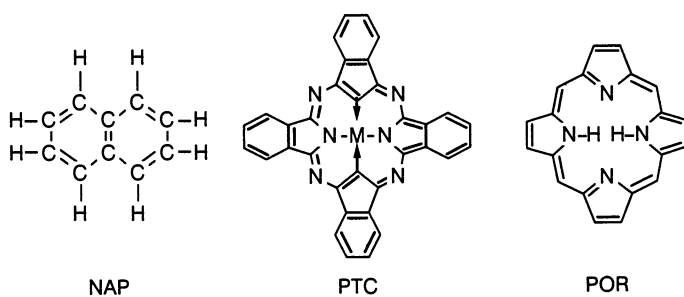


Figure 1. Organic precursors used in this study, NAP = naphthenate, PTC = phthalocyanine, and POR = porphyrin.

Luminescence Lifetime. Luminescence lifetime measurements were made with a PRA Model 3000 system. A block diagram of the system is given in Figure 2. The excitation source is a hydrogen arc lamp operated at 30,000 Hz. Data were collected on a Tracor-Northern multichannel analyzer and were transferred to a Digital Corporation PDP-1103 computer for storage and fitting. Statistical analysis was performed using the software package Decay 3.0 purchased from PRA Corporation.

Results

With 1.29% V, the LaY crystals lose most (>80%) of their initial crystallinity, Figure 3B. With 5.0% V, the steam aged LaY samples collapse and new phases are formed, Figure 3A. In the diffractogram shown in Figure 3A, reflections at $d = 3.41\text{\AA}$, 3.22\AA and 3.00\AA indicate the presence of monoclinic LaVO_4 . Additional peaks at $d = 23.8\text{\AA}$ and 17.9\AA have been attributed to the presence of smaller amounts of tetragonal LaVO_4 . Some mullite ($\text{Al}_2\text{Si}_2\text{O}_7$) is also present, Figure 3A. Raman results are shown in Figure 4. With 5.0% V a spectrum similar to the one for unsupported LaVO_4 is obtained, Figure 4A. At lower V-levels (1.29% V), a non-descriptive spectrum with a broad and very weak band centered near 850 cm^{-1} is seen; Figure 4B.

Emission spectra of vanadyl naphthenate on LaY after various treatments are shown in Figure 5. The dried sample spectrum consists of a strong band centered at 365 nm, indicative of the naphthenate moiety, Figure 5a. After calcination, the intensity of the naphthalene band is greatly reduced and a broad weak band begins to appear in the 500-575 nm region, Figure 5b. The hydrothermally treated sample does not show the naphthalene band and the broad spectral band in the 500-575 region becomes dominant, Figure 5c. The effects of tin addition can be seen in Figure 6. Tin treated (calcined or steamed) samples do not luminesce in the 400-500 nm region.

Emission spectra of vanadyl mesotetraphenyl porphyrin on LaY, when excited at 310 nm, are shown in Figure 7. After calcination and hydrothermal treatment, the porphyrin band in the 350 nm region is still present (Figures 7b and 7c); the spectrum for the dried sample shows more fine structure in the 330-370 nm range, Figure 7a. After calcination, some of the fine structure is lost and there is a slight decrease in intensity of the spectral bands. In the dried and in the calcined samples, evidence of metal free porphyrin is indicated by the broad band in the 390-475 nm region. The effects of tin addition are shown in Figure 8. The tin loaded LaY sample exhibits, after calcination, a weak band at 370 nm. After steam aging, fine structure appears in the 340-425 nm region.

Vanadyl porphyrin on LaY, when excited at 468 nm, gives the spectra shown in Figure 9. The dried and the calcined samples give similar spectra, Figures 9a-b. The bands in the 640-750 nm range correspond to porphyrin and at liquid nitrogen temperatures fine structure is seen in these bands, Figure 10. Steam-aged vanadyl porphyrin does not luminesce in this region and the spectrum is dominated by a broad band near 530 nm. Both the calcined and steam aged tin loaded samples exhibit very weak spectra that are one quarter the magnitude of the samples free

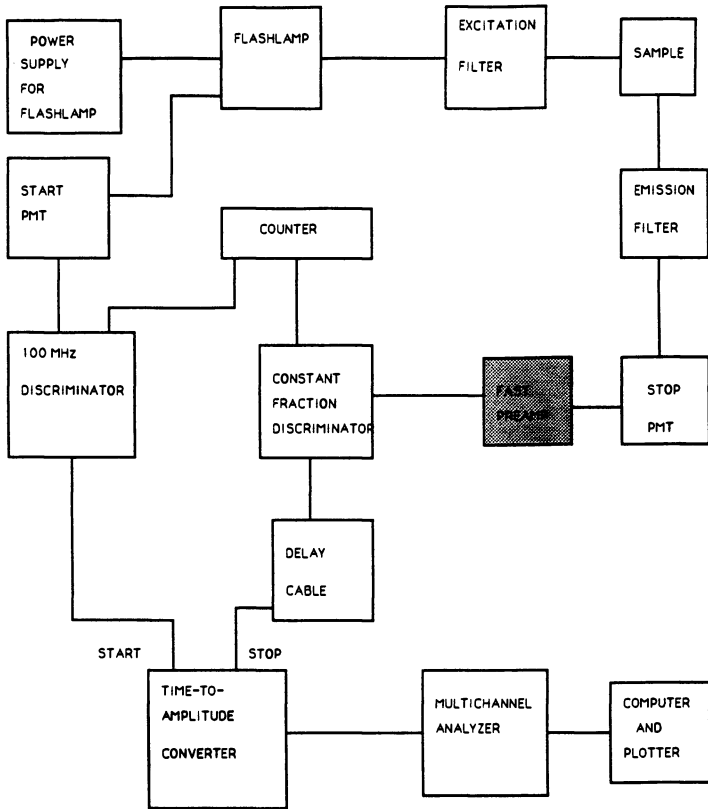


Figure 2. Schematic diagram of a single-photon counting nanosecond fluorometer.

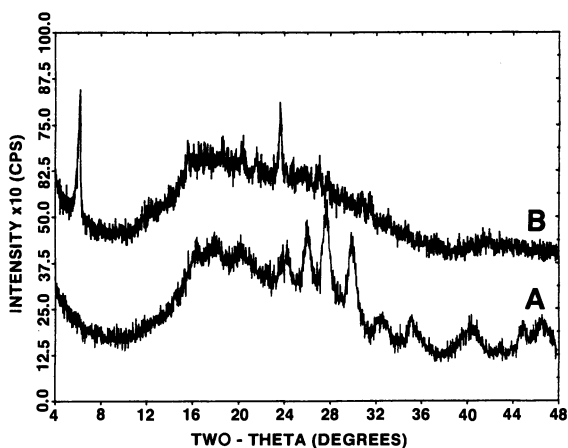


Figure 3. X-ray diffractograms of LaHY crystals steam-aged in the presence of: (A) 5% and (B) 1.2% vanadium.

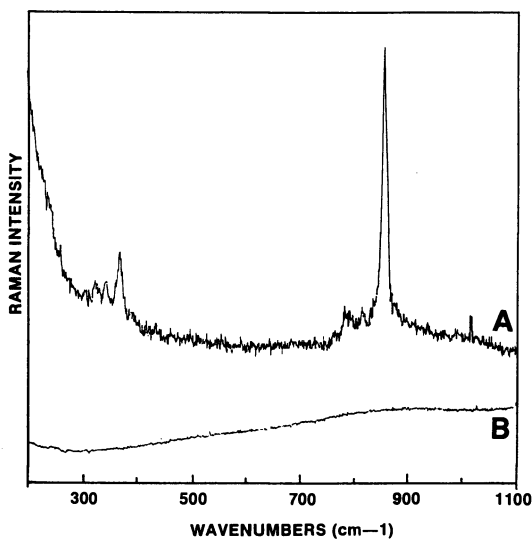


Figure 4. Laser Raman spectra of LaHY crystals steam-aged in the presence of: (A) 5% and (B) 1.2% vanadium.

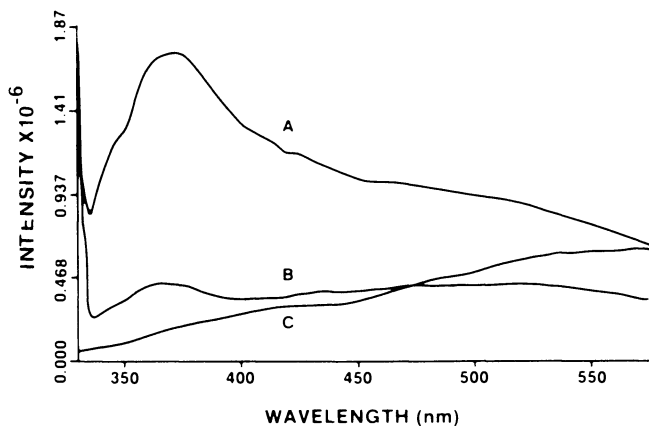


Figure 5. Luminescence spectra for vanadyl naphthenate on LaY: (A) before and (B) after calcination and (C) steam aging. The excitation wavelength was 300 nm.

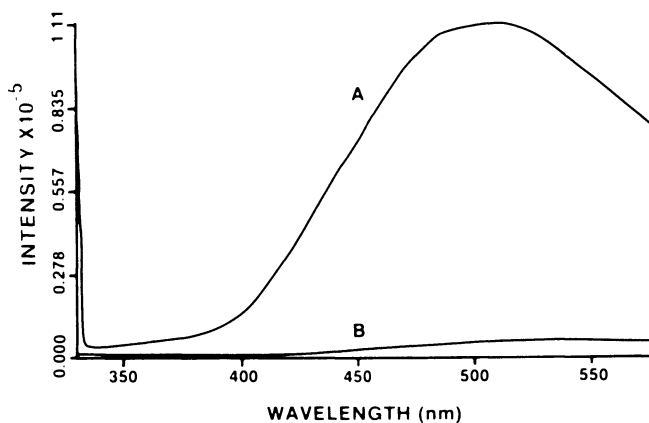


Figure 6. Luminescence spectra of vanadyl naphthenate on LaY steam aged: (A) without and (B) with tin addition. The excitation wavelength was 300 nm.

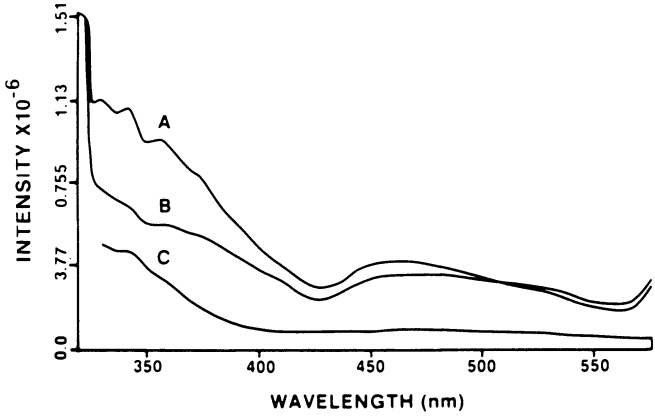


Figure 7. Luminescence spectra of vanadyl porphyrin on LaY: (A) before and (B) after calcination and (C) after steam aging. Excitation wavelength was set at 310 nm.

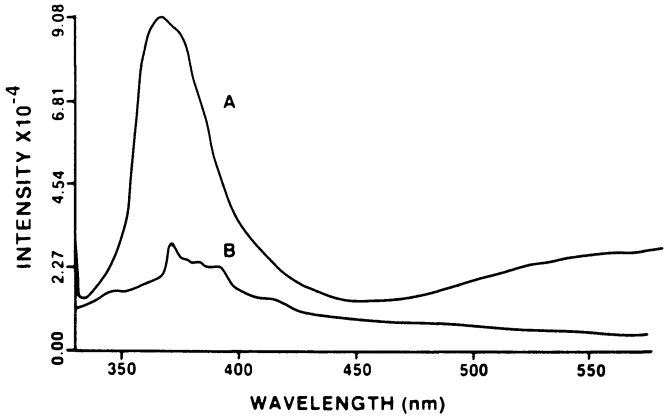


Figure 8. Luminescence spectra of tin loaded LaY at 77 K after vanadyl porphyrin impregnation and calcination; (A) was taken before and (B) after steam aging. The excitation wavelength was set at 300 nm.

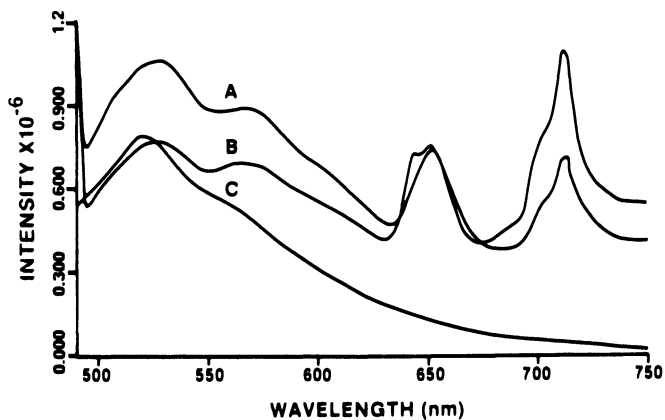


Figure 9. Luminescence spectra of vanadyl porphyrin on LaY: (A) before and (B) after calcination and (C) steam aging. Excitation wavelength was set at 468 nm.

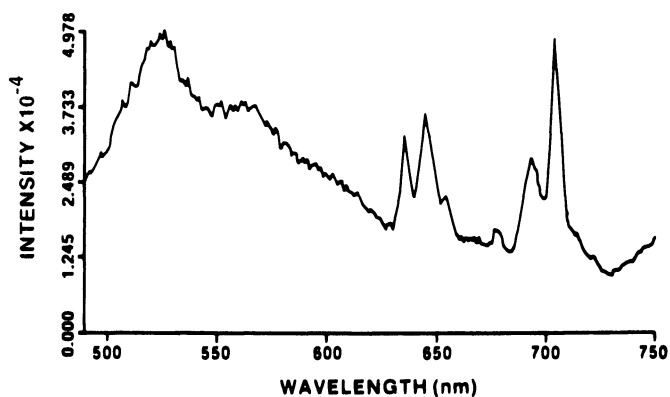


Figure 10. Luminescence spectrum of calcined vanadyl porphyrin on LaY at 77K with the excitation wavelength set at 468 nm.

of tin, Figure 11. The calcined tin loaded LaY has a broad band centered near 540 nm; a shoulder in the 700 nm region suggests the presence of residual porphyrin, Figure 11a. Porphyrin moieties are not present in hydrothermally treated samples containing tin, Figure 11b.

Vanadyl phthalocyanine freshly deposited on LaY shows a broad weak band at 450 nm, Figure 12a. Upon calcination more fine structure appears; steam aging increases band intensity five-fold, however the shoulder at 415 nm remains, Figure 12c. Tin addition decreases band intensity by a magnitude of four; nonetheless, some of the fine structure is still present. The emission spectra of vanadyl phthalocyanine, when the excitation is set at 400 nm, are shown in Figure 13. A broad band centered at 470 nm dominates the spectra of the dried and calcined phthalocyanine samples, Figure 13a. Upon calcination the band nearly doubles in intensity, Figure 13b. Steam aging broadens this band. Tin addition results in a very weak spectrum without luminescent behavior in the 500-575 nm region, Figure 14. At 650-675 nm, a new band begins to emerge.

For comparison purposes, the spectrum of LaVO_4 (excited at 330 nm) is given in Fig. 15. The spectra for steam aged LaY crystals containing low (1.29%) V levels is shown in Fig. 16. Luminescent lifetime data are given in Tables I and II. In all cases there are two components, (T_1 and T_2), present. The T_2 species are very short often exceeding limits of detection.

TABLE I. LUMINESCENCE LIFETIME DATA FOR LaY

<u>V Precursor</u>	<u>Treatment</u>	<u>T_1</u>	<u>T_2</u>	<u>X^2</u>
NAP	Fresh	3.46	0.47	1.5
PTC	Fresh	3.74	0.40	1.4
POR	Fresh	4.85	0.17	1.1
NAP	Calcined	4.86	0.85	1.2
PTC	Calcined	5.71	0.31	1.1
POR	Calcined	6.37	0.21	1.3
Vanadia	Calcined	5.24	0.34	1.2
LaVO_4	Neat	2.16	0.85	1.3

Calcined = 540°C, in air, 10 hr.

Steamed = 740°C, 95% steam, 5% N_2 , 10 hr.

T_1 and T_2 in nanoseconds.

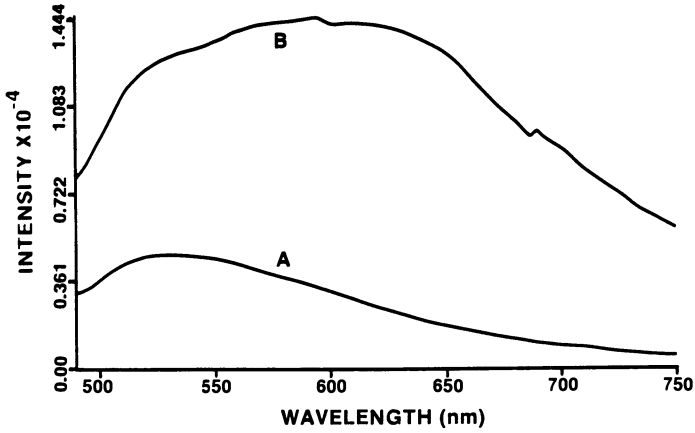


Figure 11. Luminescence spectra of tin loaded LaY impregnated with vanadyl porphyrin: (A) calcined and (B) steam aged. The excitation wavelength was set at 468 nm.

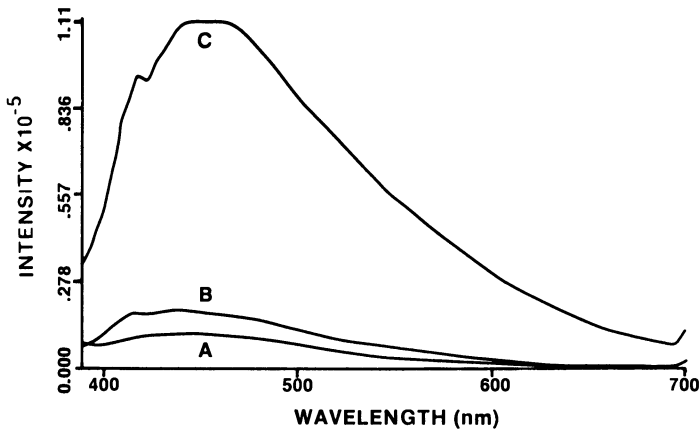


Figure 12. Luminescence spectra of vanadyl phthalocyanine on LaY: (A) before and (B) after calcination and (C) steam aging. The excitation wavelength was set at 365 nm.

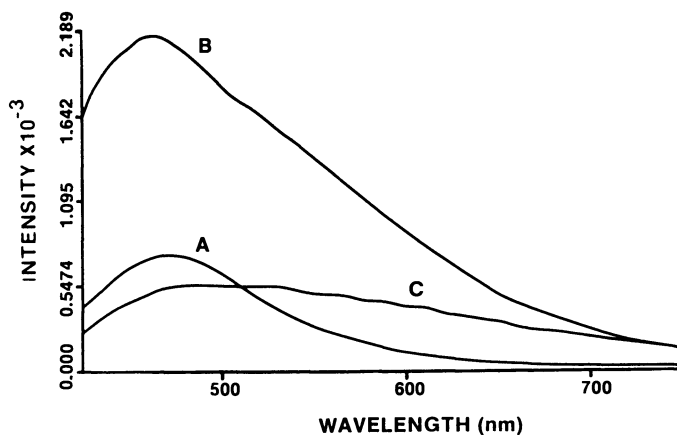


Figure 13. Luminescence spectra of vanadyl phthalocyanine on LaY: (A) before and (B) after calcination and (C) steam aging. The excitation wavelength was set at 400 nm.

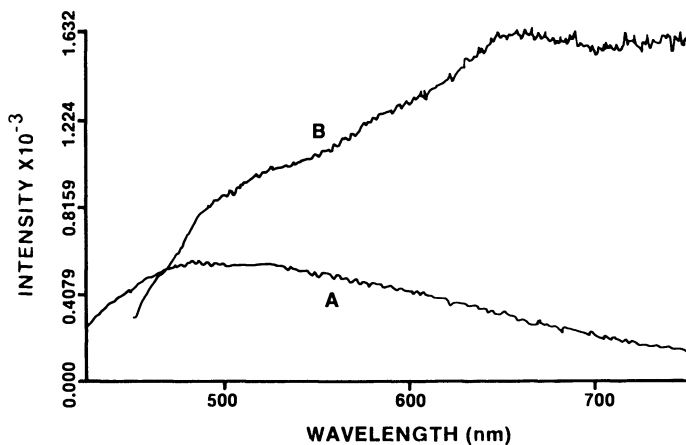


Figure 14. Luminescence spectra of vanadyl phthalocyanine on steam aged LaY: (A) without and (B) with tin addition.

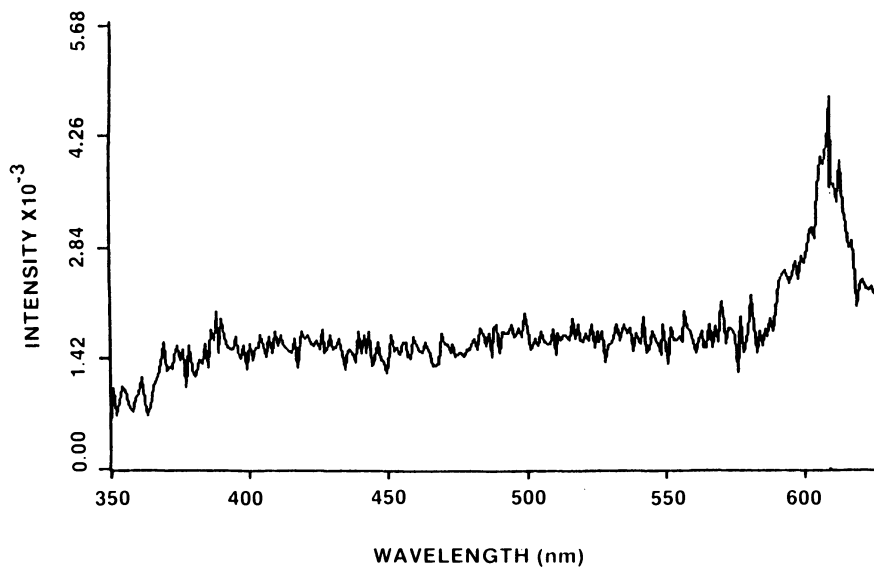


Figure 15. Luminescence emission of LaVO_4 . The excitation wavelength was 330 nm.

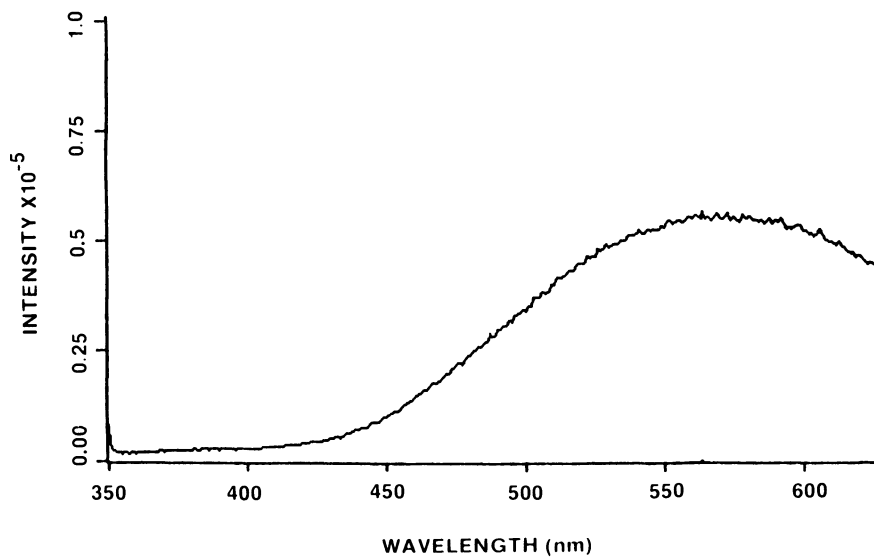


Figure 16. Luminescence emission of steam aged LaY crystals loaded with 1.29% V. The excitation wavelength was 330 nm.

TABLE II. LUMINESCENCE LIFETIME DATA FOR Sn PASSIVATED SAMPLES

<u>V Precursor</u>	<u>Treatment</u>	<u>T₁</u>	<u>T₂</u>	<u>χ²</u>
NAP	Sn, Fresh	4.01	0.57	1.1
PTC	Sn, Fresh	3.12	0.59	0.9
POR	Sn, Fresh	4.85	0.17	1.1
NAP	Sn, Calcined	5.59	0.34	1.6
PTC	Sn, Calcined	6.07	0.24	1.2
POR	Sn, Calcined	7.50	0.07	1.5
NAP	Sn, Steamed	6.37	0.46	1.2
PTC	Sn, Steamed	2.94	0.04	1.3
POR	Sn, Steamed	7.26	0.41	1.5

Calcined = 540°C, in air, 10 hr.

Steamed = 740°C, 95% steam, 5% N₂, 10 hr.

Discussion

In agreement with published results (25) steam-aging LaHY crystals containing high (5.0%) V-levels caused a total collapse of the faujasite structure with formation of LaVO₄ and some mullite (36, 37), see Figure 3a. Vanadate formation can be easily observed also by LRS, Figure 4a. At lower (1.29%) V-levels the steam aged crystals retain some crystallinity; however V-compounds such as V₂O₅ or LaVO₄ could not be observed either by XRD or LRS, see Figures 3b; 4b. These compounds, in samples containing low concentrations of V, can be observed by luminescence techniques.

The spectrum for LaY impregnated with vanadyl naphthenate shows a characteristic band at 365 nm that loses most of its intensity after calcination, Figs. 5a, 5b. This is not surprising since Pompe et al (30), using TGA/DTA data, have shown that the oxidative decomposition of the vanadyl naphthenate is complete at 500°C. Electron paramagnetic resonance (EPR) studies have shown that vanadium (after calcination) is stabilized mainly in the form of vanadyl (VO²⁺) cations in the zeolite supercages (29).

The naphthenate band at 365 nm disappears after steam aging the V-loaded (1.29%) catalysts and a broad band in the 450-575 nm region is formed, Fig 5C; both V₂O₅ and LaVO₄ exhibit spectral bands in this region. In the present study, V₂O₅ formation has been ascertained by taking the luminescence spectrum at 77 K.

The presence of V₂O₅ (together with EuVO₄) has also been observed by Anderson et al (29) after steam-aging vanadyl naphthenate on EuY crystals. Roozenboom

et al (31) have shown that V_2O_5 forms on the surface of SiO_2 and Al_2O_3 . Iwamoto et al. (32) and Anpo et al. (33) have reported the phosphorescence spectrum of V_2O_5 , observed when vanadyl naphthenate was steam aged. The generation of a V_2O_5 phase on several supports (free of RE-ions) impregnated with vanadyl naphthenates and steam aged has also been observed using Laser Raman spectroscopy for V concentrations above 4% (22-25). Mauge et al (34), using SEM, TEM and energy dispersive X-ray emission (EDX) have shown that when LaY crystals are loaded with naphthenate, steaming induced a reaction between the La^{+3} ions and vanadium with formation of a $LaVO_4$ phase.

Spectral bands in the 500-575 nm region are quenched when the LaY zeolite is loaded with 1% tin, suggesting that tin addition minimizes V_2O_5 formation. Mössbauer studies have indicated that tin is in the +4 state after calcination (26-31); the reduction in intensity seen when comparing Figures 6a and 6b could be due to the formation of $V^{+5}-O-Sn^{+4}$ linkages (26).

After deposition, vanadyl porphyrin (like vanadyl naphthenate) covers the LaY surface, Figs. 7-10. EPR results have indicated that, again, V in these samples is in the +4 state. A similar conclusion was also reached by Roth et al (35) after depositing vanadyl porphyrin on NdY crystals. FTIR results were reported (35) that indicated loss of porphyrin structure after calcination. DTA data (35) were used to show that the porphyrin moiety lost aromatic structure after heating in the 200°-300°C temperature range; vanadyl porphyrin fully decomposed in air below 500°C (30). In LaY crystals, residual porphyrins are still present after calcination at 540°C, but totally disappear after steam aging; a broad band centered between 400-550 nm (attributed to V_2O_5) is observed, Fig. 7. In the presence of both Sn and V, samples give a spectrum with weak bands in which neither porphyrins or V_2O_5 bands can be observed, Fig. 8.

Luminescence spectra in Fig. 9 show strong bands for the vanadyl mesotetraphenyl porphyrin moiety after deposition and after calcination indicating little degradation of the complex after thermal treatment. On steaming there is considerable loss of band intensity between 640 and 750 nm. These bands (not seen in Figs. 7,8) are now observable since the excitation wavelength used corresponds to direct excitation of the porphyrin, Fig. 9. Luminescence data taken at 77 K for the calcined vanadyl mesotetraphenyl porphyrin loaded LaY crystals show fine structure of the porphyrin ring again indicating that little breakdown of this complex had occurred, Fig. 10.

Spectra of tin loaded LaY containing vanadyl mesotetraphenyl porphyrin show a significant decrease in luminescence intensity with respect to tin free samples after calcination (27). These data suggest that tin deposition influences the emissive properties of the porphyrin perhaps by quenching. It is not believed that Sn deposition catalyzes the breakdown of the porphyrin. On steaming there is significant intensity in the 550-750 nm region indicating that some porphyrin is still present, Fig. 11b.

The phthalocyanine band increases in intensity and acquires a shoulder near 420 nm on calcination, Fig 12. There is almost a ten-fold increase in band intensity after steam aging, Fig 12c. In contrast to what is shown in Figs. 5 and 7, band

intensity for vanadyl phthalocyanine increases after steam aging, Fig. 12. This luminescence enhancement has been attributed to the phosphorescence of benzene containing fragments resulting from the thermal degradation of the phthalocyanine moiety, Fig. 12. The luminescence enhancement after calcination could be due to self absorption effects. Vanadyl phthalocyanine appears to be less stable than vanadyl mesotetraphenyl porphyrin complexes, Figs. 7, 12. These results are consistent with bioinorganic literature data. When the excitation wavelength is set at 400 nm (instead of 365 nm) a band at 470 nm appears, Figs 13a,13b; this band broadens and shifts to near 530nm after steaming, Fig. 13c. Spectra for calcined (or steamed) samples containing tin do not exhibit a band near 470 nm; however, a peak in the 650-725 nm region begins to appear, Fig. 14.

Loss of structure in the 520-550 nm region of the luminescence emission spectrum is apparent after tin addition, Figs. 7-14. This vibrational structure is indicative of V_2O_5 , and is inhibited by tin addition. On the other hand, samples containing both Sn and V show quenched luminescence emission in the 520 - 550 nm region. These data suggest that a V_2O_5 -like environment is present in these materials which may have tin incorporated into V_2O_5 . This Sn-0-V species is amorphous and may be responsible for V passivation in these LaY samples. Luminescence lifetime data are in agreement with this suggestion. The luminescence emission spectra of steamed samples containing both Sn and V show that a vanadium oxide-like environment has been formed. The luminescence emission spectra of this species do not have vibrational fine structure even when data are collected at liquid nitrogen temperature indicating that V_2O_5 itself is not present; a conclusion supported also by lifetime data.

Luminescence lifetime behavior in all samples showed two species, Table 1. The T_2 is very short, often exceeding the instrumental limits. In all cases the lifetimes changed after calcination and steam aging suggesting the formation of different vanadium species. The calcined samples have T_1 values that approach that of calcined V-loaded LaY. Tin addition affects the lifetimes of the vanadium species, Table 2. When the naphthenate was used as the precursor all the tin treated samples exhibited higher T_1 values than tin-free samples. Steam aging the porphyrin-containing samples changed T_1 by one half. When phthalocyanine was used to load V, tin addition had little effect on the samples' T_1 values.

Unsupported $LaVO_4$ crystals have an emission band at 610 nm, Fig. 15. This band is not observed in any V loaded LaY crystals. The emission of the vanadia-like specie at 540 nm is so intense that it extends past 600 nm toward the red region, Fig. 16. Thus the emission of any $LaVO_4$ formed when steam aging V-loaded LaY could have been covered by the strong emission of the V_2O_5 -like phase.

In conclusion, luminescence can be used as a probe for tracking V_2O_5 formation and for monitoring disappearance and changes in the state of the organic precursor. The nature of the vanadium precursor controls the stage at which the ligand leaves. Naphthenate is lost at much lower temperatures and treatment times than porphyrin or phthalocyanine ligands. In all tin-free supports tested, vanadia forms either during calcination (naphthenate, phthalocyanine) or steaming (porphyrin). These data suggest that porphyrin precursors are most stable. In all cases, tin addition results in reactions with vanadium with concomitant prevention (or minimization) of V_2O_5 formation.

Luminescence is more sensitive than LRS and can detect the presence of V_2O_5 in V-loaded LaY crystals even at low ($\sim 1\%$ V) levels. Luminescence lifetime experiments at 610 nm will need to be performed with a more powerful light source and with a monochromator placed between the sample and the detector in order to observe $LaVO_4$ formation at low V concentrations. Such experiments are now in progress in our laboratory.

Acknowledgments

Support for this research was from the National Science Foundation under the Kinetics and Catalysis Program through grant CBT-08814974.

Literature Cited

1. Thomas, J. M.; Vaughan, D. E. W. *J. Phys. Chem. Solids*, 1989, **50**, 445.
2. Koenig, S. A. H.; Ring, T. A. *Hydrocarbon Processing* 1985, 61.
3. Hettinger, W. P., Jr.; Carruthers, J. D.; Watkins, W. D. Eur. Patent 65,626 (1981).
4. Upson, L. L. Katalistiks 5th FCC Symposium, Vienna, May 1984.
5. Ocelli, M. L.; Kowalczyk, D. C.; Kibby, C. L. *App. Catal.*, 1985, 227.
6. Upson, L. L. Katalistiks 5th FCC Symposium, Vienna, May 1984.
7. Otterstedt, J. E.; Zhu, &-M; Sterte, J. *App. Catal.* 1988, **38**, 143.
8. Woolery, G. L.; Chin, A. A.; Kirker, G. W.,; Huss, A. Jr. *Physica B*, 1989, **158**, 213.
9. Hettinger, W. P. Jr. Eur. Patent 69,842 (1982).
10. Otterstedt, J. E. A.; Jaras, S. G.; Pudas, R.; Upson, L. L., U.S. Patent 4,515,903 (1985).
11. Meyers, V. K.; McKay, B. E. Jr.; Busch, L. E., U.S. Paent 4,464,250.
12. Bowes, E.; Farcasiu, m.; Scott, E. J., U.S. Paent, 4,548,709 (1985).
13. Meyerson, A. S.; Ernst, W. R., U.S. Patent, 4,599,313 (1985).
14. Ocelli, M.L.; and Swift, H. E. in U.S. Patent No. 4,466,884 (1984).
15. Mitchell, B. R.; Swift, H. E., U.S. Patent 4,101,417 (1978).
16. Campagna, R. J.; Krishna, A. S. Katalistiks 5th FCC Symposium Vienna, May 1984.
17. Roberts, J. S.; Bertus, B. J.; McKay, D. L.; Mark, W., U.S. Patent 4,397,767 (1983).
18. Durante, V. A.; Olszanski, D. J.; Reagan, W. J.; Brown, S.M., U.S. Patent 4,430,199 (1984).
19. Beck, W. H.; Carruthers, J. D.; Cornelius, E. B.; Hettinger, W. P. Jr.; Kovack, S. M.; Palmer, J. C.; Zandona, O. J., U.S. Patent 4,432,890 (1984).
20. Roberts, J. S.; McKay, D. L.; Bertus, B. J.; Mark, H. W., U.S. Patent 4,257,142 (1981).
21. Mauge, F.; Gallezot, P.; Courcelle, J. C. Fr. Demande FR. 2,567,142 (1968).
22. Ocelli, M. L. in "Fluid Catalytic Cracking: Role in Modern Refining." ACS Symposium Series, Vol. 375; M. L. Ocelli, Ed., ACS, Washington, D.C., p. 162 (1989).
23. Ocelli, M. L. and Stencel, J. M. in "Zeolite as Catalysts, Sorbents and Detergent Builders." H. G. Karge and J. Weitkamp Eds.; Elsevier, p. 127 (1989).

24. Occelli, M. L. and Stencel, J. M. in "Fluid Catalytic Cacking: Role in Modern Refining," ACS Symposium Series, Vol. 375; M. L. Occelli Ed., ACS Washington, D.C., p. 195 (1989).
25. Occelli, M. L. and Stencel, J. M. in "Proc. 8th IZA Meeting," Amsterdam, The Netherlands (in press).
26. Anderson, M. W.; Occelli, M. L.; Suib, S. L.; J. Mol. Catal. (In press).
27. Anderson, M. W.; Occelli, M. L.; and Suib, S. L.; J. Catal., 112, 375 (1990).
28. Occelli, M. L.; Psaras, D.; Suib, S. L., J. Catal. 96, 336 (1986).
29. Anderson, M. W.; Occelli, M. L.; Suib, S. L. J. Catal. 1989, 118, 31.
30. Pompe, R.; Jaras, S. and Vannenberg, N., Appl. Catal., 13, 171 (1984).
31. Roozenboom, F.; Mittelmeijer-Hazeleger, M. C.; Moulign, J. A.; Mecima, J.; deBeer, V. H. J.; Gellings, P. J. J. Phys. Chem. 1980, 84, 2783.
32. Iwamoto, M.; Furukawa, H.; Matsukami, K.; Tekenaka, T.; Kakawa, S. J. Am. Chem. Soc. 1983, 105, 3719.
33. Anpo, M.; Tanahashi, I.; Kubokawa, Y. S. J. Phys. Chem. 1980, 84, 3440.
34. Mauge, F.; Courcelle, J. C.; Engelhard, Ph.; Gallezot, P. Grosmaning, J. Proceedings of the 7th Int. Zeolite Conf. Murakami, Y.; Iijima, A. T.; Word, J. W. Eds. 1986.
35. Marshall, C. L.; Delgass, W. N. J. Catal. 1987, 108, 214.
36. Yoshimura, M., and Sata, T., Bull. Chem. Soc. Japan 42, 3195 (1969).
37. Le Flem G., and Olazcuaga R., Bill. Soc. Chem. Fran. 2769 (1968).

RECEIVED August 28, 1990

Chapter 15

Vanadium-Contaminated Aluminas and Aluminosilicate Gels

⁵¹V NMR Spectroscopic Characterization

P. S. Iyer¹, H. Eckert², M. L. Occelli¹, and J. M. Stencel³

¹Science and Technology Division, Unocal Corporation, Brea, CA 92621

²University of California, Santa Barbara, CA 93106

³Center for Applied Energy Research, University of Kentucky,
Lexington, KY 40506

⁵¹V wideline solid state NMR spectroscopy has been used to differentiate between various vanadium (V^{+5}) species present on vanadium-loaded pseudo-boehmite and aluminosilicate gels. The observed speciation has been found to be sensitive to vanadium loadings and to hydrothermal and dehydration pre-treatments. Low loadings (<2%V) result in the formation of 4-coordinate surface species. Higher loadings (>2%V) favor 6-coordinate vanadium species formation. Dehydration studies have confirmed that hydrous species such as H_2O and/or OH do indeed participate in some of these 6-coordinate environments. The relative amounts of 4- and 6-coordinate vanadium species is principally governed by the support surface area retention after calcination and steaming. The aluminosilicate gel, on the other hand, responds to hydrothermal treatment by forming a new, highly hydrated, V_2O_5 -like phase, that has not been identified before by NMR studies.

Recent studies at microactivity test (MAT) conditions have shown that VO^{+5} -Naphthenate decomposes on fluidized cracking catalysts (FCC) forming vanadium species that during steam aging allow intra particle transfer of V to occur (1-3). Once on the catalyst surface, V can dramatically reduce cracking activity by decreasing the crystallinity of its cracking centers (the zeolite). Migrating

Note: Based in part on a paper presented at the 1989 Fall Meeting of the California Catalysis Society, University of California at Los Angeles, Los Angeles, CA.

vanadium can be selectively sorbed and passivated by adding to the FCC a second particle capable of forming unreactive and heat stable vanadium compounds (4-6). By preventing (or minimizing) vanadium from reaching the FCC, it has been possible to generate dual function cracking catalysts (DFCC) mixtures capable of retaining 70-80% of their original cracking activity even in the presence of high (1.0-1.5%) vanadium levels (7-9). Vanadium transport and the selective sorption of vanadium by a second particle (alumina) has recently been observed by Kugler and Leta (10) in their SIMS analysis of equilibrium FCC from a US refinery. Vanadium-alumina interactions have also been investigated by XPS, Raman (4-6,11) and ^{51}V NMR (12) spectroscopy.

Solid state NMR of quadrupolar nuclei has become an increasingly popular tool to probe the structure of metal oxide surface species on catalysts (12-17). Although the ^{51}V nuclide has favorable NMR characteristics, the number of ^{51}V solid state NMR applications to the characterization of V^{+5} oxide surface phases on catalysts has been somewhat limited (12-15). Recently, extensive studies of crystallographically well-defined model compounds have shown that the anisotropic ^{51}V chemical shift tensors obtained from static (wideline) NMR experiments at high field strengths ($> 7 \text{ T}$) can distinguish unambiguously between four- and six-coordinate V^{+5} environments (12). These insights have helped to clarify the structural properties of the V^{+5} surface oxide phases present on a variety of metal oxide supports (12). The present study extends this work to the hydrated and dehydrated forms of pseudo boehmite and aluminosilicate gels of the type used in preparing V-resistant cracking catalyst mixtures (5).

Experimental

Room temperature wideline and MAS solid state NMR measurements were carried out using a General Electric GN-300 spectrometer, equipped with an Explorer high speed digitizer and a 7 mm multi-nuclear MAS-NMR probe (zirconia stator and spinner) from Doty Scientific. Ambient samples were studied within zirconia spinners, while dehydrated samples were studied in flame-sealed evacuated pyrex ampules. The 90° pulse length for liquid VOCl_3 was measured to be 7-8.5 μs . Spectra were typically obtained using a simple one-pulse sequence (Bloch decay) using a pulse length of 1 μs and a pre-acquisition delay of 10 μs with a dwell time of 1-2 μs . Relaxation delays of 1 second were usually found sufficient for quantitative signal detection in all the samples. Although the use of Bloch decays will result in somewhat distorted lineshapes with more accentuated valleys between peaks and shoulders, it is the preferred method here, since it avoids complications arising from varying degrees of excitation selectivity that become important with the longer pulse lengths needed to generate 90° and 180° pulses for spin echoes. All chemical shifts are reported with liquid VOCl_3 as a reference.

Detailed descriptions of the catalysts' properties as well as descriptions of the method of procedures used in preparing V-contaminated materials, has been given elsewhere (18).

Dehydration of the alumina samples, prior to ^{51}V NMR analysis, was performed for 22 hours at -200°C under -10^{-6} torr pressure. The gel samples were dehydrated at -150°C for 4 hours under the same vacuum.

Results and Discussion

NMR spectra of quadrupolar nuclei are influenced by the interaction of the nuclear electric quadrupole moment with electrostatic field gradients generated at the nuclear sites by asymmetric electron distributions due to chemical bonding. To a first order approximation the energy levels of a spin split yielding 2I transitions; I is the nuclear spin-quantum number. For half-integer nuclei such as ^{51}V ($I=7/2$), the central $+1/2$ to $-1/2$ transition remains unaffected. Previous studies (12) have shown that this situation is usually valid for ^{51}V NMR obtained at sufficiently high fields (≥ 7 T), where second-order effects on experimentally observed lineshapes can be neglected (12). However, as previously described, even in this limit the quadrupolar interaction manifests itself in the pulsed excitation behavior. The selective excitation of the central $+1/2$ to $-1/2$ transition thus affects the nuclear precession frequency of the spins in the applied radio frequency field necessary for NMR detection. As described below, this effect will be used. However, the main focus will be on chemical shift information available from the static NMR lineshapes. In this paper, results obtained on V^{+5} surface oxide deposited on pseudo boehmite and aluminosilicate gels will be discussed and compared.

Vanadium and Pseudo-Boehmite Alumina. The 79 MHz wide-line ^{51}V NMR spectra of these steam aged samples containing only 0.5 to 5.0% V (loaded using VO^{+2} -Naphthenate) are shown in Figure 1. Two principal signal components, "type a" (favored at high surface coverages and assigned to distorted-octahedral V^{+5} species) and "type b" (favored at low surface coverages and indicative of a distorted tetrahedral environment) can be easily distinguished. The relative signal intensity ratios of these two species are similar to those observed by Eckert and Wachs (12) where $\text{VO}(\text{OC}_2\text{H}_7)_3$ in methanol was used to load γ -alumina powders (Figure 2). The similarity in the spectra is particularly interesting considering the differences in the nature of the precursor, alumina support and the fact that impregnation was simply followed by calcination at 450°C for 16 h; steam aging was not performed (12). The main difference between both sets of samples is the vanadium level needed before crystalline V_2O_5 is detected e.g. 5% in the present study vs 11.2% V in the case of γ -alumina support. This is largely due to the reduction of the surface area encountered upon steaming, and is a clear manifestation of the detrimental effect of vanadium on the stability of the support surface (see Table 1, Ref. 18).

At the lowest loadings, 4-coordinate vanadium is indicated by a broad "type-b" signal. This resonance is much broader than usually observed for monomeric $\text{Q}^{(0)}$ (e.g. orthovanadate, VO_4^{3-}) and dimeric $\text{Q}^{(1)}$ (e.g. pyrovanadate, $\text{O}_3\text{V-O-VO}_3^{4-}$) species, which show only small differences between the chemical shift components σ_{11} , σ_{22} , and σ_{33} . As discussed previously for V^{+5} oxide on γ -alumina (12), the

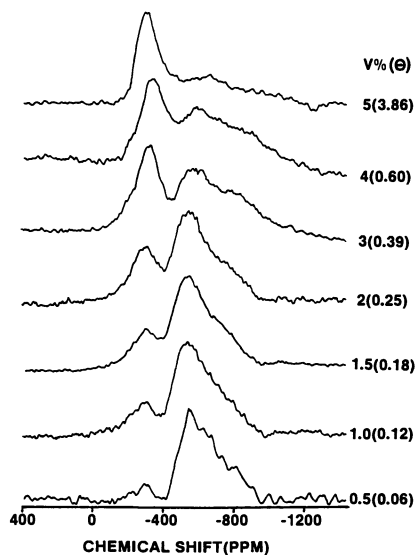


Figure 1. ^{51}V wide line NMR spectra at 79 MHz for aluminas (boehmite) V-loaded with VO_2 naphthenate in benzene and steam aged. The numerals indicate V loadings and (θ) surface coverage by V.

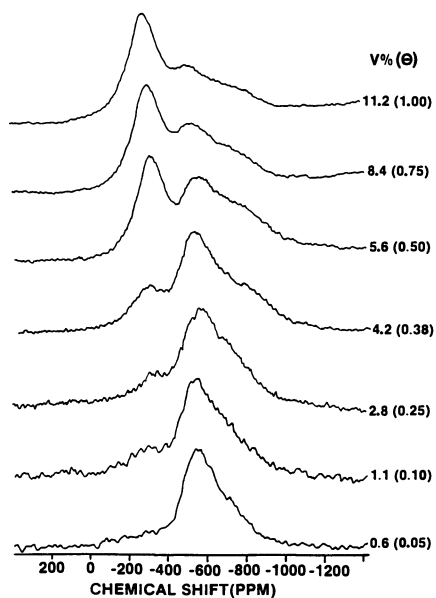


Figure 2. ^{51}V wide line NMR spectra at 79 MHz for γ -aluminas V-loaded with $\text{VO}(\text{OC}_2\text{H}_5)_3$ in methanol and calcined at $450^\circ\text{C}/16$ h (12). The numerals indicate V loadings and (θ) surface coverage by V.

spectroscopic parameters are most consistent with a $Q^{(2)}$ species. It was not possible to achieve line narrowing by MAS, indicating the presence of a wide chemical shift distribution. This distribution probably also includes vanadium atoms with different numbers of non-bridging oxygen atoms.

The intensity of the "type a" signal increases monotonically with increasing V-loadings, Figures 1,2. Reference to the appropriate model compounds indicate that the local structure of this species is quite different from that of crystalline V_2O_5 and suggests a distorted octahedral structure similar to that observed in ZnV_2O_6 , PbV_2O_6 and $Na_6V_{10}O_{28} \cdot 18 H_2O$. At 5% loading, the NMR spectrum shows that the majority of vanadium is present as crystalline V_2O_5 . This is accompanied by a total structural collapse of the support with formation of a bulk δ -alumina phase. Formation of bulk $AlVO_4$ was not observed in any of the samples studied. While significant signal intensity is observed in the region near 800 ppm (which overlaps with the chemical shift range for $AlVO_4$), we believe that this signal is simply due to the upfield component of the chemical shift anisotropy powder pattern belonging to the octahedral V^{+5} species.

As observed previously for γ -alumina, ^{51}V NMR spectra of surface V^{+5} oxide on pseudo-boehmite are very sensitive to the state of hydration, Figure 3. The sample containing 5% vanadium remains unaffected, as expected for a situation where most of the signal is due to bulk crystalline V_2O_5 . At lower loadings the octahedral species diminished dramatically upon dehydration in vacuo. The extremely broad signals observed for the 3% and 4% samples indicate that dehydration in vacuum causes the formation of a distribution of different four-coordinate V^{+5} species, which span a very wide chemical shift range. A narrower and more well-defined signal ("type c") is observed at 2% loading. The lineshape indicates an approximately axial chemical shift tensor, consistent with a vanadium (V) environment that possesses a local unique axis (12). Such symmetric units could also be present at higher loadings, but cannot be discerned clearly from the broad lineshapes observed in those cases, see other traces in Figure 3. Recent in-situ Raman results, obtained on dehydrated V(V) oxide surface phases on various metal oxide supports, show Raman bands in the 1020-1040 cm^{-1} region, indicating that the vanadium species possesses a single strong $V=O$ bond (19-21). These species are also observed on V-loaded, steam-aged pseudo-boehmite aluminas (metal loaded with VO_4^{2-} naphthenate in benzene) but only after surface dehydration (18).

Aluminosilicate gels. Figure 4 shows the ^{51}V NMR results obtained on vanadia-loaded aluminosilicate gels. While no readily apparent trend is visible, it has to be borne in mind that the interpretation of the spectra is complicated here by the limited hydrothermal stability of the gel when loaded with V, (18). Due to these complications, only the spectra obtained at the lowest surface coverages (0.5% and 1%) are interpretable in terms of surface- V^{+5} oxide species. Figure 4 reveals that the distorted octahedral environments ("type a" signals) dominate at these V-loadings. As the vanadium loading increases the gel structure collapses rapidly, e.g., with only 1.25% V there is a 46% reduction in surface area,

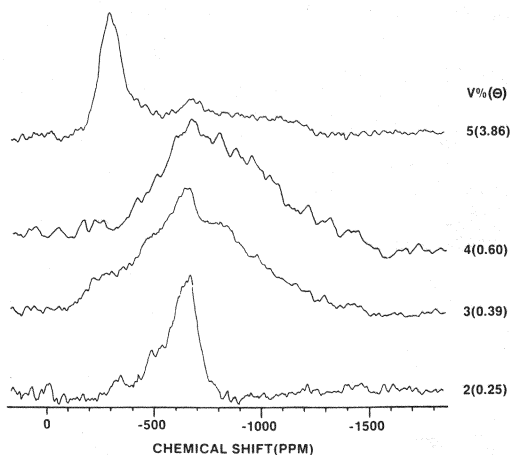


Figure 3. ^{51}V wide line NMR spectra at 79 MHz of V loaded aluminas after dehydration in vacuo at 220°C.

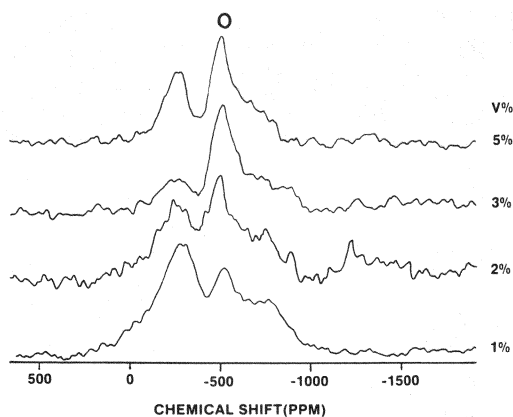


Figure 4. ^{51}V wide line NMR spectra at 79 MHz of V loaded aluminosilicate gels.

accompanied by the formation of bulk phases such as mullite and tridymite that can be easily⁵¹V observed by XRD (18).

As in the case of V^{+5} on pseudo boehmite, this structural collapse is induced by the steaming process rather than the calcination step. Accordingly, the spectra observed for samples with V-contents exceeding 1wt.%, show two new types of signals: a sharp feature near 500 ppm ("type d"; symbol o in Figure 4) and an extremely broad signal ("type e") whose spectral parameters are reminiscent of V_2O_5 . Based on its spectroscopic parameters, the sharp 500 ppm feature is assigned to a tetrahedral V^{+5} species. It most likely arises from V^{+5} incorporated in one of the bulk phases, whose formation is induced by the presence of vanadium upon steaming. This assignment is further supported by the fact that surface dehydration has no influence on this site (vide infra).

The broad "type e" signal, whose contribution increases with increasing V content, shows NMR behavior that is consistent with the presence of bulk V_2O_5 : (1) the wideline NMR pattern resembles that of crystalline V_2O_5 , (2) intense spinning sideband patterns are present under MAS conditions (not shown) and (3) the pulsed excitation behavior indicates weak quadrupolar coupling similar to that observed in crystalline V_2O_5 . Figure 5 illustrates that it is possible to detect this signal selectively by using pulses of sufficient length to cause relaxation of the other NMR signals in the rotating frame of the applied radio frequency field. Thus, at a pulse length of $7\mu s$, the sharp 500 ppm feature, which arises from ^{51}V nuclei with significantly stronger quadrupolar interactions, remains undetected.

Although the presence of a V_2O_5 -like phase is detected by Raman analysis (18), there was no evidence for the formation of a crystalline phase by XRD. Thus, in spite of the analogies between the species giving rise to the "type e" NMR signal and crystalline V_2O_5 , the signal is assigned to an amorphous V_2O_5 phase.

Further insight into this problem is provided by the ^{51}V NMR spectra of the corresponding dehydrated samples, Figure 6. As observed for V loaded aluminas, the octahedral "type a" surface species, seen at low coverages, has been replaced by the tetrahedral "type c" species (most likely a $Q^{(3)}$ unit). The same type of unit appears to arise from dehydration of samples containing the amorphous V_2O_5 precursor, indicating that this phase must be highly hydrated under ambient conditions. Finally, the tetrahedral "type d" species, already identified as a signal arising from the bulk in the ambient samples remains unaffected upon dehydration of the surface (see symbol o in Figure 6.)

Summary and Conclusions

^{51}V wideline solid state NMR has proven to be a very useful technique for differentiating between various vanadium (V^{+5}) surface species present on vanadia-loaded metal oxide substrates. The results confirm the previous trends observed for vanadium on alumina and titania supports, which can be summarized as follows:

- (1) low surface coverages favor the formation of a highly disordered four-coordinated vanadium species;

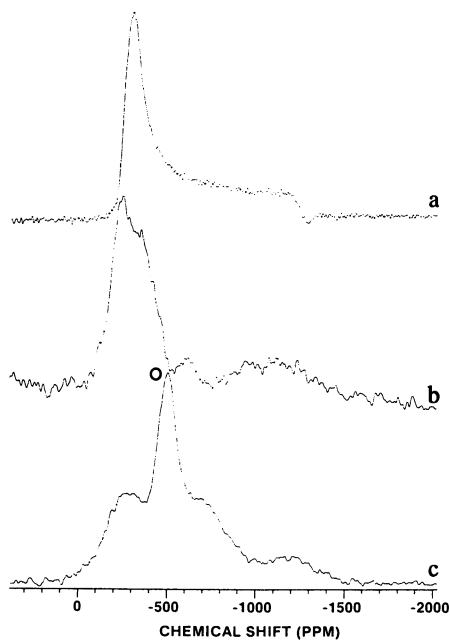


Figure 5. Effects of pulse length on ^{51}V wide line NMR spectra of aluminosilicate gels containing: (a) 5% V, $7\mu\text{s}$ pulse length, resulting in exclusive detection of bulk V_2O_5 ; (b) 3% V, $7\mu\text{s}$ pulse length, resulting in exclusive detection of amorphous V_2O_5 and (c) 3% V, $1\mu\text{s}$ pulse length, resulting in a spectrum representative of all V^{+5} species present.

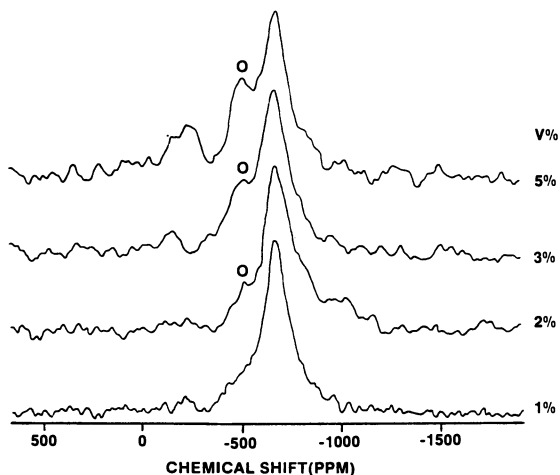


Figure 6. ^{51}V wide line NMR spectra at 79 MHz of V loaded aluminosilicate gels after dehydration in vacuo at $150^\circ\text{C}/4\text{h}$.

- (2) as the surface coverage increases, an increasing amount of vanadium is present in a six-coordinate environment under ambient conditions;
- (3) hydrous species (H_2O and/or OH) participate in this six-coordinate environment, and upon dehydration a highly characteristic V^{+5} oxide with an axially symmetric $V(V)$ point symmetry is formed.

Beyond confirmation of these previously obtained results, the present study also illustrates the utility of ^{51}V NMR to probe the processes that lead to the collapse of vanadia-loaded surfaces upon hydrothermal treatment. In the case of pseudo boehmite, the four- and six-coordinate V^{+5} oxide surface species simply redistribute to account for the gradual loss in surface area upon steaming, yielding results in close analogy to those obtained on calcined (but unsteamed) samples. In contrast, the aluminosilicate gel responds to hydrothermal treatment by forming a new amorphous, highly hydrated, V_2O_5 -like phase, which has not been identified before by NMR studies of other substrates. Further details of the mechanism of catalyst deactivation by V are the subject of continuing investigations in our laboratories by ^{51}V solid state NMR, XPS, and Raman spectroscopy.

Acknowledgment

The authors thank Mr. R. Ortiz and Dr. M. Sollberger for assistance in sample preparation.

References

1. Ocelli, M. L. in "Fluid Catalytic Cracking: Role in Modern Refining," ACS Symposium Series, Vol. 375; M. L. Ocelli, Ed., ACS, Washington, D. C., p. 162 (1989).
2. Ocelli, M. L. and Swift H. E. U. S. Patent No. 4, 466, 884 (1984).
3. Ocelli, M. L. in "Advances in Catalytic Chemistry IV" Snowbird, Utah (1989).
4. Ocelli, M. L. And Stencel, J. M. in Fluid Catalytic Cracking: Role in Modern Refining," ACS Symposium Series, Vol. 375; M. L. Ocelli Ed., ACS Washington, D. C., p. 195 (1989).
5. Ocelli, M. L. and Stencel, J. M. in "Zeolites as Catalyst, Sorbents and Detergent Builders," H. G. Karge and J. Weitkamp Eds.; Elsevier, p. 127 (1989).
6. Ocelli, M. L. and Stencel, J. M. "Proc. 8th IZA" Amsterdam (1989).
7. Ocelli, M. L. and Kennedy, J. V. in G. B. Patent No. 2, 116, 062A (1983).
8. Ocelli, M. L. and Kennedy, J. V. in U. S. Patent No. 4, 465, 588 (1984).
9. Ocelli, M. L. in U. S. Patent No. 4,615,996 (1986)
10. Kugler, E. L. and Leta, D. P., J. Catal. 109, 387 (1988).
11. Repelin, Y., Husson, E., Abello, L. and Lucazeau, G., Spectrochim. Acta, 41A, 993 (1985).

12. Eckert, H. and Wachs, I. E., *J. Phys. Chem.* **93**, 6796, 1989.
13. Eckert, H. and Wachs, I. E., *Mater. Res. Soc. Symp. Proc.* **111**, 455 (1988).
14. Le Costumer, L. R., Taouk, B., Le Meur, M., Payen, E., Guelton, M. and Grimblot, J., *J. Phys. Chem.* **92**, 1230 (1988)
15. Taouk, B., Guelton, H., Grimblot, J. and Bonnelle, J. P., *J. Phys. Chem.* **92**, 6700 (1988).
16. Cheng, J. T. and Ellis, P. D., *J. Phys. Chem.* **93**, 2549 (1989).
17. Morris, H. D. and Ellis, P. D., *J. Am. Chem. Soc.* **111**, 6045 (1989).
18. Occelli, M. L., and Stencel, J. M., This Volume.
19. Went, G. and Bell, A., personal communication, *J. Phys. Chem.* 1990, in press.
20. Wachs, I. E., *J. Catal.* 1990 (in press).
21. Wachs, I. E., *Chem. Eng. Science*, 1990 (in press).

RECEIVED August 28, 1990

Chapter 16

Laser Raman and X-ray Photoelectron Characterization of V-Contaminated Components of Fluidized Cracking Catalysts

M. L. Occelli¹ and J. M. Stencel²

¹Science and Technology Division, Unocal Corporation, Brea, CA 92621

²Center for Applied Energy Research, University of Kentucky,
Lexington, KY 40506

In recent years, a variety of spectroscopic techniques have been used to study the nature of the compounds formed from vanadium deposition on metal oxide surfaces. Using laser Raman spectroscopy (LRS) it was observed that V, when deposited on layered magnesium silicates (such as sepiolite), is passivated in the form of $\beta\text{-Mg}_2\text{V}_2\text{O}_7$ and that the nature of the vanadate formed depends on the clay composition (1). Roozenboom et al (2) have proposed that on alumina, tetrahedrally coordinated vanadia monomers and octahedrally coordinated vanadia oligomers are formed at low V-loadings. At high V loadings, a crystalline V_2O_5 phase has been observed by several investigators (2-6). Wachs et al (6) have proposed that the observed monomeric species are dioxovanadates a conclusion supported also by EXAFS measurements (7,8). However, several other authors have proposed instead that the monomeric species formed at low V-loading on alumina surfaces are mainly monoxovanadyl groups bonded to the surface by Al-O-V linkages (9-13). The dependence of the nature of the V species formed and V-loading on alumina granules (after steam aging at 760°C/5h, 100% steam), has revealed that at least three type of V species can be present, (4). Vanadyls (VO^{+2}) groups, V_2O_7 -groups (with at least three different V-O-V bond angles) and a crystalline V_2O_5 phase have been observed when the V-loaded alumina contained <1%, 1% to 4% and >4% vanadium, respectively (4). Monomeric vanadyls, one and two dimensional vanadate chains, and crystallites of V_2O_5 have been found to form as the V loading is increased on SiO_2 , TiO_2 and Al_2O_3 supports (14).

Spectroscopic and modelling studies of V_2O_5 xerogels have comprehensively examined the vibrational characteristics of $\text{V}_2\text{O}_5 \cdot n\text{H}_2\text{O}$ gels (21-24). These gels contain broadened vibrational bands as compared to crystalline V_2O_5 . Vanadia gels with $n > 0.5$

have been described as having a two dimensional fiber or ribbon structure. For $n = 1.6$ these ribbons have been measured to be $2.7 \times 0.36 \times 100$ nm (a x b x c) in size and to orient with layers parallel to the smooth substrates on which they are deposited (21-23). The presence of H_2O , either as trapped molecules between the layers of V_2O_5 , or terminally bonded to V_2O_5 crystallites, or interacting with individual V-O bonds in vanadia gels, has been shown to produce a Raman band on the high frequency side of the normally intense 998 cm^{-1} V=O stretching band (24-27). Thus, the presence of bands (or shoulders) in the $1010 - 1040\text{ cm}^{-1}$ region of spectra showing V_2O_5 speciation have been attributed to H_2O present in the vanadia structure. This type of 'blue shift' in vibrational frequency indicated that H_2O , besides weakening V=O bonds by pi back donation (thereby decreasing V=O stretching frequencies), can also strengthen other V=O terminal bonds. The purpose of this paper is to investigate V-interactions on steam-aged aluminosilicates of the type used in FCC preparation. The properties of the V species formed will be compared to those of V compounds observed on similarly prepared V-loaded alumina samples.

EXPERIMENTAL

Catalysts Preparation

Vanadyl naphthenate (in benzene) was used to metal load aluminas and aluminosilicate gels according to an established procedure (15); the naphthenate was obtained from Pfaltz and Bauer, Inc., and contained 2.9 wt% V. Decomposition of the naphthenate was performed by calcining the impregnated materials for 10 hours at 540°C in air. All catalysts were then steam-aged for five hours with ~100% steam at 760°C in a fluidized bed.

The amorphous aluminosilicate gel (AAA-alumina) used in this study contains about 80.4% SiO_2 , 19.4% Al_2O_3 and 0.056% Na_2O . Mercury porosimetry measurements have indicated a $479\text{ m}^2/\text{g}$ surface area and 1.67 cc/g pore volume; the average pore diameter of the dried gel was 134 \AA .

The 100×325 mesh granules of Catapal SB Alumina used gave an x-ray pattern in excellent agreement with JCPDS (Joint Committee on Powder Diffraction Standards) pattern No. 21-1307 for AlOOH (boehmite); minor amounts of $Al(OH)_3$ (nordstrandite with possible gibbsite polymorphs) are also present. After steam-aging ($760^\circ\text{C}/5\text{h}$) this alumina had a mercury surface area of $118\text{ m}^2/\text{g}$ and pore volume of 0.98 cc/g .

Catalysts Characterization

(i) XPS Measurements. Materials were analyzed by X-ray photoelectron spectroscopy (XPS) after calcination (C), steaming (S) and after H_2 -treatment (H_2). Powders were pressed into thin, 13-mm diameter wafers and then mounted on a heatable sample probe attached to a Leybold-Hereaus LHS-11 XPS/Auger/ISS instrument. The instrument base pressure was 2×10^{-10} bar; samples were generally

analyzed at a pressure of 2×10^{-8} bar. During H_2 -treatment, materials were exposed to 25 ml/min flowing H_2 at a pressure of 2.5 bar and at temperatures of 325-400°C for periods of 15 to 120 minutes in a high pressure-high temperature reactor attached to the side of the LHS-11 analysis chamber. After exposure to H_2 , the samples were cooled while the reactor was evacuated to 10^{-2} bar. Then the samples were moved into a preparatory chamber and finally into the analysis chamber. A typical time to cool, evacuate and move the sample to the analysis position was 10 minutes.

All binding energies reported have been corrected for charging by comparing the location of the C 1s bands with that for Al 2p. Correction of the Al 2p band to 74.7 eV coincided with peak fitting of the C 1s bands in which a prominent carbon peak was within ± 0.3 eV of the ubiquitous C 1s assumed to be at 284.6 eV. Hence, peak positions for vanadium were corrected using the Al 2p at 74.7 eV.

The V 2p is a doublet, the $2p_{1/2}$ peak of which is obscured by the O 1s peak while an oxygen satellite is located between the V $2p_{3/2}$ and $2p_{1/2}$ peaks. Hence, manipulation of the spectra included a satellite elimination routine, followed by a nonlinear background subtraction, to produce a well-separated V $2p_{3/2}$ peak on which an estimation of the presence of multiple oxidation states for vanadium was made. This estimation involved the deconvolution of the V $2p_{3/2}$ to include either a singlet, doublet, or triplet Gaussian fit. The number of peaks used in this fitting procedure was determined by comparing the FWHM of the fitted V peaks to those obtained for the Si and Al peaks, relating fitted peak positions to those from standards, and by minimizing the least squares difference between fitted and experimental data.

(ii) Raman Spectroscopy. Raman spectra were recorded on a Spex Ramalog 1403 spectrometer (Spec Industries, Metuchen, NJ) equipped with a cooled RCA GaAs photomultiplier tube (CA 31034-02). The 488nm line of a model 165 Ar⁺ laser (Spectra Physics, Mountain View, CA) was used to generate Raman scattered light. The laser power impinging on the sample was limited to approximately 50 mW. All spectra were recorded with a spectral resolution of 5 cm^{-1} ($350 \mu\text{m}$ slit width). Signal pulses from the photomultiplier tube were passed through a model 1182 amplifier/discriminator (Princeton Applied Research, Princeton, NJ) and counted by a Nicolet 1280 data system (Nicolet Instrument Corp., Madison, WI). Typically, 50-100 scans per sample were averaged in order to obtain spectra with adequate signal-to-noise ratios. A data point was acquired every 0.7 cm^{-1} . Samples were prepared for Raman measurements by grinding the catalysts in an agate mortar and pestle. The powdered samples were then pressed into 1 cm diameter wafers under a pressure of approximately 1000 psi. Each wafer was mounted in a spinning sample holder and placed in the spectrometer sample chamber. The angle between the incident laser beam and the sample surface was 30° ; samples were spun at approximately 500 rpm to minimize thermal modifications.

RESULTS AND DISCUSSION

Surface Properties

The boehmite used (Catapal SB Alumina) after V-loading and calcination in air (at 540°C) formed some poorly crystallized delta-alumina (4); the BET surface area of the calcined material remained essentially unchanged for V loadings up to 5%, table 1. After steam-aging (760°C/5h, 100% steam) the alumina surface area (SA) decreased to 130 m²/g and the crystallinity of the delta-alumina phase improved (4). During steam aging, the surface area monotonically decreased with V-loading, table 1. With 4% V, the steam aged alumina retained 76% of its initial surface area. Above 4% V, there is a collapse of the microporous structure. With 5% V, the surface area decreased to 18 m²/g and formation of a crystalline V₂O₅ phase together with (well crystallized) delta-alumina could be observed in the x-ray diffractograms of the sample (4); formation of AlVO₄ was not observed in any of the V-loaded aluminas studied (4).

The high field aluminum-27 MAS NMR spectrum of the aluminosilicate gel under study contains resonances near 0 ppm 30 ppm and 58 ppm indicating the presence of aluminum in octahedral, pentahedral and tetrahedral coordination (16,17), see Fig. 1. Luminescence as well as EPR data have shown that after metal deposition, the vanadyl ions (VO²⁺) formed are quite mobile (18,19) and able to migrate possibly to charge compensate Al(IV) present in the gel thereby forming Si-O-Al(IV)-OVO²⁺ groups (20).

It is believed that, when steaming the gel at high temperatures, the VO²⁺ attacks and breaks the Si-O-Al bonds promoting mullite formation and the collapse of the gel macroporous structure (3). The XRD pattern in Fig. 2B shows that mullite formation in the gel can be observed with only 1.5% V and when this occurs, there is a 81% decrease in surface area, Table 1. Mullite level increased with V-loadings, see Fig. 2. Data in the literature (20) indicates that when the steaming temperature is decreased to 730°C from 760°C (as in the present work) gel stability to V improved and only a 23% reduction in surface area was observed in a similar gel loaded with 1.5% V. Aluminosilicate gels are clearly less resistant than aluminas to V attack at hydrothermal conditions, Table 1.

Laser Raman Spectroscopy

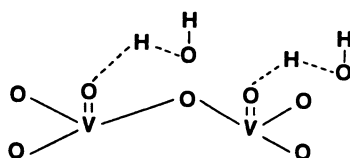
Laser Raman spectra of steamed (760°C/5hr) pseudoboehmite aluminas metal loaded with solutions of vanadyl naphthenate in benzene are shown in Fig. 3; band positions are listed in Table 2. Some of these results have already been discussed in details elsewhere (3,4). At low V-loadings, the spectrum is characterized by an intense band near 925 cm⁻¹, Fig. 3B. This band has been attributed to V=O stretching modes resulting from the presence of isolated vanadyl ions on the alumina surface. Hydrogen bonding, resulting from steaming, is believed responsible for the broad nature of this band.

TABLE 1. Steaming (760°C/5h, 100% steam) effects on the surface area (SA, m²/g, ±5%) of V-loaded aluminas and aluminosilicate gels (AAA-alumina). Data obtained from N₂-porosimetry measurements.

Wt% V	Support*			
	Alumina		Gel	
	<u>C</u>	<u>S</u>	<u>C</u>	<u>S</u>
0.0	238	130	480	191
0.25	---	---	---	166
0.5	232	126	---	146
1.0	232	124	448	127
1.25	---	---	---	88
1.5	230	116	---	35
2.0	229	113	424	33
3.0	228	109	396	22
4.0	227	96	392	17
5.0	224	18	371	13

* C = calcined at 540°C/10h in air; S = steamed at 760°C/10h, 100% steam at 1 atm.

As the V-levels on the alumina support increase, the band at 925 cm⁻¹ decreases in intensity and shifts to higher wavelengths; simultaneously new bands in the 300 cm⁻¹ to 850 cm⁻¹ region appear, Figs. 3C-3D. The band near 790 cm⁻¹ has been attributed to the formation of octahedral-like species and to V-O stretching vibrational modes (4). It has been proposed that for V concentrations between 1% and 4%, dimeric species such as:



are formed on the alumina surface (4). Bands near 660 cm⁻¹ and bands in the 350 cm⁻¹ - 600 cm⁻¹ region have been assigned to V-O-V asymmetric and symmetric stretching modes; these V₂O₇ units probably have three different VOV bond angles (4). If samples containing more than 4% V, steaming cause a drastic reduction in the alumina surface area (Table 1) and formation of V₂O₅, Fig. 3 H. This V₂O₅ phase is also easily observed by XRD (4).

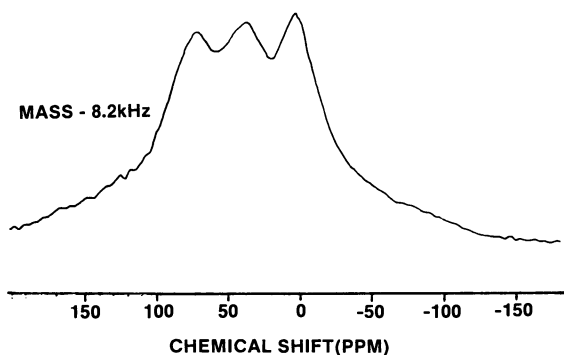


Figure 1. Aluminum 27 MAS NMR spectrum at 130 MHz of the parent aluminosilicate gel.

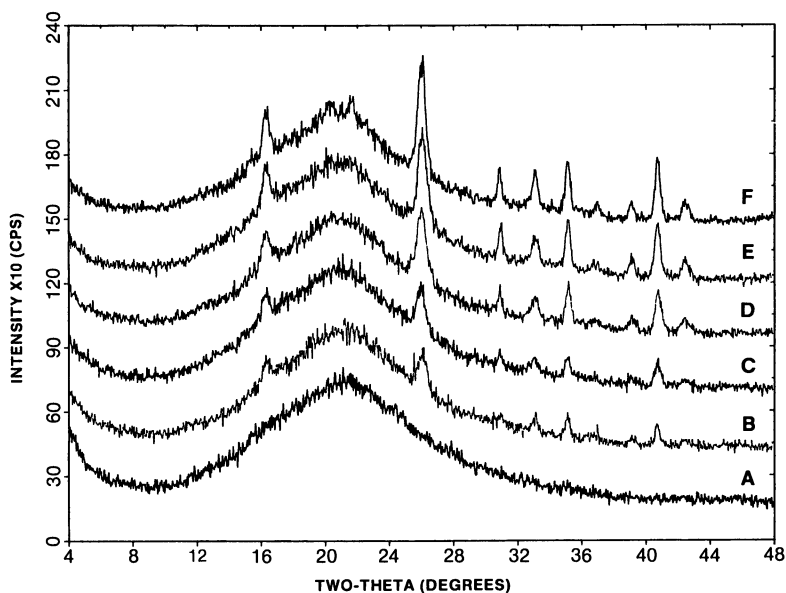


Figure 2. X-ray Diffractograms of steam aged aluminosilicate gels loaded with (A) 1.0%; (B) 1.5%; (C) 2.0%; (D) 3.0%; (E) 4.0% and (F) 5.0% vanadium.

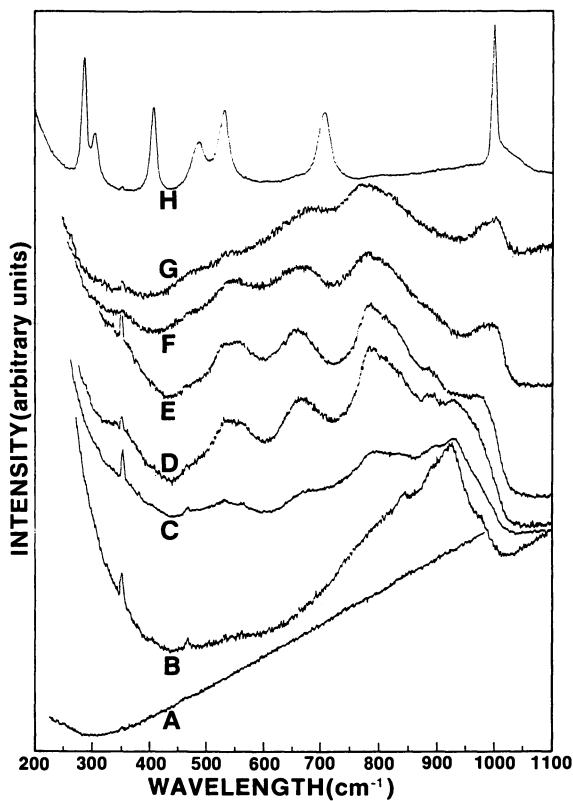


Figure 3. Laser Raman spectra of Catapal SB alumina (A) after loading with : (B) 0.5%; (C) 1.0%; (D) 1.5%; (E) 2.0%; (F) 3.0%; (G) 4.0%; (H) 5% V and steaming (4).

The LRS of similarly prepared V-loaded aluminosilicate gels (AAA-aluminas) are shown in Fig. 4; band positions are listed in Table 3. These spectra are essentially featureless for V concentrations below the 1%V level, Fig.4. For loadings in the 1.0 to 3.0% V range, relatively intense bands near 517 cm^{-1} and 700 cm^{-1} , together with a broad shoulder centered near 815 cm^{-1} and a very weak band near 1020 cm^{-1} can be seen in the Raman spectra of these samples, Figs. 4B-4D. Recently, Wokaun, et. al. (25) have shown Raman spectral characteristics for SiO_2 supporting low V loadings which are similar to those in Fig. 4 but did not indicate whether H_2O influenced their results.

For steamed gels containing more than 3%V, Raman spectra show formation of a supported V_2O_5 phase, Figs. 4E-4F. When V loadings increased to 5% from 4%, the relative intensity ratio of the 525 cm^{-1} to the 475 cm^{-1} band (i.e. I_{525}/I_{475}) increases to 1.83 from 1.35. Furthermore, the intensity of the 405 cm^{-1} band changed relative to the intensity of the $525\text{-}475\text{ cm}^{-1}$ doublet as loading of V increased to 5%.

Spectra of aluminosilicates gel containing 4% and 5%, V exhibit a strong band at 995 cm^{-1} with a shoulder at 1020 cm^{-1} , Figs. 4E,4F. The high frequency band is different from that resulting from the presence of monomeric vanadyl species observed at low V loadings (21) and has been attributed to water sorbed in the V_2O_5 -like phase during steam-aging.

TABLE 2. Raman Band Positions for the V-Loaded Aluminas shown in Fig.3.

% V	Positions (cm^{-1})									
0.5	---	---	---	---	---	842	890	925	978	---
1.0	---	528	560	665	790	835	895	928	978	---
1.5	352	535	560	665	785	835	890	930	978	---
2.0	355	532	555	660	780	828	888	---	978	---
3.0	350	540	---	660	777	---	---	---	978	---
4.0	---	480	535	---	670	770	---	---	978	1000
5.0	405	485	530	---	---	704	---	---	978	997

Vanadium speciation for concentrations below 4%V is not easily ascertained. In general, for V-containing compounds, terminal $\text{V}=\text{O}$ band frequencies have values greater than 900 cm^{-1} ; these bands appear only when the presence of V_2O_5 is observed, Figs. 4E-4F.

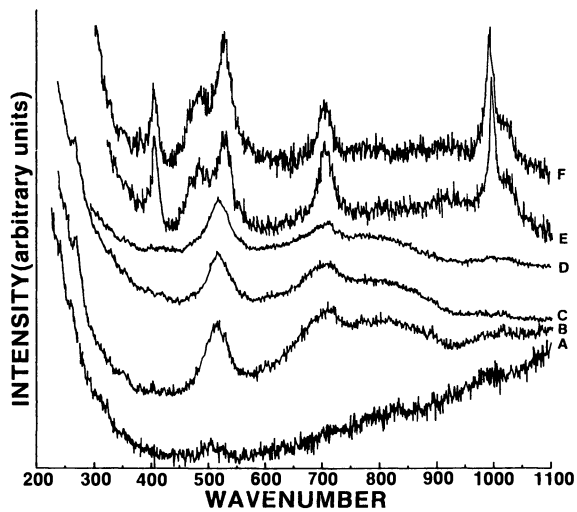


Figure 4. Laser Raman spectra of an aluminosilicate gel after loading with (A) 1.0%; (B) 1.5%; (C) 2.0%; (D) 3.0%; (E) 4.0%; (F) 5% V and steaming.

TABLE 3. Raman Band Positions for the V-Loaded Aluminosilicate Gels in Fig. 4.

% V	Positions (cm ⁻¹)								
1.0%	----- 517 -----								
1.5%	265	---	517 (685),	715	805	---	---	---	(1020)
2.0%	264	---	517 (685),	715	805 (867)	(968)	---	---	(1020)
3.0%	265	---	517	707	805	---	---	---	(1020)
4.0%	---	405	482,527	704	---	---	---	995	1020
5.0%	282	405	485,527	704	---	---	---	994	1020

Tetrahedral (VO₄)³⁻ species in aqueous solutions contain an intense V-O stretching vibrational band at 827 cm⁻¹ and relatively intense V-O bending modes near 330 cm⁻¹ (26). In condensed VO₄ systems, the V-O stretching vibration increases in position and has a range of values from 830 to 915 cm⁻¹ (27). In metavanadates, (i.e., MVO₃-type molecules which consist of V₂O₆ chains connected by VO₄ groups) the intense bands in the 890 to 950 cm⁻¹ region have been assigned to V-O stretching vibrations (28-30). In addition, metavanadate chain structures produce relatively intense vibrational bands due to V-O-V stretching in the 500 and 200-300 cm⁻¹ regions (28-30). Intense bands in the 820-950 cm⁻¹ or in the 200-300 cm⁻¹ region were not observed in the gel spectra for V-loadings below 4%, (Figs. 4A-4F). Thus concentration of condensed VO₄ or V₂O₆ chains is expected to be insignificant in these steam-aged aluminosilicates containing less than 4% V.

When V-levels decreased to 3% from 4% V, the intense bands at 995 cm⁻¹ and 405 cm⁻¹ disappeared and a singlet at 517 cm⁻¹ formed from the doublet at 482 cm⁻¹ and 527 cm⁻¹ seen in Figs. 4E,4F. Furthermore, the band at 704 cm⁻¹ decreased in intensity forming a band near 715 cm⁻¹ with shoulder at 685 cm⁻¹. Samples containing 1-3% V exhibit also a (weak) broad band in the 725-925 cm⁻¹ region, see Figs. 4B-4D. These spectral changes are similar to those reported for V₂O₅·nH₂O xerogels with n>0 (21-24).

Characteristic bands for aluminosilicates containing less than 4% V that can be reasonably assigned are in the 400 and 750 cm⁻¹ region. For V₂O₅ these bands are assigned to V-O stretching vibrations (685-705 cm⁻¹) and -V-O bending vibrations (480-500 cm⁻¹). The structural model of vanadia gels involves relatively long V-O-V chains which contain four coordinated V having distorted tetrahedral symmetry. Such a chain structure necessitates relatively intense vibrational bands in the 100-350 cm⁻¹ region which are the result of concerted vibrational motions of O and V atoms in the chain.

However, the multiplicity of bands and relatively intense character of these concerted vibrational modes are not observed in the V loaded gels under study. Thus, significant development of long ribbons of $V_2O_5 \cdot nH_2O$, or a polymeric nature of this surface species, is not expected to exist in the V-loaded aluminosilicates under study.

In summary, it is proposed that at low V levels, steam-aging (760°C/5h) generates highly hydrated vanadia islands containing distorted tetrahedral and octahedral V atoms (31). Hydration would change terminal V-O bond orders and/or cap terminal vanadyl groups (21,22), thereby removing strong Raman bands above 850 cm^{-1} , broadening V-O stretching bands in the 700-900 cm^{-1} region and weakening bands below 350 cm^{-1} . Vanadia formation is favored by the limited hydrothermal stability of the gel, Table 1. The V_2O_5 structure at low V concentrations would support easily the development of three dimensional V_2O_5 as the V concentration is increased to 4%. Hence, a hydrated layered vanadia model is envisioned which does not contain terminal vanadyl groups because of H-bonding effects and decreased V-O bond order due to H_2O sorbed during steaming. Thus, the vanadia present would be a highly disordered or poorly condensed phase similar in structure to $V_2O_5 \cdot nH_2O$ where $n > 1.6$.

XPS Results

XPS results for (steam aged) V-loaded aluminosilicate gels and aluminas are shown in Figs. 5-8. At low (0.5%) V levels, the two supports contain both V^{4+} and V^{5+} species in the near-surface region; V^{5+} formation in samples containing as little as 0.5% V has been observed also by ^{51}V -NMR (31). Surface concentration of V^{4+} rapidly decreases with V-loadings, Fig. 5. With 2% V only V^{5+} is observed on the gel and 5% V is needed before all the V^{4+} present is oxidized to V^{5+} on the alumina surface, Fig. 5. Electron paramagnetic (EPR) studies of gels contaminated with 1% V have indicated that, following the oxidative decomposition of the naphthenate, 95% of the vanadium was present as V^{5+} (18). After steam aging, the sample, assumed a yellow/green coloration indicative of the presence of V_2O_5 which could be verified also by Luminescence techniques (19).

The reducibility of the vanadium on the gel (i.e., the amount of V^{4+} or V^{3+} observed in H_2 treated samples) is less than that on the alumina; V^{3+} formation is observed only at 5% V loadings, Fig. 6. This difference can be easily observed in Fig.7 where the percentage of the V^{4+} originating only from V^{5+} is plotted. At 5% V loading, and after H_2 treatment, some of the vanadium on the gel remained in the V^{5+} state whereas on the Al_2O_3 , all of the vanadium was converted to either V^{4+} or V^{3+} , Fig. 6. Hence, conversion (or nucleation) of vanadium to a V_2O_5 species was probably more complete on the Al_2O_3 than on the gel. This conversion difference to V_2O_5 at a 5% V loading can also be inferred from Raman data where the signal-to-noise (S/N) for 5% V/ Al_2O_3 is significantly

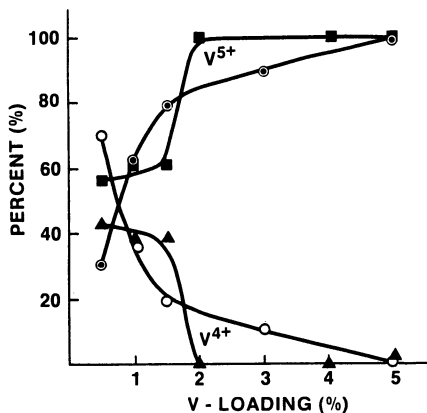


Figure 5. Percent distribution of V⁵⁺ (⊙) and V⁴⁺ (○) after steaming V-loaded aluminas; V⁵⁺ (■) and V⁴⁺ (▲) after steaming aluminosilicate gels.

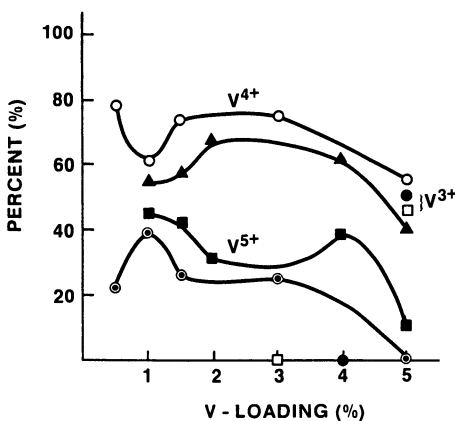


Figure 6. Percent distribution of V⁵⁺ (⊙), V⁴⁺ (○) and V³⁺ (□) after reducing in H₂ steam aged V-loaded aluminas. Data for similarly prepared gels is indicated by (■) V⁵⁺, (▲) V⁴⁺ and (●) V³⁺.

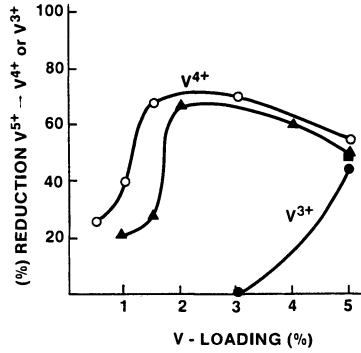


Figure 7. Reducibility in H_2 of steam aged V-loaded aluminas to V^{+4} (\circ) and (\bullet) V^{+3} . Data for similarly prepared gels is indicated by (\blacktriangle) V^{+4} and (\blacksquare) V^{+3} .

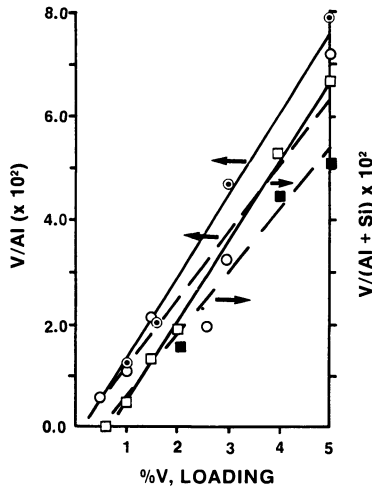


Figure 8. Surface V/Al and V/Si+Al ratios in V-loaded and steam aged alumina and aluminasilicate gels before [\odot , \square] and after [\circ , \blacksquare] reduction in H_2 .

better than the S/N for 5%V/gel and confirms the amorphous nature of the V_2O_5 present on the aluminosilicate matrix.

Comparison of V/Al atomic ratios for Al_2O_3 and V/(Si+Al) atomic ratios for V-loaded gels are presented in Fig. 8. Overall, and somewhat independent of whether or not the samples have been subjected to H_2 reduction, these ratios for the gel are approximately 30% smaller than the values observed for V on Al_2O_3 . The least squares linear regression fits to the V/ Al_2O_3 data extrapolates near the origin whereas the corresponding data for V/gel does not, Fig. 8. Hence, V dispersion on the gel surface, as monitored by XPS, is lower than on Al_2O_3 . The hydrothermal instability of V loaded gel (Table 1) is probably responsible for the lower V dispersion and for the lower V/Al+Si ratios seen in Fig. 8.

Raman and NMR (31) data indicate that with up to 2% V, a significant amount of the vanadium is in tetrahedral coordination on both supports. That is, poorly formed $V_2O_5 \cdot nH_2O$ ($n > 0$) on the gel and V compounds on the alumina in tetrahedral coordination. At loadings above 2%, the coordination of vanadium on Al_2O_3 becomes more octahedral but, until a loading of approximately 4%, contains isolated V_2O_7 units instead of a condensed V_2O_5 network. Hence, considering the XPS data on reducibility and the Raman data, it seems to be possible to stabilize V against H_2 reduction while having vanadium in different coordination and speciation, but essentially in identical dispersion and isolated units.

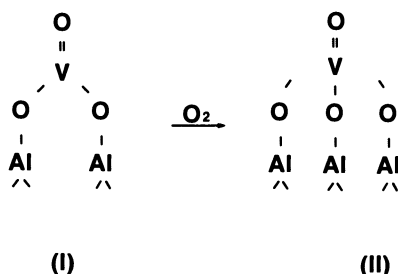
SUMMARY AND CONCLUSIONS

XRD, XPS, and Raman characterization of V supported on pseudoboehmite alumina or on amorphous aluminosilicate gels (metal loaded with a solution of VO^{+2} Naphthenate in benzene) have indicated the presence of tetrahedrally and octahedrally coordinated vanadium (31) having speciation and dispersion that depends on vanadium concentration (and surface area) present on the steamed (760°C/5h) samples.

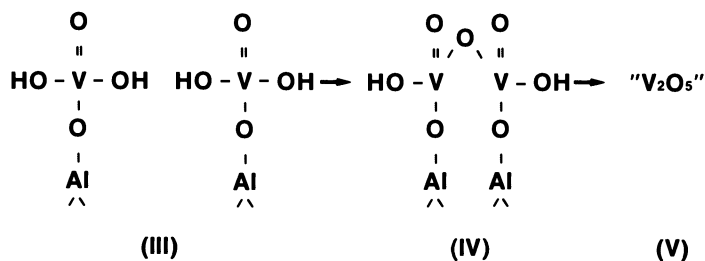
Oxycations of V (VO_2^+ or VO^{+2}) can easily penetrate the gel microspace and break Si-O-Al bonds causing the collapse of the gel microstructure and mullite formation even at low (1.5%) V levels. Excess V generates an x-ray amorphous, V_2O_5 -like species which is highly hydrated and less susceptible to chemical reduction than bulk V_2O_5 .

In (pseudoboehmite) alumina, Al-O-Al bonds are not easily broken by oxycations of V and condensed species, -(V-O-V)-, resistant to reduction are formed. In fact, it is believed that following the oxidative decomposition of the naphthenate precursor, VO^{+2} cations

are deposited on the alumina surface where they can be oxidized to VO^{+3} species (scheme I and II)



In the presence of steam (760°C/5h) hydroxy vanadyl ions (and other protonated species) are formed (scheme III and scheme IV)



As V loadings increase, condensation of these monomeric species yield divanadates units (V_2O_7) that at high (5%) V levels collapse the alumina microspace and form a crystalline V_2O_5 phase.

Surface vanadium appears to be most stable (to reduction) at low (<1%) V concentration when present as monomeric vanadyl units. Its stability decreases with increasing V levels. It is least stable (to reduction) at high (5%) V levels when present as a supported Vanadia phase. This difference in reactivity with V concentrations is believed responsible for the rapid decline in cracking activity observed in dual function cracking catalysts containing alumina when V start to exceed the 1.0-1.25 wt.% level (4). Further details of the mechanism of catalyst deactivation by V are the subject of continuing investigations in our laboratories by ^{51}V solid state NMR, XPS, and Raman spectroscopy.

Acknowledgments

The authors gratefully acknowledge the help received from Mr. R. Ortiz during sample preparation. Special thanks are due to Dr. P. S. Iyer for providing NMR data and to Dr. P. Ritz for LRS measurements.

References

1. Ocelli, M. L. in "Fluid Catalytic Cracking: Role in Modern Refining," ACS Symposium Series, Vol. 375: M. L. Ocelli, Ed., ACS, Washington, D. C., p. 162 (1989).
2. Rooseboom, F.; Mittelmeijer-Hazeleger, M. C. Moulijn, J. A.; Medema, J.; de Beer, V. H. J.; Gellings, P. J. J. *Phys. Chem.* 1980, 84, 2783.
3. Ocelli, M. L. and Stencel, J. M. in "Zeolites as Catalyst, Sorbents and Detergent Builders," H. G. Karge and J. Weitkamp Eds.; Elsevier, p. 127 (1989).
4. Ocelli, M. L. and Stencel, J. M. "Zeolites: Facts, Figures, Future" P. A. Jacobs and R. A. Van Santen, Eds.: Elsevier, p. 1311 (1989).
5. Wachs, I. E., Hardcastle, F. D. and Chan, S. S., *Mat. Res. Soc. Symp. Proc.* Vol. III, 353 (1988).
6. Wachs, I.E.; Saleh, R. Y.; Chan, S. S.; Cherisch, C. C. *Appl. Catal.* 1985, 15, 339.
7. Kozłowski, R.; Pettifer, R. F.; Thomas, J. M. *J. Phys. Chem.* 1989, 87, 5176.
8. Haber, J.; Kozłowska, A.; Kozłowski, R. *J. Catal.* 1986, 102, 52.
9. Anpo, M.; Tanahashi, I.; Kubokawa, Y. *J. Phys. Chem.* 1980, 84, 3440.
10. Anpo, M.; Sunamoto, M.; Che, M. *J. Phys. Chem.* 1989, 93, 1187.
11. Anpo, M.; Suzuki, T.; Yamada, Y.; Che, M. *Proc. 9th Int. Cong. Catal.* 1988, 1513.
12. Cristiani, C.; Forzatti, P.; Busca, G. *J. Catal.* 1989, 116, 586.
13. Oyama, S. T.; Went, G. T.; Lewis, K. B.; Bell, A. T.; Somorjai, G. A.; *J. Phys. Chem.* 1989, in press.
14. Went, G. T., Oyama, S. T. And Bell, A. T. *J. Phys. Chem.* (submitted)
15. Mitchell, B. D. *Ind. Eng. Chem. Prod. Res. Dev.* 19, 209 (1980)
16. Gilson, J. P.; Edwards, G. C.; Peters, A. K.; Rajagopalan, K.; Wormsbecher, R. F.; Roberie, T. G.; Shatlock, M. P., *J. Chem. Soc. Chem. Comm.* 1987, 91.
17. Samoson, A.; Lippmaa, E.; Engelhardt, G.; Lohse, D.; Jerschwitz, H. g., Chemical Physics Letters 1987, 134, 589.
18. Anderson, M. W.; Ocelli, M. L.; Suib, S. L., *J. Catal.*, in press.
19. Anderson, M. W.; Ocelli, M. L.; Suib, S. L., *J. Catal.*, in press.
20. Ocelli, M. L. and Stencel, J. M. in "Proc. 9th Int. Congress Catalysts," Phillips, M. J. and Ternan, M., Eds.; Vol. 1, p. 214 (1988).
21. Abello, L., Husson, E., Repelin, Y. and Lucazeau, G., *J. Solid State Chem.* 56, 379 (1985).
22. Repelin, Y., Husson, E., Abello, L. and Lucazeau, G., *Spectrochim. Acta*, 41A, 993 (1985).
23. Abello, L., Husson, E., Repelin, Y. and Lucazeau, G., *Spectrochim. Acta*, 39A, 641 (1983).

24. Sanchez, C., Livage, J. and Lucazeau, G., Raman Spectrosc. 12, 68 (1982).
25. Wokaun, A., Schraml, M. and Baiker, A., J. Catal. 116, 595 (1989).
26. Vilchez, F. G. and Griffith, W. P., J. C. S., Dalton, 1416 (1972).
27. Griffith, W. P. and Lesniak, P. J. B., J. Chem. Soc. (A), 1066 (1969).
28. Park, Y. S. and Shurwell, H. F., J. Raman Spectrosc. 18, 247 (1987).
29. Baran, E. J., Cabello, C. I. and Nord, A. G., J. Raman Spectrosc. 18, 405 (1987).
30. Seetharaman, S., Bhat, H. L. and Narayanan, P. S., J. Raman Spectrosc. 14, 401 (1983).
31. Iyer, P. S., Eckert, H., Occelli, M. L. and Stencel, J. M., this volume.

RECEIVED August 28, 1990

Chapter 17

Petroleum Cracking Catalyst Characterization

Secondary Ion Mass Spectrometry Imaging Processing Methods

D. P. Leta, W. A. Lamberti, M. M. Disko, E. L. Kugler¹,
and W. A. Varady

Exxon Research and Engineering Company, Annandale, NJ 08801

The characterization of petroleum cracking catalysts, with which a third of the world's crude oil is processed, presents a formidable analytical challenge. The catalyst particles are in the form of microspheres of 60-70 micron average diameter which are themselves composites of up to five different micron and submicron sized phases. In refinery operation the catalysts are poisoned by trace concentrations of nickel, vanadium and other contaminant metals. Due to the replacement of a small portion of equilibrium catalyst each day (generally around 1% of the total reactor inventory) the catalyst particles in a reactor exist as a mixture of differing particle ages, poisoning levels and activities.

Direct imaging SIMS has been shown to be capable of viewing both the phases and contaminants within individual catalyst particles, and differences from particle to particle. Multiple image processing techniques now allow the rapid analysis of the relative concentrations of several elements (normally 6-8) on a large number of particles (50-100) using multiple low magnification SIMS images. Using the fact that nickel concentrations increase systematically with a particle's age permits the analysis of poisoning and elemental composition as a function of a particle's "time in the reactor." Within individual particles, SIMS views coupled with elemental image ratios and overlays have also allowed the measurement of the quantity of each phase (such as zeolite and alumina) and the distribution of nickel and vanadium poisons in relationship to those phases.

The technique of Imaging Secondary Ion Mass Spectrometry (SIMS) has proven to be very well suited to the characterization of fluidized petroleum cracking catalysts (FCC).⁽¹⁻⁴⁾ The ability to view

¹Current address: West Virginia University, Morgantown, WV 26506

elemental distributions with 0.5 micron spatial resolution at concentrations in the ppm range is well suited to the analysis of the submicron phases and low concentration contaminants present in commercial multi-component FCC particles. The use of ultra-low light level imaging systems⁽⁵⁾ with the intrinsically sensitive SIMS technique makes real time viewing of many of the elements important in FCC catalysts possible. Aluminum, silicon and the rare earth elements serve to define the major phases present within each catalyst particle, while the transition row elements and all of the alkali and alkaline elements may be seen at trace concentrations. Of particular importance is the use of the technique to study the distributions of nickel and vanadium which are the most deleterious of the contaminant metals.⁽⁶⁾ Modern image processing computers and software now allow the rapid quantitative analysis of SIMS elemental images in order to more clearly reveal the locations of the catalyst phases and the quantitative distributions of the contaminant metals on those phases. Although the analysis techniques discussed in this study may be applied to any of the contaminant elements, for simplicity we will limit our examples to the major catalyst elements, and the nickel and vanadium contaminants.

EXPERIMENTAL METHODS

Catalyst Preparation. All of the FCC catalyst samples used in this study were prepared by embedding the as-received particles in thermosetting copper doped epoxy (commercially available from metallurgical supply distributors) to provide electrical conductivity. The hardened epoxy blocks were then polished to expose the interiors of the catalyst particles (approximate cross-sections) using silicon carbide paper to 600 grit. The polishing is carried out without water to avoid the possibility of elemental redistribution. Prior to data collection it is necessary to pre-sputter areas of interest for 10-15 minutes, which atomically removes several microns of material, cleaning away embedded polishing grit and exposing the undisturbed particle interiors.

SIMS Instrumentation. A CAMECA IMS-3f ion microprobe/microscope, modified by the addition of a high sensitivity video based imaging system⁽⁵⁾ was used for elemental viewing of the FCC particles. Oxygen as O_2^+ was used as the primary bombarding ion, at an impact energy of 10.5 keV and positive secondary ions were used for data collection. Generally, integration times of 8-30 seconds were sufficient to obtain good signal-to-noise characteristics in the images. All of the images in this study were collected using either a nominal 150 or 400 micron field-of-view. The type of image integration used sets the final intensity of the brightest pixel in each image to a standard value, ensuring viewability. As such, the brightness within one image may be used to gauge an element's relative concentration from region to region, but no conclusions should be drawn between different images without using the mass spectral count rates and comparison to suitable standards. For this study, the digitized brightness within the images were

used without attempt to convert to actual concentration, and as such all values represent "relative concentration."

Image Processing. In our image processing/collection system the SIMS instrument's internal multichannel plate / fluorescent screen is viewed using an ultrahigh gain video camera capable of viewing the bursts of light generated by individual ions. This analog video signal is digitized and integrated using a "Crystal" image processor (MCI Consultants) and the integrated images stored as analog signals using an Optical Laser Disk which provides inexpensive hi-fidelity image storage. Post analysis image processing is accomplished by re-digitizing the images with a Microvax II hosted Gould/DeAnza 8500 image processing computer system and using a combination of in-house and commercial software routines. Prior to the use of any image comparative calculations, sets of images are accurately registered with each other using cross-correlation techniques. For all steps of image handling and processing, resolutions of approximately 512x512 with 256 brightness levels are maintained.

RESULTS AND DISCUSSION

Distributions Within Single Catalyst Particles

Silicon/Aluminum Ratio Images. Many types of FCC catalyst particles are heterogeneous mixtures of zeolite, clay, alumina and silica/alumina binder phases. Each of these phases contains silicon and aluminum as the major elements, with varying Si/Al ratios in each phase. It is possible to generate a "phase map" of single catalyst particles by taking advantage of these differing Si/Al ratios. Division of the SIMS Si ion image by the Al ion image produces a Si/Al intensity ratio image which often clearly shows the positions of the phases. Image division also provides the additional benefit of eliminating most of the intensity variations caused by topography or by nonuniform primary beam illumination of the sampled region.

Figure 1a and 1b show 150 micron field-of-view Si and Al ion images, respectively, taken of a fresh FCC catalyst particle of a type which contains no rare earth exchanged zeolites. When rare earth elements are present (see later discussion) they greatly simplify the identification of the zeolite phase. Inspection of the Si and Al images shows that although brightness variations are present in both images it is very difficult to "see" where the various phases reside. Division of the Si image by the Al image yields figure 1c which shows the Si/Al intensity ratio image, re-normalized to a viewable brightness. In this ratio image the various grey levels (brightnesses) corresponding to the different phases may be much more clearly discerned. Silica (as silica impurities or as aggregated binder phase) gives the highest Si/Al ratios and is therefore the brightest in the intensity ratio image, followed by zeolite > clay > added bulk alumina.

The use of line profile methods to determine the digital grey levels (0-255) present across the ratio image is demonstrated in

figure 1d. At this point in the analysis it is necessary to determine the "cutoff" grey levels which demark each of the phases. Our experience has shown that although the eye seems to be reasonably able to "see" the position of the phases in the Si/Al intensity ratio image, perhaps because of the brain's ability to see "objects" instead of "grey levels", it is often difficult to accurately pick the grey level cutoffs for each phase. Absolute comparison of the grey levels present in a set of images with those determined using standard single phase samples is difficult due to "day-to-day" changes in instrument transmission, primary ion beam stability and uniformity, and to the "autoranging" of the image collection system (which increases the system's gain for weaker signals to make the final images viewable). For comparison to separate standards, normalization of the brightness levels using a separate measurement of the ion counts-per-second for each element arising from the entire field of view must be done. For these reasons it is best and most convenient to use known phases within the analysis field of view itself, either within the particles being analyzed or added as "internal standards" to the mounting material, to determine the grey levels representative of each phase. After the grey level representative of each phase is determined from large and well defined regions the difficulty still remains as to how to assign the "pixels" whose values fall between the grey levels determined as "average" for each phase. Due to the limits of resolution of the technique (about 0.5 micron), the intimate mixing of the phases, and the ubiquitous presence of binder, there exists a range of measured grey levels for each phase. Normally the selection of a grey level evenly spaced between the average of two phases may be used as a cutoff level to delineate the boundaries of each phase. Figure 1e shows the grey level cutoffs chosen to indicate the high silica (clumped binder), zeolite, clay and alumina phases present in this catalyst particle. Experience has shown that the average area concentrations determined on standard materials with known concentrations of zeolite and alumina phases agrees within $\pm 20-30\%$ relative once the conversion from weight concentration to volume concentration has been made. Improvement, automation, and mathematical justification of this process will be a goal of future study.

Once the grey levels representing each of the phases have been determined, a "semi-quantitative phase map" such as that shown in figure 1f may be generated. The white areas in this image show the high silica phase, the light grey shows the zeolite phase, the dark grey the clay phase and the very dark grey the added bulk alumina. From such an analysis both the position and the "area concentration" for each phase may be determined. It must be kept in mind that the area concentrations of each phase determined by viewing cross-sectioned catalyst particles are proportional to the occupied volume fractions but must be corrected both for a phase's absolute and "packed" densities before comparing the "area concentrations" to conventional weight fractions.

Distribution of Nickel and Vanadium Between Phases. Along with the determination of the amount of each phase present in individual catalyst particles it is very useful to be able to quantify the

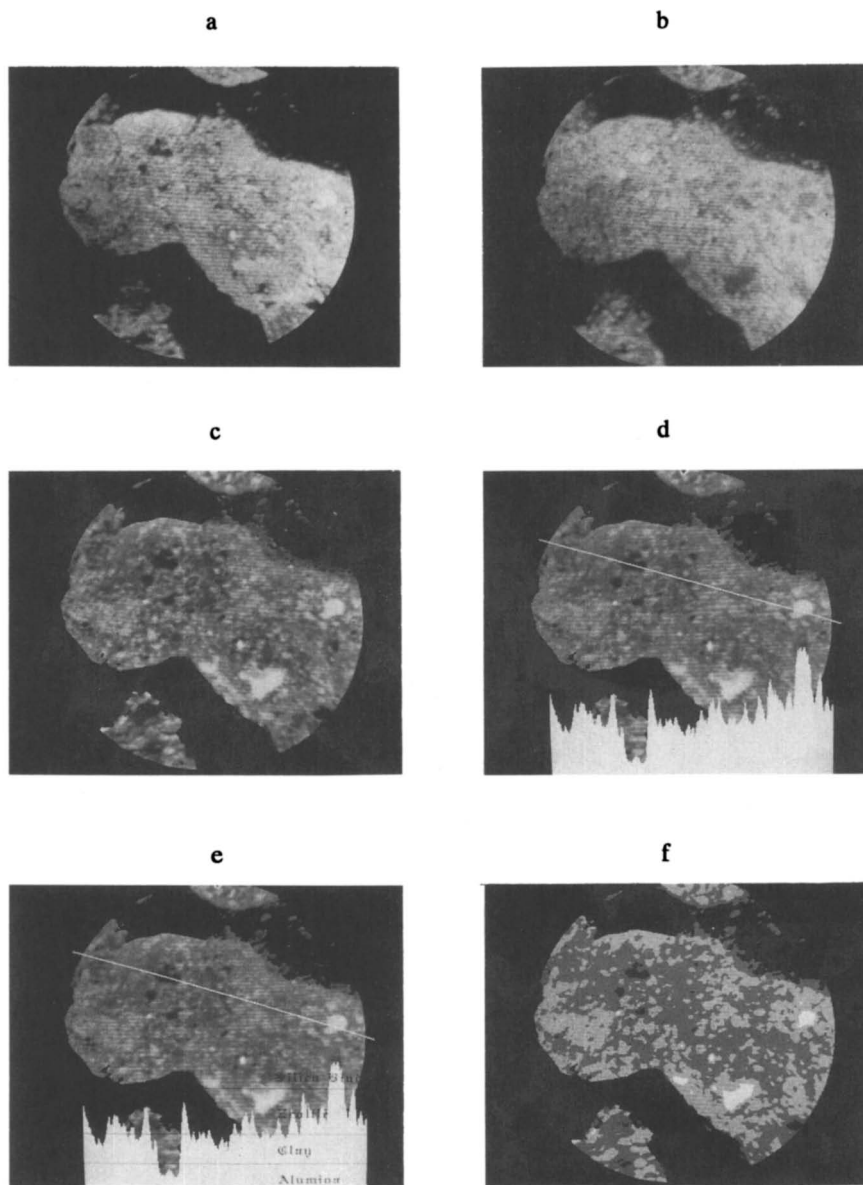


Figure 1. Phase identification using Si/Al ratio images. a) silicon b) aluminum c) Si/Al ratio image d) Si/Al intensity profile e) selection of intensity cut-offs f) "semi-quantitative" phase map

distribution of trace poisons such as nickel and vanadium between those phases. Of particular importance is the degree to which vanadium resides on the zeolite phase of a catalyst. It has been found that vanadium deactivates cracking catalysts by decrystallizing the zeolite component.⁽⁷⁾ In general, we have seen that the greater the fraction of vanadium which resides on the zeolite phase the greater the activity loss suffered due to vanadium attack. This is true for both laboratory doped and equilibrium catalysts. Although laboratory methods of vanadium doping may not quantitatively mimic the distributions of vanadium found in equilibrium catalysts, final vanadium distributions as discernible by imaging SIMS in either situation seem to correlate well with the degree of deactivation experienced (in that situation). We have also seen that while vanadium has a significant degree of mobility both within and between particles under normal FCC conditions, nickel tends to be immobilized once deposited. As such, nickel distributions may be used to both determine the approximate time a particle has been recirculating in an FCC unit⁽⁸⁾, as well as to show on which phases the cracking occurs for the nickel porphyrin type molecules present in FCC feeds.

At this point it may be appropriate to briefly discuss the mechanism of signal formation in the SIMS process. A primary ion beam impinges upon the sample surface and causes the sputtering of atoms and small molecular clusters, some of which are ionized by the energy of collision, usually several thousands of eV. The ions thus created are available for analysis by collection using electrostatic acceleration and mass spectrometric separation followed by sequential ion counting or direct image formation (the type of instrument used in this study actually keeps the sputtered ions focussed as they are mass separated through the use of ion lenses). In the sputtering event itself a significant amount of atomic mixing of the outer 20-30 angstroms of a material occurs, creating an amorphous and well-mixed region. It is from the top few atomic layers of this region, which is in steady state with the several angstroms per second sputtering recession of the surface, that the collected ions are created. The rapid sputtering and mixing situation prevalent in the "dynamic SIMS" process here has several beneficial characteristics when applied to the characterization of FCC catalyst particles. First, the rapid sputtering allows the top several microns of prepared cross-sectional surface to be removed in a reasonable period of time, thus atomically removing mixing and smearing effects which might have occurred during polishing. Secondly, the atomic mixing of the surface tends to eliminate "overlayer" effects which might cause one element to "conceal" another. Thirdly, in the case of oxide catalysts such as these, the atomic mixing phenomena tends to distribute oxygen throughout the sputtering region in a relatively uniform manner, where it has the effect of "buffering" any matrix effects on elemental ion yields. Although the ion yields for the elements (i.e. the ions created ratioed to the atoms sputtered) vary greatly from element to element, for any one element this oxide buffering effect minimizes the changes in ion yield from phase to phase thus greatly reducing the difficulties normally encountered in making SIMS results even "semi-quantitative."

SIMS ion images taken of the Al, Si, La, V and Ni distributions on several particles of equilibrium catalyst are shown in Figure 2a-2e, respectively. This catalyst is of the type designed to crack vacuum gas oils and contains only rare earth exchanged zeolite, clay and binder. In this catalyst type, much of the zeolite is present in 5-10 micron diameter clumps. This clumping makes the visualization of this phase possible either as dark grey areas in the aluminum image or as the bright areas in the lanthanum image which directly shows the rare earth doping in the zeolites. Qualitatively, vanadium may be seen to be present at higher concentrations (brighter) in the regions of the particles which contain zeolite, while nickel shows a strong "rim" distribution on these cross-sectional views. Closer inspection of the nickel image also reveals that while much of the interior of the particles has a low, but visible amount of nickel, the regions where zeolite is present show almost no nickel signal. As previously stated nickel's apparent lack of mobility, here demonstrated even within individual catalyst particles, has caused the nickel to be found in the locations where the porphyrin molecules were cracked. Very reasonably, in this case where the zeolite crystals are clumped together and allow little access to their external surface areas, the nickel may be seen to be excluded from these regions because of the large porphyrin molecules' inability to diffuse into zeolitic channels.

Figure 3a-3e demonstrates an image processing methodology useful for the generation of "binary phase masks" which may be used to define areas from which the integrated intensities of other elements, such as nickel and vanadium, may be determined. Figure 3a shows a binary image generated by using either the Si or the Al image and setting all intensity values above a cutoff value to white, to define the regions of the images representing the entire catalyst particles. Vanadium and nickel integrated intensities (summed grey levels) from within this region, divided by the number of pixels in the region, i.e. the mean pixel intensity value, gives the total "relative concentration" of the elements on the catalyst particles. Generation of a binary map of the zeolite phase is the next step in determining the trace element phase distributions. Since the binder phase is very homogeneously distributed (as is normally the case) it will not be considered as a separate phase (primarily due to our inability to separately view it). Thus the determination of the zeolite distribution will subtend the images into two phases, zeolite and clay.

As previously discussed, the formation of a Si/Al intensity ratio image gives a useful map of the phases within the catalyst particles. Regions of high Si/Al such as zeolite and clumped binder phases show up as bright areas in the ratio image. Figure 3b shows such an image for these "gas oil" catalyst particles. Conservative selection of a high cutoff value to include both the zeolite and binder regions leads to the generation of the binary image shown in figure 3c. Since this type of catalyst contains rare earth exchanged zeolites, we may also use the La ion image to define regions of zeolite phase. Generating a binary mask from the La image leads to figure 3d. We have found that although the La image itself should provide a good mask of the zeolite phase, due to the weak signals of the rare earth elements, each often present

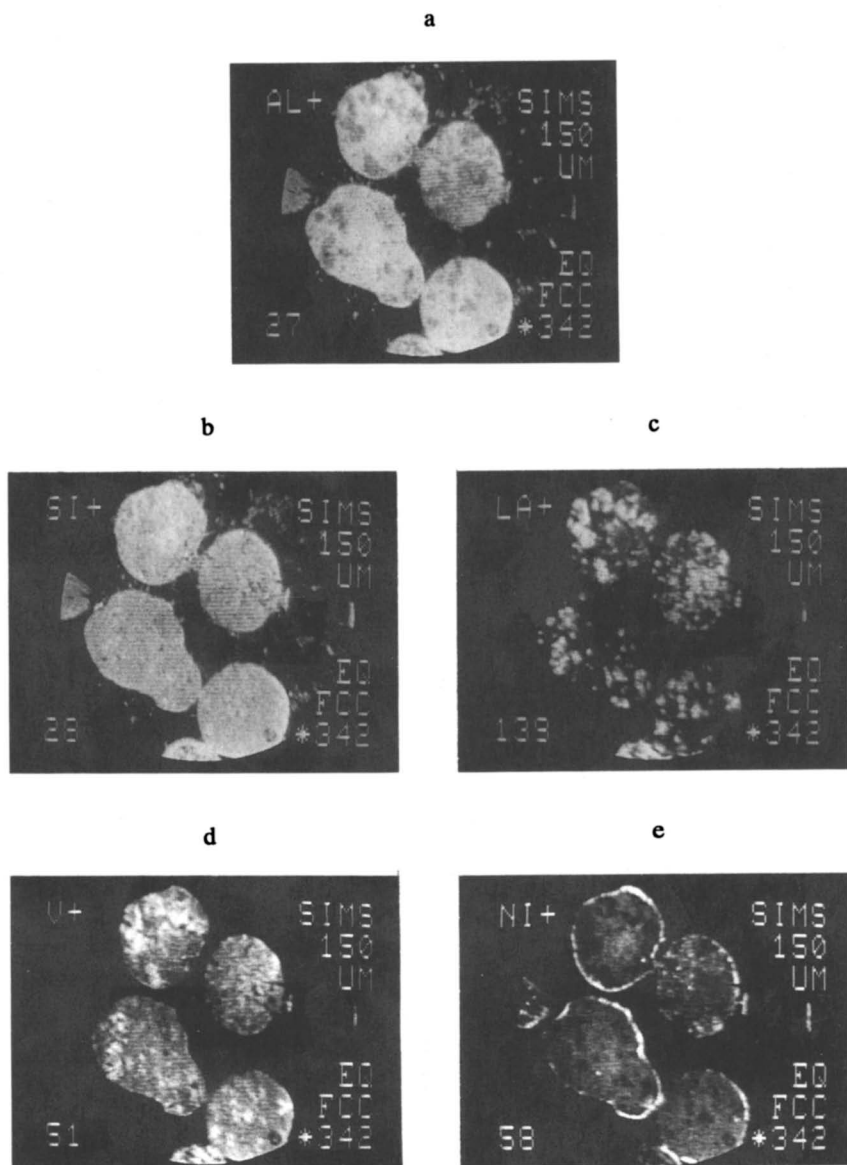


Figure 2. Ion images of equilibrium "VGO type" catalyst particles. a) aluminum b) silicon c) lanthanum d) vanadium e) nickel

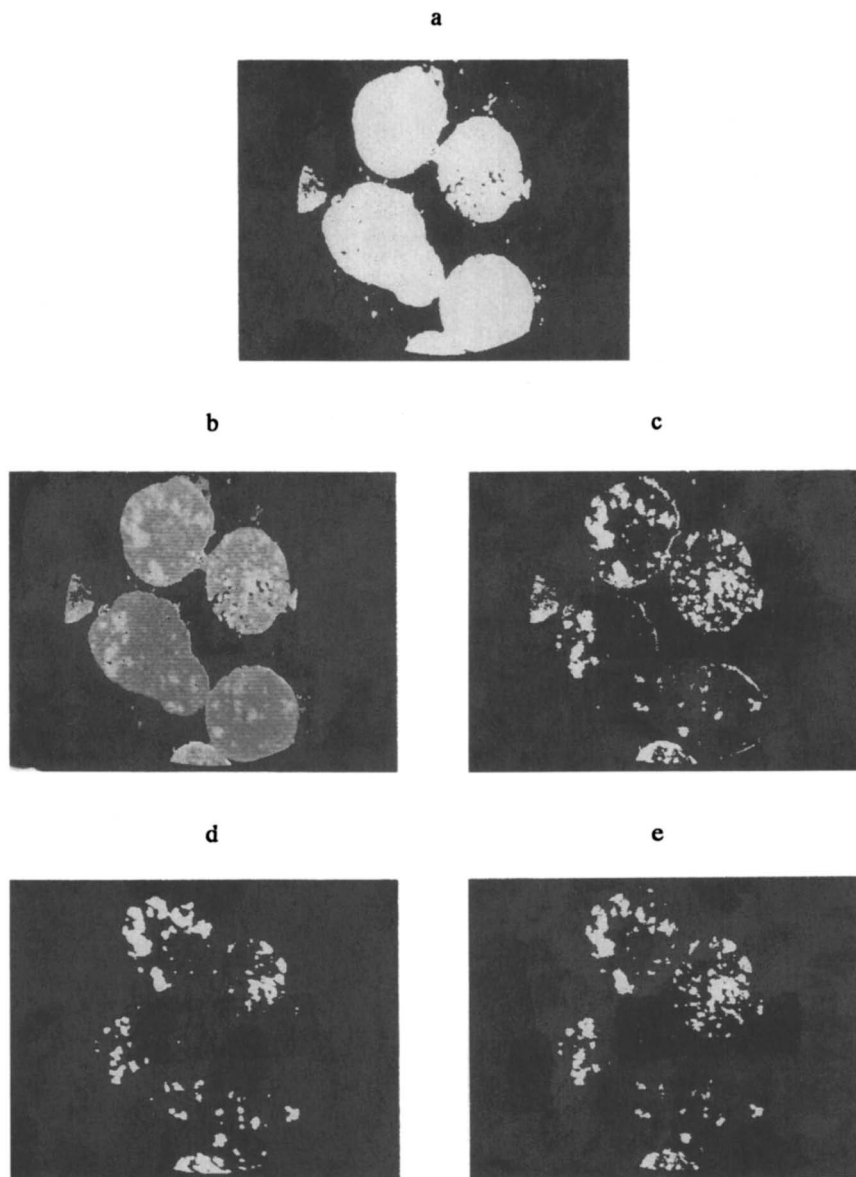


Figure 3. Binary phase masks of equilibrium VGO catalyst images. a) particle location mask b) Si/Al intensity ratio c) high Si/Al ratio mask d) high lanthanum mask e) zeolite mask (logical AND of c & d)

at tenths of percent concentrations, the images may not show sufficient clarity to properly define the zeolite regions. Performing a "logical and" operation on the two binary masks, 3c and 3d, eliminates both the regions of high binder concentration shown in the Si/Al binary image and the regions in the La binary image which are caused by imperfection of focus. Such an image, which defines the zeolite phase, and by difference the clay phase, is shown in figure 3e.

TABLE 1

<u>EQUILIBRIUM "GAS OIL" CATALYST</u>		
<u>Phase Area Conc.</u>	<u>% of V (RC)</u>	<u>% of Ni (RC)</u>
13.4%	17.4% (1.30)	6.2% (0.46)
86.4%	82.6% (0.96)	93.8% (1.09)
<u>EQUILIBRIUM "RESID RESISTANT" CATALYST</u>		
<u>Phase Area Conc.</u>	<u>% of V (RC)</u>	<u>% of Ni (RC)</u>
24.3% Zeolite	28.1% (1.16)	24.4% (1.00)
3.8% Bulk Alumina	5.0% (1.32)	5.9% (1.55)
71.9% Clay	66.9% (0.93)	69.7% (0.97)

Measuring the total signal intensities of vanadium and nickel within the total particle mask and the zeolite mask regions allows the quantification of the phase distributions of these elements. The top half of Table 1 presents the results of such an analysis on these images of gas oil catalyst. The number of pixels contained in the zeolite mask divided by the number of pixels in the particle mask directly gives the "area percent" of the zeolite phase, and by difference that of the clay (the values for clay include most of the contributions of the binder phase). The fraction of the vanadium and nickel in the defined zeolite regions divided by the signals from the particle mask regions gives the numbers reported in the table as "% of V" (or Ni). This figure is the percentage of the total quantity of the trace element which resides on the zeolite phase. "RC" in the table is used to indicate the "relative concentration" factor, which is the percentage of the element on a phase divided by the area fraction of that phase. Here an RC value of 1.00 would mean that the phase contains a concentration of the element which is equal to the average concentration of the element on the total particle. RC factors greater than 1.0 mean that the phase has a higher than average concentration (and conversely for values of less than 1.0). It may be seen that in this case,

vanadium is significantly accumulated on the zeolite phase, with an RC factor of 1.3. As was seen qualitatively however, nickel is mostly excluded from the zeolite regions with an RC factor of 0.46.

SIMS elemental images taken of a second type of equilibrium commercial catalyst, marketed as "resid resistant", are shown in figure 4. Careful inspection of the Al and Si images reveals the presence of dark regions in the Si image and corresponding light regions in the Al image. These regions are bulk alumina which has been added to the catalyst during manufacture. The use of image subtraction, as demonstrated in the Si-Al image (fig. 4c), quickly reveals the locations of this alumina phase. In the subtracted ion images the alumina appears as black regions. In our system, as well as many commercial image processing systems, image subtraction (as opposed to the more calculation intensive image division operations) may be performed at video rates which makes the identification of added alumina in FCC particles possible in real time while collecting the SIMS data. The lanthanum ion image (fig. 4d) shows that in this catalyst type the distribution of the zeolite phase in this catalyst is much more homogeneous than the previously cited example. The vanadium ion image (fig. 4e) shows that the alumina phase has gettered the vanadium, which shows the brightest areas in the locations of the alumina. The alumina in the catalyst, in addition to likely providing increased "bottoms cracking", is making the catalyst somewhat "resid resistant" by gettering a fraction of the vanadium. It must be noted, however, that the zeolite phase (fig. 4d) is also "trapping" a significant portion of the vanadium. The nickel concentrations (fig. 4f) varies somewhat from particle to particle due to the particles' different residence times (ages) in the unit, but within each particle nickel may be seen to reside to a significant degree on the alumina phase and "closer to the outside" of the particles. Once again, the nickel distribution is likely indicating the locations within the particles where the organometallic nickel species were decomposed.

Image processing methodology, similar to that described earlier, may be used to quantify the phase distributions of the nickel and vanadium in these images. The quantitative results of such an analysis may be found in the bottom of Table 1. Here, the RC factor for vanadium on the zeolite has been lowered from the 1.30 observed in the gas oil catalyst example to 1.16. This may be postulated to be due to the trapping of some of the vanadium by the alumina phase, which, with an RC of 1.32 is acting as a sink for vanadium. Even if the trapping effect of the alumina is a temporary one, it decreases the effective activity of the vanadium in the regenerator. Although the quantity of vanadium trapped by the small quantity of alumina in this catalyst is only 5% of the total, it may be that this mechanism helps reduce the activity of the mobile vanadium in the regenerator enough to make a difference. As noted before, the nickel is also located on the alumina phase and here shows a 1.55 RC factor. The nickel's RC of 1.00 on the zeolite phase (average nickel content), as opposed to being reduced as shown for the gas oil catalyst, may be due to the more accessible external reactive surface of the well-distributed zeolite crystals in this catalyst type.

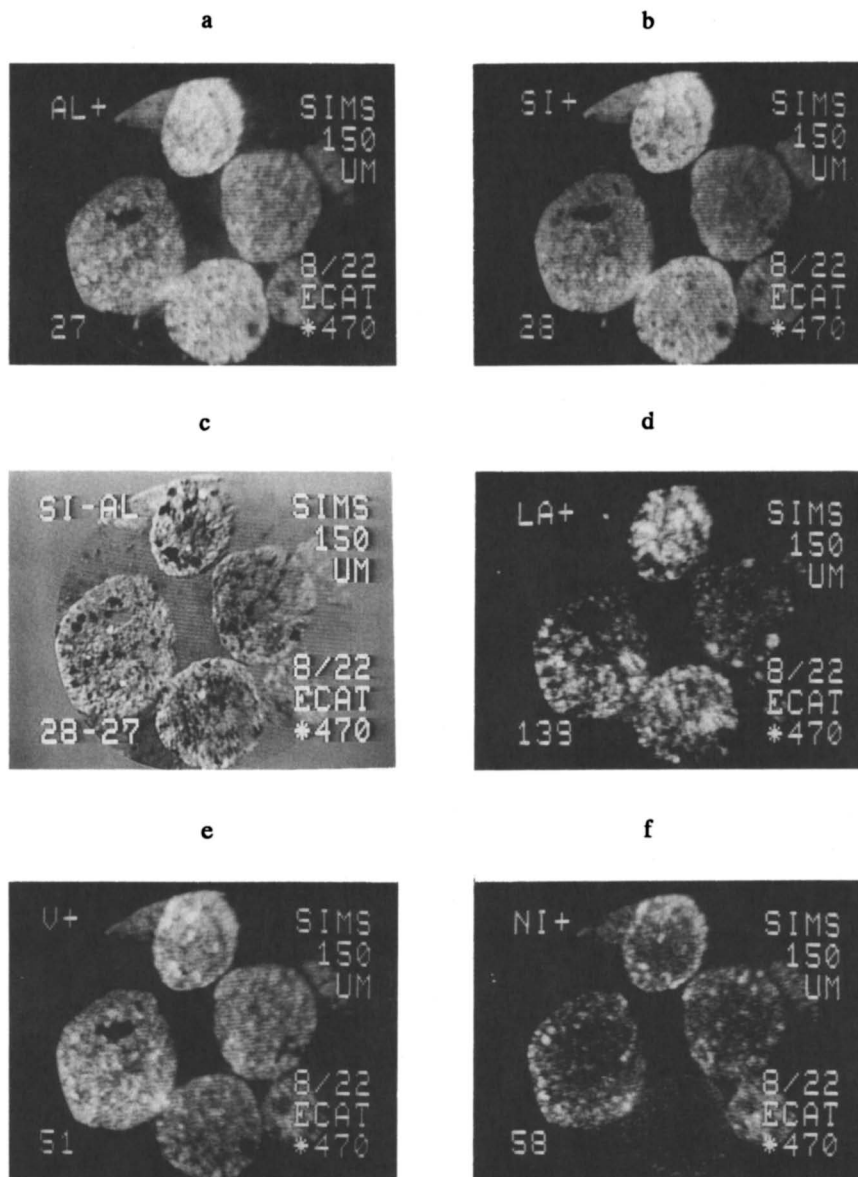


Figure 4. Ion images of equilibrium "Resid type" catalyst particles. a) aluminum b) silicon c) silicon minus aluminum d) lanthanum e) vanadium f) nickel

Distributions From Particle to Particle

One of the primary benefits in the use of the imaging SIMS technique to view FCC catalyst particles lies in its ability to identify particular catalyst particles or types in mixtures. This is particularly important in characterizing equilibrium catalyst particles where there exists a range of particle ages (i.e., time in the unit) as well as the possibility of catalysts from different vendors and/or separate additive-containing particles. Used at low magnifications and working with particles embedded at reasonably high densities, it is possible to simultaneously view as many as one hundred particle cross-sections. Although at low magnifications it may not be possible to view the phases within each catalyst particle, collecting images of all of the elements of interest in a single region followed by quantitative image processing provides the equivalent of as many as one hundred multi-element analyses.

Qualitative Observations. As an example of multi-particle imaging SIMS analysis, equilibrium catalyst sampled from an FCC unit which had recently begun adding fresh catalyst from a different vendor has been chosen. In this situation, we have a handle on the maximum length of time which a new type catalyst particle has been in the reactor, as well as the minimum time for an old type catalyst particle. (Although mixing in the fresh catalyst feed silo adds uncertainty to the situation, as will be seen in the following analysis.)

A set of ~400 micron field-of-view SIMS images of an equilibrium sample taken approximately four weeks into a catalyst type change is shown in Figure 5. It may be seen that the lanthanum (5b) and cerium (5d) distributions are not identical. Using the mass spectral mode of SIMS analysis on separate samples of the old and new catalyst types it was found that the old catalyst (longer residence time in the unit) had a lanthanum to cerium ratio of approximately twice the new type. This difference may be used to rapidly identify the vendor of each individual particle. Figure 5f shows the "cerium minus lanthanum" image in which the old particles appear very dark and the new particles appear white. The nickel intensities (5e) are, qualitatively, the inverse of this subtracted image. That is, the particles known to be older may be seen to contain more nickel. The vanadium image (5c) also shows a correlation with age, but the contrast from old to new particles is much less than for nickel. This may be interpreted to demonstrate that vanadium has exhibited a significant, but finite, degree of particle to particle mobility in the FCC unit.

Quantitative Multi-particle Analysis. In order to determine the relative concentrations of each of the elements-of-interest (here taken to mean a dimensionless measure of the variations of each element's concentration from particle to particle within the field-of-view), the silicon image is used to generate a binary mask which defines the position of each of the catalyst particles. In cases where the particles are touching, it is additionally necessary to manually draw a line of separation between them. Once

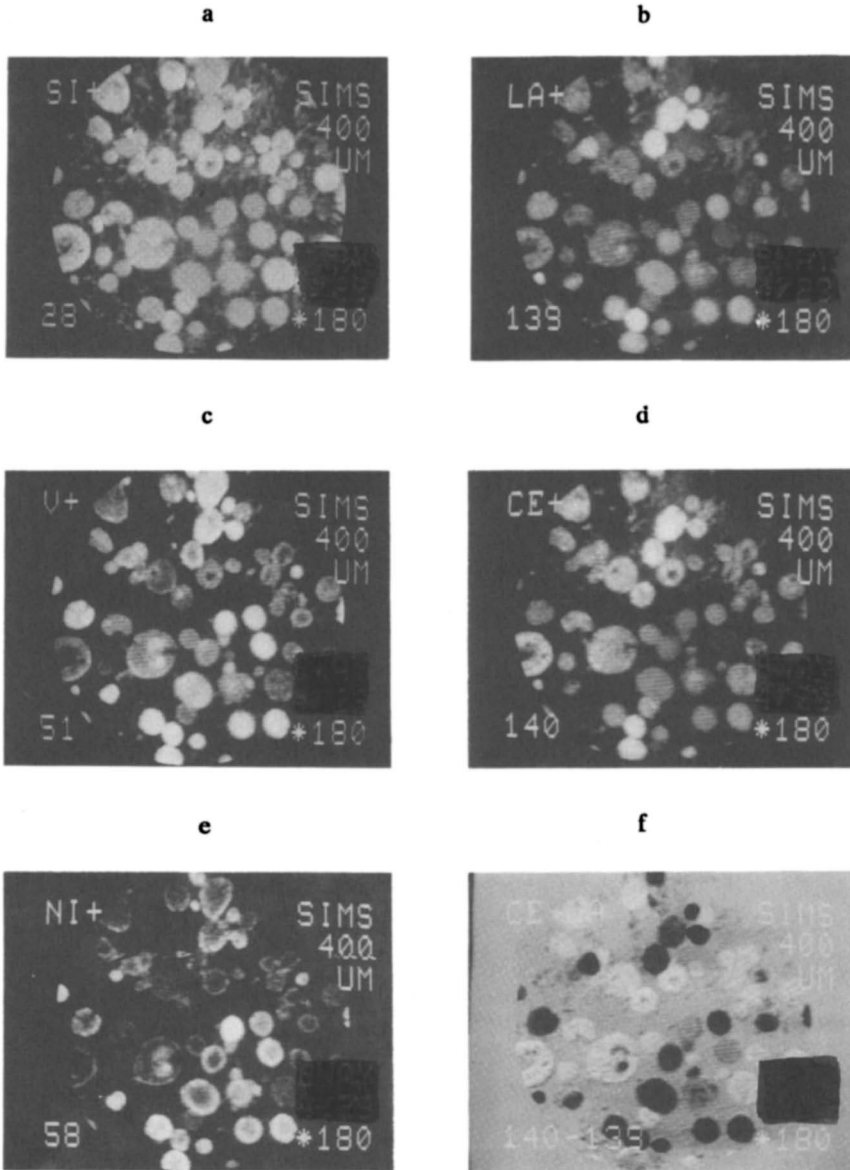


Figure 5. Low magnification ion images of equilibrium catalyst particles sampled four weeks into a catalyst type change.
 a) silicon b) lanthanum c) vanadium d) cerium e) nickel
 f) cerium minus lanthanum

this particle mask is generated, the mean intensity of each of the elements-of-interest is determined within each of the "particle" regions (proprietary software). In this case, the relative concentrations of Si, Al, La, Ce, Ni and V on each particle were determined. To show the potential of such analysis, the relationship of vanadium to the other elements was determined in order to gain insight into the factors controlling its final distribution.

Figure 6 shows the relationship of vanadium to nickel for the sample mentioned above, taken four weeks after the catalyst type change. Note that the units on this, and the following figures, are the mean grey levels from each particle, ranging from 0-255, which were digitized from the SIMS ion images. The new catalyst particles, as determined by their lower calculated La/Ce ratios, are identified by a "*".

In figure 6 the nickel concentration, shown on the X-axis, is intended to indicate the "age" of the individual particles. Although the nickel concentration of the particles is certainly proportional to their age, it is likely that the relationship is not exact, and may be affected by particle size. It has been shown that nickel is often, but not always, found to reside in a "rim" distribution on the cross-sectioned catalyst particles. This indicates that the nickel-containing molecules often crack rapidly, relative to their speed of diffusion into the catalyst particles. This diffusion limitation leads to the possibility that the "quantity of nickel on a particle per the particle's external surface area" (here meaning the area of the surface of the ~30-90 micron spheres, not the "surface area" of the catalyst) would be a more correct determinant of age than would the nickel per volume, which is the concentration. Two factors have prevented us from applying the effects of this diffusion limitation, which may lead to larger particles showing lower concentrations of nickel at equal age than smaller ones, in the calculation of the particles' age distributions. First, we have seen that the degree of "rim" distribution for nickel varies among different equilibrium catalyst samples, probably due to differences in the diffusion limitations of the catalyst types. Secondly, although we do determine the viewed area of each of the particles, we have no way of determining to what point in its cross-section an individual particle has been polished. Therefore, only a statistical analysis of large numbers of particles, combined with quantitative determination of the radial distribution functions for nickel, would allow the proper use of a factor expressing the mix between Ni/volume and Ni/surface area to be used. Combined with the necessary assumption that the concentration of nickel in the FCC unit's feed has been very constant over a year-long period (often known to be false) leads us to merely use the nickel concentration as the indicator of age. Returning to figure 6, we may note that even with all of these caveats, the use of mean nickel intensity as the age indicator has given a very good separation of the new particles ("*") on the left, from the old particles on the right. Note the one "new" particle on the extreme right of the plot. Although it appears that this particle is misplaced on the plot, an analysis of its Si/Al ratio shows it to be different from the other new particles. A check of the refinery's records revealed that although they had

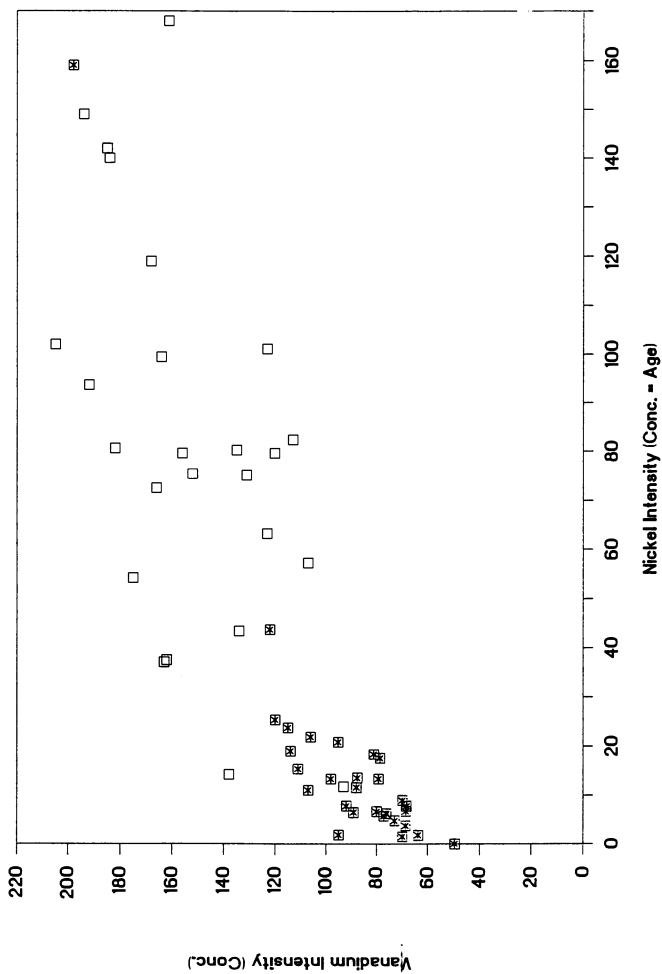


Figure 6. V vs Ni - four weeks into a catalyst type change. The "*" always indicates new catalyst type.

been using the "old" type of catalyst for about a year, prior to that time they had been using a catalyst from the same vendor as that of the "new" type. This "old old" catalyst was of a different binder type, explaining its different Si/Al ratio, but being from the same vendor, happens to have the same La/Ce ratio as our new catalyst particles.

From the vanadium concentrations shown in the figure, we immediately discern two facts. First, even at very short times in the unit the particles have become impregnated with a significant quantity of vanadium. Secondly, this rapid diffusion of vanadium does not lead to a total homogeneity of vanadium concentration regardless of age. It would seem likely that several mechanisms of vanadium binding or transport are occurring, leading to a mixture of short and long vanadium impregnation kinetics.

Figure 7 shows a similar analysis of another sample taken from the same unit four weeks later. Although not as tightly separated into old and new particles, the same general observations still hold. It is believed that some of the mixing of old and new type particles is real, occurring due to the mixing of old and new catalyst types in the "fresh catalyst feed silo" leading to a gradual change to the new catalyst type, and that some of the mixing is due to the difficulties encountered with correctly determining a particle's age. The large number of particles sampled in this case (71) as well as the more even mixture of several catalyst types, makes this data better suited for use as a data base for an empirical view of the factors affecting vanadium concentrations on individual particles.

In order to empirically remove the effects of age, as determined by the nickel concentration, from the vanadium distribution, a regression of the data was performed to determine a best fit functional form relating vanadium with nickel. With the forced use of a zero intercept, for this case (and several others, not shown) best results were obtained for functions of the type:

$$V = A*(Ni^{1/3}).$$

No fundamental explanation for this empirically derived relationship has yet been postulated. The general shape of this type of function is reasonable if one considers the mobility of vanadium and the lack of mobility of nickel. The constant "A" must be such that young particles have a greater V/Ni ratio than that of the feed and old particles have a lower V/Ni ratio than that of the feed. Given quantitative deposition of both metals from the feed to the catalyst(8), the average V/Ni ratio on the catalyst must be equal to that in the feed, but due to the transfer of vanadium, older particles are losing vanadium to younger ones. Eventually, it appears that the oldest particles approach the equilibrium situation of losing vanadium as fast as they acquire it, and their vanadium concentration asymptotically approaches a constant while their nickel concentration rises. Figure 8 presents the calculated curve and the residual values for vanadium as a function of the cube root of nickel. The fit is quite reasonable, with an R^2 of 0.70 and a fairly even scatter of the residuals.

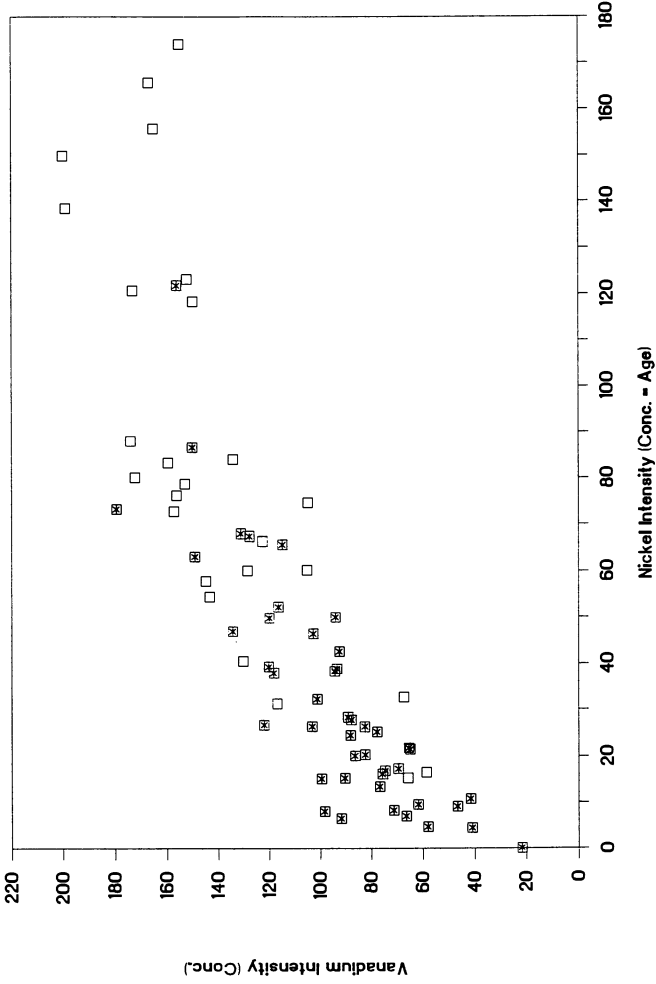


Figure 7. V vs. Ni - eight weeks into a catalyst type change.

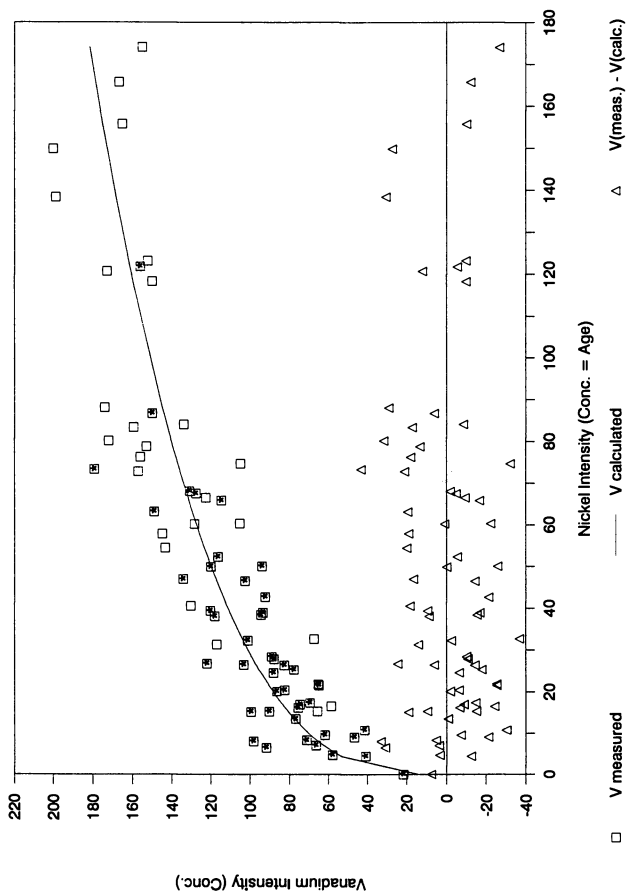


Figure 8. V vs Ni - showing an empirical curve fit based on $Ni^{1/3}$.

Searching for the next most critical determinant of the vanadium distribution revealed a relationship between vanadium and the quantity of zeolite in each particle, as measured using the La+Ce intensity value.

Figure 9 presents this relationship for the measured vanadium values (boxes), as well as for the residual vanadium values (+) after subtraction of the calculated contributions of the particles' age. Both sets of values show a weak trend for particles with more zeolite to contain more vanadium, an observation made qualitatively earlier in this study by viewing the individual phases. Including a term in our "fit" to account for this relationship in the form of

$$V = A*(Ni^{1/3}) + B*(La+Ce)$$

leads to improvement of the R^2 term to 0.79.

Further inspection of the data showed a third, but even more tenuous, relationship of vanadium with the Si/Al ratio of the particles. Figure 10 plots this relationship for the measured data and for the residual values after subtraction of the calculated effects of both age and zeolite content. Here, correction for these terms, prior to looking for a relationship, becomes even more important due to the lack of independence of the Si/Al ratios from the age and the zeolite levels. From the "measured" vanadium values shown in fig. 10 it can be seen that the new catalyst type particles have, in general, higher Si/Al ratios than do the old. It is very reasonable for them to have less vanadium merely because they have been in the unit for less time. Additionally, since zeolite has a higher Si/Al ratio than do the other phases in the catalyst particles, some softening of the apparent relationship is likely due to the changes in zeolite content (which we have found leads to more vanadium in higher Si/Al cases). Given these limitations, the residual values do show a tendency for there to be somewhat more vanadium in particles with lower Si/Al ratios. This is probably an indication of the "trapping" effect of alumina in the catalyst particles, as demonstrated earlier. Including this term in our fit to account for this relationship as

$$V = A*(Ni^{1/3}) + B*(La+Ce) + C*(Si/Al)$$

leads to improvement of the R^2 term to 0.84. The relative standard errors of the A, B and C constants are 5%, 18%, and 28%, respectively, which serves as an indication both of the quality of the fit as well as showing the relative importance of each of the parameters to the final vanadium distribution. We have not included the actual values for the A, B, and C terms since they are related only to the "grey level" measurements, and we wish to avoid any confusion with actual concentration related empirical relationships.

A presentation of the final calculated "curve" for the vanadium values, plotted against nickel (age) is shown in Figure 11. Although we have admittedly taken more liberties with our empirical fit than the probable data quality permits, we have intended an example of the types of analysis that become possible using the combination of modern image processing techniques and

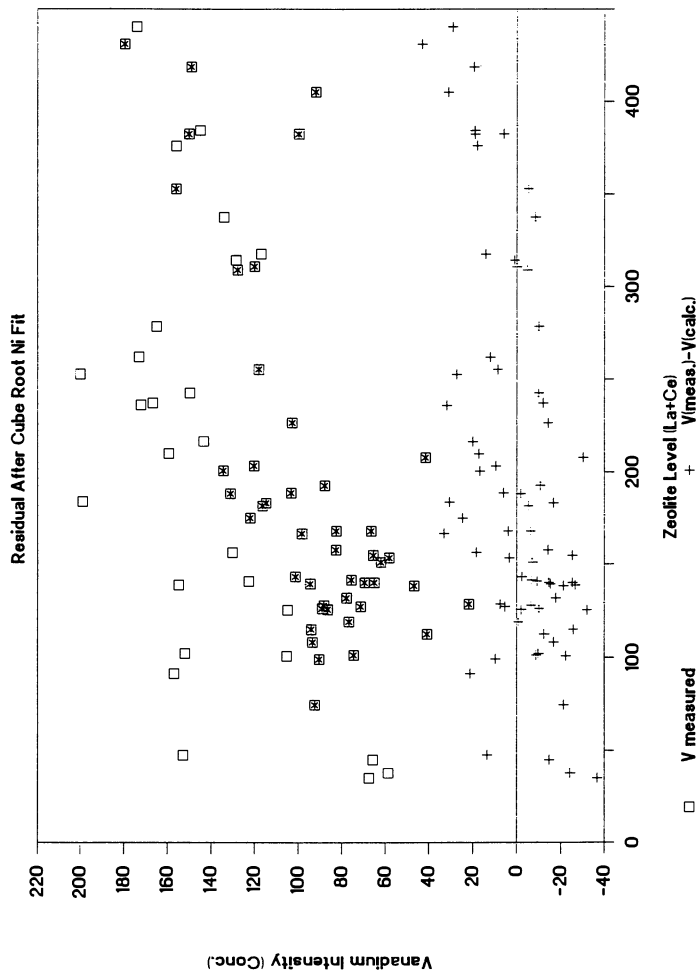


Figure 9. V vs. Zeolite Concentrations.

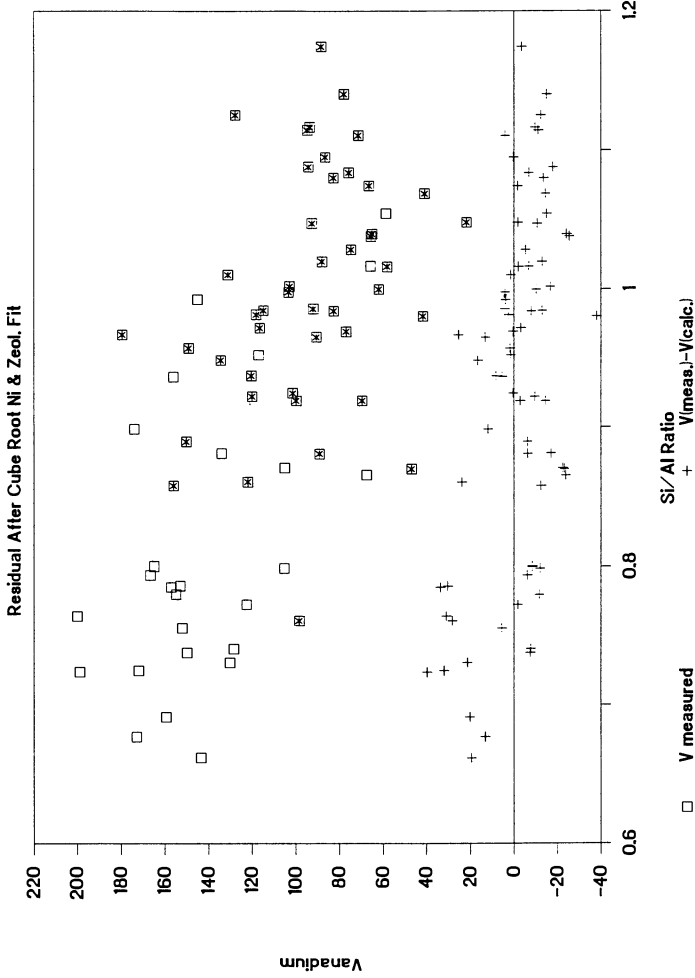


Figure 10. V vs. Si/Al ratios.

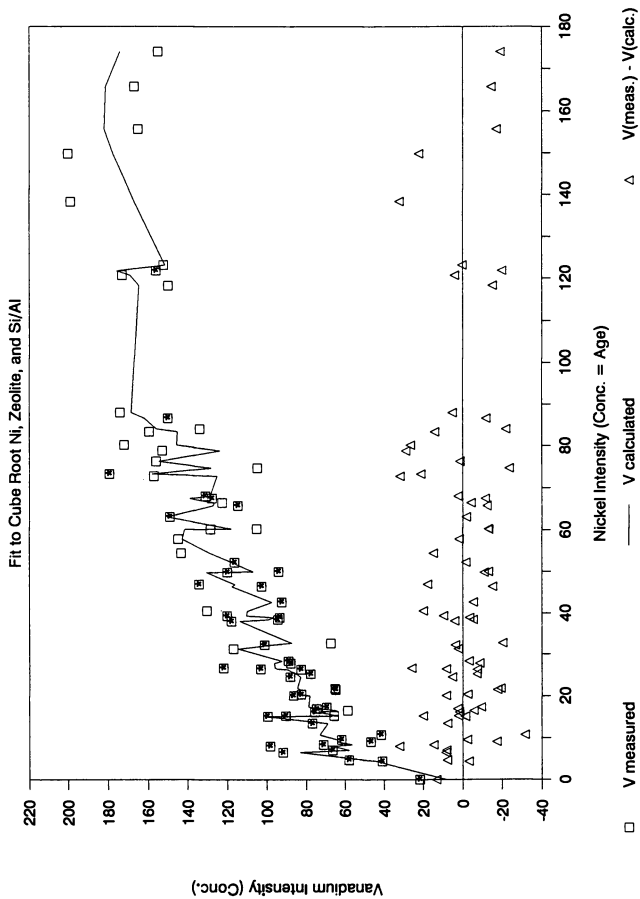


Figure 11. V vs Ni - showing an empirical curve fit based on Ni^{1/3}, zeolite concentration and Si/Al ratio.

imaging SIMS. In more controlled (but perhaps less realistic) sample preparations done in the laboratory, such an analysis might be expected to reveal more dependable relationships.

REFERENCES

1. Jaras, S., *Appl. Catal.*, **2**, 207 (1982).
2. Kugler, E. L., and Leta, D. P., *J. Catal.*, **109**, 387 (1988).
3. Leta, D. P., and Kugler, E. L., "Imaging SIMS in Catalysis", SIMS VI, Secondary Ion Mass Spectrometry, A. Benninghoven, A. M. Huber, H. W. Werner, eds., 373 (1987).
4. Leta, D. P., and Kugler, E. L., American Chemical Society Symposium Series 411, "Characterization and Catalyst Development," S. A. Bradley, M. J. Gattuso, R. J. Bertolacini, Eds., ACS, Washington, D.C., 1989, pp. 354-364.
5. Leta, D. P., "Springer Series in Chemical Physics 44", A. Benninghoven, R. J. Colton, D. S. Simons and H. W. Werner, eds., Springer-Verlag, Berlin, 1986, p. 232.
6. Mills, G. A., *Ing. Eng. Chem.* **42**, 182 (1950).
7. Ritter, R. E., Rheume, L., Welsh, W. A., and Magee, J. S., *Oil and Gas J.*, **103**, (July 6, 1981).
8. Palmer J. L., and E. B. Cornelius, *Journal of Applied Catalysis*, vol. **35** (1987), pages 217-235.

RECEIVED June 8, 1990

Chapter 18

Aluminum-Exchanged Sepiolite as a Component of Fluid Cracking Catalysts

A. Corma, V. Fornés, A. Mifsud, and J. Pérez-Pariente

Instituto de Tecnología Química, UPV-CSIC, Universidad Politécnica de Valencia, Camino Vera S/N, 46022 Valencia, Spain

Sepiolite has been made exchangeable by chemical treatments and Mg^{2+} at the border of the channels has been substituted by Al^{3+} . In this way sepiolite with mild acidity, controlled mesopore, and improved stability has been obtained. This material is active for gasoil cracking, giving a good bottom conversion, and light cycle oil products without excessive gas and coke formation. Meanwhile, it is active for vanadium passivation.

Sepiolite is a fibrous magnesium silicate, which is formed of talc-like ribbons arranged in such a way that the tetrahedral sheet is continuous but inverts apical directions in adjacent ribbons (1). In this way, channels of $10.8 \times 4.0 \text{ \AA}$ in a cross-section perpendicular to the length of the fibre (C axis) are generated. The average fibre length of the mineral varies between 0.5 and $1.0 \mu\text{m}$, and reagent molecules have only access to a small portion of the interior of the channels. Natural (2-4), acid leached (5), and exchanged sepiolite (6-8) have been found useful for vanadium passivation in FCC catalysts. However a closer look to the structure and textural properties of the sepiolite strongly suggests that this material, conveniently modified, could play a more extensive role in FCC catalysts. Indeed, the properties of the natural material such as surface area and pore volume could be adequate for use in catalysis. However, and more specifically for FCC catalysts, sepiolite presents a limitation derived from its very low acidity. Furthermore, it becomes difficult to introduce directly any acidity, due to the very low ion exchange capacity of this material. The structure of the sepiolite given in Figure 1, shows that the octahedral

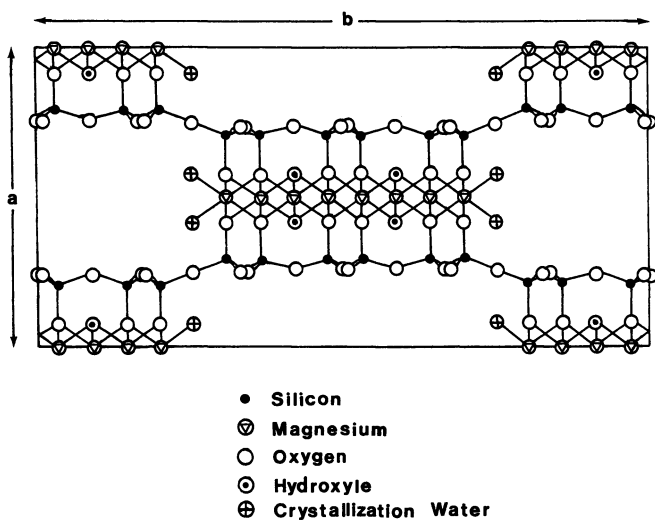


Figure 1. (001) projection of the unit cell of the sepiolite.

layer is composed mainly by Mg^{2+} ions, 25% of which are located at the edges which form the "walls" of the channels, running along the fibre. These Mg^{2+} , which are coordinated with four oxygens and two water molecules, are mobile and can, under the hydrothermal conditions in the regenerator, migrate to the zeolite component of the FCC, and to decrease the stability of the zeolite. This phenomena has been observed in commercial samples of FCC catalysts (5). Nevertheless, sepiolite has been proved to be an excellent vanadium scavenger (4).

In our case, we have modified the sepiolite in order to improve the textural characteristics, while removing the Mg^{2+} ions of the border and introducing other cations which can give acid properties to this material. In the present work, the acidity, stability and textural properties of modified sepiolites are presented, and its implications in gasoil cracking and vanadium trapping have been studied.

Experimental

Materials

Sepiolite from Vallecas (Spain) with a chemical composition given in Table I, was used as starting material. Following the procedure described previously (8), between 1.7 and 2 meq $^{-1}$.g $^{-1}$ of Na^+ , La^{3+} , Al^{3+} , Cr^{3+} and H^+ were introduced in the octahedral sheet of the silicate, replacing the magnesium ions located at the edges of the fibres in natural sepiolite (Figure 1).

Table I. Chemical composition of natural Vallecas-type sepiolite (wt%).

SiO_2	60.31
Al_2O_3	1.88
Fe_2O_3	0.48
CaO	0.27
MgO	25.48
Na_2O	0.12
K_2O	0.26
TiO_2	0.22
Weight loss on calcination at 1000°C	10.88

The catalysts studied were prepared by dispersing 20 wt% of a USY zeolite with a 2.433 nm of unit cell size in either silica (BASF (D-11-11)) or aluminic sepiolite (SA1). The final catalyst was steamed at 750°C in a 100% steam for 6 hours.

Acidity Measurements

Acidity measurements were carried out following adsorption/desorption of pyridine at different temperatures by I.R. spectroscopy. Wafers of 10 mg.cm^{-2} of pure sample were pretreated two hours at 10^{-2} Pa and temperatures varying between 100 and 450°C , in a greaseless conventional pyrex IR cell. After that, 6.10^2 Pa of pyridine were introduced in the cell and desorbed for 1 h at 150, 300 and 450°C ; after each treatment, the I.R. spectrum was recorded at room temperature in a Perkin Elmer 580 B spectrophotometer equipped with Data Station.

From the intensity of the bands of adsorbed pyridine we can measure the Lewis (1450 cm^{-1}) and Brönsted acidity (1540 cm^{-1}) (8,9). When intensity of Brönsted I.R. band is too low, we can use the intensity of 1490 cm^{-1} band assigned to pyridine adsorbed on both Lewis and Brönsted acid sites. After Hughes and White (10), the apparent molar extinction coefficient ratio of the 1490 and 1450 cm^{-1} bands of pyridine adsorbed on Lewis sites can be estimated as $\epsilon_{1450}^L/\epsilon_{1490}^L = 6$. In consequence we can calculate the contribution of Brönsted sites to the intensity of the 1490 cm^{-1} band from equation

$$I_{1490}^B = I_{1490} - I_{1450}^L/6 \quad [1]$$

In this paper we will call "b" parameter the values of calculated I_{1490}^B .

Catalytic experiments

The experiments were carried out in a fixed-bed tubular reactor, heated by an electric furnace divided into three heating zones. Prior to each experiment the catalyst was stripped with N_2 at 482°C (reaction temperature) for 20 minutes. Then the reactant (which characteristics are given in Table II) was charged at the top of the reactor by a constant-rate positive-displacement pump. The catalyst to oil ratio with respect to the zeolite content was varied between 0.09 and 0.23 g.g^{-1} by changing gasoil feed ($4.45\text{--}1.78 \text{ g}$) while keeping the weight of zeolite constant (0.40 g).

In all experiments the time on stream was kept constant at 60 seconds. During the reaction, the liquid products were collected after passing through a condenser located below the reactor; the gaseous products were trapped downwards by displacement of water in a gas burette. At the end of each run, the reactor was purged with nitrogen and the purged gases were collected for analysis in the burette. Finally, the catalyst was regenerated "in situ" by burning off the coke with a stream (6 l h^{-1}) of air at 530°C for five hours.

The gaseous products were analyzed by gas chromatography with a double column of Poropak-Q and

Silica, while the liquid products were analyzed by simulated distillation. The amount of coke was measured from the weight of water and carbon dioxide generated during regeneration.

Table II. Properties of the vacuum distilled gas oil.

API gravity at 15°C	26.3	K-UOP	11.5
Conradson carbon/wt	0.14	Freezing point/°C	24
Hydrogen/wt%	11.9	Pensky Martens/°C	130
Sulfur/wt%	2.14	Viscosity/C.S 40°C	11.54
N ₂ /ppm	562		

Distillation curve D-1160 (°C)

IBP	5	20	30	40	50	60	70	80	95	FBP	
	240	307	323	345	362	378	390	405	420	465	512

Results and Discussion

The acidity of the different sepiolite samples has been compared at 200°C of pretreatment temperature. In Tables III and IV, are given the values of the intensity of the I.R. bands, corresponding to pyridine adsorbed on Lewis sites (cations included) at 1450 cm⁻¹, and on Brönsted sites calculated as "b" parameter, from the intensity of 1490 and 1450 cm⁻¹ I.R. bands.

From the results presented, it can be seen that only the sepiolite derivatives whose exchange cations have high charge/radium ratio, present Brönsted acidity. In fact, the origin of Brönsted acidity in metal exchanged clays (11) and in sepiolite derivatives is the highly polarized water molecules bonded to the cations situated at the interlamellar space and at the edges of the octahedral sheet. Consequently, the higher the polarizing power of the cation, the higher the acidity of the resulting sepiolite derivative is. Indeed, only SAL, SCr and SH show Brönsted acidity (b parameter), while SMg, SNa and SLa do not. This is confirmed by the results presented in Figure 2, where we show the I.R. spectra in the 1800-1300 cm⁻¹ range, of the adsorbed pyridine after subtraction of spectra of the sample pretreated at 200°C and vacuum before adsorbing pyridine. It is evident that only the Al³⁺, Cr³⁺ and H⁺ sepiolite derivatives show bands at 1540 cm⁻¹ and 1640 cm⁻¹ characteristic of the protonated pyridine.

By plotting the Brönsted acidity (b parameter) versus desorption temperature for these three samples, one can obtain a picture of the strength distribution for the

Table III. Intensity of the I.R. bands of pyridine adsorbed on sepiolite derivatives. b parameter calculated from equation 1, with an estimated error of ± 0.02 .

SAMPLE	PRETREAT. oC	$I_{1450 \text{ cm}^{-1}}$			$I_{1490 \text{ cm}^{-1}}$			b parameter		
		150	300	450	150	300	450	150	300	450
SMg	100	-	-	-	-	-	-	-	-	-
	200	.43	.08	.03	.04	.01	-	-	-	-
	300	.27	.05	.03	.02	-	-	-	-	-
	450	.34	.03	-	.02	-	-	-	-	-
SNa	100	.07	.01	-	.01	-	-	-	-	-
	200	.11	-	-	.01	-	-	-	-	-
	300	.03	-	-	-	-	-	-	-	-
	450	.04	-	-	-	-	-	-	-	-
SLa	100	.62	.27	.17	.05	.02	.01	-	-	-
	200	.25	.13	.06	.04	.01	-	-	-	-
	300	.20	.05	.01	.03	-	-	-	-	-
	450	.13	.04	-	.02	-	-	-	-	-

Table IV. Intensity of the I.R. bands of pyridine adsorbed on sepiolite derivatives. b parameter calculated from equation 1, with an estimated error of ± 0.02 .

SAMPLE	PRETREAT. oC	$I_{1450 \text{ cm}^{-1}}$			$I_{1490 \text{ cm}^{-1}}$			b parameter		
		150	300	450	150	300	450	150	300	450
SA1	100	.61	.55	.20	.27	.16	.04	.17	.07	-
	200	.90	.65	.22	.34	.17	.04	.19	.06	-
	300	.67	.48	.50	.18	.10	.01	.07	.02	-
	450	.30	.21	.20	.07	.03	-	.02	-	-
SCr	100	1.40	.74	.08	.32	.12	-	.08	-	-
	200	1.04	.66	.07	.24	.11	-	.07	-	-
	300	.62	.39	.03	.12	.06	-	.02	-	-
	450	.45	.23	.01	.06	.03	-	-	-	-
SH	100	1.20	.58	.06	.22	.11	-	.02	.01	-
	200	.76	.47	.05	.16	.08	-	.04	-	-
	300	.42	.20	.02	.09	.03	-	.02	-	-
	450	.32	.12	.01	.05	.02	-	-	-	-

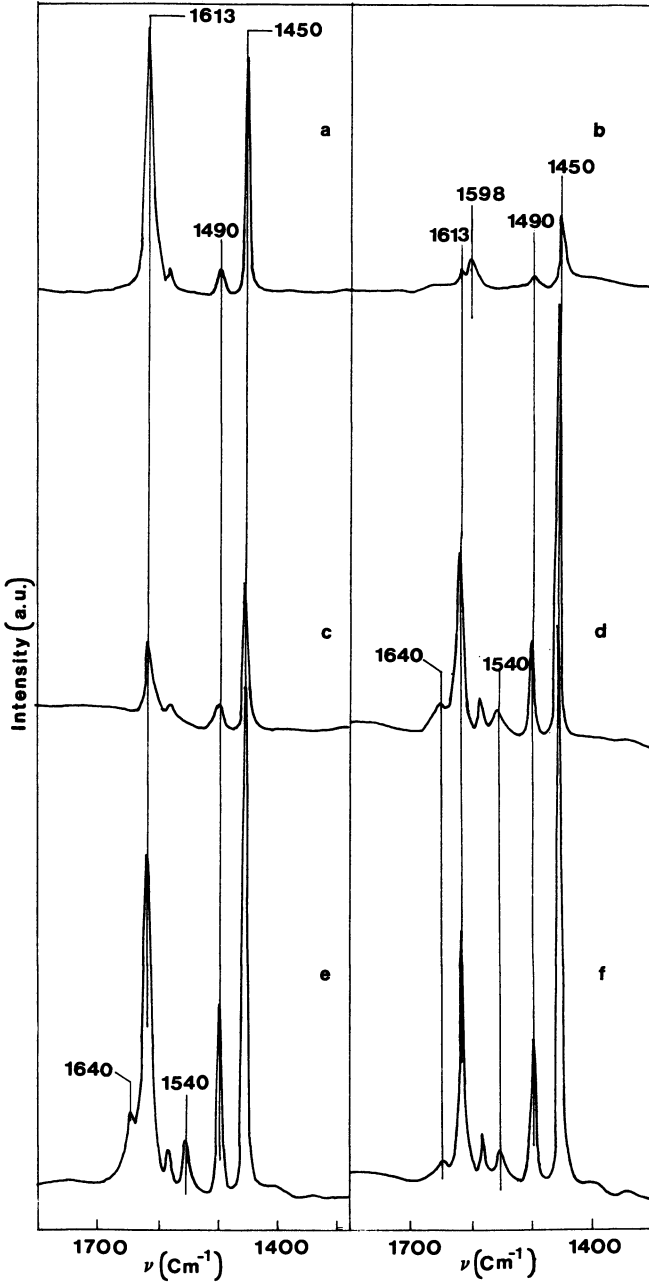


Figure 2. I.R. spectra of pyridine adsorbed on different sepiolite derivatives after degassing at 150°C and 10^{-3} Pa. a) Mg; b) Na; c) La; d) protonic; e) Al; f) Cr sepiolites.

protonic acidity of the different samples. Figure 3 shows that maximum in Brönsted acidity corresponds to acid centers of medium strength (150°C of desorption temperature (T_d)), and that only the aluminium derivative has some acid centers of strong acidity ($T_d=300^{\circ}\text{C}$). Sites with very strong acidity ($T_d > 400^{\circ}\text{C}$) have not been found in the sepiolite derivatives. On a comparative basis we have obtained a "b" parameter of 0.10 for a commercial amorphous silica-alumina (25% Al_2O_3), degassed at 150°C and 10^{-3} Pa.

It is known (12) that, depending on the cation, the position of the 8a ($1600-1625\text{ cm}^{-1}$) I.R. band assigned to pyridine coordinated to cations varies (i.e. 1623 cm^{-1} - Al^{3+} ; 1606 - La^{3+} ; 1612 - Ni^{2+} ; 1598 - Na^+ , etc...). Then, if Lewis acidity is due to the presence of cations at the edges of the channels, the spectra of the pyridine coordinated to Lewis acid sites will change with the exchanged cation. However, the spectra of all the sepiolite derivatives show a band at 1613 cm^{-1} . The sodium derivative of the sepiolite shows two 8a pyridine bands, one at 1613 , and another appearing at 1598 cm^{-1} assigned to $[\text{Py}: \text{Na}^+]$ interaction, showing that in sepiolite, besides the Lewis acidity associated to the cations at the border ($1598-1606\text{ cm}^{-1}$) there is Lewis acidity due to the presence of "intrinsic" defects in the structure of the clay silicate framework. If this is so, the difference of intensity of the pyridine coordinated I.R. bands must be ascribed to differences in accessibility to potential Lewis site centers. In fact, treatments with low pH solutions (Al^{3+} , Cr^{3+} , H^+) increases the amount of accessible Lewis sites with respect to that of natural sepiolite (SMg), while treatments with basic solutions blocks the porosity and consequently the amount of the observed Lewis sites decreases. This behaviour, which can already be seen in Figure 2, is more clearly observed in Figure 4 where intensity of Lewis band (1450 cm^{-1}) for different samples and at different desorption temperature has been presented. Another possible explanation for changes in Lewis acidity can be related with the thermal stability of the exchanged samples with respect to natural sepiolite which prevents the folding (13) of the structure and consequently the decrease in surface area (14).

Gasoil cracking

At this point we have an aluminum type sepiolite which shows mild acidity and could be used as a component for FCC catalysts. Then, we have checked if the aluminium containing sepiolite can also passivate vanadium. To do that, two FCC catalysts containing 20% of a REHY zeolite in either 80% of a 23 wt% Al_2O_3 containing silica-alumina, or 80% of aluminic sepiolite were prepared. Both samples were impregnated to incipient wetness with a V naphthenate/xylene mixture (15), in order to introduce 6000 ppm of vanadium. Both samples were steam deactivated

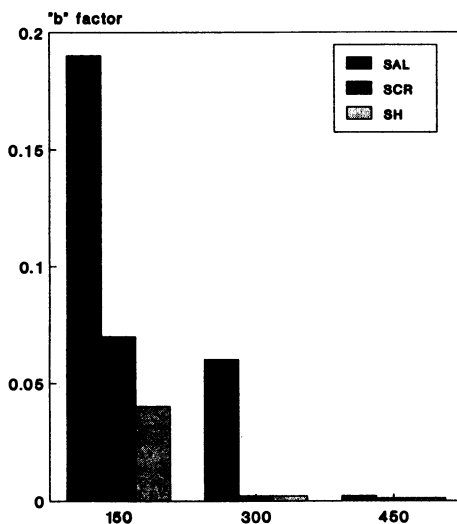


Figure 3. Brønsted acidity ("b" factor), as a function of the desorption temperature for the different sepiolite derivatives. SAL, aluminium; SCR, chromium; SH protonic, sepiolites.

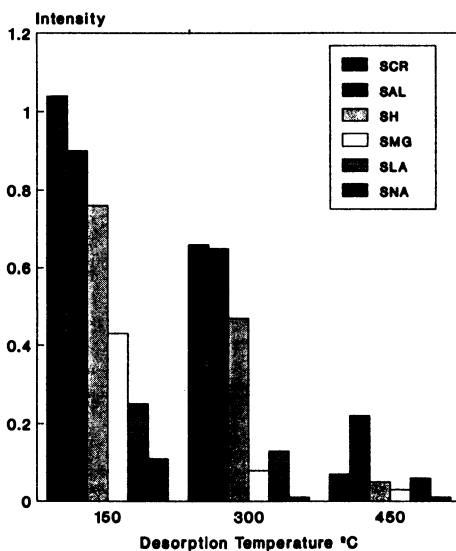


Figure 4. Lewis acidity. Intensity of the 1450 cm^{-1} pyridine I.R. band as a function of the desorption temperature.

at 750°C for 12 hours, and the X-Ray diffractograms are given in Figure 5. It can be seen there that while most of the zeolite crystallinity in silica-alumina containing catalyst (a) has been lost, the crystallinity of the zeolite in the catalyst containing aluminium sepiolite (b) is retained in much higher degree. Therefore, this sepiolitic material is active for vanadium passivation.

The hydrothermal stability of the SAL sample has been compared with that of the original SMg in Figure 6. The X-Ray diffraction pattern of an Al sepiolite before (a) and after (b) steaming at 700°C, 100% steam; and a natural sepiolite (SMg) also steamed at 700°C (c). The results indicate that after this thermal treatment an important fraction of the aluminic sepiolite remains unaltered, while the natural sample is completely folded. The folding of the sepiolite is shown by the disappearance of the (1,10) reflexion at 7.2, 2 θ , and the appearance of a new reflexion at 8.9, 2 θ (16). Moreover, the adsorption of pyridine shows the presence of a residual Brönsted acidity in the SAL after the hydrothermal treatment which is approximately 30% of the untreated sample.

To study the gasoil cracking behaviour of this material, two samples have been prepared with 20% of a USY zeolite embedded in either silica, or SAL. These samples were steamed at 750°C, and the resultant U.C. of the zeolite was 24.31 Å. The gasoil cracking results obtained with the two samples are given in Figures 7 and 8. The introduction of the aluminic sepiolite in the matrix is useful, not only for vanadium passivation as was shown above, but also introduces additional cracking activity to the catalyst (Fig. 7). The SAL does not produce a sensible increase in gases and coke, but its main cracking benefit is in the bottoms conversion, giving a sensible increase in the production of diesel (Fig. 8). As can be seen in Figure 9, the increase in diesel generation due to the introduction of S-Al occur at the expense of the slurry oil fraction.

Conclusions

- It is possible to prepare, by a conventional treatment, sepiolites in which the magnesium at the borders of the channels has been substituted by Al³⁺.
- These samples show a much higher acidity and hydrothermal stability than natural sepiolites, most of the acidity being in the range of mild strengths.
- Aluminic sepiolites while being good for vanadium passivation, do not present the inconvenience due to Mg migrations to the zeolite (if in the same particle) shown by natural sepiolite.
- They present a good gasoil cracking activity and selectivity, specially useful for bottoms conversion.

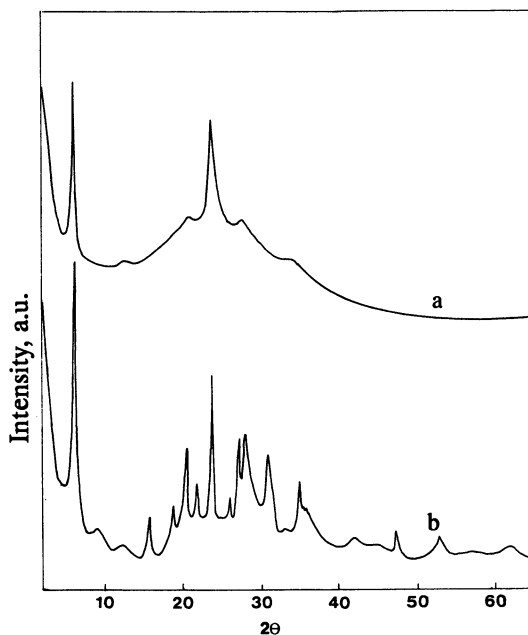


Figure 5. X-Ray diffraction pattern of the catalyst after steaming in the presence of vanadium. a) REHY + silica-alumina; b) REHY + sepiolite.

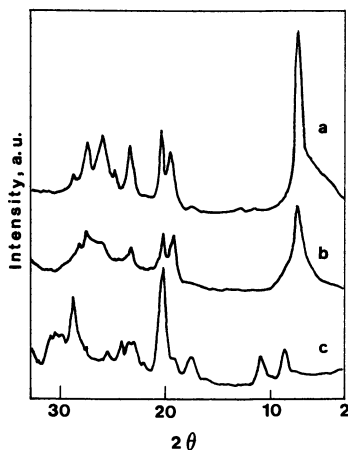


Figure 6. X-ray diffraction pattern of: natural sepiolite (a); aluminium exchanged sepiolite after steaming at 973 K (b); natural sepiolite after steaming at 973 K (c).

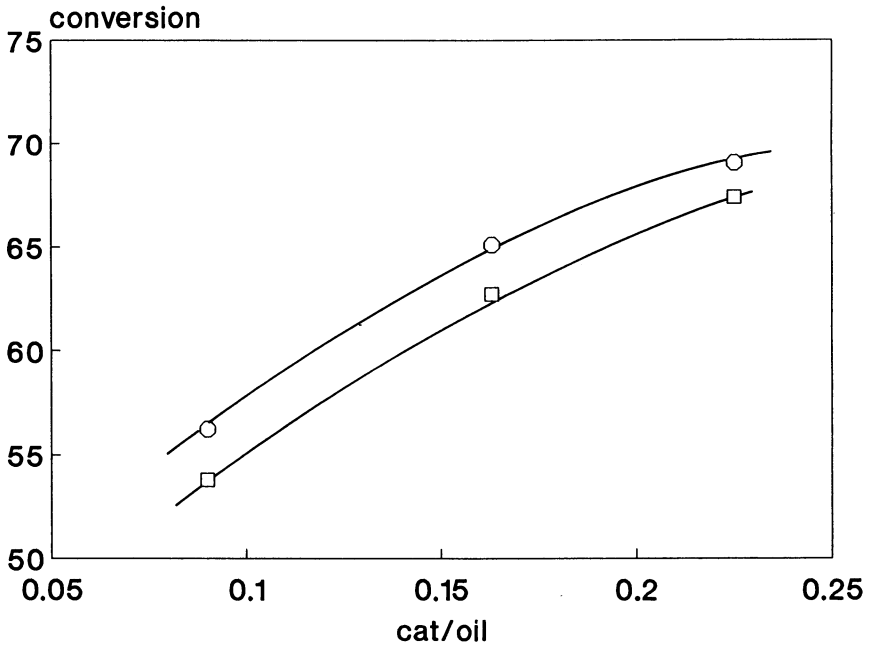


Figure 7. Gasoil cracking conversion on USY + silica (\square) and USY + SA1 (\circ) catalysts.

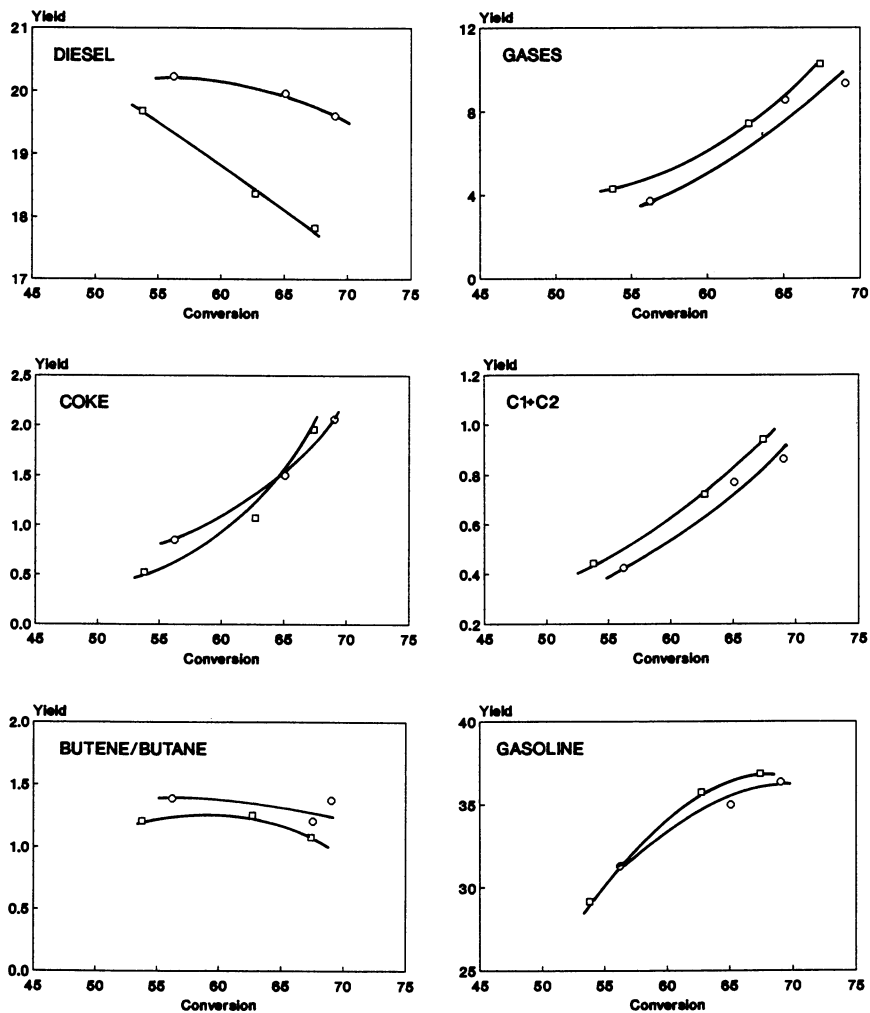


Figure 8. Yields of gasoline, diesel, gases and coke, at different levels of conversion, on USY + silica (\square), and USY + SA1 (\circ) catalyst.

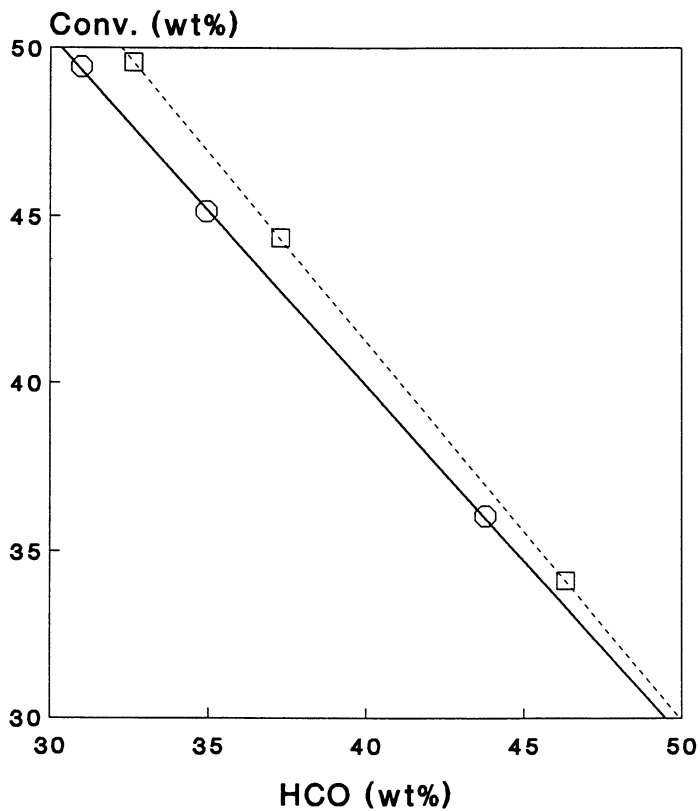


Figure 9. Gasoil conversion (gases + coke + gasoline) versus slurry oil, (\square) USY + SA1, and (\circ) USY + Silica.

All these characteristics make aluminium sepiolites materials worth to be tested in a larger scale for catalytic cracking of residues.

Acknowledgments

Financial support by the CICYT (Project MAT 88-0147) is gratefully acknowledged.

Literature Cited

1. Brauner K.; Preinsinger, A. Struktur und Entstehung des Sepioliths. *Tschermaks Miner. U. Petrog. Mitt.* 1956, 6, 120.
2. Ocelli, M.L.; Kennedy, J.V., U.S. Pat. 4 465 588, 1984.
3. Ocelli, M.L.; Kennedy, J.V., U.S. Pat. 4 465 779, 1984.
4. Ocelli, M.L. Fluid Catalytic Cracking Role in Modern Refining, Ocelli, M.L. ed., ACS Symp. Ser., 1988, 375, 162.
5. de Jong, Jan Ide, Europ. Pat., 832018352, 1984.
6. Corma, A.; Mifsud, A.; Pérez-Pariente, J., SP Pat. 510013, 1982.
7. Corma, A.; Fornés, V.; Mifsud, A.; Pérez-Pariente, J., SP Pat. 527756, 1983.
8. Corma, A.; Mifsud A.; Pérez-Pariente, J., US Pat. 4 542 002, 1985.
9. Basila, M.R.; Kantner T.R.; Rhee, K.H. J. Phys. Chem. 1964, 68, 3197.
10. Hughes, T.R.; White, H.M. J. Phys. Chem. 1967, 71, 2192.
11. Farmer, V.C.; Mortland, M.M. J. Chem. Soc. (A) Inorg. Phys. Theor. 1966, 344.
12. Vázquez, M.I.; Corma, A.; Fornés, V. Zeolites 1986, 6, 271.
13. Pérez-Pariente, J.; Fornés, V.; Corma, A.; Mifsud, A. Appl. Clay. Sci. 1988, 3, 299.
14. Fernandez Alvarez, T.; R. Hisp. Belg. Min. Arcilla, Madrid, 1970, p. 202.
15. Mitchell, B.R. IEC PRD 1980, 19, 209.
16. Preinsinger, A. Clays and Clay Minerals, Proc. 6th Conf., Pergamon Press, Oxford, 1959, p. 61.

RECEIVED June 8, 1990

Chapter 19

Long-Residue Processing in a Riser Pilot Plant

Vida J. Stripinis

Oakville Research Centre, Shell Canada Limited, Oakville,
Ontario, Canada

Pilot plants are often used for studying the FCC process. In order for results to be meaningful, it is necessary that pilot plant operation be consistent with that of commercial units. When processing feedstocks containing residue, this becomes even more important. Failure to pay attention to details, such as feed/catalyst contacting, can lead to problems with data integrity and with coke buildup in the equipment. A riser pilot plant has been successfully used to process heavy feedstocks with Conradson carbon contents as high as 10%w.

A number of different types of laboratory scale units have been developed to simulate commercial catalytic crackers. These include fixed bed (MAT), fluidized bed, and riser units. (1,2,3) In particular, for simulating commercial riser FCC units which process residue, a riser pilot plant is the preferred choice. The catalyst and oil are in plug flow and the contact time is short so that secondary reactions are avoided and catalyst deactivation by coke formation is properly simulated. The resulting product selectivity, then, is similar to commercial units. Experimental results from a laboratory scale unit can thus be translated to commercial units.

This paper describes experience with residue processing in catalytic cracking units in the industry, both on a commercial and pilot plant scale. Specific changes which have been made to the design and operating procedures of the Shell Canada Oakville Research Centre (ORC) riser pilot plant are also discussed. These have allowed processing of residues containing up to 9.9% Conradson Carbon Residue (CCR).

Commercial Experience

A number of refiners have processed residue containing feedstocks in commercial FCC units. Feeds with as much as 5.1%w RCR (~6.5%w CCR) and 85 ppm Ni + V have been processed in Phillips' Borger Refinery.(4) Ashland has processed feedstocks of up to 7.1%w RCR (~8.5%w CCR) and 85 ppm Ni + V in their RCC (Reduced Crude Conversion) process.(5,6) A commercial scale ART (Asphalt Residual Treating) unit has processed residues containing levels of contaminants as high as 13.5%w RCR and 300 ppm Ni + V (7,8). However, in typical day-to-day operation of residue cat crackers, feedstock quality is not as extreme as those illustrated above.

The above data indicates that some commercial units can already process long residue from a number of available world crudes. This is illustrated in Figure 1 (9), a plot of metals versus Conradson carbon content for long residues from various crudes. A box is drawn indicating the limitations of current FCC technology for handling metals and Conradson carbon. A number of long residues fall within this box, although an even larger number fall outside it. The challenge is to develop FCC technology to enable economical processing of poorer quality feedstocks.

Pilot Plant Experience

Development of technology is generally done using laboratory scale units. Experimental data can be obtained with less expense and with more accuracy and flexibility than by attempting to do the same test on a commercial scale. In the laboratory, smaller quantities of feedstock and catalyst are needed and lower manpower and capital costs are incurred. By necessity, bench scale units must process feedstocks which are at least as difficult as those processed commercially.

Processing residue on a laboratory scale poses a number of challenges. Residue-containing feedstocks are more difficult to vapourize and have a higher coke forming tendency than gas oils. Particular attention must be paid to pilot plant design and operating procedures in order to avoid coke formation and plugging of the small tubing in pilot plants and to ensure meaningful data.

Gulf has reported problems conducting resid cracking studies in pilot scale units.(10) The difficulties included feed injector plugging and catalyst flow problems in small lines in their 0.2 B/D gasoil cracking unit. They have built a somewhat larger, 1.0 B/D pilot plant, specifically for high carbon residue feedstocks, and they have processed feedstocks containing up to 7.66%w CCR. Engelhard has operated a modified ARCO Lab unit with a feedstock of 2.5% RCR (~3.5% CCR).(11) Kellogg has a 1/3 B/D unit used for studies in conventional gas oil FCC, HOC (Heavy Oil Cracking) and ART.(12) North Sea residue, containing 3.9%w CCR, has been processed in their unit.(13) The ART process has, for the most part, been developed in much larger units, namely, a 200

B/D demonstration plant and a 10,000 B/D commercial unit which have both processed poorer quality feedstocks.

Total (15) reports that operation of their pilot plant is not satisfactory for feedstocks with a viscosity greater than 80 cSt at 100°C. They state that thermal shock simulation and feedstock atomizing and evaporation are unsatisfactory in their laboratory scale unit.

Shell Canada's Oakville Research Centre has had a riser pilot plant in operation for about ten years. A series of modifications have been made to the unit over the years in order to improve its ability to process heavier feedstocks. In spite of a rather low feedrate of 0.52 g/s (approximately 0.3 B/D), poorer quality feedstocks have been processed than those described above. To date, feedstocks with Conradson carbon contents up to 9.9%w and viscosities up to 120 cSt at 100°C have been successfully run in the ORC pilot plant. Operating experience with the pilot plant is summarized in Table I, and a schematic is shown in Figure 2.

Experience has shown that there are four key aspects of design and operation of the pilot plant that must be considered in order for it to operate successfully with residue-containing feedstocks:

- 1) Feedstock atomization and vaporization
- 2) Feed/catalyst mixing
- 3) Spent catalyst stripping
- 4) Product handling

These items will each be discussed separately below. The resolution of problems encountered in the ORC laboratory unit while processing heavy feedstocks will be described.

Feedstock Atomization and Vaporization

Feedstocks containing residue are more difficult to vapourize and tend to coke more easily. Atomizing the oil feed to small droplets results in more surface area for heat transfer and quicker vapourization of the higher boiling materials in it. The atomizing nozzle in use on the ORC pilot plant achieves average droplet sizes of less than 60 microns. This is illustrated in Figure 3, which is a plot of Sauter mean diameter of the droplets produced versus atomizing gas flow. The data was collected at conditions chosen to simulate pilot plant operation on a residue-containing feedstock.

In catalytic cracking, a large amount of heat needs to be supplied at the reactor inlet to vapourize the feed and provide the heat of reaction. In commercial units, this heat is provided by the hot catalyst recirculated from the regenerator. High heat transfer rates are achieved when the fluidized catalyst is mixed with the feed. In some experimental units, feed and catalyst are injected at reactor temperature. The heat of reaction must then be supplied by an external heating element, at much slower rates of heat transfer. The product selectivity from such laboratory units cannot be expected to simulate that of commercial units

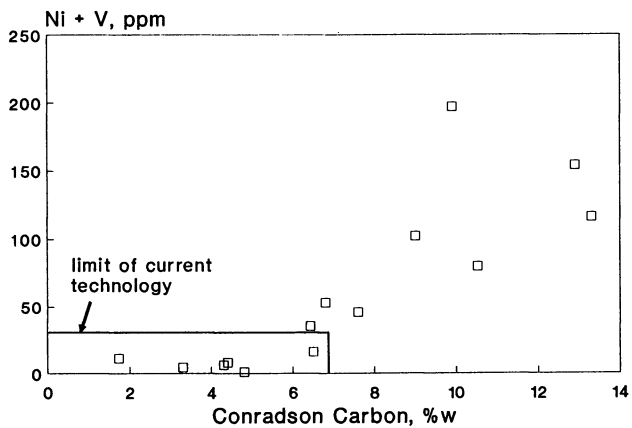


Figure 1 - Long Residue from Various Crudes

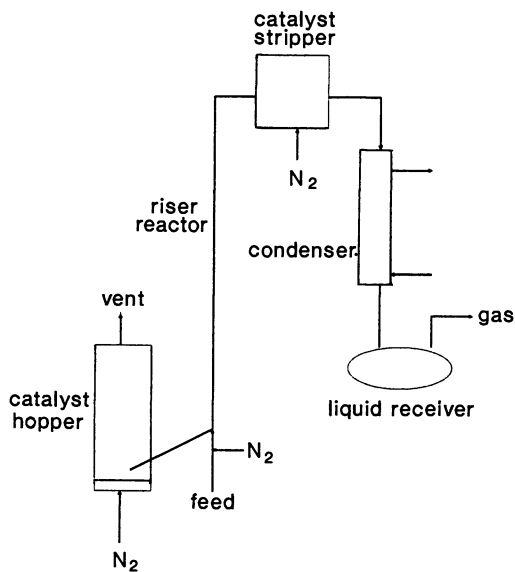


Figure 2 - Schematic of Riser Pilot Plant

Table I. Riser Pilot Plant Operation

Feed Rate	0.52 g/s (approx 0.3 B/D)
Cat/Oil Ratio	2.5 to 16 w/w
Reactor Outlet Temp.	up to 540°C
Feed Temperature	up to 300°C
Catalyst Temperature	up to 800°C
Feed CCR up to 9.9%w	
Feed Viscosity	up to 120 cSt @ 100°C
Reactor Pressure	1 bar

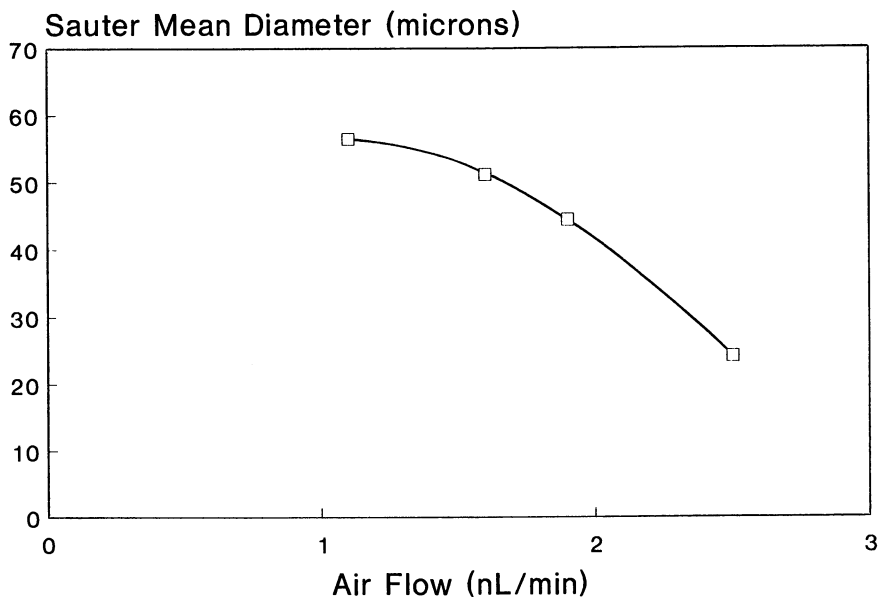


Figure 3 - Atomizing Nozzle Performance

very well. The preferred way to supply the heat required by the process is using hot catalyst, the same as in a commercial unit.

Heating the feed to reactor temperature, usually greater than 500°C, causes an additional problem. Coke is formed by thermal reactions of the feed in the preheater and feed injection system. The coking tendency is more severe for heavy feedstocks which have higher concentrations of coke precursors. This can be avoided by limiting the feed temperature to 300°C or less.

The practice at ORC has been to preheat the feedstock to a temperature sufficiently high to reduce its viscosity enough to ensure good atomization without causing coke formation in the feed system. The heat of vaporization and reaction is supplied by the much hotter catalyst. Good simulation of commercial FCC units has been achieved using this operating strategy.

Feed/Catalyst Mixing

Once the feedstock has been atomized, it must be mixed with the catalyst in a uniform way to ensure efficient heat transfer and fast vapourization of the oil. Oil droplets must not be allowed to hit the wall of the reactor where they would deposit on the wall and form coke. They must come in contact with a catalyst particle first. Coke formation on the wall can lead to flow restrictions in the unit and an inability to operate it successfully.

In the past, ORC experienced plugging from exactly this type of phenomenon. When processing residue-containing feedstocks, coke would build up just above the feed injection nozzle causing the flow to the riser reactor to become restricted. As a result, runs would have to be ended prematurely. The coke build-up tended to be the worst at low catalyst-to-oil ratios when catalyst flow rates were also low. It was thought that the density of the catalyst being supplied to the mixing zone was not constant. During moments of low density, feed droplets would come in contact with the wall and form coke deposits. The catalyst is supplied from a hopper which is fluidized with nitrogen. Bubbles of gas from the fluidized bed were getting entrained with the catalyst to the mixing zone and causing variations in catalyst density.

The operation of the catalyst hopper was examined keeping in mind known facts about catalyst fluidization behavior. Figure 4 illustrates the fluidization behavior of a typical FCC catalyst. Catalyst bed height is plotted against superficial velocity of the fluidizing gas. At gas velocities between zero and minimum fluidization velocity (U_{mf}), the bed height remains unchanged. Once the minimum fluidization velocity is reached, the bed starts to expand. When gas flow is increased further, the minimum bubbling velocity (U_{mb}) is reached. At this point, the gas starts to rise through the catalyst bed in the form of bubbles. The bed height then starts to drop and slowly increases again with increasing superficial velocity.

The catalyst hopper had, at times, been operated at gas velocities above the minimum bubbling velocity. This caused bubbles as well as catalyst to be carried to the feed/catalyst

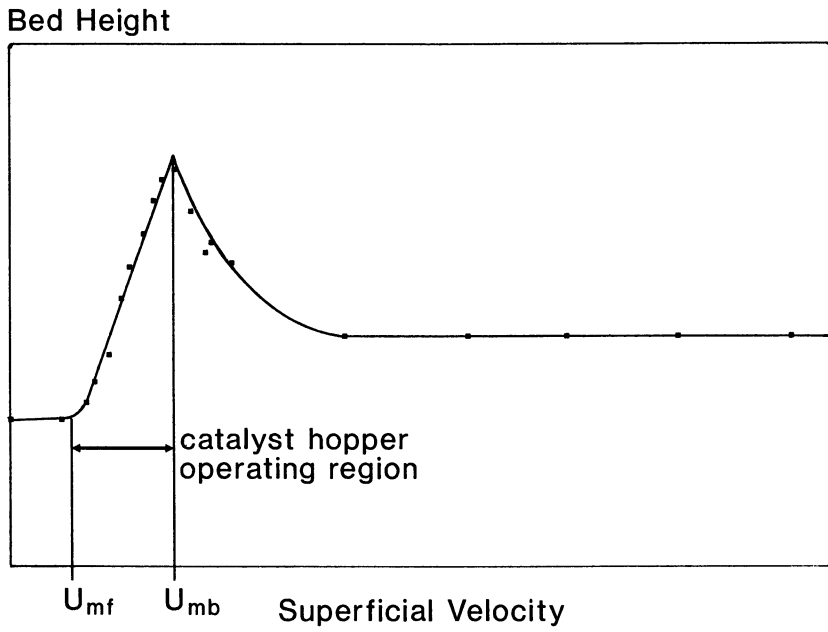


Figure 4 - FCC Catalyst Fluidization Behaviour

mixing zone and resulted in variations in catalyst density and the formation of the coke deposits. To correct this, the gas flow was reduced to eliminate bubbles from the catalyst being supplied to the reactor and the catalyst was instead supplied in dense phase flow.

This change in catalyst hopper operation virtually eliminated the formation of coke deposits in the feed mixing zone. Catalyst-to-oil ratios as low as 2.5 have been achieved even with very heavy feedstocks.

Catalyst Stripping

Good stripping is important in order to minimize coke formation. When catalyst is stripped effectively, higher boiling materials are recovered as product rather than being quantified as coke. In order to achieve this, equipment to strip the spent catalyst must be carefully designed. Stripping nitrogen and catalyst residence time must then be optimized in order to achieve good stripping. If more nitrogen is used than necessary, the product gas is diluted, making accurate gas analysis for yield determination more difficult.

Such a study to optimize spent catalyst stripping has been done for the ORC riser pilot plant. After making changes to the design of the stripper, a series of tests were done with varying stripping nitrogen flow while keeping other operating conditions constant to determine the optimum flow. The flow rate chosen for future operation was one for which the observed coke yield had reached a minimum. The unit operates in a batch mode with the catalyst being collected and stripped in the same vessel. As a result, another variable which affects catalyst stripping is the length of time that the catalyst is stripped after the run is finished. A study was done to optimize this stripping time. Overall, the changes in stripper design and operation resulted in a coke yield reduction of 1.5%w at constant conditions.

Product Handling

Residue-containing feedstocks produce products that are heavier and more viscous than normal. Therefore, operating temperature in the product condenser must be chosen with care. If the temperature is too low, the high boiling, viscous portion of the product deposits on the condenser tube walls and gets retained in the condenser rather than being recovered as product. On the other hand, if the temperature is too high, light liquids are not condensed and get carried over into the gas stream. If the gas sample is allowed to cool, these light liquids can then condense and not get analyzed.

Experience at ORC has shown that a condenser operating temperature of 0°C is too low when processing residue-containing feedstocks. The product recovery is reduced by 5% or more due to retention of heavy ends in the condenser. A temperature of 38°C is sufficiently high to avoid this problem. In order to ensure that, in spite of this, light liquids are condensed and not

carried over to the gas stream, the product receiver is cooled to -24°C and the gas stream knock-out pot also to -24°C .

Summary and Conclusions

By paying particular attention to FCC pilot plant design and operating procedures, feedstocks containing significant amounts of residue can be successfully processed in a small-scale unit. The critical aspects can be itemized as follows:

- o atomization of oil to small droplet sizes;
- o feed temperature adequate to avoid coke formation in the feed system;
- o use of hot catalyst to supply heat to the system, as is done in commercial units;
- o consistent catalyst flowrate to the feed/catalyst mixing zone by selecting fluidizing nitrogen flow rate to stay below the minimum bubbling velocity of the catalyst;
- o uniform mixing of the feed and catalyst in the bottom of the reactor to ensure quick vapourization and avoid coke formation in the mixing zone;
- o optimized design and operation of the spent catalyst stripper to ensure that coke yields are minimized without diluting the product gas more than necessary; and
- o proper selection of condenser operating temperature in order to avoid retaining the heavy, viscous fraction of the product on the condenser tube walls.

By focussing on the above points, cat cracking experiments can be performed in laboratory equipment with residue-containing feedstocks. With proper choice of operating conditions, the resulting product yields and selectivity simulate those in commercial units quite well.

Literature Cited

- 1) P. O'Connor and M.B. Hartkemp, "A Microscale Simulation Test for FCC Development", ACS Los Angeles Meeting, Sept. 25-30, 1988, pp. 656-662.
- 2) J.E. Creighton, G.W. Young, "Fluid Cracking Catalyst Evaluation: A Comparison of Testing Strategies", The Catalysis Society, 8th North American Meeting, May 1-4, 1983, Philadelphia, Pennsylvania.
- 3) W.H. Humes, "ARCO's Updated Cat-Cracking Pilot Unit", CEP, February 1983, 51-54.
- 4) J.B. Rush, P.V. Steed, "HDS + Cracking Ups Capacity, Yields", OGI, May 28, 1984, 96-103.

- 5) L.E. Busch, W.P. Hettinger, Jr., Richard P. Krock, "Reduced Crude Oil Conversion in Commercial RCC and ART Process Operations" (Paper No. AM-84-50), 1984 NPRA Annual Meeting, March 25-27, 1984, San Antonio, Texas.
- 6) L.E. Busch, W.P. Hettinger, Jr., R.P. Krock, "RCC Complex Now Cornerstone of Ashland Refinery", OGJ, December 10, 1984, 79-84.
- 7) D.B. Bartholic and R.P. Haseltine, "Development of Engelhard's Art Process", API, 46th Mid-Year Meeting, May 11-14, 1981, Chicago, Illinois, pp. 335-339.
- 8) R.P. Haseltine, A.K. Logwinuk, D.L. Caldwell, "The ART Process Offers Increased Refinery Flexibility" (Paper No. AM-83-43), 1983 NPRA Annual Meeting, March 20-22, 1983, San Francisco, California.
- 9) Oil & Gas Data Book, 1986 ed. Pennwell Publishing Co., Tulsa, Oklahoma.
- 10) R.J. Campagna, A.S. Krishna, S.J. Yanik, "Research and Development Directed at Resid Cracking", OGJ, October 31, 1983, 128-134.
- 11) D.B. Bartholic, R.P. Haseltine, "Utilizing Laboratory Equipment in New Residual Oil Development" (Paper No. AM-81-45), 1981 NPRA Annual Meeting, March 29-31, 1981, San Antonio, Texas.
- 12) M. Schlossman et al, "Riser Pilot Plant for Catalytic Cracking Studies", Katalistiks 7th Annual FCC Symposium, Venice, Italy, May 12-13, 1986.
- 13) H. Torgaard, "North Sea Resid Tested as FCC Feedstock", OGJ, January 10, 1983, 100-103.
- 14) D.F. Barger, C.B. Miller, "Convert Resid for Flexibility", Hydrocarbon Processing, May 1983, 68-70.
- 15) M. Denmar, A. Triki, J.P. Franck, "Advanced Analyses Improve Delta Coke Prediction for Resids", OGJ, Sept. 15, 1986.

RECEIVED June 8, 1990

Chapter 20

Concepts for Future Residuum Catalyst Development

P. O'Connor¹, A. W. Gevers¹, A. Humphries², L. A. Gerritsen³,
and P. H. Desai⁴

¹Akzo Chemicals BV, P.O. Box 975, 3800 AZ Amersfoort,
The Netherlands

²Akzo Chemicals, Inc., 3250 East Washington Boulevard,
Los Angeles, CA 90023

³Akzo Chemicals BV, P.O. Box 15, 1000 AA Amsterdam,
The Netherlands

⁴Akzo Chemicals, Inc., 13000 Bay Park Road,
Pasadena, TX 77058

This paper reviews some main concepts for Resid Catalyst development.

In the area of catalyst architecture, the effect of an enhanced accessibility of the active sites by the larger resid molecules, can significantly improve both conversion and bottoms cracking.

Several generations of vanadium metal catchers have been developed (1, 2), leading to an improved activity retention at high vanadium levels on catalyst. The recent progress in nickel tolerance with new nickel encapsulation technologies is just as dramatic. The reduced coke, gas and hydrogen make of these types of catalysts open the road to a significant increase in resid processing.

Developments in the zeolite field in terms of non-framework alumina control, leading to super low delta coke zeolites and the advent of enhanced surface activity zeolites, seem promising for the resid cracking field (3).

Resid upgrading in the refining industry

Several forecasters (4) have predicted that the world's crude reserves are weighted about two to one in favor of heavy versus light crudes. Consequently the inevitable trend is that the average crude processed will become heavier. Market forces, regional demand, environmental considerations and other factors will determine the economics and justification for heavy oil conversion. But it is clear that in the global scene, there will be an increasing supply of heavy oil.

On the other hand, a steady decline in fuel oil consumption in different regions has been reported (5, 6). Increasing supply, combined with decreasing demand for oil, challenges the refineries to investigate creative solutions to the resid problem. The main objective is to convert the heavy resid to desirable transportation fuels.

Several hydrocarbon processes are available for upgrading resid: hydrotreating, Fluid Catalytic Cracking (FCC), coking etc., some more capital intensive than others. The most widely prevalent process is the FCC process. Therefore any advances in processing resid in FCC units will have wide application. This paper deals with concepts for developments in resid cracking, particularly in resid FCC development, evaluation and application.

Whereas worldwide demand for gasoline is expected to remain more or less constant, demand for middle distillates (diesel, kerosene, jet fuel) is expected to increase. Resid cracking to yield gasoline does not always lead to favorable economics. Making mid-distillates from resid however, may offer interesting opportunities.

Resid Processing

From an FCC viewpoint, there is not a clear definition of resid cracking. If we consider the overall refinery scheme, all materials not qualifying for gas oil type specifications are resid, which in fact means that the traditional FCC feed, Vacuum Gasoil (VGO), is nearly 100% resid, or to be more specific a fuel oil.

The fact that a traditional VGO FCC unit is also a "fuel oil" cracker, can be illustrated by the fact that processing of VGO in a FCC unit in a refinery running on Middle East crude, will reduce the heavy fuel oil production of the refinery by about 10% wt on crude (7).

For conventional VGO cracking the sharpness of the vacuum separation between the flashed distillate and residue is not really important, provided that the undesirable non-volatile asphaltenes and metal compounds are left in the residue.

Entrainment is kept at a minimum by a wash oil section in the vacuum unit and checked with a colour specification on the FCC feed. The "real" FCC resid cracking seems to start, when the wash oil stream in the vacuum column is also routed to the FCC unit, obviously the colour of the FCC feed will deteriorate strongly.

Depending on the crude origin, already the introduction of dirty wash oil can have a significant impact on the metal content of the FCC feed and hence the catalyst. Several deasphalting processes open up the possibility to cut deeper, but also more selective in terms of asphaltene and metal content into the resid.

High temperature deep flashing and vacuum flashing of thermally cracked distillate also contributes to increasing the percentage of the crude, which can be routed to the FCC unit.

In the ultimate case, depending on the feedstock origin and the FCC unit operational constraint, even 100% atmospheric residue can sometimes be processed in the FCC unit. (Table I.)

Table I. Resid Cracking in FCC

- VGO Cracking	- Vacuum Gasoil clear, no metals	- Vacuum Flashed distillate from atmospheric resid
- HVGO/DAO	- Heavy VGO, Wash oils - Deep Flashed VGO - Flashed Cracked residues - Deasphalted Oil	- Cutting deeper into the barrel, while trying to avoid excessive asphaltenes and metals
- Resid Cracking	- Atmospheric Residue (AR)	- Crude selection to avoid excessive asphaltenes and metals - Pretreatment to reduce asphaltenes and metals

Processability of resids in FCC units

It is well known that the processing of heavier, more contaminated feedstocks (metals, asphaltenes) tends to increase the production of coke and gas and deactivates the catalyst. This is mainly the results of (8):

- (1) A larger feed fraction that does not vaporize under conventional cracking conditions. For this reason resid in FCC is sometimes defined as the fraction of the feed boiling above an effective "cutpoint" of the flash in the bottom of the FCC riser. Depending on the expected bottom mix temperature, cutpoints of 530 up 560°C are mentioned in the literature.
- (2) Contamination by heavy metals (V, Ni). To maintain the metal content on catalyst constant, usually a large increase in catalyst consumption (from an average of 0.15 lb/bbl up to and above 0.5 lb/bbl) is required. Alternatively special metal resistant catalyst can be applied in order to minimize catalyst consumption. Arbitrarily a metals content (Ni + V) of above 1500 ppm on catalyst is sometimes considered to be a metals contaminated resid operation.
- (3) A higher concentration of basic and polar molecules, i.e. nitrogen compounds that are readily adsorbed on to the catalyst acidic sites, leading to an instant, but temporary deactivation. Polycyclic aromatics also strongly contribute to coke formation.

(4) Other poisons as alkali contaminants (Na, K....).

The higher coke production of resid feedstocks will also tend to increase the temperature of the regenerator and hence the deactivation of the catalyst.

From the foregoing it becomes obvious that the FCC processability of resid feedstock and the choice of a possible FCC feed pretreatment (for instance Resid Hydroprocessing) will depend on the feed quality and hence its origin.

Naber et al (9) have demonstrated that FCC still has a considerable potential to remain the (resid) conversion "workhorse" of the oil industry. At present about 45% of the world's crude can be envisioned to be within the frontiers of Resid FCC (figure 1). Apart from the importance of FCC feed pretreatment and FCC unit design, also the impact of FCC catalyst performance is crucial to allow the processing of heavier feeds.

The Catalyst Role in Resid FCC

Reviewing the main challenges in Resid FCC, we can establish the areas in which FCC catalyst improvements can play a role in enhancing the processability of resids. (see Table II.)

- (a) Vaporization and cracking of large hydrocarbons:
This leads to a poor conversion and higher coke and fuel gas yields. In order to improve the conversion of large molecules, new modifications in the FCC Catalyst Architecture and Active Site Accessibility, are required in terms of Pore Size and Pore Acidity distribution.
- (b) Contamination by heavy metals (V, Ni):
Several catalysts on the market today contain special vanadium traps or vanadium scavengers in order to protect the active ingredients against poisoning and/or destruction by Vanadium. These "Metal Traps" limit the mobility of the vanadium pentoxide compounds under FCC conditions (2, 10). The nickel problem needs to be approached differently: and more recently, progress has been made towards reducing the dehydrogenation activity of nickel dispersed on FCC catalysts (11).
- (c) Poisoning and coke formation by basic and polar compounds:
High nitrogen resistant catalysts and/or nitrogen traps are available nowadays; unfortunately, no real breakthroughs have been made in reducing the effect of polycyclic aromatics (Conradson Carbon Catchers?). At present super low delta coke catalysts are produced to allow for the additional coke produced by these polycyclic aromatics.
- (d) Active site poisoning by Sodium, Potassium; etc.....
The Sodium resistance of the active ingredients in FCC catalysts can also be tackled by high activity and stability catalysts.
- (e) Severe Hydrothermal regeneration conditions:
An improvement in coke selectivity can have a large impact on

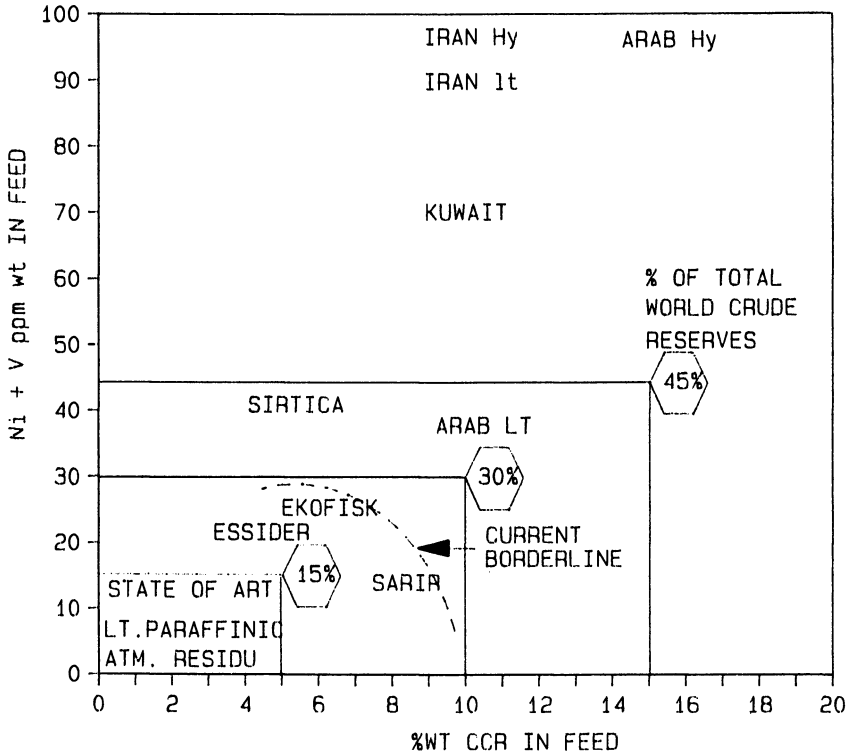


Figure 1 : Resid (370 °C TBP+) properties in relation to FCC processability (see Ref. 9). Reprinted with permission from National Petroleum Refiners Association publication AM-90-42. Copyright 1990.

Table II. Resid Processing Challenges and Catalyst Development

<u>A</u>	- Vaporization and cracking of large hydrocarbon molecules	- Unvaporized feed results in poor conversion and higher coke and fuelgas production	- Catalyst Architecture
<u>B</u>	- Contamination by heavy metals	- Catalyst deactivation by Vanadium - Dehydrogenation activity of Nickel	- Vanadium Catcher/Resistance - Reduction of Nickel Activity
<u>C</u>	- Basic and polar compounds	- active site poisoning by Nitrogen - Coke formation and acid site blocking by poly-cyclic aromatics	- Nitrogen Catcher/Resistance - Conradson Carbon Catcher?
<u>D</u>	- Other poisons	- Active site poisoning by e.g. Sodium	- Sodium Catcher/Resistance
<u>E</u>	- Severe Hydrothermal Conditions	- Catalyst deactivation/ stability problems	- High Activity and Stability Catalysts

the activity stability via the regenerator temperature reduction. High activity and stability catalysts are required.

It is obvious that depending on the type and severity of FCC feed pretreatment (Coking, Hydrogenation/Demetallization) and the type of FCC unit design and operating philosophy the priority of the foregoing aspects may differ considerably. An interesting example is the comparison between the operation of FCC units with and without heat removal. (Table III.)

Although the table gives a very exaggerated comparison between the two cases, it does clearly distinguish their priorities.

It is also clear that in the case of FCC with heat removal, the frontier of resid processability can at a certain moment be determined by the coke selectivity of the catalyst, while on the other hand the conversion of resid in a unit without heat removal may also be limited by the metal resistance of a catalyst.

Catalyst Accessibility and Architecture

i. Diffusion and active site accessibility

The accessibility of active sites plays an important role in the activity and selectivity of FCC. For resid cracking diffusion and accessibility effects can become of prime importance.

In a previous paper (7), we have illustrated that diffusion in FCC takes place in the non-steady regime and that this explains the failure of several attempts to relate laboratory measurements on FCC catalysts to theories on steady state diffusion. Apart from the diffusion aspects, Nace (13) has also indicated the limited accessibility of the zeolite portal surface area by comparing the cracking rates of various model compounds with an increasing number of naphthenic rings on zeolite and amorphous FCC catalysts, figure 2.

With an increase in the number of naphthenic rings, the crackability of the hydrocarbon molecule increases (vide data with $\text{SiO}_2\text{-Al}_2\text{O}_3$ catalyst), while the relative cracking rate by zeolites drops off due to the limited accessibility of the acid sites in the zeolite.

It becomes clear that significant conversion benefits can be obtained by increasing the activity contribution in the meso pore range (about 20 to 200 Angström diameter) in a catalyst, Table IV. Results obtained from testing various catalysts with Vacuum gasoil (VGO) and Atmospheric Residue (AR) confirm that indicated improvement of FCC conversion.

Table III. Resid FCC Operating Strategy

<u>Strategy</u>	<u>Without heat removal</u>	<u>With heat removal</u>
<u>Typicals</u>		
Catalyst to oil ratio	low	high
Coke production	low	high
Regenerator temperature	high	low
Delta Coke on catalyst	low	high
<u>Catalyst priority</u>	<ol style="list-style-type: none"> 1. Super low delta coke 2. Hydrothermal stability 3. Catalyst architecture 4. Metal resistance 	<ol style="list-style-type: none"> 1. Metal resistance 2. High activity/stability 3. Catalyst architecture 4. Low delta coke
<u>Operating goal</u>	"MAXIMIZE CTO"	"MAXIMIZE ACTIVITY"
<u>Catalyst development Category</u>	RESID-2	RESID-1

Table IV. Impact of enhanced accessibility on conversion

Catalyst	Mesopore Surface area	Mesopore activity	Conversion in MST test, wt%		
			VGO	AR	Delta
A	low	low	63	63	0
B	high	high	63	65	+ 2
C	medium	medium	62	64	+ 2
D	high	medium	68	74	+ 6
Development	medium	medium	66	74	+ 8

MST = Micro Simulation Test (14);

High Temperature, Short contact Time MAT (560°C, 15 seconds)

VGO = Kuwait

AR = North Sea

Catalyst Deactivation: 5 hrs 788°C, 100% steam, 1500 ppm Ni

Although an increase in meso pore surface area and activity will result in an increase in conversion and resid conversion, Table IV also shows that there is no simple correlation between the observed catalyst properties and these results. Apparently other aspects such as pore size distribution and pore chemistry also play an important role.

Another aspect which needs to be considered is the effect of catalyst to oil ratio. In a commercial unit the effective meso pore activity will be a function of the meso pore activity of the catalyst and of the catalyst to oil ratio (CTO):

$$\text{Effective meso porosity} = \text{Mesoporosity} \times \text{CTO}$$

Mesoporosity is expressed in terms of surface area as measured by Hg adsorption in the 20 to 100 Angström range. Figure 3 indicates how the effective meso pore activity has a strong effect on conversion of bottoms in the case of Atmospheric Residue, while this effect is much less pronounced in the case of VGO feedstock. For a commercial unit this implies that we need to enhance the meso pore activity while avoiding a drop in CTO due to (for instance) a higher delta coke of the catalyst.

ii. Pore Size Acidity Distribution

In an idealized situation one can optimize several stages in the cracking of a resid molecule:

Stage one : Catalyst sorbs non volatile or partially volatile resid. Large asphaltenes crack and decompose nearly instantaneously, and metals are deposited on the catalyst surface.

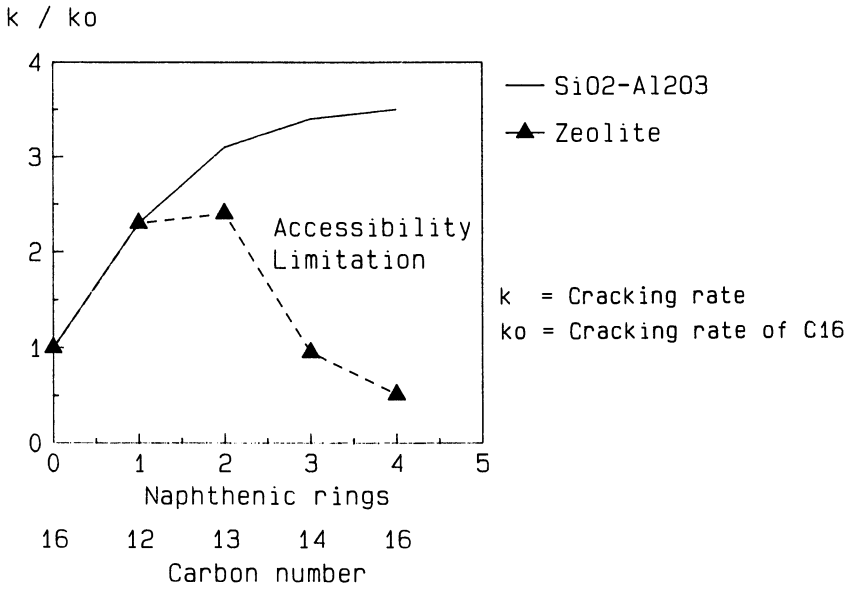


Figure 2 : Active Site accessibility (13).

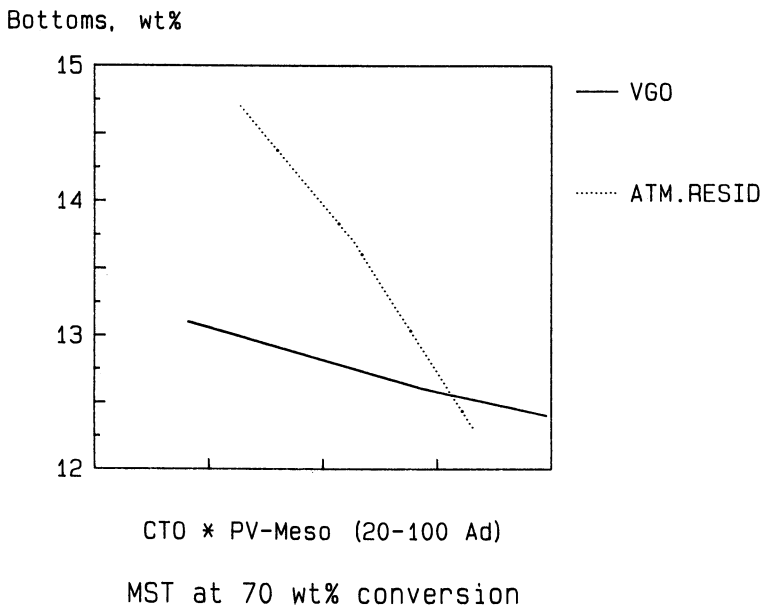


Figure 3 : Effective Mesoporosity concept.

Stage two : Large hydrocarbon molecules precrack in meso pores.

Stage three: Hydrocarbon cracking on surface of and in zeolite pores.

Hettinger et al (7) have presented this staged cracking concept as a useful model for FCC resid catalyst design (figure 4). Based on this model we can envision a very specific Pore Size Acidity Distribution (figure 5), which would be necessary to achieve an improvement in resid conversion.

We have noted that regarding the necessity of special large "Liquid catching" (LC) pores, there is a very significant impact on coke and fuel gas selectivity.

Figure 6 shows an example of the coke selectivity in the MST unit with a normal VGO feedstock.

Another interesting feature is that these LC pores result in an increase in the overall conversion. This effect is most pronounced when the catalyst is impregnated with Nicel (1500 ppm Nickel in MST) and at high coke yields. From this it seems obvious that pore mouth blocking is also a factor in Resid FCC, and that the presence of LC pores can be beneficial in this respect. Meso pores, are essential for reduction of the bottoms yield with aromatic and/or naphthenic feedstocks. (Table V.)

Table V. Impact of meso pore activity

Bottoms yield in the MST at 4 wt % coke [*])		
	Aromatic/Napthenic Feedstock	Paraffinic Feedstock
Cat. A - high zeolite activity - low meso pore activity	14.5	11.5
Cat. B - medium zeolite activity - high meso pore activity	12.0	13.2
Cat. C - medium zeolite activity - high meso pore activity	11.0	10.5

* MST test with 1500 ppm Ni, catalyst deactivated 5 hours at 788°C.

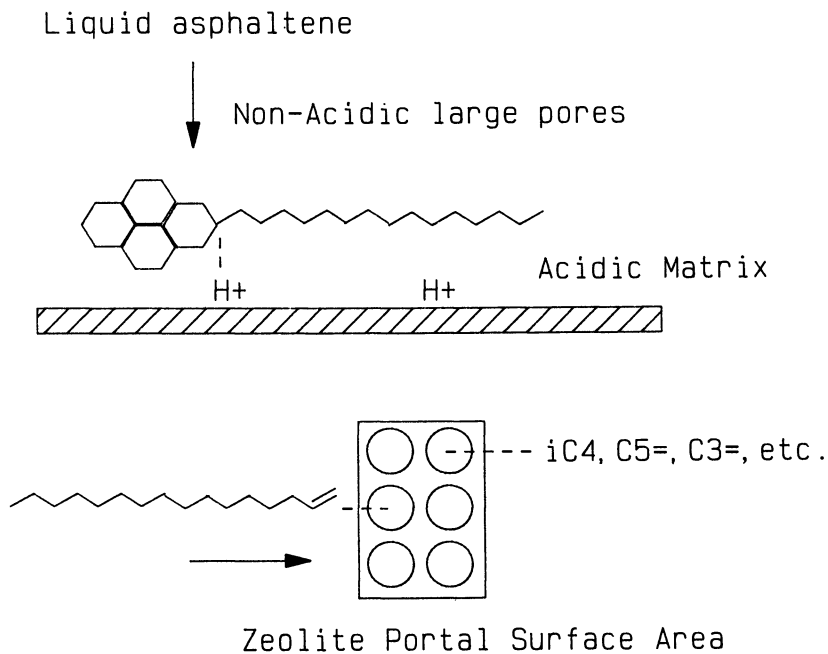


Figure 4 : Staged Cracking Model (15).

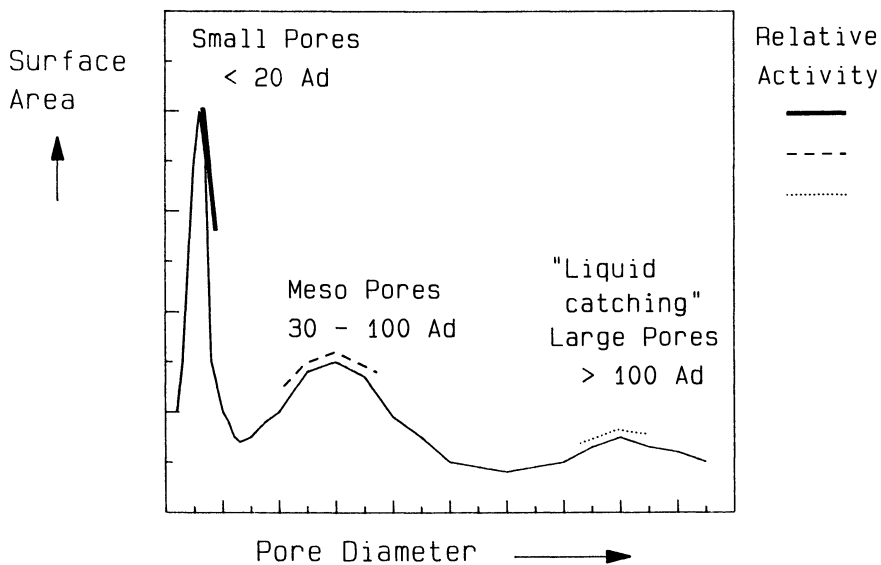


Figure 5 : Poresize Acidity Distribution.

Table 5 indicated the large effect of mesopore activity on the reduction of bottoms yield with Aromatic/Naphthenic feedstocks. For the paraffinic feedstocks tested, the impact of the zeolite activity is much more pronounced, and the catalyst with the highest zeolite activity and lowest mesopore activity generates the lowest bottoms yield.

These results seem to correlate well with the "conceptual picture" of staged cracking as presented by Hettinger (figure 5) and the influence of molecular structure (large number of rings vs low number of rings) on the effectiveness of the zeolite activity as indicated by Nace (figure 2). A salient point of table 5 is the further reduction of bottoms yields obtained with a special technology high mesopore activity catalyst (Cat. C).

Figure 7 illustrates that there is an essential difference in the pore size architecture between catalysts produced with this technology (Cat. C) and those produced with the other manufacturing technologies (Cat. A,B). With the Cat. C Technology (high meso pore activity catalysts) there is a shift towards more pores in the "larger" meso pore area (Table IV.)

Catalyst Resistance to Deactivation by Metals

i. Strategies to reduce vanadium effects

There are several good review articles which cover the research of the mechanism of vanadium deactivation of FCC catalysts (see 2, 8). Basically the vanadium present in the large metal porphorin molecules is deposited on the outer surface of the catalyst, due to the fast decomposition of these molecules.

At high temperatures and in the presence of steam, vanadium becomes mobile and moves into other parts of the catalyst. In a FCC unit this takes place during the regeneration phase (average 700°C and 5-25% steam atmosphere). Vanadium oxide V_2O_5 formed during regeneration can react with the zeolite, RE_2O_3 , Na and Al_2O_3 , promoting destabilization and collapse of the zeolite structure (16, 17). Even in the case that a very stable zeolite is able to withstand this attack, activity losses can occur due to neutralization of the zeolite and matrix acid sites.

FCC catalyst development to reduce the effect of vanadium has been aimed at reduction of vanadium mobility: the application of special ingredients in the catalyst which function as metal scavengers or metal catchers. In the past (2, 10) transport experiments were used to show that during steam-aging, intraparticle transfer of vanadium occurs and that migrating vanadium can be irreversibly sorbed by a metal trap such as sepiolite (2) in the form of a heat stable vanadate.

A simple vanadium mobility test can be setup, in which the vanadium which migrates from vanadium-loaded catalyst towards non-vanadium loaded catalyst can be measured under catalyst aging (usually steaming) conditions (2).

The method we applied is as follows: The catalyst is sieved into a coarse and a fine fraction. The coarse fraction of the catalyst (PSD > 75 μm) is impregnated homogeneously with about 4000 ppm vanadium by a traditional pore volume impregnation method.

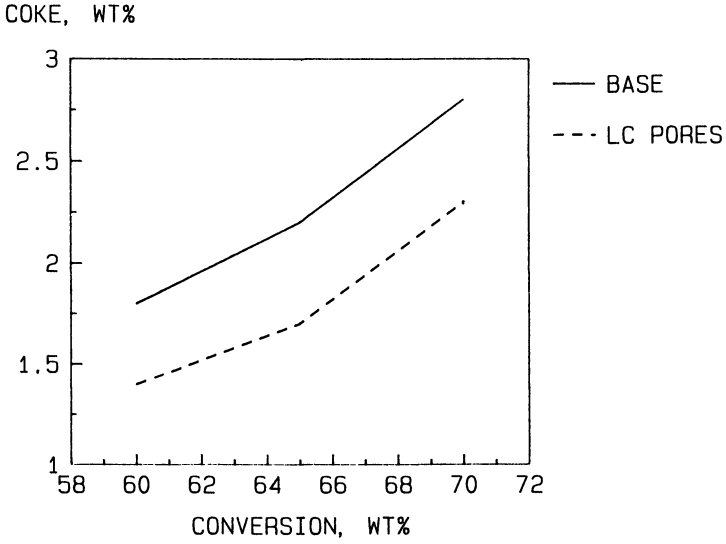


Figure 6 : Selectivity benefit of improved pore architecture.

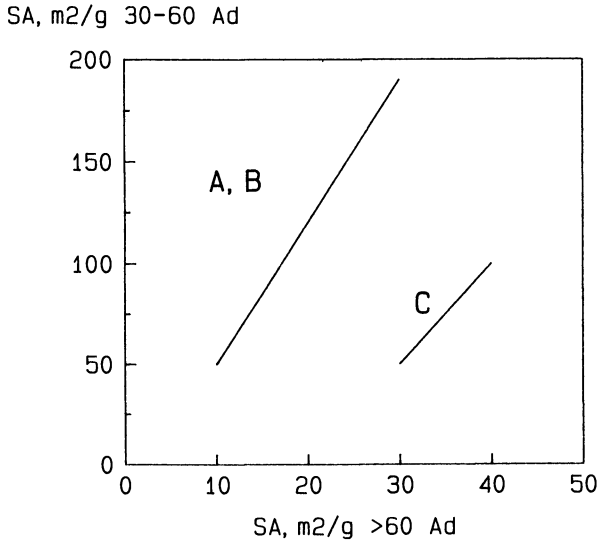


Figure 7 : Simplified Pore Architecture of fresh catalysts.

After this both fractions are mixed together again, and the mixture is steamed in a fixed bed for 5 hours at 788 or 830°C, with 100% steam. The steamed mixture is then sieved again and the vanadium content of the coarse fraction ($PSD > 75 \mu\text{m}$) is measured. This approach minimizes the effects of catalyst attrition phenomena on the vanadium mobility determination.

The vanadium mobility (VM) is then defined as follows:

$$VM (\%) = \frac{V_{C_1 \text{ start}} - V_{C_1 \text{ end}}}{V_{C_1 \text{ start}}} * 100$$

$V_{C_1 \text{ start}}$ = Vanadium level of coarse fraction ($> 75 \mu\text{m}$), before mixing and steaming (ppm wt)

$V_{C_1 \text{ end}}$ = Vanadium level of coarse fraction ($> 75 \mu\text{m}$) after mixing and steaming (ppm wt)

The following table (Table VI), shows an example of vanadium mobility and its dependence on catalyst composition.

Table VI. Reduction of vanadium mobility

<u>Catalyst</u>	<u>Vanadium mobility</u> (% V migration)
USY	61.5
USY + Active Al_2O_3	52.7
USY + Active Al_2O_3 + MTT*)	33.0

*) MTT = A metaltrap, as described in Reference (18).

In FCC units which exhibit a high tendency to vanadium migration, the application of metal traps can be very beneficial.

Factors that influence vanadium mobility in commercial FCC units are:

1. The oxidation state of the vanadium (see also 2)
2. Regenerator temperature; it has been observed that the vanadium mobility can double with 40°C regenerator temperature (see figure 8).
3. The presence of steam and carbon on catalyst.
4. The vanadium level and the catalyst replacement on inventory.

Figure 8 illustrates the effect of temperature on vanadium mobility (measured on equilibrium catalysts from three FCC units) and the large impact of certain unit variables. For these measurements the coarse equilibrium catalyst was tested in a mobility test using the method described above by substituting sieved coarse equilibrium catalyst for vanadium impregnated catalyst.

In case of a relatively low vanadium mobility, the deactivation by vanadium will be less, and so will be the effect of incorporating a metal trap. Still it also appears to be important to address the strategy to combat vanadium in this case. If vanadium is only present on the outer layer and in the larger pores of a catalyst, the effect on zeolite deactivation might be decreased. However owing to deactivation of acid sites in these mesopores, the bottoms cracking potential of the catalysts will be strongly affected. Thus the presence of vanadium catching capability in these larger pore regions becomes essential. This is clearly visible with more resid in the feestock.

Since the method of metal impregnation will also have a large impact on the profile of vanadium deposition of the catalyst, we clearly need to review this aspect of catalyst testing. Via cyclic metal impregnation and catalyst deactivation, we can approach "Real-World" conditions far better. (Table VII.)

Table VII. Effect of accessibility

Conversion in MST, % wt	100% VGO	60% VGO/ 40% North Sea AR
Catalyst A	66	66
Catalyst B "Accessible" vanadium catcher	68	71

*) 5000 ppm V metal level, impregnation by a cyclic deactivation method.

The route of catalyst deactivation via a cyclic metal impregnation and deactivation method has produced significant improvements in approaching realistic vanadium and nickel profiles over the catalyst particles. From electron microprobe analyses of Ni and V loaded catalyst it has been established that after pore volume saturation, Ni and V are rather homogeneously distributed over the catalyst. In cyclic impregnated catalysts, Ni is mainly present on the catalyst surface. In contrast a vanadium profile over the particle is found. In the case that no steam is applied in the regeneration stage of the cyclic deactivation procedure, the V remains mainly concentrated at the surface of the catalyst particles. Other methods as imaging SIMS (19) and Luminescence (20) are also being applied to monitor and compare the Ni and V distribution of deactivated

catalysts versus commercially deactivated equilibrium catalysts.

Careful selection of the deactivation conditions (metals per cycle, regenerator temperature, % wt steam in can also allow us to distinguish between catalyst deactivation by metals and by hydrothermal effects. (Table VIII.)

Table VIII. Metals tolerance by cyclic deactivation

Conversion loss (wt % in MST)			
<u>Catalyst</u>	<u>Zeolite</u>	<u>Low metals</u> cycles	<u>High metals</u> cycles
g	Z-14 US	2.8	5.5
K	LZ-210	2.4	4.8
Akzo	ADZ-40	2.3	3.5
Akzo	ADZ-41	2.6	3.0

Low metals : 1000 ppm V, 500 ppm Ni

High metals: 3000 ppm V, 1000ppm Ni

It can be observed that the magnitude of conversion loss of 1 to 2 points MST per 1000 ppm V corresponds quite well with commercial data. Note that this is only true for V levels below 5000 ppm that is, at relatively low V levels.

ii. Nickel effects and encapsulation

In the eighties, more and more FCC units processed nickel rich feedstocks, especially nickel rich paraffinic atmospheric resids from the North Sea and Asia Pacific sources.

Although nickel has only a marginal effect on catalyst deactivation, nickel itself is activated especially on alumina surfaces and works as a dehydrogenation agent catalyzing the reactions forming coke, gas and especially hydrogen (2). Also as a consequence of the higher localized coke formation, blocking of the pores will take place, resulting in a loss of activity. Apart from the use of Sb or Bi passivators on the catalyst side, up to very recently the only approach has been to minimize the active alumina surface in the catalyst and consequently sacrifice bottoms conversion for nickel resistance.

A new technology of catalyst production (11) is capable of generating materials in which the nickel activity as dehydrogenation agent has been stopped by a multi-step strategy. (Table IX.)

V - Mobility

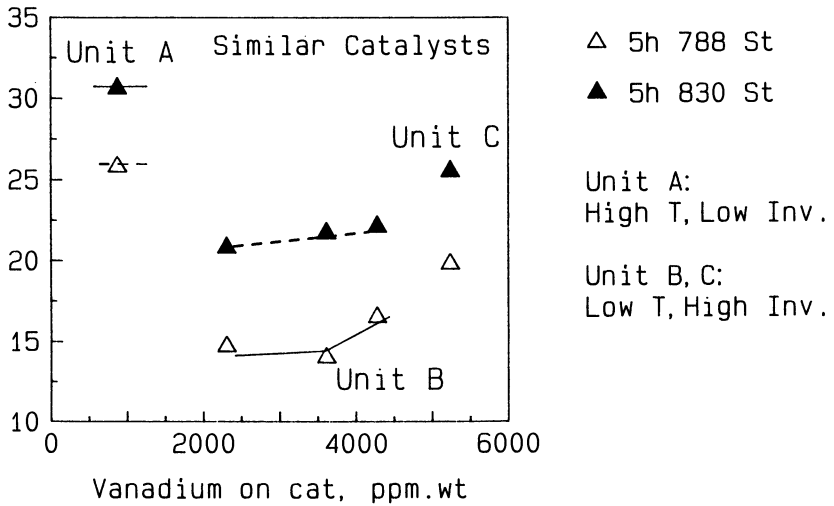


Figure 8 : Vanadium Mobility on FCC catalysts.

Table IX. Strategy to combat Nickel

<u>Silica Rich Surface</u>	Formation of large crystallites and stable inert Ni-silicates
<u>Alumina rich Surface</u>	Encapsulation of nickel in non-active alumina tetrahedral structures
<u>Zeolite</u>	Non-framework Alumina Control (ADZ)

Figure 9 demonstrates the clear benefit of nickel encapsulation in reducing the activity for hydrogen production. The observed RE_2O_3 effect on hydrogen production, is related to the formation of zeolite surface non-framework alumina. Progress in nickel tolerance of FCC catalyst with these new technologies is at least as dramatic as in vanadium tolerance (2).

Commercial FCC operations with nickel on equilibrium catalyst (above 2000 ppm) without the use of passivator, have become feasible. This new technology also allows further optimization of the mesopore activity, the conceptual figure 10 illustrates this point, which now has been confirmed in commercial FCC operations (21).

As with vanadium under relatively low mobility conditions, nickel remains mainly deposited in the larger pores of the catalyst.

Hence to investigate nickel effects as realistically as possible, Cyclic Deactivation (CD) methods are recommended.

Table X. demonstrates this, showing how the catalyst ranking can be influenced by the deactivation procedure used.

Table X. Influence of catalyst ranking by type of deactivation procedure.

Method	pore volume impregnation		cyclic deactivation	
	LCMR	ES	LCMR	ES
Catalyst *)	LCMR	ES	LCMR	ES
MST yield	70 % wt			
Conversion				
H ₂	0.16	0.22	0.17	0.15
Dry gas	3.1	3.1	3.0	2.5
Gasoline	44.2	44.0	44.0	45.2
Bottoms	13.1	12.2	14.2	12.6
Coke	3.4	3.8	4.2	3.7
C ₄ =/C ₄ tot	0.63	0.70	0.60	0.65

*) Catalyst Characteristics:

LCMR : Minimum mesopore activity with MR metal trap
 ES : High mesopore activity with ADVANCE technology

Catalyst Resistance to Deactivation by Other Poisons

Other catalyst poisons besides nickel and vanadium are:

1. Poisons which neutralize or destroy acid sites, as for instance sodium, potassium, nitrogen.
2. Poisons (such as basic and polar compounds in the feed) which primarily enhance the formation of coke and hence indirectly also cause the deactivation of the catalyst.

For the first type of poisons, we can either try to apply the same approach as with vanadium; meaning specific catchers or offer a sufficient excess of acid sites: sacrificial sites in order to reduce the relative impact of the poisoning. For instance, in the case of a nitrogen resistant catalyst, usually the catalyst design will involve a relatively high rare-earth and high zeolite content catalyst with the option of additional sacrificial sites in the form of active alumina (12).

Obviously such a type of formulation could have some negative consequences for the catalyst: primarily a higher coke make and probably also some octane penalty.

With regards to sodium we also need to consider the stability resistance of the zeolite. Fortunately, some of the newer zeolites are able to maintain their structural integrity, in the presence of high sodium levels. However, the acid sites present remain still very susceptible to neutralization by sodium.

We can also distinguish a few lines of approach regarding catalyst poisons which deactivate the catalyst by coke formation, that is by blocking of pores and the catalyst active sites,

1. Conversion of these coke precursors prior to the formation of the coke. It is to some extent debatable whether this can be done. Some improvements are possible using an improved catalyst pore architecture and acidity distribution.
2. Adapt catalyst design to minimize the effect of coke on catalyst. This is an aspect which clearly deserves attention, as we might expect significant deposition of coke in the very beginning of the riser when processing resids.
3. Reduce the catalytic coke formation of the catalyst in order to allow some room for the additional coke formed by these poisons. In this approach we accept that the extra coke formed is unavoidable, and that we need to compensate by improving the coke selectivity of the catalyst.

The main strategies for addressing these types of catalyst poisons are summarized in Table XI.

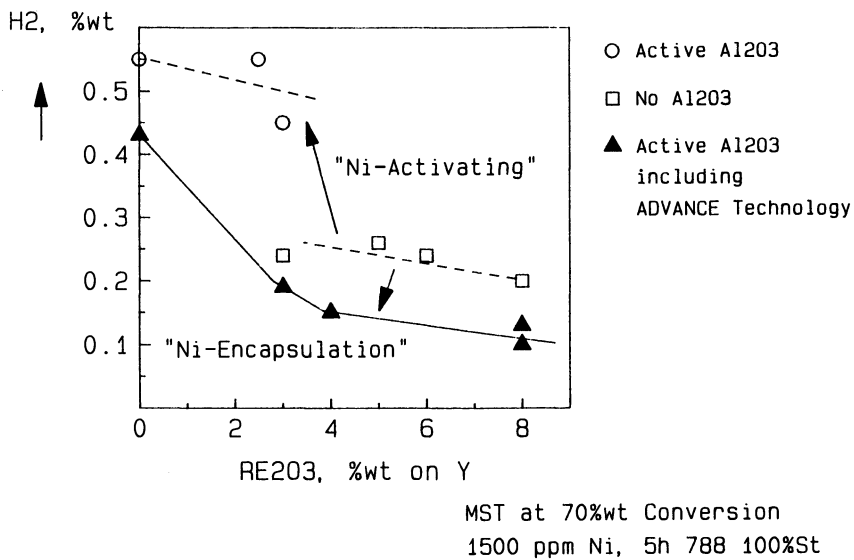


Figure 9 : Hydrogen production vs Catalyst design.

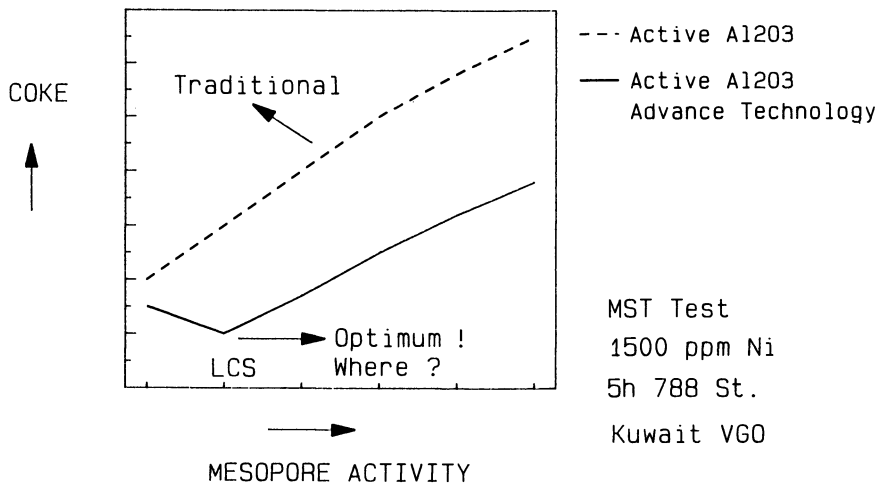


Figure 10 : Coke selectivity vs Mesopore activity.

Table XI. Strategies for addressing catalyst poisons

<u>Type of Poison</u>	<u>Examples</u>	<u>Strategy</u>	<u>Remarks</u>
Poisons which neutralize or destroy acid sites	Na, K, nitrogen	- specific poison catchers - sacrificial sites: high	- not successful yet - need to compensate for coke-selectivity
Poisons which deactivate sites and block pores by extra coke formation	basic and polar compounds	- convert coke precursors - min. effect of coke on catalyst - reduce catalytic coke formation	- special pore acidity distr. - need to compensate for coke selectivity

We can conclude that an improvement in coke selectivity plays an important role in the strategies to cope with both type of poisons.

Catalyst Selectivity and Stability

As discussed in the previous sections any improvements in coke selectivity can be utilized to extend the frontiers of resid processing as several types of poisons in the resid feed, most of all the polar hydrocarbons will increase the coke formed. Also for fuel gas we can observe that non-optimal vaporization and cracking conditions with resid will strongly enhance gas formation. A low coke and gas catalyst is hence a big plus for resid processing. (Table XII.)

Table XII. Low coke and gas catalyst

Zeolite	Non-framework control (3), also low coke with medium/high RE ₂ O ₃ levels.
Active Al ₂ O ₃	Fuel gas decreases with higher RE ₂ O ₃ levels
Catalyst	Modified surface chemistry to reduce coke and gas formation (11, 20)
Architecture	Special pore size Acidity Distribution reduces coke and gas formation

Based on the "idealized objectives" outlined in Table XIII., we can arrive at the following catalyst characteristics for optimum coke and gas reduction

RESID-1	Minimum gas	Medium rare earth zeolite with medium to high mesopore activity.
RESID-2	Minimum coke	Low rare earth zeolite with low mesopore activity.

The progress in coke selectivity and bottoms or resid cracking is illustrated in Table XIII below:

Table XIII. Resid conversion at constant coke

RC, Resid conversion = 100-bottoms-coke, in MST

	RC	Delta RC
Base	79.3	-
ADVANCE	80.6	1.3
DEV-1*)	82.8	3.5
DEV-2*)	83.8	4.5

RE-USY catalyst with medium mesopore activity, deactivated 5 hours at 788°C, 100% steam and 1500 ppm Ni.

*) Experimental laboratory samples

It is clear that the zeolite delta coke will have a strong effect on the regenerator temperature and hence on the catalyst deactivation. Depending on the trend in FCC regenerator temperatures, the aspect of hydrothermal stability might become of greater importance.

It has been observed that, the indirect effect of delta coke on catalyst deactivation, and the direct effect of delta coke on the blocking of acid sites (early) in the riser seems to be a prime factor, which dominates conversion and selectivity effects in a resid type of operation.

Future Perspectives

From the foregoing chapters it should be clear that the development of a successful FCC resid catalyst depends on several aspects the relative priorities of which will be determined by the refinery objectives, feedstock, FCC unit configuration and limitations. Still, it is worthwhile to distinguish certain "idealized objectives" in order to focus the catalyst development in this field. The advances in resid FCC catalyst development up to now have been mainly in the field of metal tolerance (metal traps), while also progress has

been made in cracking the larger hydrocarbon molecules. For the future we need to address some other critical points touched upon in this review as (Table XIV.)

Table XIV. Some future challenges

-
- How to reduce the formation and the detrimental effect of the feed coke or coke formed by polar compounds
 - Development of traps for poisons, without negatively affecting the catalyst selectivity
 - Accessibility and effectiveness of vanadium trapping
 - Further reduction of "catalytic" coke and fuel gas production in order to allow more room for resid processing
 - Cracking of certain "difficult" molecules
-

It is also clear that a good understanding of the FCC process objectives, limitations and configuration will be of crucial importance for the development of an optimized resid FCC catalyst formulation.

REFERENCES

1. See for example:
 - (a) M.L. Occelli and J.V. Kennedy in GB 2.116.062 A (1983)
 - (b) M.L. Occelli and J.V. Kennedy in US 4.465.588 (1984)
 - (c) M.L. Occelli and H.E. Swift in US 4.466.884 (1984)
 - (d) M.L. Occelli in US 4.615.996 (1986)
 - (e) J.I. de Jong in US 4.519.897 (1985)
2. M.L. Occelli in "Fluid Catalyst Cracking: Role in Modern Refining", ACS Symposium Series, vol 375, M.L. Occelli, Ed. ACS Washington D.C., p 162 (1989).
3. See for example:
 - (a) J. Scherzer in "Catalytic Materials: Relationship between structure and reactivity", ACS Symposium Series, vol 248 T.E., Whyte, R.A.D. Betta, E.G. Derouane and R.T.K. Baker, Editors, ACS Washington D.C., p 157 (1983)
 - (b) R.J. Pellet, C.S. Blackwell and J.A. rabo; J. Catalysis 114, 71-89 (1988)
 - (c) B. de Kroes, C.J. Groenenboom and P. O'Connor; "New Zeolites in FCC", Akzo Catalyst Symposium 1986, May 25-28, The Netherlands. H.Th. Rijnten, and H.J. Lovink editors.
4. See for example:

G.J. Thompson, R.H. Hensen, C.N. Cabrera and E.J. Houde; "Processing requirements and economic analysis of Heavy Oil and syncrude refining", in the 12th World Petroleum Congress, Houston 1987, John Wiley & Sons ltd.

5. C. Carter; NPRA Annual meeting 1986, AM-84-27
6. J.A. Dudley; AIChE 1989, Spring National Meeting, Houston
7. P. O'Connor and F.W. van Houtert; "The role of diffusion in bottoms conversion", Akzo Catalyst Symposium 1986, May 25-28, The Netherlands. H.Th. Rijntjen and H.J. Lovink editors.
8. J.L. Mauleon and J.B. Sigaud; "Characterization and selection of heavy feeds for upgrading through fluid catalytic cracking process" in the 12th world Petroleum Congress, Houston 1987, John Wiley & Sons Ltd.
9. J.E. Naber, P.H. Barnes and M. Akbar; J.P.I. Petroleum Refining conference, Tokyo - Japan, October 1988.
10. M.L. Occelli and J.M. Stengel in "Fluid Catalytic Cracking: Role in Modern Refining", ACS Symposium Series, vol 375, M.L. Occelli, Ed. ACS Washington D.C., p 195 (1989).
11. C. Lam, P. O'Connor and C.P. Smit; "The Advance Catalyst Series", Akzo Catalyst Symposium 1988, May 29-June 1, The Netherlands, H.J. Lovink editor.
12. J. Scherzer and d.P. McArthur; "Catalytic Cracking of High Nitrogen Petroleum Feedstocks: Effect of Catalyst Composition and Properties", Ind. Eng. Chem. Res. 1988, 27, p 1571-1576.
13. D.M. Nace; Ind. Eng. Chem. 9 (2), 203, 1970.
14. P. O'Connor and M.B. Hartkamp in "Characterization and Catalyst Development", ACS Symposium series, vol 411, S.A. Bradley, M.J. Gatturo and R.J. Bertolacini, editors ACS Washington DC, p 135 (1989).
15. P. Hettinger in "Fluid Catalytic Cracking: Role in Modern Refining", ACS Symposium Series, Vol 375, M.L. Occelli, editor ACS Washington DC, p 308 (1989).
16. M.L. Occelli and J.M. Stengel in "Zeolite as Catalysts, sorbents and Detergent Builders" H.G. Karge and J. Weitkamp, editors Elsevier, p 127 (1989).
17. M.L. Occelli and J.M. Stengel in "Zeolites, Facts, Figures, Future", P.A. Jacobs, P.A. Vanjarter, editor Elsevier, part B p 1311, 1989.
18. C. Groenenboom in "Zeolites as Catalysts, Sorbents and Detergent Builders", H.G. Karge, editor Elsevier, p 199, 1989.
19. D.P. Leta and E.L. Kugler; "Secondary Ion Mass Spectrometry Proc. Int. Conf.", 6th 1987, p 373 (1988).
20. M.L. Occelli; Journal of Catalysis, 96, 1985, 2, p 363-370.
21. A.W. Gevers, P. O'Connor and E. Brevoort; "Advance: an exceptional FCC Catalyst design", Akzo Catalysts South American Catalyst Seminar, 1989, October 19-20, 1989, H.J. Lovink editor.

RECEIVED October 5, 1990

Chapter 21

Metal-Resistant Fluid Cracking Catalysts Thirty Years of Research

M. L. Occelli

Science and Technology Division, Unocal Corporation, Brea, CA 92621

Although the deleterious effects of metals such as V, Cu, Ni and Fe have been known for well over forty years (1-19), the study of metal resistant fluidized cracking catalysts (FCC) became an area of intense research in industrial and academic laboratories only in the early seventies when the Arab Oil embargo induced nearly a four-fold increase in crude prices and greatly reduced overseas crude availability (2).

Metal levels (Ni+V) on equilibrium catalysts from U.S. refineries have been monotonically increasing with time since the early sixties (20). This trend continued during the 1980-1986 period (Figure 1) when crude prices decreased to about \$25/bbl from \$38/bbl, Figure 2. Following the 1986 oil price collapse (crudes sold for \$9.35/bbl in August 1986), V level started to decrease somewhat, probably because of the refiners selection of more paraffinic crudes. However, Ni levels on equilibrium catalysts has remained unchanged. Thus, the importance of processing metals contaminated feeds has not significantly changed through the years and it has been projected that by 1995, 25% to 30% of the world's FCC units will be partially operating as resid crackers (21).

It is the purpose of this paper to review the progress made in understanding and designing zeolite-containing fluidized cracking catalysts capable of negating the deleterious effects of metals such as nickel and vanadium.

The development of metal resistant FCC requires extensive experimentation and rapid testing. Pilot-plant evaluation and screening of experimental FCC formulations (although more realistic) are not practical because they are time consuming and therefore costly. Thus, the investigation of metal containing FCC as well as the design of metal resistant FCC has been performed in industrial laboratories (perhaps at the cost of accuracy) using bench-scale microreactors similar to the one developed by Ciapetta and Anderson (22).

A spectroscopic study of 23 domestic crude oils has revealed the presence of 28 elements (23). Representative metal types and levels usually found in petroleum are shown in Table 1; Ni and V are, in general, the most abundant metals found.

TABLE 1. Metal Contaminants (PPM) Levels in Petroleum

Fe	0.1	-	5.0
As	0.5	-	1.0
Cr	0.001	-	0.01
Co	0.03	-	13.0
Cu	0.14	-	7.0
Mn	0.50	-	2.5
Mo	0.008	-	0.05
Ni	50.0	-	350.0
Se	0.020	-	2.0
V	4.0	-	300.0
Pb	0.10	-	0.40

Equilibrium FCC from a refinery contains these metals at levels that are usually below the limit of detection of most spectroscopic techniques of catalyst characterization. Furthermore, the simultaneous presence of several elements and coke further complicate the study of the effects that individual metals may have on catalyst performance.

Although several metal-containing heterocyclic compounds (such as porphyrins, phthalocyanines, naphthenates) are present in oil fractions most of the bench-scale research has been based on relatively rapid Ni, V, or Ni/V deposition procedures in which experimental FCC formulations have been artificially metal contaminated with solutions of Ni and/or V naphthenate dissolved in benzene (or toluene) (24). Metal levels in these novel FCC are usually above 0.5%; that is well above the concentration that today exist on equilibrium FCC, see Figure 1. High metal concentration facilitate the study and characterization of Ni and V effects by modern characterization techniques such as X-ray photoelectron spectroscopy (XPS), Laser Raman spectroscopy (LRS), X-ray diffraction (XRD), electron microscopy, secondary ion mass spectrometry (SIMS), and ^{51}V nuclear magnetic resonance (NMR).

Nickel-Containing Cracking Catalyst

The role of metals in catalyzing the nonselective cracking of gas oils has been well documented in the literature for several types of fluidized cracking catalysts (1-29). During the cracking process, Ni and V-containing porphyrins and porphyrins-like complexes decompose, leaving metal contaminants on the catalyst surface (15). Metals such as Ni (and to a lesser extent Fe) have little effect on cracking activity (and surface area), but change product distributions and increase coke, hydrogen, and light gas yields at the expense of the (more valuable) gasoline fraction (13, 18, 25, 26), Figure 3. In metals-tolerant FCC, it is believed that inactive metal silicates or even aluminates are formed on the catalyst surface (27). Metals-surface interactions, that is metals passivation, strongly depend on the composition of the cracking catalyst surface.

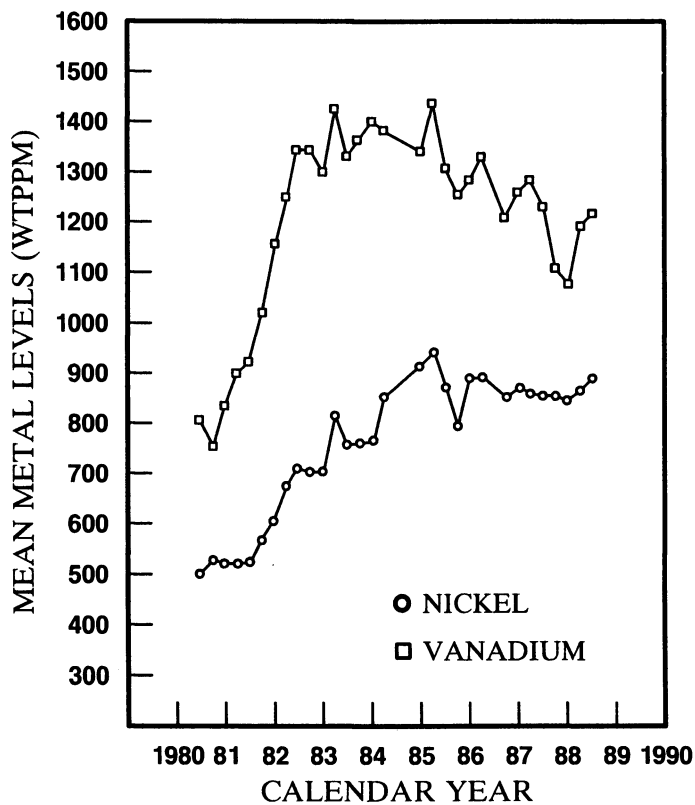


Figure 1. Metal level trends in equilibrium fluid cracking catalysts (FCC). Data based on Davison analysis of samples from 96% of fluid units in the USA and Canada.

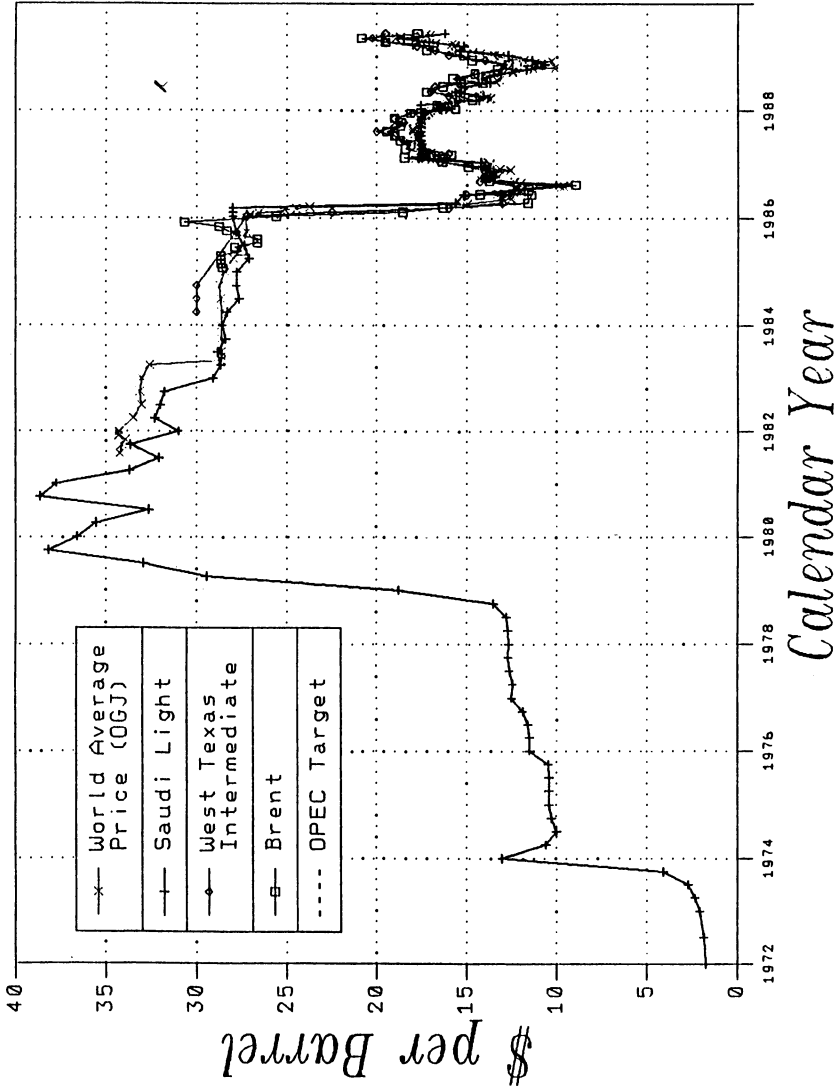


Figure 2. Crude oil prices for the 1980-1990 period.

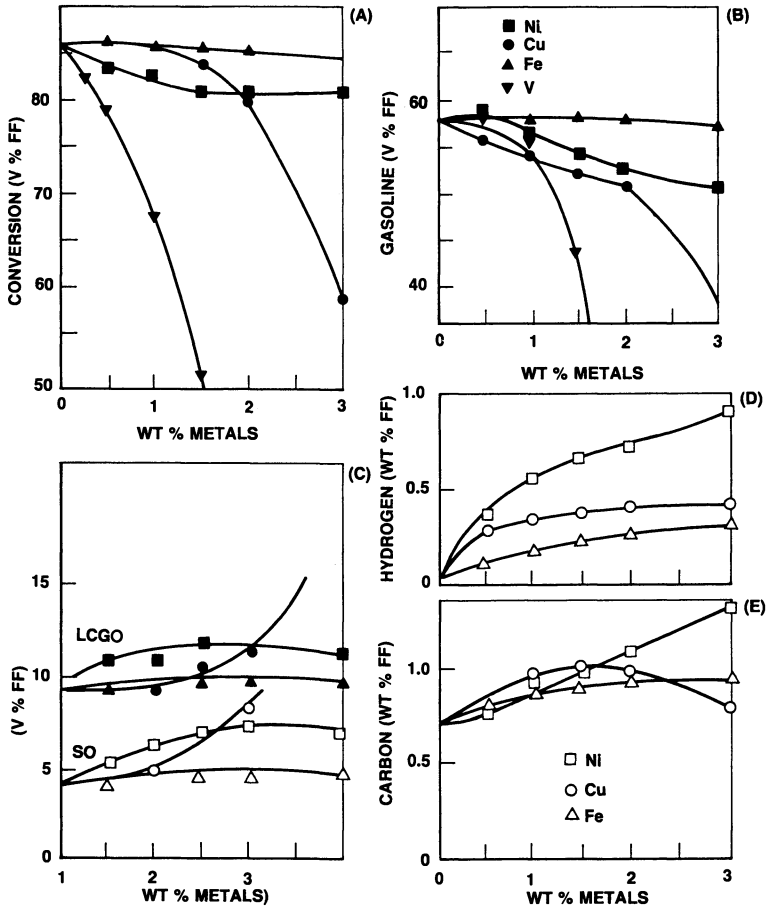


Figure 3. Metal effects on: (A) conversion, (B) gasoline, (C) LCGO and SO, (D) hydrogen and (E) carbon generation. Partially adapted from Ref. 25.

i. The Effects of Catalyst Composition. A study of the interaction of Ni with typical components (the gel, clay and the zeolite) of a fluid cracking catalyst (FCC) has shown that after calcination, Ni is present mainly as an easily reducible NiO-like phase on all the supports tested (27). However, after steam-aging, Ni interacts with the clay and the gel to form a NiAl_2O_4 surface specie. In a FCC, steaming causes Si to migrate to the surface where, in the presence of Ni, it can form inert NiSiO_3 -like compounds (27). The ability of a matrix to minimize Ni dispersion and of the matrix components to form chemically inert Ni-compounds will control the activity of this metal for catalyzing those secondary cracking reactions during gas oil conversion that generates light gases and coke at the expense of gasoline make (10,18,27,28,31). Recently, it has been reported that the deleterious effects of Ni can be reduced by FCC whose matrix consists of a partially dealuminated kaolin mineral embedded in a SiO_2 -rich support (16,18).

Nickel tolerance in FCC can also be induced by addition of particles (such as sepiolite, attapulgite, crysotile) which can irreversibly sorb and passivate metals (29-31). The excellent agreement between the Raman spectrum of natural garnierite (an hydrous magnesium-nickelsilicate) and the spectra of calcined or steam aged Spanish sepiolite loaded with 5% Ni has confirmed the presence of NiSiO_3 -like structures (such as Ni crysotile) resulting from Ni-sepiolite interactions induced by the various heat treatments used to age the catalyst (28). It is believed that clays, in addition to improving the FCC physical properties, can interact with metal contaminants like Ni and form surface compounds (such as Ni-aluminates or Ni-silicates) which are less deleterious to the cracking process than supported NiO-like species. Thus, a Ni-resistant cracking catalyst should contain a clay and a matrix capable of minimizing metals dispersion while forming inert Ni-compounds (27).

ii. Nickel Passivation. Resistance to metal poisoning in a cracking catalyst can be achieved by adding to the feed metals [such as Sb(32), Bi (33), Sn (34), Sn-Sb combinations (35), Ba (36), P and B (37)], thought capable of forming inert residues on the catalyst surface. Initially the bulk of the successful work, was performed by researchers at Phillips (32, 36, 38-42) using artificially impregnated as well as equilibrium FCC evaluated at microactivity test (MAT) conditions. It was reported that when using an equilibrium FCC with 0.31% Ni and 0.45% V, addition of 0.5% Sb increase (at 75% conversion) the gasoline make by 12%; coke and hydrogen decreased by 15% and 55% respectively (43). An organo-antimony compound (Phil-Ad^(R) CA) was used as the Sb-loading agent in bench scale, pilot plant as well as in the commercial testing conducted at the Phillips Borger refinery in Texas. The equilibrium FCC from this refinery contained high (0.22-3.0% Ni and 0.48-0.90% V) metal levels. Nonetheless, Sb injection to the feed increased (at a certain reactor T) gasoline make by 6.1% while hydrogen, dry gas and coke decreased by 44.6%, 27.5%, and 15.3%, respectively (43). As a result of improved selectivities, a net increase in product value of 41 cents/barrel of oil converted was obtained (43).

Antimony, although effective in reducing the dehydrogenation activity of Ni can be volatile, thus capable of contaminating a FCC unit internals and generate products on the EPA list of hazardous material. Bi-based passivators may offer the benefit of Sb-based technology without the concern that volatile Sb-compounds

pose to refiners (46). Metals passivation with Bi has been demonstrated in five commercial units during the 1986-87 period (46). However, Bi may not be as effective as Sb in passivating Ni contaminants in a FCC unit (47). Recently, it has been suggested that Sb volatility could be reduced by introducing into a FCCU diluents, such as aluminas and clays, loaded with Sb (30). The controlled release of Sb from the diluent surface to the host catalyst particle and to the gas phase, would then moderate the dehydrogenation activity of Ni contaminants in the feed and on the catalyst surface.

Other methods of metal passivation reported in the patent literature have proposed the use of H₂S (48,49), steam and methane gas (50-52). With H₂S, Nickel is converted to a sulfide and then oxidized to a washable sulfate that can be recovered.

iii. Characterization of Ni Containing FCC. Overcracking by nickel can be diminished by a variety of passivating agents. The most commonly used agent is Phillips Petroleum's Phil-Ad CA which consists of an organic antimony compound (32,53). However, the study of these systems has been conducted mainly on supported binary mixtures of Sb and Ni. Parks and co-workers have used XPS to show that nickel and antimony form an alloy in which nickel is covered by antimony (39,40). Nickel (II) antimonates formation was later suggested also by Woltermann and Magee (54).

Polycrystalline Ni-Sb alloys, unsupported Sb-loaded Ni powders, artificially contaminated as well as equilibrium FCC (from a heavy oil cracker) have been studied using X-ray diffraction (XRD), Auger spectroscopy and x-ray photoelectron spectroscopy (XPS) by workers at Phillips in what was one of the first examples of a multi-characterization technique approach to FCC study (39,40). XPS results have indicated that in an equilibrium FCC, 50 to 80% of the surface Sb and 30% to 50% of the surface Ni could be reduced to metal. This XPS data suggested that Ni and Sb were present on at least two different sites (that can be differentiated by their reducibility at 500°C/H₂) and that reduction caused a twofold increase in the Ni/Sb ratio due to greater Ni dispersion.

At the higher metal level (2.0-4.5% Ni with up to 2% Sb) used to study artificially contaminated materials, XRD results have shown the formation of Ni-Sb alloys (NiSb_x, x<0.08) whereas XPS data have indicated that a non-reducible antimony oxide, a well dispersed reducible Sb phase together with reducible Sb (that form an alloy with reducible Ni), were present. Selective chemisorption data for unsupported Ni-powders, showed that one surface structure can effectively passivate 2-3 Ni atoms with respect to H₂ chemisorption. XPS examination confirmed that Sb segregates at the surface of Ni particles where it can drastically affect the electron properties of neighboring Ni atoms thus reducing their activity.

Transmission electron micrographs and XPS results have been used to show that a catalyst, with a high silica content in the matrix, prevents nickel dispersion (16,18). In fact, in a FCC with a Si-rich (Si/Al = 4.3) surface, XPS data has indicated that calcination and steaming cause nickel (and vanadium) migration to the cracking catalyst surface where nickel sinters. As a result, nickel crystallites 50

to 70Å in size have been observed by transmission electron microscopy (TEM), Figure 4. The SiO₂-rich matrix prevents good Ni distribution on the surface; large Ni crystallites and inert NiSiO₃ formation are believed responsible for the catalyst's low carbon and hydrogen generation during gas oil cracking at MAT conditions (16,18). XRD, scanning transmission electron microscopy (STEM), and x-ray fluorescence have also been used to observe nickel crystallites formation on a catalyst surface (55). Formation of these type of silicates on amorphous supports have also been proposed by Meisenheimer (8).

XPS has been used also to show that Ni may be present as Ni⁺² or as Ni⁺³ on the surface of regenerated FCC (56). Initially, Ni was found to be homogeneously distributed on the catalyst surface; then as Ni levels increased above 2%, surface enrichment of Ni occurred (56). Ni migration can be correlated with the luminescence quenching of the rare-earths (RE) containing Y-zeolite (REY) present in the FCC matrix (16). Steaming induced Ni migration from the luminescence centers (REY crystals) and partial restoration of band intensity was observed (16). XPS and TEM data have indicated that Ni can move to the catalyst surface were sintering occurs, see Figure 4. Nickel distribution has also been investigated using secondary ion mass spectrometry (SIMS) (12). Nickel and vanadium effects can be additive (56,57).

Vanadium-Containing Cracking Catalysts

Vanadium is present in crudes mainly in the +4 state (58). In fact, up to 50% of the total vanadium in crude oil can be found as VO²⁺ in organometallic compounds such as porphyrins and naphthenates (59-63). During the cracking reaction in a FCCU, these compounds deposit V (probably in the form of VO⁺² cations) on the catalyst surface. Then, after steam-stripping and catalyst regeneration, formation of V⁺⁵ surface phases occur. The effects of vanadium on FCC properties are more severe than any of the other metals present in petroleum feedstocks. In fact, vanadium causes an irreversible loss of cracking activity which is the result of a decrease in crystallinity, pore volume and surface area of the catalyst, Figure 5.

i. Characterization of V-Containing FCC. The ever increasing availability and application of modern spectroscopic techniques of catalyst characterization have provided invaluable guidance to the study of vanadium effects and interaction in cracking catalysts. Thermogravimetric (TGA) and differential thermal analysis (DTA) data have shown that vanadium naphthenates and porphyrins readily decompose exothermally under reactor (reduction) conditions. In air, vanadium compounds are less stable and fully decompose below 500°C forming V₂O₅. This oxide has also been observed in RE-free materials using luminescence (13), Laser Raman spectroscopy (28) and XPS (27) measurements.

SIMS (61,64,86), microscopy (65), XPS (56), electron microprobe techniques (14,66), electron paramagnetic resonance (EPR) (67) and luminescence experiments (68) have been successfully employed to probe and study V mobility and reactivity on a catalyst surface. TEM, STEM and energy dispersive X-ray emission (EDX) measurements have indicated that V interaction with REY-crystals induced vanadate clusters formation (65). Vanadium was also found capable of reacting with rare-earths outside the zeolite cavities to form LaVO₄

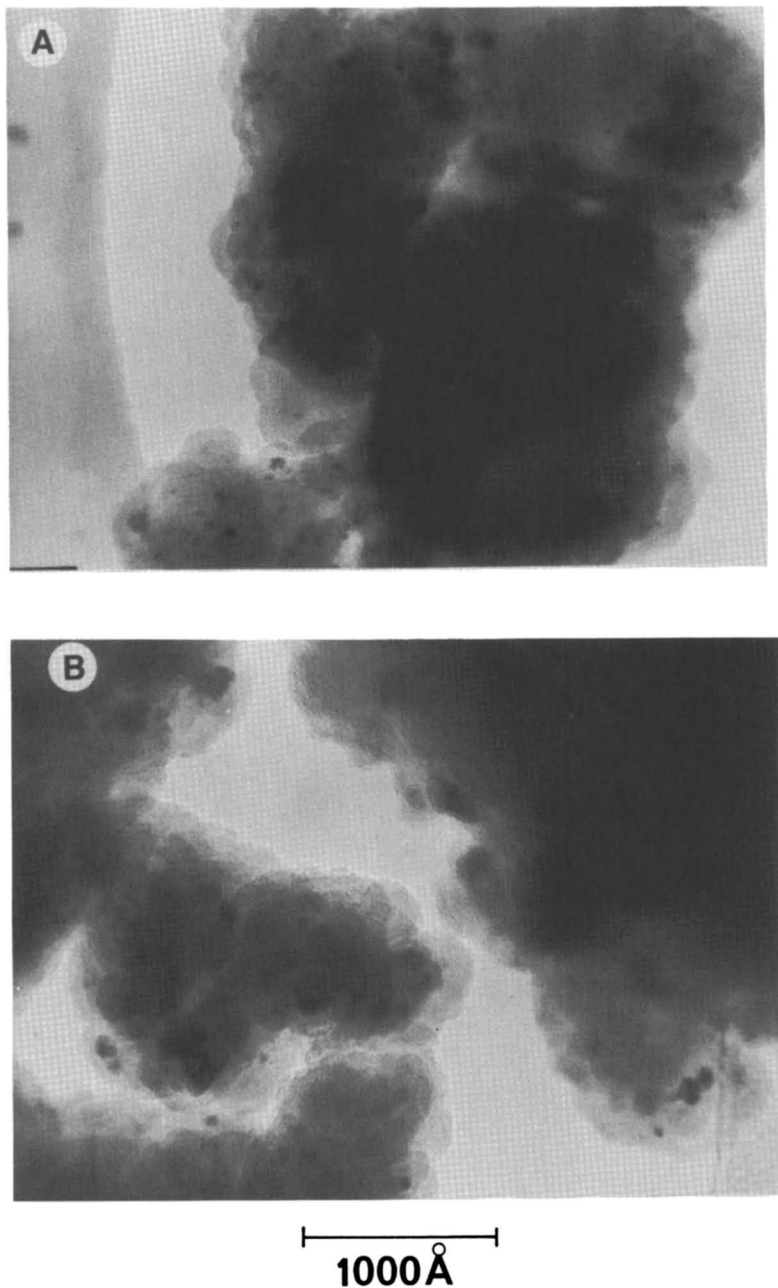


Figure 4. Transmission electron micrographs of 2% Ni on catalyst (A) before and (B) after steaming. Steam-aging has little effect on Ni distribution and crystallite size stays unchanged at 50-70Å .

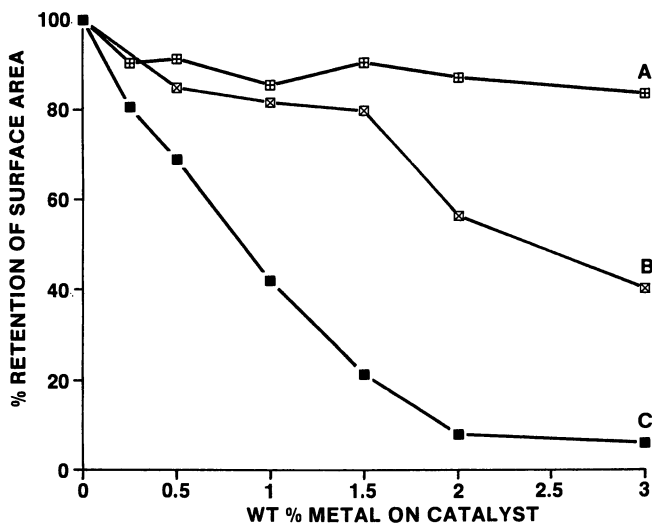


Figure 5. The effects of V levels on an FCC surface area after heating for 10 h at: A) 540 °C in air, B) 730 °C in air and C) 730 °C with 95% steam. Reprinted with permission from Ref. 13. (Copyright 1985 Academic Press)

(65). Radial electron diffraction patterns (65), XRD and Laser Raman spectroscopy (69) have confirmed the formation of REVO₄ type phases.

X-ray absorption spectroscopy has indicated that, after deposition, vanadium is in the +4 state and converts to the +5 state after regeneration (70). Similar conclusion has been reported from XPS measurements (56). Owing to the polar nature of vanadium porphyrin complexes, vanadium is initially deposited on the catalyst outer surface, where during regeneration in air, forms V₂O₅. Then vanadia, at regeneration condition, becomes a highly mobile fluid capable of migrating into the FCC macroporous structure where it interacts with and degrades zeolite crystallinity (56).

Analysis of vanadium-loaded model materials (such as EuY, amorphous aluminosilicate gels and EuY-gel mixtures) by electron paramagnetic resonance (EPR) has provided information concerning metal oxidation state and stereochemistry (67). EPR data has indicated that when vanadyl cations are introduced in the form of vanadyl naphthenate, they were stabilized in a zeolite with the faujasite structure as pseudo-octahedral VO²⁺ even after calcination at 540°C. Upon steaming, these VO²⁺ cations were then converted almost entirely to V⁺⁵ species (67). The formation of EuVO₄ was verified but the concentration of this vanadate was never proportional to the total rare-earth content of the zeolite. In EuY-gel mixtures the gel preferentially sorbed vanadium where it was stabilized mainly in the form of V₂O₅.

Luminescence experiments (68) have shown that vanadium after being preferentially sorbed by the gel, did not migrate during calcination but did migrate between the zeolite and the matrix during steaming. After heating in air at 575°C, vanadium was found to be in the form of VO²⁺ cations on the zeolite and primarily in the form of V₂O₅ on the gel matrix. The environment of Eu³⁺ cations is very sensitive to heat treatment; these cations can react with V during steaming to form EuVO₄ (68).

ii. Mechanisms of Vanadium-FCC Interactions. It has been proposed that V-REY interactions generate RE-V₂O₅ eutectics that, because of their low (630°C) melting points can flow (during regeneration) into the FCC macroscale where they can limit (or inhibit) the availability of the cracking centers to the diffusing hydrocarbons molecules (5,57,71). The formation of RE-V₂O₅ eutectics has been proposed also by other authors (61,62). However, Wormsbecker et al (14) have shown experimentally that by heating at 760°C in air V-loaded catalysts (containing less than 5%V) deactivation did not occur and disputed the importance of rare-earth eutectics formation during catalyst regeneration.

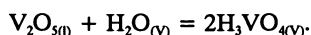
DTA/TGA studies have shown an endothermic melting point of pure V₂O₅, indicating a reaction between the zeolite and V₂O₅ before V₂O₅ liquefaction. (57,72) Analysis of the mixture by XRD has shown the formation of a tetragonal REVO₄ thought to be the product of a reaction between V₂O₅ and the rare-earth cations present in the zeolite. Pompe et al (72) further proposed that since vanadate formation requires more oxygen than V₂O₅ can supply, oxygens were removed from the zeolite lattice



during vanadate formation, causing the collapse of the crystal structure. Sodium in the system lowers the melting point of the REVO₄ eutectic, thus promoting the ease of zeolite destruction (72). This mechanism of REY collapse by V has been rejected by Mauge and co-workers (65).

Mauge et al (65) have proposed a mechanism of REVO₄ generation that did not require the removal of framework oxygen atoms since it involve a reaction between V₂O₅ and the La-(OH)-La linkages present in the zeolite sodalite cages (65). The presence of steam was not necessary for this reaction to occur; LaVO₄ was observed after calcination at 600 °C/air of V-loaded LaY crystals (65). Formation of LaVO₄ after calcination at 760°C/5h in air has been observed also by LRS (69).

Speronello and Reagan (26) have proposed that vanadium migrates along the catalyst matrix and then, during regeneration, reacts with the zeolite. Wormsbecher et al (14) have attributed vanadium mobility to vanadic acid formation during steam aging (87):



At the V-levels used, it was observed that only after steam-aging V contaminants were found capable to decrease zeolite crystallinity. Vanadic acid was believed capable of leaching Al from the zeolite framework in the form of AlVO₄, thus causing reduction in crystallinity and therefore cracking activity (14). However, experimental evidence for AlVO₄ formation could not be obtained by XRD, LRS (28,73,74) or by ⁵¹V NMR (75,76). This vanadate is not thermally stable at test conditions. In fact, the DTA profile of a reference (unsupported) AlVO₄ has indicated that this compound begins to decompose at about 650°C (74).

Losses in cracking activity in a FCCU can be minimized by prudent unit design. In fact, Hettinger (77) has reported that by maintaining a small amount of coke on regenerated FCC it is possible to minimize the oxidation of V contaminants to (mobile and reactive) V₂O₅ and keep most of the V as V₂O₄. Lower valence vanadium oxides melt at temperatures much higher than those encountered in a FCCU regenerator. The properties of these oxides are described below in Table 2 (88).

Table 2. Some physicochemical properties of vanadium oxides.

	<u>V₂O₅</u>	<u>VO₂</u>	<u>V₂O₃</u>	<u>VO</u>
Color	Orange	Blue	Gray-Black	Gray
Melting Point (°C)	658	1640	1970	950
Density (g/cc)	3.34	4.34	4.84	5.55
ΔH _f (kcal/mole)	373	342	296	117
structure	Trig. Bipy.	Rutile	Corundum	NaCl

Lower valences of V can also be obtained by exposing V-contaminated FCC to a reducing atmosphere. Vanadia can be reduced to V_2O_4 under relatively mild conditions ($\Delta G = -33.5$ kcal/mol); reduction of V_2O_4 to V_2O_3 is more difficult ($\Delta = -17.4$ kcal/mol).

Catalyst deactivation could also result from blockage of the zeolite and FCC microporous structure by the presence of Vanadia and debris generated by V-zeolite interactions (78). It has been claimed that, by removing these type of contaminants, part of the catalyst's original activity can be restored (78).

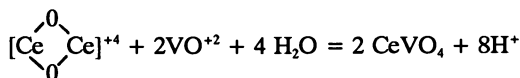
^{29}Si and ^{27}Al MASNMR spectroscopy has been used to show that on calcination, cracking components such as HY, Si-enriched HY, REHY and CREY, undergo dealumination and that steam aging increases the presence of extra framework Al in these zeolites; dealumination was more severe in HY type materials (73,74). Faujasite crystals (with or without RE-ions) are thermally stable at $760^\circ\text{C}/5\text{h}$ in air for V loading up to 4%. When the V on catalyst levels are raised to 5%, the crystal structure collapses indicating that, at this V concentration and temperature, the presence of steam is not required to promote zeolite destruction (73,74). However, when the same thermal treatment is repeated in the presence of steam (at 1 atm), the ease with which V destroys the zeolite crystallinity greatly increases; CREY crystals (containing a 3.5% Na_2O) collapse with only 0.4% V (73,74). The zeolite V-resistance seems to decrease when RE-ions are present and increases with increasing extra framework Al in the following order:



Extra framework Al in HY-type zeolites (generated during calcination and steaming) could directly react with VO^{+2} cations and form stable complexes thus increasing the crystal tolerance to V.

HY-type crystals as well as X-ray amorphous aluminosilicate gels (AAA alumina), form mullite ($\text{Al}_6\text{Si}_2\text{O}_{13}$) when heated at 1200°C in air. In the presence of V, these materials form mullite at lower temperatures (760°C) indicating that V acts as a mineralizing agent (69). In addition to mullite and tridymite, an X-ray amorphous V_2O_5 phase is formed. At the high temperatures used for FCC regeneration, oxyocations of vanadium (VO_2^+ or VO^{+2}) could attack the Al-O bond in HY causing dealumination and lattice collapse. The amorphous product re-crystallizes then into a vanadium-containing mullite phase and the excess silica and vanadium form tridymite and a supported V_2O_5 phase (69). In the presence of steam, hydroxy vanadyl ions and other protonated species resulting from the interaction of V compounds (such as V_2O_5) with steam, could accelerate Al-removal from the faujasite structure thus increasing the ease of mullite formation.

In REHY and in calcined rare earths exchanged Y-zeolites (CREY) containing about 7.6% Ce_2O_3 , 4.0% La_2O_3 , 2.8% Nd_2O_3 and 0.9 Pr_2O_3 crystals, it is believed that Ce^{+4} ions, present as an oxycerium complex, undergo a redox reaction with oxyvanadyl cations (VO^{+2}) and form a stable orthovanadate (74):



Vanadate formation (LaVO_4) occur also in LaY crystals (69). Removal of other charge compensating cations (such as Na^+ ions) in the form of vanadates further destabilize the crystal lattice thus promoting and enhancing zeolite destruction.

iii. Vanadium Passivation. Addition of antimony organics to cracking catalysts can drastically reduce the dehydrogenation activity of Ni contaminants. However, vanadium passivation has not been as successful, although tin has been reported capable of reducing the deleterious effects of V impurities (79-80). In fact, tin concentrations between 0.2 wt% and 2.50 wt% have been shown effective in preventing the breakdown of the zeolite structure (82).

The effects of Sn on V-contaminated model catalysts have been recently studied using luminescence experiments (68), EPR (67) and Mossbauer spectroscopy (83). Luminescence experiments have provided useful information on the environment of the rare-earth cations present in the zeolite and were used to monitor V-migration between the zeolite and the catalyst matrix even in the presence of Sn. Tin-119 Mossbauer spectroscopy has indicated that Sn-V interactions take place only during steam-aging forming $\text{Sn}^{4+}\text{-O-V}^{5+}$ complexes; V-Sn alloys were not observed (88). EPR data has shown that tin promotes the oxidation of VO^{+2} to V^{+5} during steam aging with formation of $\text{Sn}^{4+}\text{-O-V}^{+5}$ complexes. It is believed that these complexes inhibit V-zeolite interactions thus helping in preserving zeolite crystallinity and cracking activity when fluidized cracking catalysts are contaminated with V-compounds. The presence of excess tin seems to minimize oxidation to V^{+5} and promotes the formation of EuVO_4 ; thus excess tin is to be avoided (67). The deleterious effects of V on a FCC are best negated (at MAT conditions) by the use of V-scavengers.

Although vanadium mobility on a FCC surface has been recognized by several researchers, intraparticle transport of vanadium has been observed (at MAT conditions) only a few years ago (66). It has been reported in the patent literature that vanadium (and nickel) resistance in a FCC can be significantly enhanced by the addition of certain diluents capable of acting as metal scavengers (29-31). In fact, addition of alumina and alumina-containing materials with (30) or without (29) passivating agents (such as Sn or Sb) or addition of natural layered magnesium silicates as well as addition of certain natural zeolites (31) can inhibit the deleterious effects that metal contaminants (like Ni and V) in gas oils have on the cracking activity and selectivity of commercial fluid cracking catalysts. Specifically, sepiolite addition to a high activity commercial FCC, can generate dual-functional cracking catalyst (DFCC) mixtures that, even when metal contaminated with as much as 1.5 wt% vanadium, have been found capable of retaining useful cracking activity (70% conversion) when cracking a light gas oil (with an API gravity of 29.6) at microactivity test (MAT) conditions, see Figures 6,7. Improved coke and hydrogen selectivity were also observed.

Investigation of nickel and vanadium mobility under hydrothermal conditions has been studied by analyzing surfaces of the steamed materials by electron microprobe (66). Probe analysis of two DFCC containing 2% vanadium alternatively on the host catalyst and on the diluent (sepiolite or alumina particles) has indicated that heating in air at 540°C does not induce any significant migration of vanadium from particle to particle. However, when heating was performed in a fluidized bed in the presence of 100% steam, vanadium was found to migrate from the FCC to the

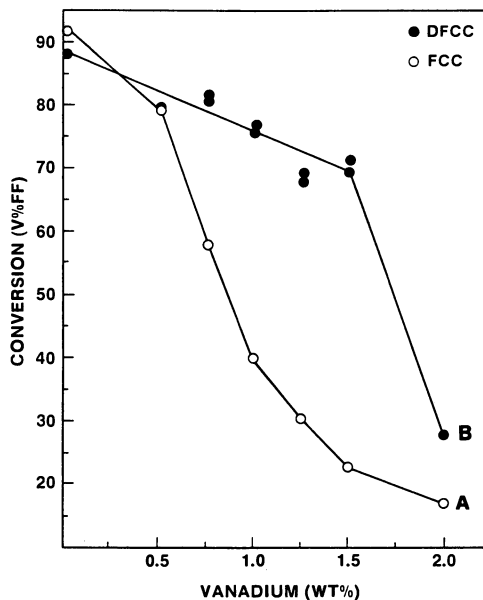


Figure 6. Retention of cracking activity in the presence of V before A) and after B) addition of Sepiolite. Reproduced with permission from Ref. 66. (Copyright 1989 American Chemical Society)

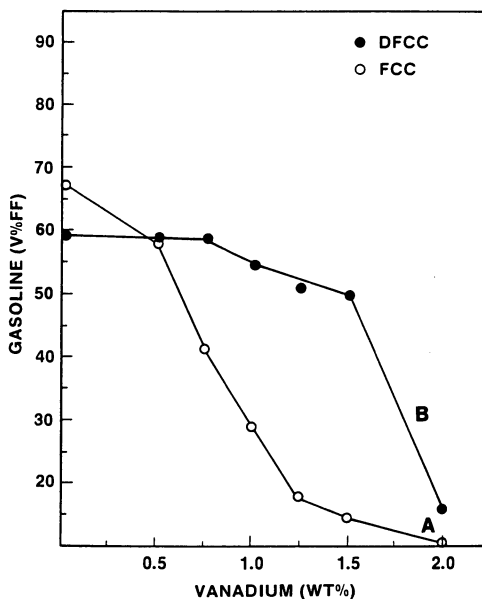


Figure 7. Retention of gasoline make in the presence of V before A) and after B) addition of Sepiolite. Reproduced with permission from Ref. 66. (Copyright 1989 American Chemical Society)

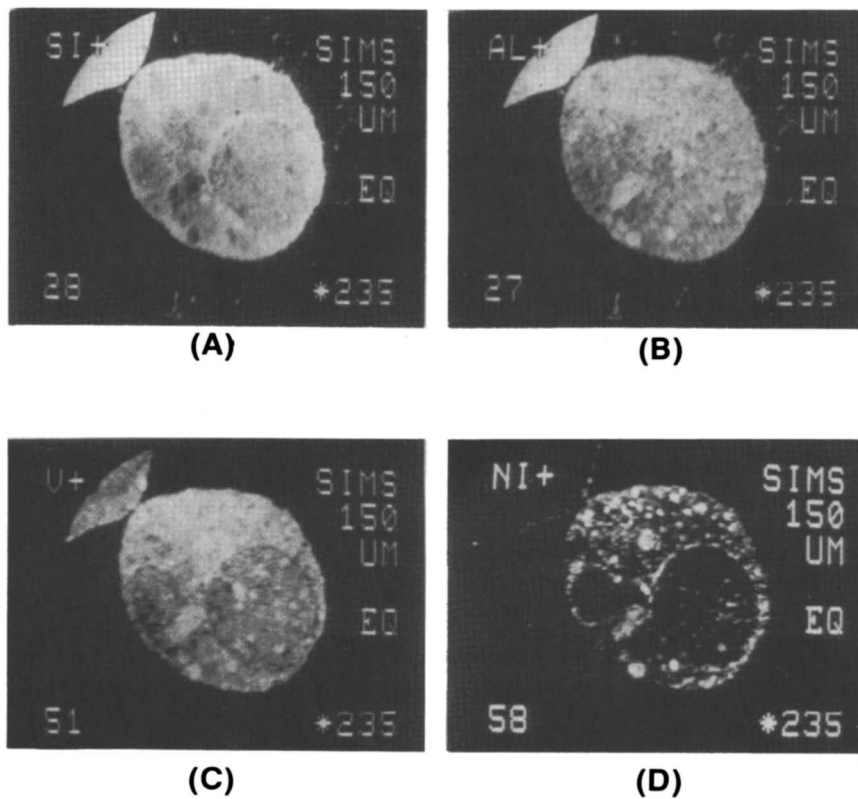


Figure 8. Cross sections of equilibrium FCC containing alumina particles. Ion images show A) silicon, B) aluminum, C) vanadium, and D) nickel. The aluminum and vanadium ion image are almost identical, thus showing V accumulation on alumina. Reproduced with permission from Ref. 86. (Copyright 1988 Academic Press)

sepiolite or alumina granules surface but not vice versa. Analysis of two nickel-containing DFCC revealed that neither heating in air or in steam induced intraparticle transfer of nickel at the thermal and hydrothermal conditions used to age the fresh catalysts (66) prior to microactivity testing.

LRS characterization of DFCC system tested at MAT conditions, have indicated that in steam aged catalysts containing more than 1% V, $[V_2O_7]$ units are formed lending support to the experimental work of Glemser and Muller (84) in which the reaction: $V_2O_{5(s)} + 2H_2O(g) = H_4V_2O_{7(g)}$ was reported. Thus it is believed that $H_4V_2O_7$ is one of the volatile V-compounds that can be generated in the steam-stripping zone of a FCC unit. Yannopoulos (87) has proposed that vanadia react with steam to form vanadic acid. Experimental evidence of H_3VO_4 formation in V-loaded FCC has not (to date) been presented.

Vanadium mobility has also been observed at pilot plant test conditions (85). Furthermore, Kugler and Leta (86) using data from imaging secondary ion mass spectrometry (SIMS) have observed recently that an equilibrium FCC containing alumina granules accumulates V preferentially on the alumina particulates thus supporting laboratory and pilot plant results (85) that have indicated that V-contaminated surfaces can react with steam and form volatile compounds capable of migrating from particle-to-particle, Figure 8. In summary, transport experiments at MAT conditions, together with pilot plant results (85) have indicated that the DFCC enhanced vanadium resistance can be attributed to the gas phase transport of this metal from the host catalyst to the diluent (sepiolite) where it is sorbed and passivated.

DFCC systems appear to have the necessary metals tolerance to process residual oils and the abundant, cheaper, but heavily vanadium-contaminated, Venezuelan and Mexican crudes (66). Therefore, the dual function fluid cracking catalyst (DFCC) concept could lead to the generation of important catalysts for U.S. refineries should Middle East politics cause another sudden escalation in crude oil prices and availability. The concept is practical and easily implementable and it may offer a cost advantage over conventional commercial cracking catalysts (66).

Acknowledgments

The skilled assistance received from Mr. B. McCormick in evaluating experimental cracking catalysts during the 1979-1985 period is gratefully acknowledged. Other aspects of catalysts characterization and testing was made possible by the support and cooperation received from Dr. S. L. Suib (University of Connecticut), Dr. J. M. Stencil (University of Kentucky), Dr. E. Goldish, and Dr. P. Ritz (Unocal). Special thanks are due to Dr. D. Leta (Exxon) for providing the micrographs shown in Figure 8. Finally, I would like to thank Ms. Seneti Kongaika for typing this manuscript.

Literature Cited

1. Mills, G. A., *Ing. Eng. Chem.* 42, 182 (1950).
2. Duffy, B. J. and Hart, W. M., *Chem. Eng. Prog.* 48, 344 (1952).
3. McEvoy, J. E., Milliken, T. H., Mills, G. A., *Ind. Eng. Chem.* 49, 865 (1957).
4. Rothrock, J. J., Birkhimer, E. R., and Leum, L. N., *Ind. Eng. Chem.* 49, 272 (1957).
5. Conner, J. E., Rothrock, J. J., Birkhimer, E. R., and Leum, L. N., *Ind. Eng. Chem.* 49 (2), 276 (1957).
6. Donaldson, R. E., Rice, T., and Murphy, J. R., *Ind. Eng. Chem.* 53 (9), 721 (1961).
7. Grane, H. R., Conner, J. E., and Masologites, G., P., *Pet. Ref.* 40 (5) 168 (1961).
8. Meisenheimer, R. G., *J. Catal.* 1,356 (1962).
9. Cimbalo, R. N., Foster, R. L., and Wachtel, S. J., *Oil Gas J.*, 112 (1972).
10. Magee, J. S., Ritter, R. E., and Rheume, L., *Hydrocarbon Process*, 123 (1979).
11. Ritter, R. E., Rheume, L., Welsh, W. A. and Magee, J. S., *Oil Gas J.*, 103 (1981).
12. Jaras, S., "Applied Catalysts," p. 207, Elsevier, Amsterdam, 1982.
13. Occelli, M. L., Psaras, D. and Suib, S. L., *J. Catal.*, 96, 363 (1985).
14. Wormsbecher, R. F., Peters, A. W. and Maselli, J. M., *J. Catal.* 100, 130 (1986).
15. Agrawal, B. B., and Gulati, F. B., *Pet. Hydrocarbons* 6, 193 (1972).
16. Occelli, M. L., Psaras, D., Suib, S. L., and Stencel, J. M., *App. Catal.*, 28, 143 (1986).
17. Plank, C. J., "Proceedings, 3rd International Congress on Catalysis, Amsterdam, 1964," p. 727. North-Holland, Amsterdam, 1965.
18. Occelli, M. L., Kowalczyk, D. C. and Kibby, C. L., *Appl. Catal.*, 16, 227 (1985).
19. Magee, J. S. and Blazek, J. J., ACS Monograph No. 171, Chapter 11 (1976).
20. Occelli, M. L. in "Fluid Catalytic Cracking: Role in Modern Refining." ACS Symposium Series Vol. No. 375; M. L. Occelli, Ed; p. 1, 1988.
21. *Chemical Week*, p. 20, June 24 (1987).
22. F. Ciapetta and D. Henderson, *Oil and Gas Journal*, 65, 88 (1967).
23. Yen, T. F. in "The Role of Trace Metals in Petroleum." Ann Arbor Science Publisher Inc., Ann Arbor, Michigan 1975.
24. Mitchell, B. R., *Ind. Eng. Chem. Prod. Res. Dev.* 19, 209 (1980).
25. Occelli, M. L., Psaras, D. and Suib, S. L., "Proc. Int. Symp. Zeolite Conf.," Siofok, Hungary, p. 423 (1985).
26. Speronello, B. K.; Reagan, W. J., *Oil & Gas J.*, Jan. 30, 1984.
27. Occelli, M. L. and Stencel, J. M., "Proc. 9th Int. Conf. Catal.," Phillips, M. J. and Ternan, M., Eds., Vol. 1, p. 214 (1988).
28. Occelli, M. L. and Stencel, J. M., in "Fluid Catalytic Cracking: Role in Modern Refining." ACS Symposium Series Vol. No. 375; M. L. Occelli Ed p. 195 (1988).
29. Occelli, M. L. and Kennedy, J. V., U.S. Patent No. 4, 465, 588 (1984).
30. Occelli, M. L. and Swift, H. E., U.S. Patent No. 4, 466, 884 (1984).
31. Occelli, G. B. Patent No. 2, 145, 345A (1985).
32. McKay, D. L., U.S. Patent No. 4, 153, 536, (1979).

33. Readal, T. C., McKinney, J. D. and Titmus, R. A., U.S. Patent No. 3, 977, 963 (1976).
34. Mitchell, B. R. and Swift, H. E., U.S. Patent No. 4, 101, 417 (1978).
35. Briel, R. F., U.S. Patent No. 2, 901, 419 (1959).
36. Bertus, B. J., and McKay, D. K., U.S. Patent No. 4, 377,494 (1983).
37. Mathy, E. V. and Helmers, C. J., U.S. Patent No. 2, 564, 268 (1951).
38. Dreiling, M. J., and Schaffer, A. M., *J. Catal.*, **56**, 130 (1979).
39. Parks, G. D., *Appl. Surf. Sci.*, **5**, 92 (1980).
40. Parks, G. D., Schaffer, A. M., Dreiling, M. J., and Shiblom, C. M., *ACS Div. Pet. Chem. Prepr.*, **25**, 334 (1980).
41. Dale, G. H., and McKay, D. L., *Hydrocarbon Processing*, **56**, 97 (1977).
42. Gray, E. H., Scharf, D. R., Dale, G. H., and Rush, J. B., A Presentation National ACS Meeting Atlanta, Symposia on Residua Upgrading (1981).
43. McKay, D. L., Schaffer, A. M. and Bertus, B. J., Paper presented at the Southwest Catalysis Society's Symposium.
44. Johnson, M. M. and Taber, D. C. in U.S. Patent No. 3, 711, 422 (1973).
45. McKay, D. L. and Bertus, B. J., *Preprints Div. Petro. Chem. ACS*, **24**, 645 (1978).
46. Ramamorthy, P., English, A. R., Kennedy, J. V., Jossens, L. W. and Krishna, A.S., NPRA Annual Meeting, March 20-22, San Antonio, TX, 1988.
47. Bohmer, R. W., McKay, D. L., and Knopp, K. G., NPRA Annual Meeting, paper No. AM89-51 (1989).
48. Yoo, J. S.; Karch, J. A.; Burk, e. H. Jr. *Ind. Eng. Chem. Prod. Res. Dev.*, **25**, 549 (1986).
49. Meyerson, A. S.; Ernst, W. B., U.S. Patent No. 4, 599, 313 (1985).
50. Castillo, C; Hayes, J. C., U.S. Patent No. 4, 361, 496 (1982).
51. Castillo, C; Hayes, J. C., U.S. Patent No. 4, 404, 090 (1983).
52. Sata, G.; Ogata, M.; Masuda, T.; Ida, T., *Eur. Patent No.* 176, 150 (1985).
53. McCarthy, W. C.; Hutson, T. Jr.; Mann, J. W. *Katalistiks 3rd FCC Symposium, Amsterdam* (1982).
54. Wolterman, G. M.; Magee, J. W., *Katalistiks 5th FCC Symposium, Vienna* (1984).
55. Davis, T. R.; Rase, H. F., *Ind. Eng. Chem. Fundam.* **25**, 581, 1986.
56. Anderson, S. L. T., Lundin, S. T., Jaras, S. and Otterstedt, J., *Applied Catalysis*, **9**, 317 (1984).
57. Upson, L. L.; Jaras, S. J.; Dalin, I., *Katalistiks 3rd FCC Symposium, Amsterdam, May 1982*.
58. Saveceno, A. J.; Fanale, D. T.; Coggeshal, N. D. *Anal. Chem.*, 1961, **33**, 500.
59. Skinner, D. A., *Ind. Eng. Chem.*, **44**, 1159, 1952.
60. Sundararaman, P. *Anal. Chem.*, **57**, 2204, 1985.
61. Jaras, S. *App. Catal.*, 1982, **2**, 207.
62. Jaras, S., First *Katalistiks FCC Symposium, Bordeaux, France, Oct. 1980*.
63. Fish, R. H.; Komlenic, J. J., *Anal. Chem.*, 1984, **56**, 510.
64. Upson, L.; Jaras, S.; Dalin, I. *Oil & Gas J.*, 1982, 135.
65. Mauge, F.; Courcelle, J. C.; Engelhard, Ph.; Gallezot, P.; Grosmaning, J. *Proceedings of the 7th Int. Zeolite Conf.*, Murakami, Y.; Iijima, A. & Word, J. W. eds (1986).
66. Ocelli M. L. in "Fluid Catalytic Cracking: Role in Modern Refining." ACS Symposium Series, Vol. 375: M. L. Ocelli, E., ACS, Washington, D.C., p. 162 (1989).

67. Anderson, M. W., Ocelli, M. L. and Suib, S. L., J. Catal., 112, 2, p. 375 (1990).
68. Anderson, M. W., S. L. Suib, and Ocelli, M. L., J. Catal., 118, 31 (1989).
69. Ocelli, M. L. in Advances in Catalytic Chemistry IV, Snowbird, Utah, October 1-7 (1989).
70. Woolery, G. L., Chin, A. A., Kirker, G. W. and Huss, A. M. in "Fluid Catalytic Cracking: Role in Modern Refining." ACS Symposium Series, Vol. 375: M. L. Ocelli, Ed., ACS, Washington, D.C., p. 215 (1989).
71. Murphy, J. R., Katalistiks 3rd FCC Symposium, Amsterdam, May 1982.
72. Pompe, R.; Jaras, S.; Vanneberg, N. -G. App. Catal. 1984, 13, 171.
73. Ocelli, M. L. and Stencel, J. M. in "Zeolites as Catalysts, Sorbents and Detergent Builders." H. G. Karge and J. Weitkamp Eds.; Elsevier, p. 127 (1989).
74. Ocelli, M. L. and Stencel, J. M. in "Zeolites, Facts, Figure, Future." P. A. Jacobs, R. A. Van Santen, Eds., Elsevier, Part B, p. 1311 (1989).
75. Eckert, H. and Wachs, I. E., J. Phys. Chem. 93 6796 (1989).
76. Iyer, P. S., Eckert, H., Ocelli, M. L. and Stencel, J. M. this volume.
77. Hettlinger, W. P. in "Fluid Catalytic Cracking: Role in Modern Refining." ACS Symposium Series, Vol. 375: M. L. Ocelli, Ed., ACS, Washington, D.C., p. 308 (1989).
78. Elvin, F. J., Oil & Gas J., Mar. 2, 42, 1987.
79. Roberts, J. S., Bertus, B. J., McKay, D. L., Mark, W. U.S. Patent No. 4, 397, 767 (1983).
80. Meyers, V. K., McKay, B. E. Jr., Busch, L. E. U.S. Patent No. 4, 464, 250 (1984).
81. Mitchell, B. R., Swift, H. E. U.S. Patent No. 4, 101, 417 (1978).
82. English, A. R., Kowalczyk, D. C. Oil and Gas J. 127, July 16, 1984.
83. Anderson, M. W., Ocelli, M. L. and Suib, S. L., J. Mol. Cat. (In press), 1990.
84. Glemser, O. and Muller, A., Z. Anorg. Allg. Chem. 325, 220 (1963).
85. Ocelli, M. L., Unpublished Gulf Research results (1982).
86. Kugler, E. L. and Leta, D. D., J. Catal. 109, 387 (1988).
87. Yannopoulos, L. N., J. Phys. Chem. 72, 9, 3293 (1968).
88. Clark, R. J. in "The Chemistry of Vanadium and Titanium." Elsevier (1968).

RECEIVED August 28, 1990

Author Index

- | | |
|--------------------------|--------------------------------|
| Beyerlein, R. A., 109 | Kurihara, L. K., 224 |
| Bohmer, Robert W., 183 | Lamberti, W. A., 269 |
| Cheng, W.-C., 198 | Leib, T. M., 144 |
| Corella, J., 165 | Leta, D. P., 269 |
| Corma, A., 12, 79,293 | Lunsford, Jack H., 1 |
| Desai, P. H., 318 | Marchal, C., 212 |
| Disko, M. M., 269 | Marshall, C. L., 109 |
| Dorémieux-Morin, C., 212 | McKay, Dwight L., 183 |
| Dwyer, J., 56 | Meyers, B. L., 109 |
| Eckert, H., 242 | Mifsud, A., 293 |
| Feng, Y., 27 | Miller, S. J., 96 |
| Fornés, V., 12,79,293 | Mocholf, F. A., 12,79 |
| Fraissard, J., 212 | Montón, J. B., 12 |
| Francés, E., 165 | Ocelli, M. L., 224,242,252,343 |
| Franco, M. J., 79 | O'Connor, P., 318 |
| Fyfe, C. A., 27 | Pappal, D. A., 45 |
| Gerritsen, L. A., 318 | Pérez-Pariente, J., 79,293 |
| Gevers, A. W., 318 | Rajagopalan, K., 198 |
| Grondy, H., 27 | Rawlence, D. J., 56 |
| Gruia, M., 212 | Rey, F., 12 |
| Hall, J. B., 109 | Sapre, A. V., 144 |
| Hsieh, C. R., 96 | Schipper, P. H., 45 |
| Huggins, B. J., 109 | Stencel, J. M., 242,252 |
| Humphries, A., 318 | Stripinis, Vida J., 308 |
| Iyer, P. S., 242 | Suib, S. L., 224 |
| Knopp, Kelly G., 183 | Tamborski, G. A., 109 |
| Kokotailo, G. T., 27 | Thoret, J., 212 |
| Kugler, E. L., 269 | Varady, W. A., 269 |

Affiliation Index

- | | |
|---|---|
| Akzo Chemicals, 318 | Universidad Politécnica de Valencia (Spain),
12,79,293 |
| Amoco Corporation, 109 | Université Pierre et Marie Curie, 212 |
| Chevron Research and Technology
Company, 96 | University of British Columbia, 27 |
| Crosfield Catalysts, 56 | University of California—Santa Barbara, 242 |
| Exxon Research and Engineering
Company, 269 | University of Connecticut—Storrs, 224 |
| Mobil Research and Development Corporation,
45,144 | University of Kentucky—Lexington, 242,252 |
| Phillips Petroleum Company, 183 | University of Manchester Institute of Science
and Technology, 56 |
| Shell Canada Limited, 308 | University of Zaragoza (Spain), 165 |
| Texas A&M University, 1 | Unocal Corporation, 224,242,252,343 |
| | W. R. Grace and Company—Conn., 198 |

Subject Index

A

- Activity, cracking 14,16–20
- Aluminum atoms, distribution of types in faujasites, 1,2*f*
- Aluminum-exchanged sepiolite as components of fluid catalysis cracking catalysts
acidity measurement procedure, 296
- Brønsted acidity vs. desorption temperature, 297,300,301*f*
- catalytic experimental procedure, 296,297*t*
- experimental materials, 295*t*
- gas-oil conversion vs. slurry oil, 302,306*f*
- gas-oil cracking, 300,302,303–306*f*
- gas-oil cracking conversion on ultrastable Y zeolite catalysts, 302,304*f*
- Lewis acidity, 300,301*f*
- natural Valdecas-type sepiolite, chemical composition, 295*t*
- pyridine adsorbed on derivatives
intensity of IR bands, 297,298*t*
- IR spectra, 297,299*f*
- vacuum-distilled gas oil, properties, 296,297*t*
- X-ray diffraction pattern
catalyst, 300,302,303*f*
- sepiolite forms, 302,303*f*
- yields of gasoline, diesel, gases, and coke, 302,305*f*
- Amorphous silica–alumina cracking catalysts, replacement with synthetic faujasites, 27
- Amorphous silica–alumina matrix
role in resid feed cracking, 198
- selectivity, 199–210
- Antimony metals passivation process
applications, 183,187
- development, 183

B

- β zeolites, effect on octane enhancement, 79–80

C

- Carbenium ion, isomerization, 105,106*f*
- Catalyst accessibility and architecture,
future development, 324–331

- Catalyst composition, effect on nickel tolerance in FCC, 348
- Catalyst deactivation
effect of Ni, 335,336*t*,337*f*,338
- resistance to poisons, 338,339*t*
- simulation methods, 109–110
- Catalyst density
carbon, effect on catalyst, 140
- estimation of contribution by factors, 139
- excluded volume, effect on change, 141–142
- factors contributing to change, 139–142
- incremental addition of heteroatom species, effect on change, 139–141
- metals, effect on catalyst, 140–141
- Catalyst pore architecture, 330,331*f*
- Catalyst selectivity and stability,
improvements, 339–340*t*
- Catalytic cracking, octane enhancement with high-silica zeolites, 96–108
- Cation mobility, synthetic faujasite, 31,34*f*
- Chemical extraction of Al, synthesis of dealuminated synthetic faujasites, 35
- Coke-conversion kinetics
effect of feedstock quality and oil partial pressure on coking, 147
- reaction(s), 146
- reaction rate per unit volume for gas-oil cracking, 147–148
- Coke-conversion selectivity,
definition, 149
- Commercial fluid cracking catalysts,
composition, 198
- Commercial metals passivation systems,
examples, 192
- Crackability, definition, 149
- Cracking activity
influencing factors, 14,16–20
- SAPO-37, 88,90,91*f*,92,93*f*
- Cracking selectivity, influencing factors, 20,21–24*f*
- Crude oil, 1980–1990 prices, 343,346*f*
- Cumene dealkylation, effect of framework Al concentration on activity, 3–4,5*f*
- Cyclic metal impregnation and deactivation, advantages for catalyst deactivation, 334,335*t*

D

- Dealuminated synthetic faujasite advantages, 31
- ^{27}Al magic angle spinning NMR spectra
 - highly dealuminated Y zeolite samples, 40,41f
 - hydrothermally treated samples, 35,37f,38
- hydroxyl group concentration determination, 40
- relationship of Si/Al ratio to unit cell dimension, 31,35
- ^{29}Si magic angle spinning NMR spectra
 - highly dealuminated Y zeolite samples, 40,41f
 - hydrothermally treated samples, 35,36f,38
- synthesis, 35–41
- Dealuminated Y zeolites, origin of strong acidity, 1–10
- Dealumination, effect on zeolite activity, 3
- Dealumination process, effect on Al distribution in framework, 3
- Dempsey–Mikovsky–Marshall model of acid strength, relationship of Al distribution in framework to acid strength, 1,3
- Density separation of precoked catalyst, description, 110–111
- Divalent exchange, synthetic faujasite, 29–33
- Durabead 5, replacement of amorphous silica–alumina cracking catalysts, 27
- Dynamic activity, definition, 149

E

- Effective mesoporosity, definition, 326
- Equilibrium catalyst separation, monitoring of FCC catalyst deactivation profile, 109–142
- Equilibrium cracking catalyst, density separation, 110–111
- Excluded volume, effect on charge-density change, 141–142
- Extensive zeolite crystallites, analytical electron microscopic investigation, 131,132–134f
- Extraframework aluminum
 - catalytic role during gas-oil cracking, 13
 - effect on superacid site formation, 13
 - elimination, effect on gas-oil cracking behavior, 13–20
 - method and conditions of formation, effect on catalytic role, 13
 - role in strong acidity of Y zeolites, evidence, 7,8f,9

F

- Faujasite, framework structure, 28,30f
- Feedstock quality, effect on metals passivation, 193,194t,195
- Fixed-bed microactivity tests
 - comparison of conversion for catalysts with that of fixed-fluid-bed reactor experiments, 144,145f,146
 - problems with conversion to riser reactor performance, 146
- Fixed-bed test, description, 97
- Fixed-fluid-bed reactor
 - estimates of model parameters, 162,163t
 - model, 148–149
 - operating conditions, 148,149t
- Fixed-fluid-bed reactor experiments
 - conversion for catalysts, comparison with that of fixed-bed microactivity tests, 144,145f,146
 - conversion to riser reactor performance, problems, 146
- Fluid catalytic cracking (FCC)
 - application, 224
 - modeling of riser reactor, 165–178
 - process, 224
- Fluid catalytic cracking catalyst(s)
 - aluminum-exchanged sepiolite as components, 295–306
 - factors affecting laboratory evaluation, 109–110
 - metal level trends, 344,345f
- Fluid catalytic cracking catalyst
 - deactivation profile monitoring by equilibrium catalyst separation activity profile for increasingly severe laboratory deactivations, 129,130f,131
 - analytical electron microscopic investigations of equilibrium catalyst fractions, 131–137
 - catalyst age, 112–113
 - catalyst history, 111–112t,113
 - coking of equilibrium catalyst procedure, 113
 - cumene cracking activity, 116,118t
 - deactivation profile, 128–129,130f,131
 - density of steam-deactivated vs. fresh catalyst, 121,123t
 - density variations for heaviest fractions, 127–128

- Fluid catalytic cracking catalyst
 deactivation profile monitoring by
 equilibrium catalyst separation—
Continued
 digisorb analyses of coked and
 regenerated equilibrium catalyst
 fractions, 114,117*t*
 distribution of catalyst fractions,
 114,115*f*,116
 equilibrium catalyst fraction
 properties, correlation with fraction
 density–age, 114–123
 excluded volume, effect on solvent
 accessibility, 123–128
 experimental procedure, 113–114,115*f*
 factors leading to density variation, 125
 feedstock contaminant metal material
 balance on catalyst, 111,112*t*
 fraction analytical procedure, 114
 gravimetric reactor used in cumene
 cracking studies, 114,115*f*
 laboratory steam deactivations,
 comparison, 128–129
 laboratory-steamed catalyst,
 comparison with equilibrium
 fractions, 121,122*t*
 metal content of catalyst, 111*t*
 metal deposition vs. catalyst age, 118–119,120*f*
 micropore structure vs. solvent
 accessibility, 123,124*f*,125
 properties of equilibrium catalyst
 fractions, 114,116*t*
 properties of fresh and steam-
 deactivated catalyst, 121–122*t*
 quantitative estimates of density
 variations, 125,126*t*,127
 rare earth material balance catalyst, 111,112*t*
 rate of dealumination compared with rate
 of zeolite destruction, 128
 separation method, 113–114
 surface area–micropore volume loss for
 equilibrium catalyst,
 117*t*,119,120*f*,121–122*t*
 testing of cumene cracking reactions on
 separated fractions, 114,115*f*
- Fluid catalytic cracking catalyst design,
 objective, 79
- Fluid catalytic cracking catalyst
 gasoline, effect of ZSM-5 zeolite
 addition, 56–77
- Fluid catalytic cracking catalyst metals
 passivation
 antimony
 effect of maintenance on optimization
 concentration, 190,194*f*
 effect of type on optimization, 190,192
 effect on CO combustion promoters and
 SO_x catalysts, 186–187
 passivation effects on charge rate,
 187,188*t*,189
 case studies, 187,188*t*
 catalyst V/Ni ratio effects on hydrogen
 generation, 189–190,191*f*
 commercial application, 186
 commercial systems, 192
 effect on environment, industrial
 hygiene, and metallurgy, 186
 effectiveness of elements for hydrogen
 yield reduction, 184,185*t*
 evaluation results for 75 vol %
 conversion, 184,185*f*
 future application and development, 192–193
 hydrogen reduction vs. metal levels,
 187,188*f*
 industry-wide acceptance, 187–191
 mechanism, 186
 modeling of effects, 193,194*t*,195
 optimization of benefits, 190,192
 research and development,
 184,185*t,f*,186
 technology transfer to commercial use,
 190,191*f*
- Fluidized-bed tests, description, 97
- G
- Gas-oil cracking
 effect of ZSM-5 zeolite, 58,59*t*,60
 superacid sites, effect in ultrastable
 Y zeolites, 13–20
- Gasoline cracking
 effect of Y zeolite, 60,62*t*,63,64*t*
 effect of ZSM-5 zeolite, 60,62*t*,63,64*t*
- H
- Hexadecane cracking, effect of total Al
 content, 39

- Hexagonal prism atom distribution, stereoscopic view, 31,32f
- Hexane cracking
effect of framework Al concentration on activity, 3
effect of framework Al content, 7,8f,9
- High-silica zeolites, octane enhancement in catalytic cracking, 96–108
- Hydrogen generation, effect of catalyst V/Ni ratio, 189–190,191f
- Hydrogen transfer index test
description, 97,100
procedure, 97
values for catalysts vs. linear hexane conversion, 100,102f
- Hydrothermal stability, SAPO-37, 82–89
- Hydrothermal treatment, synthesis of dealuminated synthetic faujasite, 35–41
- Hydroxyl groups in dealuminated synthetic faujasite, determination of total concentration, 40
- Hydroxyl IR bands of Y zeolites, effect of sodium, 4,6f,7
- H–Y zeolite, effect of dealumination on activity for acid-catalyzed reactions, 1
- I**
- Intimate mixture of crystalline and collapsed zeolite, analytical electron microscopic investigation, 131,135f,136,137f
- Isoolefins, effect of zeolite addition on reactions in gasoline, 63,70–73
- L**
- Laboratory steam deactivations, disadvantages for equilibrium catalyst simulation, 110
- Laser Raman spectroscopy, characterization of vanadium-contaminated components of FCC, 252–262
- Linde X zeolite
replacement of amorphous silica–alumina cracking catalysts, 27
synthesis, 28
- Linde Y zeolite, synthesis, 28
- Long residue, metals vs. Conradson carbon content, 308
- Long residue processing in riser pilot plant
atomizing nozzle performance, 310,312f
catalyst stripping, 315
commercial experience, 309,311f
FCC catalyst fluidization behavior, 313,314f
feed–catalyst mixing, 313,314f,315
feedstock atomization, 310,312f
feedstock vaporization, 310,313
operating conditions of plant, 310,312t
pilot plant experience, 309–310,311f,312t
problems with laboratory-scale processing, 309–310
product handling, 315–316
requirements, 316
schematic representation of plant, 310,311f
- Luminescence as probe of metal effects in fluid catalytic cracking catalysts
calcination, effect on vanadyl porphyrin spectra, 227,232f,238
catalyst preparation, 225
excitation wavelength, effect on vanadyl phthalocyanine, 233,235f,239
laser Raman spectra of steam-aged LaHY crystals, 227,229f,237
LaVO₄, spectra, 233,236f,239
luminescence lifetime data, 227,228f
LaY, 233t,240
Sn-passivated sample, 233,237t,240
luminescence procedure, 225
organic precursors used, 225,226f
single photon counting nanosecond fluorometer, schematic diagram, 227,228f
steam-aged LaHY crystals, X-ray diffractograms, 227,229f,237
steam-aged LaY crystals, spectra, 233,236f,239
tin addition
effect on vanadyl naphthenate spectra, 227,230f,238
effect on vanadyl phthalocyanine spectra, 233,235f,239
effect on vanadyl porphyrin spectra, 227,231f,238
tin-loaded LaY impregnated with vanadyl porphyrin, spectra, 227,233,234f,238

Luminescence as probe of metal effects in fluid catalytic cracking catalysts—

Continued

treatments

effect on vanadyl naphthenate spectra, 227,230f,237

effect on vanadyl phthalocyanine spectra, 233,234f,238–239

effect on vanadyl porphyrin spectra, 227,231f,238

wavelength, effect on vanadyl porphyrin spectra, 227,232f,238

M

Mesopore, impact of activity, 328t,330

Metal contaminants

effect on product distributions and yields, 344,347f

levels in petroleum, 344t

Metal effects in fluid catalytic cracking catalysts

avoidance techniques, 224–225

use of luminescence as probe, 225–240

Metal-resistant fluid catalytic cracking catalysts

developmental problems, 343–345

nickel-containing cracking catalyst, 344–351

vanadium-containing cracking catalysts, 350–359

Metals passivation

advantages, 183–184

development and application for FCC catalysts, 184–195

integration into overall refining

optimization models, 183

modeling effects, 193,194t,195

Methanol dehydration, effect of framework Al concentration on activity, 3

Microactivity fixed bed

estimates of model parameters, 162,163t

model, 150–151

operating conditions, 149t

Model for strong acidity

description, 9–10

validity, 10

Modified zeolites, advantages, 212

Molar expansion parameter, definition, 162

Motor octane increase using ZSM-5 in catalytic cracking

C₅ and C₆ olefin composition vs. catalyst, 49,51t

effect of ZSM-5 zeolite on gasoline composition, 53,54t

experimental procedure, 46,47–48t

FCC gasoline composition, 49,50t

iso/normal paraffin ratios for C₅–C₉ for catalysts with and without ZSM-5 zeolite, 53f

isoparaffin yields for C₅–C₉ for catalysts with and without ZSM-5 zeolite, 51,52f,53

octane yields at 70 vol % conversion, 46,48t,49

olefin yields for C₅–C₉ for catalysts with and without ZSM-5 zeolite, 51,52f

paraffin–olefin–N–catalyst A composition of gasolines at 70 vol % conversion, 49t

N

Na₂O, effect on framework dealumination, 39

Nickel, effect on catalyst deactivation, 335,336t,337f,338

Nickel-containing cracking catalyst characterization, 349–350,351f

effect of catalyst composition, 348

nickel passivation, 348–349

role of nickel, 344,347f

Nickel passivation, procedure, 348–349

NMR-invisible Al, characterization method, 39–40

Nonselective adsorption, effect on charge-density change, 142

Numerical method, description, 151

O

Octane enhancement

effect of SAPO-37, 79–94

effect of ZSM-5 zeolite addition to FCC catalysts, 56–77

Octane enhancement in catalytic cracking with high-silica zeolites additives
 effect on iso/normal paraffin composition, 100,101f
 effect on selected hydrocarbon types, 97,100t
 C₄ olefinicity vs. Si/Al ratio, 97,98–99f
 catalyst preparation, 96–97
 fixed-bed tests, 97
 fluidized-bed tests, 97
 hydrogen transfer index test, 97,100,102f
 isomerization of normal carbenium ion, 105,106f
 oligomerization of olefins, 105,107,108f
 pilot plant test, 103t,104f,105t,106f
 selectivity, 108
 selectivity to C₅ plus vs. Si/Al ratio, 97,98–99f

P

Petroleum, metal contaminant levels, 344t
 Petroleum cracking catalyst characterization via secondary ion MS imaging advantages, 269–270
 binary-phase masks of equilibrium V gas-oil catalyst images, 275,277f,278
 calculated curve and residual values for V vs. Ni^{1/3}, 285,287f
 calculated curve and residual values vs. Ni^{1/3}, zeolite concentration, and Si/Al ratio, 288,291f,292
 catalyst preparation, 270
 distributions from particle to particle, 281–292
 image processing, 271
 ion images of equilibrium resid-type catalyst particles, 279,280f
 ion images of equilibrium V gas-oil catalyst particles, 275,276f
 low-magnification ion images of equilibrium catalyst particles sampled 4 weeks into catalyst-type change, 281,282f
 multiparticle analysis
 qualitative, 281,282f
 quantitative, 281,283–292
 nickel and vanadium distribution between phases, 273–280
 phase distributions for vanadium and nickel vs. catalyst, 278t,279

Petroleum cracking catalyst characterization via secondary ion MS imaging—
Continued
 Si/Al ratio images, 271,272f,273
 signal formation in SIMS, mechanism, 274
 SIMS instrumentation, 270–271
 V vs. Ni concentration 4 weeks into catalyst-type change, 283,284f,285
 V vs. Ni concentration 8 weeks into catalyst-type change, 285,286f
 V vs. Si/Al ratios, 288,290f
 V vs. zeolite concentrations, 288,289f
 Pilot plant test
 gasoline composition vs. additive, 105t
 incremental measured octane differences, 103,104f
 incremental octane yield differences, 103,104f
 product inspections, 103t
 relative carbon number yields vs. base case, 105,106f

Poisoning studies of Y zeolites
 effect of sodium on hexane cracking, 4,5f
 mechanisms for effectiveness, 4

Pore-size acidity
 distribution, 326,328t,329f
 selectivity, 328,331f

R

Rare earth form of Y zeolite, replacement of amorphous silica–alumina cracking catalysts, 27–28
 Refining industry, resid upgrading, 318–319
 Resid catalyst development, future catalyst resistance to deactivation metals, 330,332–338
 poisons, 338,339t
 catalyst role in resid FCC, 321,323t,324,325t
 catalyst selectivity and stability, 339–340t
 concepts for the future, 318–341
 diffusion and active site accessibility, 324,325–326t,327f
 future challenges, 340,341t
 mesoporosity concept, effective, 326,327f
 nickel, effect on catalyst deactivation, 335,336t,337f,338

- Resid catalyst development, future—*Continued*
 pore-size acidity distribution, 326,328–331
 processability of resids in FCC units,
 320–321,322*f*
 resid processing, 319,320*t*
 resid upgrading in refining industry, 318–319
 vanadium effects, reduction strategies,
 330,332*t*,333*f*,334–335*t*
- Resid cracking
 definition, 319
 description, 319,320*t*
 model, 328,329*f*
 stages, 326,328
- Resid fluid catalytic cracking, improvements in
 catalyst role, 321,323*t*,324,325*t*
- Resids in fluid catalytic cracking catalyst units,
 processability, 320–321,322*f*
- Riser pilot plant
 advantages, 308
 long residue processing, 308–316
- Riser pilot plant composition analyses of
 motor octanes
 C₅ and C₆ olefin composition vs.
 catalyst, 49,51*t*
 catalyst properties, 46,47*t*
 catalyst steaming conditions, 46,47*t*
 experimental procedure, 46,47–48*t*
 FCC gasoline composition, 49,50*t*
 feedstock properties, 46,48*t*
 iso/normal paraffin ratios for C₅–C₉ for
 catalysts with and without ZSM-5
 zeolite, 53*f*
 isoparaffin yields for C₅–C₉ for
 catalysts with and without ZSM-5
 zeolite, 51,52*f*,53
 octane yields at 70 vol % conversion,
 46,48*t*,49
 olefin yields for C₅–C₉ for catalysts
 with and without ZSM-5 zeolite, 51,52*f*
 paraffin–olefin–N–catalyst A composition
 of gasolines at 70 vol % conversion, 49*t*
 ZSM-5 zeolite, effect on gasoline
 composition, 53,54*t*
- Riser reactor(s)
 estimates of model parameters, 162–163
 model, 151
 operating conditions, 149*t*
- Riser reactor of fluid catalytic cracking unit
 assumptions of model, 167–168
 calculation of product distribution, 172
- Riser reactor of fluid catalytic cracking unit—
Continued
 data input to program or model, 177
 deactivation kinetics, 172
 description, 165
 five-lump model, 168,170
 flow rate
 in riser inlet, 172
 vs. riser height, 169,170*f*
 mean molecular weight of feedstock, 169,171
 model(s)
 examples, 177–178,180*t*,*f*
 output, 178,180*t*
 previous models, 166–167
 modeling, 173–174,175*f*
 nomenclature, 174,175*f*
 operating conditions, 165–166
 procedure, 174,176–177
 product distribution at exit, 177
 residence time of catalyst in riser, 171
 temperature along riser height, 171
 total pressure, effect, 178,180*f*
 volumetric flow rate, 169
 weight fraction of feedstock at inlet, 173
- S
- SAPO-37
 activation temperature, effect on
 crystallinity, 88,89*f*
 chemical composition, 81*t*
 cracking activity, 88,90–93
 experimental procedure, 81*t*,82
 hydrothermal stability, 82–89
 IR spectra
 sample treated at several conditions,
 85,86–87*f*,88
 sample treated in vacuum at
 increasing temperatures, 83,84*f*,85
 selectivity, 92,93*f*
 silicon concentration, effect on
 cracking activity, 88,90,91*f*
 synthesis, 80–81
 thermal stability, 82–89
- Secondary ion MS (SIMS) imaging, petroleum
 cracking catalyst characterization,
 269–292
- Selective sorption, effect on charge-density
 change, 142

- Selectivity, cracking 20,21–24f
- Selectivity of silica–alumina matrices
- activity and selectivity of hydrothermally pretreated catalysts, 208,209f
 - activity per unit surface area for gas-oil cracking, 205,206f
- ²⁷Al-NMR characterization of catalysts, 200,202f,204t
- composition and pretreatment
- effect on coke selectivity, 205,207f
 - effect on H₂ selectivity, 205,206f
- experimental materials, 199
- experimental procedure, 199–200
- light hydrocarbon selectivity of hydrothermally pretreated catalysts, 208,210f
- pretreatment time, effect on catalyst surface area, 200,201f
- product distribution vs. composition, 208,209–210f
- properties of catalysts, 199t
- properties of sour, imported heavy gas oil, 200t
- ²⁹Si-NMR characterization of catalysts, 200,203f,204
- XPS characterization, 200,204t
- Sepiolite
- applications, 293
 - description, 293
 - effect on vanadium-containing cracking catalysts, 356,357f,359
 - modification for use in FCC catalysts, 295–306
 - structure, 293,294f,295
- Silica–alumina matrix, amorphous, *See* Amorphous silica–alumina matrix
- Silicon, effect of amount of SAPO-37
- cracking activity, 88,90,91f
- Slip velocity, definition, 165
- Sodalite cage atom distribution, stereoscopic view, 31,33f
- Sodalite cage complex, stereoscopic view, 29,30f
- Sodium, effect on hydroxyl IR bands of Y zeolites, 4,6f,7
- Sodium poisoning, effect on hexane cracking of Y zeolites, 4,5f
- Solid–solid reaction between Y zeolite and vanadium pentoxide
- adsorption isotherms, 214,218f,219
 - electron paramagnetic resonance spectrum, 219,220f,221
- Solid–solid reaction between Y zeolite and vanadium pentoxide—*Continued*
- experimental materials, 213
 - experimental procedure, 213–214
 - ²⁹Si-NMR spectrum, 214
 - transmission electron microscopic results, 221
 - ¹²⁹Xe-NMR spectrum, 219
 - ¹²⁹Xe chemical shift vs. number of adsorbed Xe atoms, 219,220f
 - X-ray data, 214,216–217t
 - X-ray spectra vs. V/(Al + Si), 214,215f
- Solid-state NMR of quadrupolar nuclei, use in probing structure of metal oxide surface species on catalysts, 243
- Solid-state reactions between zeolites and salts
- analytical techniques, 212–213
 - examples, 212–213
- Strong acidity origin in dealuminated Y zeolites
- extraframework Al, role, 7,8f,9
 - framework Al concentration, effect, 3–4,5f
 - hydroxyl IR bands, 4,6f,7
 - model, 9–10
 - poisoning studies, 4,5f
- Superacid site effects on gas-oil cracking in ultrastable Y zeolites
- acidity measurements vs. degassing temperatures, 14,16t
 - cracking activity, 14,16–20
 - cracking selectivity, 20,21–24f
 - effect on cracking selectivity levels of conversion, 20,21f
 - (NH₄)₂SiF₆, 20,23f
 - unit cell size, 20,22f
 - zeolite, 20,24f
 - experimental procedure, 13–14
 - gas-oil cracking activity, 14,16,17f
 - n*-heptane cracking activity, 18,19f,20
 - physicochemical characteristics of samples, 14,15t
- Synthetic faujasite
- cation mobility, 31,34f
 - chemical extraction of Al, 35
 - divalent exchange, 29,31
 - hexagonal prism atom distribution, stereoscopic view, 31,32f
 - hydrothermal treatment, 35–41
 - replacement of amorphous silica–alumina cracking catalysts, 27–28

Synthetic faujasite—*Continued*

- site designations, 29
- sodalite cage atom distribution, stereoscopic view, 31,33*f*
- sodalite cage complex, stereoscopic view, 29,30*f*
- trivalent exchange, 29
- X-ray diffraction patterns, 31,34*f*

T

- Thermal stability, SAPO-37,82–89
- Translation of laboratory fluid catalytic cracking catalyst characterization tests to riser reactors
 - catalyst deactivation functions for RE Y zeolite and ultrastable Y zeolite catalysts, schematic representation, 155,156*f*
 - catalyst deactivation rate, impact on predicted conversions, 155,157*f*
 - heat of reaction, impact on conversions, 155,157*f*
 - model parameters, estimates, 162,163*t*
 - parametric studies, 153,154*t*
 - potential erroneous ranking of catalysts, 151,152*t*
 - predicted coke-conversion selectivity vs. catalyst activity
 - RE Y zeolite catalysts, 154,156*f*
 - ultrastable Y zeolite catalysts, 155,158,160*f*
 - predicted product selectivities vs. conversion, 159,160*f*
 - quantitative predictions, 152,153*t*
 - reaction network for gas-oil cracking, 158–159
 - RE Y zeolite catalysts, 154–155,156*f*
 - ultrastable Y zeolite catalysts, 155,156–157*f*,158,160*f*
- Trivalent exchange, synthetic faujasite, 29,30*f*,31

U

- Ultrastable Y zeolite
 - effect of superacid on gas-oil cracking, 13–20
 - formation techniques, 12–13
 - mechanism of octane enhancement, 31

V

- V₂O₅ · nH₂O gels, vibrational characteristics, 252–253
- Vacuum gas oil, characteristics, 81*t*,82
- Vanadium, strategies to reduce effects on FCC catalysts, 330,332*t*,333*f*,334–335*t*
- Vanadium-51 NMR characterization of vanadium-contaminated aluminas and aluminosilicate gels
 - γ-aluminas, 244,245*f*,246
 - aluminosilicate gels, 246,247*f*,248,249*f*
 - effect of nuclear electric quadrupole moment–electrostatic field gradient interaction, 244
 - experimental materials, 243–244
 - experimental procedure, 243
 - pseudoboehmite alumina, 244,245*f*,246,247*f*
 - pulse length, effect on spectra of aluminosilicate gels, 248,249*f*
 - sensitivity of spectra to hydration state aluminosilicate gels, 248,249*f*
 - pseudoboehmite, 246,247*f*
- Vanadium-containing cracking catalysts
 - alumina particles, effect, 358*f*,359
 - characterization, 350,353
 - sepiolite addition, effect, 356,357*f*,359
- V levels, effects on FCC surface area after heating, 350,352*f*
- V–FCC interactions, mechanisms, 353,354*t*,355–356
- vanadium passivation, 356,357–358*f*,359
- Vanadium-contaminated aluminas and aluminosilicate gels, vanadium-51 NMR characterization, 243–250
- Vanadium-contaminated components of fluid catalytic cracking catalyst characterization
 - ²⁷Al magic angle spinning NMR spectrum of parent aluminosilicate gel, 255,257*f*
 - aluminosilicate gel loaded with V, laser Raman spectra, 258,260*t*,261*f*,262
 - catalyst characterization procedure
 - Raman spectroscopy, 254
 - XPS measurements, 253–254
 - catalyst preparation, 253
 - effect of steaming on surface area, 255,256*t*
 - percent distribution of V⁵⁺ and V⁴⁺ after steaming, 262

- Vanadium-contaminated components of fluid catalytic cracking catalyst characterization—*Continued*
- percent distribution of V⁵⁺, V⁴⁺, and V³⁺ after reduction, 262,263*f*
- pseudoboehmite aluminas loaded with V, laser Raman spectra, 255–256,258*t*,259*f*
- reducibility in H₂ to V⁴⁺ and V³⁺, 262,264*f*,265
- steam-aged aluminosilicate gels loaded with V, X-ray diffractograms, 255,257*f*
- surface properties, 255,256*t*,257*f*
- surface V/Al and V/(Si + Al) ratios before and after reduction, 262,264*f*,265
- V-loaded aluminosilicate gels and aluminas, XPS, 262,263–264*f*,265
- Vanadium mobility
- definition, 332
- dependence on catalyst composition, 332*t*
- effect of accessibility, 334*t*
- influencing factors, 332,333*f*,334
- Vanadium naphthenate, effect on cracking activity, 242–243
- Vanadium on alumina and titania supports, trends, 248,250
- Vanadium oxides, physicochemical properties, 354*t*
- Vanadium pentoxide, solid-state reaction with Y zeolite, 213–221
- X**
- X-ray photoelectron spectroscopy (XPS), characterization of vanadium-contaminated components of FCC, 252–255,262–265
- Y**
- Y zeolite
- effect on cyclic structure reactions, 72,74–78
- effect on gasoline cracking, 60,62*t*,63,64*t*
- effect on isoolefin distribution, 63,68*f*
- effect on olefin reactions, 63,71*t*,72,73*f*
- effect on *n*-olefin distribution, 63,69*f*
- effect on total hydrocarbon distribution, 63,65*f*
- effect on total olefin distribution, 63,67*f*
- effect on total paraffin distribution, 63,66*f*
- experimental procedure, 57–58
- parent gasoline composition, 60,61*t*
- role, 57
- ZSM-20 zeolite
- effect on octane enhancement, 79–80
- framework structure, 28
- intergrowth occurrence, 28–29
- synthesis, 28
- Z**
- Zeolites, effect on reactions in gasoline
- cyclic structures, 72,74–77
- cycloolefins, 72,74*f*,75–77
- cycloparaffins, 72,75–77
- ZSM-2 zeolite
- framework structure, 28
- synthesis, 28
- ZSM-3 zeolite
- framework structure, 28
- synthesis, 28
- ZSM-5 zeolite
- applications, 45
- effect on octane enhancement in catalytic cracking, 96–108
- increase of motor octane, 46–54
- shape-selective behavior, 45–46
- use in catalytic cracking applications, 45
- ZSM-5 zeolite addition to fluid catalytic cracking catalysts
- description, 56
- effect on cyclic structure reactions, 72,74–78
- effect on gas-oil cracking, 58,59*t*,60
- effect on gasoline cracking, 60,62*t*,63,64*t*
- effect on isoolefin distribution, 63,68*f*
- effect on olefin reactions, 63,71*t*,72,73*f*
- effect on *n*-olefin distribution, 63,69*f*
- effect on total hydrocarbon distribution, 63,65*f*
- effect on total olefin distribution, 63,67*f*
- effect on total paraffin distribution, 63,66*f*
- experimental procedure, 57–58
- parent gasoline composition, 60,61*t*
- role, 57
- ZSM-20 zeolite
- effect on octane enhancement, 79–80
- framework structure, 28
- intergrowth occurrence, 28–29
- synthesis, 28